JOURNAL OF THE ELECTROCHEMICAL SOCIETY

LECTROCHEMICAL
CIENCE AND TECHNOLOGY

LID-STATE
ENCE AND TECHNOLOGY

VIEWS AND NEWS
Call for Papers
San Diego, California, Meeting



VOL. 133, NO. 2 FEBRUARY 1986

JESOAN 133 (2) 241-456, 41C-64C

FUTURE MEETINGS

BOSTON, MASSACHUSETTS—MAY 4-9, 1986—HEADQUARTERS AT SHERATON BOSTON HOTEL

Final program to be published in the March 1986 issue of **This Journal.**

SAN DIEGO, CALIFORNIA—OCTOBER 19-24, 1986—HEADQUARTERS AT THE TOWN AND COUNTRY HOTEL

See the detailed Call for Papers published in the December 1985-April 1986 issues of **This Journal.** Final program to be published in the August issue of **This Journal.**

PHILADELPHIA, PENNSYLVANIA—MAY 10-15, 1987—HEADQUARTERS AT ADAM'S MARK HOTEL

The detailed Call for papers will be published in the July-November 1986 issues of **This Journal.** Final program to be published in the March 1987 issue of **This Journal.**

Planned symposia for the Philadelphia Meeting include the following Divisions, Groups, Subcommittee, and subjects. **Battery**—General Session. **Corrosion**—General Session. **Dielectrics and Insulation**—Nonblodgett Monomolecular Films. **Electronics**—Large Diameter Crystal Growth; Smart Power and High Voltage Devices. **Electronics/Dielectrics and Insulation**—Contactless Testing; Contacts to Compound Semiconductors; First International Symposium on ULSI Science and Technology; High Current for Silicon Implantation; Joint General Session; Joint Recent News Papers Session; State-of-the-Art Program on Compound Semiconductors VI. **Electronics/Luminescence and Display Materials**—BICMOS and Other Mixed Processes. **Energy Technology**—General Session. **Energy Technology/Corrosion**—Electrochemistry of Coal Slurries. **Energy Technology/Industrial Electrolytic**—Applications of Fuel Cell Electrodes in Electrolytic Industries. **Energy Technology/Physical Electrochemistry/Electrodeposiiton/Corrosion**—Electrochemistry and Tribology. **Energy Technology/Physical Electrochemistry/Organic and Biological Electrochemistry**—Applications of Macromolecules in Energy Conversion. **High Temperature Materials**—Rapidly Solidified Materials. **High Temperature Materials/Corrosion/Dielectrics and Insulation/Physical Electrochemistry**—In Situ Nonelectrochemical Techniques for Study of Electrode Reactions. **High Temperature Materials/Dielectrics and Insulation**—Chemical Interactions in Ceramic Composites: Laser Induced Chemical Reactions. **High Temperature Materials/Physical Electrochemistry/Electronics/Dielectrics and Insulation**—Electrical Properties and Applications of Amorphous Materials. **Industrial Electrolytic**—General Session. **Organic and Biological Electrochemistry**—Heterogeneous Electron Transfer Kinetics; Synthetic Processes with Conducting Membranes; Transfer Processes in Membranes; General Session. **Physical Electrochemistry**—The Electrical Double Layer; Quantum Effects in Electrochemistry; General Session. **Physical Electrochemistry/Battery**—Nonaqueous Electrochemistry. **Physical Electrochemistry/Battery/Energy Technology**—Electrode Materials and Processes for Energy Conversion and Storage. **Physical Electrochemistry/New Technology Subcommittee**—Magnetic Effects in Electrochemistry. **New Technology Subcommittee**—Numerical and Analog Simulation of Heat Mass and Fluid Flows Applied to Process Technologies.

HONOLULU, HAWAII—OCTOBER 18-23, 1987—HEADQUARTERS AT HILTON HAWAIIAN VILLAGE

Cosponsored by The Electrochemical Society of Japan and with the cooperation of The Japan Society of Applied Physics.

The detailed Call for Papers will be published in the December 1986-April 1987 issue of **This Journal.** Final program to be published in the August 1987 issue of **This Journal.**

Planned symposia for the Honolulu Meeting include the following Divisions, Groups, and subjects. **Battery**—Lithium Batteries; Load Leveling; Manganese Dioxide; General Session. **Battery/High Temperature Materials/Corrosion**—High Temperature Fuel Cells. **Corrosion**—Corrosion and Catalysis of Metallic Glasses; Statistical Aspects of Corrosion Science and Engineering; General Session. **Corrosion/High Temperature Materials**—Corrosion in High Temperature Aqueous Solutions. **Corrosion/Physical Electrochemistry**—Stress Corrosion Cracking. **Dielectrics and Insulation**—Processing for Cryogenic Devices. **Dielectrics and Insulation/Electronics**—Dielectric Films for Compound Semiconductor Technology; Laser Assisted Processing; Polymeric Materials for IC's. **Dielectrics and Insulation/Luminescence and Display Materials/Electronics**— Patterning Science and Technology. **Electrodeposition**—Electroless Deposition; Surface Finishing for Electronics; General Session. **Electrodeposition/Corrosion**—Corrosion Resistance of Electrodeposited Metals. **Electronics**—Amorphous Semiconductors; Second International Symposium on Silicon Molecular Beam Epitaxy. **Electronics/Dielectrics and Insulation**—Automated IC Manufacturing III; State-of-the-Art Program on Compound Semiconductors VII; Joint General Session; Joint Recent News Papers Session. **Electronics/Dielectrics and Insulation/High Temperature Materials/Japan Society of Applied Physics**—Symposium on Special Materials. **Energy Technology**—Energy Storage Systems for Remote Applications; Mechanical Properties of Photovoltaic Device Structure. **Energy Technology/Dielectrics and Insulation/High Temperature Materials**—Materials and New Processing Technologies for Photovoltaics. **Energy Technology/Electronics/Dielectrics and Insulation**—Scale-Ups of Deposition Processing Apparatus for Photovoltaics. **Energy Technology/Industrial Electrolytic/Physical Electrochemistry**—Membrane Processes in Electrosynthesis. **Energy Technology/Organic and Biological Electrochemistry**—Biomass Electrochemistry. **Energy Technology/Physical Electrochemistry**—Electrosynthesis on Semiconductor Electrodes. **High Temperature Materials**—High Temperature Materials Chemistry IV. **High Temperature Materials/Dielectrics and Insulation**—Electro-Ceramics; Properties and Processing of Magnetic Thin Films. **High Temperature Materials/Dielectrics and Insulation/Electronics**—Tenth International Conference on Chemical Vapor Deposition. **Industrial Electrolytic**—Electrochemical Engineering; The Future of Chlor-Alkali Industry; Industrial Processes for the Production of Organic and Specialty Chemicals. **Industrial Electrolytic/Organic and Biological Electrochemistry**—Electro-Organic Chemistry as a Tool in Industrial Organic Synthesis. **Luminescence and Display Materials**—CRT Manufacture and New CRT Technologies; Electroluminescence; Optical Imaging's IR Light Sources, Detectors, and Imaging Techniques; Physics and Chemistry of CRT Phosphors; Science and Technology of Laser Materials; Rare Earth Phosphors: Spectroscopy and Technology; General Session; Recent News Papers Session. **Luminescence and Display Materials/Dielectrics and Insulation**—Materials and Fabrication Techniques for Storage Displays. **Organic and Biological Electrochemistry**—Redox Mechanisms and Interfacial Behavior of Molecules of Biological Importance; Recent Advances in Organic Electrosynthesis; General Session. **Physical Electrochemistry**—Modified Electrodes; Photoelectrochemistry; Research in Electrochemical and Spectroelectrochemical Chemistry; General Session. **Physical Electrochemistry/High Temperature Materials**—Sixth International Symposium on Molten Salts. **Joint Society Symposium**—Sensors.

THE ELECTROCHEMICAL SOCIETY BOOKS IN PRINT

Society Proceedings Series
1980-1985

The following softbound proceedings volumes are sponsored and published by The Electrochemical Society, Inc., 10 South Main Street, Pennington, NJ 08534-2896. Orders filled at the list price given, subject to availability. Enclose payment with order.

Electronic and Optical Properties of Polycrystalline or Impure Semiconductors and Novel Silicon Growth Methods. K. V. Ravi and B. O'Mara, Editors. A 1980 symposium. 280 pages, **$15.00.**

Electron and Ion Beam Science and Technology, Ninth International Conference. R. Bakish, Editor. A 1980 symposium. 672 pages, **$28.00.**

Lithium Nonaqueous Battery Electrochemistry. E. B. Yeager, B. Schumm, Jr., G. Blomgren, D. R. Blankenship, V. Leger, and J. Akridge, Editors. A 1980 workshop. 328 pages, **$18.00.**

Ion Exchange: Transport and Interfacial Properties. R. S. Yeo and R. P. Buck, Editors. A 1980 symposium. 396 pages, **$15.00.**

Materials and New Processing Technologies for Photovoltaics. J. A. Amick, E. Sirtl, P. Rai-Choudhury, and J. P. Dismukes, Editors. A 1980 symposium. 368 pages, **$14.00.**

Lithium Batteries, H. V. Venkatasetty, Editor. A 1980 symposium, 516 pages, **$26.00.**

Semiconductor Silicon 1981. H. R. Huff, R. J. Kriegler, and Y. Takeishi, Editors. A 1981 symposium. 1064 pages, **$25.00.**

Electrocrystallization. R. Weil and R. G. Barradas, Editors. A 1981 symposium. 352 pages, **$13.00.**

Corrosion and Corrosion Protection. R. P. Frankenthal and F. Mansfeld, Editors. A 1981 symposium. 304 pages, **$10.00**

Third International Symposium on Molten Salts. G. Mamantov, M. Blander, and G. P. Smith, Editors. A 1981 symposium, 600 pages, **$23.00.**

Second International Symposium on Molten Salts. J. Braunstein and J. R. Selman, Editors. A 1978 symposium. 420 pages, **$16.00**

High Temperature Materials Chemistry. D. D. Cubicciotti and D. I. Hildenbrand, Editors. A 1981 symposium. 498 pages, **$21.00.**

Electrocatalysis. W. E. O'Grady, P. N. Ross, Jr., and F. G. Will, Editors. A 1981 symposium. 428 pages, **$18.00.**

Photoelectrochemistry: Fundamental Processes and Measurement Techniques. W. L. Wallace, A. J. Nozik, S. K. Deb, and R. H. Wilson, Editors. A 1981 symposium. 736 pages, **$35.00**

The Nickel Electrode. R. G. Gunther and S. Gross, Editors. A 1981 symposium. 324 pages, **$15.00.**

Semiconductor Technology. D. A. Doane, D. B. Fraser, and D. W. Hess, Editors. A 1982 symposium. 264 pages, **$18.00.**

Plasma Processing. J. Dieleman, R. G. Frieser, and G. S. Mathad, Editors. A 1981 symposium. 528 pages, **$25.00.**

VLSI Science and Technology. C. J. Dell'Oca and W. M. Bullis, Editors. A 1982 symposium. 392 pages, **$20.00.**

Materials and New Processing Technologies for Photovoltaics. J. P. Dismukes, E. Sirtl, P. Choudhury, and L. P. Hunt, Editors. A 1982 symposium. 544 pages, **$25.00.**

Inorganic Resist Systems. D. A. Doane and A. Heller, Editors. A 1982 symposium. 320 pages, **$15.00.**

Transport Processes in Electrochemical Systems. R. S. Yeo, T. Katan, and D-T. Chin, Editors. A 1982 symposium. 288 pages, **$18.00.**

Corrosion in Batteries and Fuel Cells and Corrosion in Solar Energy Systems. C. J. Johnson and S. L. Pohlman, Editors. A 1981 symposium. 554 pages, **$22.00.**

Electron and Ion Beam Science and Technology, Tenth International Conference, R. Bakish, Editor. A 1982 symposium. 474 pages, **$30.00.**

Membranes and Ionic and Electronic Conducting Polymers. E. B. Yeager, B. Schumm, Jr., K. Mauritz, K. Abbey, D. Blankenship, and J. Akridge, Editors. A 1982 symposium. 380 pages, **$22.00.**

Aggregation Phenomena of Point Defects in Silicon. E. Sirtl and J. Goorissen, Editors. A 1982 symposium. 216 pages, **$15.00.**

Corrosion in Fossil Fuel Systems. I. G. Wright, Editor. A 1982 symposium. 522 pages, **$20.00.**

Electrochemical Process and Plant Design. R. C. Alkire, T. R. Beck, and R. D. Varjian, Editors. A 1982 symposium. 288 pages, **$20.00.**

High Temperature Materials Chemistry II. Z. A. Munir and D. Cubicciotti, Editors. A 1983 symposium. 480 pages, **$30.00.**

Silicon Nitride Thin Insulating Films. V. J. Kapoor and H. J. Stein, Editors. A 1983 symposium. 522 pages, **$25.00.**

Defects in Silicon. W. M. Bullis and L. C. Kimerling, Editors. A 1983 symposium. 660 pages, **$30.00.**

Plasma Processing. G. S. Mathad, G. C. Schwartz, and G. Smolinsky, Editors. A 1983 symposium. 660 pages, **$35.00.**

Materials and New Processing Technologies for Photovoltaics. J. A. Amick, V. K. Kapur, and J. Dietl, Editors. A 1983 symposium. 512 pages, **$25.00.**

Electroplating Engineering and Waste Recycle—New Developments and Trends. D. D. Snyder, U. Landau, and R. Sard, Editors. A 1982 symposium. 428 pages, **$22.00.**

III-V Opto-Electronics Epitaxy and Device Related Processes. V. G. Keramidas and S. Mahajan, Editors. A 1983 symposium. 289 pages, **$25.00.**

Lithium Batteries. A. N. Dey, Editor. A 1983 symposium. 460 pages, **$35.00.**

Fourth International Symposium on Molten Salts. M. Blander, D. S. Newman, M-L. Saboungi, G. Mamantov, and K. Johnson, Editors. A 1983 symposium. 776 pages, **$35.00.**

Fundamental Aspects of Corrosion Protection by Surface Modification. E. McCafferty, C. R. Clayton, and J. Oudar, Editors. A 1983 symposium. 364 pages, **$25.00.**

Advances in Battery Materials and Processes. J. McBreen, R. S. Yeo, D-T. Chin, and A. C. C. Tseung, Editors. A 1983 symposium. 320 pages, **$26.00.**

The Electrochemistry of Carbon. S. Sarangapani, J. R. Akridge, and B. Schumm, Editors. A 1983 symposium. 648 pages, **$32.00.**

Ninth International Conference on Chemical Vapor Deposition. McD. Robinson, C. H. J. van den Brekel, G. W. Cullen, J. M. Blocher, Jr., and P. Rai-Choudhury, Editors. A 1984 symposium. 824 pages, **$36.00.**

VLSI Science and Technology/1984. K. E. Bean and G. A. Rozgonyi, Editors. A 1984 symposium. 520 pages, **$30.00.**

Porous Electrodes: Theory and Practice. H. C. Maru, T. Katan, and M. G. Klein, Editors. A 1982 symposium. 492 pages, **$18.00.**

Equilibrium Diagrams; Localized Corrosion. R. P. Frankenthal and J. Kruger, Editors. A 1984 symposium. 611 pages, **$36.00.**

Electrochemistry in Mineral and Metal Processing. P. E. Richardson, S. Srinivasan, and R. Woods, Editors. A 1984 Symposium. 677 pages, **$30.00.**

Advances in the Chlor-Alkali and Chlorate Industry. M. M. Silver and E. M. Spore, Editors. A 1984 Symposium. 374 pages, **$18.00.**

The Chemistry and Physics of Electrocatalysis. J. D. E. McIntyre, M. J. Weaver, and E. B. Yeager, Editors. A 1983 symposium. 684 pages, **$27.00.**

Molten Carbonate Fuel Cell Technology. J. R. Selman and T. D. Claar, Editors. A 1982 Symposium. 533 pages, **$15.00.**

Advances in Lead-Acid Batteries. K. R. Bullock and D. Pavlov, Editors. A 1984 Symposium. 548 pages, **$28.00.**

Plasma Processing. G. S. Mathad, G. C. Schwartz, and G. Smolinsky, Editors. A 1984 symposium. 636 pages, **$40.00.**

High Temperature Lamp Chemistry. E. G. Zubler, Editor. A 1985 symposium. 340 pages, **$25.00.**

Computer Aided Acquisition and Analysis of Corrosion Data. M. W. Kendig, U. Bertocci, and J. E. Strutt, Editors. A 1984 symposium. 276 pages, **$17.00.**

Manganese Dioxide Electrode Theory and Practice for Electrochemical Applications. B. Schumm, Jr., R. L. Middaugh, M. P. Grotheer, and J. C. Hunter, Editors. A 1984 symposium. 696 pages, **$40.00.**

VLSI Science and Technology/1985. W. M. Bullis and S. Broydo, Editors. A 1985 symposium. 572 pages, **$35.00.**

Electromigration of Metals/Multilevel Metallization and Packaging. J. R. Lloyd, R. A. Levy, J. Pierce, and R. G. Frieser, Editors. A 1984 symposium. 201 pages, **$16.00.**

Silicon Molecular Beam Epitaxy. J. C. Bean, Editor. A 1985 symposium. 455 pages, **$36.00.**

The Chemistry and Physics of Composite Media. M. Tomkiewicz and P. N. Sen, Editors. A 1985 symposium. 373 pages, **$35.00.**

Materials and New Processing Technologies for Photovoltaics. V. K. Kapur, J. P. Dismukes, and S. Pizzini, Editors. A 1984 symposium. 432 pages, **$27.00.**

10/85

JOURNAL OF THE

EDITOR
Norman Hackerman
Jackie Bourne, Assistant to the Editor

DIVISIONAL AND GROUP EDITORS

BATTERY
R. J. Brodd
Elton J. Cairns
Eugene G. Gagnon
G. F. Nordblom
Darrel Untereker

CORROSION
J. W. Faust, Jr.
R. P. Frankenthal
H. S. Isaacs
Barry R. MacDougall
Florian Mansfeld
Ken Nobe
W. H. Smyrl

DIELECTRICS AND INSULATION
Robert S. Alwitt
Rudolf G. Frieser
Dennis Hess
Vikram J. Kapoor
S. P. Murarka
George L. Schnable
Alan W. Swanson

ELECTRODEPOSITION
Ugo Bertocci
Huk Y. Cheh
Y. Okinaka
Mordechay Schlesinger

ELECTRONICS
John M. Andrews
Ted F. Ciszek
George R. Cronin
James S. Harris
Subhash Mahajan
David L. Nelson
Bertram Schwartz
Thomas O. Sedgwick
Don W. Shaw
Ben Streetman
C. C. Wang
P. Wang
J. M. Woodall

ENERGY TECHNOLOGY GROUP
A. R. Landgrebe
S. Srinivasan
M. Tomkiewicz

HIGH TEMPERATURE MATERIALS
William A. Adams
E. D. Cater
J. V. Cathcart
Daniel Cubicciotti
Lee P. Hunt
Peter J. Meschter
Zuhair A. Munir
T. A. Ramanarayanan
David A. Shores
Donald R. Vissers
Gene F. Wakefield

INDUSTRIAL ELECTROLYTIC
Richard C. Alkire
Ronald L. Dotson
Scott Lynn

LUMINESCENCE AND DISPLAY MATERIALS GROUP
Harry G. Brittain
Henry F. Ivey
Simon Larach
Melvin Tecotzky

ORGANIC AND BIOLOGICAL ELECTROCHEMISTRY
Martin Blank
Glenn Dryhurst
John H. Wagenknecht
Stanley Wawzonek

PHYSICAL ELECTROCHEMISTRY
Gregory C. Farrington
David S. Ginley
Adam Heller
Nathan S. Lewis
Joseph T. Maloy
Gleb Mamantov
Barry Miller
William E. O'Grady
Robert A. Osteryoung
C. W. Tobias
Ronald H. Wilson

News Editor—Jack H. Westbrook

JOURNAL OF THE
ELECTROCHEMICAL SOCIETY
(USPS 284-140)
ISSN 0013-4651

The JOURNAL OF THE ELECTROCHEMICAL SOCIETY (USPS 284-140) is published monthly by The Electrochemical Society, Inc. at 215 Canal St., Manchester, NH 03108. The address for the Executive Offices, Editorial and Advertising Office, and Circulation Department of The Electrochemical Society, Inc., is 10 South Main St., Pennington, NJ 08534-2896. Subscription to members as part of membership service; subscription to nonmembers $195.00 plus $20.00 for postage outside U.S. and Canada. Single copies $8.00 to members, $18.00 to nonmembers. © Copyright 1986 by The Electrochemical Society, Inc. Second Class Postage paid at Pennington, New Jersey and at additional mailing offices.

POSTMASTER: Send address changes to THE ELECTROCHEMICAL SOCIETY, INC., 10 South Main St., Pennington, NJ 08534-2896.

February 1986

ELECTROCHEMICAL SCIENCE AND TECHNOLOGY

TECHNICAL PAPERS

Structural Properties of the PbO_2 Active Mass Determining Its Capacity and the "Breathing" of the Positive Plate during Cycling
D. Pavlov, E. Bashtavelova 241

Protection of n-Si Photoanode against Photocorrosion in Photoelectrochemical Cell for Water Electrolysis
R. C. Kainthla, B. Zelenay, J. O'M. Bockris 248

Corrosion Studies on Zinc in a Methanol/Water/Lithium Chloride/Oxygen System
J. Banás, K.-G. Schütze, E. Heitz 253

Cathodic Polarization Behavior of Ag-Al_2O_3 Electrode in Silver Thiocyanate Solution Containing Al_2O_3 Particles
Y. Suzuki, M. Wajima, O. Asai 259

***In Situ* ^{119}Sn Conversion Electron Mössbauer Study of the Surface of Tin Layers as Deposited by an Electroless Process**
H. M. van Noort, B. C. M. Meenderink, A. Molenaar 263

Photoelectrochemical Generation of Hydrogen at Electrochemically Deposited p-CdTe Films: Effect of Heat-Treatment, Surface Modification by Platinum and Surface Oxide Layer on Conversion Efficiency
M. Takahashi, K. Uosaki, H. Kita 266

The High Aqueous Solubility of K_2S and Its Effect on Bulk and Photoelectrochemical Characteristics of Cd(SeTE)/$S_x^=$ Cells. I. Polysulfide Variation at Constant Sulfur/Sulfide Ratio
S. Licht, J. Manassen, G. Hodes 272

The High Aqueous Solubility of K_2S and Its Effect on Bulk and Photoelectrochemical Characteristics of Cd(SeTe)/$S_x^=$ Cells II. Variation of Sulfur/Sulfide Ratio
S. Licht, J. Manassen 277

Electrolyte Loss and Performance Decay of Molten Carbonate Fuel Cells
C. D. Iacovangelo, E. C. Jerabek 280

Computer-Aided Simulation of Electrochemical Process Flowsheets by a Computer-Based Method
R. Alkire, R. La Roche, G. Cera, M. Stadtherr 290

Photocharge Transfer Mediation by Adsorbed Ions: Simulation of Photocurrent-Voltage Curves Based on Results of Photoluminescence Transient Measurements
M. Evenor, D. Huppert, S. Gottesfeld 296

Polymer Films on Electrodes. XIX. Electrochemical Behavior at Polypyrrole-Nafion and Polypyrrole Clay Thin Films on Glassy Carbon Electrodes.
F.-R. F. Fan, A. J. Bard 301

Effect of Counterions on the Formation of Ohmic Contact Between p-Si and Poly(pyrrole) Film. An AC Impedance Analysis
G. Nagasubramanian, S. DiStefano, J. Moacanin 305

Electronically Conductive Composite Polymer Membranes
R. M. Penner, C. R. Martin 310

ELECTROCHEMICAL SOCIETY

Vol. 133 • No. 2

Phase Diagrams and Conductivity Characterization of Some PEO-LiX Electrolytes
C. D. Robitaille, D. Fauteux 315

Aluminum Bromide-1-Methyl-3-Ethylimidazolium Bromide Ionic Liquids
I. Densities, Viscosities, Electrical Conductivities, and Phase Transitions
J. R. Sanders, E. H. Ward, C. L. Hussey 325

Electron Transfer at the WO_3-Electrolyte Interface under Controlled Mass Transfer Conditions
J. Desilvestro, M. Grätzel, T. Pajkossy 331

Electrochemical Behavior of Azide Ions on Platinum Electrodes
H. Miyama, Y. Nosaka, T. Fukushima 336

Time-Resolved Photocurrent of WSe_2 Photoanode Studied with a Nanosecond Pulse Laser
T. Sakata, E. Janata, W. Jaegermann, H. Tributsch 339

TECHNICAL NOTES

A Platinized Titanium Anode for Chromium Electroplating
F. Hine, K. Takayasu, N. Koyanagi 346

Deposition of Zinc Selenide Thin Films by Solution Growth Technique
P. Pramanik, S. Biswas 350

A 12% Efficient Photoelectrochemical Cell Based on Polycrystalline n-$CuInSe_2$ Electrodes
G. Razzini, L. P. Bicelli, B. Scrosati, L. Zanotti 351

Polythiophene/PolyTHF: A Multicomponent Electrically Conducting Polymer
M. A. Druy 353

Time-Dependent Degradation in Sodium-Beta″ Alumina Solid Electrolytes
D. C. Hitchcock, L. C. De Jonghe 355

Semiconductor Electrodes. LX. Photoelectrochemistry of p-ReS_2 and p-$ReSe_2$ in Aqueous Solutions
B. L. Wheeler, J. K. Leland, A. J. Bard 358

SOLID-STATE SCIENCE AND TECHNOLOGY

TECHNICAL PAPERS

Analysis of Corrosion on Aluminum Double-Layer Metallization
T. Wada, H. Higuchi, T. Ajiki 362

CVD Growth and Properties of "phoslon" Dielectric Films
P. C. Li, L. C. Hsia 366

The Effect of Bulk Traps on the InP Accumulation-Type MISFET
L. G. Meiners 372

Selective Growth of Polysilicon
Y. Furumura, F. Mieno, T. Nishizawa, M. Maeda 379

Deep Melting of Silicon Wafers
L. O. Wilson, G. K. Celler, L. E. Trimble 383

Sidewall Spacer Technology for MOS and Bipolar Devices
S. H. Dhong, E. J. Petrillo 389

ห้องสมุดกรมวิทยาศาสตร์บริการ

DIVISION AND GROUP OFFICERS

Battery Division
Sidney Gross, Chairman
Eugene Gagnon, Vice-Chairman
James McBreen, Secretary-Treasurer
Brookhaven National Laboratory
DAS Building 815
Upton, NY 11973
William H. Tiedemann, Division Advisor

Corrosion Division
Edward McCafferty, Chairman
Robert A. Rapp, Vice-Chairman
Ronald B. Diegle, Secretary-Treasurer
11515 Manitoba NE
Albuquerque, NM 87111
Glenn Dryhurst, Division Advisor

Dielectrics and Insulation Division
Laura Rothman, Chairman
Robert B. Comizzoli, Vice-Chairman
D. L. Flowers, Treasurer
J. P. Dismukes, Secretary
Exxon Research & Engineering Company
Clinton Township
Route 22 East
Annandale, NJ 08801
Werner Kern, Division Advisor

Electrodeposition Division
Mordechay Schlesinger, Chairman
David S. Lashmore, Vice-Chairman
Uziel Landau, Secretary-Treasurer
Department of Chemical Engineering
Case Western Reserve University
Cleveland, OH 44118
William H. Tiedemann, Division Advisor

Electronics Division
Patricia L. Castro, Chairman
W. Murray Bullis, Vice-Chairman (Semiconductors)
Howard R. Huff, Vice-Chairman (New Electronic Technologies)
Kenneth E. Bean, Treasurer
Stella W. Pang, Secretary
Massachusetts Institute of Technology
Lincoln Laboratory
244 Wood St.
Lexington, MA 02173
Werner Kern, Division Advisor

Energy Technology Group
V. K. Kapur, Chairman
H. Maru, Vice-Chairman
V. Jalan, Treasurer
D. S. Ginley, Secretary
Sandia National Laboratories
P.O. Box 5800
Albuquerque, NM 87185
Glenn Dryhurst, Group Advisor

High Temperature Materials Division
Wayne L. Worrell, Chairman
Zuhair A. Munir, Senior Vice-Chairman
Vishu D. Dosaj, Junior Vice-Chairman
David A. Shores, Secretary-Treasurer
Corrosion Research Center
151 Amundson Hall
421 Washington Ave. SE
Minneapolis, MN 55455
Werner Kern, Division Advisor

Industrial Electrolytic Division
Robert S. Karpiuk, Chairman
W. Bruce Darlington, Vice-Chairman
Marino Y. C. Woo, Secretary-Treasurer
930 Brown Road
Bridgewater, NJ 08807
William H. Tiedemann, Division Advisor

Luminescence and Display Materials Group
C. W. Struck, Chairman
R. O. Petersen, Vice-Chairman
W. M. Yim, Secretary-Treasurer
RCA Laboratories
David Sarnoff Research Center
Princeton, NJ 08540
Willaim H. Tiedemann, Group Advisor

Organic and Biological Electrochemistry Division
P. Zuman, Chairman
D. Evans, Vice-Chairman
G. Dryhurst, Secretary-Treasurer
Dept. of Chemistry
University of Oklahoma
620 Parrington Oval
Norman, OK 73019
Glenn Dryhurst, Division Advisor

Physical Electrochemistry Division
Larry R. Faulkner, Chairman
Barry Miller, Vice-Chairman
Rolf H. Muller, Secretary-Treasurer
30 High Gate Rd.
Berkeley, CA 94707
Glenn Dryhurst, Division Advisor

SOCIETY OFFICERS AND STAFF

Richard C. Alkire, President
Dept. of Chemical Engineering
University of Illinois
Urbana, IL 61801

Ronald E. Enstrom, Vice-President
RCA Laboratories
Princeton, NJ 08540

Fritz G. Will, Vice-President
General Electric Company
Research and Development Center
Schenectady, NY 12301

Bruce E. Deal, Vice-President
Fairchild Camera & Instrument Corporation
Palo Alto, CA 94304

James A. Amick, Secretary
Exxon Research & Engineering Company
Clinton Township
Route 22 East
Annandale, NJ 08801

Jerome Kruger, Treasurer
Department of Materials Science and Engineering
Johns Hopkins University
Baltimore, MD 21218

V. H. Branneky, Executive Secretary
The Electrochemical Society, Inc.
10 South Main Street
Pennington, NJ 08534-2896

Roque J. Calvo, Assistant Executive Secretary
The Electrochemical Society, Inc.
10 South Main Street
Pennington, NJ 08534-2896

PUBLICATION STAFF

Sarah A. Kilfoyle, **Director of Publications**
Andrew C. Litz
Anne McGovern
William G. Sheahan

PUBLICATION COMMITTEE

Robert P. Frankenthal, **Chairman**
James A. Amick
Norman Hackerman
Bertram Schwartz
Lee P. Hunt
Rolf H. Muller
Boone B. Owens
Klavs F. Jensen

Manuscripts submitted to the JOURNAL should be sent in triplicate to the Editorial Office at 10 South Main Street, Pennington, NJ 08534-2896. They should conform to the revised "Instructions to Authors" available from Society Headquarters. Manuscripts so submitted, as well as papers presented before a Society technical meeting, become the property of the Society and may not be published elsewhere in whole or in part without written permission of the Society. Address such requests to the Editor.

The Electrochemical Society does not maintain a supply of reprints of papers appearing in its JOURNAL. A photoprint copy of any particular paper may be obtained from University Microfilms, Inc., 300 N. Zeeb St., Ann Arbor, MI 48106.

Inquiries regarding positive microfilm copies of issues should be addressed to University Microfilms, Inc., 300 N. Zeeb St., Ann Arbor, MI 48106.

Walter J. Johnson, Inc., 355 Chestnut St., Norwood, NJ 07648, have reprint rights to out-of-print volumes of the JOURNAL, and also have available for sale back volumes and single issues with the exception of the last two calendar years.

The JOURNAL OF THE ELECTROCHEMICAL SOCIETY combines the JOURNAL and TRANSACTIONS OF THE ELECTROCHEMICAL SOCIETY. Statements and opinions given in articles and papers in the JOURNAL OF THE ELECTROCHEMICAL SOCIETY are those of the contributors, and The Electrochemical Society, Inc. assumes no responsibility for them.

Claims for a missing issue should be reported within 60 days of normal delivery date to the Circulation Dept., The Electrochemical Society, Inc., 10 South Main Street, Pennington, NJ 08534-2896.

Notice of a change in address should be sent to the Circulation Dept., The Electrochemical Society, Inc., 10 South Main Street, Pennington, NJ 08534-2896. Include the mailing label or the number from the mailing label from your previous issue of the JOURNAL to ensure proper identification.

SOLID-STATE SCIENCE (Cont.)

Analytical Model for Phosphorus Diffusion in Silicon
K. O. Jeppson, D. Anderson 397

Fabrication of Highly Reliable Tungsten Gate MOS VLSI's
N. Yamamoto, H. Kume, S. Iwata, K. Yagi, N. Kobayashi, N. Mori, H. Miyazaki 401

Characterization and Control of Silicon Surface Modification Produced by CCl_4 Reactive Ion Etching
A. Rohatgi, P. Rai-Choudhury, S. J. Fonash, P. Lester R. Singh, P. J. Caplan, E. H. Poindexter 408

Highly Sensitive Impurity Analysis of GaAs Using SIMS and Chemical Preparation
T. Tanaka, S. Kurosawa 416

Thermodynamics of the Silicon-Chlorine-Hydrogen System: Chemical Potential for Homogeneous Nucleation
K. D. Allen, H. H. Sawin 421

Thermochemical Stability of β- and β''-Alumina Electrolytes in Na/S Cells. I. The Activities of Na_2O, and Al_2O_3
N. S. Choudhury 425

Thermochemical Stability of β- and β''-Alumina Electrolytes in Na/S Cells. II. Assessment
N. S. Choudhury 429

Thermochemistry and Structure of Low Pressure Chemically Vapor Deposited and Bulk SiO_2-P_2O_5 and SiO_2-GeO_2 Glasses
M. Huffman, A. Navrotsky, F. S. Pintchovski 431

Releasing Material for the Growth of Shaped Silicon Crystals
Y. Maeda, T. Yokoyama, I. Hide, T. Matsuyama, K. Sawaya 440

TECHNICAL NOTES

Evaluations of Plasma Silicon-Oxide Film (P-SiO) by Infrared Absorption
A. Takamatsu, M. Shibata, M. Ishida, H. Sakai, T. Yoshimi 443

Thermal Oxidation of Undoped LPCVD Polycrystalline-Silicon Films
C. Y. Lu, N. S. Tsai 446

Rapid Isothermal Annealing of Sputtered Phosphorus-Doped Silicon Films
T. Serikawa, A. Okamoto 447

Temperature Response of GaAs in a Rapid Thermal Annealing System
T. R. Block, C. W. Farley, B. G. Streetman 450

ACCELERATED BRIEF COMMUNICATIONS

Potential Corrosion of Metals by Atmospheric Organic Acids
T. E. Graedel, C. McCrory-Joy, J. P. Franey 452

A Self-Contained Miniature Hydrogen Reference Electrode
F. G. Will 454

REVIEWS AND NEWS

NEWS 45C

Call for Papers—San Diego, California, Meeting 57C

JOURNAL OF THE ELECTROCHEMICAL SOCIETY

ELECTROCHEMICAL SCIENCE AND TECHNOLOGY

FEBRUARY 1986

Structural Properties of the PbO_2 Active Mass Determining Its Capacity and the "Breathing" of the Positive Plate during Cycling

D. Pavlov* and E. Bashtavelova

Central Laboratory of Electrochemical Power Sources, Bulgarian Academy of Sciences, 1040 Sofia, Bulgaria

ABSTRACT

By measuring the distribution of the volume and surface area of the pores in positive active masses (PAM's) having various structures, it was found that depending on their size the pores perform two functions: the macropores build up the transportation systems, along which the fluxes of ions taking part in the reaction flow, and the micropores, which provide the active surface, onto which the reactions occur. It was established that the plate capacity is determined by the volume of the transport pores and depends also on the surface area of the active mass. During discharge both the volume and the surface area of the pores decrease, while the plate thickness grows. This is related to the newly formed nonequilibrium $PbSO_4$ crystals, which generate internal stresses tending to expand the skeleton of the active mass. When discharged plates are kept for a longer period at the open-circuit potential, the $PbSO_4$ crystals recrystallize, this resulting in a contraction of the plate. During charge the active mass continues to shrink but the initial thickness of the plate cannot be restored in all cases. This "breathing" of the plate during discharge and charge becomes more and more pronounced as the number of cycles grow. This process is associated with the deterioration of the mechanical integrity of the skeleton structure. The "breathing" brings about an irreversible swelling of the active material, deterioration of the contacts between the PbO_2 agglomerates, and decay of the plate capacity. The advancement of this process results finally in the ultimate failure of the positive plate of the lead acid battery.

In a previous paper (1) a model was advanced for the organization of the structure of the positive active mass (PAM). It contains two levels: the first one is the microstructure and is built up of small PbO_2 crystallites in the form of grains, prisms, plates, and needles, organized in a porous agglomerate. The second level is the macrostructure or skeleton. The separate agglomerates, having various arrangements screwlike, spherical, or rock-like, are linked together in a macroporous skeleton, which mechanically supports the active material, conducts the electric current and represents the memory, where the method of the PAM preparation is recorded. The present paper is a continuation of our effort to develop a model of the structure of PAM. It is aimed at revealing the effect of the structure on the volume and surface area of the pores of the PAM, as well as the influence of the latter on the plates' capacity.

Previous investigations of PAM have been basically concerned in elucidating the phenomena determining the life of the battery. Thus Simon *et al.* (2) relate the decline of capacity with the formation of a coraloid structure, which does not at all or very slightly takes part in the current-generating process. Rand *et al.* (3) consider that the capacity loss is brought about by the formation of amorphous PbO_2, while Caulder *et al.* (4, 5) assign the plate failure to the formation of inactive PbO_2, assuming that the activity of PbO_2 is associated with the content of hydrogen in the crystal lattice of PbO_2. Hill (6) concludes, however, that there is not any relation beween the capacity and the content of hydrogen in the crystal lattice of PbO_2. In our paper (1) it was shown that the active material undergoes an evolution during cycling, whereby the macrostructure falls apart to separate crystallites or chains of crystallites. The contact between the latter deteriorates and the plate loses its capacity. It appears that the destruction of the structural organization of the PAM is the factor limiting its life. It is the second purpose of this paper to reveal the phenomena, which bring about this destruction.

*Electrochemical Society Active Member.

Experimental

Preparation of plates with various structure of the active mass.—The variations in structures of PAM were attained by preparation of pastes with different phase compositions. The latter were obtained by changing the ratio H_2SO_4/PbO and the temperature during the paste mixing. Table I presents the conditions for the preparation of the pastes used in the present study.

For each H_2SO_4/PbO ratio pastes with three different densities were prepared in the ranges shown in Table I. 5 kg of commercial leady oxide (63% PbO) with the necessary amounts of water and H_2SO_4 (d = 1.4) were loaded in a laboratory mixer and were agitated for 1h at a constant temperature. The paste was applied manually on SLI battery grids, cast from a lead alloy containing 6% Sb, 0.1% As, and 0.1% Sn. Regardless of the type of paste used, one

Table I. Conditions for the preparation of the pastes and their phase composition

H_2SO_4/PbO ratio (%)	Temperature of paste mixing (°C)	Range of densities (g/cm³)	Phase composition
1	30	4.30-5.0	tet-Pbo + small amounts of $3PbO \cdot PbSO_4 \cdot H_2O$
6	30	3.60-4.20	$3PbO \cdot PbSO_4 \cdot H_2O$ + small amounts of tet-PbO
6	80	3.70-4.70	$4PbO \cdot PbSO_4$ + small amounts of tet-PbO
12	30	4.00-4.80	$PbO \cdot PbSO_4$ + small amounts of $3PbO \cdot PbSO_4H_2O$ + tet-PbO

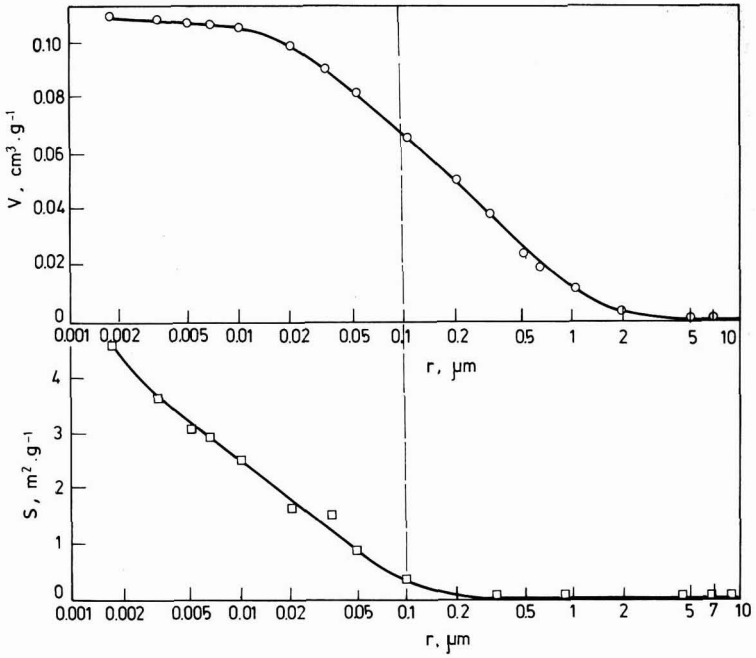


Fig. 1. Distribution of the volume and surface area of the pores of PAM formed from a 3PbO · $PbSO_4$ · H_2O paste. The pore radius of 0.1 μm is assumed as the limit between the micro-(agglomerate) and the macro-(transport) pores.

and the same amount was applied on the grids. The calculated rated capacity of the plate (C_N) was 11 Ah at 50% utilization of PAM. The plates were cured in a chamber, first at 30°C and 100% RH for 48h, and then at 40°C and 60% RH for 24h. The content of metallic lead in the paste after curing did not exceed 1%.

The plates were formed in cells assembled with 3 positive and 4 negative plates in H_2SO_4 (d = 1.05) at 5 mA/cm² and 30°C for 24h. They were then cycled for 5 or 30 cycles in H_2SO_4 (d = 1.28): charged for 7h and discharged for 5h at 2A. The cells were charged to a definite state of charge after which the pore volume, the surface area of PAM, and the capacity of the plates were determined.

The pore size and pore surface area distribution were determined by an Autopore 9200 Micrometrics (Georgia) mercury porosimeter. The surface area of PAM was measured by the BET method using a Strohlein (Düsseldorf, Germany) adsorbtion apparatus. The apparent density of the active mass was assessed by a mercury pycnometer. The plate capacity was determined at 4h rate discharge at a constant current i = 0.25 C_N Ah, until the final potential of + 600 mV *vs.* Hg/Hg_2SO_4 of the positive half-cell was reached.

Results and Discussion

Dependence of the volume and surface area of the pores on their radius.—Figure 1 depicts the pore volume (Fig. 1a) and the pore surface area (Fig. 1b) distribution *vs.* the pore radius of an active mass formed from a 3PbO · $PbSO_4$ · H_2O paste.

The integrated volume and the surface area of the pores grow with the decrease in the pore radius. The ranges of

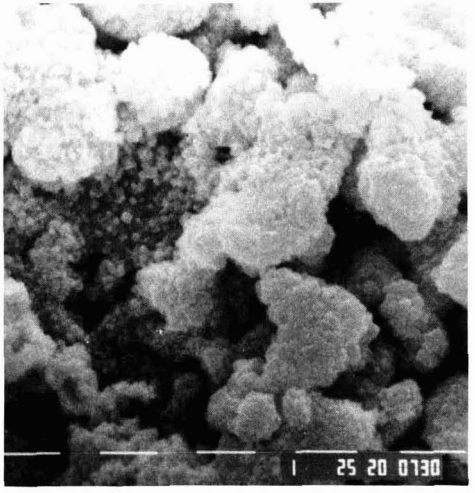


Fig. 2. SEM picture of the skeleton (macro) structure of a PAM prepared from a 3PbO · $PbSO_4$ · H_2O paste. White lines = 1 μm.

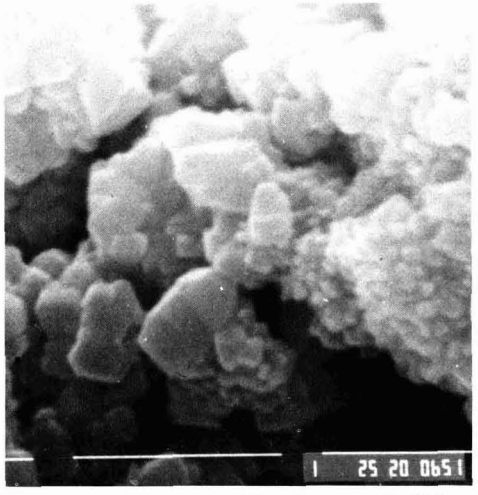


Fig. 3. SEM picture of the crystal (micro) structure of a PAM prepared from a 3PbO · $PbSO_4$ · H_2O paste. White lines = 1 μm.

the steep rise of these parameters are shifted with respect to each other. Thus, the pore volume begins to rise at 1 μm, while the surface area starts growing from 0.1 μm. At 0.1 μm the pore volume is 0.065 cm^3/g, which is *ca.* 62% of the total pore volume. At the same pore size the surface area is only 6% of the total surface area of the active material. This result demonstrates that at this pore size the pore volume is almost completely built up in the skeleton level of the structure. It can be asserted that these pores serve as main transport ducts for the flux of ions between the bulk solution and the agglomerates inside the plate, *i.e.*, that they build up the basic ionic transport system.

Figure 2 gives a SEM picture of the macrostructure of the same active material, where the transport pores are clearly visible.

The size of the transport pores evidently depends on the type and size of the agglomerates and the density of the PAM. As it was established the latter are determined by the phase composition and the crystal morphology in the paste (1).

According to the model for the structure of the PAM (1) each agglomerate contains a large number of separate PbO_2 crystallites, between which the micropores (agglomerate pores) are confined. The PbO_2 crystallites and the agglomerate pores build up the PAM microstructure. At this level the pores are smaller than 0.1 μm and they form the main part of the PAM surface area. They can be seen in the SEM picture in Fig. 3, made at a higher magnification than that in Fig. 2.

Figure 1 shows that the pore volume in the agglomerates is comparatively small. It will depend on the morphology of the PbO_2 crystallites (platelike, needle-like, grains, etc.).

The idea for this distinction of two types of pores according to their radius and the functions which they perform in the PAM was advanced in our earlier papers (1, 7). Recently Chang (8) also classified the pores into 2 classes, macropores larger than 0.5 μm, and micropores smaller than that. Figure 1 shows that as a limit between the agglomerate pores (micropores) and the transport pores (macropores) one can assume the pore radius, at which the pore surface area begins steeply to rise. It can be expected that this radius will depend on the type of the PAM structure.

Effect of the volume and surface area of the pores on the plate capacity.—Using the pastes described in Table I (with several densities of each type) we prepared plates, which after formation were subjected to 5 charge-discharge cycles. After this we determined the distribution of the pore volume of the charged plates, the BET surface area, and the plate capacity at a 4h rate.

Figure 4 presents the porograms and the pore surface area distribution of part of the active materials studied. The data for chemically prepared PbO_2 (Merck) are also given for comparison.

The following conclusions can be drawn from the data in this figure. When the PAM is obtained by the formation of basic lead-sulfate pastes, the pore volume grows gradually in a broad range of radii (0.005-1.2 μm). For the chemically obtained PbO_2 the total pore volume attains its limiting value in a very narrow range of radii. The steep rise in the surface area in the case of PAM prepared from pastes is observed when the pore radius drops be-

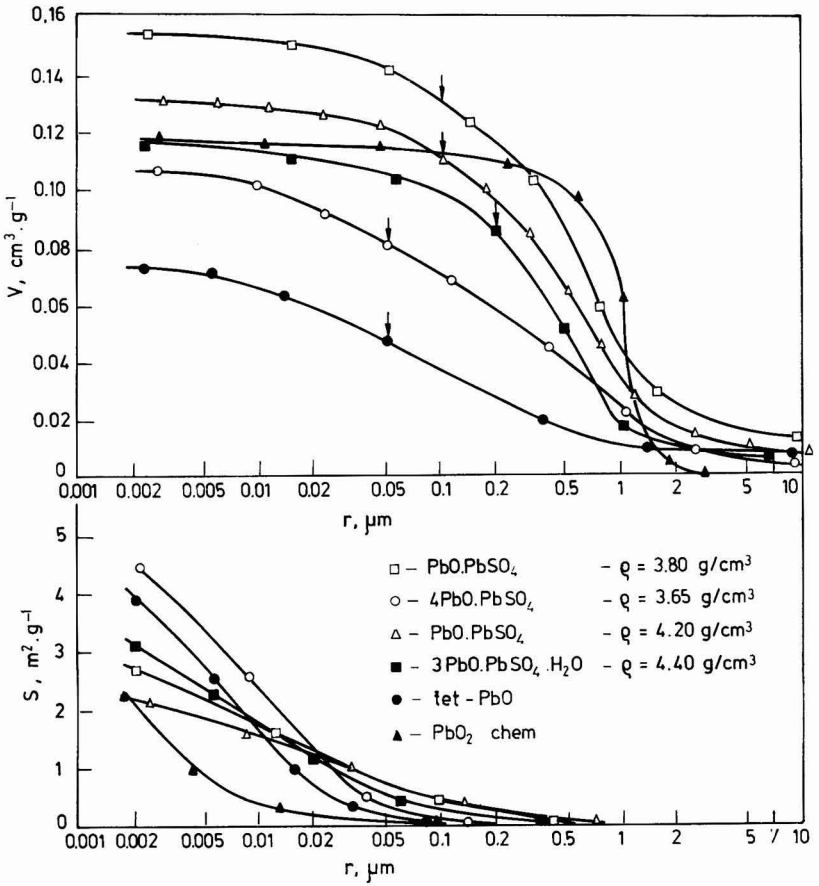


Fig. 4. Distribution of the volume and surface area of pores for PAM's formed from pastes with various phase compositions. The arrows mark the assumed limit between micro- and macropores.

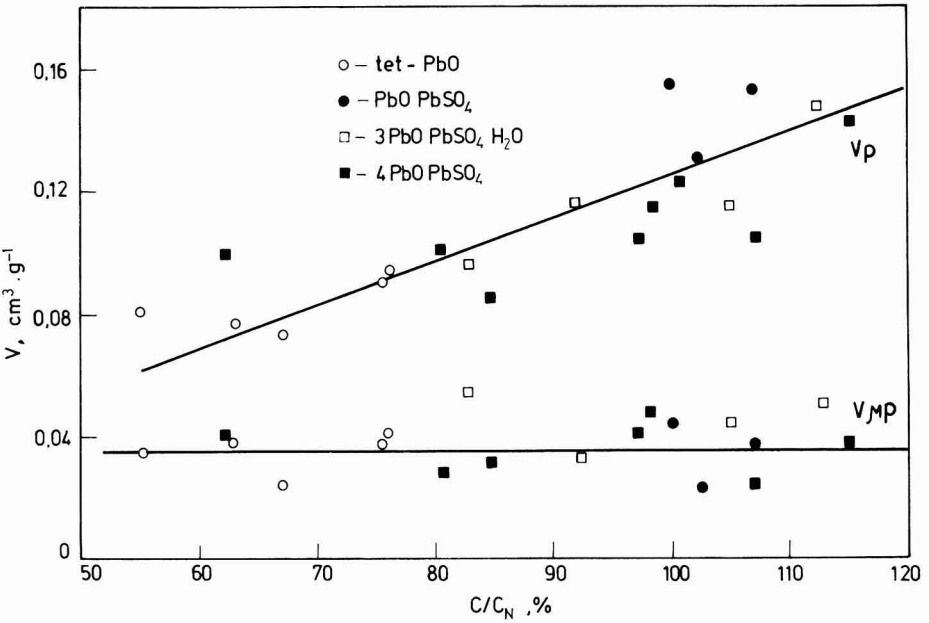


Fig. 5. Dependence of the capacity on the total volume of pores (V_p) and the volume of micropores ($V_{\mu p}$) of PAM's prepared from pastes with various phase composition.

low 0.5-0.1 μm, while in the case of the chemically obtained PbO_2 this rise appears at a radius ten times lower (0.01 μm). The pore volume of the PAM is strongly dependent on the phase composition of the paste. Pastes obtained from tet-PbO exhibit a low pore volume of the active material, while those of PbO · $PbSO_4$ have an exceptionally large volume. The pore volume diminishes with the increase in the paste density at one and the same phase composition. These experiments reveal that the porosity of the active material can be controlled by the phase composition and the density of the paste.

Let us assume the beginning of the steep rise in the surface area as a tentative limit between the agglomerate and transport pores. This limit is marked with arrows in Fig. 4. The total volume V_p of these two types of pores for a statistical number of PAM's, obtained under the conditions described in Table I, is presented as a function of the plate capacity in Fig. 5, together with the volume of the micropores ($V_{\mu p}$).

It is seen that the plate capacity increases with the total pore volume. The experimental points are, however, rather scattered. The active mass obtained from a tet-PbO paste (1% H_2SO_4/PbO) has a low total volume and a capacity lower than 80%, whereas that prepared from a PbO · $PbSO_4$ paste has a large total volume and a capacity over 100%. Figure 5 reveals also that the volume of the micro-

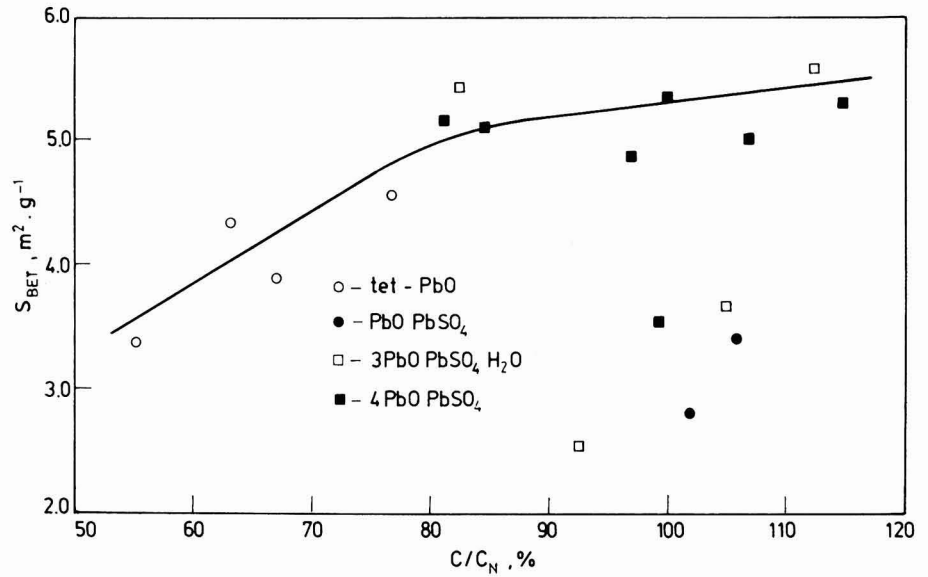


Fig. 6. Plate capacity as a function of BET surface area of PAM's prepared from pastes with various phase composition

pores varies between 0.025 and 0.055 cm^3/g. The capacity is almost unaffected by the volume of the micropores. This unexpected result induced the tests of a statistical number of plates with various active materials.

The difference between the total pore volume and that of the micropores gives the volume of the transport pores. It is worth mentioning that all plates had one and the same amount of the active material, and their rated capacity was calculated at 50% active material utilization. From Fig. 5 it follows that the volume of the transport pores is the capacity limiting parameter.

The surface area of the charged active materials was measured by the BET method, and Fig. 6 shows the results.

It is seen that in general the plate capacity grows with the BET surface area. Several plates exhibited comparatively low BET surface areas but high capacities. It can be supposed that the active material structure of these plates is such, that its surface area although comparatively low, is not a capacity limiting factor.

From the results in Fig. 5 and 6 it follows that the structure is a capacity limiting factor mainly through the volume of the transport pores and in a smaller degree by the surface area which is built up in the agglomerates. The first parameter determines the transport hindrances for the fluxes of ions taking part in the reactions, while the second one provides the surface area upon which the electrochemical reaction can take place.

The influence of these parameters was exhibited at the fifth cycle, *i.e.*, in the beginning of the battery life. It might be supposed that toward the end of the battery life the ohmic resistance between the agglomerates or the crystallites could also become a capacity limiting factor, which is likewise a structural parameter of the active material.

Variation of the volume and surface area of the pores during discharge.—Figure 7 presents the variation in the distribution of the pore volume *vs.* pore radius of two types active masses. During discharge the pore volume decreases, in virtue of the larger molar volume of $PbSO_4$ compared to that of PbO_2. The reduction of the total pore volume during discharge ΔV_p in cm^3/g can be estimated by the electric charge q_i in Ah consumed by the plate (using Faraday's law)

$$\Delta V_p = \frac{0.431\ q_i}{P_{AM} - 1.2q_i}\ cm^3/g$$

where P_{AM} is the weight of the active mass in grams. Table II presents the calculated and the experimental values of the variation in the total pore volume during discharge.

The good agreement between the calculated and experimental values is evident. The error is related to the inadequate precision in the estimation of the electric charge and to the insufficient mechanical stability of the structure which might not resist the pressure during the porosity measurements so that the pores would contract prior to the intrusion of mercury into them.

Such a situation is quite feasible since the newly formed $PbSO_4$ crystallites reduce the pore cross section at certain points and thus bottlenecked pores with a larger radius are formed. The intrusion of mercury into these pores requires a higher pressure in order to overcome the reduced pore cross section. This increased pressure could cause the larger pores to shrink whereby one may erroneously observe a larger pore volume contraction during the discharge of the plate.

On the other hand, the data in Table II reveal that the experimentally observed pore volume contraction per Ah is only slightly dependent on the type of the active material structure.

The curves of the surface area distribution *vs.* the pore radius, measured by mercury porosimetry, do not correctly reflect the actual distribution, due to the bottlenecking effect by the newly formed $PbSO_4$ crystallites. In order to eliminate this error the variation of the surface

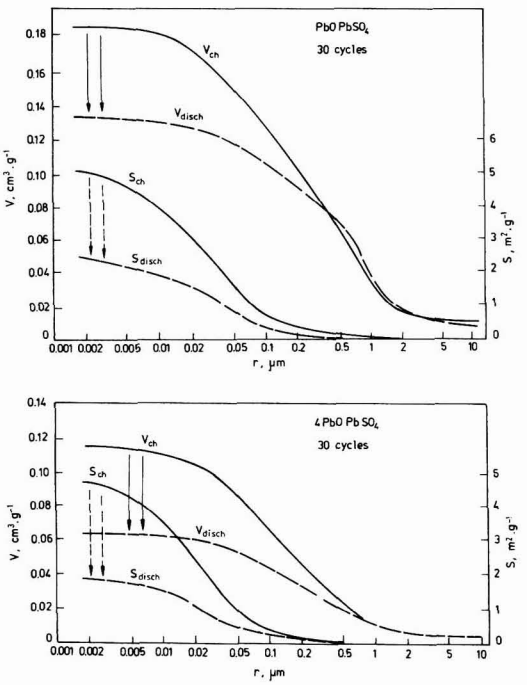


Fig. 7. Variation in the distribution of the volume and surface area of pores for PAM's prepared from PbO · $PbSO_4$ and 4PbO · $PbSO_4$ pastes at the 30th cycle, after discharge.

Table II. Calculated and experimentally found total volume of the pores for PAM's prepared from pastes with various phase composition at the 5th cycle

Active mass prepared from	V_p, calc., (cm^3/g)	V_p, exper. (cm^3/g)	Error (%)	ΔV_{exp}/Ah
3PbO · $PbSO_4H_2O$	0.043	0.044	−2	0.411
tet-PbO	0.035	0.034	+2.8	0.451
PbO · $PbSO_4$	0.049	0.052	−6	0.424
4PbO · $PbSO_4$	0.037	0.040	−8	0.339

Table III. Experimental values of the BET surface area of charged and discharged plates at the 5th cycle of PAM's prepared from paste with various phase composition

PAM formed from	Ah/g	S charged plate $m^2\ g^{-1}$	S disch. plate $m^2\ g^{-1}$	S/Ah $m^2 \cdot Ah^{-1}$
3PbO · $PbSO_4$ · H_2O	0.1070	3.60	2.75	7.94
tet-PbO	0.0754	4.55	3.34	16.05
PbO · $PbSO_4$	0.1226	6.99	3.09	31.81
4PbO · $PbSO_4$	0.1023	3.54	1.63	18.67

Table IV. Total pore volume and apparent density of charged PAM's prepared from pastes with various phase composition after the 5th and the 30th cycle

	5th cycle		30th cycle	
PAM formed from	V_{ch} ($cm^3 \cdot g^{-1}$)	Apparent density ($g \cdot cm^{-3}$)	V_{ch} ($cm^3 \cdot g^{-1}$)	Apparent density ($g \cdot cm^{-3}$)
3PbO · $PbSO_4$ · H_2O	0.115	4.3419	0.137	3.9105
tet-PbO	0.092	4.8240	0.102	4.2892
PbO · $PbSO_4$	0.183	3.3300		2.6885
4PbO · $PbSO_4$	0.115	4.5013	0.134	3.6789

ห้องสมุดกรมวิทยาศาสตร์บริการ

area during discharge was determined by the adsorption BET method.

The reduction in the active surface area ΔS_i per gram active material during discharge is expressed by

$$\Delta S_i = \Delta S_{PbSO_4} - \Delta S_{PbO_2} - S_{PbO_2/PbSO_4}$$

where ΔS_{PbSO_4} is the surface area of the newly formed $PbSO_4$ crystallites, ΔS_{PbO_2} is that of the reduced PbO_2 crystallites, and $S_{PbO_2/PbSO_4}$ is the contact surface area of PbO_2 onto which $PbSO_4$ crystallites have precipitated, thus separating it from the solution. We shall assume this area to be small enough so that ΔS_i will be determined basically by the difference $\Delta S_{PbSO_4} - \Delta S_{PbO_2}$. It will depend on the volume of the $PbSO_4$ crystallites. Since the volume of the $PbSO_4$ crystallites is larger than that of the initial PbO_2 ones, the surface area of the discharged active material will be smaller than that of the charged one. Table III presents the experimental BET surface areas of charged and discharged plates of the 4 types of active materials at their fifth cycle.

The data in Table III present the reduction in the surface area of the active material during discharge. This implies that the $PbSO_4$ crystallites have a much larger volume than that of the PbO_2 ones. The data in this table also demonstrate that the different structures of the active material exhibit different variations in the BET surface area per 1 Ah of electric charge. This implies that the active material structure controls the size of the $PbSO_4$ and PbO_2 crystallites. Finally this table reveals that the capacity of the plate is not unequivocally related to the variations in its surface area.

Variations in porosity and surface area of the active material and the thickness of the plate during cycling.— Test cells assembled with plates prepared from the 4 types of PAM were subjected to 30 charge-discharge cycles. After cycling, the following tests were performed: distribution of the volume and surface area of the pores, BET surface area, apparent density of the active mass, and plate thickness in charged and discharged state.

Table IV shows the values of the pore volume and the apparent densities of the charged plates for the 4 types of the active materials at the 5th and the 30th cycle.

It appears that during cycling the structure undergoes changes leading to the increase in the pore volume and a reduction in the apparent density of the active material. Since no shedding was observed up to the 30th cycle (with the exception of some of the plates prepared from the $PbO \cdot PbSO_4$ paste) it follows that the volume of the PAM grows during cycling. This was checked also by direct measurements of the thickness of plates in charged and discharged state. Besides this, part of the plates of each type of active mass were allowed to stand after discharge for 16h at open circuit (OC) in the cell, and their thickness was measured again. The thickness measurements were performed by a micrometer at fixed points of the plate. Table V illustrates the results.

The juxtaposition of the data for the 5th and the 30th cycle reveals the growth of the plate thickness on cycling. The rate of growth depends on the stability of the skeleton structure. This rate is the highest with the PAM obtained from $PbO \cdot PbSO_4$. In fact, this active material is most apt to shed and is mechanically unstable (1). The thickness of the plates, prepared from the $4PbO \cdot PbSO_4$ paste, is practically invariable. This material is the most rigid one, and the plates exhibit the longest cycle life.

Table VI. BET surface area of plates: charged, discharged, and discharged and kept for 16h at open circuit at the 30th cycle

PAM formed from	Charged plate $m^2 \cdot g^{-1}$	Discharged plate $m^2 \cdot g^{-1}$	Discharged + OC $m^2 \cdot g^{-1}$
$3PbO \cdot PbSO_4 \cdot H_2O$	5.49	2.12	1.62
tet-PbO	6.04	2.19	1.96
$PbO \cdot PbSO_4$	6.29	2.89	2.24
$4PbO \cdot PbSO_4$	5.94	2.07	1.89

Table V also shows the thickness variations within one charge-discharge cycle. The thickness of the charged plate is smaller than that of the discharged one implying that the processes taking place during the discharge cause an expansion of the plate. By keeping the discharge plates at OC in the solution their thickness diminishes. It can be supposed that some recrystallization processes occur in the active material leading to a relaxation of the mechanical stress developed during the discharge and a contraction of the skeleton. During the next charge the plate thickness is restored to its initial value or close to it. In some of the charge cycles in the skeleton of the active material certain irreversible structural changes occur whereby the plate thickness cannot be recovered to its initial value and remains larger. These irreversible changes bring about the swelling of the PAM. Hence, in each of the charge-discharge cycles the positive active mass is "breathing" since during the discharge, mechanical stresses are generated and the plate volume expands while during the rest and the charge period, the stresses are relieved as a result of the processes occurring and the plate shrinks.

During the initial cycles when the skeleton is rigid enough, the variations in the volume of the active material are small. The skeleton can sustain the mechanical stresses. This accounts for the good agreement between the experimental and the calculated variations in the pore volume. With the increase of the number of cycles, the strength of the skeleton declines and the volume variations increase leading to the swelling of the active material. This contributes, on its part, to the deterioration of the contact between the agglomerates which results in a capacity decay and in the ultimate failure of the plate. If the active material is confined in a mechanically strong wrap, the latter could sustain the mechanical loads during the "breathing" of the plate, the swelling would be eliminated, and the battery life could be increased. This is the case with the tubular electrodes, which exhibit a cycle life twice as long as that of the pasted-type electrodes.

Table VI shows the value of the BET surface area of charged, discharged, and discharged and left for 16h at open-circuit plates for the 4 types of active materials at the 30th cycle.

During discharge the surface area of the active material diminishes. This diminution continues during the rest period of the discharged plates at the OC. As pointed out in the preceding section these processes are associated with the ratio between the volumes of $PbSO_4$ and PbO_2. The decrease in the surface area during the rest period is probably caused by the recrystallization of the small $PbSO_4$ crystallites in larger ones.

Table V. Thickness of plates: charged, discharged, and discharged and kept for 16h at open circuit at the 5th and 30th cycle

	5th cycle			30th cycle			
PAM formed from	Char. (mm)	Disch. (mm)	Disch. + OC (mm)	Char. (mm)	Disch. (mm)	Disch. + OC (mm)	Char. (mm)
$3PbO \cdot PbSO_4 \cdot H_2O$	2.390	2.440	2.410	2.790	3.010	2.820	2.790
tet-PbO	2.380	2.420	2.410	2.580	2.750	2.590	2.590
$PbO \cdot PbSO_4$	2.580	2.740	2.630	3.260	3.610	3.280	3.260
$4PbO \cdot PbSO_4$	2.660	2.690	2.670	2.660	2.860	2.760	2.660

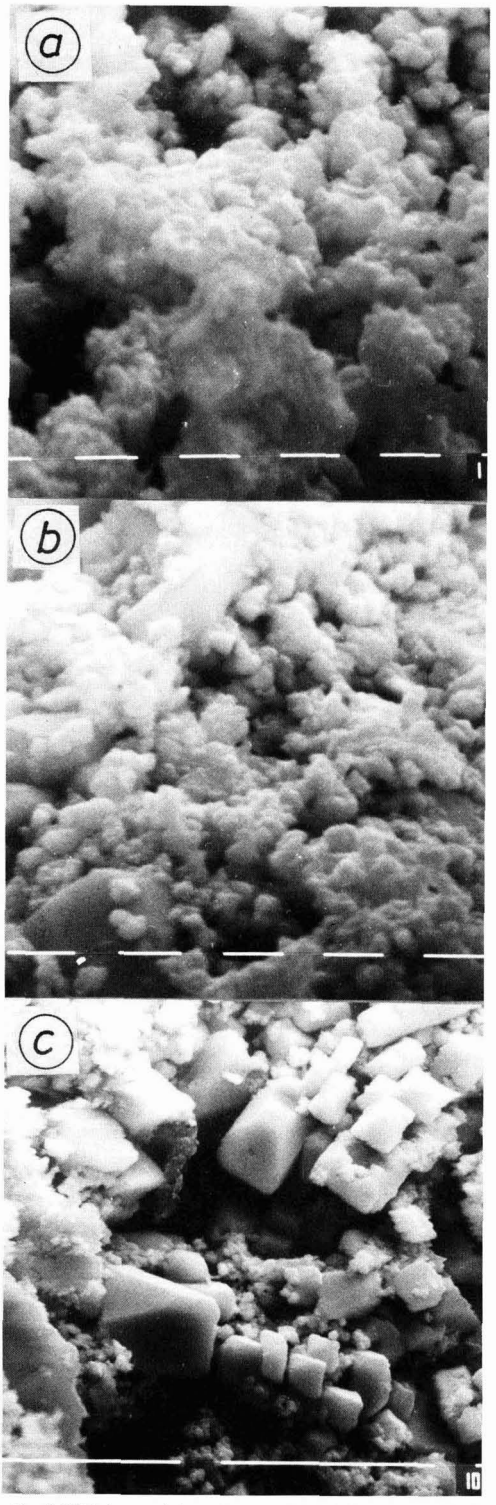


Fig. 8. SEM picture of the active material: (a) after charge; (b) after discharge; (c) after discharge and 16h rest at open circuit. (a, b) White lines = 1 μm; (c) White line = 10 μm.

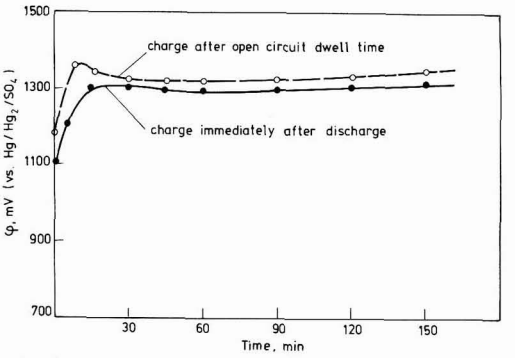


Fig. 9. Potential transients during galvanostatic charge of discharged plates immediately after discharge or after 16h rest at open circuit.

The pictures in Fig. 8 illustrate the crystal morphology and the structure of the active material, obtained from the $3PbO \cdot PbSO_4 \cdot H_2O$ paste: 8(a), after charge; 8(b), after discharge; and 8(c), after discharge and rest for 16h at the OC. The picture in 8(c) is at a 3 times lower magnification in order to more clearly see the $PbSO_4$ crystallites.

After the discharge one can discern parts of $PbSO_4$ crystallites [Fig. 8(b)] on certain sites, which are not very clearly cut, but are intimately linked to the active material. They have grown at sites of maximum supersaturation and probably have nonequilibrium planes and edges. From another point of view this process reveals the following. Due to the larger molar volume of $PbSO_4$ than that of PbO_2, the $PbSO_4$ crystallite attached to the skeleton will generate, during its growth, internal tensions tending to expand the skeleton. In case that the latter is not rigid enough it will begin to swell.

During the rest period at the OC the H_2SO_4 concentration in the active material is leveling in the entire cross section of the plate. This causes the dissolution of the nonequilibrium $PbSO_4$ crystallites and their precipitation upon equilibrium nuclei. As a result of this process we observe well-formed $PbSO_4$ crystals with equilibrium planes, edges, and corners [Fig. 8(c)].

Figure 8 exhibits that the discharge process comprises the electrochemical reduction of PbO_2 to $PbSO_4$ followed by a recrystallization process during which Pb^{2+} ions are transported in the pores and equilibrium $PbSO_4$ crystals are built up. If the last process actually takes place, then the reverse process for the electrochemical oxidation of $PbSO_4$ during the charging will depend on that whether $PbSO_4$ has recrystallized or not. Figure 9 gives polarization charge curves recorded immediately after the discharge and after a rest period of 16h at the OC of the discharged plate.

The charging of the discharged active material after the rest occurs at a higher polarization. This is especially well expressed in the initial 15-30 min of the charging.

This increased polarization could be assigned either to the hindered dissolution of the $PbSO_4$ crystals (equilibrium crystals dissolve less easily than nonequilibrium ones) or to transport hindrances. During the recrystallization, $PbSO_4$ from a certain region of the active material is collected in larger crystals. When considering the charge-discharge process as a whole, one has to take into account also the recrystallization step of $PbSO_4$ in the overall phenomena.

Acknowledgments

The authors wish to express their gratitude to K. Stambolska and V. Stoyanova for their technical assistance.

Manuscript received May 20, 1985.

REFERENCES

1. D. Pavlov and E. Bashtavelova, *This Journal*, **131,** 1468 (1984).
2. A. C. Simon, S. M. Caulder, and J. T. Stemmle, *ibid.*,

122, 461 (1975).
3. D. C. Constable, J. R. Gardner, J. A. Hamilton, J. Harris, R. J. Hill, D. A. J. Rand, S. S. Wan, and L. B. Zalman, ILZRO Project LE-290, Progress Report No. 6 (1982).
4. S. M. Caulder, J. S. Murday, and A. C. Simon, *This Journal*, **120**, 1515 (1973).
5. S. M. Caulder and A. C. Simon, *ibid.*, **121**, 1546 (1974).
6. R. J. Hill, A. M. Jessel, and I. C. Madsen, in "Advances in Lead Acid Batteries," K. R. Bullock and D. Pavlov, Editors, p. 59, The Electrochemical Society Softbound Proceedings Series, Vol. 84-14, Pennington, NJ (1984).
7. D. Pavlov, G. Papazov, and V. Iliev, *This Journal*, **119**, 8 (1972).
8. T. G. Chang, *ibid.*, **131**, 1755 (1984).

Protection of n-Si Photoanode against Photocorrosion in Photoelectrochemical Cell for Water Electrolysis

R. C. Kainthla, B. Zelenay, and J. O'M. Bockris*

Chemistry Department, Texas A&M University, College Station, Texas 77843

ABSTRACT

The photoelectrochemical behavior of n-type Si electrode in aqueous solutions was investigated. Protection of the electrodes against photocorrosion was achieved by chemically depositing a thin film of manganese oxide on the surface. The electrodes have shown complete stability during oxygen evolution under continuous illumination of more than 650h. The electrodes have been characterized in terms of surface topography, surface analysis, and flatband potential using scanning electron microscopy, x-ray photoelectron spectroscopy (XPS), and capacitance-potential characteristics, respectively. Mn in the film is observed to be present in the +3 state. The XPS analysis of the electrode that has been producing oxygen shows that the photogenerated holes on the electrode surface oxidize water to oxygen and do not oxidize the Mn^{3+} to higher valence state. Mott-Schottky plots have been used to determine the flatband potential of the electrode. They show that the flatband potential of the protected electrode shifts in the cathodic direction with an increase in the pH of the solution.

The use of small-bandgap n-type nonoxide semiconductors as photoanodes to electrolyze water is hampered by the instability of these electrodes under conditions of oxygen evolution. Because of its wide use and availability, n-Si is of special interest. However, n-Si is photooxidized in aqueous solution to produce an insulating film of SiO_2. A number of methods (1-12) of preventing this passivation have been reported. In general, the electrode has been protected by depositing thin coatings on the n-Si surface. However, most of these protected electrodes (1-9) have been used to carry out redox reactions, which occur at much lower potentials than oxygen evolution, for which only a few electrodes have demonstrated feasibility (8, 10-12). For use in water photoelectrolysis, the n-Si electrodes have been protected by depositing thin films of indium tin oxide (ITO) (10), iron oxide (11), Pt-doped SiO_2 (12), and iridium silicide (8). These films have been deposited by spray pyrolysis, vacuum evaporation, and electrochemical and vacuum evaporation techniques, respectively. In this communication, we report the stabilization of n-Si electrode under conditions of oxygen evolution by deposition of manganese oxide film using a chemical deposition technique that is simple, inexpensive, and known to yield uniform films (13). Various properties of the protected electrode are also described.

Experimental

Anode preparation.—Single-crystal n-Si of 2-5 Ω-cm resistivity was obtained from Monsanto Corporation. Wafers of 1.0 mm thickness were etched in $HCl:HNO_3:HF$ (3:1:2) bath for 5 min followed by etching in 48% HF for 5 min and rinsing in triply distilled water for 1 min. The wafer was provided with Ga-In back ohmic contact, and one monolayer of Pd was deposited on the front surface by galvanostatic pulse method in the dark at a current density of 0.4 mA-cm^{-2} from 10% $PdCl_2$ solution. The sample was then immersed in a bath containing $3 \times 10^{-2}M$ $MnCl_2$, $0.25M$ NH_4Cl, and $1.4M$ NH_4OH aqueous solution. The solution was stirred continuously and maintained at room temperature. After a few minutes, a light brown precipitate of $Mn(OH)_2$ started forming. The sample was left in the bath for 15 min. At the end of the reaction, the sample was washed in triply distilled water and, after drying, transferred to a glass tube that was evacuated to 2×10^{-5} torr. The sample was then heated at 250°C for 15 min. The heating in vacuum resulted in loss of water, thereby leaving a thin film of manganese oxide (Mn_2O_3) behind (13).

Thickness measurement.—To determine the thickness of the Mn-oxide film, the film was deposited on polished n-Si wafer and also on a glass slide. The thickness was determined by a Rudolph Research Automatic Fourier Transform Ellipsometer (Model 2000 FT) to be 200 ± 50Å.

Photocurrent-potential measurements.—The electrode with Ga-In-backed ohmic contact was placed on a copper disk soldered to a copper wire. The assembly was mounted in a Teflon holder with a Teflon O ring between the holder and the electrode (14). No epoxy cement was used, as the arrangement was found to be leakproof. The area of the electrode exposed to the light was about 0.2 cm^2.

The photoresponse of the electrodes was measured in a $0.5M$ K_2SO_4 solution and in $0.2M$ NaOH solution using a PARC 363 potentiostat with a PARC 175 universal programmer under 100 mW-cm^{-2} light intensity from a Xe arc lamp. Three electrode geometries were employed for the cell with platinum foil as the counterelectrode.

Photocurrent-wavelength measurements.—The photocurrent-wavelength measurements at different electrode potentials were carried out with a high intensity monochromator (Bausch and Lomb). The intensity of light at each wavelength was measured by an Eppley radiometer. The spectral response was calculated by subtracting the dark current from the photocurrent and dividing the resultant current by the incident light intensity at each wavelength.

Capacitance-voltage characteristics.—The capacitance of the electrode-electrolyte interface at various electrode potentials was measured with a Solartron frequency response analyzer (Model 1170) and a Solartron electrochemical interface (Model 1186).

* Electrochemical Society Active Member.

Surface topography.—Surface topography and composition of the electrode were determined using a JEOL (JSM-35U) scanning electron microscope with energy dispersive x-ray spectrometer. A 10 keV electron beam with a beam current of microamps was used.

Surface analysis.—The surface analysis of the electrode was made with a KRATOS XSAM-800 scanning Auger microprobe and x-ray photoelectron spectrometer using monochromatic Mg Kα x-ray source. The angles of incidence were 0° and 60°. The pressure of the analyzer chamber was 1×10^{-9} torr. Initially, a survey scan was recorded to identify the elements present on the surface. Subsequently, the data were recorded over a narrow energy range (25 eV window width). The spectral acquisition and signal averaging were performed by a 'DIGITAL' computer. Standard spectra recorded were Si(2p), Mn(2p), and O(1s). The peak position, half-width, and area under the peak were determined by fitting the synthesized peak to the observed peak using peak synthesis routine with Gaussian peaks. All peaks were referenced to C(1s) peak at 285.0 eV.

Results and Discussion

Photoactivity of the Mn-oxide-coated n-Si electrode.—Figure 1 shows the current-potential characteristics of the Mn-oxide-coated n-Si electrode in 0.5*M* K_2SO_4 solution [Fig. 1(c) and 1 (d)] and in 0.2*M* NaOH solution [Fig. 1(a) and 1(b)]. The I-V curves were obtained by scanning the electrode potential between +0.5V and +1.3V (*vs.* NHE) in NaOH solution and between +0.9V and +1.9V in K_2SO_4 solution at a scanning rate of 50 mV · s^{-1}. Under dark conditions, the current [Fig. 1(b) and 1(d)] is negligible as compared to the current under illumination [Fig. 1(a) and 1(c)]. Under illumination, the onset of the anodic current occurs at +0.51V in NaOH solution (*p*H 13.0) and at +1.12V in K_2SO_4 solution (*p*H 4.7). This shift in the onset potential is due to the different *p*H of the solution and corresponds to a similar shift in the reversible potential for oxygen evolution (V_{rev}) with change in the *p*H of the solution.

The photocurrent-potential curves show some hysteresis due to the formation of oxygen on the electrode surface. However, the cathodic sweep shows little or no reduction of the oxide. If the electrode is cycled continuously, a slight decrease in photocurrent is observed due to the formation of oxygen bubbles on the electrode. The photocurrent-potential curve returns to the initial curve when the bubbles leave the electrode. The observation of no significant change in current-potential curves with cycling suggests that the electrodes are stable in both K_2SO_4 solution and NaOH solution.

As Fig. 1 shows, the photocurrent has a tendency to saturate for potentials anodic of +1.8V and +1.3V in K_2SO_4 solution and in NaOH solution, respectively. The saturation current is about 5.0 mA · cm^{-2}, which is only 20-25% of the value expected for silicon. However, the photocurrent is due to photogeneration of carriers in Si and not in Mn-oxide, as the Mn-oxide film deposited on Ti and indium-tin-oxide(ITO)-coated glass does not show any photogenerated current (see below). The lower saturation current cannot be attributed to absorption by the Mn-oxide film, as the transmittance of the film deposited on a glass slide shows that the intensity of the light decreases by ~10% only on passing through the film. Therefore, it seems that the main decrease in photocurrent is due to the presence of interface states at the Si/Mn-oxide interface or surface states at the Mn-oxide electrolyte interface, which act as recombination centers and, therefore, reduce the photocurrent. The decrease in photocurrent due to surface recombination is also shown by the spectral response measurements reported later. Interface states are known (15) to occur at the interface between two dissimilar materials. However, it is known (10) that, for example, for the Si/ITO interface the density of interface states can be reduced by optimizing the deposition of ITO on Si. Since the purpose of the present study is to determine the stability of the Mn-oxide-coated n-Si electrode, no attempts were made to optimize the catalytic properties of the surface.

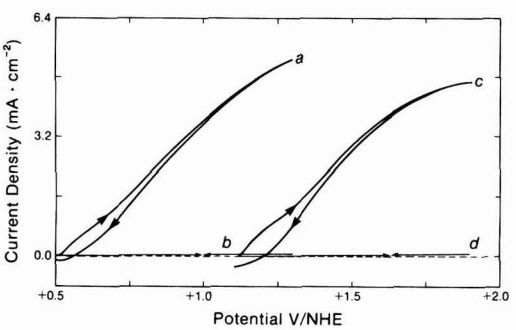


Fig. 1. Current-potential characteristics of manganese-oxide-coated n-Si electrode in 0.2*M* NaOH solution (a, b) and in 0.5*M* K_2SO_4 solution (c, d), in dark (b, d) and under illumination (a, c).

The comparison of the onset potentials for oxygen evolution on Mn-oxide-coated n-Si electrodes reveals that the onset potential lies in the same range as observed by other workers for oxygen evolution on n-Si electrode protected by different coatings. Thus, the onset potential on RuO_2 and IrSi-coated n-Si occurred at about V_{rev} (8), and that on RuO_2 and ITO-coated n-Si occurred at about 100 mV cathodic of V_{rev} (10), while on SiO_2(Pt)-covered n-Si it occurred at about 250 mV anodic of V_{rev} (12). On IrSi-coated Si and ITO-coated Si, RuO_2 was used as an electrocatalyst for oxygen evolution, while in Pt-doped silica-coated Si, no electrocatalyst was used. In Mn-oxide-coated n-Si electrode without any electrocatalyst in NaOH solution, the onset occurs at about 60 mV anodic of V_{rev}. However, when Ag is chemisorbed on the Mn-oxide surface, the onset potential has been observed to shift to +0.3V, which is about 150 mV cathodic of V_{rev} and, therefore, is comparable to those on RuO_2 and ITO-coated n-Si. Hence, photoactivity on Mn-oxide-coated Si can be catalyzed.

Stability of the electrode.—To test the long-term stability of the Mn-oxide-coated n-Si electrode, the electrode was maintained at +1.3V *vs.* NHE in 0.5*M* K_2SO_4 solution. Figure 2(a) shows the dependence of current density on time over a typical period of 1h. A slight decrease in current with time is observed, but the current is restored when the bubbles leave the surface. Figure 2(b) shows the results of the continuous illumination over long periods of time. Except for a small decay in current in the first few hours of testing, the sample has shown no decay in current for ~650h of continuous operation, after which the exposure was stopped. Even after eight months of sporadic use, the electrode is still working without any decrease in current.

Comparison of the electrode stability data with other coated n-Si electrodes used for oxygen evolution reveal that, in earlier work, the stability has been studied for time periods shorter than that of the present study. Thus, Ir-Si-coated n-Si electrode was shown to be stable up to seven days during chlorine evolution (8) and the ITO-coated n-Si for 65h during chlorine evolution (1), after which time experiments were discontinued. The Pt-doped silica-coated n-Si was shown to be relatively stable up to 100h, but decayed sharply after about 120h (11). In the present work, the stability has been studied at current densities around 1 mA · cm^{-2}, whereas, on IrSi-coated n-Si or ITO-coated n-Si electrodes during chlorine evolution, the current density was 10-20 mA · cm^{-2}. However, the time period over which the stability has been proven is 5-10 times longer.

Photoactivity of Mn-oxide films.—Figure 3 shows the current-potential characteristics of the Mn-oxide film deposited on Ti substrate in K_2SO_4 solution and in NaOH solution under dark and under illumination. There is no

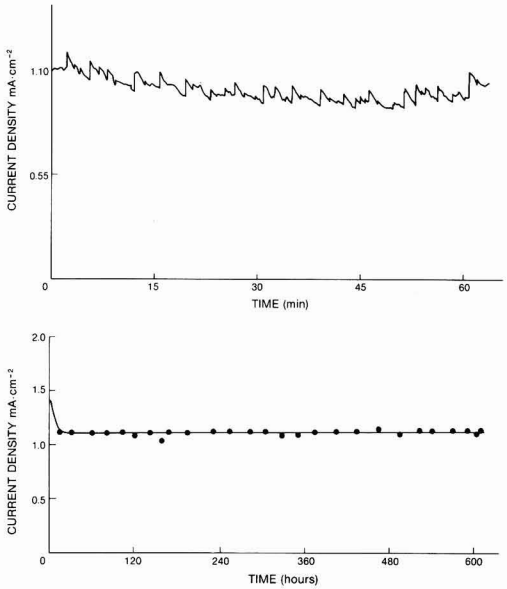


Fig. 2. (a, top) Photocurrent density as a function of time, showing fluctuation in current as a result of buildup of O_2 gas bubbles on the surface at +1.3V vs. NHE in 0.5M K_2SO_4 solution. (b, bottom) Photocurrent density as a function of time of continuous illumination (light intensity = 100 mW-cm^{-2}, Xe arc lamp).

photogenerated current, and the dark and light current-potential curves coincide. In K_2SO_4 solution and NaOH solution, appreciable anodic current is obtained for potentials anodic of about 1.4V and 0.8V, respectively. Comparison of these results with Mn-oxide film on n-Si electrode (Fig. 1) shows that, under the influence of light for Mn-oxide on n-Si, the oxygen evolution is shifted by about 0.3V in the cathodic direction as compared to Mn-oxide on Ti substrate.

Photocurrent as a function of wavelength.—The spectral response (see above) of the manganese-oxide-protected n-Si electrode at electrode potentials of +1.3V (*vs.* NHE) and +1.5V (*vs.* NHE) in 0.5*M* K_2SO_4 solution is plotted in Fig. 4. The figure shows that the electrode responds to entire visible radiation. The gradual decrease in photoresponse into the short wavelength region (or higher photon energies) is indicative of surface recombination of photogenerated minority carriers due to surface states. Application of higher anodic bias to electrode results in the expected increase in photocurrent, but the surface recombination component is not reduced (*cf.* response at +1.3V and +1.5V *vs.* NHE).

Flatband potential.—The flatband potential of the electrode was measured in 0.5*M* K_2SO_4 solution and in 0.2*M*

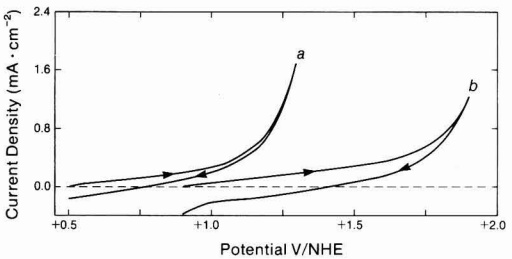


Fig. 3. Current-potential characteristics of manganese-oxide-coated Ti electrode in (a) 0.2M NaOH solution and in (b) 0.5M K_2SO_4 solution. There is no difference between dark and photo characteristics.

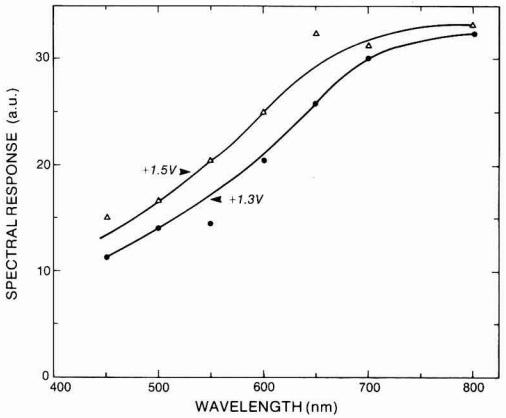


Fig. 4. Spectral response of Mn-oxide-coated n-Si electrode in 0.5M K_2SO_4 solution at +1.3V and +1.5V (vs. NHE) electrode potentials.

NaOH solution. The flatband potential was determined by measuring the capacitance of the electrode-electrolyte interface at various frequencies and at different electrode potentials and by plotting $1/C^2$ as a function of electrode potential.

Figure 5 shows the plot of $1/C^2$ *vs.* electrode potentials for Mn-oxide-coated n-Si electrode in 0.5*M* K_2SO_4 solution. The figure shows change in the capacitance with frequency, but the intercept on the potential axis is nearly the same. The values of the flatband potential for Mn-oxide-coated n-Si electrodes in 0.5*M* K_2SO_4 solution and 0.2*M* NaOH solution are 0.12 ± 0.02V and −0.50 ± 0.02V, respectively. The change in the capacitance with frequency is typical of a semiconductor electrolyte interface, which has a large density of surface states (16).

The comparison of the onset potential for the anodic photocurrent (U_{onset}) with the flatband potential (U_{FB}) shows that the onset potential is ~1.0V anodic of the flatband potential. The flatband potential and the onset potential are expected to coincide for those interfaces only where the number of surface states is low and the rate of charge transfer from the electrode to the ions in solution is high. The oxygen evolution reaction is kinetically slow, and, thus, the difference between the onset potential and the flatband potential can be rationalized. The difference between U_{FB} and U_{onset} of >0.6V has been reported earlier by various workers (17-19). Thus, for hydrogen evolution on p-GaP (17) and p-GaSe (18) and for

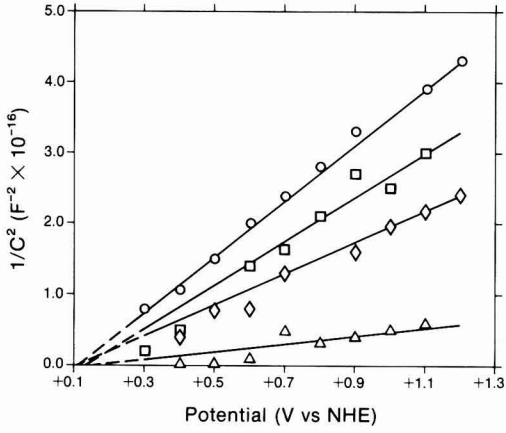


Fig. 5. Mott-Schottky plots of Mn-oxide-coated n-Si electrode in 0.5M K_2SO_4 solution at various frequencies (circle) 10 kHz, (square) 3 kHz, (diamond) 1 kHz and (triangle) 300 Hz.

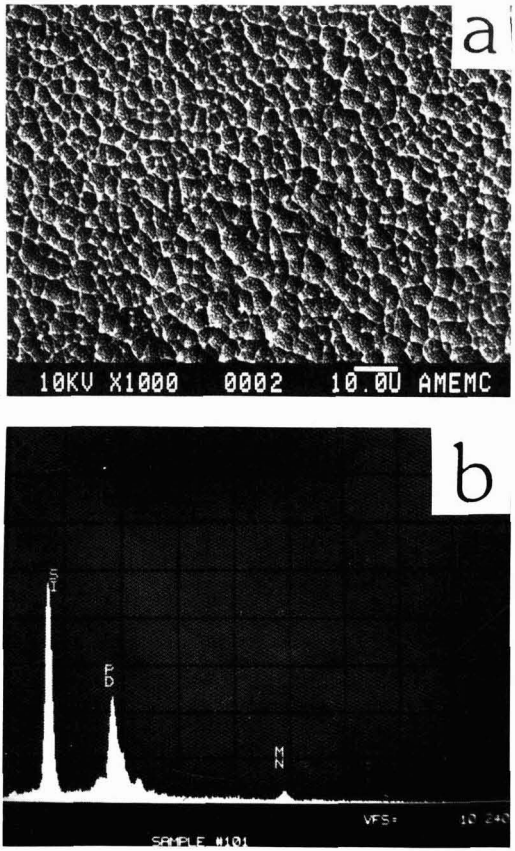


Fig. 6. (a) Surface topography of Mn-oxide-coated n-Si electrode. (b) EDAX plot of Mn-oxide-coated n-Si electrode, showing the presence of Si, Mn, and Pd.

S^{2-} oxidation on n-CdSe (19), differences of 0.6V, 0.8V, and 0.6V, respectively, have been reported. For oxygen evolution on n-In_2O_3 and n-$CaTiO_3$, differences of 0.85V and 0.94V, respectively, have been observed (18).

Scanning electron microscopy.—Figure 6(a) shows the surface topography of the manganese-oxide-protected n-Si electrode. The electrode is uneven, but no cracks were observed even at magnification of 15,000. The manganese oxide film covers the hills and valleys produced by the etching of Si in $HCl:HNO_3:HF$ solution uniformly.

Figure 6(b) shows the elemental EDAX analysis of the electrode surface. Since the penetration depth of electrons at beam energy of 10 keV is hundreds of angstroms, a relatively large concentration of Si is observed. In addition, as expected, Pd and Mn are also observed.

X-ray photoelectron spectroscopy.—The broad x-ray photoelectron spectrum of the n-Si electrode coated with Mn-oxide film, which has not been used to photoelectrolyze water (as prepared electrode) over the whole binding energy range (0-1253.6 eV), shows the presence of Mn, O, C, and Cl, only. Contrary to the EDAX analysis, no signal due to Si is observed, suggesting that the manganese oxide film covers the Si surface uniformly without any cracks or pin holes. The presence of Cl is due to the use of $MnCl_2$ and NH_4Cl during the deposition of the film.

The x-ray photoelectron spectrum in the region of Mn(2p) is shown in Fig. 7(1) for the electrode before use. Two peaks corresponding to binding energies at 641.8 eV and 653.5 eV are obtained. The peaks match well with the

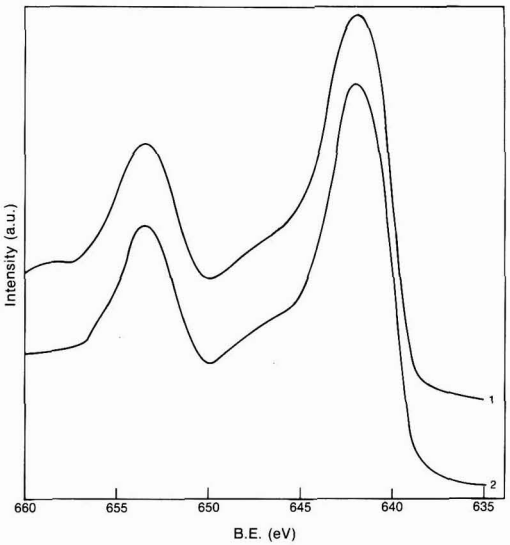


Fig. 7. Photoelectron spectrum of Mn-oxide-coated n-Si electrode, showing Mn(2p) region of (1) as-prepared electrode and (2) electrode that has been photoevolving oxygen for 16h.

$2p_{3/2}$ and $2p_{1/2}$ peaks reported for Mn_2O_3 and MnO(OH) (20). Thus, Mn in the Mn-oxide film is present in 3+ state.

Figure 8 shows the O(1s) spectrum. A single peak with a shoulder is obtained. The peak can be resolved into three peaks at 530.05 eV, 531.9 eV, and 533.8 eV, with FWHM of 1.75 eV, 2.09 eV, and 1.50 eV, respectively (Fig. 9). These peaks can be assigned to O(1s) in Mn_2O_3 (530.1 eV), MnO(OH), and water, respectively (20, 21). The relative area under these peaks is 50.2, 45.5, and 4.3, respectively.

The presence of MnO(OH) and water in the manganese oxide film is not surprising, as the film is deposited from an aqueous solution. Also, the initial stage of formation is $Mn(OH)_2$, which, in contact with O_2 atmosphere, changes to MnO(OH) (13). Heating MnO(OH) at 250°C in vacuum is known to convert MnO(OH) to Mn_2O_3 (13, 20). The presence of MnO(OH), even after heat-treatment at 250°C for 15 min in vacuum may be due to the short time used for the heat-treatment.

The broad photoelectron spectrum of the Mn-oxide-coated n-Si electrode, which has been producing oxygen for 16h in aqueous solution, again shows the presence of Mn, O, C, and Cl only. Again, Si is not detected, showing that the operation of the electrode does not damage the

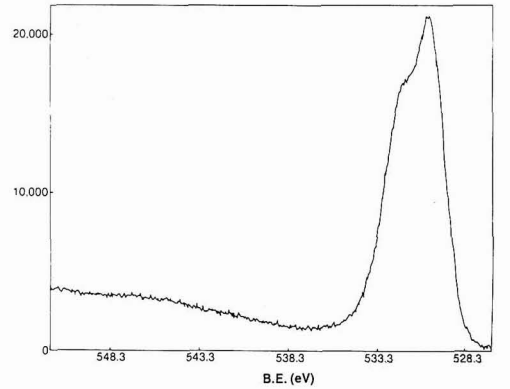


Fig. 8. Photoelectron spectrum of Mn-oxide-coated n-Si electrode in the region of O(1s) (as-prepared electrode).

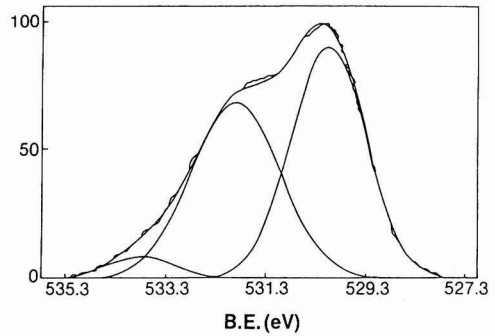


Fig. 9. Resolution of O(1s) peak into component peaks

protective coating. Also, contrary to some polymer films used earlier to protect the n-type semiconductor electrodes (22), the film does not peel off when oxygen is evolved on the electrode.

Figure 7(2) shows the Mn(2p) spectrum for the Mn-oxide-coated electrode that has been used to evolve oxygen. No change in peak position or peak shape is observed, showing that Mn is still in the 3+ state. Thus, we conclude that photogenerated holes on the electrode surface only oxidize water to oxygen and do not oxidize the Mn^{3+} to higher valence state.

Figure 10(2) shows the O(1s) spectrum for the Mn-oxide coated n-Si electrode that has been used to photoelectrolyze water. Again, a single peak with a shoulder is obtained. Although the peak position is the same, there is a change in the peak shape implying surface modification as a result of oxygen evolution or immersion in aqueous solution. This change in surface composition, together with the oxygen bubbles on the electrode surface, is probably responsible for the slight decay (10-20%) in the photocurrent observed in the first few hours of operation of the electrode [*cf.* Fig. 2(b)].

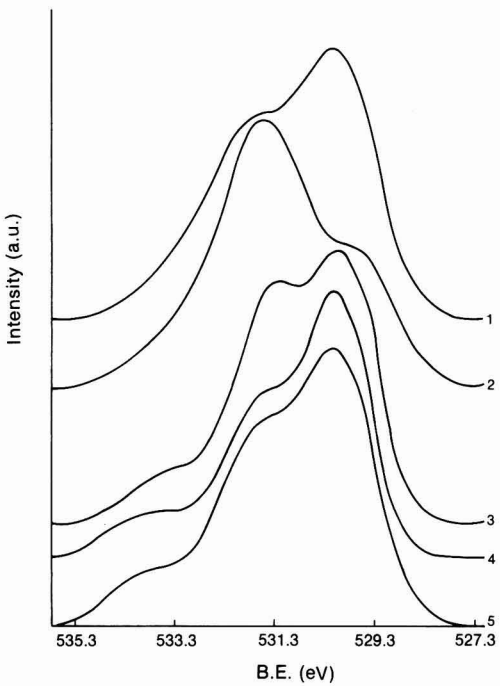


Fig. 10. X-ray photoelectron spectra in the region of O(1s) (1) for as-prepared electrode and (2-5) for the electrode that has been photoevolving oxygen for 16h, after Ar^+ ion etching for different times: (2) 0 min, (3) 5 min, (4) 10 min, and (5) 20 min.

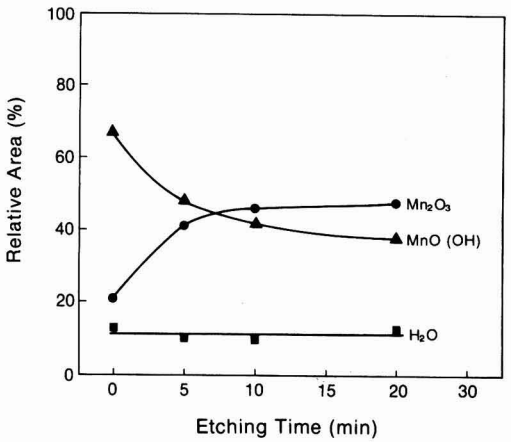


Fig. 11. Relative area under each peak as a function of Ar^+ ion etching time.

The O(1s) peak can still be resolved into three peaks corresponding to Mn_2O_3, MnO(OH), and H_2O, but the relative concentrations of MnO(OH) and H_2O are higher than the corresponding concentration in the as-prepared electrode.

The effect of etching the electrode with Ar^+ ions on the O(1s) peak is shown in Fig. 10 (3-5), which shows the O(1s) spectrum after different etching times. The peak in each case can still be resolved into three peaks, but the relative concentration of Mn_2O_3 and MnO(OH) changes with Ar^+ ion etching, while the water concentration remains essentially constant. The etching with Ar^+ ions shows a decrease in the MnO(OH) concentration and a corresponding increase in the Mn_2O_3 concentration away from the surface. The relative areas of the peaks corresponding to Mn_2O_3, MnO(OH), and H_2O are plotted as a function of Ar^+ etching time in Fig. 11. The figure shows that the relative composition in the bulk of the electrode is almost identical to the as-prepared electrode. Thus, we conclude that the O_2 evolution and/or immersion of the electrode in aqueous solution converts Mn_2O_3 to MnO(OH) on the surface, but without affecting the bulk composition. Slightly higher concentration of water in these films as compared to as-prepared films is understandable, due to long time of immersion of these films in aqueous solution.

Conclusions

In conclusion, it has been shown that (*i*) n-Si electrode can be stabilized against photocorrosion under the condition of oxygen evolution for times of many months by chemically depositing a thin film of manganese oxide on the surface: (*ii*) the photocurrent is due to photogeneration of carriers in Si and not in Mn-oxide; (*iii*) Mn in Mn-oxide is in the +3 state, and the valence state is not changed by the photogenerated holes on the electrode surface, which only oxidize H_2O to O_2; and (*iv*) photoevolution of oxygen and/or immersion of the electrode in aqueous solution changes the surface to MnO(OH) without affecting the bulk composition.

Acknowledgments

The authors wish to thank the Electric Power Research Institute and the other sponsors of the Hydrogen Research Center, namely, the National Science Foundation, the Gas Research Institute, Koppers, and Standard Oil of Ohio, and Dr. Hampton Robinson for the support in developing hydrogen as a fuel.

Manuscript submitted April 15, 1985; revised manuscript received Aug. 26, 1985.

Texas A&M University assisted in meeting the publication costs of this article.

REFERENCES

1. Y. Nakato, T. Ohishi, and H. Tsubomura, *Chem. Lett.*, 883 (1975).
2. P. A. Kohl, S. N. Frank, and A. J. Bard, *This Journal*, **124**, 225 (1977).
3. R. Noufi, D. Tench, and L. F. Warren, *ibid.*, **127**, 2709 (1980).
4. T. Skotheim, I. Lundstrom, and J. Prejza, *ibid.*, **128**, 1625 (1981).
5. R. Noufi, A. J. Nozik, J. White, and L. Warren, *ibid.*, **129**, 2261 (1982).
6. F. R. F. Fan, G. A. Hope, and A. J. Bard, *ibid.*, **129**, 1647 (1982).
7. G. Cooper, R. Noufi, A. J. Frank, and A. J. Nozik, *Nature*, **295**, 578 (1982).
8. F. R. F. Fan, R. G. Keil, and A. J. Bard, *J. Am. Chem. Soc.*, **105**, 220 (1983).
9. Y. Nakato, A. Tsumura, and H. Tsubomura, *Chem. Lett.*, 1071 (1982).
10. G. Hodes, L. Thompson, J. Dubow, and K. Rajeshwar, *J. Am. Chem. Soc.*, **105**, 324 (1983).
11. T. Osaka, K. Ejiri, and N. Hirota, *This Journal*, **131**, 1571 (1984).
12. A. Q. Contractor and J. O'M. Bockris, *Electrochim. Acta*, **29**, 1427 (1984).
13. K. L. Chopra, R. C. Kainthla, D. K. Pandya, and A. P. Thakoor, "Physics of Thin Films," Vol. 12, p. 167, G. Hass, M. H. Francombe, and J. L. Vossen, Editors, Academic Press, New York (1982).
14. M. Szklarczyk and J. O'M. Bockris, *J. Phys. Chem.*, **88**, 1808 (1984).
15. S. M. Sze, "Physics of Semiconductor Devices," Chap. 7, John Wiley and Sons, New York (1981).
16. See, for example, M. P. Dave Edwards, A. Hamnett, and P. R. Trevellick, *J. Chem. Soc. Faraday Trans. 1*, **79**, 2111 (1983), and references therein.
17. M. P. Dave Edwards, A. Hamnett, and J. B. Goodenough, *J. Electroanal. Chem.*, **119**, 109 (1981).
18. J. F. McCann, Ph.D. Thesis, Flinders University of South Australia, Adelaide (1980).
19. K. Rajeshwar, L. Thompson, P. Singh, R. C. Kainthla, and K. L. Chopra, *This Journal*. **128**, 1744 (1981).
20. M. Oku, K. Hirokawa, and S. Ikeda, *J. Electron. Spectrosc. Relat. Phenom.*, **7**, 465 (1975).
21. J. C. Fuggle, in "Handbook of X-ray and Ultraviolet Photoelectron Spectroscopy," Chap. 8, D. Briggs, Editor, Heyden, London (1977).
22. R. Noufi, *This Journal*, **130**, 2126 (1983).

Corrosion Studies on Zinc in a Methanol/Water/Lithium Chloride/Oxygen System

J. Banaś,[1] K.-G. Schütze,[2] and E. Heitz

Dechema-Institut, Frankfurt/M., Germany

ABSTRACT

The corrosion of zinc displays different effects in methanolic and aqueous chloride solutions. Since there is no surface layer formation, corrosion takes place at a higher rate in methanol than in aqueous solutions. An evaluation of the polarization curves gives different kinetic parameters. The marked effect of chloride ions in methanol solutions is noticeable even in the ppm region, as well as the rise in acidity in aqueous solutions with a high chloride ion concentration. Small amounts of water in methanol have an inhibiting effect. At higher water content, the structure of the solution exerts an influence, and a corrosion rate maximum is reached in the region of 10 to 20 $moll^{-1}$. Zinc corrosion in ethanol is similar to that in methanol, but the rates are lower.

There is increasing interest in the corrosion of metals in systems with methanol as the principal solvent, with methanol becoming more significant as a fuel, for example as an alternative fuel for motor vehicles. Since zinc and zinc alloys are widely used materials in fuel systems the substitution of hydrocarbons by methanol is associated by a number of corrosion problems.

Corrosion processes in alcohols differ from the processes in aqueous media in a number of ways. Depending on the chain length of primary aliphatic alcohols, varying physicochemical characteristics are apparent. These include the dielectric constant, the dissociation equilibrium, and the solubility of the reactants and products of the corrosion reaction (1). It is important to note that some metals cannot passivate in nonaqueous solvents, a fact which has considerable influence on corrosion behavior (2, 4, 5).

Most corrosion studies have in the past concentrated on practical problems during methanol production and application. Mechanistic studies by electrochemical investigations have mainly been performed on ferrous materials and transition metals such as titanium and zirconium. To overcome the disadvantage of low conductivity in methanolic solutions, the majority of electrochemical tests have been performed with additions of inorganic acids such as HCl and H_2SO_4 or high concentrations of conducting salts (3-12). It should also be mentioned that combinations of electrochemical measurements with other methods such as mass loss measurements scarcely have been used. In one of the cited works, however, ellipsometric determination of film thickness as a function of the applied potential is described (11).

Despite these obvious limitations in methodology a number of useful conclusions have been drawn. The crucial role of water on passivity and passivity breakdown by pitting has been shown in the system titanium/methanol + water + HCl or H_2SO_4 (10, 12). Another study quoted in (9) investigates the influence of water and chlorides on the electrochemical behavior of ferrous materials in alcohols of differing structures, arriving at the following conclusions: (*i*) Iron does not passivate in anhydrous, oxygen free, $LiClO_4$ containing methanol. (*ii*) Water has a passivating effect in the system 304L stainless steel/methanol + HCl. (*iii*) Electrochemical processes in alcohol/water mixtures are more dependent on water concentration in less water-like alcohols.

Zinc and zinc alloys have not been subject of detailed mechanistic investigations. Only in Ref. (4) polarization curves in the system $Zn/CH_3OH + H_2O + HCl$ are cited which reveal that a rise in the water content increases the cathodic polarization but gives no change in anodic behavior.

The present study aims at obtaining quantitative data on free corrosion and the influence of low concentration of chlorides and water, as well as providing electrochemical information.

Since some of the systems under discussion showed a high ohmic potential drop which had to be eliminated, a computer-controlled interrupter method was developed.

[1]Present address: University of Mining and Metallurgy, Institute of Foundry Engineering, Krakow, Poland.
[2]Present address: Degussa AG, ZN Wolfgang, Abt. Forschung Chemie-PH/W, Hanau, Germany.

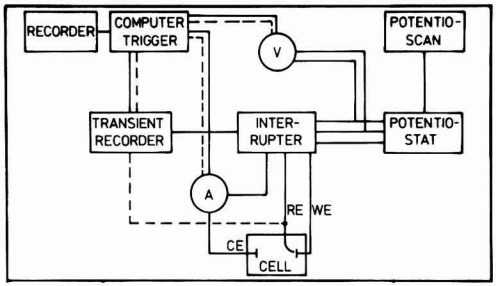


Fig. 1. Flow diagram of the computer-controlled measuring equipment used to eliminate ohmic potential drop.

Experimental

The experiments were carried out using polycrystalline pure zinc (99.999%). The test pieces were prepared by grinding with abrasive paper, rinsing in water-free ethanol and drying in air at room temperature. Nonaqueous methanol (<0.01% H_2O) and nonaqueous lithium chloride were used for the preparation of the solutions. The corrosion losses were determined analytically as the portion of the metal dissolved in the solution, using atomic absorption spectroscopy (AAS).

The electrochemical measurements were made using computer controlled measuring equipment as in Fig. 1. This consists basically of an electronic interrupter (own construction), a transient recorder (VuKO, VKS 22-16), and two digital multimeters (Keithley 179 A TRMS) for measuring the set voltage and current connected to the computer (Hewlett-Packard, HP 85) via a parallel interface. The potentiostat (Wenking LB 75 M) and set voltage generator (potentioscan, Wenking VSG 72) correspond to the instruments in common use for electrochemical measurement. The method is based on a setup which has been successfully used to eliminate ohmic potential drop at gas-evolving electrodes at high current densities (13) and will be described in detail elsewhere (14).

The reference electrodes used were silver/silver chloride electrodes placed in the corresponding electrolyte solution with reference to the SHE (omitting the diffusion potential). Unless otherwise stated, all the polarization curves were recorded using solutions gassed with nitrogen. The zinc test pieces were polarized cathodically (to about -1.3 V_{SHE}) immediately after immersion, and the current *vs.* potential curve recorded from this potential to the corrosion potential. This procedure was repeated three or four times, until the last two curves coincided. These curves were then evaluated. It is therefore safe to assume that the measurements were taken on an oxide-free metal surface. Fresh solutions were used for the anodic curves, and again the polarization curves were recorded three or four times.

The polarization curves have been taken potentiostatically point-to-point after having obtained a quasi steady state at each point.

Results and Discussion

Zinc in methanol/LiCl solutions.—Figure 2 gives the polarization curves for zinc in nonaqueous (<0.03% H_2O) methanol with the chloride concentration as a parameter.

The cathodic curves show a linear relationship between log i and the potential over a wide potential range, with a Tafel gradient of 120-130 mV. This curve corresponds to the reduction of methanol according to the following reaction

$$2CH_3OH + 2e^- \rightarrow 2CH_3O^- + H_2 \qquad [1a]$$

with the mechanism having the Volmer reaction as the rate-determining step. The influence of stirring in the region of low cathodic overpotential ($U < -1.1$V) can be interpreted as a reduction of solvated protons, as follows

$$2CH_3OH_3^+ + 2e^- \rightarrow 2CH_3OH + H_2 \qquad [1b]$$

The equilibrium potential of the anodic dissolution of zinc has highly negative values, so reaction [1a] is a cathodic reaction step in the corrosion process for zinc. In unstirred solution in particular, with the extremely low limiting current density of reaction [1b], reaction [1a] is the decisive factor.

The anodic portions of the polarization curves fan out in relation to the chloride content and show two Tafel regions at low chloride concentration, the larger with a slope of 35 to 40 mV and the smaller with 120 to 150 mV.

The reaction order with respect to the chloride ions is determined from the relationships between current den-

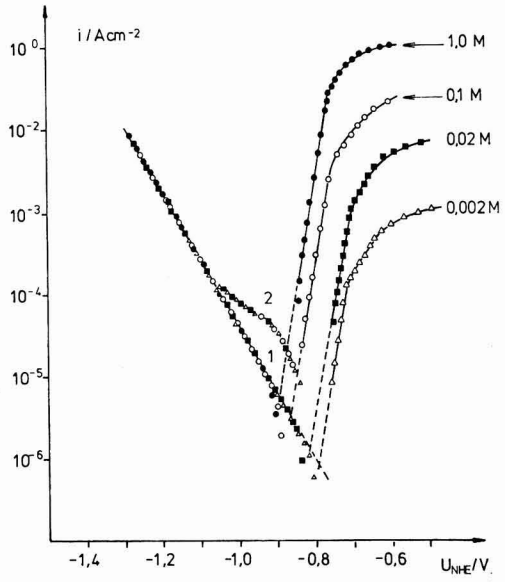


Fig. 2. Steady-state polarization curves for zinc in CH_3OH/LiCl, water free, gassed with N_2. 1, stirred; 2, unstirred.

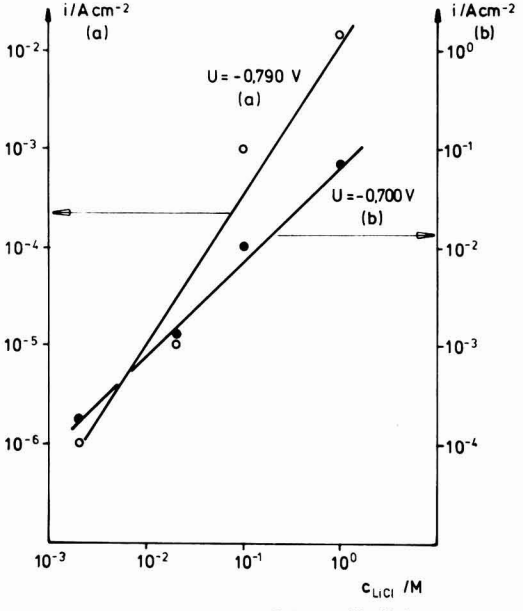


Fig. 3. Anodic current densities of zinc *vs.* chloride ion concentration at two potentials in methanol, nonaqueous, gassed with N_2.

sity and chloride ion concentration at two constant anodic potentials, as shown in Fig. 3. For the potential −0.790V (region of Tafel slope $b_+ = 40$ mV) the value for electrochemical reaction order $d \log i/d \log c$ is 1.5. The value of $d \log i/d \log c$ at a potential of −0.700V ($b_+ = 120$ mV) is 1.0. Stirring has no effect anywhere in the potential range.

The kinetic data obtained are similar to the data for aqueous solutions of complexing agents (15), in which the dissolution of zinc takes place via intermediate compounds of monovalent zinc (15-18). In contrast to this, the electrochemical reaction order with respect to chloride for iron in methanol with HCl content was found to be 1.82 (7). The results under discussion are therefore best interpreted as a succession of anodic steps, as follows

$$Zn + Cl^- \rightarrow ZnCl_{ads}^- \quad [2a]$$

$$ZnCl_{ads}^- \rightarrow ZnCl_{ads} + e^- \text{ (rate determining)} \quad [2b]$$

$$ZnCl_{ads} + Cl^- \rightarrow Zn^{2+} + 2Cl^- + e^- \quad [2c]$$

or

$$Zn + Cl^- \rightarrow ZnCl_{ads}^- \quad [2d]$$

$$ZnCl_{ads}^- \rightarrow ZnCl_{ads} + e^- \quad [2e]$$

$$ZnCl_{ads} + Cl^- \rightarrow ZnCl_2 + e^- \text{ (rate determining)} \quad [2f]$$

$$ZnCl_2 \rightarrow Zn^{2+} + 2Cl^- \quad [2g]$$

The reaction steps [2a] to [2c] would indicate a first-order reaction with respect to chloride ions, whereas [2d] to [2g] indicate a second-order reaction. Within these two limiting cases the reaction orders obtained in the present study have to be placed.

It should also be noted that the polarization curves were plotted at different ionic concentrations, which could falsify the kinetic data such as Tafel slopes and reaction orders.

Extrapolation of the Tafel lines in Fig. 2 gives corrosion potentials and corrosion current densities, and these are compared in Fig. 4 and 5 with the data from experiments with free corrosion and analytically determined zinc concentration. The results are sufficiently similar, taking into account the fact that the measurements were obtained under different conditions: (i) condition of surface after 4h free corrosion, and (ii) condition after repeated polarization curve measurements.

For the kinetic parameters from Fig. 2, $b = 120$ mV, $b_+ = 40$ mV, and for $d \log i_a/d \log c = 1.5$, the relationship between the corrosion potential and the log of the chloride ion concentration $dU_{corr}/d \log c$ should equal −45 mV.

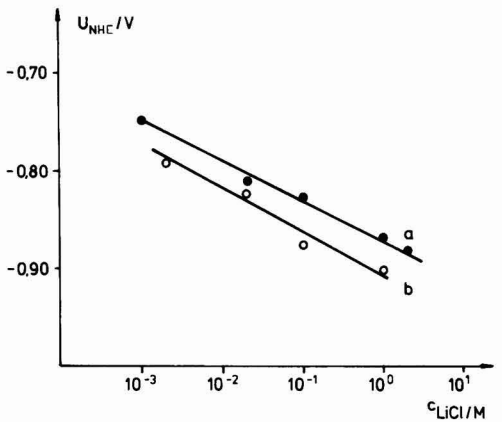


Fig. 4. Corrosion potential of zinc vs. chloride ion concentration in CH_3OH/LiCl, gassed with N_2. (a) After 4h free corrosion and (b) by extrapolation of the Tafel gradients in Fig. 2.

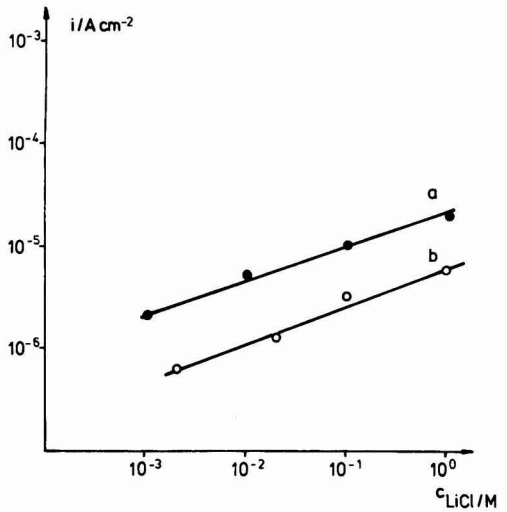


Fig. 5. Corrosion current densities of zinc vs. chloride ion concentration in CH_3OH/LiCl, water free, gassed with N_2. (a) After 4h free corrosion and (b) by extrapolation of the Tafel lines in Fig. 2.

This value is in accordance with the relationship $dU_{corr}/d \log c = -44$ mV obtained from free corrosion experiments (Fig. 4). The relationship $d \log i/d \log c$ also shows a good correlation. The values for free corrosion give 0.34, whereas the value obtained from kinetic parameters reaches 0.38.

All the experimental evidence indicated that there is no surface layer formation in methanol solutions.

Zinc in H_2O/LiCl solution.—The following corrosion experiments in aqueous solutions provide a basis for comparison with methanol solutions. As shown in Fig. 6, the corrosion rate rises with increasing chloride ion concentration and with stirring. In contrast to the experiments with methanol solutions (Fig. 13, upper line), however, the corrosion rate decreases with time (exception: 2*M* LiCl).

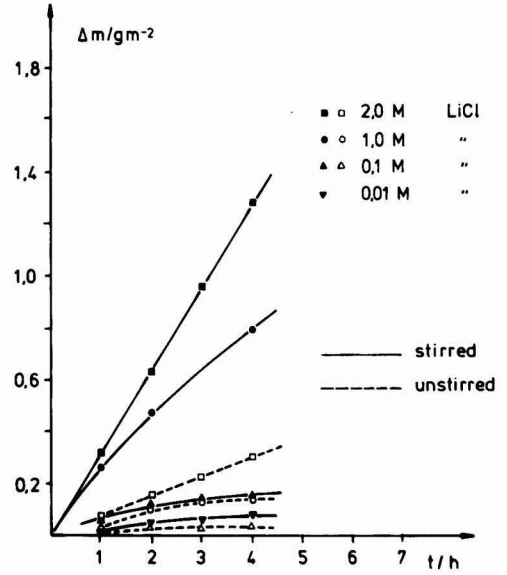


Fig. 6. Mass loss of zinc vs. time in aqueous solutions of LiCl, gassed with N_2.

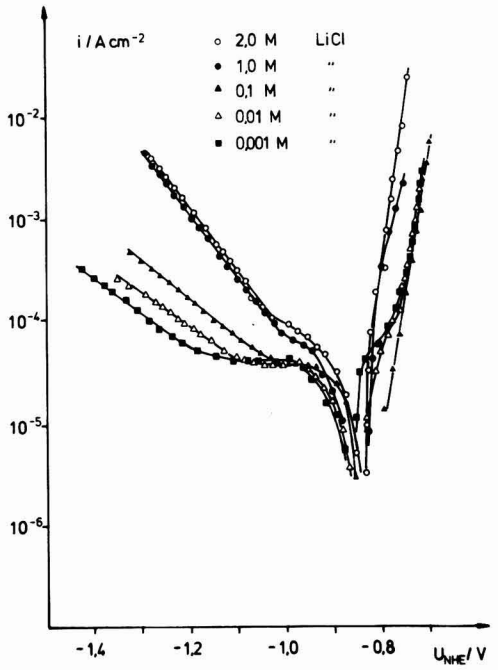


Fig. 7. Steady-state polarization curves for zinc in H_2O/LiCl, gassed with N_2.

The decrease in the corrosion rates with time can be explained by the passivating effect of hydroxide ions. As the equilibrium potential Zn/Zn^{2+} is highly negative (for $c_{Zn^{2+}} = 10^{-6}$ moll^{-1}, $U_{Zn/Zn^{2+}} = -0.943$V), the reduction of water can take place on the pure zinc surface. Hydroxide ions are a product of this reaction, and form hydroxide layers with the zinc ions.

The shape of the polarization curves points to the formation of surface layers (Fig. 7). In the anodic region a plateau occurs in dilute solutions, whereas the cathodic

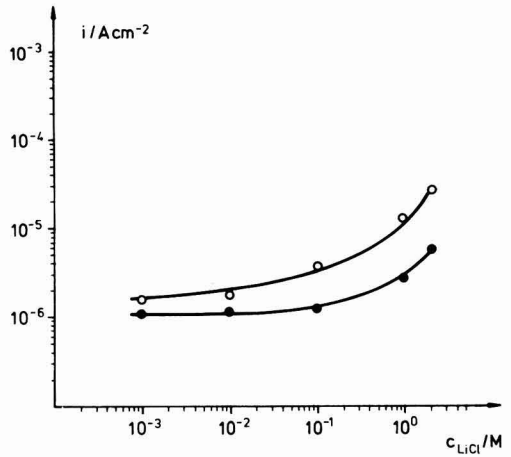


Fig. 9. Corrosion current density (from analysis of Zn^{2+}) with relation to LiCl concentration in aqueous solutions, gassed with N_2. ○ Stirred and ● unstirred.

curves show Tafel slopes beween 150 and 250 mV, indicating the presence of surface layers. The existence of oxide/hydroxide layers on zinc surfaces in neutral solutions is confirmed by the literature (19-22).

In the concentrated solutions (1 to 2 moll^{-1}) the hydroxide layer more or less dissolves, and the kinetic parameters of zinc dissolution approach the parameters of zinc dissolution in methanol solutions. This is probably attributable to a rise in hydrogen ion activity with increasing salt concentration, as shown in Fig. 8. Above a chloride ion concentration of 10^{-1} moll^{-1} there is a rise in hydrogen ion activity and corrosion potential. A similar relationship, qualitatively speaking, appears when the corrosion rate (given as corrosion current density) is plotted against the LiCl concentration (Fig. 9).

Comparison of corrosion rates in Fig. 9 with corrosion rates from polarization curves in Fig. 7 give sufficient agreement in those cases in which the anodic Tafel lines can be extrapolated to the corrosion potential. This is the case for LiCl concentrations larger than 0.1*M*. Generally, extrapolation of Tafel lines is prevented by the formation of surface layers which give curved Tafel lines.

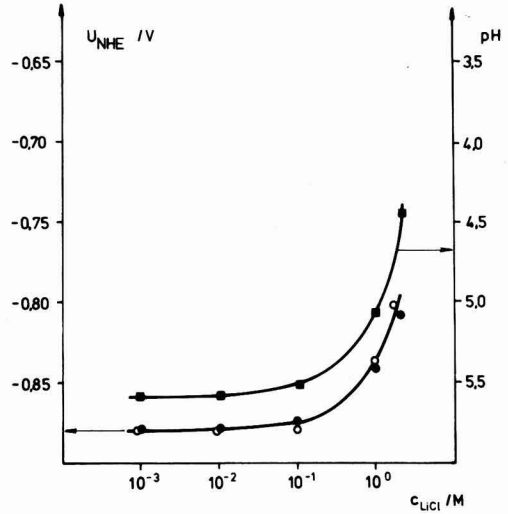


Fig. 8. Graph of corrosion potential (○, ●) and pH (□) values vs. LiCl concentration in aqueous solutions, gassed with N_2.

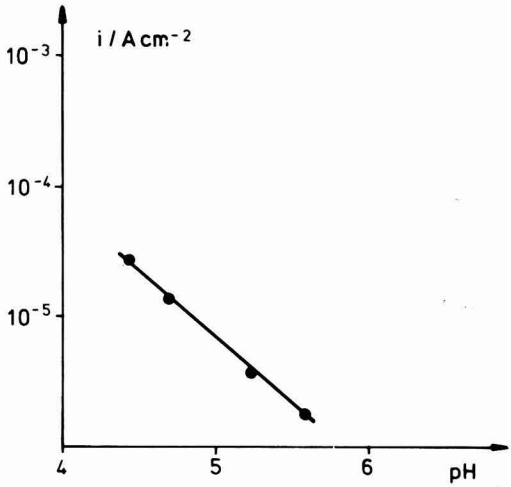


Fig. 10. Graph of corrosion current density vs. pH value of aqueous LiCl solutions gassed with N_2, stirred.

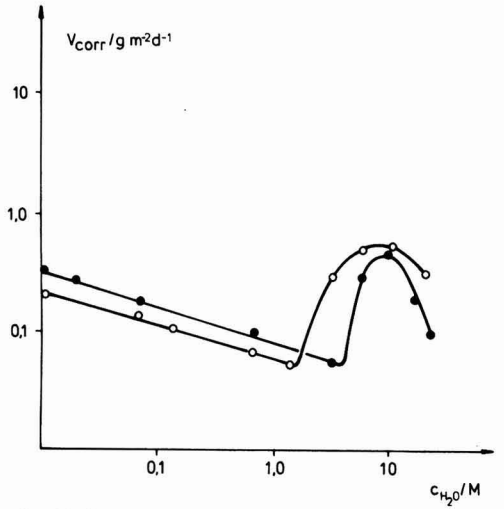


Fig. 11. Corrosion rates for zinc in methanol solutions of differing water content, 50 ppm LiCl. ● Gassed with nitrogen and ○ gassed with oxygen.

Figure 10 gives the curve for corrosion current density *vs.* pH value. The value of $d \log i_{corr}/d\text{pH}$ is -1. This indicates that the corrosion of zinc is controlled by the cathodic reduction of hydrogen ions. In the pH region under discussion, this process is dependent on the convective diffusion of the hydrogen ions (23-25), so the corrosion of zinc in aqueous solutions of lithium chloride is dependent on stirring (Fig. 9).

According to Schwabe, the decrease in pH value with salt concentration can be explained by a rise in the activity coefficient of the H^+ ions (26, 27). The effect is particularly apparent in the presence of lithium ions, because of their high charge density.

To summarize, the dominant factor in the case of free corrosion for the cathodic partial steps is the evolution of hydrogen from H_2O in dilute (aqueous) solutions, and from H_3O^+ in concentrated solutions. The anodic intermediate steps are influenced mainly by the simultaneous cathodic formation of hydroxide ions and the resulting surface layers.

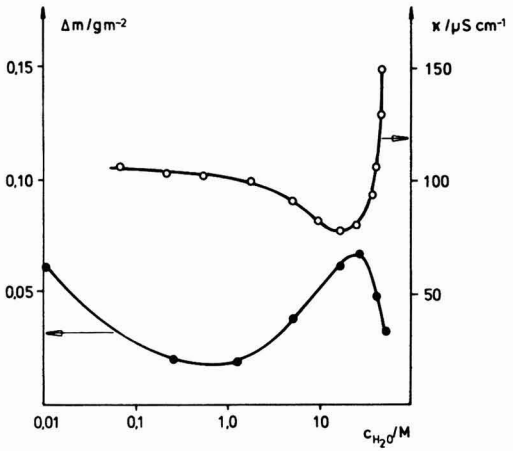


Fig. 12. Relationship of mass loss and conductivity to water content in methanol with 50 ppm LiCl, gassed with N_2, duration of experiment 4h.

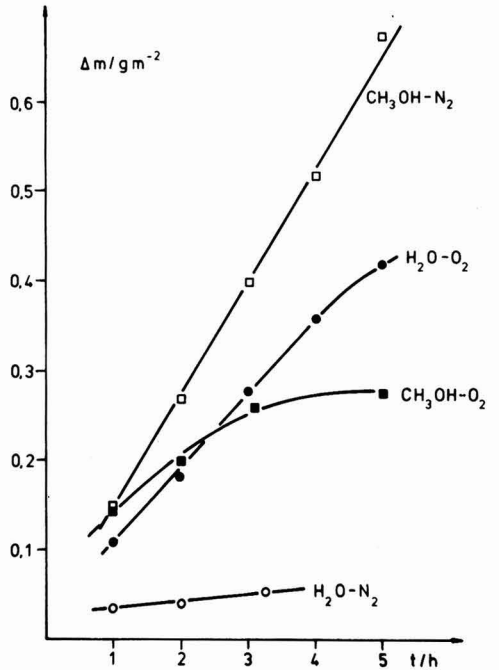


Fig. 13. Mass loss of zinc in methanolic and aqueous solutions with and without oxygen, 50 ppm Cl^-.

Zinc in CH_3OH/H_2O/LiCl solutions.—Influence of oxygen.—The corrosion behavior of zinc in CH_3OH/H_2O mixtures is of theoretical and practical relevance. The results are given in Fig. 11 as a graph of corrosion rate *vs.* water concentration in methanol (technical grade) at a constant LiCl concentration of 1.5×10^{-3} moi^{-1} (50 ppm). The analyses of the curve is complex, in solutions with low concentrations of water, the water has an inhibiting effect (up to about 1 moll^{-1}); at higher concentrations a

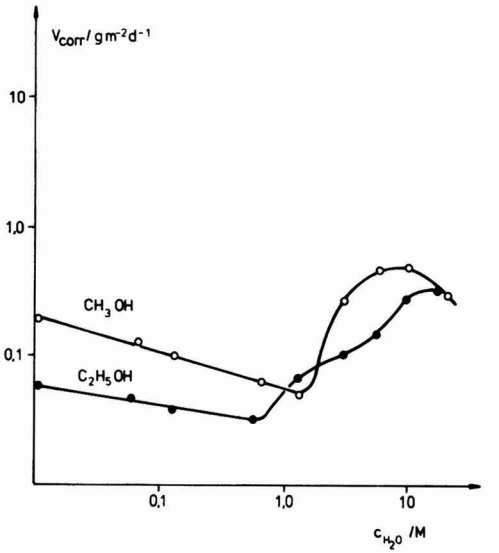


Fig. 14. Corrosion rates for zinc in CH_3OH/H_2O/50 ppm Cl^- and C_2H_5OH/H_2O/50 ppm Cl^-; duration of experiment 48h, gassed with oxygen.

Table I. Comparison of partial reactions in methanolic and aqueous solutions

Components	CH_3OH	H_2O
Gassed with nitrogen	Cathodic (C): $2CH_3OH + 2e^- \rightarrow 2CH_3O^- + H_2$ Anodic (A): $Zn \rightarrow Zn^{2+} + 2e^-$ No layer formation	C: $2H_2O + 2e^- \rightarrow 2\,OH^- + H_2$ A: $Zn \rightarrow Zn^{2+} + 2e^-$ Layer formation: $Zn^{2+} + 2\,OH^- \rightarrow Zn(OH)_2$
Gassed with oxygen	C: $1/2\,O_2 + CH_3OH + 2e^- \rightarrow CH_3O^- + OH^-$ A: $Zn \rightarrow Zn^{2+} + 2e^-$ Inhibition by layer formation: $Zn^{2+} + 2\,OH^- \rightarrow Zn(OH)_2$	C: $1/2\,O_2 + H_2O + 2e^- \rightarrow 2\,OH^-$ A: $Zn \rightarrow Zn^{2+} + 2e^-$ Stimulation by layer dissolution: $Zn^{2+} + 2\,OH^- \rightarrow Zn(OH)_2$ $Zn(OH)_2 + 2\,OH^- \rightarrow Zn(OH)_4^{2-}$
Chloride ions	Anodic stimulation (also in ppm region) No cathodic effect	Cathodic stimulation Weak anodic effect

rise in the rate of dissolution can be observed with increasing water content; at water concentration of about 10 $moll^{-1}$ the rate of dissolution reaches a maximum. Alongside an acidity maximum (27), a maximum of the interaction effect between methanol and water molecules can be observed at these concentrations. This results in a strengthening of the structure of the electrolyte. An example is given in Fig. 12, where mass loss and conductivity are plotted against the concentration of water. The two effects counteract each other. Other physicochemical characteristics of the methanol/water system reach a minimum at this concentration, such as mole volume and solvation enthalpy (28-30). The corrosion rate maximum in this region could be attributed to a minimum in the solvation enthalpy of the proton, which is necessary for the cathodic partial step.

The effect of oxygen is different. It inhibits corrosion at low water concentrations and stimulates it at high ones (Fig. 11). This can be seen more clearly in Fig. 13. In the oxygen-free methanol solution the value of the corrosion rate is constantly high, decreasing in the presence of oxygen. This is related to the formation of surface layers.

In aqueous solutions, the presence of oxygen has the reverse effect. The cathodic reduction of oxygen causes a strong alkalization of the surface, resulting in the dissolution of the passive layer.

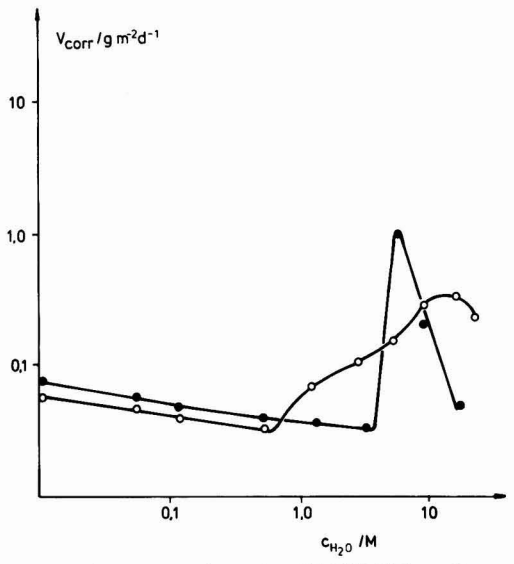


Fig. 15. Corrosion rates for zinc in a C_2H_5OH/H_2O/50 ppm Cl^- system; duration of experiment 48h. ● Gassed with nitrogen and ○ gassed with oxygen.

Exploratory Experiments in Ethanol Solutions

Figure 14 shows the results of experiments in methanol and ethanol of varying water content with the addition of 50 ppm Cl and gassed with oxygen. Similar behavior may be observed in both media, except that the corrosion rates are low in ethanol, as expected. Figure 15 gives the results from experiments with and without oxygen. As is the case for methanol solutions (Fig. 11) the oxygen inhibits its corrosion in ethanol solutions with low water content and stimulates it in solutions with high water content.

Anodic and Cathodic Partial Reactions and Conclusions

In Table I the anodic and cathodic partial reactions in methanol and water are compared. Main differences in oxygen free solutions are the nature of the cathodic partial step (different proton donors) and the layer formation capability. In presence of air both reactions in methanol and in water lead to the formation of surface layers. With regard to corrosion rates oxygen has an opposite effect. In methanol solutions it decreases and in aqueous solutions it increases the corrosion rates. Also chloride ions influence the partial reactions in a different way. In methanol solutions they stimulate the anodic and in aqueous solution the cathodic step.

The various effects of the zinc corrosion parameters can be summarized as follows:

1. In nonaqueous methanol solutions the zinc surface remains free of surface layers; in aqueous solutions oxide/hydroxide surface layers are formed.

2. The evolution of hydrogen in methanol is less kinetically controlled than in water. The corrosion rates in methanol solutions are thus higher than in aqueous solutions.

3. Chlorides have an anodically stimulating effect in methanol; they have no cathodic effect. In water chlorides influence the surface layers, as is particularly evident from the cathodic polarization curves. With rising chloride ion concentrations the acidity of the aqueous solution increases, and with it the corrosion rates. Chloride ion concentrations in the ppm region have a marked effect in methanol solutions ($d \log i_{corr}/d \log c_{LiCl} = 0.34$), but not in aqueous solutions.

4. Small amounts of water, as well as the presence of oxygen, have an inhibiting effect on the dissolution of zinc in methanol solutions. At water concentrations <1 $moll^{-1}$ the corrosion rate of zinc is dependent on the structure of the solution. At water concentrations in the region 10-20 $moll^{-1}$ the methanol/water interaction reaches a maximum. This strengthening of the structure causes an increase in the activity of hydrogen ions, and the rate of dissolution reaches maximum values.

5. Zinc displays similar corrosion behavior in the ethanol/water/50 ppm LiCl system to that in methanol/water/50 ppm LiCl.

Acknowledgments

This work was carried out with the financial aid of the research program on corrosion and corrosion prevention of the Bundesministerium für Forschung und Technologie (Project management: DECHEMA, Frankfurt) and by the Alexander von Humboldt Foundation (for J. B.), which is gratefully acknowledged.

Manuscript submitted July 9, 1985; revised manuscript received Oct. 17, 1985.

REFERENCES

1. E. Heitz, in "Advances in Corrosion Science and Technology," M. Fontana and R. Staehle, Editors, Vol. 4, Plenum Press, New York (1974).
2. K. Schwabe, S. Hermann, and W. Oelssner, in "Passivity of Metals," R. P. Frankenthal and J. Kruger, Editors, p. 413, The Electrochemical Society, Princeton, NJ (1978).
3. C. Farina, G. Faita, and F. Olivani, *Corros. Sci.*, **18,** 465 (1978).
4. P. Hronsky, *Werkst. Korros.*, **31,** 619 (1980).
5. B. Elsener, H. Böhni, and P. Hronsky, *ibid.*, **33,** 213 (1982).
6. Z. Szklarska-Smialowska and J. Mankowski, *Corros. Sci.*, **22,** 1105 (1982).
7. S. Sternberg and V. Branzoi, *Electrochim. Acta*, **29,** 15 (1984).
8. Y. Roques, G. Mankowski, G. Chatainier, and F. Dabosi, *Corrosion*, **40,** 561 (1984).
9. P. L. DeAnna, *Corros. Sci.*, **25,** 43 (1985).
10. F. Mansfeld, *This Journal*, **118,** 1412 (1971).
11. T. Smith and F. Mansfeld, *ibid.*, **119,** 663 (1972).
12. F. Mansfeld, *ibid.*, **120,** 188 (1973).
13. M. Kuhn, G. Kreysa, and B. Haakanson, Proc. 34th ISE-Meeting, Abstract 0539, Erlangen, 1983.
14. M. Kuhn, K.-G. Schütze, G. Kreysa, and E. Heitz, Dechema Monograph Vol. 103, 1985, In press.
15. K. E. Heusler and R. Knödler, *Electrochim. Acta*, **13,** 855 (1973).
16. L. Gaiser and K. E. Heusler, *ibid.*, **15,** 161 (1970).
17. C. Cachet and R. Wiart, *J. Electroanal. Chem.*, **111,** 235 (1980).
18. C. Cachet and R. Wiart, *ibid.*, **129,** 103 (1981).
19. L. M. Bough, *Electrochim. Acta*, **24,** 657 (1979).
20. K. G. Boto and L. F. G. Williams, *J. Electroanal. Chem.*, **77,** 1 (1970).
21. L. M. Bough, R. J. Field, and J. A. Lee, *Electrochim. Acta*, **25,** 751 (1980).
22. L. M. Bough, F. L. Tye, and N. C. White, *J. Appl. Electrochem.*, **13,** 623 (1983).
23. Z. Zembura and L. Burzyńska, *Corros. Sci.*, **17,** 871 (1977).
24. J. Sedzimir and M. Gmytryk, Extended Abstract of Papers presented at 2nd International Congress of Metallic Corrosion, New York, 1963.
25. M. Gmytryk and J. Sedzimir: Sci. Bull. Univ. of Mining and Metallurgy 201, Kraków (1969).
26. H. Kelm and K. Schwabe, *Z. Phys. Chem. (Leipzig)*, **255,** 3, 475 (1974).
27. K. Schwabe, *Österr. Chem. Ztg.*, **65,** 11, 339 (1964).
28. K. Schwabe, *Ber. Sächs. Akad. Wissenschaften Leipzig*, **109,** 6 (1972).
29. M. A. Neidig, R. T. Yinking, K. L. Lockwood, and T. G. Tates, *J. Chem. Educ.*, **42,** 309 (1965); **42,** 7, 369 (1965).
30. K. P. Mischenko, G. M. Poltoratskii, "Termodinamika i stroenie vodnych i nevodynch rastvorov i elektrolitov" Chimija, Leningrad (1976).

Cathodic Polarization Behavior of Ag-Al_2O_3 Electrode in Silver Thiocyanate Solution Containing Al_2O_3 Particles

Y. Suzuki,* M. Wajima, and O. Asai

Hitachi Research Laboratory, Hitachi, Limited, 4026, Ohmika, Kujimachi, Hitachi, Ibaraki, Japan

ABSTRACT

Mechanisms for the codeposition of Al_2O_3 particles from silver thiocyanate solution have been investigated. The codeposition rate of Al_2O_3 onto composite coatings was found to increase with slight agitation near the cathode surface and with larger cathodic overvoltages. The actual cathodic current density was smaller, at low overvoltage, for solutions containing Al_2O_3 than for those without it. However, the opposite was true at high overvoltage. On the basis of the experimental results, it was felt that Al_2O_3 dispersion particles suppressed the electrodeposition reaction of silver, since the particles were absorbed on the cathode at low overvoltage. Stirring near the electrode surface promoted the reactions.

Composite coatings deposited from solutions containing insoluble particles have been studied to improve the characteristics of deposits (1, 2), and several theories for codeposition mechanisms have been proposed (3-8). However, there is no uniform theory, in part because it is difficult to investigate quantitatively the codeposition state of dispersion particles.

This paper describes results of mechanism studies for particles codeposited from solutions containing insoluble particles. The results were obtained from cathodic polarization curves measured in the stationary state.

Experimental

The plating solution was a silver thiocyanate bath and had the following composition: AgSCN, 0.18*M*; KSCN, 3.00*M*; KI, 200 μM; and Al_2O_3, 100 g/l, (Al_2O_3: mean size, 2.0 μm; density, 3.9 g/cm^3). The tests were conducted at 30.0° ± 0.1°C and the solution pH was adjusted to 7.0 using NaOH. The starting cathode was Ag, which was electrodeposited on a rolled Pt foil from the silver thiocyanate bath at an overvoltage (ΔE) of −0.037V. The mean deposit thickness was 2 μm. One side of the cathode was covered with a polyester tape. The anode, made of Ag foil (purity: 99.99%), was also masked in the same way. The electrodes were mounted on the inner wall of the cell using the polyester tape (thickness: 100 μm). The electrode surfaces were in the same plane as the inner wall surface of the cell.

The flow velocity of the plating solution was set at 5 or 40 cm/s with a pump. All solutions were deoxygenated with Ar (99.999%) for 30 min before the measurements were made and during them. The electrochemical characteristics of Ag and Ag-Al_2O_3 electrodes were studied in the cell shown in Fig. 1. A potentiostat (Hokuto Denko Company, Type HA-303) was used to control the electrode potential. A saturated calomel electrode was used as the reference electrode. The scan rate of the electrode potential was 0.020 V/min. The Ag-Al_2O_3 composite coatings were dissolved with HNO_3 to determine their Ag content, and then the solutions were diluted with distilled water before their Ag^+ ion concentration was measured by atomic absorption. The Al_2O_3 content of the coatings was determined by subtracting the weight of Ag from the total coating weight.

Results

Curves showing current density (i) *vs.* overvoltage (ΔE) on the Ag electrode in solutions with and without Al_2O_3

*Electrochemical Society Active Member.

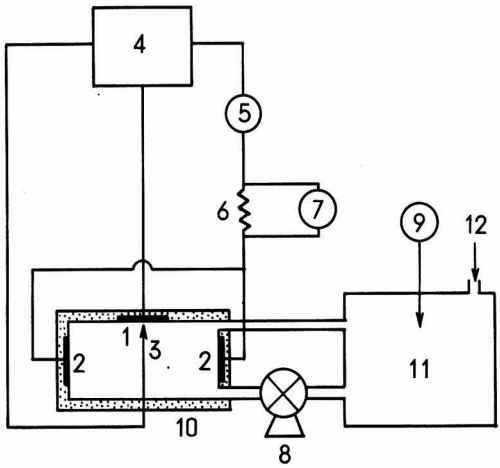


Fig. 1. Apparatus for the electrodeposition of composite coatings and polarization measurements: 1: cathode; 2: anode; 3: reference electrode; 4: potentiostat; 5: coulometer; 6: resistor; 7: recoder; 8: recirculating pump; 9: thermostat; 10: electrolytic cell; 11: preliminary tank; 12: Ar gas inlet.

are plotted in Fig. 2 for a nonstationary state. The amount of polarization with Al_2O_3 is larger than it is without it at low overvoltage. The relation is independent of the flow velocity (v) of the solution on the electrode surface. In the region of high overvoltage, the amount of polarization on the Ag electrode in the solution containing Al_2O_3 is larger than that in the solution without it if the solution flow velocity near the electrode surface is slow. However, the relation between the former and the latter is reversed if the flow velocity is faster. Accordingly, it is difficult to examine closely codeposition mechanisms of Al_2O_3 during electrodeposition in the nonstationary state.

Therefore, we examine the relation between cathodic polarization characteristics of Ag deposition and that of Ag-Al_2O_3 codeposition in the stationary state. Figure 3 shows profiles of current density *vs.* charge (q) under potentiostatic conditions at a surface flow velocity of 5 cm/s. Figure 4 shows the profiles where the velocity is 40 cm/s. The solid lines indicate the profiles obtained for current density *vs.* charge in solutions without Al_2O_3, while the dashed lines correspond to solutions containing 100 g/l of Al_2O_3.

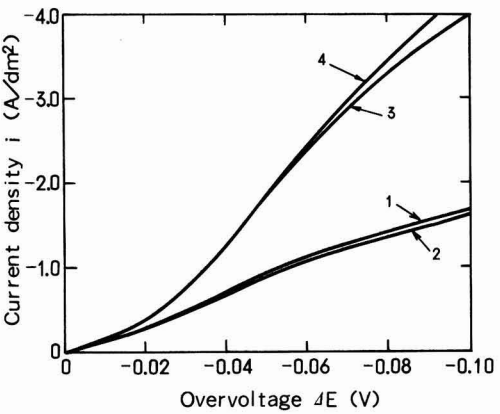


Fig. 2. Effects of agitation on the cathodic polarization during electrodeposition of Ag coatings and Ag-Al_2O_3 composite coatings: 1: Al_2O_3 = 0 g/l, v = 5 cm/s; 2: Al_2O_3 = 100 g/l, v = 5 cm/s; 3: Al_2O_3 = 0 g/l, v = 40 cm/s; 4: Al_2O_3 = 100 g/l, v = 40 cm/s.

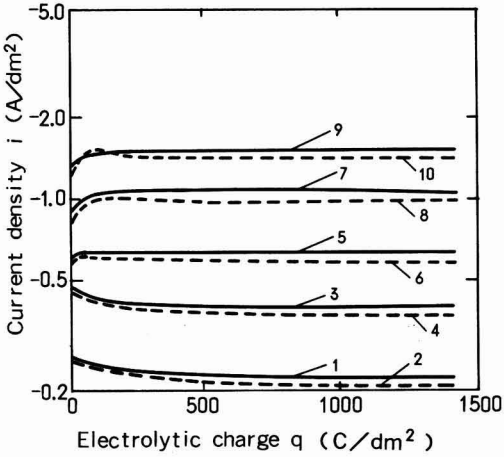


Fig. 3. Relation between current density and electrolytic charge consumed by coating. v = 5 cm/s: solid line: Al_2O_3, 0 g/l; dashed line: Al_2O_3, 100 g/l. Overvoltage (ΔE): 1, 2: −0.017V; 3, 4: −0.027V; 5, 6: −0.037V; 7, 8: −0.057V; 9, 10: −0.087V.

The cathodic current density becomes larger at the start of the electrolysis as Al_2O_3 is added to the silver thiocyanate solution in the overvoltage region of −0.057 to −0.087V. The effect of flow velocity near the electrode surface on the relationship is very slight. When the cathodic charge is increased, the cathodic current density decreases monotonously and independently of added Al_2O_3 in the overvoltage region of −0.017 to −0.027V in Fig. 3 and 4. Changes in cathodic current density *vs.* cathodic charge are small at the overvoltage of −0.037V. From −0.057 to −0.087V, cathodic current density in the solution containing Al_2O_3 has a maximum value at 100 C/dm². After 500 C/dm², it has a nearly constant value. Cathodic current density reaches a stationary state at 1000 C/dm² and overvoltage of −0.017V, and at 500 C/dm² and −0.027V. These results suggest that the polarization curves in Fig. 2 are measured in a nonstationary state at overvoltages of 0.0 to −0.087V. Generally, at the time of metal deposition on the cathode, crystallization nuclei are formed there, and the metals deposit on them. A maximum is frequently observed in curves of current density

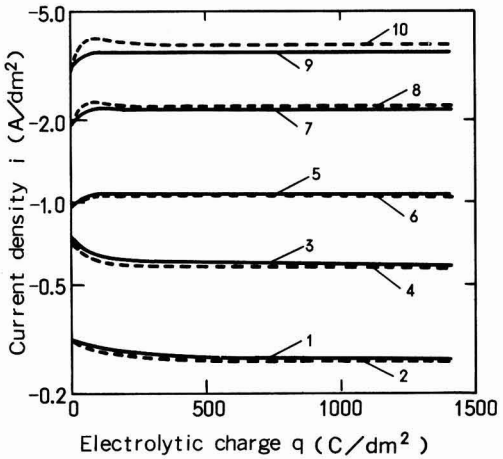


Fig. 4. Relation between current density and electrolytic charge consumed by coating. v = 40 cm/s: solid line: Al_2O_3, 0 g/l; dotted line: Al_2O_3, 100 g/l. Overvoltage (ΔE): 1, 2: −0.017V; 3, 4: −0.027V; 5, 6: −0.037V; 7, 8: −0.057V; 9, 10: −0.087V.

vs. time obtained by chronoamperometry (9, 10). Such maxima disappear at small charges (<<1 C/dm²). Reasons proposed to explain such behavior are the low diffusion rate of ions taking part in the cathodic reaction on the electrode surface and changes in the ion concentrations with the charge. However, the charge required for the maxima to disappear in Fig. 3 and 4 is above 100 C/dm². Accordingly, it is difficult to attribute this disappearance in the solution containing Al_2O_3 to the above reasons only. Additional reasons must be put forth.

Budevski *et al.* have examined cathodic polarization behavior of single crystalline Ag, without any defects, in a solution of 6*N* $AgNO_3$ (11). The single crystalline Ag acted as an ideal polarization electrode at overvoltages from 0.0 to −0.010V; above −0.010V, two-dimensional nuclei form on the electrode, and a faradaic reaction occurs. Vermilyea has examined the cathodic polarization characteristic of a copper whisker electrode in copper sulfate solution (12). He indicated that the faradaic reaction was almost nonexistent in the range of overvoltages from 0.0 to −0.100V, but that it occurred when nuclei were formed above those values. It appeared that dislocations were nonexistent in copper whisker (13). Haruyama and Kaneko have reported that the apparent exchange current density was 3×10^{-4} A/dm² at 20°C for a copper whisker electrode, which was about 10^{-3} as much as that for polycrystalline copper electrode (14). Kita *et al.* have reported that the number of effective steps for crystal growth increased abruptly with increasing overvoltage (15).

Silver electrodeposition coatings at the overvoltage of −0.037V from thiocyanate solutions are used as substrate in Fig. 3 and 4. If Ag-Al_2O_3 composite coatings are formed at overvoltages above −0.037V, the numbers of crystal nuclei and defects increase with increased charge. Consequently, cathodic current density increases. On the other hand, if Ag-Al_2O_3 composite coatings are formed at overvoltages below −0.037V, the numbers of crystal nuclei and defects decrease with increased charge, and cathodic current density decreases. The figures show that, for low overvoltages, a large charge is needed to reach stationary values for the cathodic current densities. It is assumed that this is related to the crystals electrodeposited at low overvoltage, which grow to a larger size than those deposited at high overvoltage.

Figure 5 shows the surface morphology of Ag-Al_2O_3 composite coatings. Part of the surface of Ag-Al_2O_3 codeposits is covered by codeposited Al_2O_3.

Naitoh obtained the actual surface area contribution to the electrode reaction using Saifullin's equation (16). In accordance with the equation, the surface area covered by codeposited particles is obtained by assuming that the particles are spherical, that they occupy all the corner sites of a cube, and that the sphere centers exist on the surface of the deposits. But, for a surface area covered by codeposited particles, it seems better to assume that each of the spheres exists on the surface of deposits in an averaged distribution.

Then, we obtain the ratio ($R_{Al_2O_3}$) between the surface area covered by codeposited Al_2O_3 to the apparent surface area

$$R_{Al_2O_3} = V_{Al_2O_3}/(V_{Ag} + V_{Al_2O_3}) \quad [1]$$

where $V_{Al_2O_3}$ and V_{Ag} are the volumes of Al_2O_3 and Ag codeposited in a unit volume, respectively. The actual cathodic current density ($i_{ac(Ag\text{-}Al_2O_3)}$) is obtained with [2]

$$i_{ac(Ag\text{-}Al_2O_3)} = i_{ap(Ag\text{-}Al_2O_3)}/(1 - R_{Al_2O_3}) \quad [2]$$

where $i_{ap(Ag\text{-}Al_2O_3)}$ is the apparent cathodic current density. Figure 6 shows the relation between $R_{Al_2O_3}$(%) and electrolytic charge at different overvoltages. The ratios become larger than the flow velocity near the electrode surface is slower or the cathodic current density is larger. The actual cathodic current density is calculated by consideration of the area covered by Al_2O_3 and using the results of Fig. 3, 4, and 6. Figure 7 shows the relations between the actual cathodic current density and electrolytic charge for different overvoltages. The maxima at the start of electrodepositing for high overvoltages from −0.057 to −0.087V in solution containing Al_2O_3 seen in Fig. 3 and 4 are not observed in Fig. 7. Accordingly, the reasons why the maxima are seen in Fig. 3 and 4 are as outlined below: (*i*) many nuclei and defects appear on the crystal surface as growth progresses, and (*ii*) the effective surface area of the electrode reaction decreases with codeposition of Al_2O_3. The effect of item (*i*) is greater than (*ii*) at the start of electrodeposition. However, the latter becomes greater as the reaction progresses. The low codeposition ratio of Al_2O_3 in the initial stage can be attributed to the deposit being too thin to hold the Al_2O_3.

The effects of Al_2O_3 on Ag electrodeposition reaction in the stationary state are investigated next. Figures 3 and 4 indicate that the reactions between the cathodic current density and charge reach the stationary state at 1000 C/dm². Figure 6 indicates that the relation between ratio of codeposited Al_2O_3 and charge also reaches the stationary state at 1000 C/dm². Then relationships to overvoltage between the ratios of both apparent and actual cathodic current densities ($i_{ap(Ag\text{-}Al_2O_3)}$ and $i_{ac(Ag\text{-}Al_2O_3)}$) in the solution containing Al_2O_3 to cathodic current density in the solution without Al_2O_3 (i_{Ag}) are examined at 1000 C/dm². Figure 8 shows the relation between $\Delta i_{ap}/|i_{Ag}|$($\Delta i_{ap} = |i_{ap(Ag\text{-}Al_2O_3)}| - |i_{Ag}|$) and ΔE (dashed line) and the relation between $\Delta i_{ac}/|i_{Ag}|$ ($\Delta i_{ac} = |i_{ac(Ag\text{-}Al_2O_3)}| - |i_{Ag}|$) and ΔE (solid line).

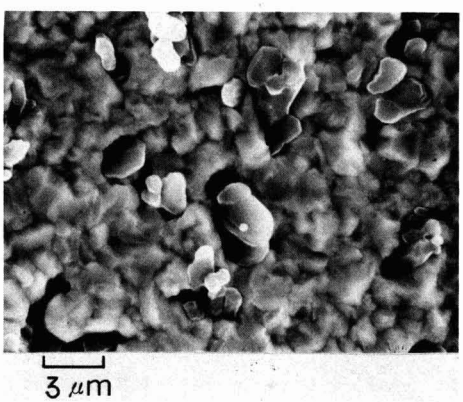


Fig. 5. Surface morphology of Ag-Al_2O_3 composite coating. ΔE: −0.057V; *v*: 5 cm/s.

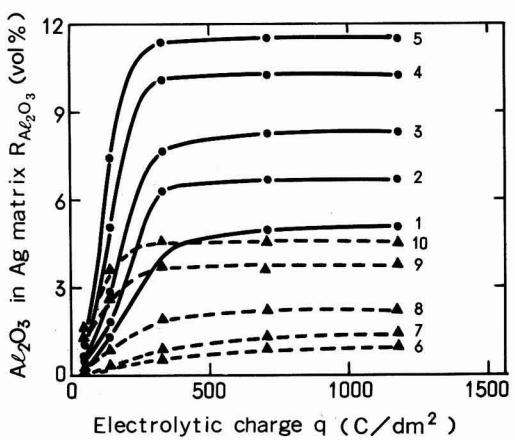


Fig. 6. Relation between amount of Al_2O_3 contained in composite coatings and electrolytic charge: solid line, circles: 5 cm/s; dotted line, triangles: 40 cm/s. Overpotential (ΔE): 1, 6: −0.017V; 2, 7: −0.027V; 3, 8: −0.037V; 4, 9: −0.057V; 5, 10: −0.087V.

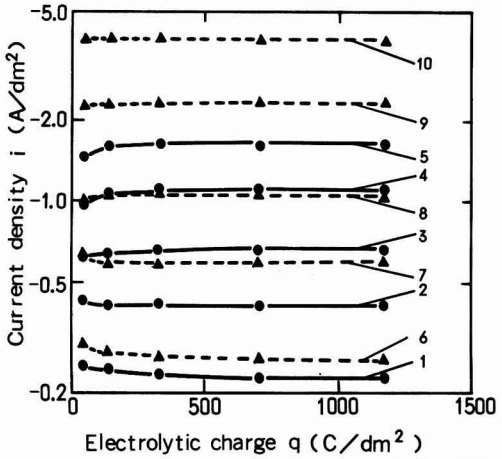


Fig. 7. Relation between actual current density and electrolytic charge consumed by deposition. Al_2O_3: 100 g/l. Solid line, circles: v (5 cm/s); dotted line, triangles: v (40 cm/s). Overvoltage (ΔE): 1, 6: −0.017V; 2, 7: −0.027V; 3, 8: −0.037V; 4, 9: −0.057V; 5, 10: −0.087V.

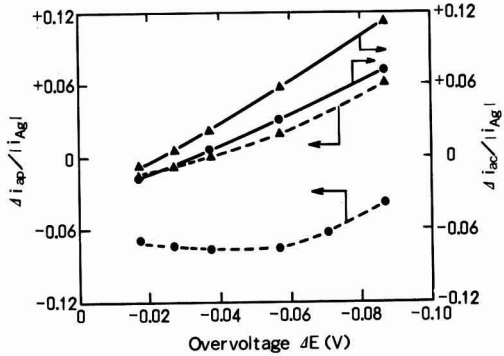


Fig. 8. Normalized difference of current density between Ag-Al_2O_3 composite coating and Ag coating as a function of overvoltage. $\Delta i_{ap} = |i_{ap(Ag\text{-}Al_2O_3)}| - |i_{Ag}|$. $\Delta i_{ac} = |i_{ac(Ag\text{-}Al_2O_3)}| - |i_{Ag}|$. Dotted line, circles: $\Delta i_{ap}/|i_{Ag}|$, v (5 cm/s). Dotted line, triangles: $\Delta i_{ap}/|i_{Ag}|$, v (40 cm/s). Solid line, circles: $\Delta i_{ac}/|i_{Ag}|$, v (5 cm/s). Solid line, triangles: $\Delta i_{ac}/|i_{Ag}|$, v (40 cm/s).

Values of $\Delta i_{ap}/|i_{Ag}|$ and $\Delta i_{ac}/|i_{Ag}|$ for fast velocity flow near the electrode surface are larger than those for slow flow at overvoltages from −0.017 to −0.087V.

Discussion

The effects of dispersion particles on cathodic polarization curves differ with electroplating conditions. Metzger and Tombrink reported that SiC particles in Ni electroplating solution increased the cathodic current (17). Furukawa and Hayashi also reported the same phenomenon with the addition of Al_2O_3 (18). They suggested it was due to (18): (*i*) dispersion particles causing vigorous agitation near the cathode surface; (*ii*) an increase in cathode surface area due to addition of dispersion particles; and (*iii*) a contribution to the cathodic reaction by Ni^{2+} ions being adsorbed on the dispersion particle surfaces. But, Melnikov *et al.* reported that the cathodic current decreased with addition of BeO to the Ag electroplating solution (19). In silver thiocyanate plating solution, cathodic polarization curves change in a complicated way on addition of Al_2O_3. For the relation between $\Delta i_{ap}/|i_{Ag}|$ and ΔE (in Fig. 8), if the flow velocity near the electrode surface is slow, cathodic current density decreases for overvoltages from −0.017 to −0.087V on addition of Al_2O_3, but if the flow velocity is fast, the cathodic current density decreases in the range from −0.017 to −0.027V and increases in the range from −0.037 to −0.087V on addition of Al_2O_3. On the relation between $\Delta i_{ac}/|i_{Ag}|$ and ΔE, the cathodic current density decreases at low overvoltage and increases at high overvoltage with addition of Al_2O_3 for both low and high flow velocities. As a result of the relation between $\Delta i_{ac}/|i_{Ag}|$ and ΔE, it appears that the main factor determining the rate of Ag deposition differs at low and high overvoltages: Al_2O_3 dispersed in the solution has few characteristics of colloids as their average particle diameter is 2.0 μm (20). Accordingly, it is estimated that the number of Al_2O_3 particles codeposited in the composite coatings supplied to the cathode by mechanical movement is more than that by diffusion. As a result of the movement, the width of the diffusion layer of Ag $(SCN)_n^{-(n-1)}$ becomes narrower with addition of Al_2O_3. Accordingly, at high overvoltage, the absolute value of actual cathodic current densities calculated by consideration of the area covered by Al_2O_3 $[|i_{(Ag\text{-}Al_2O_3)}|]$ is larger than the cathodic current density in the solution without Al_2O_3 $[|i_{Ag}|]$. This is because the supply of Ag $(SCN)_n^{-(n-1)}$ to the cathode can be carried out easily since the width of the diffusion layer on the electrode surface in a solution containing Al_2O_3 is thinner than that in a solution without it. But, at low overvoltage, the concentration of Ag $(SCN)_n^{-(n-1)}$ on the electrode surface is sufficient for the cathodic reaction at both low and high flow velocities. At low overvoltage, it seems that Al_2O_3 in the solution functions to suppress the cathodic reaction through Al_2O_3 adsorption on the cathode (21). Accordingly, for the low overvoltage, $|i_{ac(Ag\text{-}Al_2O_3)}|$ is smaller than $|i_{Ag}|$, because the effective area of the electrode reaction of a solution containing Al_2O_3 is smaller than that in a solution without it.

Acknowledgments

The authors wish to thank T. Narahara and H. Yagi for their helpful discussions.

Manuscript submitted April 8, 1985; revised manuscript received Oct. 24, 1985.

Hitachi, Limited, assisted in meeting the publication costs of this article.

REFERENCES

1. M. Pushpavanam, G. Vanadajan, S. Kvishnamurthy, and B. A. Shenoi, *Electroplat. Met. Finish.*, **27**, 10 (1974).
2. R. V. Williams and P. W. Martin, *Trans. Inst. Met. Finish.*, **42**, 182 (1964).
3. F. K. Sautter, *This Journal*, **110**, 557 (1963).
4. T. W. Tomaszewsky, L. C. Tomaszewsky, and H. Brown, *Plating*, **56**, 1234 (1969).
5. P. K. Sinha, N. Dhananjayan, and H. K. Chakrabarti, *ibid.*, **60**, 55 (1973).
6. D. W. Snaith and P. D. Groves, *Trans. Inst. Met. Finish.*, **50**, 95 (1972).
7. A. M. J. Kariapper and J. Foster, *ibid.*, **52**, 87 (1974).
8. N. Guglielmi, *This Journal*, **119**, 1009 (1972).
9. Y. Ogata, K. Yamakawa, and S. Yoshizawa, *J. Appl. Electrochem.*, **12**, 449 (1982).
10. H. Gerischer, *Z. Elektrochem.*, **59**, 604 (1955).
11. E. Budevsky, W. Bostanov, T. Kaishav, Z. Stojnov, A. Kotzeva, and R. Kaishev, *Phys. Status Solidi*, **13**, 577 (1966).
12. D. A. Vermilyea, *J. Chem. Phys.*, **27**, 814 (1957); *ibid.*, **28**, 717 (1958).
13. O. Nittono and S. Nagakura, *Jpn. J. Appl. Phys.*, **8**, 1186 (1969).
14. S. Haruyama and M. Kaneko, *Corros. Sci.*, **15**, 35 (1975).
15. H. Kita, M. Enyo, and J. O'M. Bockris, *Can. J. Chem.*, **39**, 1670 (1961).
16. K. Naitoh, *Kinzoku Hyomen Gijutsu*, **30**, 185 (1979).
17. W. Metzger and H. H. Tombrink, Paper A2, Interfinish 8, Basel, Switzerland (1972).
18. N. Furukawa and T. Hayashi, *Kinzoku Hyomen Gijutsu*, **28**, 527 (1977).
19. P. C. Melnikov, R. S. Saifullin, and G. S. Vozdvizhenskii, *Zashch. Met.*, **7**, 616 (1971).
20. P. Sennet and J. P. Olievier, *Ind. Eng. Chem.*, 32 (1965).
21. G. R. Lakshminarayanan, E. S. Chen, and F. K. Sautter, *This Journal*, **122**, 1589 (1975).

In Situ ^{119}Sn Conversion Electron Mössbauer Study of the Surface of Tin Layers as Deposited by an Electroless Process

H. M. van Noort, B. C. M. Meenderink, and A. Molenaar

Philips Research Laboratories, 5600 JA Eindhoven, The Netherlands

ABSTRACT

In situ ^{119}Sn conversion electron Mössbauer spectroscopy has been used to investigate the process of autocatalytic (electroless) tin deposition in a strong alkaline solution using a rotating disk. It is very likely that a tin(II) compound—probably some tin(II) hydroxide complex—is present at the surface during the Sn-metal depositing disproportionation reaction. The results obtained in a tin(II) solution with a *p*H of 6.1 indicate the presence at the surface of what is probably a tin(II) chloride compound.

Tin can be deposited on other metals (*e.g.*, copper) to produce a corrosion resistant or solderable coating. Such layers are usually made by immersion plating, electrodeposition, or dip-soldering. Immersion plating, which involves a replacement of the substrate metal by tin, is restricted to layers with a limited thickness. Autocatalytic plating gives the possibility of selective deposition of metals to unlimited thickness. It was found that autocatalytic tin deposition is possible by a disproportionation reaction (1), in which the oxidation of one tin(II) ion at the surface supplies the two electrons for the reduction of a second tin(II) ion to metallic tin. The metallization solution contains tin(II) chloride, sodium hydroxide, and sodium citrate at a temperature of about 70°C. Because the solution is stable for days, the disproportionation agent must be an active tin(II) complex on the growing surface. This active complex can be formed from an inactive tin(II) complex in the solution. Using Mössbauer spectroscopy, it should, in principle, be possible to identify the active tin(II) compound by means of the isomer shift (*IS*) and quadrupole splitting (*QS*).

It is advantageous to study surfaces with conversion electron Mössbauer spectroscopy (CEMS). This is a well-established technique for ^{57}Fe, but ^{119}Sn is also very suited for CEMS (2). The conversion electrons, emitted on deexcitation of the ^{119}Sn nuclei, have an energy of about 20 keV. Due to the small escape depth of these conversion electrons, only a surface layer with a thickness of about 1 μm is measured with about 2/3 of the electrons originating from the outermost 0.5 μm (3). Because the recoil-free fraction of SnO_2 is nine times that of β-Sn, this technique is very sensitive for thin surface oxide layers. For instance, the spectrum of a sample consisting of tin metal, covered with 100Å SnO_2, will consist of contributions of the oxide amounting to 30% (3). Kordesh *et al.* (4) have developed a new technique that allows CEMS on a continuously immersed electrode using a cell design similar to that reported by Rath and Kolb (5). The electrode is a disk with its lower half in the electrolyte and its upper half close to the conversion electron detector. The disk rotates slowly, in order to measure continuously a freshly reacted surface. A similar setup is used to investigate the above-mentioned process of autocatalytic tin deposition. We also examined the surface of tin layers immersed in a tin(II) solution with a *p*H of 6.1, a solution in which a tin(II) compound is also formed at the surface.

Experimental

The setup for *in situ* CEMS is shown in Fig. 1. A Teflon disk, on which a thin copper disk is mounted, is slowly rotated by a motor at a speed of 1/4 rpm. The lower half of the disk is immersed in a bath and its upper half is close to the conversion electron detector. This detector is a proportional counter using a He/4% CH_4 gas flow. The perspex box, in which the whole setup is mounted, is filled with helium gas. A radioactive source with 5 mCi ^{119m}Sn in a $CaSnO_3$ matrix is used, which emits γ-rays with an energy of 23.9 keV. All isomer shifts are against $CaSnO_3$, and the velocity was calibrated using a ^{57}Co source and a standard α-Fe foil. The average measuring time for one spectrum is two days. The copper disk has been connected to earth potential.

The copper disk, mounted on the Teflon disk, was pretreated in the following way: it was immersed for one minute at room temperature in a solution containing 55 volume percent H_3PO_4, 25 v/o HAc, 20 v/o HNO_3, and 0.5 v/o HCl, to remove the passive film on the copper surface. This pretreatment was followed by intensive rinsing with deionized water for 30s. The cleaned copper disk was then treated with a solution containing 0.02*M* tin(II) chloride, 0.6*M* thiourea, and 0.2*M* sulfuric acid for 10 min at room temperature. Copper ions are dissolved and tin metal is deposited. Such tin layers were used as substrates for autocatalytic tin deposition. After rinsing with deionized water for 15s, the substrate was placed in the solution for autocatalytic deposition at 70°C containing 0.33*M* tin(II) chloride, 3.85*M* sodium hydroxide, and 0.66*M* sodium citrate. Before the Mössbauer spectrum was measured, we waited a few hours in order to have a tin layer thickness of more than 3 μm so as to avoid contributions to the spectrum of tin atoms near the copper-tin interface.

We also measured a number of tin surfaces with a thickness of more than 5 μm using a solution containing 0.1*M* tin(II) chloride, 0.66*M* sodium citrate, and 0.08*M* sodium hydroxide. This solution has a *p*H of 6.1. All solutions were prepared with oxygen-free deionized water.

Results and Analysis of the Mössbauer Spectra

Before we measured with the rotating disk, we checked the effect on autocatalytic tin deposition of repeatedly bringing the surface of the disk in and out of the solution. The deposition process continues when the surface is reimmersed in the solution.

The conversion electron Mössbauer spectrum of a slowly rotating disk with its lower half in the metallization solution at 70°C is shown in Fig. 2a. After this spectrum was measured, the disk was stopped and again the Mössbauer spectrum was collected at room temperature, at which no disproportionation takes place (Fig. 2b). From this latter spectrum the Mössbauer parameters of SnO_2 and of metallic tin are obtained. In the literature, values of the *IS* of metallic tin vary between 2.55 and 2.65 mm/s. From our spectrum, we obtained for β-tin an isomer shift of 2.60 mm/s and a linewidth of 0.90 mm/s. The line belonging to SnO_2 was fitted with a single Lorentzian line with an *IS* of 0.00 mm/s and a linewidth of 1.1 mm/s. The statistics of the spectra were not good enough to resolve the quadrupole splitting of SnO_2. The spectrum obtained with the rotating disk has been analyzed using these parameters, and a good fit could only be obtained by taking two Lorentzian lines for the resonance near 2.5 mm/s: one line originating from β-tin, with the above-mentioned parameters, which are kept fixed during the fit, and a second line with an isomer shift of 2.2 mm/s and a linewidth of 0.8 mm/s. When we took just one Lorentzian line for the resonance near 2.5 mm/s, we obtained an isomer shift of 2.48 mm/s and a linewidth of

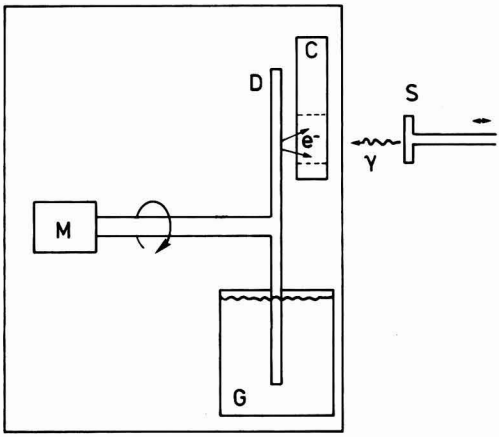


Fig. 1. Schematic diagram of the setup for *in situ* conversion electron Mössbauer spectroscopy. (M) Motor, (G) glass cuvet containing the tin(II) solution, (D) Teflon disk on which a thin copper disk is mounted, (C) conversion electron detector, (S) radioactive ^{119m}Sn source. The whole setup is mounted in a perspex box filled with helium gas.

1.1 mm/s. These parameters deviate significantly from those of β-tin.

In a similar way, we measured and analyzed the conversion electron Mössbauer spectrum of a disk that slowly rotated with its lower half in a tin(II) solution with a pH of 6.1 at room temperature. The line near 2.5 mm/s in the spectrum of the rotating disk could be analyzed using two Lorentzian lines: one originating from β-tin and a second line with an isomer shift of 2.9 mm/s and a linewidth of 0.8 mm/s (see Fig. 3a). The values of β-tin are obtained from the spectrum of the stationary disk (see Fig. 3b).

Discussion

Before we discuss the results, a number of experimental circumstances that could possibly account for the observed changes in the Mössbauer spectra must be considered: (*i*) to check whether the rotation itself could cause changes in the spectrum, we measured a copper disk covered with tin and observed identical spectra for the rotating and stationary disk; (*ii*) to check whether the presence of a thin layer of the solution could be responsible for the differences in the spectra, we took the same disk as mentioned in (*i*) and measured the spectra of the dry disk and of the disk rotating with its lower half in water, and again, identical spectra were found; and (*iii*) the decrease in temperature between the rotating disk (70°C) and the disk when it is stationary (25°C) causes an increase of the isomer shift of β-tin of 0.016 mm/s (6). This small temperature-dependent shift has been taken into account. We therefore conclude that the observed extra singlet in the conversion electron Mössbauer spectrum during the reaction is not an instrumental artifact but indicates the presence of a tin species at the surface during the disproportionation reaction. The measured Mössbauer parameters, IS = 2.2 mm/s and QS = 0 mm/s, are rather unusual for a tin(II) compound. It has been shown by a number of authors that tin(II) compounds can have isomer shifts as low as 1.8 mm/s, *i.e.*, in the tin(IV) region (7, 8). On the other hand, a tin(IV) compound with an isomer shift larger than 2.0 mm/s can be excluded (6).

The absence of a quadrupole splitting is more difficult to explain. It has been shown that tin(II) compounds with low isomer shifts often have a large quadrupole splitting (6). However, the quadrupole splitting strongly depends on the structure of the compound, in contrast to the isomer shift, which is not very sensitive to the structure. Most literature values of tin(II) compounds were obtained from powdered samples, whereas we measured thin surface layers on a wet disk. It has also been shown by Donaldson *et al.* that some tin(II) compounds, known to contain tin in lone-pair distorted sites, nevertheless have sharp singlet Mössbauer lines (9).

It is possible to obtain a small quadrupole splitting if we fit the observed spectra in a somewhat different way.

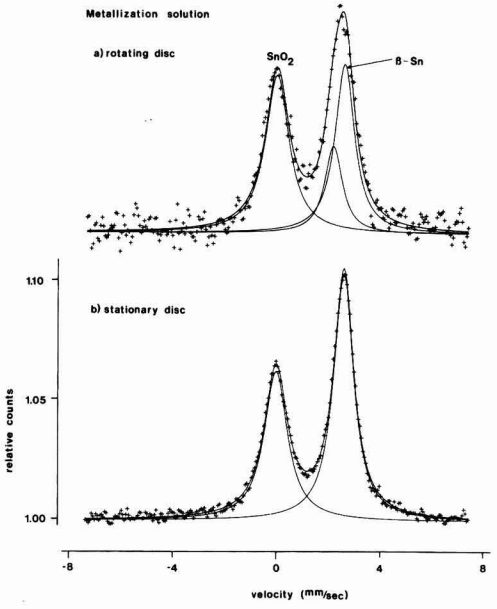


Fig. 2. (a) ^{119}Sn conversion electron Mössbauer spectrum of a rotating disk with its lower half in the metallization solution. (b) Mössbauer spectrum of the stationary disk.

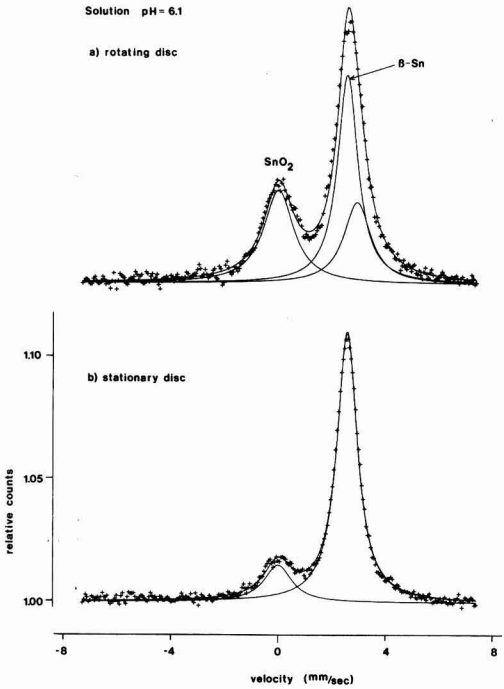


Fig. 3. (a) ^{119}Sn conversion electron Mössbauer spectrum of a rotating disk with its lower half in the tin(II) solution with a pH of 6.1. (b) Mössbauer spectrum of the stationary disk.

It is known that some tin compounds, especially when adsorbed on a surface, can exhibit the Gol'danskii-Karyagin effect due to anisotropy of the recoilless fraction (10, 11). In a quadrupole split spectrum, this effect will result in a difference in intensity between the two lines of the doublet. With increasing temperature, this effect becomes even more pronounced, and the intensity ratio of the two lines can be as high as 2.5 (12). Bearing this in mind, we fitted the spectrum of the rotating disk with one singlet originating from β-tin and a doublet with IS = 2.5 mm/s, QS = 0.6 mm/s, and an intensity ratio of the two lines of 2. This type of analysis and that previously described yielded equally good fits. As a third possibility, the spectrum can be fitted assuming that the observed extra singlet during rotation of the disk is the high-velocity component of a doublet with a quadrupole splitting of 2.2 mm/s, with its low-velocity component hidden under the SnO_2 peak around 0.0 mm/s. This doublet must then be assigned to a tin(IV) compound, since it has an isomer shift of about 1.2 mm/s. We now have three possibilities to fit the observed spectrum of the rotating disk all of which are mathematically equivalent: (*i*) SnO_2, β-Sn, and a singlet with IS = 2.2 mm/s and QS = 0 mm/s; (*ii*) SnO_2, β-Sn, and a doublet with IS = 2.5 mm/s and QS = 0.6 mm/s; and (*iii*) SnO_2, β-Sn, and a doublet with IS = 1.2 mm/s and QS = 2.2 mm/s. It is, however, very unlikely that a tin(IV) compound will not be present after the rotation of the disk has stopped, when it is present during the rotation. It is also very unlikely that only a tin(IV) compound is present during the rotation and no tin(II) compound. Although the Mössbauer parameters do not correspond to those of a known tin(II) compound, the value of the isomer shift points to the presence of a tin(II) compound at the surface during the disproportionation reaction.

The observed extra singlet, measured during the rotation of the disk with its lower half in a solution with a pH of 6.1, also points to the presence of a tin(II) compound. The value of the isomer shift of 2.9 mm/s is very close to the value reported by Cohen and West (13) who studied tin-palladium sols. They observed an extra singlet, with IS = 2.7 mm/s and QS = 0 mm/s, which cannot be ascribed to any known tin(II) compound. They attributed this singlet to Sn^{2+} ions, probably giving $(SnCl_3)^-$ complexes, which form a stabilizing layer surrounding palladium sol particles.

We will now discuss the possible tin(II) compounds, which may be present at the surface of the disk during the reaction. The effect of chloride ions in the metallization solution on the autocatalytic process has previously been studied. Both a metallization solution made with tin(II) chloride and a solution without chloride ions made by oxidation of metallic tin gave the same deposition rate on a catalytic surface. A tin(II) chloride compound as the disproportionating agent on the tin surface can, therefore, be excluded. It is suggested in Ref. (1), using thermodynamic arguments, that some tin(II) hydroxide complex or hydroxo-bridged tin(II) species may be present at the surface during the disproportionation reaction. It is probable that some tin(II) chloride compound is present at the surface of the disk when it is immersed in the solution with a pH of 6.1. This possibility is supported by the observations of some authors that tin(II) chloride hydroxide has an isomer shift that is at least 0.4 mm/s larger than that of tin(II) hydroxide oxide (14, 15).

Finally, as regards the amount of tin(II) compound present, it is known that tin(II) oxides have a recoil-free fraction that is about nine times that of β-tin (2). It is also known that our tin surfaces are fairly rough, giving rise to a large effective surface area. This means that only a few atomic layers of the tin(II) compound are likely to be present (3).

Acknowledgment

We would like to thank H. G. Bosklopper for technical assistance.

Manuscript submitted June 17, 1985; revised manuscript received Oct. 22, 1985.

Philips Research Laboratories assisted in meeting the publication costs of this article.

REFERENCES

1. A. Molenaar and J. J. C. Coumans, *Surf. Technol.*, **16,** 265 (1982).
2. F. A. Deeney and P. J. McCarthy, *Nucl. Instrum. Methods*, **159,** 381 (1979).
3. G. P. Huffman and G. R. Dunmyre, *This Journal*, **125,** 1652 (1978).
4. M. E. Kordesh, J. Eldridge, D. Scherson, and R. W. Hoffmann, *J. Electroanal. Chem.*, **164,** 393 (1984).
5. D. L. Rath and D. M. Kolb, *Surf. Sci.*, **109,** 641 (1981).
6. "Mössbauer Isomer Shifts," G. K. Shenoy and F. E. Wagner, Editors, p. 593, North Holland, Amsterdam (1978).
7. W.-W. Du Mont, J. L. Lefferts, and J. J. Zuckerman, *J. Organomet. Chem.*, **166,** 347 (1979).
8. A. B. Cornwell and P. G. Harrison, *J. Chem. Soc., Dalton Trans.*, 1486 (1975).
9. J. D. Donaldson, D. G. Nicholson, D. C. Puxley, and R. A. Howie, *ibid.*, 1810 (1973).
10. R. H. Herber and A. E. Smelkinson, *Inorg. Chem.*, **16,** 953 (1977).
11. B. Y. K. Ho, K. C. Molloy, J. J. Zuckerman, F. Reidinger, and J. A. Zubieta, *J. Organomet. Chem.*, **187,** 213 (1980).
12. I. P. Suzdalev, A. S. Plachinda, and E. F. Makarov, *Sov. Phys. JETP*, **26,** 897 (1968).
13. R. L. Cohen and K. W. West, *This Journal*, **120,** 502 (1973).
14. C. G. Davies and J. D. Donaldson, *J. Chem. Soc. (A)*, 946 (1968).
15. S. Ichiba and M. Takeshita, *Bull. Chem. Soc. Jpn.*, **57,** 1087 (1984).

Photoelectrochemical Generation of Hydrogen at Electrochemically Deposited p-CdTe Films: Effect of Heat-Treatment, Surface Modification by Platinum and Surface Oxide Layer on Conversion Efficiency

Makoto Takahashi, Kohei Uosaki,* and Hideaki Kita

Department of Chemistry, Faculty of Science, Hokkaido University, Sapporo 060, Japan

ABSTRACT

The effects of heat-treatment, Pt modification of the surface and surface oxide layer on the efficiency for the photoelectrochemical generation of hydrogen were investigated at p-CdTe films deposited electrochemically at −0.35V (*vs.* Ag/AgCl) from an aqueous sulfuric acid solution of *p*H = 1.4 containing 1*M* $CdSO_4$ and 1 m*M* TeO_2. By heat-treatment in a He atmosphere, the crystalline diameter increased and, thus, the number of grain boundaries at which effective electron-hole recombination takes place decreased. Free metallic Te existing near the surface, which acts as a recombination center, was removed by the treatment at the temperatures above 350°C. The cathodic photocurrent was increased by the heat-treatment due to these two effects. The cathodic photocurrent was decreased and even the anodic photocurrent was observed at the films treated at too high a temperature and for too long a time. The films were converted to n-type by these treatments because of the removal of the lattice Te from CdTe crystal. Pt modification, either vacuum deposition or codeposition, improved the efficiency, but the photocurrent is small, suggesting that the major reason for the low efficiency is still the bulk recombination. The oxide layer was easily formed on the CdTe films by exposure to air but dissolved by contacting with solution and had no effect on the photoelectrochemical properties of the film.

Recently strong attention has been paid to photoelectrolysis of water by using semiconductor electrodes as one of the useful means to convert solar energy into chemical energy, hydrogen (1). To make this process practical, it is essential to find an economical method for the production of polycrystalline semiconductors which have appropriate photoelectrochemical characteristics (2).

Cadmium telluride (CdTe) has the following attractive properties for solar energy conversion devices. The bandgap energy is 1.45 eV (3) from which one expects a high solar energy conversion efficiency (4). The direct optical transition (5) results in a large absorption coefficient which makes the use of thin film solar cells possible. Both p- and n-type forms can be prepared (6). Thus, the application of CdTe to solid-state solar cells (7) and photoelectrochemical cells (8) have been studied very extensively. One of us found p-CdTe is a stable cathode material for the photoelectrochemical generation of hydrogen (9).

The electrochemical deposition has been studied extensively as a useful method for preparing large area, polycrystalline Cd-chalcogenides (10). The photoelectrochemical properties of electrochemically deposited Cd-chalcogenide thin films have also been reported by many research groups but most of the reports are on n-type materials (11).

We have recently investigated the electrochemical deposition of CdTe thin films from the solution containing $CdSO_4$ and TeO_2 and reported the effect of preparation conditions, *e.g.*, deposition potential, on the composition and optical and electronic properties of the deposited films (12-14). We also studied the photoelectrochemical generation of hydrogen at the electrochemically deposited p-CdTe films (12, 14). The conversion efficiency at the as-grown films was poor compared with that at single crystal electrodes. The following are considered to be the reasons for the low efficiency: (*i*) There are many grain boundaries in the films at which effective recombination takes place. (*ii*) Free excess metallic Te which acts as recombination center exists near the surface. (*iii*) The hydrogen evolution reaction rate at the semiconductor electrode is low.

In this paper, to overcome the above difficulties and to improve the efficiency, the effects of heat-treatment and surface modification by platinum on the photoelectrochemical generation of hydrogen at electrochemically deposited p-CdTe films are investigated. The effect of surface oxide layer which was reported to affect the efficiency at p-InP (15) is also examined.

*Electrochemical Society Active Member.

Experimental

p-CdTe thin films were deposited on Ti sheet, which was degreased by a chloroform, then by an ethanol vapor, etched by 10% HF solution, and washed by deionized water before use from an aqueous sulfuric acid solution of *p*H = 1.4 containing 1*M* $CdSO_4$ and 1 m*M* TeO_2(4). The deposition potential was usually −0.35V (*vs.* Ag/AgCl) and the deposition current was *ca.* 0.15 mA · cm^{-2}. The thickness of as-grown CdTe film was usually 3 μm and the deposition took *ca.* 15h. The reagent grade H_2SO_4, $CdSO_4$ (purity 99.5%), and TeO_2 (purity 99%) of Wako Pure Chemicals, Incorporated were used without further purification. Water was purified by a Milli Q water purification system (Millipore Corporation). A usual three-electrode cell was used both for the electrochemical deposition and for the photoelectrochemical measurements. A platinum sheet and a Ag/AgCl electrode were used as a counter and a reference electrode, respectively. A potentiostat (Wenking Model 68 FRO.5 or Nikko Keisoku NPGS-301 s) was used to control the electrode potential. The deposition of films and the photoelectrochemical measurements were carried out at room temperature after the electrolyte solution was deaerated by passing a purified He gas through the solution for about 20 min. The photoelectrochemical measurements were carried out in 1*M* NaOH. A 500W Xe lamp (Usio Denki Company Limited) with an IR absorbing filter (Toshiba IRA-20) was used as a light source. The intensity of the light at the electrode surface was *ca.* 17 mW · cm^{-2}.

The heat-treatment of the films was carried out in a quartz tube under a He gas flow. The temperature was measured with a Chromel-Alumel thermocouple and controlled by using a thermocontroller (Model E560, Chino Work, Limited) within an accuracy of ±5°C. Temperature was raised to a preset value with a rate of *ca.* 100°C/h.

Two methods were employed to modify the electrode surface with Pt. The first one was the codeposition of Pt. Just before the electrodeposition of CdTe was completed, H_2PtCl_6 solution was added to the electrolyte solution so that Pt concentration of the solution became 0.4 m*M*. The amount of Pt deposited was calculated from the difference between the charge passed when Pt was added and

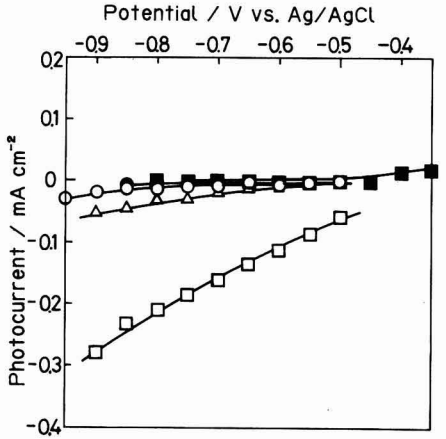


Fig. 1. Photocurrent-potential relations of p-CdTe films deposited on Ti sheet at −0.35V (vs. Ag/AgCl) from an aqueous sulfuric acid solution of pH = 1.4 containing 1M $CdSO_4$ and 1 mM TeO_2. The measurements were carried out in 1M NaOH with 500W Xe lamp illumination. ●: As-grown. Other films were annealed in a He atmosphere for 4h at 200°C (○), 350°C (□), 400°C (△), and 500°C (■).

that without Pt addition. Heat-treatment was carried out as for the films without modification. In the other method, Pt was vacuum deposited on the films by using Ulvac, EBH-6. In this case, the thickness of Pt was measured by using an interference microscope (Mizojiri Optical Company Limited, Model 2).

The type of semiconductivity of the CdTe films were determined by measuring the potential difference between a hot and a cold contact. X-ray diffraction patterns and reflection spectra were obtained by using Toshiba XC-40 x-ray diffractometer and a Beckman DK-2 reflectometer, respectively. X-ray photoelectron spectroscopy (XPS) measurements were carried out by using a V. G. Scientific, Limited, ESCA3.

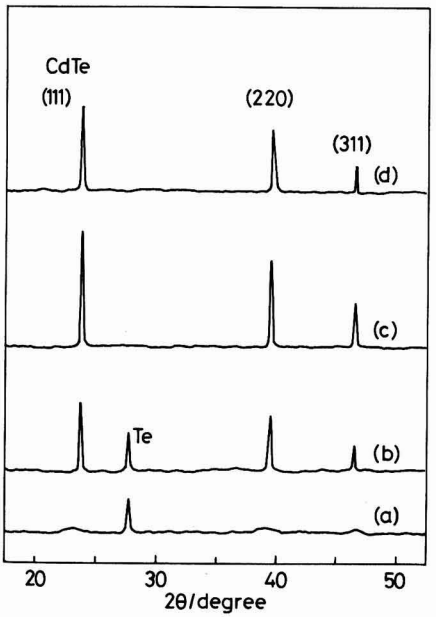


Fig. 2. X-ray diffraction patterns of the CdTe films used for the experiments presented in Fig. 1. (a) As grown, (b) annealed at 200°C, (c) annealed at 350°C, and (d) annealed at 500°C.

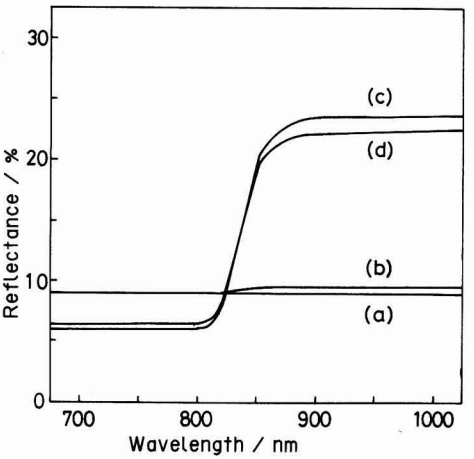


Fig. 3. Reflection spectra of the CdTe films used for the experiments presented in Fig. 1. (a) As grown, (b) annealed at 200°C, (c) annealed at 350°C, and (d) annealed at 500°C.

Results

Effect of heat-treatment.—Figure 1 shows the photocurrent-potential relations of electrochemically deposited p-CdTe films annealed for 4h at several temperatures.[1] The cathodic photocurrent increased with the increase of annealing temperature up to 350°C and then decreased at higher temperatures as at 400° and 500°C. Even the anodic photocurrent was observed at the films treated at the temperatures above 400°C.

The x-ray diffraction patterns of the annealed films shown in Fig. 2 demonstrate that the diffraction peak due to free metallic Te which existed in as-grown films remained at the films treated at 200°C but disappeared on annealing at higher temperatures. The intensity of diffraction peaks due to CdTe increased and the full width at half maximum (FWHM) of the peaks decreased by the

[1] Each data point in most of the figures represents the average value of 2-4 independent experiments. The deviation of data was within the size of the symbols (○, □, etc.) in the figures.

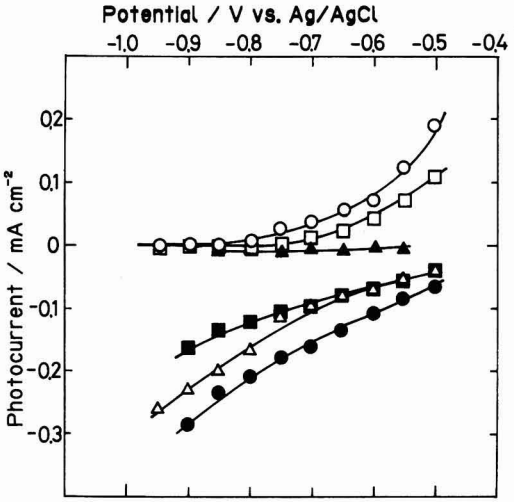


Fig. 4. Photocurrent-potential relations of p-CdTe films. Experimental conditions for the deposition and the photoelectrochemical measurements were the same as those in Fig. 1. ▲: As grown. Other films were annealed in a He atmosphere at 350°C for 2h (■), 4h (●), 6h (△), 7h (□) and 12h (○).

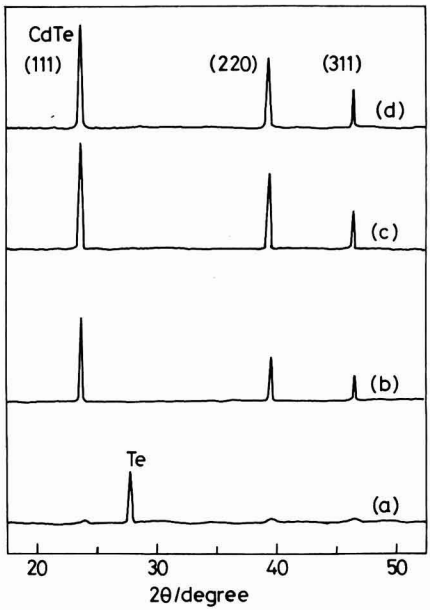


Fig. 5. X-ray diffraction patterns of the CdTe films used for the experiments presented in Fig. 4. (a) As grown, (b) annealed for 2h, (c) annealed for 4h, (d) annealed for 12h.

heat-treatment. The higher the temperature, the stronger the intensity of the peaks. The intensity, however, became weaker by the treatment at 500°C. The crystalline diameter calculated by using Scherrer's equation (16) with the value of FWHM increased by annealing and are larger than 50 nm, which is the upper limit of the present arrangement, for the films treated above 350°C.

The reflection spectra of the above-mentioned samples are shown in Fig. 3. The reflectance was almost constant for the as-grown films but changed around 820-860 nm for the annealed films. The bandgap energy determined from the spectra is *ca.* 1.45 eV which is in good agreement with the value reported for CdTe single crystals (3).

Although the as-grown film was p-type, the semiconductivity of the annealed films differed depending upon the annealing temperature. The films treated below 350°C were p-type and those treated above 350°C were n-type. The semiconductivity of films treated around 350°C were difficult to determine by the method employed here.

Effect of the annealing time was also examined. Figure 4 shows the photocurrent-potential relations of the electrochemically deposited p-CdTe films annealed at 350°C for 0-12h. The cathodic photocurrent increased with the increase of annealing time up to 4h and then decreased. The anodic photocurrent was observed at the films treated for longer than 7h.

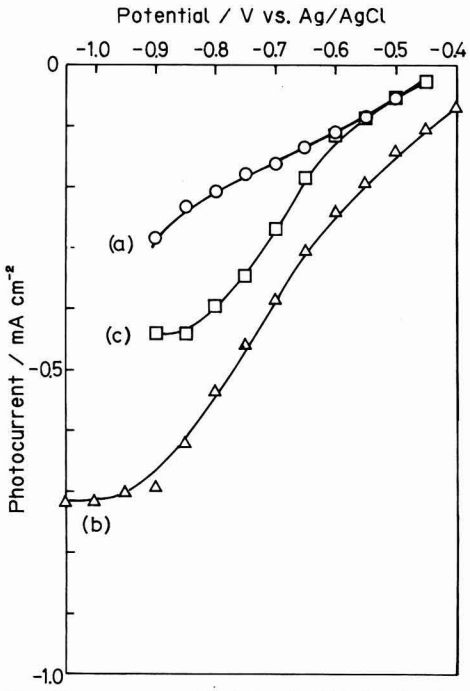


Fig. 6. Photocurrent-potential relations of p-CdTe films. Experimental conditions for the deposition and the photoelectrochemical measurements were the same as those in Fig. 1. (a) Annealed in a He atmosphere at 350°C for 4h (sample 2 of Table I), (b) modified with Pt by codeposition then annealed in a He atmosphere at 350°C for 4h (sample 4 of Table I), and (c) annealed in a He atmosphere at 350°C for 4h then modified with Pt by vacuum deposition (sample 7 of Table I).

The x-ray diffraction patterns of the films used for the measurements presented in Fig. 4 are shown in Fig. 5. The diffraction peaks due to CdTe faces became stronger and sharper by the longer treatment. The diffraction peak due to free Te disappeared after 2h treatment.

The films remained as p-type up to 6h treatment. The semiconductivity of the films treated for 7h was hard to be determined and that of those treated for longer than 8h was n-type. As already reported, if the films were treated at 200°C, the films remained p-type with the x-ray diffraction peak due to free Te even after 12h treatment (14).

Pt modification.—The effect of Pt modification was investigated as listed in Table I. The photocurrent was always increased by Pt modification either by codeposition or by vacuum deposition, although it was small at the films without annealing (sample 3 and 6). Figure 6 shows the photocurrent-potential relations of sample 4 and 7 as well as that of the annealed film without Pt modification (sample 2).

Table I. Effect of Pt modification on the photocurrents at the CdTe films

Sample	Pt modification	Annealing*	Photocurrent** at −0.8V/mA · cm^{-2}
1	—	— (as-grown)	−0.01
2	—	Annealing only	−0.20
3	Codeposition	—	−0.07
4	Codeposition	After Pt modification	−0.55
5	Electrodeposition	Before Pt modification	−0.28
6	Vacuum deposition	—	−0.06
7	Vacuum deposition	Before Pt modification	−0.40
8	Vacuum deposition	After Pt modification	−0.43

* Annealing treatments were carried out in a He atmosphere at 350°C for 4h.
** Photocurrents were measured in 1*M* NaOH under 500W Xe lamp illumination.

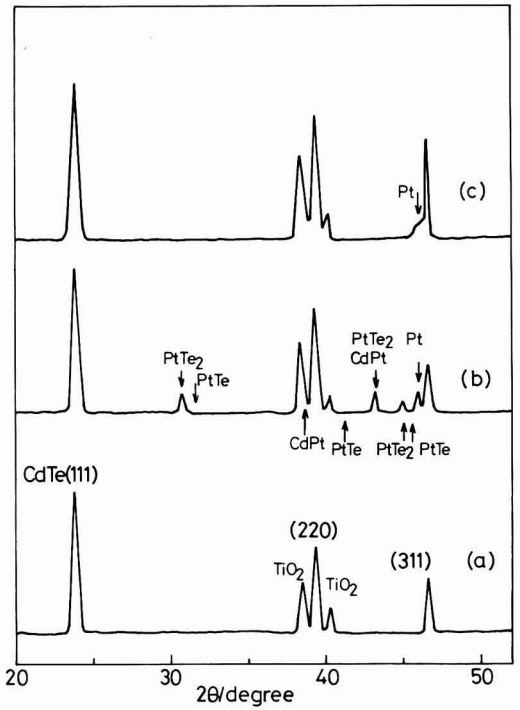


Fig. 7. X-ray diffraction patterns of the CdTe films used for the experiments presented in Fig. 6. (a) Annealing only (sample 2), (b) Pt codeposition followed by annealing, and (c) annealing followed by Pt vacuum deposition. Peaks corresponding to TiO_2 which existed on substrate (Ti) were also observed. In Fig. 2 and Fig. 5, no peaks due to TiO_2 can be seen because TiO_2 portion was covered with epoxy resin when x-ray diffraction patterns were obtained.

X-ray diffraction patterns of the films used for the measurements shown in Fig. 6 are shown in Fig. 7. In addition to CdTe peaks (2θ = 23.8°, 39.3°, and 46.4°) (17), additional peaks at 2θ = 46.2° and 81.3° corresponding to Pt (17) were observed with sample 7 (Fig. 7c).[2] Similar patterns were observed with sample 6. If the annealing was carried out after the Pt modifications, Pt reacted with CdTe and several Pt alloys were formed. Figure 7b shows the x-ray diffraction patterns of sample 4 and the diffraction peaks due to PtTe (2θ = 31.6°, 41.2°, and 45.8°) (17), $PtTe_2$ (2θ = 30.7°, 43.5°, and 45.1°) (17), and CdPt (2θ = 38.6°, 43.5°, and 76.1°) (17) were also observed.[3] Similar patterns were observed at sample 8.

XPS spectra of sample 4 and 7 show that platinum existed as metallic (Pt(0)).[4]

The photocurrent-potential relations were not much affected at the thickness of Pt between 5 and 300Å.

Growth of surface oxide layer and its effect on the photoelectrochemical behavior.—It has been reported by Werthen *et al.* that surface oxide layer grows on CdTe single crystal (18). XPS spectra of the CdTe films which were annealed at 300°C in a He atmosphere for 4h, then

[2] Figure 7 shows only diffraction peaks between 2θ = 17° and 2θ = 52°.

[3] Some of the peaks were very weak and are not obvious in Fig. 7.

[4] Peaks corresponding to Pt ($4f_{5/2}$) and Pt ($4f_{7/2}$) appeared only at 75.0 eV and 71.5 eV, respectively, which are known to be due to Pt (0).

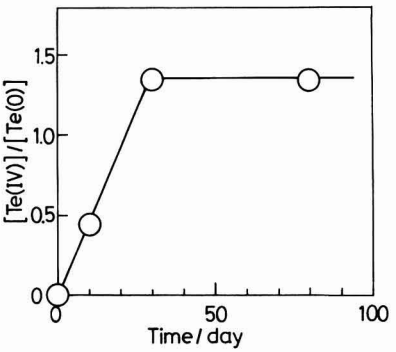


Fig. 9. The ratio of XPS peaks corresponding to Te(IV) and Te(0) as a function of air-exposed time.

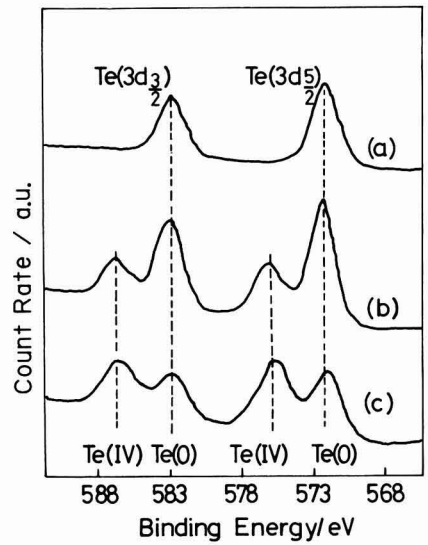


Fig. 8. XPS spectra of p-CdTe films in the region of Te $3d_{5/2}$ and $3d_{3/2}$ peaks. The deposition conditions of the films were the same as those in Fig. 1. The films were annealed in a He atmosphere at 300°C for 4h then exposed to air for (a) 15 min, (b) 10 days, and (c) 80 days.

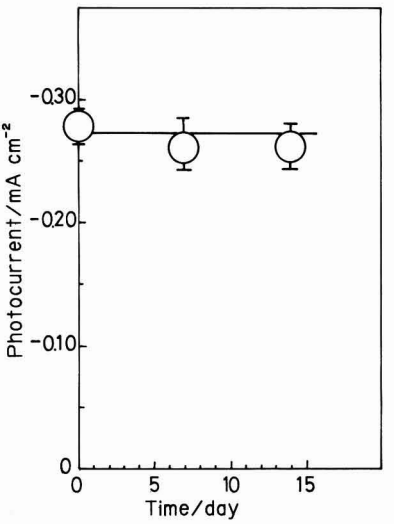


Fig. 10. The photocurrent under illumination of 500W Xe lamp at −0.70V (vs. Ag/AgCl) in 1M NaOH at the CdTe films as a function of air-exposed time. The films were deposited and annealed in the way shown in Fig. 8.

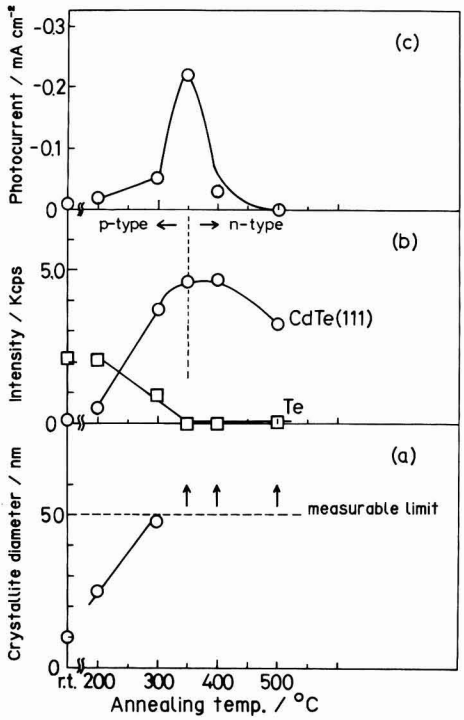


Fig. 11. (a) The crystalline diameter as a function of annealing temperature, (b) the intensity of x-ray diffraction peaks corresponding to CdTe (111) face (○) and free Te (□), and (c) the photocurrent at −0.80V (*vs.* Ag/AgCl). The experimental conditions for the deposition and the photoelectrochemical measurements were the same as those in Fig. 1. The films were annealed in a He atmosphere for 4h at the temperature shown as abscissa. The upper limit of the crystallite diameter to be determined in the present experimental arrangement is 50 nm.

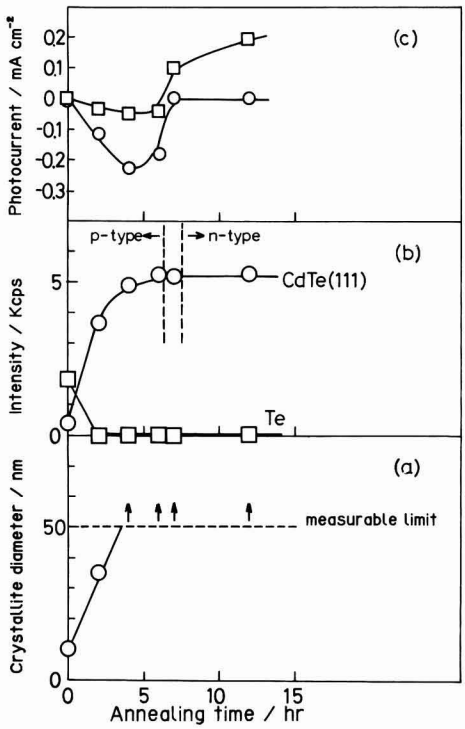


Fig. 12. (a) The crystallite diameter as a function of annealing time, (b) the intensity of x-ray diffraction peaks corresponding to CdTe (III) face (○) and free Te (□), and (c) the photocurrents at −0.80V (○) and at −0.50V (□). The experimental conditions for the deposition and the photoelectrochemical measurements were the same as those in Fig. 1. The films were annealed in a He atmosphere at 350°C for a period shown in abscissa.

exposed to air for 15 min, 10 days, and 80 days are shown in Fig. 8 in the region of Te $3d_{5/2}$ and $3d_{3/2}$ peaks. The peaks at 572.5 and 583.0 eV correspond to Te(0) and those at 576.0 and 586.5 eV correspond to Te(IV) (18, 19).[5] While only peaks due to Te(0) were observed at the films exposed to air for 15 min, peaks due to Te(IV) were also observed at the films exposed to air for longer time periods. The ratio of Te(IV)/Te(0) increased at the beginning with the increase of the time of exposure to air and reached a constant value as shown in Fig. 9. The shape and the intensity of the peaks which correspond to Cd $3d_{5/2}$ and $3d_{3/2}$ were not affected by the air exposure. These results suggest the formation of TeO_2 near the surface by air exposure as proposed by Werthen *et al.* (18). Air-exposure time did not affect the cathodic photocurrent as shown in Fig. 10. XPS spectra taken after the films were immersed in 1*M* NaOH showed no peaks due to Te(IV), suggesting that the surface oxide dissolved in the solution.

Discussion

As mentioned before, the major reasons for low efficiencies at as-grown films are the bulk recombination at grain boundaries, the surface recombination due to the existence of excess free Te metal, and the slow hydrogen evolution reaction. The annealing treatments were carried out primarily to increase the crystalline diameter so that the number of grain boundaries should be decreased.

[5] Although White *et al.* showed the existence of Te^{2-} in CdTe (19), Werthen *et al.* suggested that Te existed as Te(0) in CdTe. In our measurements, the position of Te peaks of sputtered CdTe films agreed with that of Te peaks of sputtered elemental Te within experimental error, suggesting that Te existed as Te(0) in CdTe.

Crystalline diameter, intensity of x-ray diffraction peaks, and photocurrents are plotted as a function of the annealing temperature (Fig. 11) and of the annealing time (Fig. 12 at 350°C and Fig. 13 at 200°C). As shown in Fig. 13 the annealing at 200°C increased the crystalline diameter but did not affect the free Te concentration. In this case the increase of the photocurrent is solely due to the increase of crystalline diameter. The annealing above 300°C not only increased the crystalline diameter but also removed the free Te which existed near the surface and acted as the surface recombination center. Thus, the annealing improved the efficiency due to these two effects. The cathodic photocurrent, however, declined by the annealing at too high temperature or for too long time (Fig. 11, 12). The films were converted to n-type by these treatments and even anodic photocurrents were observed (Fig. 12). This is due to the removal of the lattice Te from CdTe crystal. The Te vacancy is known as a donor center (20). Although the details of the effect of the annealing on the composition and the electronic properties of the films will be reported elsewhere (21), it should be emphasized here that the effect of the annealing on the photocurrent is the result of the increase of the crystalline diameter, the decrease of free Te concentration and the change of the electronic properties.

Pt modification was carried out with the hope that the hydrogen evolution reaction is enhanced by Pt which is known as a good catalyst for this reaction (22). The results shown in Table I, Fig. 6, and Fig. 7 support that this expectation was correct. However, the increment by the treatment is not as large as those reported for p-type single-crystal electrodes, *e.g.*, p-InP (23), and the photocurrent at RHE is still small. Thus, it can be concluded

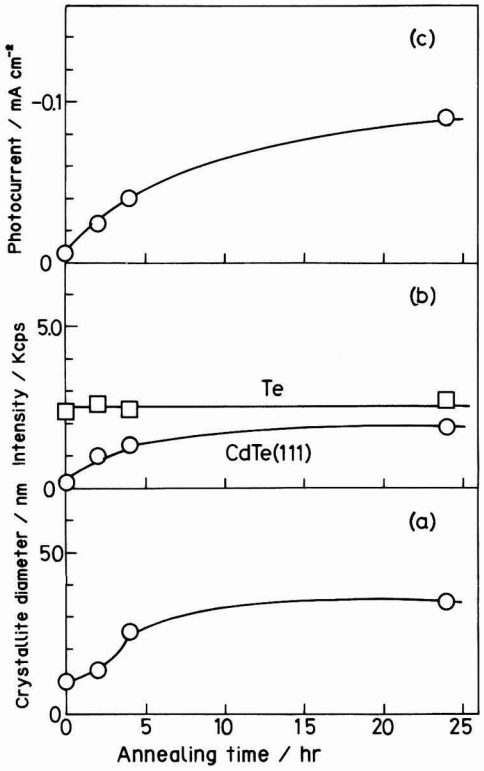


Fig. 13. (a) The crystallite diameter as a function of annealing time, (b) the intensity of x-ray diffraction peaks corresponding to CdTe (111) face (○) and free Te (□), and (c) the photocurrent at −0.80V. The films were annealed at 200°C. Other conditions were as same as those in Fig. 12.

that the bulk recombination is still the major reason for the low efficiency at these films. The role of Pt alloys found in the films annealed after the Pt modification is not clear.

According to Heller, surface oxide layer plays an important role in determining the efficiency for photoelectrochemical hydrogen evolution reaction at p-InP (15). In the present case, however, although the surface is very easily oxidized by exposing it to air, the oxide layer thus formed disappears just by immersing the film into 1*M* NaOH, and, therefore, cannot play any role in the photoelectrochemical properties of CdTe films. This result agrees with the fact that there is no *p*H dependence of the flatband potential (24), which also suggests no oxide layer at the surface in contact with solution.

Acknowledgments

Thanks are due to Professor T. Yokokawa and Dr. T. Maekawa and to Professor Y. Matsunaga for the help in the x-ray diffraction measurements and reflection spectra measurements, respectively. Vacuum deposition was carried out with the help of Dr. M. Taniwaki for which we are most grateful. Mr. Kiya is acknowledged for constructing electrochemical cells. This work was partially supported by a Grant-in-Aid for Scientific Research, Ministry of Education, Science and Culture.

Manuscript submitted April 2, 1985; revised manuscript received July 9, 1985.

Hokkaido University assisted in meeting the publication costs of this article.

REFERENCES

1. (a) A. Fujishima and K. Honda, *Nature*, **238**, 37 (1972); (b) A. Heller, *Acc. Chem. Res.*, **14**, 154 (1981); (c) A. J. Bard, *J. Phys. Chem.*, **86**, 172 (1982).
2. (a) B. Miller and A. Heller, *Nature*, **262**, 680 (1976); (b) W. J. Danaher and L. E. Lyons, *ibid.*, **271**, 139 (1978); (c) J. F. McCann and M. Skyllas Kazacos, *J. Electroanal. Chem.*, **119**, 409 (1981).
3. K. W. Böer and A. Rothwarf, *Ann. Rev. Mater. Sci.*, **6**, 303 (1976).
4. S. Wagner, in "Solid State Chemistry and Energy Conversion and Storage," J. B. Goodenough and M. S. Whittingham, Editors, p. 109 Adv. in Chem. Ser. of ACS, No. 163 (1977).
5. B. M. Basol and O. M. Stafsudd, *Thin Solid Films*, **78**, 217 (1981).
6. S. S. Chern, H. R. Vydyanath, and F. A. Kröger, *J. Solid State Chem.*, **14**, 33 (1975).
7. J. G. Werthen, J-P. Häring, A. L. Fahrenbruch, and R. H. Bube, *J. Appl. Phys.*, **54**, 5982 (1983).
8. A. B. Ellis, S. W. Kaiser, J. M. Bolts, and M. S. Wrighton, *J. Am. Chem. Soc.*, **99**, 2839 (1977).
9. J. O'M. Bockris and K. Uosaki, *This Journal*, **124**, 1348 (1977).
10. (a) L-S. R. Yeh, P. G. Hudson, and A. Damjanovic, *J. Appl. Electrochem.*, **12**, 153 (1982); (b) D. K. Roe, L. Wenzhao, and H. Gerischer, *J. Electroanal. Chem.*, **136**, 323 (1982); (c) I. Markov and M. Ilieve, *Thin Solid Films*, **74**, 109 (1980); (d) M. Cocivera, A. Darkowski, and B. Love, *This Journal*, **131**, 2514 (1984); (e) M. P. R. Panicker, M. Knaster, and F. A. Kröger, *ibid.*, **125**, 566 (1978).
11. (a) J. H. Reeves and M. Cocivera, *This Journal*, **131**, 2042 (1984); (b) G. J. Houston, J. F. McCann, and D. Haneman, *J. Electroanal. Chem.*, **134**, 37 (1982); (c) G. Hodes, J. Manassen, and D. Cahen, *Nature*, **261**, 403 (1976); (d) M. Skyllas Kazacos and B. Miller, *This Journal*, **127**, 869 (1980); (e) M. Tomkiewicz, I. Ling, and W. S. Parsons, *ibid.*, **129**, 2016 (1982).
12. K. Uosaki, M. Takahashi, and H. Kita, *Electrochim. Acta*, **29**, 279 (1984).
13. M. Takahashi, K. Uosaki, and H. Kita, *J. Appl. Phys.*, **55**, 3879 (1984).
14. M. Takahashi, K. Uosaki, and H. Kita, *This Journal*, **131**, 2304 (1984).
15. A. Heller, *J. Vac. Sci. Technol.*, **21**, 559 (1982).
16. J. R. Anderson, "Structure of Metallic Catalysts," p. 365, Academic Press, London (1975).
17. ASTM X-Ray Powder Data, 15-770, 19-193, 19-192, 14-7, 18-976, 17-920.
18. J. G. Werthen, J-P. Höring, and R. H. Bube, *J. Appl. Phys.*, **54**, 1159 (1983).
19. H. S. White, A. J. Ricco, and M. S. Wrighton, *J. Phys. Chem.*, **87**, 5140 (1983).
20. D. de Nobel, *Philips Res. Rep.*, **14**, 361 (1959).
21. M. Takahashi, K. Uosaki, and H. Kita, *J. Appl. Phys.*, **58**, 4292 (1985).
22. J. F. Llopis and F. Colom, in "Encyclopedia of Electrochemistry of the Elements," Chap. VI-4, A. J. Bard, Editor, Marcel Dekker, Inc., New York and Basel (1976).
23. W. D. Johnston, Jr., H. J. Leamy, B. A. Parkinson, A. Heller, and B. Miller, *This Journal*, **127**, 90 (1980).
24. J. L. Sculfort, R. Triboulet, and P. Lemasson, *ibid.*, **131**, 209 (1984).

The High Aqueous Solubility of K_2S and Its Effect on Bulk and Photoelectrochemical Characteristics of Cd(SeTe)/$S_x^=$ Cells

I. Polysulfide Variation at Constant Sulfur/Sulfide Ratio

Stuart Licht,*,[1] Joost Manassen,* and Gary Hodes*

Department of Materials Research, The Weizmann Institute of Science, Rehovot 76100, Israel

ABSTRACT

The aqueous solubility of K_2S is measured to be 5.6, 8.9, and 11.3*m* at 0°, 25°, and 72°C, respectively. The high K_2S solubility, compared to that of Na_2S, is discussed. An increase in potassium sulfide concentration in polysulfide solutions containing a fixed ratio of dissolved sulfur to alkali sulfide is shown to: (*i*) modify the distribution of polysulfide species in solution, (*ii*) increase the solution-absorbance of light, (*iii*) negatively shift the redox potential, (*iv*) increase the calculated disproportionation-limited lifetime of the solution, and (*v*) decrease potassium ion activity. Thin film Cd(SeTe) photoelectrochemical solar cells were investigated with polysulfide electrolytes containing 0.5 to 8.5*m* K_2S. At either lower or higher sulfide concentrations, photocurrent, fill factor, and conversion efficiency are depressed. A relative gain in efficiency >30% is achieved with electrolytes of intermediate concentration containing 1 to 2*m* potassium sulfide.

Thin film cadmium-chalcogenide/aqueous polysulfide photoelectrochemical solar cells (CdX/$S_x^=$ PEC's) are a potentially inexpensive method for solar-to-electrical energy conversion. The complexity of the aqueous polysulfide system has impeded study of the solution chemistry aspect of these cells. Recently a computer model was developed to predict the relative activities of H_2O, alkali cations, OH^-, H^+, H_2S, HS^-, $S^=$, $S_2^=$, $S_3^=$, $S_4^=$, and $S_5^=$ species in polysulfide solution upon input of the nominal sulfur, sulfide, and hydroxide concentrations in solution (1).

Polysulfide solution modification can have significant effects on CdX/$S_x^=$ PEC performance. Photoelectrode operating lifetime has been shown to increase with increasing concentration of polysulfide in the electrolyte (2, 3). However, these studies were performed in polysulfide electrolyte containing added alkali hydroxide, which was shown recently to be detrimental to CdX/$S_x^=$ PEC photovoltage, photocurrent, and solar-to-electrical energy conversion efficiency (4). The general effects of sulfide concentration variation on CdX/$S_x^=$ PEC photocurrent, photovoltage, and efficiency have not yet been reported.

The maximum nominal polysulfide concentration used in PEC's has been limited by the solubility of sodium sulfide. At room temperature, the solubility of sodium sulfide in aqueous polysulfide varies from approximately 2 to 3*m*, depending on the concentrations of added hydroxide and sulfur. The solubilities of the other alkali sulfides have not been previously reported, although in 1887 Bock reported working on very concentrated aqueous solutions of K_2S (6).

Alkali cation species (7, 8) and hydroxide concentration (4), as well as the optimization of sulfur to sulfide ratio in solution (5), have been shown to influence greatly the behavior of CdX/$S_x^=$ PEC's. Here we report on the aqueous solubility of potassium sulfide and the effect of its extremely high solubility on CdX/$S_x^=$ PEC performance.

Experimental

Alkali hydrosulfide solutions were prepared by saturation of aqueous alkali hydroxide solution with H_2S

$$MOH + H_2S \rightarrow MHS + H_2O; (M = Na^+, K^+) \quad [1]$$

The reaction is exothermic and results in an increase in volume, a proportional mass increase, and a *p*H decrease, all of which are consistent with Eq. [1]. Saturation with H_2S was monitored by mass change yielding 98.5 ± 1% reaction. Alkali sulfide was then nominally formed upon addition of equimolar hydroxide

$$MOH + MHS \rightleftharpoons M_2S + H_2O \quad [2]$$

Polysulfide solutions were obtained by addition of sulfur. Solutions were prepared with analytical grade reagents and doubly distilled, deionized water, and they were prepared, stored, and utilized under argon to prevent solution oxidation.

K_2S aqueous solubilities, as a function of observed temperature, were determined both by gradual cooling of supersaturated solutions and by gradual heating of saturated solutions containing excess K_2S crystals. The measured solubilities were accurate to an estimated ±2%, limited by the analytical purity of the materials and the small uncertainty in temperature measurement.

Many of the procedures were as previously described (4). Potassium ion activities were determined by measuring the potential response in solution of a Beckman 39137 cationic selective electrode and a Radiometer K401 standard calomel electrode (SCE). The electrodes were calibrated and found to respond linearly to potassium activity (K^+) according to the relationship

$$E_{K^+} = 0.219V + 0.590 \log (a_{K^+}) + E_j \quad [3]$$

where E_j represents the liquid junction potential arising over the solution/SCE interface.

The electrodeposition of thin films of $CdSe_{0.65}Te_{0.35}$ on titanium substrates and the photoelectrochemical etching of these films were also previously described (4).

Standard equipment was used to measure solution conductivity and light transmission and for obtaining the photocurrent *vs.* applied potential (I-V) data and redox potentials. A constant distance (5 mm) from the front wall of the test cell to the photoelectrode, and also a constant distance from the stabilized tungsten/halogen lamp to the photoelectrode, were maintained during the experiments. In order to insure that the observed I-V changes were reproducible and reversible, each I-V curve measurement was both preceded and followed by an additional I-V curve that was measured using the same electrode but in a polysulfide solution set aside for this standardization. The I-V measurements reported here represent the average of repeated results on two or more photoelectrodes.

Results and Discussion

Bulk solution characteristics.—The measured aqueous solubility of K_2S, compared to the known solubilities of Na_2S, NaOH, and KOH, is presented in Fig. 1. The solubility of K_2S (molecular weight 110.27 g/mole) varies from 5.6*m* (62g K_2S/100g H_2O) at 0°C to 8.9*m* (98g K_2S/100g H_2O) at 25°C and increases to 11.3*m* (125g K_2S/100g H_2O) at 72°C. At 25°C, this is approximately a factor of 3 higher than the known molal solubility and a factor of 4.5 higher than the weight solubility of Na_2S (9).

The relative solubilities are related to the solid hydrated alkali salts with which the solutions are in equilibria. In

*Electrochemical Society Active Member.

[1]Present address: Department of Chemistry, Massachusetts Institute of Technology, Cambridge, Massachusetts 02139.

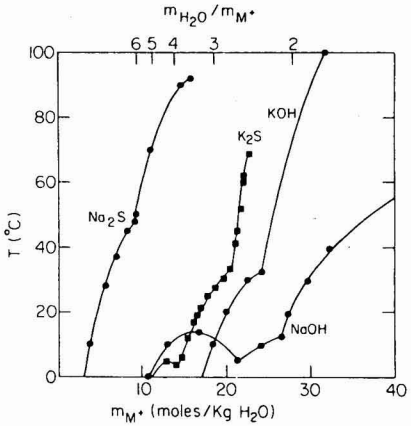


Fig. 1. The aqueous solubilities of K_2S, Na_2S, KOH, and NaOH as a function of temperature. Na_2S, KOH, and NaOH data are from Ref. (9); K_2S data are from this work.

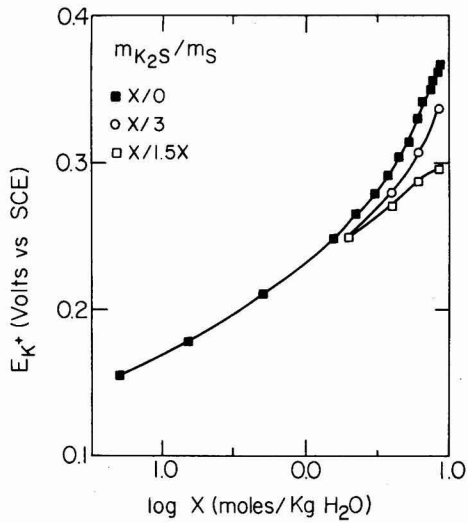


Fig. 2. The voltage response, as a function of potassium ion concentration, of a Beckman 39137 cationic selective electrode, measured vs. a Radiometer K401 SCE, in aqueous potassium sulfide and polysulfide solutions at 25°C.

the solution, as the temperature increases, the ratio of molal water (55.51 moles H_2O/Kg H_2O) to molal dissolved salt approaches the limit of the number of water molecules in these solid hydrated salts. Saturated KOH solutions are known to be in equilibria with solid KOH · $2H_2O$ for temperatures from below freezing through approximately 33°C and in equilibria with KOH · H_2O from 33 through 143°C (9). Hence, when compared to the upper horizontal axis in Fig. 1, values of KOH solubility begin to approach a molal water:dissolved salt ratio of two in the temperature range from 0 to 33°C, and a ratio of one as the temperature is increased further. Similarly, saturated NaOH solution is in equilibria with NaOH · H_2O and anhydrous NaOH, respectively, in the temperature range from 12.3 to 64.3°C, and for temperatures above 64.3°C. In the temperature range from −30 to 12°C, saturated NaOH solutions are in a complex equilibria with NaOH · xH_2O (x = 7, 5, 4, 3, and 2); the more heavily hydrated salts predominate at the lower temperatures (9). Thus, the solubility of Na_2S is limited by the highly hydrated salt with which the solution equilibrates. These are known to be $Na_2S \cdot 9H_2O$ ($m_{H_2O}/m_{Na^+} = 4.5$) in the temperature range from 0 to 48°C and $Na_2S \cdot 7H_2O$ in the temperature range from 48° to 91.5°C (9). In Fig. 1, K_2S approaches a molal water:dissolved salt ratio of 5 ($m_{H_2O}/m_{K^+} = 2.5$) in the temperature range from 7° to 38°C and a ratio of approximately 4 for temperatures above this. It is these relatively low hydration levels that permit the high solubility of K_2S.

Sulfide may hydrolyze according to the reaction

$$S^= + H_2O \rightleftharpoons HS^- + OH^- \qquad [4]$$

which has the equilibrium constant

$$K'' = (a_{HS^-} - a_{OH^-})/(a_{H_2O}\, a_{S^=}) = K_w/K_2 \qquad [5]$$

where K_2 is the aqueous second acid dissociation constant for H_2S and K_w is the water dissociation constant. Spectroscopic (10, 11) and potentiometric (12) studies indicate that, at 25°C, K_2 is less than 10^{-17}, which is several orders of magnitude smaller than previously accepted. K'' is greater than 1000, and a solution prepared with molal concentrations of alkali sulfide will contain mainly hydroxide and hydrosulfide species in solution. Therefore, it is not unreasonable that the solubilities of potassium sulfide and potassium hydroxide, as seen in Fig. 1, exhibit a parallel behavior. However, it is not clear why a saturated solution of sodium sulfide is in equilibria, at a given temperature, with a salt which is much more heavily hydrated than that for the equivalent sodium hydroxide solution.

The cation electrode couple response in potassium sulfide and polysulfide solutions is presented in Fig. 2. Potassium ion activities were calculated from Eq. [3], using the data in Fig. 2 and assuming zero liquid junction potential variation. The results are presented in Fig. 3 along with several other bulk properties measured in these solutions.

Activity coefficients larger than one in concentrated aqueous solutions result from immobilization of water within the sphere of ionic hydration. This decrease in free solvent concentration acts to raise activities. Thus, potassium hydroxide activity coefficients vary from near unity, in dilute solutions, to 33 (for 17.5m KOH at 25°C (13)). The measured potassium activities in sulfide and particularly in polysulfide solutions are depressed compared to the potassium activities in these hydroxide solutions. We attribute this, in part, to considerable ion association in solution. The addition of potassium sulfide to solution, by increasing the cation concentration in solution, increases the probability of association of potassium ions to sulfide or polysulfide ions. A mechanism and evidence for ion association in alkali salt solutions has been presented by Harned and Robinson (14) and others (15, 7).

From Fig. 3, it is also evident that the addition of sulfur to a solution of fixed K_2S concentration depresses measured K^+ activity. This is consistent with alternate physical explanations: (i) increased ion pairing or incomplete dissociation in potassium polysulfide compared to potassium sulfide solutions, and (ii) very large variations, with concentration, of liquid junction potentials across the potassium polysulfide-SCE interface. Accurate theoretical calculation or experimental measurement of the variation of the liquid junction potential in concentrated aqueous solutions is not available, although Licht has indicated that the variation is small in concentrated KOH solutions (16).

The specific conductivity in potassium sulfide and polysulfide solutions is also presented in Fig. 3. The high conductivity of these solutions reflects the known high mobility of the hydroxide species (17) that occurs from the hydrolysis of sulfide (Eq. [4]). In all solutions, maximum conductivity is found at approximately 4m potassium sulfide. With increasing concentration, the decreasing specific conductivity of very concentrated potassium hydroxide solutions is known to be paralleled by depressed dielectric constant and sharply increasing viscosity (18).

It is also interesting to note the effect of sulfur dissolution on the specific conductivity of a solution containing

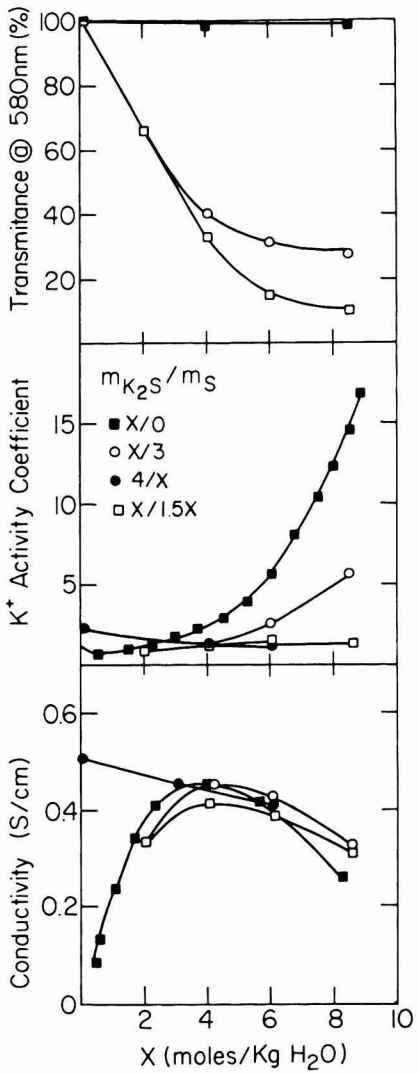


Fig. 3. The concentration dependence of specific conductivity, potassium ion activity, and transmittance at 580 nm for various aqueous potassium sulfide and potassium polysulfide solutions. The activity results are at 25°C and were determined using Eq. [3], from data in Fig. 2. Spectral data were measured at room temperature. The specific conductivity results for polysulfide were measured at 25°C; those for K_2S are at 18°C and are from Ref. (9) and (24).

a fixed potassium sulfide concentration. Protonated polysulfide species are not found in alkaline polysulfide solutions (19). Addition of sulfur to sulfide solutions produces polysulfide species according to the reaction

$$OH^- + HS^- + xS \rightarrow S_{x+1}^{=} + H_2O \qquad [6]$$

Hence, addition of sulfur depletes the concentration of the highly mobile hydroxide ion, which decreases conductivity, as is seen in Fig. 3.

Polysulfide solutions absorb light strongly at near UV and visible wavelengths. Therefore, concentrated polysulfide solutions act as cutoff filters for shorter-wavelength light. This will diminish the amount of solar irradiation incident on the photoelectrode in aqueous polysulfide based PEC's and thereby reduce conversion efficiencies. As expected, and as seen in Fig. 3, increasing polysulfide concentrations decrease solution transmittance. Surprisingly, it is seen that in a solution of fixed sulfur concentration, the 580 nm transparency is also a strong function of potassium sulfide concentration. This is despite the fact the potassium sulfide solutions, not containing sulfur, are essentially transparent to 580 nm light. In 1 cm path-length cells with aqueous solutions containing 3*m* sulfur and 2, 4, 6, or 3.47*m* potassium sulfide, 20% of incident light was absorbed at respective wavelengths of 595, 615, 630, or 642 nm.

Known equilibria constants (19, 20) and the known variation of aqueous potassium hydroxide mean solution activity (13) were incorporated into an iterative computer model (1). This was used to calculate the distribution of species in polysulfide solutions, as a function of nominal potassium sulfide and sulfur in solution. The results of these calculations are presented in Table I, and show that the main ionic components of these solutions are K^+, OH^-, HS^-, $S_3^=$, and $S_4^=$. Additionally the polysulfide solutions containing concentrated K_2S have significant activities of $S^=$ and $S_2^=$. It is also seen that a primary effect of the addition of concentrated sulfide is an increase in the $S_3^=:S_4^=$ ratio. The $S_4^=$ species displays peak absorbance at 368 nm and the $S_3^=$ species at 417 nm (21). The transmission measurements in Fig. 3 reflect the long wavelength shoulders of these peaks. Hence, as an increasing sulfide concentration is added to polysulfide solutions, the concentration of $S_3^=$ increases, shifting the solution transmission spectra from the near UV toward the visible and significantly decreasing the transparency of the solution.

Thermodynamically, aqueous polysulfide solutions are unstable. Giggenbach observed that polysulfide spontaneously disproportionates in solution according to the reaction (22)

$$S_5^= + 3\ OH^- \rightarrow S_2O_3^= + 3HS^- \qquad [7]$$

The half-life of a polysulfide solution may be defined as the time required for half of the free sulfur (as polysulfide) to disproportionate. This time, t_h (seconds), is given by (22)

$$t_h = 10^{(5600/T - 11.66)}\ C_s\ (\alpha_{HS^-})^2/(\alpha_{OH^-}\ \alpha_{S_5^=}) \qquad [8]$$

where c_S is the concentration of sulfur initially added to the solution, a_{HS^-} and a_{OH^-} are the activities of HS^- and OH^- in solution, and T is the temperature in degrees Kelvin. Temperatures over 60°C have been measured for $CdX/S_x^=$ PEC's operating under normal insolation (23). At these temperatures, the calculated useful half-life of polysulfide solutions is seen, in Table II, to increase with the concentration of added sulfide.

Photoelectrochemical characteristics.—Potentiostatic current-voltage measurements were made for illuminated 1 cm^2 $CdSe_{0.65}Te_{0.35}$ electroplated thin film electrodes immersed in a variety of polysulfide solutions. Optimal $CdX/S_x^=$ PEC I-V characteristics are known to occur in polysulfide electrolytes in which a sulfur:potassium sulfide ratio of between 1.5:1 and 2:1 has been maintained (5). Results of measurements made using both of these ratios are presented in Fig. 4 and 5. Use of a cutoff filter negated differences in light absorbance by the different polysulfide solutions. In Fig. 4, measurements were made using a cutoff filter, which allowed light of wavelengths longer than 665 nm to be incident on the photoelectrode. Similar results are obtained in Fig. 5 and are also compared to measurements in which the full spectral output of the lamp was incident on the cell.

Redox potentials of various polysulfide electrolytes are included in Fig. 4 and 5. The measured redox potential of the bulk electrolyte becomes increasingly negative with increasing polysulfide. In Fig. 4, the open-circuit voltage, V_{OC}, is seen to fall with increasing polysulfide concentration, indicative that there is not a commensurate shift in flatband potential to the observed redox potential shift. It may be that the electrode surface approaches satura-

Table I.

The calculated distribution of species, at 25°C, in polysulfide solutions at a fixed ratio of K_2S to sulfur. The calculation is based on equilibria constants in Ref. (19) and (20) according to the method presented in Ref. (1). The activity coefficient of all species in solution is considered unity except for F, the activity coefficient for OH^- and K^+, and A_w, the activity coefficient of water. F and A_w are the values for KOH solutions of the same ionic strength (13).

	Nominal concentration (moles/kg H_2O)				
K_2S	1.0	2.0	4.0	6.0	8.47
S	1.5	3.0	6.0	9.0	12.7
	Assumed activity coefficients				
F	0.867	1.34	3.75	10.2	30.5
A_w	0.921	0.818	0.572	0.343	0.153
	Calculated activities				
H_2S	1.0×10^{-7}	5.0×10^{-8}	1.5×10^{-8}	3.3×10^{-9}	5.0×10^{-10}
HS^-	0.46	0.87	1.5	1.9	1.8
$S^=$	0.00018	0.0011	0.013	0.092	0.53
$S_2^=$	0.0021	0.011	0.081	0.30	0.83
$S_3^=$	0.12	0.37	1.2	2.5	4.1
$S_4^=$	0.41	0.74	1.1	1.2	1.2
$S_5^=$	0.0074	0.0079	0.0055	0.0032	0.0019
OH^-	0.40	1.2	5.7	19.0	54.0
H^+	2.4×10^{-14}	7.3×10^{-14}	1.0×10^{-15}	1.8×10^{-16}	3.0×10^{-17}
K^+	1.7	5.3	30.0	120.0	52.0
H_2O	51.0	45.0	32.0	19.0	8.8

tion with $S_x^=$ as the concentration increases. In Fig. 5, in which the sulfur:sulfide ratio is fixed at 2:1, the trend is somewhat less evident, perhaps indicative that the electrode surface is not fully saturated with polysulfide at the lowest sulfide concentrations studied.

From Fig. 4 and 5, it is seen that short-circuit photocurrent, I_{SC}, decreases below 1m sulfide, remains relatively stable from 1 to 2m sulfide, and drops sharply at potassium sulfide concentrations greater than 4m. Presumably, the drop in I_{SC} at lower concentrations of potassium sulfide reflects mass transport limitations on the current through the cell. At concentrations of potassium sulfide greater than 4m, the drop in I_{SC} is paralleled by the observed drop in solution conductivity, Fig. 3, and also by the known increase in viscosity with increasing KOH concentration (18), and may be attributed to one or more of the following effects. (*i*) The activity measurements indicated that ion pairing increases with potassium sulfide concentration. This will remove photo-oxidizable species from solution and thereby diminish the rate of charge transfer kinetics and the measured current. (*ii*) Lando *et al.* have suggested dissolution of the photo-oxidized product as the rate-limiting step in the overall PEC reaction (25). Alkali hydroxide solutions are characterized by a sharp increase in viscosity at very high concentrations (18), and, presumably, this will be paralleled by a decrease in solution diffusivity. Diminished diffusion rates will inhibit dissolution from the photoelectrode, which will tend to impede the ongoing process of charge transfer. (*iii*) As we have shown, increasing sulfide will increase hydroxide and decrease $S_4^=$ concentration in solution. If we hypothesize that the kinetically-preferred, photo-oxidized species is $S_4^=$, then suppression of this species will decrease the charge transfer rate and, thus, the current. (*iv*) An increase in OH^- species in solution may have some direct negative effect on charge transfer.

Table II.

The calculated time for half the free sulfur to disproportionate to thiosulfate and hydrosulfide in aqueous polysulfide solutions containing various concentrations of potassium sulfide and sulfur but maintaining a 1.5:1 ratio of sulfur to potassium sulfide. The half-life, t_h, is calculated from Eq. [8].

	Nominal concentration (moles/kg H_2O)				
K_2S	1.0	2.0	4.0	6.0	8.47
S	1.5	3.0	6.0	9.0	12.7
	Calculated time of 50% sulfur disproportionation (days)				
t_h (25°C)	16,000	38,000	68,000	79,000	60,000
t_h (60°C)	180	440	870	1,100	1,200

As seen in Fig. 5, the fill factor, calculated as the ratio of the maximum measured photopower to the product $V_{OC}I_{SC}$, varies with potassium sulfide concentration in a similar qualitative manner to the variation of I_{SC}, although the decrease in fill factor is most pronounced at the lowest concentrations of potassium sulfide. Hence, there is a region of maximum conversion efficiency between 1 and 2m potassium sulfide. Efficiency drops sharply at both low and very high concentrations of sulfide. Relative efficiency drops by 30% from 2 to 3.47m sulfide, before the additional relative losses due to the decrease in solution transparency are considered.

In order to simulate roughly the real operating conditions for these PEC's, performance was tested under nonfiltered, artificial illumination at an intensity approximating peak insolation. These measurements are compiled in Fig. 5. The higher light intensity employed in these measurements is paralleled by larger charge transfer requirements. Hence, in an electrolyte that is mass-transport limited, such as the 0.5m sulfide solution when compared to the measurement at lower light intensity, a large relative drop in short-circuit photocurrent and efficiency is observed. As expected, the decreasing light transmittance by the electrolyte, with increasing polysulfide concentration, further decreases the relative I_{SC}. This tends to lower the optimal concentration of polysulfide down towards 1m, although we point out that the magnitude of this shift is dependent on the proximity of the photoelectrode to the cell wall and that the calculated lifetime of the electrolyte (Table II) increases with increasing polysulfide concentration.

In $CdX/S_x^=$ PEC's, the photoelectrode undergoes photocorrosion, typified by a decrease in photocurrent in time. We report here preliminary stability results on photoetched thin film $CdSe_{0.65}Te_{0.35}$ electrodes. An aqueous electrolyte containing 2m K_2S and 3m S was measured to increase photoelectrode lifetime compared to an electrolyte containing 6m K_2S and 9m S, suggesting that the maximum photoelectrode stability is attained in an electrolyte of intermediate polysulfide concentration. These results are consistent with a model that suggested that any factor increasing quantum yield will also increase

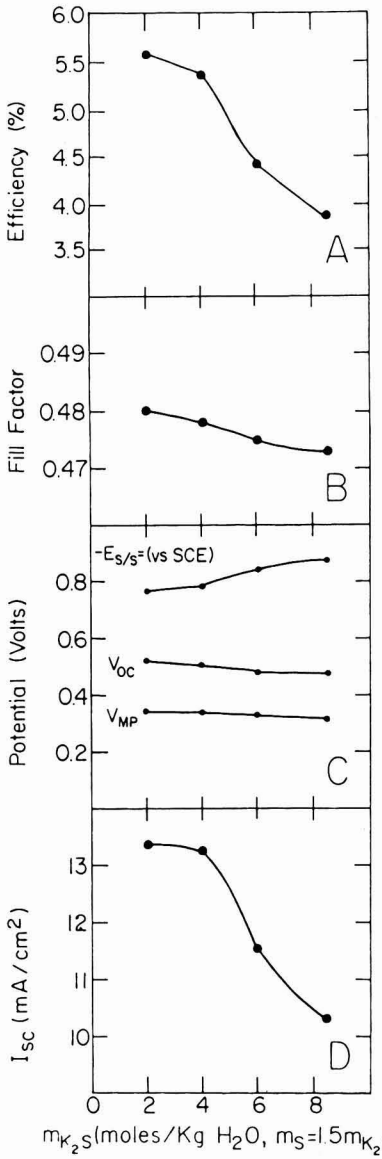


Fig. 4. The variation with potassium sulfide concentration, in a solution containing 1.5:1 ratio of potassium sulfide to sulfur, of polysulfide redox potential, and of various current and voltage related properties for an illuminated one cm^2 electroplated thin film $CdSe_{0.65}Te_{0.35}$ electrode, at room temperature. $E_{S/S^=}$, V_{OC}, V_{MP}, and I_{SC} refer to the polysulfide redox potential, the open-circuit voltage, the voltage at the I-V point of maximum power, and the short-circuit current, respectively. The light source was a tungsten halogen lamp with a cutoff filter to eliminate radiation below 665 nm. Illumination intensity was approximately equivalent to sunlight of 60 mW/cm^2.

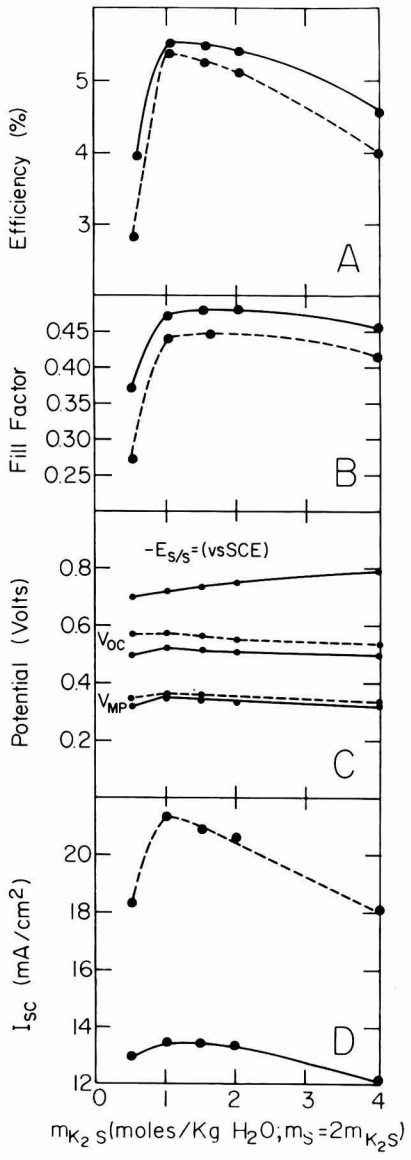


Fig. 5. As Fig. 4, but in a solution containing a 2:1 ratio of potassium sulfide to sulfur. The light source was (a) as in Fig. 4 (solid line) or (b) a tungsten halogen lamp (without cutoff filter) providing an illumination intensity equivalent to sunlight of approximately 100 mW/cm^2 (dashed line).

electrode stability (3). A more detailed and quantitative report will be presented in a future publication.

Conclusions

The measured high aqueous solubility of potassium sulfide, compared to Na_2S, resulted in the preparation of a novel series of polysulfide electrolytes for use in CdX/$S_x^=$ PEC's. In these electrolytes, containing a fixed ratio of dissolved sulfur to potasium sulfide, an increase in potassium polysulfide concentration has been shown to (*i*) significantly shift the distribution of species in solution, (*ii*) increase the solution absorbance of light, (*iii*) significantly affect solution activity, (*iv*) shift, negatively, the redox potential, and (*v*) increase the calculated disproportionation-limited lifetime of the solution. At very high potassium sulfide concentrations, effects (*i-iv*) have a negative influence on CdX/$S_x^=$ PEC photocurrent, photovoltage, fill factor, and conversion efficiency. However, low potassium sulfide concentration results in reduced mass transport, which imposes kinetic limitations. In CdX PEC's containing polysulfide electrolytes maintaining a sulfur:sulfide ratio of 1.5-2:1, optimal CdX/$S_x^=$ PEC's performance was observed with 1*m* to 2*m* potassium sulfide

concentration. We note that these optimal concentration regions are also accessible with Na_2S, although single-crystal $CdX/S_x^=$ studies have shown the beneficial effects of K^+ and Cs^+, compared to Na^+, cations (7, 8).

Successful application of photoelectrochemical cells is contingent on increases in their solar:electrical conversion efficiencies and operating lifetimes. As demonstrated in this study, modification of the cell solution chemistry has an important role in realizing these goals.

Manuscript submitted Dec. 10, 1984; revised manuscript received Aug. 25, 1985.

REFERENCES

1. S. Licht, G. Hodes, and J. Manassen, *Inorg. Chem.*, In press.
2. B. Miller, A. Heller, M. Robbins, S. Manezes, K. C. Chansan, and J. Thomson, Jr., *This Journal*, **124**, 1019 (1977).
3. R. Tenne, N. Muller, Y. Mirovsky, and D. Lando, *ibid.*, **130**, 852 (1983).
4. S. Licht and J. Manassen, *ibid.*, **132**, 1076 (1985).
5. G. Hodes, J. Manassen, and D. Cahen, *Sol. Energ. Mater.*, **4**, 373 (1981).
6. O. Bock, *Wied. Ann.*, **30**, 631 (1887).
7. S. Licht, R. Tenne, H. Flaisher, and J. Manassen, *This Journal*, **131**, 950 (1984).
8. S. Licht, R. Tenne, H. Flaisher, and J. Manassen, *ibid.*, **133**, 52 (1986).
9. J. W. Mellor, "A Comprehensive Treatise on Inorganic and Theoretical Chemistry," Vol. II, pp. 502-503, 624-626, 644, Longmans, London (1960).
10. W. Giggenbach, *Inorg. Chem.*, **10**, 1333 (1971).
11. B. Meyer, K. Ward, K. Koshlap, and L. Peter, "Proc. of 185th ACS National Meeting," Seattle, Washington, March 20-25, Abstr. 9 (1983).
12. S. Licht and J. Manassen, To be published.
13. G. Akerlof and P. Bender, *J. Am. Chem. Soc.*, **70**, 2366 (1948).
14. R. A. Robinson and H. S. Harned, *Chem. Rev.*, **28**, 419 (1941).
15. R. M. Diamond, *J. Am. Chem. Soc.*, **80**, 4808 (1958).
16. S. Licht, *Anal. Chem.*, **57**, 514 (1985).
17. J. O'M. Bockris and A. K. N. Reddy, "Modern Electrochemistry," Vol. 1, p. 366, Plenum Press, New York (1970).
18. "CRC Handbook of Chemistry and Physics," 62nd ed., C. R. Weast, Editor, CRC Press, Inc., Boca Raton, Florida (1981).
19. W. Giggenbach, *Inorg. Chem.*, **13**, 1724 (1974).
20. A. Iverson, *J. Phys. Chem.*, **68**, 515 (1964).
21. W. Giggenbach, *Inorg. Chem.*, **11**, 1201 (1972).
22. W. Giggenbach, *ibid.*, **13**, 1730 (1974).
23. N. Muller and D. Cahen, *Sol. Cells*, **9**, 220 (1983).
24. N. A. Lange, "Handbook of Chemistry," 10th ed., p. 1208, Handbook Pub., Inc., Sandusky, Ohio (1957).
25. D. Lando, J. Manassen, G. Hodes, and D. Cahen, *J. Am. Chem. Soc.*, **101**, 3969 (1979).

The High Aqueous Solubility of K_2S and Its Effect on Bulk and Photoelectrochemical Characteristics of $Cd(SeTe)/S_x^=$ Cells

II. Variation of Sulfur/Sulfide Ratio

Stuart Licht*,[1] and Joost Manassen*

Department of Materials Research, The Weizmann Institute of Science, Rehovot 76100, Israel

ABSTRACT

Variation of sulfur/alkali sulfide ratio (X_S) is shown to modify significantly transparency, redox potential, and half-life of aqueous polysulfide solutions. In electrolytes containing $3m$ total sulfur and various concentration of K_2S, shift in X_S from 2.5 to 0.4 is calculated to change the primary polysulfide species from $S_4^=$ to $S_3^=$ in solution. When these electrolytes are employed in $Cd(SeTe)/S_x^=$ photoelectrochemical solar cells, a decrease in X_S, from 2.5 to 1.8, increases relative optical to electrical conversion efficiencies by 50%, due primarily to improvement in fill factor, paralleled by an increase in $[HS^-]$. At $X_S < 1.8$, photovoltage, photocurrent, and fill factor are depressed. Photovoltage decrease is attributed to negative shifts in redox potential not paralleled by commensurate shifts in flatband potential. At low X_S, an observed decrease in fill factor and photocurrent are related to a decrease in $[S_4^=]$ in solution and to ion pairing.

Aqueous polysulfide solutions ($S_x^=$) are the most successfully applied electrolyte in cadmium-chalcogenide (CdX) photoelectrochemical solar cells (PEC's). Yet relatively little was known about the effect of solution chemistry modification on PEC performance. In a recent series of articles that includes this work, modification of each of the components comprising the alkali polysulfide solution is shown to have an important effect on $CdX/S_x^=$ PEC's performance (1-5).

In polysulfide electrolyte, added alkali hydroxide has been shown to be detrimental to $CdX/S_x^=$ PEC photocurrent, photovoltage, efficiency, electrode stability, solution stability, and solution transparency (1). The recent synthesis of extremely concentrated polysulfide solutions indicated that intermediate concentrations (1-2m in K_2S) provide optimal cell performance (2), modifying earlier indications that increases in alkali sulfide concentration were beneficial (6, 7). Alkali cations, although not directly involved in the photo-oxidation process, have a pronounced effect on cell performance, which improves with electrolyte in the order $Li_2S_x < Na_2S_x < K_2S_x < Cs_2S_x$ (3, 4). Lando *et al.* (8) suggested that sulfur dissolution was the rate-determining step in $CdX/S_x^=$ PEC performance. Hartler *et al.* (9) indicated that in polysulfide solutions, the maximum rate of sulfur dissolution occurs at a sulfur:alkali sulfide ratio (X_S) of approximately 1.4:1. Hodes *et al.* (10) found a maximum PEC stability in solutions of X_S approximately 2:1. The effect of X_S variation on PEC efficiency has not been previously reported.

The high solubility of K_2S allows for a variation of sulfide concentration between wide limits. In a previous article we reported on the influence of sulfide concentration at constant sulfur:sulfide ratio. In this study we report on the influence of varying the X_S on both the physical properties of polysulfide solutions and on the performance of $CdX/S_x^=$ photoelectrochemical solar cells.

Experimental

The procedures employed in this study, including aqueous polysulfide electrolyte preparation, the electrodeposition of thin film Cd(Se, Te) on titanium substrates, and measuring techniques, are as previously described (1, 2).

Results and Discussion

Bulk solution characteristics.—Known equilibria constants (11, 12) and the known variation of aqueous potassium hydroxide mean solution activity (13) were incorporated into an iterative computer model (14). This was used

* Electrochemical Society Active Member.

[1] Present address: Department of Chemistry, Massachusetts Institute of Technology, Cambridge, Massachusetts 02139.

Table I.

The calculated distribution of species in polysulfide solutions containing 3*m* sulfur and various concentrations of potassium sulfide. The calculation is based on equilibria constants in Ref. (11) and (12) according to the method presented in Ref. (14). The activity coefficient of all species in solution is considered unity except for *F*, the activity coefficient for OH^- and K^+, and A_w, the activity coefficeint of water. *F* and A_w are the values for KOH solutions of the same ionic strength (13).

	Temperature (°C) and nominal concentration (moles/kg H_2O)				
T	25.0	25.0	25.0	60.0	25.0
K_2S	1.2	2.0	4.0	4.0	8.47
X_S	2.5	1.5	0.75	0.75	0.35
	Assumed activity coefficients				
F	0.937	1.34	3.75	2.76	30.5
A_w	0.902	0.818	0.572	0.596	0.158
	Calculated activities				
H_2S	9.4×10^{-8}	6.0×10^{-8}	1.5×10^{-8}	1.0×10^{-7}	5.1×10^{-10}
HS^-	0.18	0.87	2.6	2.6	3.9
$S^=$	0.000028	0.0011	0.039	0.019	2.6
$S_2^=$	0.00084	0.011	0.12	0.099	0.89
$S_3^=$	0.11	0.37	0.86	0.83	0.96
$S_4^=$	0.88	0.74	0.38	0.41	0.0062
$S_5^=$	0.037	0.0079	0.00090	0.0011	0.000021
OH^-	0.16	1.2	9.7	7.3	120.0
H^+	5.7×10^{-14}	7.3×10^{-15}	6.1×10^{-16}	7.7×10^{-15}	1.4×10^{-17}
K^+	2.2	5.3	30.0	22.0	52.0
H_2O	50.0	45.0	32.0	33.0	8.8

to calculate the distribution of species in polysulfide solutions, as a function of X_S in solutions maintaining a constant nominal sulfur concentration. The results of these calculations, for varying X_S, are presented in Table I. In the table, it is interesting to note that X_S has a relatively small influence on the main polysulfide species in solution. Despite an eightfold decrease in X_S (from 2.5 to 0.35), the number of zero valent sulfurs contained in the predominant polysulfide species changes only by one (from $S_4^=$ to $S_3^=$). The solutions have high activities in K^+, OH^-, HS^-, $S_3^=$, and $S_4^=$. The activities of $S^=$ and $S_2^=$ increase sharply in the polysulfide solutions with concentrated K_2S. At large values of X_S, hydrosulfide and hydroxide activities decrease sharply. In Table I, it is seen that the distribution of species is not a strong function of temperature.

As stressed in our previous papers, concentrated polysulfide solutions act as cutoff filters for light of wavelengths less than approximately 580 nm. This will diminish the amount of solar irradiation incident on the photoelectrode in aqueous polysulfide based PEC's and thereby reduce conversion efficiencies. In a cell of 1 cm path length, a solution containing 2*m* K_2S and 3*m* sulfur transmits 67% of 580 nm light and 90% of 615 nm light. The $S_4^=$ species displays peak absorbance at 368 nm and the $S_3^=$ species at 417 nm (15). Solution transparency reflects the long wavelength shoulders of these peaks. Hence, a decrease of X_S from 1.5 to 1.33 (that is, to 4*m* K_2S and 3*m* S), which, as seen in Table I, increases $S_3^=$ activity, decreases 580 nm light transmittance to 40%. Addition of sulfur introduces competing effects on visible light absorbtion by the solution: (*i*) it increases total polysulfide in solution, which tends to decrease solution transparency, and (*ii*) it decreases the $S_3^=$:$S_4^=$ ratio, which tends to have the opposite effect. A solution containing 4*m* K_2S and 6*m* S transmits 34% of 580 nm light.

As discussed in part I of this series, polysulfide solutions are thermodynamically unstable (2, 16). Temperatures over 60°C have been measured for CdX/$S_x^=$ PEC's operating under normal insolation (17). In Table II it is seen that, at these temperatures, the useful half-life of polysulfide solutions as a function of X_S, calculated by varying nominal sulfide concentration, rises with decreasing X_S.

Photoelectrochemical characteristics.—The first paper in this series reported the effect on the PEC performance of a wide range of polysulfide electrolytes maintaining a fixed sulfur:alkali sulfide ratio (2). Now we observe the significant effect of X_S variation on photoelectrochemical behavior for illuminated 1 cm^2 $CdSe_{0.65}Te_{0.35}$ electroplated thin film electrodes immersed in a variety of polysulfide solutions. These potentiostatic photocurrent-voltage measurements are presented in Fig. 1, in which a cutoff filter was used to eliminate light of wavelengths below 665 nm, and in Fig. 2, in which the full spectral output of the lamp was incident on the cell. Use of the cutoff filter negated differences in light absorbance by the different polysulfide solutions.

Redox potentials of polysulfide electrolytes prepared with 3*m* S, as a function of X_S, are included in Fig. 1 and 2. As previously observed (18), the redox potential of the bulk electrolyte becomes increasingly positive with increasing X_S. If one makes the assumption that the electrode is saturated with polysulfide and, hence, that the flatband potential of the Cd(SeTe) photoelectrode remains approximately the same in each of these solutions, then the observed redox potential variation should be reflected in an open-circuit voltage (V_{OC}) that increases with increasing X_S, and, in Fig. 1, this is indeed seen to be the case.

In Fig. 1 the variation of short-circuit photocurrent (I_{SC}) is shown to increase towards maximum with increasing X_S. This variation of I_{SC} is consistent with one or more of the following trends: (*i*) preferential photo-oxidation of $S_4^=$ compared to $S_3^=$ (see Table I), (*ii*) preferential dissolution of the photo-oxidized product in the less concentrated and, hence, less viscous solutions, or (*iii*) an increase in ion pairing as the ionic strength of the solution in-

Table II.

The calculated time for half the free sulfur to disproportionate to thiosulfate and hydrosulfide in aqueous polysulfide solutions containing 3*m* sulfur and various concentrations of potassium sulfide. The half-life, t_h, is calculated using data from Table I, by Eq. [8] in Ref. (2).

	Nominal concentration (moles/kg H_2O) and [S]/[K_2S]			
K_2S	1.2	2.0	4.0	8.47
X_S	2.5	1.5	0.75	0.35
	Calculated time of 50% sulfur disproportionation (days)			
t_h (25°C)	2,340	38,000	350,000	2,800,000
t_h (60°C)	27	440	4,300	66,000

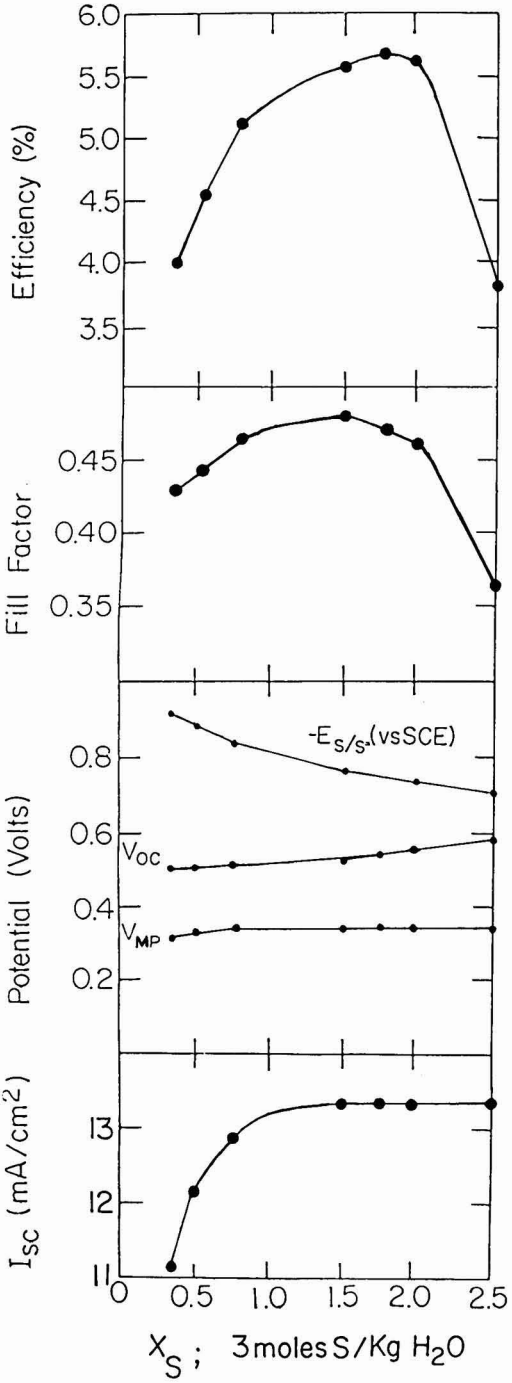


Fig. 1. The variation with X_S of polysulfide redox potential and of various current- and voltage-related properties for an illuminated one cm^2 electroplated thin film $CdSe_{0.65}Te_{0.35}$ electrode, at room temperature. X_S is the ratio of sulfur to K_2S in solution. The sulfur concentration remains fixed at 3m. $E_{S/S^=}$, V_{OC}, V_{MP}, and I_{SC} refer to the polysulfide redox potential, the open-circuit voltage, the voltage at the I-V point of maximum power, and the short-circuit current, respectively. The light source was a tungsten halogen lamp with a cutoff filter to eliminate radiation below 665 nm. Illumination was approximately equivalent to a solar intensity of 60 mW/cm^2.

creases. Ion pairing, of the form previously discussed (1-4), tends to reduce free polysulfide in solution, which impairs charge transfer and thereby reduces current.

As opposed to the variation of V_{OC} and I_{SC}, both of which improve with X_S, the fill factor, calculated as the ratio of the maximum measured photopower to the prod-

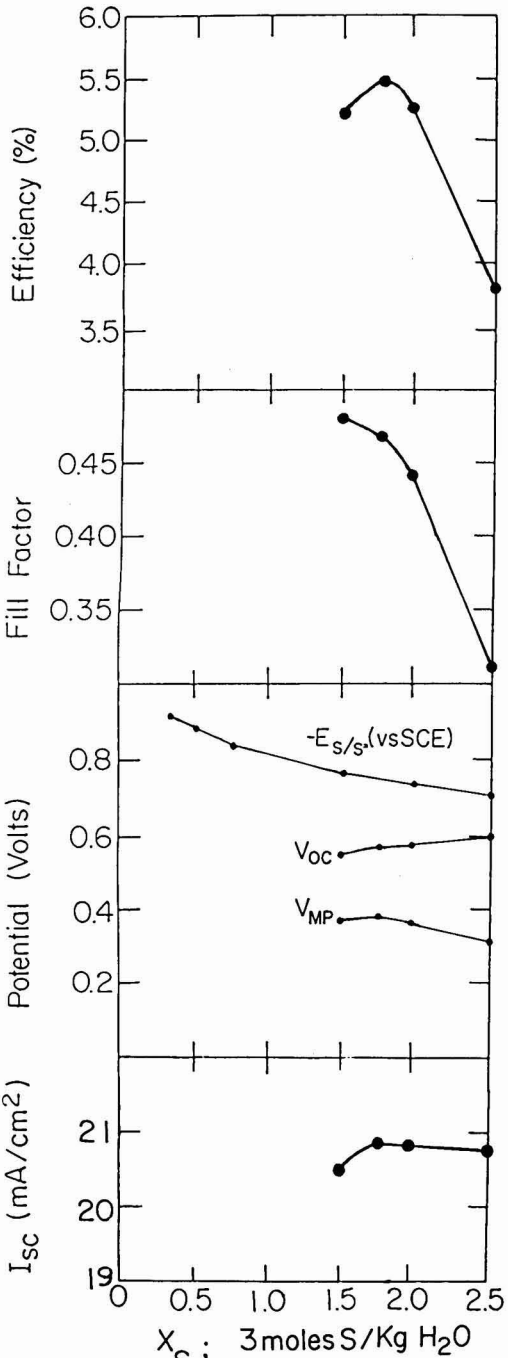


Fig. 2. As Fig. 1, but the light source was a tungsten halogen lamp (without cutoff filter) providing an illumination equivalent to sunlight of approximately 100 mW/cm^2.

uct $V_{OC}I_{SC}$, is seen in Fig. 1 to display a maximum at X_S of approximately 1.5. Both hydrosulfide and hydroxide activities have been shown to decrease with increasing X_S (Table I). Added hydroxide is generally detrimental to fill factor and overall performance (1). Hence, it appears that some minimum hydrosulfide activity is necessary to maintain satisfactory fill factors. In Fig. 1, the optimal optical to electrical conversion efficiency, strongly influenced by the sharp variation in fill factor, displays a maximum at approximately $X_S = 1.8$.

In order to roughly simulate real operating conditions for these PEC's, performance was tested under non-filtered artificial illumination at an intensity approximating peak insolation. These measurements are compiled in Fig. 2. Trends are similar to those seen in Fig. 1, with the additional pertinent features: (*i*) absorbance of light by the solution results in a small drop in conversion efficiency, and (*ii*) at large X_S, a drop in fill factor and I_{SC} is observed. These measurements were conducted at higher light intensities (compared to those in Fig. 1). It is suggested that at the resulting higher charge densities, a depletion of hydrosulfide in solution impairs either charge transfer or sulfur dissolution, which in turn causes the observed drop in I_{SC} and fill factor. To emphasize the importance of X_S optimization, it should be noted in Fig. 2 that a 50% improvement in relative efficiency is gained by adding 0.5*m* K_2S to an electrolyte containing 1.2*m* K_2S and 3*m* sulfur.

In situations where higher current densities are to be maintained by the electrode, the relative importance of improved charge transfer kinetics should increase. Therefore, if the PEC were to be illuminated under concentrated light, or if electrodes of higher conversion efficiencies were employed, then one would expect the relative increase in efficiency be removal of hydroxide to be even higher. This is reflected in recent outdoor measurements on a $CdSe_{0.65}Te_{0.35}$ single crystal in which relative efficiency improved by 65% to an absolute efficiency of 12.7% when the cell electrolyte containing 1*m* NaOH, 1*m* Na_2S, and 1*m* S was replaced by an electrolyte consisting of 1.8*m* Cs_2S and 3*m* S (5). The improvement results from an optimization of both X_S and nominal sulfide concentration by (*i*) not adding hydroxide and (*ii*) changing the alkali cation in solution.

In $CdX/S_x^=$ PEC's, the photoelectrode undergoes photocorrosion, typified by a decrease in photocurrent in time. In a solution containing 1*m* KOH, 1*m* Na_2S, and various sulfur concentrations, Hodes *et al.* (10) found a maximum thin film CdSe stability at an X_S of approximately two. A general rule had been formulated that those factors increasing relative quantum yield (normalized short-circuit current density compensated for solution transparency) will also improve photoelectrode stability (7, 8). However, as seen in Fig. 1, it appears that fill factor and not short-circuit current displays a maximum of X_S similar to those found in the stability study, although it should be noted that these studies have employed significantly different polysulfide electrolytes.

Manuscript submitted Dec. 10, 1984; revised manuscript received Aug. 25, 1985.

REFERENCES

1. S. Licht and J. Manassen, *This Journal*, **132**, 1076 (1985).
2. S. Licht, J. Manassen, and G. Hodes, *ibid.*, **133**, 264 (1986).
3. S. Licht, R. Tenne, H. Flaisher, and J. Manassen, *ibid.*, **131**, 950 (1984); *ibid.*, **133**, 54 (1985).
4. S. Licht, *J. Phys. Chem.*, In press.
5. S. Licht, R. Tenne, G. Dagan, J. Manassen, G. Hodes, D. Cahen, R. Triboulet, J. Rioux, and C. Levy-Clement, *Appl. Phys. Lett.*, **46**, 608 (1985).
6. B. Miller, A. Heller, M. Robbins, S. Menezes, K. C. Chansan, and J. Thompson, Jr., *This Journal*, **124**, 1019 (1977).
7. R. Tenne, N. Muller, Y. Mirovsky, and D. Lando, *ibid.*, **130**, 852 (1983).
8. D. Lando, J. Manassen, G. Hodes, and D. Cahen, *J. Am. Chem. Soc.*, **101**, 3969 (1979).
9. N. Hartler, J. Libert, and A. Teder, *Ind. Eng. Chem., Process Des. Dev.*, **6**, 398 (1967).
10. G. Hodes, J. Manassen, and D. Cahen, *Sol. Energ. Mater.*, **4**, 373 (1981).
11. A. Iverson, *J. Phys. Chem.*, **68**, 515 (1964).
12. W. Giggenbach, *Inorg. Chem.*, **13**, 1724 (1974).
13. G. Akerlof and P. Bender, *J. Am. Chem. Soc.*, **70**, 2366 (1948).
14. S. Licht, G. Hodes, and J. Manassen, *Inorg. Chem.*, In press.
15. W. Giggenbach, *Inorg. Chem.*, **11**, 1201 (1972).
16. W. Giggenbach, *Inorg. Chem.*, **13**, 1730 (1974).
17. N. Muller and D. Cahen, *Sol. Cells*, **9**, 220 (1983).
18. G. Hodes, D. Cahen, J. Manassen, and M. David, *This Journal*, **127**, 2252 (1980).

Electrolyte Loss and Performance Decay of Molten Carbonate Fuel Cells

Charles D. Iacovangelo* and Elihu C. Jerabek

General Electric Company, Corporate Research and Development, Schenectady, New York 12301

ABSTRACT

Postmortem chemical analysis, gas chromatography, electrode polarization studies, atomic adsorption spectroscopy, and Hg intrusion porosimetry have been employed in studies of the extent of electrolyte loss from cell components and the resultant performance decay. This study has identified electrolyte creep, hardware corrosion, and chrome lithiation as the pivotal electrolyte consumption mechanisms. The principal mechanisms of performance decay are increased cell resistance, increased cathode polarization, and deteriorating gas compositions due to gas crossover and parasitic reactions at the wet seal edges of the cell.

Commercialization of cost-effective, high efficiency, molten carbonate fuel cells necessitates a stack life approaching 40,000h. In order to achieve such a life, electrolyte loss from operating cells and electrolyte redistribution among the active cell components must be understood and controlled. Electrolyte loss from operating cells occurs through four basic mechanisms: lithiation of the anode and cathode, hardware corrosion, vapor loss, and electrolyte migration from the cell (creep).

Lithiation of the anode, or, more specifically, of the chromium content of the anode, can occur chemically (reaction [1]) in typical fuel environments: $P_{O_2} = 10^{-17}$-10^{-21}.

$$2Cr + Li_2CO_3 + O_2 \rightarrow 2LiCrO_2 + CO \qquad [1]$$

This reaction more likely occurs by the electrode reaction

* Electrochemical Society Active Member.

[2]

$$Cr + Li^+ + 2CO_3^= \rightarrow LiCrO_2 + 2CO_2 + 3e^- \quad [2]$$

which is potential dependent. Analyses of cells that operated between 24 and 2000h have shown that lithiation of chromium is limited by diffusion of Cr out of the Ni-chrome alloy, leveling out after ~300h at 80% lithiation (1).

Lithiation of the cathode involves incorporation of lithium ions into the nickel oxide lattice with subsequent formation of Ni^{+++} ions. This equilibrium has been modeled by Bronstein *et al.* (3) according to reaction [3]

$$1/2\ x\ Li_2CO_3 + NiO + 1/4\ x\ O_2 = x\ LiNiO_2 + 1/2\ x\ CO_2 + (1 - x)\ NiO \quad [3]$$

In a manner similar to that of lithiation of chromium in the anode, lithiation of the cathode probably occurs by means of the electrode reaction [4]

$$1/2\ x\ O_2 + NiO + x\ Li^+ + xe^- \rightarrow x\ LiNiO_2 + (1 - x)\ NiO \quad [4]$$

where x = atomic fraction of Li^+ and Ni^{+++}.

As Eq. [3] and [4] show, the equilibrium percent Li in lithiated NiO is dependent upon the activity of Li_2CO_3 in the melt, which is constantly decreasing in operating cells, upon the cathode gas atmosphere, and upon the cathode potential. Analyses of cathodes from operating cells (2, 11) have shown these effects to be minor. Under standard operating conditions, the cathode should contain ~0.04 atomic fraction Li.

Li_2CO_3 consumption in the cell due to corrosion of the cathode hardware has proven to be one of the more difficult values to assess. In general, corrosion rates on the order of 4 μm/1000h have been measured for the operating conditions of standard 100 cm² cells (4). The corrosion product has been shown to be a duplex layer consisting of a protective outer $LiFeO_2$ layer and an inner Cr_2O_3 layer. The quantity of Li_2CO_3 consumed by such a corrosion layer in a 100 cm² cell (~200 cm² of 300 series stainless steel) would be ~0.14g. It should be noted, however, that the protective oxide layer may crack during thermal cycling, causing continued lithiation and corrosion (4).

The amount and composition of electrolyte that is lost from operating cells due to vapor loss by equilibration with the fuel gases exiting from the cell has been an elusive parameter. Ong and Claar (5) have measured weight loss from varying electrolyte compositions under fuel and oxidant gases as a function of temperature and pressure. These results were found to correlate with carbonate loss from the 10,000h cell test: 3.7 *vs.* 3.3g/10,000h. Modeling of vapor loss by Wilemski *et al.* (6) and Bale *et al.* (7) has demonstrated sufficient correlation with experimental results obtained by Ong and Claar (5) in the oxidant gas, but suggest higher vapor losses in the fuel gas. It is clear from the 10,000h cell test, however, that vapor loss is not appreciably larger than indicated by the measurements of Ong and Claar. In fact, Kunz (8) has recently suggested that vapor loss from operating cells is much smaller than measured in out-of-cell tests (9), although earlier, good correlation between in-cell and out-of-cell measurements was reported (10). Several short time vapor loss tests conducted at General Electric Company (11) to establish background weight loss rates in support of corrosion studies agreed with the reported results of Ong and Claar. Their data was used to predict and allow for vapor loss in this study. For this purpose, the equilibrium composition of vapor was assumed to be established with the exiting gas composition and flow rate. On the basis of these assumptions, one may conclude that a standard 100 cm² cell operating at 160 mA/cm² on a fuel of 60% H_2 40% CO_2, humidified at 140°F at 75% utilization, would consume ~0.104g of Li_2CO_3/1000h. The corresponding loss at the cathode, 75% air 25% CO_2, humidified at 140°F and 50% utilization, would be ~0.06g/1000h. It should be noted that vapor loss has been shown to be a strong function of electrolyte composition. Particularly in comparing lithium/potassium and lithium/sodium carbonate melts. However, little change in vapor loss due to the changing Li/K ratio in the range of this test was anticipated. Therefore, no attempt was made in this study to correct vapor loss for changing electrolyte composition with time.

Electrolyte loss from the cell due to electrolyte creep on the external cell hardware or within external manifold designs has been modeled by Kunz (8). In this study, the effect of electrolyte creep on performance decay is examined.

Experimental

Electrolyte loss from four 100 cm² (active area) laboratory cells was examined. Each cell was operated continuously at 650°C, 1 atm, and 160 mA/cm² on (0.48 H_2, 0.32 CO_2, and 0.20 H_2O) fuel and (0.13 O_2, 0.20 CO_2, 0.20 H_2O, and 0.47 N_2) oxidant. Flow rates of fuel and oxidant were set for 75 and 50% utilization, respectively. All cells employed 0.038 cm (0.015 in.) thick ~80% porous nickel cathodes and 0.051 cm (0.020 in.) thick hot-roll-milled (HRM) electrolyte tapes (11). Two of the cells, M70 and M86, operated with state of the art (SOA) 0.076 cm (0.030 in.) thick Ni-10 Cr anodes (~65% porous), and two, M71 and M87, had 0.076 cm (0.030 in.) thick (70% porous) metal plated-ceramic anodes (12-15). The remaining difference among the cells was the initial electrolyte composition, which was 62 mole percent (m/o) Li_2CO_3:38 m/o K_2CO_3 in cells M70 and M71, and ~70 m/o Li_2CO_3:30 m/o K_2CO_3 in the remaining cells. The electrolyte composition in the latter cells was increased in Li_2CO_3 content to allow for Li_2CO_3 loss early in life so that the final electrolyte composition of the cells after 2000h would be ~62 m/o Li_2CO_3:38 m/o K_2CO_3.

Final electrolyte contents were determined from weight loss of cell components after leaching the carbonates in 50% aqueous acetic acid under vacuum. The leachant was analyzed by atomic adsorption spectroscopy for Li, K, Ni, Cr, Fe, and Cu to allow comparison of weight loss data with Li_2CO_3 and K_2CO_3 contents and, also, to correct the carbonate content for species present in the melt other than Li_2CO_3 and K_2CO_3. Analyses were carried out on small individual samples of anode, cathode, matrix, and hardware to examine differences in electrolyte composition and quantity among the cell components and at different locations within the cell. These samples accounted for ~20% of the cell package, and the remainder of the cell package was leached in bulk with no differentiation among individual components. The distribution of electrolyte within the cell components was determined using an Aminco Model 7121B Hg-intrusion porosimeter by comparing pore size and pore volume distribution before and after leaching the electrolyte.

Performance decay with time was evaluated by periodic measurements of: cell performance, anode and cathode polarizations, cell impedance, and exiting gas compositions. Anode and cathode polarizations were measured using a Keithley Model 616 digital electrometer against an O_2/CO_2/Au reference electrode placed at the cathode/electrolyte matrix interface (16, 17). Cell impedance measurements were made with a Hewlett Packard Model 4275A LCR meter at 100, 1000, and 10,000 Hz. Gas analysis was done on a dry basis using a Hewlett Packard Model 5880A gas chromatograph.

Results and Discussion

Electrolyte loss.—Listed in Table I is the initial electrolyte loading in each of the four cells examined. This initial loading is broken down according to where the electrolyte was anticipated to be located in the anode, cathode, and electrolyte matrix. These loadings were based on the percentage of small pores ($\leq$2 μm) typically observed in operating cells (18, 19). Table I also lists the amount of electrolyte initially loaded in the cell to compensate for the various loss mechanisms described earlier. As Table I demonstrates, only cells M86 and M87 had enough electrolyte loaded initially to allow for elec-

Table I. Postmortem cell analysis of carbonate

Cells M70, M86: Ni-10 Cr anode; M70 570h; M86 1766h.
Cells M71, M87: Ni-Cu-plated $SrTiO_3$; M71 640h; M87 1766h.

	M70 (g)	M71 (g)	M86 (g)	M87 (g)
Initial Electrolyte Loading Composition				
Anode fill (62:38)	3.124	3.184	3.007	0.568
Anode lithiation (Li_2CO_3)	—	—	1.763	—
Cathode fill (62:38)	1.106	1.115	1.097	1.144
Cathode lithiation (Li_2CO_3)	—	—	0.184	0.207
Matrix fill (62:38)	8.480	8.321	8.863	8.740
Hardware lithiation (Li_2CO_3)	—	—	0.140	0.140
Vapor loss (62:38)	—	—	0.500	0.500
Total electrolyte loading	12.710	12.620	15.554	11.299
Final Electrolyte Contents				
Theoretical[a]	10.617	11.979	13.616	10.748
Measured	10.270	11.598	13.804	10.639
Difference	0.347 (3.3%)	0.381 (3.2%)	0.188 (1.4%)	0.109 (1.0%)
Final Electrolyte Composition				
Theoretical Li_2CO_3/K_2CO_3	51:49	60:40	64:36	63:37
Measured	49:51	58:42	65:35	63:37

[a] Theoretical value is based on actual anode and cathode lithiation.

trolyte loss and still fill the active components to the anticipated levels. In cells M70 and M71 electrolyte loss would come from draining electrolyte from the active components. In all cells, the electrolyte was added to the cathode flow field and allowed to percolate through the cathode to fill the active components.

Hardware corrosion, as shown, accounted for only ~1% of the total electrolyte content. To allow for vapor loss, 0.5g of 62:38 carbonate was added (~4% of the total electrolyte content). It should be pointed out that vapor loss was expected to be predominantly in the form of KOH and represents loss of K_2CO_3 from the cell. The addition of 62:38 eutectic, therefore, added additional Li_2CO_3 over and above the amount required in the cell. Based on the electrolyte breakdown shown in Table I, it was concluded that the initial electrolyte compositions of cells M70, M71, M86, and M87 were 62:38, 62:38, 71:29, and 64:36 Li_2CO_3:K_2CO_3, respectively.

Also listed in Table I are the final electrolyte contents of each cell. These values are compared with the theoretical contents anticipated after allowing for each of the loss mechanisms described previously. As can be seen, good correlation between anticipated and measured electrolyte contents was obtained with and without electrolyte added to allow for electrolyte loss. The differences observed are within the error limits of the analysis technique. The closer agreement in the latter two cells, M86 and M87, was due principally to three key factors. First, two problems were encountered with weight-loss measurements. Ensuring that all the electrolyte leached from the small pores was particularly difficult with the anode. Also, it was found that careful drying of $LiAlO_2$ in the matrix was necessary, to avoid hydration effects that introduced appreciable errors in the weight-loss values. Detailed attention was given to these factors for the latter two cells. Thirdly, to ensure that the weight-loss values were accurate, the leachants from the latter cells were analyzed by atomic absorption for Li, K, Ni, Cr, Cu, and Fe. These values were used to correct the weight-loss values, which resulted in a change of ~5%. The values listed in Table I are the corrected values.

The results for cells M70 and M71 show that, in a relatively short time, a marked percentage of the initial electrolyte was lost—19.2 and 8.1%, respectively. The pivotal difference between the two cells was the lithiation of the chrome in the anode of cell M70, which consumed 1.65g of Li_2CO_3 (13% of total electrolyte loading). As will be shown later, this loss in electrolyte caused a marked drainage of electrolyte from the electrolyte matrix, resulting, subsequently, in a high performance decay. In comparison, although cells M86 and M87 lost a similar amount of electrolyte (11.3 and 5.8%, respectively), sufficient electrolyte remained in the cell to fill the matrix. This resulted in a greatly reduced performance decay.

Of equal importance for determining the quantity of electrolyte lost from operating cells was the composition of the remaining electrolyte. If the loss mechanisms postulated earlier are accurate, then the final electrolyte composition should be predictable. Excellent correlation between measured and anticipated electrolyte compositions, shown in Table I, was obtained. This demonstrates the preferential loss of lithium from the electrolyte. Table I shows that, without additional electrolyte added to the cells (M70 and M71), the cells were actually operating with a reduced Li_2CO_3 electrolyte, which was ~50:50 Li_2CO_3:K_2CO_3 for cells with SOA anodes. It was mentioned earlier that the anticipated final electrolyte compositions for cells M86 and M87 were 62:38. The values listed in Table I, however, were corrected for the measured degree of lithiation of the anode and cathode, which was lower than anticipated. Also, as described earlier, 62:38 Li_2CO_3:K_2CO_3 was added to allow for vapor loss, although the predominant loss was of K_2CO_3. These corrections were larger for cell M86 than M87, resulting in theoretical compositions of 64:36 and 63:37, respectively. As seen, the measured electrolyte compositions were extremely close, 65:35 and 63:37.

Electrolyte distribution.—In order to maintain initial cell performance, it is critical to understand and control electrolyte distribution among the active cell components. The electrolyte content and location in each of the active components of these four cells was determined. Shown in Fig. 1 and 2 are the electrolyte contents of the Ni-Cr anodes from cells M70 and M86. The electrolyte content of these anodes filled ~31 and 42% of the void volume and resided in pores $\leq$ ~0.6 and 1.0 μm, respectively.

It has been shown (18) that these pores are associated with a porous $LiCrO_2$ skin on the surface on the Ni-Cr strands. A comparison of these two electrodes, shown in Fig. 3, demonstrates the concern over the large percentage of small pores in SOA anodes. After 1766h on-test, ~40% of the pores in the anode are smaller than the pores in the electrolyte matrix (see Fig. 6 and 7), causing considerable drainage of electrolyte from the matrix.

In contrast, the electrolyte content of metal plated-ceramic anodes was very small. Shown, for example, in Fig. 4 is the distribution for the anode from cell M87 after 1766h on-test. This electrode had only ~4% of the void volume filled with electrolyte. This results from the elimination of lithiation and subsequent formation of small pores and from a large wetting angle of carbonate on metals compared to a zero wetting angle on oxides (20).

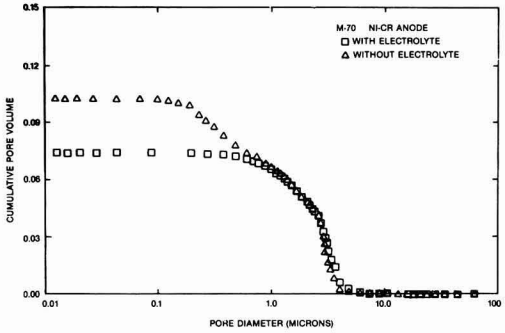


Fig. 1. Pore distributions of a Ni-Cr anode, with and without electrolyte, after testing in cell M70 for 570h.

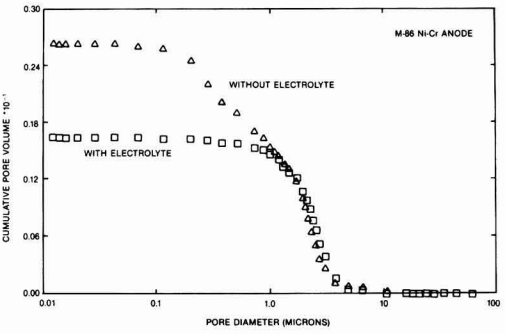


Fig. 2. Pore distribution of a Ni-Cr anode, with and without electrolyte, after testing in cell M86 for 1766h.

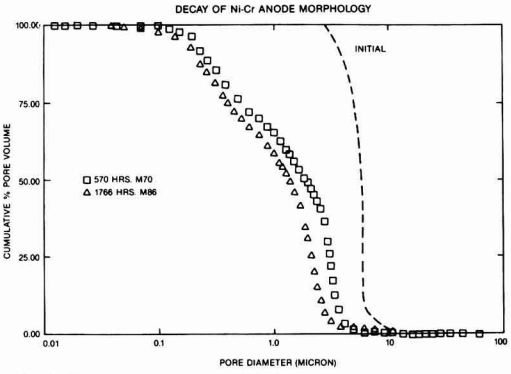


Fig. 3. Comparison of pore size distribution for two Ni-Cr anodes after cell testing for 570 and 1766h.

Like the anode, the cathode also forms small pores due to the conversion of Ni to lithiated NiO (19). Unlike the anode, however, the percentage of small pores is formed early in life and remains constant. Little difference was found between the pore distribution after ~500h and after 1766h.

Shown in Fig. 5 is the pore distribution of the cathode from cell M87 after 1766h. This electrode contained ~27% of the void volume filled with electrolyte. Although the percentage of small pores formed in the cathode is relatively consistent, the percentage filled with electrolyte is dependent upon the amount of electrolyte present in the cell package and the type of anode employed. This effect was pronounced in cell M71, where enough electrolyte was added to the cell to fill ~35% of the anode. As was shown earlier, however, plated-ceramic anodes do not retain high electrolyte contents. Thus, this excess electro-

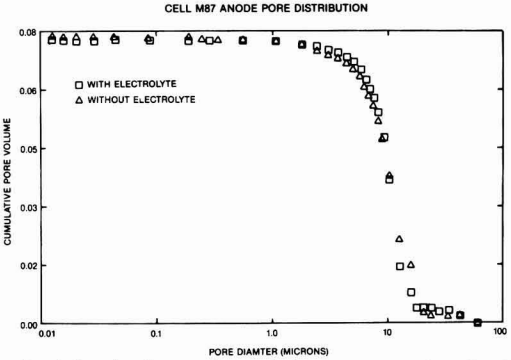


Fig. 4. Pore distributions of a metal plated-ceramic anode, with and without electrolyte, after cell testing for 1766h.

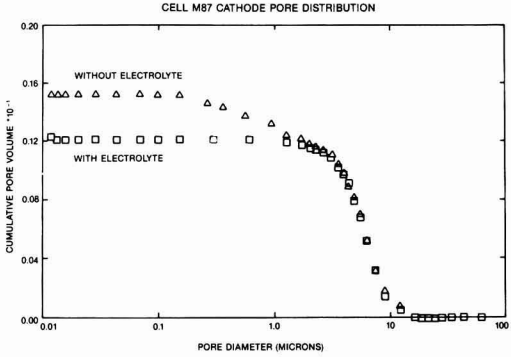


Fig. 5. Pore distributions of a NiO cathode, with and without electrolyte, after cell testing for 1766h.

lyte was retained in the cathode, filling ~40% of the open porosity. Over-filling of the cathode has been shown to result in extremely poor cathode performance (21) and emphasizes the need to coordinate the amount of electrolyte and the pore distributions in each component (22).

Shown in Fig. 6-8 are the pore size distributions of all three active components for cells M70, M86, and M87. Listed in Table II are the carbonate contents of all four cells. Figure 6 and Table II show that at end of life, due to carbonate consumption, cell M70 had only enough electrolyte left in the cell to fill pores $\leq$~0.6 μm. The filled pores are those to the left of the vertical dashed line in Fig. 6-8. This resulted in filling of 31, 13, and 85% of the anode, cathode, and matrix, respectively. Cell M71, in

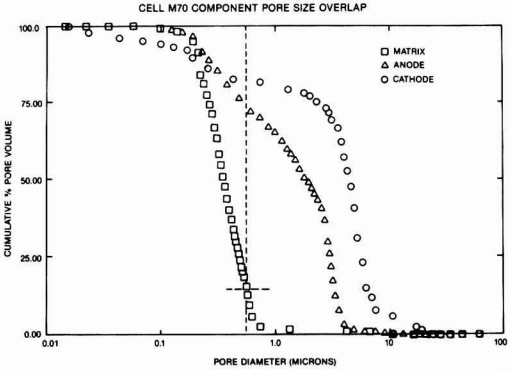


Fig. 6. Overlap of pore size distributions of the anode, cathode, and matrix from cell M70.

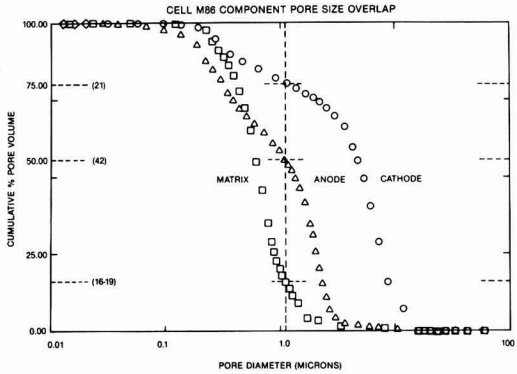


Fig. 7. Overlap of pore size distributions of the anode, cathode, and matrix from cell M86.

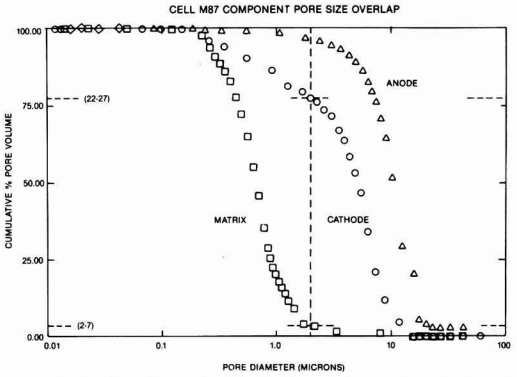


Fig. 8. Overlap of pore size distributions of the anode, cathode, and matrix from cell M87.

contrast, due to the low carbonate content of the anode (~12%), had sufficient carbonate to fill completely the matrix and ~40% of the cathode. Although cells M86 and M87 had excess electrolyte added initially to allow for electrolyte loss, complete fill of the matrix was not found. In cell M86, Fig. 7, the largest pore size filled with electrolyte was ~1.0 μm compared to 0.6 μm for cell M70. However, the increased anode fill of 42% and the large percentage of pores greater than 1 μm in the matrix (~15%) resulted in only 84% fill of the matrix. Cell M87, Fig. 8, in comparison, had sufficient electrolyte to fill pores up to ~2 μm in size. However, as shown, the matrix used in this cell had ~5% of the pores present larger than 2 μm, resulting in only a 93% fill of the matrix.

These results point out several important features of cell design. First, it is imperative to add sufficient electrolyte to allow for electrolyte loss. It is clearly evident that the pore size in the matrix must be kept below ~1 μm for complete fill. It is also apparent that, in order to store electrolyte for continued performance, one must store the electrolyte in precisely controlled pore size regions within the cell, or flooding of the electrodes will occur. In cells with plated ceramic anodes, this flooding occurs in the cathode. The tolerances of pore sizes allowable for such electrolyte storage concepts depend strongly on the type of anode used.

Table II. Postmortem electrolyte distribution

Component	Cell % fill M70	M71	M86	M87
Anode anticipated	35	—	35	—
Anode measured	31	12	42	4
Cathode anticipated	20	20	20	20
Cathode measured	13	40	21	27
Matrix anticipated	100	100	100	100
Matrix measured	85	100	84	93

Cell performance.—Adding sufficient electrolyte to account for electrolyte loss with time had a dramatic effect on cell performance and decay. Shown in Fig. 9 are life plots for cells M86 and M87, which had significantly higher electrolyte contents than cell M70. Cell M70 exhibited the largest decay rate, ~70 mV in 500h, compared to cell M86, which exhibited a constant decay rate of ~30 mV/1000h. Cell M86 had a peak performance of 0.776V, which was within 56 mV of the theoretical exit Nernst potential of 0.832V. After 1766h, this cell had a voltage of 0.706V. Cell M87 has a slightly lower peak performance of 0.760V and exhibited a slightly higher decay rate of ~50 mV/1000h. The cell voltage after 1766h was 0.652V, which was falling more rapidly after 1694h. Of critical importance in each cell was the mechanism of performance decay. These cells were analyzed with respect to the following mechanisms: changing gas composition due to increased crossover and wet seal/furnace atmosphere reactions, increased IR due to voiding of the electrolyte matrix and increased contact resistances, and increased electrode polarization. The effect of these mechanisms as a function of time and current is shown in Table III, which lists the following: the exit fuel gas composition (with percentage of theoretical shown in parenthesis), calculated cell Nernst potential based on the measured gas compositions, measured cell voltage, calculated anode Nernst potential (*vs.* a 0.16 O_2, 0.25 CO_2/Au reference electrode), measured anode potential against the same reference electrode, anode overpotential (η_A) calculated as the difference between anode potential and anode Nernst potential, cell overpotential (η_C) calculated as the difference between the cell voltage and cell Nernst voltage, and the cell IR loss at 16A.

The most notable change shown in this table is the decreasing H_2 content in both cells. Neither cell started with theoretical H_2 contents, which accounts for the low open-circuit voltages of 0.973 and 0.980V, compared to a theoretical 0.984V. The H_2 content of each cell continued to deteriorate with time with only 69 and 76% of incoming H_2 being present at end of life. It should be noted that the listed fuel gas compositions cannot be derived by assuming only cathode gas crossover. Instead, these gases simulated utilized fuel conditions that were low in H_2 and high in CO_2, with little N_2 present. The reasons for utilized fuel gas are hypothesized as parasitic reaction at the wet seal involving hardware corrosion and electrolyte pumping. These effects will be discussed in further detail. It is of interest, however, to note that, although cell M87 showed little increase in N_2 content, 0.3% at end of life, the H_2 content was still only 76% of theoretical, and CO_2 content increased to 132%. The effect of electrolyte deficiency on

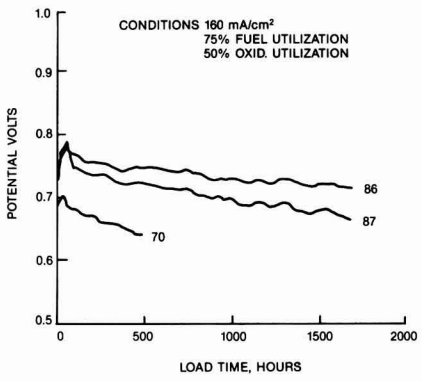


Fig. 9. Comparison of life performance of cell M86, M87, and M70

Table III. Gas composition and performance correlations

Cell no.	Test hours	I (A)	Exit fuel gas composition (% theor.) H_2	CO_2	CO	H_2O[a]	N_2	Performance (volts) Cell[b] Nernst (V)	Cell voltage (V)	Nernst[c] A/R (V)	Measured A/R (V)	η (V)	η_{cell} (V)	16A IR (V)
86	24	0	0.321 (88)	0.228 (113)	0.107 (91)	0.332 (105)	0.012	0.974	0.973	0.987	0.987	—	—	0.025
87	24	0	0.331 (91)	0.224 (111)	0.111 (94)	0.325 (102)	0.007	0.976	0.980	0.989	0.989	—	—	0.029
86	192	0	0.314 (86)	0.232 (115)	0.110 (93)	0.339 (107)	0.005	0.970	0.969	0.984	0.982	—	—	—
86	192	16	0.070	0.508	0.049	0.369	0.004	0.844	0.759	0.890	0.869	0.021	0.085	0.028
87	192	0	0.335 (92)	0.214 (106)	0.108 (92)	0.341 (108)	0.002	0.976	0.976	0.989	0.988	—	—	—
87	192	16	0.073	0.499	0.049	0.378	0.001	0.846	0.745	0.891	0.890	0.001	0.101	0.035
86	1766	0	0.249 (69)	0.286 (142)	0.107 (91)	0.339 (107)	0.019	0.953	0.938	0.966	0.959	—	—	—
86	1766	16	0.050	0.525	0.036	0.376	0.014	0.829	0.706	0.875	0.865	0.010	0.123	0.044
87	1766	0	0.277 (76)	0.267 (132)	0.110 (93)	0.344 (108)	0.003	0.960	0.933	0.973	0.973	—	—	—
87	1766	16	0.063	0.509	0.043	0.384	0.003	0.838	0.652	0.884	0.877	0.007	0.186	0.047

Cell no.	Test hours	I (A)	Dry exit cathode gas composition (% theor.) O_2	CO_2	H_2O	N_2
86	1766	0	0.0901 (56)	0.3036 (121)	—	0.6063 (103)
87	1766	0	0.0891 (56)	0.2978 (119)	—	0.6131 (104)

[a] Calculated from dry gas assuming shift equilibrium.
[b] Calculated assuming no cathode gas change.
[c] Calculated against 0.16 O_2 0.25 CO_2/Au reference cathode.

gas crossover is reflected in this table. Cell M87, which maintained 93% fill of the electrolyte, had only 0.3% N_2 at end of life, compared to cell M86, which, with only 84% fill of the matrix, exhibited 1.4% N_2 in the fuel at end of life. Although the loss of hydrogen was significant in these cells, the effect on anode polarization was minimal. As shown in the table, the exit Nernst potential under load decreased 15 and 7 mV for cells M86 and M87, respectively, resulting in actual anode polarization increases of ~4 and 13 mV. This effect is also demonstrated in Fig. 10, in which the anode polarization is plotted for each cell at 192 and 1766h on-test. Shown as dotted lines are the Nernst potentials of the measured exit fuel compositions at 16A. The overpotentials for the anodes at end-of-test were 10 and 7 mV, respectively.

The decrease in cell performance due to increasing cell resistance is reflected in Tables III and IV. The IR loss for cell M86 increased 19 mV from 25 to 44 mV, while the IR loss of cell M87 increased 18 mV from 29 to 47 mV at 16A. A portion, but not all, of this increase can be correlated to decreasing carbonate content of the matrix by assuming a resistivity dependence on porosity as modeled by Zhuravela (23)

$$\rho = \rho_o (1 - \theta)^{-y} \quad [4]$$

where ρ_o = resistivity of the conducting carbonate phase

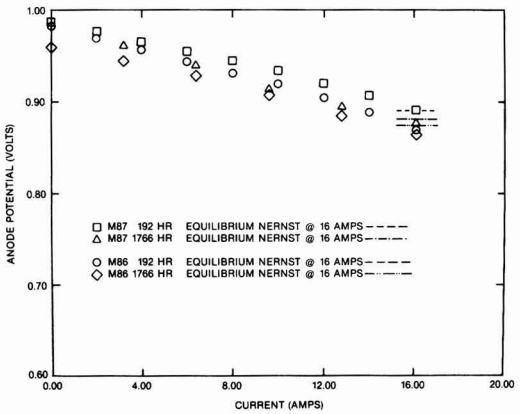


Fig. 10. Anode performance from cells M86 and M87 as a function of time on-test. Cell M86 contained a Ni-Cr anode. Cell M87 used a metal plated-ceramic anode.

Table IV. Summary cell performance decay

Mechanism	Loss M86 (mV)	Loss M87 (mV)
Anode Nernst (OCV/16A)	21/15	16/7
Anode polarization	10	7
IR	19 (13)[a]	18 (6)[a]
Cathode Nernst OCV	15	27
Cathode polarization	15[b]	46[b]
Total decay	74	105

[a] Theoretical increase based on electrolyte loss from matrix.
[b] Includes increased Nernst loss at 16A over theoretical Nernst at 16A.

(Ω-cm), θ = fraction of the nonconducting phase ($LiAlO_2$), and y = 2. Values for y ranging from 1.5-3.0 have been reported. A detailed summary of conduction in heterogeneous systems was given by Meredith and Tobias (24), who recommended a value for x of 1.5. It should be noted that, in these systems, modeling was based on low volume percents of the nonconducting phase. Experiments conducted by the General Electric Company (11) on hot-roll-milled structures having a ~50 v/o nonconducting phase have demonstrated a value of ~2. The calculated theoretical increase in resistance due to loss of the carbonate phase, shown in parenthesis in Table IV, was 13 and 6 mV for cells M86 and M87, compared to measured increases of 19 and 18 mV. Thus, the measured increase in cell IR was considerably higher than can be explained independently of the choice of value for y. The cause of the additional increase in resistance is suspected to be due to cathode hardware corrosion products.

The final cause of cell performance decay was associated with cathode polarization. Shown in Fig. 11 are cathode IR-free polarizations for these cells at 192 and 1766h on-test. Part of the increase in polarization was due to a dramatic drop in O_2 content of the cathode gas (~44%). Adequate measurement of the H_2O content was not made, which makes accurate determination of expected Nernst changes impossible. It is clear, however, from measured cell voltages at open circuit (see Table III) that voltage losses for these cells due to changing cathode gas compositions under no load conditions were ~15 and 27 mV for cells M86 and M87, respectively. The increases in cathode polarization at 16A were 30 and 39 mV. Whether these changes were due to a decreased O_2 activity or deteriorating cathode morphology was not determined.

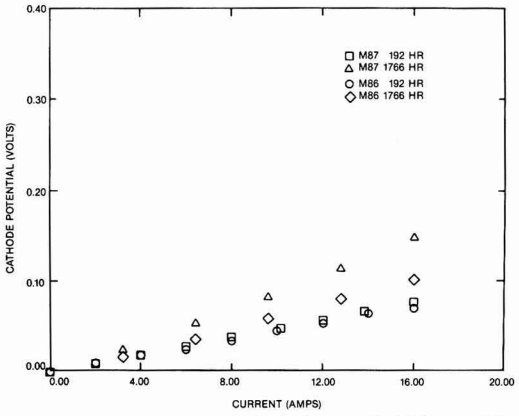


Fig. 11. Cathode performance (IR-free) from cells M86 and M87

However, it is noted that the poorer performance and greater deterioration was associated with cell M87, which had a higher than anticipated carbonate loading, suggesting a cathode "flooding" problem. It should be noted that these performance decays are somewhat larger than reported by other contractors. For example, Ong and Claar (5) reported decay rates of 10 mV/1000h. Such decay, however, was with 0.18-0.25 cm thick hot-pressed electrolytes. It is clear that performance decay due to electrolyte loss would be less in their cells. Researchers at the Energy Research Corporation have reported decay of 10 mV/1000h, again with thick, hot-pressed structures and with repeated electrolyte additions. Results with thin tape cast structures appear mixed. It should also be noted that no attempt was made in these cells to minimize decay by adding or storing additional electrolyte to minimize performance decay. These cells, rather, demonstrate the performance decay that will occur if additional steps are not taken to compensate for electrolyte loss, *i.e.*, storage electrodes, bubble pressure barriers, electrolyte addition, *etc.*

Analysis of parasitic reactions.—In addition to the decay mechanisms described above, two other causes of performance decay can occur in operating cells: gas crossover and chemical reactions on the cell housing. These two mechanisms occur simultaneously in operating cells. As will be shown, the individual effect of each one can be assessed by analysis of the exiting gas.

Gas crossover is defined herein as bulk transport of gas from one electrode chamber to the other through cracks or open porosity in the matrix. This is shown schematically in Fig. 12a. This problem has been shown to be pervasive with hot-pressed electrolyte structures and was greatly diminished with the use of hot-roll-milled electrolyte structures or bubble pressure barrier electrodes (11). Table V lists the equilibrium theoretical fuel and oxidant gas compositions at open circuit (OC) and at 75% fuel utilization-55% oxidant utilization. As can be seen in the table, the pivotal difference between the fuel and oxidant gases at open circuit is that H_2 and CO are present in the fuel, whereas O_2 and N_2 are in the oxidant. If the cathode gas is allowed to crossover to the anode, H_2 and O_2 react to form H_2O, thereby decreasing the H_2 concentration and increasing the H_2O content. Since the activity of CO_2 is essentially identical in the two gases, its activity changes only slightly due to dilution effects. Most importantly, N_2 would be present in the fuel gas, and thus the presence of N_2 in the fuel gas is indicative of cathode gas crossover to the anode.

This decay mechanism can be modeled by assuming a flow rate of cathode gas mixing with the fuel gas in the anode chamber. Shown in Table VI is the resultant fuel composition for the case in which the oxidant crossover rate is 5% of the inherent fuel flow rate. A detailed description of this analysis is given in the Appendix, in

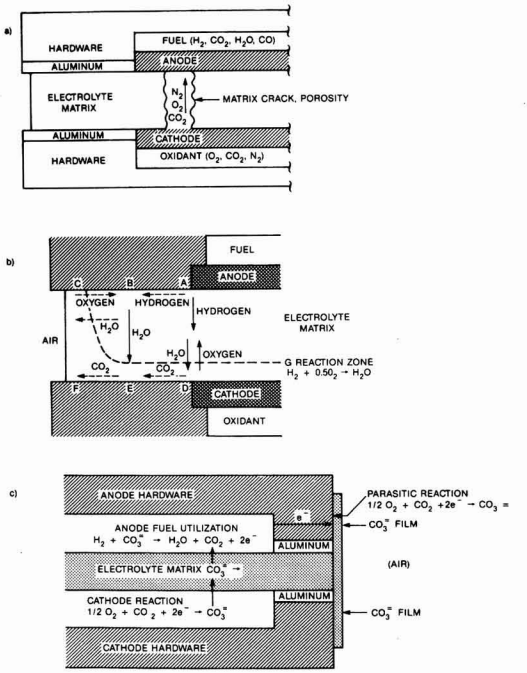


Fig. 12. Schematic representation of parasitic reactions. a) Gas crossover, b) gas flux-reprinted from (26), c) O_2 reduction on anode cell hardware in the presence of electrolyte creep.

which water gas shift equilibrium is assumed. The net effect is a drop in the anode Nernst potential of 3 mV and a decline in the limiting current (I_L) of 4%, based on available fuel.

It should be noted that, in addition to gas crossover, loss of fuel and oxidant can occur due to diffusion and reaction within the electrolyte matrix. This phenomena, represented in Fig. 12b, has been modeled recently by Donado *et al.* (26) with respect to corrosion of cell hardware. Since the combined solubility and diffusivity of H_2 is much greater than that of O_2, the reaction zone where H_2O is formed (*G*) is close to the cathode and the outer edge of the wet seal. As pointed out by Donado *et al.*, this has significant impact on corrosion regions within the cell. Moreover, it affects the gas compositions. The gas flux of species (*J*) from the anode and cathode chambers can be assessed by assuming diffusion through the melt

$$J_J = D_J \cdot S_J \cdot (P_{JA} - P_{JC})/\delta \quad \text{(mol/s cm}^2\text{)} \qquad [5]$$

where D = diffusivity (cm²/s), S = solubility (mol/(cm$_3$ · atm)), P_{JA} = partial pressure in the fuel gas (atm), P_{JC} = partial pressure in the oxidant (atm), and δ = diffusion

Table V. Equilibrium compositions and potentials of reactions in various locations of the cell at 650°C (Potentials vs. a 33% O_2 67% CO_2 reference electrode)

Region	Gas compositions (%) H_2	CO_2	CO	H_2O	O_2	N_2	Potential (V)
Anode (open circuit)	36.3	20.2	11.9	31.6	—	—	−1.051
Anode (75% util.)	5.6	46.9	3.2	44.2	—	—	−0.931
Cathode (open circuit)	—	20.1	—	19.8	12.8	47.3	−0.058
Cathode (55% util.)	—	9.0	—	7.3	24.8	58.9	−0.110
Ambient air	—	0.03	—	2.5	20.5	77.0	−0.316

Table VI. Fuel gas analysis and modeled parasitic reactions at 650°C (anode potential vs. 0.1286 O_2, 0.2009 O_2 reference electrode)

Condition	Parasitic reactions: Crossover (%)	Parasitic reactions: H_2 util. (%)	Fuel composition: H_2	CO_2	CO	H_2O	N_2	Anode potential $-E_{A/R}$ (V)	Limiting current i_L (mA/cm²)	Fuel util. at 160 mA/cm² (%)	Fuel loss (%)
Theoretical	0	0	0.3631	0.2025	0.1189	0.3155	—	0.984	216	75	0
Modeled	5	0	0.3378	0.2063	0.1099	0.3234	0.0226	0.980	207	77	4
Modeled	0	5	0.3319	0.2225	0.1134	0.3322	—	0.975	202	79	5
Cell 1											
Measured	—	—	0.1949	0.2832	0.0800	0.3489	0.0930	0.942	—	—	—
Modeled	20	22	0.1946	0.2872	0.0790	0.3592	0.0800	0.940	152	105	30
Cell 2											
Measured	—	—	0.2630	0.2434	0.0805	0.4038	0.0076	0.954	—	—	—
Modeled	2	22	0.2712	0.2496	0.0909	0.3797	0.0086	0.957	178	90	18
Cell 3											
Measured	—	—	0.3262	0.2129	0.0926	0.3650	0.0032	0.972	—	—	—
Modeled	1	8	0.3250	0.2203	0.0997	0.3504	0.004	0.972	202	79	6.5

distance (cm). As written, positive transport is from the anode to the cathode. Shown in Table VII are values of D, S, and J and corresponding loss of H_2 and O_2 for a 0.0508 cm (0.020 in.) electrolyte structure at 650°C. It is readily apparent that this loss is negligible compared to the magnitude of change shown in Table V for gas crossover.

A final cause of performance decay was associated with parasitic reactions on the cell hardware, shown schematically in Fig. 12c. Theoretically, the oxidizing gases that surround the cell can, in the presence of electrolyte, undergo the same reaction on the cell hardware as that occurring at the cathode

$$^{1/2}O_2 + CO_2 + 2e^- \rightarrow CO_3^= \quad [6]$$

This reaction is compensated by oxidation of the fuel

$$H_2 + CO_3^= \rightarrow H_2O + CO_2 + 2e^- \quad [7]$$

The driving force for this reaction is the same as that for the cell, *i.e.*, a potential difference between the reducing environment on the inside and the oxidizing environment on the outside of the anode hardware. Shown in Table V are the equilibrium potentials for reaction [6] at the cathode and the cell hardware and reaction [7] at the anode *vs.* a 0.333 O_2, 0.667 CO_2 reference electrode. The potential difference between the inside and outside of the anode chamber is ~735 mV at open circuit and ~615 mV under load.

The pivotal difference between reaction [6] occurring on the outside of the anode hardware or at the cathode is that the hardware is in electrical contact with the anode. The electrons, therefore, pass freely through the hardware. The net result is electrochemical utilization of the fuel gas, *i.e.*, loss of H_2, without generating current in the external circuit. In addition, this mechanism postulates pumping of electrolyte out of the cell. In externally manifold stack designs this has been shown (8) to cause considerable transport of electrolyte from cell to cell within the stack. Further, this reaction predicts the formation of CO_2 in the anode compartment. This last effect differentiates this decay mechanism from gas crossover and diffusion through the melt, which both result in the loss of CO_2 from the fuel gas. This parasitic utilization of fuel can be modeled by assuming a given utilization of the fuel gas. Shown in Table VI is the resultant fuel gas composition for the case of 5% utilization of the fuel. A detailed description of this analysis is given in the Appendix. The net effect, as shown, is a decrease in the H_2 concentration from 0.3631 to 0.3319, an increase in CO_2 from 0.2025 to 0.2225, a loss in open-circuit voltage from 0.984 to 0.975V, and a 5% loss in available fuel.

Table VII. Gas flux into the electrolyte melt at 650°C [data from Gelb (6)]

Gas	D [cm²/s (× 10⁵)]	S [mol/(cm³-atm) (× 10⁶)]	δ (cm)	J_m[a] [mol/s (× 10⁸)]	J_l[b] [mol/s (× 10⁴)]
H_2	1.58	5.79	0.0492	6.740	1.104
CO_2	0.94	11.66	0.0508	0.003	0.736
O_2	1.11	0.39	0.0016	3.370	0.867

[a] Flux of dissolved gas into the melt.
[b] Input flux of gas to the cell.

As discussed above, the net result of gas crossover on the fuel composition is a decrease H_2 and CO and an increase H_2O and N_2. Crossover should have little effect on the CO_2 concentration, since the CO_2 activity in the cathode gas is similar. Thus, only a dilution effect would occur. In contrast, utilization results in an increase in CO_2 and H_2O, without introducing N_2. Thus, the N_2 and CO_2 concentrations in the fuel gas provide a valuable handle to assess the causes of the fuel gas deterioration. Shown in Table VI are measured fuel gas compositions for three 12 in. by 12 in. sheet metal cells (11). Beneath each measured gas composition is the modeled gas composition, assuming the listed amount of gas crossover and parasitic utilization of the fuel due to O_2 reduction on the cell hardware. Table VI also includes the measured and modeled anode potential against a 0.1266 O_2, 0.2009 CO_2 reference electrode at open circuit, with the limiting current density (mA/cm²) based on available H_2 and CO (I_L), the corresponding fuel utilization at 160 mA/cm², and the loss in available fuel (% loss). As shown, a standard cell with no crossover or parasitic reactions would yield an anode potential of 0.984V, a limiting current of 216 mA/cm², 75% fuel utilization at 160 mA/cm², and a fuel composition of 0.3631 H_2, 0.2025 CO_2, 0.1189 CO, and 0.3155 H_2O. Cell 1 had insufficient electrolyte to fill the electrolyte structure and considerable coverage of the sheet metal with electrolyte. Although this cell is clearly not representative of state of the art cells, it serves to demonstrate how severe these decay mechanisms can become if not controlled. Due to the induced porosity in the electrolyte structure, Cell 1 was plagued by gas crossover and utilization of fuel gas resulting in ~30% loss in available fuel, a drop in potential of 42 mV, and a reduced limiting current of 152 mA/cm², which is below the design operating current density of 160 mA/cm². This severe deterioration was due to insufficient carbonate filling of the matrix. In contrast, Cell 2, which had sufficient electrolyte to fill the electrolyte matrix, displayed a marked decrease in gas crossover to ~2%. The fuel gas, however, was still highly utilized (22%), due to reaction on the anode hardware of the air environment in the furnace. The limiting current was enhanced (178 mA/cm²), but it was still considerably lower than the theoretical 216 mA/cm². The fuel gas listed

for Cell 2 was similar to cell M86 at end of life (see Table III). In Cell 3, the furnace was flushed with a 10% H_2/N_2 gas to eliminate oxygen and, hence, the potential gradient across the anode hardware. It should be noted that the furnace was not a sealed system and O_2 most likely was not completely eliminated. If the mechanism described, however, was responsible for the fuel gas decay, it should be greatly diminished. The results were significant. The utilization of the fuel was reduced to ~8%, the anode potential was within 12 mV of theoretical, the limiting current was 202 mA/cm², and 75% utilization of the fuel would occur at 152 mA/cm².

These results demonstrate the impact of gas crossover and O_2 reduction on the anode hardware. The severity of these reactions depends on many factors, most of which are design-related. For example, gas crossover is related to the ability of the electrolyte structure to remain filled and crack-free. Oxygen reduction on the cell hardware is dependent upon the potential difference across the anode hardware. This in turn depends on: anode fuel composition and polarization, the gas environment surrounding the cell, the catalytic activity of the hardware and corrosion products, the amount of electrolyte present on the cell hardware, and the exposed area of cell hardware. With respect to the last item, it should be noted that the relative exposed area in a stack is greatly diminished compared to that in single cell tests in which electrolyte can creep and cover large areas. Each of these debilitating factors can be eliminated or reduced. One approach would be to render the exposed area nonwetting, to prevent electrolyte transport. A second would be to isolate electron transfer across the hardware and eliminate catalytic activity by coating the hardware with Al_2O_3. The final alternative is to control the ambient environment.

Summary

This work has shown that vapor loss, lithiation of the anode and cathode, electrolyte creep, and hardware corrosion all contribute to electrolyte loss in operating cells. The magnitude of electrolyte loss and compositional changes of the electrolyte were found to correlate with modeled values. Lithiation of the anode was found to have a pronounced effect on lithium consumption early in cell life. This consumption can be eliminated by the use of metal-plated ceramic anodes. The critical factors affecting long-term electrolyte loss are hardware corrosion and electrolyte creep. Electrolyte creep, in addition to causing increased gas crossover by draining electrolyte from the matrix, has been found to cause parasitic reactions on the cell hardware. These reactions were manifested as appreciable utilization of the fuel gas consuming H_2 and producing CO_2 and H_2O.

The principal mechanisms of performance decay associated with electrolyte loss were increased cell resistance, increased cathode polarization, and deteriorating gas compositions due to increased gas crossover and parasitic reaction on the hardware. Electrolyte additions to compensate for electrolyte loss were effective in decreasing gas crossover and performance decay rate. Control of blanket gas environment was effective in minimizing the parasitic reactions on the cell hardware due to electrolyte creep.

APPENDIX

Modeling of gas crossover and fuel utilization in this paper was conducted as follows. The text refers to the specific cases listed in Tables VIII and IX. Cathode gas (oxidant) crossover to the anode compartment was based on a specific flow rate of oxidant combining with fuel. In a standard cell, the flow of fuel to the anode compartment is 337.5 cm³/min of the composition shown in Table VIII. For the case of 5% crossover, an oxidant flow equivalent to 5% of the total fuel flow, *i.e.*, 16.875 cm³/min was assumed to mix in the anode chamber. H_2 and O_2 were assumed to react to completion forming H_2O

$$H_2 + {}^{1/2}O_2 \rightarrow H_2O \qquad [A\text{-}1]$$

Thus 2.17 cm³/min of O_2 would react with 4.34 cm³/min of H_2 forming 4.34 cm³/min of H_2O producing a combined flow rate of 352.205 cm³/min. The net H_2 flow rate of 157.7 cm³/min would result in a new limiting current (Eq. [A-2]) of 20.7A or 207 mA/cm², compared to the initial 216 mA/cm²

$$i_L = n\mathbf{F}\, C_{H_2} V_{H_2} \qquad [A\text{-}2]$$

where n = 2 equiv./mole, $\mathbf{F}$ = Faraday's constant (9.65 × 10^4 A-s/equiv.), C_{H_2} = concentration of H_2 (mol/cm³), V_{H_2} = volumetric flow rate of H_2 (cm³/s). The water gas reaction [A-3] was assumed to be in equilibrium

$$H_2 + CO_2 = CO + H_2O \qquad [A\text{-}3]$$

with an equilibrium constant, K, at 650°C of 1.96 (27). The validity of this assumption has been discussed previously (28). Thus H_2 and CO_2 would react to form CO and additional H_2O providing the equilibrium composition shown in Tables VI and VIII, *i.e.*, 0.3378 H_2, 0.2063 CO_2, 0.3234 H_2O, 0.1099 CO, 0.0226 N_2. The resulting equilibrium potential of this anode gas *vs.* an O_2/CO_2 reference can be calculated from the free energy of reactions [A-4]-[A-6]

$$\text{Anode:} \quad H_2 + CO_3^{=} \rightarrow H_2O + CO_2 + 2e^- \qquad [A\text{-}4]$$

$$\text{Reference:} \quad 0.5\ O_2 + CO_2 + 2e^- \rightarrow CO_3^{=} \qquad [A\text{-}5]$$

$$\text{Overall:} \quad H_2 + 0.5\ O_2 \rightarrow H_2O \qquad [A\text{-}6]$$

according to Eq. [A-7]

$$-E_{A/R} = E^\circ - \frac{RT}{n\mathbf{F}} \ln \left[\frac{(^aH_2O)\,(^aCO_2)}{(^aH_2)\,(^aCO_3^{=})}\right] \text{anode} \left[\frac{(^aCO_3^{=})}{(^aO_2)^{.5}\,(^aCO_2)}\right] \text{reference} \qquad [A\text{-}7]$$

where E° = reversible potential of [A-6] (1.0202V), R = gas constant (1.987), and T = temperature (°K). Thus the potential of the equilibrium fuel gas shown in Table VIII against a 0.1286 O_2, 0.2009 CO_2 reference is

$$-E_{A/R} = 1.0202 - 0.0398 \ln \left[\frac{(0.3234)\,(0.2063)}{(0.3379)\,(0.1286)^{.5}\,(0.2009)}\right] = 0.980\text{V} \qquad [A\text{-}8]$$

Table VIII. Calculation of 5% oxidant crossover to the anode

Condition	H_2 (cm³/min)	(%)	CO_2 (cm³/min)	(%)	H_2O (cm³/min)	(%)	CO (cm³/min)	(%)	O_2 (cm³/min)	(%)	N_2 (cm³/min)	(%)	Total (cm³/min)
Fuel input	162.0	48.00	108.0	32.00	67.50	20.00	—	—	—	—	—	—	337.5
Oxidant crossover	—	—	3.39	20.09	3.35	19.85	—	—	2.17	12.86	7.965	47.20	16.875
Combined gas	157.7	44.77	111.39	31.62	75.19	21.35	—	—	—	—	7.965	2.26	352.205
Equilibrium gas	119.0	33.78	72.6	20.63	113.9	32.34	38.7	10.99	—	—	7.965	2.26	352.205

Table IX. Calculation of 5% fuel utilization

Condition	H_2 (cm³/min)	(%)	CO_2 (cm³/min)	(%)	H_2O (cm³/min)	(%)	CO (cm³/min)	(%)	Total (cm³/min)
Fuel input	162.0	48.00	108.0	32.00	67.5	20.00	—	—	337.5
Utilized fuel	153.9	44.53	116.1	33.59	75.60	21.88	—	—	345.6
Equilibrium fuel	114.70	33.19	76.89	22.25	114.81	33.22	39.19	11.34	345.5

Modeling of fuel utilization was based upon O_2 and CO_2 in ambient air reacting on the anode hardware in the presence of electrolyte according to [A-5]. On the inside of the anode chamber, H_2 reacts according to [A-4] forming H_2O and CO_2. The extent of this reaction can be modeled by assuming a given utilization of H_2. Shown in Table IX is the case for 5% utilization of the fuel. In this example, 5% of the incoming H_2 (8.1 cm³/min) reacts with carbonate ions to form 8.1 cm³/min of CO_2 and H_2O, producing a utilized fuel flow rate of 345.6 cm³/min comprised of 0.4453 H_2, 0.3359 CO_2, and 0.2188 H_2O. The resultant limiting current density (Eq. [A-2]), based on the decreased H_2 flow of 153.9 cm³/min, is 202 mA/cm². The equilibrium gas utilized fuel flow rate of 345.6 cm³/min comprised of 0.4453 H_2, 0.3359 CO_2, 0.2188 H_2O. The resultant limiting current density (Eq. [A-2], based on the decreased H_2 flow of 153.9 cm³/min, is 202 mA/cm². The equilibrium gas composition [A-3] is 0.3319 H_2, 0.2225 CO_2, 0.3322 H_2O, and 0.1134 CO. The equilibrium potential of this gas (Eq. [A-7]) is 0.975V.

Manuscript submitted April 11, 1985; revised manuscript received Oct. 10, 1985.

The General Electric Company assisted in meeting the publication costs of this article.

LIST OF SYMBOLS

a	activity in the gas
C	concentration in the gas (mol/cm³)
D_J	diffusivity of species J in the melt (cm²/s)
$E_{A/R}$	equilibrium anode potential *vs.* O_2/CO_2 reference electrode (V)
$E°$	reversible anode/reference potential at standard states (1.0202V)
$\mathbf{F}$	Faraday constant (9.65×10^4 A-s/equiv.), (2.306×10^4 cal/V · equiv.)
i_L	limiting current density (mA/cm²)
J_J	flux of species J (mol/s cm²)
n	number of electrochemical equivalents of a chemical species reacted per mole
P_{JA}	partial pressure of species J in the anode gas
P_{JC}	partial pressure of species J in the cathode gas
R	gas constant (1.987 cal/mol K)
S_J	solubility of species J in the melt (mol/cm³ atm)
T	absolute temperature (K)
V	volumetric flow rate (cm³/s)
x	atomic fraction of Li in lithiated nickel oxide
y	expotential factor in heterogeneous conductivity (Eq. [4])
η	overpotential (V)
δ	diffusion distance (cm)
ρ	resistivity of the electrolyte matrix (Ω-cm)
ρ_o	resistivity of the Li_2O_3, K_2CO_3 eutectic (Ω-cm)
θ	fraction of nonconducting phase (Eq. [4])

REFERENCES

1. "Development of Molten Carbonate Fuel Cell Power Plant," DOE Contract No. DOE-ET-17019-14, Quarterly Report, General Electric Co., May-July, 1983.
2. C. D. Iacovangelo, Abstract 140, p. 380, The Electrochemical Society Extended Abstracts, Vol. 80-2, Hollywood, FL, October 5-10, 1980.
3. H. R. Bronstein, S. Cantor, D. H. Smith, and J. Braunstein, Abstract 142, p. 385, The Electrochemical Society Extended Abstracts, Vol. 80-2, Hollywood, FL, October 5-10, 1980.
4. D. A. Shores and P. Singh, in "Molten Carbonate Fuel Cell Technology," J. R. Selman and T. D. Claar, Editors, p. 271, The Electrochemical Society Softbound Proceedings Series, Pennington, NJ (1984).
5. E. T. Ong and T. D. Claar, in "Molten Carbonate Fuel Cell Technology," J. R. Selman and T. D. Claar, Editors, p. 54, The Electrochemical Society Softbound Proceedings Series, Pennington, NJ (1984).
6. A. Gelb and G. Wilemski, "Modeling of Long-Term Decay in the Molten Carbonate Fuel Cell," Final Report EPRI-EM-2596, Project 1085-5, September, 1982.
7. C. W. Bale, A. A. Pelton, and J. Melancon, "Calculation of Thermodynamic Equilibria in the Carbonate Fuel Cell," DOE Contract no. DE-AC02-79ET15416, Project CDT-P-501, Final Report, August, 1981.
8. H. R. Kunz, Abstract 48, p. 70, The Electrochemical Society Extended Abstracts, Vol. 84-2, New Orleans, LA, October 7-12, 1984.
9. "Evaluation of National Gas Molten Carbonate Power Plants," GRI Contract no. 5081-344-0523, FCR-4303, Quarterly Report, United Technologies Corp., January-April, 1982.
10. "Advanced Technology Fuel Cell Program," EPRI Project EM-114-2, FCR-0554/RP114-2-77, Annual Report, United Technologies Corp., June, 1977.
11. "Development of Molten Carbonate Fuel Cell Power Plant," DOE Contract no. DOE-ET-17019-20, Final Report, General Electric Co., February, 1985.
12. C. D. Iacovangelo, U.S. Pat. 4,361,631 (1982).
13. C. D. Iacovangelo, U.S. Pat. 4,386,960 (1983).
14. C. D. Iacovangelo, U.S. Pat. 4,404,267 (1983).
15. C. D. Iacovangelo, U.S. Pat. 4,423,122 (1983).
16. "Development of Molten Carbonate Fuel Cells for Power Generation," DOE Contract no. DE-AC-03-77ET11319, Final Report, General Electric Co., April, 1980.
17. A. Borucka and C. M. Sugiyama, *Electrochim. Acta.*, **13,** 1887 (1968).
18. C. D. Iacovangelo, in "Molten Carbonate Fuel Cell Technology," J. R. Selman and T. D. Claar, Editors, p. 397, The Electrochemical Society Softbound Proceedings Series, Pennington, NJ (1984).
19. C. E. Baumgartner and K. P. Zarnoch, *Am. Ceram. Soc. Bull.* **64,** (1985).
20. P. Lessing and M. Johnston, "High Temperature Fuel-Cell Research and Development," Final Technical Progress Report 10/1980-9/1981, Contract no. DE-AC03-77ET-11320, Report no. DE 83 007925, October, 1981.
21. L. J. Bregoili and H. R. Kunz, *This Journal*, **129,** 2711 (1982).
22. R. H. Arendt, *ibid.*, **129,** 942 (1982).
23. U. M. Zhuravela and A. G. Pshenichnikov, *Sov. Electrochem.*, **12,** 795 (1976).
24. R. E. Meredith and C. W. Tobias, in "Advances in Electrochemistry and Electrochemical Engineering," Vol. 2, p. 15, Interscience, New York (1966).
25. "Development of Molten Carbonate Fuel Cell Technology," DOE Contract no. DOE/ET/11304-29 Progress Report, Energy Research Corp., July-Sept., 1983.
26. R. A. Donado, L. G. Marianowski, and H. C. Marv, *This Journal*, **131,** 2535 (1984).
27. I. Barin and O. Knache, "Thermochemical Properties of Inorganic Substances," Springer-Verlag, Berlin (1973).
28. W. M. Vogel and C. D. Iacovangelo, *This Journal*, **124,** 1305 (1977).

Computer-Aided Simulation of Electrochemical Process Flowsheets

Richard Alkire,* Richard La Roche, Gary Cera,* and Mark Stadtherr**

Department of Chemical Engineering, University of Illinois, Urbana, Illinois 61801

ABSTRACT

A methodology was developed for the computer-aided design and modeling of electrochemical process flowsheets. The public version of the advanced system for process engineering (ASPEN) was modified for use in the study. ASPEN was chosen because of its electrolyte capability and adaptable programming structure. Within the ASPEN framework, enhancements made during the course of this work are portable to the electrolytic industry. In this study, the design, costing, and economic analysis of the electrochemical production of methyl ethyl ketone (MEK) was used as an example. The process steps included rigorous distillations, absorbers, an electrochemical cell model, pumps, flashes, and heat exchangers involving electrolyte systems.

The electrolytic industries are in a vigorous state of change owing to technological advances, changing costs of energy and capital, and expanded societal awareness. Existing mature processes have, for example, benefited enormously from improved cell materials and designs. In addition, new electrochemical processes emerge regularly and thus require engineering evaluation. In the past, it was common to improve processes by introducing incremental adjustments based mainly on past empirical experience. With so many new opportunities available, however, it is increasingly important to develop improved procedures for screening options at an early stage of development. In order to be cost-effective, such screening often needs to be carried out before an extensive base of empirical data is available.

In the present study, a computer-aided simulation and design procedure has been developed. The procedure was used to investigate an electro-organic synthesis process, to evaluate process design alternatives, to identify sensitive process variables, and to reveal gaps in knowledge where applied research would exert useful leverage (1, 2). The example process used to illustrate these procedures was synthesis of methyl ethyl ketone (MEK) by electrolytic oxidation of *n*-butene. The following literature review provides access to the components of the overall problem.

Process flowsheeting.—A flowsheet is a diagram which indicates the flow of material and energy between processing units used to convert reactants to products. Computer-aided simulation and design of petrochemical process flowsheets are well established. An excellent review (3) and an introductory monograph (4) are available. Commercial programs have been available for over two decades. Some currently available programs include PROCESS (Simulation Sciences), ASPEN (National Energy Software Center), ASPEN PLUS (Aspen Technology), and FLOWPACK II (ICI).

A process flowsheeting system solves the set of nonlinear equations that describe a process flowsheet. This set may contain thousands to tens of thousands of equations for a chemical process. There are three broad types of flowsheeting systems: sequential modular, equation-based, and simultaneous modular. Each category differs in the "numerical strategy" or "structure" used to solve the nonlinear set of equations.

The structure of almost all existing process flowsheeting systems is "sequential modular." In this approach, the nonlinear equations are divided into module-level and flowsheet-level equations. The module-level equations are those describing a particular unit operation. These equations are solved in a FORTRAN subroutine called a unit module. Sequential modular programs provide a library of unit modules for the most common unit operations, and the user may write his own modules for other units. Given input streams and equipment parameters, the unit module will calculate output streams from the unit. The units of a flowsheet are connected by stream connection equations. Design constraints on an overall process, such as a product purity requirement, are expressed by design specification equations. A design constraint is met by adjusting a designated variable (which may be a stream flow rate, equipment parameter, etc.) called a free variable. Stream connection and design specification equations compose the flowsheet-level set.

In the sequential modular approach, flowsheet convergence involves iterative solution of a hierarchy of nested loops. The two innermost loops are any iterative physical property evaluations and any module-level iterations within each unit module. The flowsheet-level equations are solved in the next two outer levels. In the presence of recycle streams, the stream connection equations must be solved iteratively through some form of direct or accelerated substitution method. These iteration loops are often called "tear" loops. Since the design specification equations do not generate values for the free variables, a substitution method cannot be applied. The design specifications must therefore be solved iteratively with the use of separate "control" loops. Such a hierarchy of nested loops may cause convergence to the solution of the overall flowsheeting problem to be very slow.

Despite its slow convergence properties, the sequential modular approach has several traits that make it the most widely used method. Information flow between modules strongly resembles flow between process units. This characteristic renders the method readily understood by engineers. Existing software for unit modules is abundantly available and quite robust. Even in the case of simulation failure, the engineer can retrieve partial results from the modules that are useful in diagnosis. Unfortunately, the sequential modular technique is not particularly amenable to process optimization, since this would require yet another outer iteration loop, making optimization difficult and costly.

In contrast, the "equation-based" approach involves solving the entire set of nonlinear equations simultaneously. Design specifications and optimization do not require extra nested iterations. The nested loop problem is eliminated, resulting in potentially much less computer run time. However, computer storage becomes an important consideration because of the large number of equations handled at one time. Solving this large set requires efficient sparse matrix techniques and good initial guesses to converge. Current research efforts dealing with equation-based methods are reviewed by Perkins (5). SPEEDUP is an example of a flowsheeting package that employs the equation-based structure (6).

The hybrid of the sequential modular and equation-based structures is the "simultaneous modular" approach (7, 8). The unit modules are retained. The approach involves solving the stream connection and design

*Electrochemical Society Active Member.
**Electrochemical Society Student Member.

specification equations simultaneously along with any optimization. Essentially, the three outermost levels of nested loops are combined. Computational efficiency is thereby increased, while still maintaining the advantages of the sequential modular structure.

Essentially, all flowsheeting systems commercially available to date are classified as sequential modular, though some have rudimentary simultaneous modular features. While still considered to be sequential modular, the advanced system for process engineering (ASPEN) has a structure that can be modified into a simultaneous modular approach. ASPEN, for example, already has some capability to converge stream and design specification equations simultaneously with the Broyden algorithm (9). In its present state, however, ASPEN would still require an outer control loop to optimize a process flowsheet.

Modeling of electrolyte systems.—There has been little use of flowsheeting techniques for electrochemical processes until very recently. Advances in this area are being spurred on by intense research in the modeling of electrolyte thermodynamics. Key early contributions by Criss and Cobble (10), Meissner and Tester (11), Pitzer (12), and Bromley (13) led to refined electrolyte activity coefficient models which have been to date developed with the range of applicability from dilute solutions to fused salts (14-16). These models have also been extended to mixed solvents, vapor-liquid-liquid systems, and vapor-liquid-solid systems (17, 18). Mauer gives a survey of thermodynamic models proposed for electrolyte systems (19).

While general-purpose flowsheeting programs have been available for about twenty years, these programs were, in general, limited to hydrocarbons encountered in petrochemical applications. Although Zemaitis (20) had developed a stand-alone program for certain separation operations involving electrolytes, no general-purpose flowsheeting program was available commercially for electrochemical flowsheets. The ASPEN system (21) is the first attempt. The public version of ASPEN, available from the NESC (not to be confused with Aspen Technology's proprietary system, ASPEN PLUS), includes electrolyte and solids handling capabilities (22). Other commercial flowsheeting programs have begun to offer some electrolyte capabilities.

ASPEN includes a local composition model (14) which predicts the excess Gibbs energy of electrolyte systems from dilute solutions to fused salts. The model requires two binary parameters for each solvent-ion or solvent-solvent component pair. Ion-ion binary parameters are needed only when two electrolytes are present with a common ion. In the absence of electrolytes, the model reduces to the NRTL model (23). Although the local composition model was recently extended to include mixed solvents (18), ASPEN is limited to a single solvent, water.

Although the initial version of ASPEN was capable of performing single stage equilibrium of streams containing electrolytes, the electrolyte capability was restricted to process units that did not involve multistage operations (distillations and absorbers). The present investigation (1, 2) resulted in a modified version of ASPEN capable of electrolyte multistage simulation. Enhancements were made to the rigorous distillation module, RADFRC, and to the equilibrium reactor, REQUIL.

An operational data regression system is also essential, since most electrolyte models involve binary parameters that must be regressed from vapor-liquid equilibrium (VLE) and heat of mixing data in the range of interest. There is presently no method to select these parameters in the absence of experimental data. Therefore, in this study, the ASPEN data regression system (DRS) was modified to enable the electrolyte model parameter estimation to be carried out from VLE and heat of mixing data.

Electrolytic cell modules.—For a large number of unit operations such as distillation, absorption, heat exchange, etc., modules exist for calculating output streams based on input stream data and equipment parameters. While flowsheeting systems such as ASPEN provide many such modules, they do not include modules for electrolytic cells. However, mathematical models of electrolytic cells have been developed for a number of common configurations (24-27). While sophisticated procedures are available for investigating the current and potential distribution in cells, it may be unnecessary to utilize them in the early stage of evaluation when understanding of physical processes is still primitive. In the present investigation, the cell model was extremely simple and consisted of the best operating conditions reported in the patent literature for electrosynthesis of MEK.

Development of an Example Process Flowsheet

Process selection.—An electro-organic process was chosen for evaluation since there are many such candidates currently under development (28), because interactions between the cell and recovery operations are often significant (29), and because early evaluation of economics is important (30). Electrochemical production of MEK from *n*-butenes served as the example. In a preliminary study, Beck *et al.* (28) had found the electrochemical route to be less energy intensive than the conventional petrochemical route. Worsham (31) and Griffin *et al.* (32) outlined the details involved in MEK electrochemical production. The MEK process had several attributes that made it an appropriate choice for illustrating computer-aided electrochemical process design: (*i*) The product recovery required multistage separations involving electrolytes. (*ii*) The process was closely related to the conventional route which made capital and utility cost comparison straightforward. (*iii*) Electrolytic cell operation data were readily available in the literature. (*iv*) Vapor-liquid equilibrium and heat of mixing data needed for physical property modeling were available. (*v*) Alternative product recovery schemes could be developed and compared.

This study developed a methodology for computer-aided design, costing, and economic analysis of an electrochemical flowsheet. Information concerning the ASPEN system is available in public documentation from the National Technical Information Center (9). The following paragraphs provide a general description of the methodology.

Process flowsheet synthesis.—The identification of the flow diagram and operating conditions are discussed here.

Figures 1 and 2 show the two flowsheet configurations evaluated in this study. In both, *n*-butenes are absorbed into sulfuric acid and then enter the electrolytic cell. The two flowsheets differ in the downstream separation area. In Fig. 1, MEK was recovered from the cell liquor via a four column distillation system. In Fig. 2, MEK was recovered from the cell off-gas by utilizing a condenser and a two column distillation system.

In the absorber, *n*-butene was contacted with 65 w/o H_2SO_4 at 60°C and 100 psia (31). Under these conditions, the *n*-butenes become sulfonated and subsequently hydrolyzed to 2-butanol

$$C_4H_8 + H_2SO_4 \rightarrow C_4H_9OSO_3H \quad [1]$$

$$C_4H_9OSO_3H + H_2O \rightarrow C_4H_9OH + H_2SO_4 \quad [2]$$

The overall reaction to 2-butanol is a very fast second-order reaction that proceeds quickly to equilibrium in the absorber (33).

The 2-butanol/sulfuric acid mixture proceeded to the electrochemical reactor in both configurations. A two-electron transfer process yields MEK at the anode and hydrogen at the cathode

$$C_4H_9OH \rightarrow C_4H_8O + 2H^+ + 2e^- \quad [3]$$

$$2H^+ + 2e^- \rightarrow H_2 \quad [4]$$

The electrolytic cell design was based on monopolar undivided cells with expanded Pt/PtO anodes (titanium substrate) and steel cathodes.

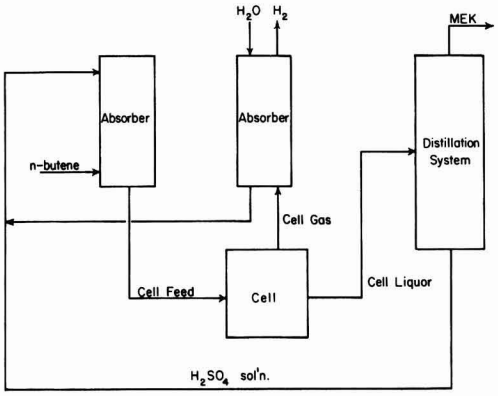


Fig. 1. MEK flowsheet 1—cell liquor recovery

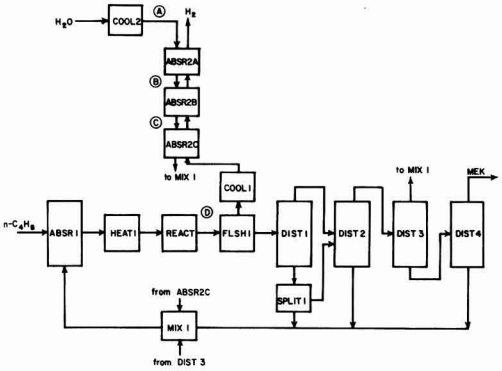


Fig. 3. ASPEN diagram for flowsheet 1

Electrochemical cell performance was based on Worsham's best operating conditions with respect to current density: 120 A/ft² at 76.7°C with 20% conversion per pass of 2-butanol (31). Griffin *et al.* (32) made successful runs up to 1:1 hydrogen ion to 2-butanol mole ratio with 65 w/o sulfuric acid. Maximum cell voltage recommended was 1.65V (31). No significant current density increase occurred above that potential. Higher voltages resulted in loss of product selectivity *via* overoxidation to produce carbon dioxide.

The flowsheet shown in Fig. 1 involved MEK recovery from the cell liquor by a system of four distillations (see Fig. 3). The first distillation separated a MEK/2-butanol/water mixture near the MEK/water azeotrope (66% MEK) from the sulfuric acid. The second distillation involved drying the mixture by the addition of a small stream of sulfuric acid at the top of the column. A MEK/2-butanol stream with trace water was taken overhead to the third distillation which removed a MEK/water azeotrope from the MEK/2-butanol. The final finishing column achieved 99% MEK product by removing 2-butanol. All other streams were recycled to the butene absorber.

The flowsheet shown in Fig. 2 recovered MEK from the electrochemical cell gas. This involved building up the MEK concentration in the recycle to increase MEK partial pressure in the hydrogen gas. Worsham (31) found that MEK concentrations of up to 22% did not adversely affect the electrochemical reaction. The MEK/hydrogen gas mixture with minor amounts of 2-butanol and water was cooled by refrigeration to 5°C. Liquid from the cooler proceeded to an azeotropic distillation to remove water and to a finishing column to attain 99% purity MEK (see Fig. 4).

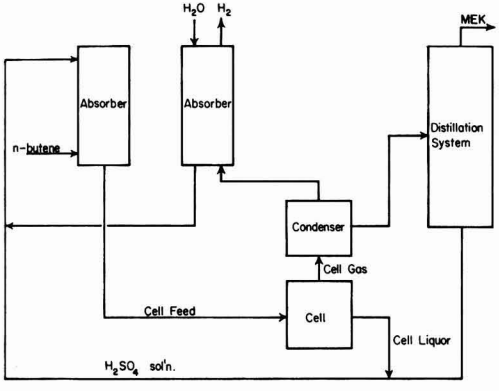


Fig. 2. MEK flowsheet 2—cell gas recovery

The effluent hydrogen stream was passed through a refrigerated water absorber in both flowsheets. The absorber removed trace amounts of MEK and 2-butanol for recycle back into the process. The relatively pure hydrogen stream was credited as by-product fuel gas.

Physical property modeling.—It is necessary to select physical property models, obtain data needed to represent the process streams, and perform data regression for binary parameter estimation.

Two physical property routines were used to predict physical properties in the MEK flowsheet. Both routines calculated vapor properties from the Redlich-Kwong equation of state. The NRTL model was used for liquid mixture properties in areas of the flowsheet that did not contain electrolytes. Chen's local composition model was used for liquid mixture properties in flowsheet sections involving electrolytes.

The ASPEN data regression system (DRS) with our modification was used to determine binary interaction parameters from literature data. Aqueous sulfuric acid VLE and heat of mixing data were used to estimate ion-water binary parameters (34, 35). Binary VLE data for each solvent-solvent pair were used for solvent-solvent parameters with ternary data used to "fine tune" the regression (36, 37). No equilibrium data were found for the organic solvents in sulfuric acid. This necessitated the assumption of negligible short-range forces between the ions and the organic molecules. The assumption should not create any significant errors since forces between the ions and water are much greater.

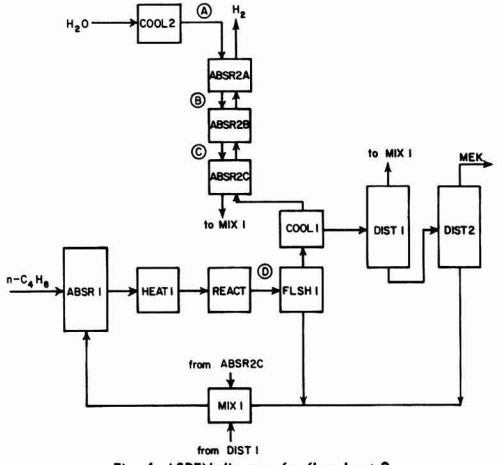


Fig. 4. ASPEN diagram for flowsheet 2

Table I describes the accuracy of the physical property model compared to the literature data values. This table shows the error between predicted and actual values for temperature, liquid mole fraction, and vapor mole fraction.

ASPEN flowsheet.—It is necessary to select ASPEN modules to represent the unit processes, and to provide additional subroutines to model special units, such as the electrolytic cell.

The process units in flowsheet 1 (Fig. 1) were simulated with the ASPEN modules shown in Fig. 3. The ASPEN modules for flowsheet 2 (Fig. 2) are shown in Fig. 4. Figures 3 and 4 describe the basic units needed to represent the material and energy balances for the flowsheets. Auxiliary equipment, such as pumps and tanks, were accounted for later in the costing routines.

The butene absorber, ABSR1, was simulated by the equilibrium reactor module, REQUIL. As previously mentioned, *n*-butenes were converted to 2-butanol (in the presence of 65 w/o sulfuric acid) by a very fast second order reaction that proceeded essentially to equilibrium. Absorber conditions were 60°C and 100 psia to maximize butanol production (31). Heat of reaction was removed by cooling water.

The butanol/sulfuric acid mixture was heated to 76.7°C by a steam supplied heat exchanger before entering the electrochemical reactor section, REACT. REACT was modeled by a simple algebraic reactor module, RYIELD, along with a user-supplied FORTRAN subroutine to portray Worsham's best cell operating conditions (31, 32). A flash module immediately followed the reactor to determine the phase condition of outlet streams.

In flowsheet 1 (Fig. 3) the cell liquid proceeded to the distillation system. All distillations used the ASPEN rigorous distillation module, RADFRC (as modified in this work). The distillation specifications were set based on preliminary runs which tested the distillation system only. DIST1 and DIST2 specifications were 92% MEK recovery and a reflux ratio of 4. The DIST3 column as an azeotropic distillation to remove trace water. Its specifications were 95% water removal and a reflux ratio of 4. The finishing column, DIST4, had a reflux ratio of 4 and attained 99% purity MEK product. All columns had fourteen equilibrium stages with a reboiler and total condenser at atmospheric pressure. Changes in the distillation specifications could be entertained in subsequent evaluations of the process if profitability would be found to be sensitive to the distillation system design.

In flowsheet 2 (Fig. 4), the MEK was removed from the electrochemical reactor gas. The gas passed through a refrigerated cooler, COOL1, which was modeled by a flash at 5°C and 30 psia. The cooler liquid advanced to a two column distillation system which was identical to DIST3 and DIST4 of the first configuration.

In both flowsheets, the by-product hydrogen gas flowed through a three-stage water absorber at 5°C and 1 atm to remove MEK for recycle. The absorbers were modeled by three flash modules assembled countercurrently. This choice was made because of difficulties modeling gas absorption with ASPEN's RADFRC and ABSORBER modules. Run time errors occurred in preliminary testing of these modules.

Design specification and convergence.—It is necessary to select design specifications, to be imposed on the flowsheet, as well as free variables, to be adjusted to meet the specifications.

The specifications for the flowsheets were a 1:1 hydrogen ion to 2-butanol mole ratio and 65 w/o sulfuric acid in the cell feed. Immediately preceding and REACT block, an ASPEN fortran block adjusted the H_2SO_4 moleflow to maintain the H^+/2-butanol ratio. This treatment handled the specification as an equipment parameter rather than an actual design specification. An ASPEN design specification block controlled the ABSR2 water flow to achieve 65 w/o sulfuric acid entering the cell. The design specification was considered converged when there was less than 0.001 kmol/h change in the absorber water flow between iterations.

A tear stream is one which is given an initial guess and then iterated upon to converge upon a recycle loop. Four tear streams were selected for each flowsheet. The tear streams for these flowsheets are designated by letters A through D in Fig. 3 and 4. The tear streams were converged when component moleflows, pressure, and total enthalpy changed by less than 0.01% between iterations. The ASPEN convergence routine employed was BROYDEN (9), which converged the design specification and tear streams simultaneously.

Costing and economic analysis.—It is necessary to select materials of construction and to specify cost module factors.

Capital and operating costs were estimated by using the ASPEN cost estimation system (CES). The CES was designed to yield a "preliminary-study grade" estimate from flowsheet heat and mass balance results. The system was based on Guthrie's modular concept for capital estimation (38). The CES contained information to determine process equipment costs (except for the electrochemical section which is discussed later). Factors to estimate the installation and indirect costs (38) were added in the ASPEN input file. Economic analysis calculated the MEK product selling price based on a 20% discounted cash flow rate of return.

The capital costs of the electrochemical reactor section were based on the work of Keating and Sutlic (39). Their cost module accounted for the cell bank, rectifier and busing, pumps, and common facilities associated with the electrochemical reactor section. Their design involved a divided membrane cell with a chlorinated polyvinyl chloride body, a precious metal oxide anode (titanium substrate), and a mild steel cathode. The costs were adjusted for the present study since only an undivided cell design was needed. The overall cost per square foot of electrode surface was \$1091 (1984\$) which included 40% indirect field costs.

Plant life was 20 years with declining balance depreciation, 13% interest on borrowed capital, 10% salvage value, and 5% yearly inflation. CES defaults (9) were used for other economic parameters such as tax rates. Construction year was 1985 in a midwest location with production beginning in 1987. Materials of construction were Incoloy 825 and Hastelloy for all process units (except the electrolytic cells) with sulfuric acid present. Units with no electrolytes were constructed of carbon steel. Plant capacity ranged from 25 to 45 kton/yr MEK produced.

Raw material (40) and utility prices (41) used for this study are listed in Table II. Another set of utility prices (Table III) was used only for utility cost comparison with conventional MEK routes. These comparisons were made with information from Rudd *et al.* (42). Cost adjustments were based on the Chemical Engineering Index.

Table I. MEK flowsheet thermodynamic data representation root mean square error analysis

Components	ΔT(°C)	Δx	Δy
Sulfuric acid/water	0.50	0.0021	—
Butanol/water	0.66	0.0035	0.030
MEK/water	0.20	0.0025	0.019
Butanol/MEK	0.49	0.0004	0.016
Butanol/MEK/water	0.31	0.0010	0.018

Results and Discussion

Table IV lists the cases that were studied in this work. MEK selling prices at 20% discounted cash flow rate of return were calculated at different plant capacities and electrolytic cell current densities. Higher current density runs were set at twice Worsham's best reported current density to investigate sensitivity of profitability to advances over current MEK cell technology. The last two

Table II. Commodity and utility prices (1984$)

Item	Unit	Price
1-butene	lb	$0.26
Process water	M gal	3.25
MEK	lb	0.36
Fuel gas	MM BTU	3.11
100 psig steam	M lb	2.71
Ammonia refrigeration	ton-day	1.63
Cooling water	M gal	0.22
Electricity	kWhr	0.056

runs were made with the use of Table III utility figures for conventional route comparisons with Rudd *et al.* (42).

Results in Table IV may be compared with the 1984 MEK price of $0.36/lb. The selling price decreases slightly with plant size. The higher current density runs show that technology advances in the MEK cell will result in improved profitability. Advances in cell design which reduce capital, such as higher current density or bipolar cell, could give advantage over the conventional route.

Base runs were made at a MEK product capacity of 45 kton/yr. Based on a 20% discounted cash flow rate of return, flowsheet 2 proved to be the better alternative with a MEK selling price of $0.391/lb. For this process, the product recovery section accounted for a minor fraction of capital costs.

Capital and utility cost comparisons were made with the conventional oxidation of *n*-butenes to MEK (Table V). These comparisons were based on conventional capital and utility costs estimated by Rudd (42). The flowsheet 2 electrochemical plant required 65% of the utility cost of the conventional route. Flowsheet 2 capital costs were 32% higher than the conventional process. These trends show that the electrochemical process could gain advantage over the conventional route in a time of energy costs rising faster than capital costs.

The MEK electrochemical process flowsheet has certain characteristics that may not be typical for electroorganic processes in general. The MEK process involves a fairly simple product recovery section. The electrochemical route eliminates the need to separate butanol from sulfuric acid, as required by the conventional process. By virtue of eliminating separation equipment, the electrochemical production of MEK may be able to compete

Table III. Utility prices for conventional route comparison (1984$)

Item	Unit	Price
Fuel gas	MM BTU	$3.16
100 psig steam	M lb	3.45
Cooling water	M gal	0.032
Electricity	kWhr	0.027

Table IV. MEK electrochemical flowsheet run summary

Capacity (kton/yr)	Flowsheet configuration	Current density (A/ft²)	MEK price ($/lb)
25	Fig. 1	120	0.424
25	Fig. 2	120	0.406
25	Fig. 1	240*	0.357
25	Fig. 2	240*	0.338
45	Fig. 1	120	0.406
45	Fig. 2	120	0.391
45	Fig. 1	240*	0.339
45	Fig. 2	240*	0.323
45	Fig. 1	120	0.395†
45	Fig. 2	120	0.379†

* These runs are for comparison only. The maximum current density achieved by Worsham was 120 A/ft².

† These runs used Table III utility prices for conventional route comparison with Rudd *et al.* (42).

Table V. Capital and utility cost comparison (1984$)

	Capital cost (MM$)	Relative yearly utility cost
Conventional oxidation of *n*-butenes	33.66	1.00
Fig. 1 electrochemical plant	51.40	1.06
Fig. 2 electrochemical plant	48.47	0.65

with the conventional route even though MEK has a relatively low unit selling price.

Typical computer run time statistics for the two flowsheet configurations are shown in Table VI. Runs were made on an IBM 4341 Model L10 computer. Core memory requirements were 4 megabytes running under the VM/SP Release 3 operating system. A simulation of flowsheet 1 required 12 iterations to converge while taking 31 CPU minutes at a cost of $37. Flowsheet 2 runs took 12 CPU min for 19 iterations at a cost of $14.

Table VI shows a breakdown of computational effort and illustrates that rigorous distillation calculations accounted for the majority of the run time. Also, distillations involving electrolytes required more CPU time than the nonelectrolyte distillations by a factor of almost four. It must be mentioned that this study used a very simple electrolytic cell model accounting for negligible run time. More complex models would undoubtedly increase computer time.

It must be emphasized that no process optimization was attempted in the present study. More detailed modeling of the electrolytic cell would be required to take full advantage of optimization techniques. At this point, the ASPEN electrolytic cell models developed in the present study are research-grade programs. All other modifications of ASPEN (REQUIL, RADFRC, and DRS) are portable to all public version ASPEN installations. Complete documentation is available from the authors.

Conclusions and Recommendations

A methodology was developed for the computer-aided simulation and design of electrolytic process flowsheets. The electrochemical production of MEK was used as an example. The methodology provides cost-effective avenues for detailed design and economic evaluation of electrochemical processes. The framework constructed in this study laid the foundation upon which a process flowsheet package capable of electrolytic process optimization could be developed.

The MEK process was found to be within the realm of economic feasibility despite the fact that MEK had a relatively low unit selling price. Electrolytic processes with high value products should show great promise competing against conventional routes. This study used a simple algebraic reactor model that portrayed the best results reported in the patent literature. This work illustrated the use of a user-supplied FORTRAN subroutine to describe an electrolytic cell in an ASPEN flowsheet.

The public version of ASPEN was enhanced to provide improved reliability and portability. The enhancements included rigorous distillation with electrolytes, and data

Table VI. Typical run time statistics

Flowsheet 1	12 iterations		$37
	2 electrolyte distillations	1397	(116/iteration)
	2 non-electrolyte distillations	372	(31/iteration)
	all other computations	75	
	1844 CPU seconds		
Flowsheet 2	19 iterations		$14
	2 non-electrolyte distillations	631	(33/iteration)
	all other computations	99	
	730 CPU seconds		

Computer: IBM 4341 Model L10

regression capability for electrolyte thermodynamic model parameters. Electrolyte distillations with the use of the modified ASPEN module, RADFRC, showed increased computation time, owing to the algorithm's difficulty in handling highly nonideal systems. It would be desirable to extend the ASPEN electrolyte thermodynamic modeling capability to liquid-liquid-gas equilibrium in order to be able to evaluate liquid-liquid extraction operations, as well as electrolytic cells with two liquid phases.

In the future, it will be important to extend computer-aided methods in order to optimize electrochemical process flowsheets. Several key problems need to be addressed in order to achieve this goal. Development of modules which are more efficient in dealing with electrolyte nonideality are required for multistage operations (absorption, distillation, extraction), and for staged equilibrium processes with chemical reactions. In order to increase computational efficiency, a multitier structure should be used for the rigor with which unit operations and electrolytic cells are modeled. Less rigorous models should be used until the flowsheet nears convergence; rigor should increase as the optimal flowsheet design is approached. ASPEN should be converted to a simultaneous modular structure. Such a structure has shown promise for process optimization (8, 43, 44).

Acknowledgments

Acknowledgment is made to the Donors of the Petroleum Research Fund, administered by the American Chemical Society, for the partial support of this research. Support was also provided by an unrestricted grant-in-aid from Monsanto, and fellowships from Amoco Oil, Chevron Oil, and Shell Oil. Computer costs were shared with the Research Board of the University of Illinois.

Manuscript received Aug. 19, 1985.

The University of Illinois assisted in meeting the publication costs of this article.

REFERENCES

1. G. D. Cera, Ph.D. Thesis, University of Illinois, Urbana, IL (1983).
2. R. D. LaRoche, M. S. Thesis, University of Illinois, Urbana, IL (1985).
3. L. B. Evans, in "Foundations of Computer-aided Chemical Process Design," **1**, R. S. H. Mah and W. Seider, Editors, p. 425, Engineering Foundation, New York (1981).
4. A. W. Westerberg, H. P. Hutchinson, R. L. Motard, and P. Winter, in "Process Flowsheeting," Cambridge University Press, Cambridge (1979).
5. J. D. Perkins, in "Proceedings of the Second International Conference on Foundations of Computer-Aided Process Design," A. W. Westerberg and H. H. Chien, Editors, p. 309, CACHE, Ann Arbor, MI (1984).
6. J. D. Perkins and R. W. H. Sargent, in "Selected Topics on Computer-Aided Process Design and Analysis," AIChE Symposium Series 214, R. S. H. Mah and G. V. Reklaitis, Editors, p. 1, American Institute of Chemical Engineers, New York (1982).
7. L. T. Biegler, in "Proceedings of the Second International Conference on Foundations of Computer-Aided Process Design," A. W. Westerberg and H. H. Chien, Editors, p. 369, CACHE, Ann Arbor, MI (1984).
8. H.-S. Chen and M. A. Stadtherr, *AIChE J.*, **31**, 1843 (1985).
9. ASPEN User Manual, U.S. Department of Energy, Vol. I (DE82020196) and Vol. II (DE82020197), National Technical Information Center, Springfield, VA (1982).
10. C. M. Criss and J. W. Cobble, *J. Am. Chem. Soc.*, **86**, 5385 (1964).
11. H. P. Meissner and J. W. Tester, *IEC Proc. Des. Dev.*, **11**, 128 (1972).
12. K. S. Pitzer, *J. Phys. Chem.*, **77**, 268 (1973).
13. L. A. Bromley, *AIChE J.*, **19**, 313 (1978).
14. C.-C. Chen, H. I. Britt, J. F. Boston, and L. B. Evans, *ibid.*, **25**, 820 (1979).
15. K. S. Pitzer, in "Thermodynamics of Aqueous Systems with Industrial Application," ACS Symposium Series 133, S. A. Newman, Editor, American Chemical Society, Washington, D.C. (1980).
16. C. Christensen, B. Sander, A. Fredenslund, and P. Rasmussen, *Fluid Phase Equilib.*, **13**, 297 (1983).
17. E. Hala, *ibid.*, **13**, 311 (1983).
18. B. Mock, C.-C. Chen, and L. B. Evans, Paper 32b presented at the AIChE Annual Meeting, San Francisco, CA., Nov. 1984.
19. G. Maurer, *Fluid Phase Equilib.*, **13**, 269 (1983).
20. J. P. Zemaitis, Jr., in "Computer Applications to Chemical Engineering," ACS Symposium Series 133, R. G. Squires and G. V. Reklaitis, Editors, p. 309, American Chemical Society, Washington, D.C. (1980).
21. L. B. Evans, J. F. Boston, H. I. Britt, P. W. Gallier, P. K. Gupta, B. Joseph, V. Mahalec, E. Ng, W. D. Seider, and H. Yagi, *Comp. Chem. Eng.*, **3**, 319 (1979).
22. C.-C. Chen, H. I. Britt, J. F. Boston, and L. B. Evans, Paper 50f presented at the AIChE Spring Meeting, Houston, TX., Apr. 1981.
23. H. Renon and J. M. Prausnitz, *AIChE J.*, **14**, 135 (1968).
24. D. J. Pickett, in "Electrochemical Reactor Design," 2nd ed. Elsevier, Amsterdam (1979).
25. R. F. Savinell, in "Tutorial Lectures in Electrochemical Engineering and Technology. II," AIChE Symposium Series 229, R. Alkire and D. T. Chin, Editors, p. 13, American Institute of Chemical Engineers, New York (1983).
26. C. Oloman, in "Tutorial Lectures in Electrochemical Engineering and Technology. II," AIChE Symposium Series 229, R. Alkire and D. T. Chin, Editors, p. 68, American Institute of Chemical Engineers, New York (1983).
27. T. Z. Fahidy, *This Journal*, **132**, 1575 (1985).
28. T. R. Beck, R. C. Alkire, N. L. Weinberg, R. T. Ruggeri, and M. A. Stadterr, in "Technique of Electroorganic Synthesis, part III," N. L. Weinberg and B. V. Tilak, Editors, p. 423, John Wiley & Sons, New York (1982).
29. C. J. H. King, in "Tutorial Lectures in Electrochemical Engineering and Technology. II," AIChE Symposium Series 229, R. Alkire and D. T. Chin, Editors, p. 79, American Institute of Chemical Engineers, New York (1983).
30. R. E. W. Jansson, *J. Appl. Electrochem.*, **12**, 163 (1982).
31. C. H. Worsham, U.S. Pat. 3,247,084, (1966).
32. L. I. Griffin, J. V. Clarke, and C. H. Worsham, U.S. Pat. 3,329,593 (1967).
33. D. S. Sanholkar and M. M. Sharma, *Chem. Eng. Sci.*, **28**, 49 (1973).
34. R. H. Perry and C. H. Chilton, Editors, in "Chemical Engineers' Handbook," 5th. ed., p. 3:64, McGraw-Hill, Inc., New York (1973).
35. D. D. Wagman, W. H. Evans, V. B. Parker, R. H. Schumm, I. Halow, S. M. Bailey, K. L. Churney, and R. L. Nuttal, *J. Phys. Chem. Ref. Data*, **11**, 2:58 (1982).
36. J. Gmehling, U. Onken, and W. Arlt, "Vapor-Liquid Equilibrium Data Collection: Aqueous-Organic Systems," supplement 1, DECHEMA, Frankfurt (1981).
37. J. Gmehling, U. Onken, and U. Weidlich, Vapor-Liquid Equilibrium Data Collection: Organic Hydroxy Compounds, supplement 2, DECHEMA, Frankfurt (1982).
38. K. M. Guthrie, in "Modern Cost-Engineering Techniques," H. Popper, Editor, p. 80, McGraw-Hill, Inc., New York (1970).
39. K. B. Keating and V. D. Sutlic, in "Electro-organic Synthesis Technology," AIChE Symposium Series 185, M. Krumpelt, E. Y. Weissman, and R. C. Alkire, Editors, p. 76, American Institute of Chemical Engineers, New York (1979).
40. Chemical Marketing Reporter, Schnell Publishing Company, New York, Oct. 29, 1984.
41. M. S. Peters and K. D. Timmerhaus, in "Plant Design and Economics for Chemical Engineers," 3rd. ed., p. 881, McGraw-Hill, Inc., New York (1980).
42. D. F. Rudd, S. Fathi-Afshar, A. A. Trevino, and M. A. Stadtherr, in "Petrochemical Technology Assessment," p. 239, John Wiley & Sons, New York (1981).
43. R. A. Trevino-Lozano, L. B. Evans, H. I. Britt, and J. F. Boston, *I Chem E Symp. Ser.*, **92**, 25 (1985).
44. L. T. Biegler, *Comp. Chem. Eng.*, **9**, 245 (1985).

Photocharge Transfer Mediation by Adsorbed Ions: Simulation of Photocurrent-Voltage Curves Based on Results of Photoluminescence Transient Measurements

M. Evenor, D. Huppert, and S. Gottesfeld[1]

Department of Chemistry, University of Tel-Aviv, Ramat-Aviv 69978, Israel

ABSTRACT

High surface capture velocities, of the order of 10^5-10^6 cm s^{-1}, for both minority and majority carriers were evaluated by us recently from measurements of photoluminescence decay in the picosecond time domain, taken for n-CdS crystals immersed in alkaline sulfide-polysulfide electrolytes. A resulting question was raised, whether an interface with high surface capture rate constants for both p and e will allow significant conversion efficiencies under normal continuous illumination conditions, as known to be obtained experimentally for this particular interface. This paper presents simulations of current-voltage curves, which demonstrate that J *vs.* V relations of desirable forms, and of good associated conversion efficiencies, may indeed be obtained in the presence of high surface capture rate constants for both holes and electrons. The condition for such behavior is that the transfer of the photogenerated minority carrier from the surface trap to an acceptor in solution proceeds with a minimum rate constant, typically of the order of $10^6 s^{-1}$. This leads to a conclusion on the possible role of surface states, particularly those derived from adsorbed anions, as mediators of photocharge transfer.

We have shown recently (1), that photoluminescence decay measurements in the picosecond time domain can serve as an efficient tool for the evaluation of surface capture velocities at the semiconductor-electrolyte interface. It has been demonstrated that the apparent surface recombination velocity increases from $S \leq 10^3$ cm/s for an etched CdS crystal immersed in water to $S = 10^5$-10^6 cm/s for an etched CdS crystal immersed in an alkaline sulfide-polysulfide solution. This apparent high value of S was shown to result from high surface capture velocities for both holes and electrons. The photoluminescence decay experiments (1) are conducted under high injection conditions, *i.e.*, under conditions where the population of the photogenerated pairs is much higher than the dark majority free-carrier concentration. Under such experimental conditions the population of both electrons and holes at the surface is high and comparable. This situation is quite different from the one that prevails under normal illumination conditions where the field in the space-charge region is responsible for a drastic lowering of the majority carrier population near the surface. The problem addressed in this paper is the following: Is it possible to obtain reasonable J *vs.* V curves under regular illumination conditions in the presence of large capture cross sections for both majority and minority carriers, as measured for CdS crystals immersed in sulfide solutions? And, if so, what are the details of the mechanism of photocharge transfer which explain such steady-state J *vs.* V curves? To answer these questions, we performed computer simulations of current-voltage curves in the presence of high surface capture cross sections for both minority and majority carriers, as evaluated from the photoluminescence decay measurements.

Several descriptions of simulations of steady-state photocurrent-voltage curves for illuminated semiconductor-electrolyte interfaces appeared recently in the literature. The effects of the finite diffusion length of minority carriers generated in the field free region (2-4), of the finite rate of photocharge transfer across the SC-electrolyte interface (3-11), of recombination in the space charge region (4, 6-10), and of the role of surface states as recombination centers (5-7, 10-12) as well as mediators of charge transfer (11, 12) have all been mostly separately considered. The approach adopted here was similar to that of Kelly and Memming (11) with three differences: (*i*) The J *vs.* V relationship is evaluated in a way that mimics a real experiment, *i.e.*, J is solved for a series of "scanned" values of V. This is in contrast to the indirect method used in (11) where the fractional filling, f_r, of the active surface levels was "scanned," and the resulting values of V and of J were solved for the "scanned" values of f_r. The advantages of the computational approach we employed will be clarified below. (*ii*) The overall current-voltage relationship, including the majority flux, is evaluated using experimentally measured parameters for the calculation of the dark current component. (*iii*) The details of the generation and recombination processes in the field free region and in the SCR are carefully considered in the simulation.

[1]On sabbatical leave at the Los Alamos National Laboratory, Los Alamos, New Mexico 87544.

Assumptions

A scheme of the model assumed is shown in Fig. 1. The following assumptions were made for the derivation of the simulated J *vs.* V curves:

1. Every photon which hits the surface is absorbed and generates an electron-hole pair.

2. The minority carriers (holes in our case) are generated in the space charge region (SCR) as well as in the field free region. They reach the SC-electrolyte interface by diffusion in the field free region and by drift in the SCR, some being lost by processes of recombination which take place in both regions.

3. Photogenerated minority carriers (holes) are transferred to solution via two parallel routes: directly from the valence band, and via a surface level. The process of the direct, VB to solution, photocharge transfer is first order with respect to the concentration of holes at the surface, and first order with respect to the concentration of acceptors in solution. The latter concentration is assumed to be very high (*e.g.*, 1M), and, therefore, this process becomes pseudo first order with respect to the hole concentration at the surface. For the same reason the process of charge transfer from the empty active surface levels to acceptors in solution is also pseudo first order with respect to their concentration.

4. A single energy level is assumed for the active surface state responsible for capture of photogenerated carriers, and its population is assumed to be determined by Hall-Shockley-Read statistics (13).

5. The active surface level is deep, *i.e.*, emission of trapped carriers back to the bands is negligible.

6. If the net charge on the surface level under steady-state illumination is different than that in the dark, this would cause a change of the potential drop across the Helmholtz layer. The charge transfer rate constants for both of the parallel hole transfer routes will be affected. The same phenomenon brings about a change in band bending at a given external applied voltage, affecting the population of minority and majority carriers at the surface and, hence, the rate of the surface recombination

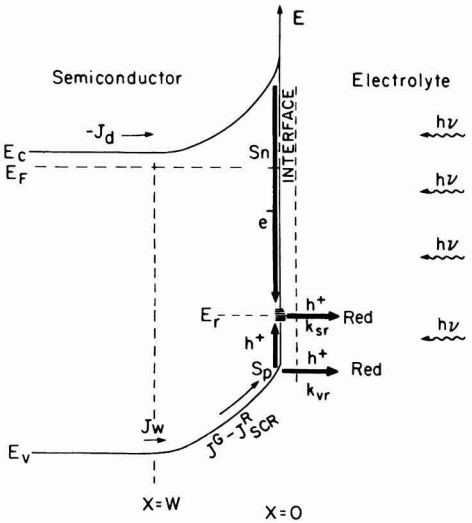


Fig. 1. Schematic presentation of the model for charge transfer. E_v, E_c, and E_r are the energy levels of the valence band, conduction band, and the surface-state level, respectively; E_F is the Fermi level; S_n and S_p are the surface capture velocities for electrons and holes, respectively; k_{vr} and k_{sr} are rate constants for hole transfer directly from the valence band and via the surface state, respectively; J_d is the dark current.

process and the level of the dark current at a given externally applied voltage are also affected.

7. It is assumed that the dark current is defined by two experimentally measured parameters for this SC-electrolyte junction (14, 15): $J_{no} = 3 \cdot 10^{-8} A cm^{-2}$ and A (ideality factor) = 2.

Equations

The following equations describe the behavior of the n-CdS/$S^=$, S^o interface under the assumptions specified above

$$J = J_p - J_n = J_p - J^*_{no}[\exp(e/AkT)(V_{sc}^o - V_{sc}) - 1] \quad [1]$$

$$J_p = e[k_{vr}P_s + k_{sr}N_r(1 - f_r)] \quad [2]$$

$$n_s = n_o \exp[-(e/kT)\, V_{sc}] \quad [3]$$

$$V = V_{sc} - V_{sc}^o + \delta V_H = \Delta V_{sc} + \delta V_H \quad [4]$$

where J is the measured current, J_p is the photocurrent density , and J_n the dark current density (Acm^{-2}), k_{vr} is the rate constant for direct hole transfer from valence band, at the surface, to the acceptor in solution (cm s^{-1}), P_s is the concentration of holes in the valence band at the semiconductor surface (cm^{-3}), k_{sr} is the rate constant for hole transfer from a surface level to an acceptor in solution (s^{-1}), N_r is the surface coverage of the active level (cm^{-2}), f_r is the fractional filling of the surface level (dimensionless), J_n is the majority current density (A cm^{-2}), J^*_{no} is the majority exchange current density measured under illumination, n_s is the surface concentration of majority carriers, and n_o is their bulk concentration (cm^{-3}). V_{sc} is the potential difference across the space charge region, defined as the potential in the bulk of the semiconductor minus the potential at the outer surface of the semiconductor phase ($x = 0$). V_{sc}^o is the value of V_{sc} at equilibrium in the dark. According to the above definition of the sign of V_{sc}, the overall potential, drop between bulk semiconductor and bulk solution in the dark is: $+V_{sc}^o + (\Delta V_H)_d$ where $(\Delta V_H)_d$ is the potential drop across the Helmholtz layer in the dark, defined as the potential at the surface minus the potential in the bulk of the solution phase. Under illumination the overall potential drop between semiconductor and solution phases will be: $+V_{sc} + (\Delta V_H)_{ill}$ and the photovoltage V will be thus given by Eq. [4] where $\delta V_H = (\Delta V_H)_{ill} - (\Delta V_H)_d$ is the change in the Helmholtz potential drop due to illumination.

The total flux of holes entering the SCR by diffusion from the field free region, at the coordinate $x = W$ is given by (4)

$$J_W = (e\phi)[L_p/(1 + L_p)] \exp(-\alpha W) - J_1(P_W/P_o - 1) \quad [5]$$

where

$$J_1 = eL_pP_o/\tau_p$$

ϕ is the incident photon flux, α the absorption coefficient for incident light, L_p the minority diffusion length in the field free region, W the width of the SCR, P_o the concentration of holes in the bulk in the dark, P_W the concentration of holes at $X = W$ at steady state, and τ_p the minority lifetime in the dark. The generation current in the SCR is given by

$$J_{SCR}{}^G = e\phi[1 - \exp(-\alpha W)] \quad [6]$$

while the recombination current in the SCR (*i.e.*, flux of minorities lost due to recombination in the SCR) is given by (16, 17)

$$J_{SCR}{}^R = J_2(W/V_{sc})(P_s/P_{so})^{1/2} \exp\{-e\Delta V_{sc}/2kT\} \quad [7]$$

where

$$J_2 = \pi e\tau_p{}^{-1}kTn_i/2$$

and where P_{so} is the surface concentration of holes in the dark, and n_i is the concentration of carriers in an intrinsic material with the same bandgap.

The overall flux of holes reaching the coordinate $x = 0$ in the semiconductor phase is given by: $J_W + J_{SCR}{}^G - J_{SCR}{}^R$, and it has to be equal at steady state to the flux of holes leaving this coordinate either directly to acceptors in solution or to the traps at the surface. Thus, at steady state

$$J_W + J_{SCR}{}^G - J_{SCR}{}^R = e[k_{vr}P_s + C_pN_rP_s] \quad [8]$$

where $C_p = \sigma_p v_{th}$, σ_p being the capture cross section for holes from the valence band by filled surface states.

Rewriting the lefthand side of Eq. [8] according to Eq. [5]-[7], while expressing P_W/P_o in Eq. [5] in terms of P_s/P_{so}, yields after some rearrangement

$$J_3 - J_1(P_s/P_{so}) \exp[-e\Delta V_{sc}/kT) - J_2(W/V_{sc})(P_s/P_{so})^{1/2} \exp[-e\Delta V_{sc}/2kT] = e[k_{vr}P_s + C_pN_rf_rP_s] \quad [9]$$

where

$$J_3 = e\phi[1 - \exp(-\alpha W)/(1 + \alpha L_p)] + J_1$$

At steady state, it is also true that $d[N_r(1 - f_r)]/dt = 0$, from which it follows that

$$C_nn_sN_r(1 - f_r) = P_sC_pN_rf_r - k_{sr}N_r(1 - f_r) \quad [10]$$

where the product C_nN_r is the surface capture velocity for electrons from the conduction band ($C_n = \sigma_n v_{th}$). Hence, at steady state

$$n_s = [C_pf_rP_s - k_{sr}(1 - f_r)]/C_p(1 - f_r) \quad [10\text{-a}]$$

The next step should be evaluation of P_s from Eq. [9] and [10]

$$P_s = J_3/be - (c/b^2)[1 - (1 + 4bJ_3/c^2e)^{1/2}] \quad [11]$$

where

$$b = J_1/(eP_{so}) \exp(-e\Delta V_{sc}/kT) + C_pN_rf_r + k_{vr} \quad [11\text{-a}]$$

$$c = (J_3/e)\, W \exp -e\Delta V_{sc}/2kT/((P_{so})^{1/2}V_{sc}) \quad [11\text{-b}]$$

In the computer calculations the rigorous Eq. [11] was employed to express P_s. However, in the system dealt with here, the following inequality holds: $4J_3b/c^2 \cdot e >> 1$ and, hence, P_s can be expressed in the simpler form

$$P_s = J_3/be - (c/b^2)(bJ_3/e)^{1/2} \quad [12]$$

Equation [12] will be used in the derivation below. Substituting P_s from Eq. [12] into Eq. [10-a], and dividing both sides by n_{so} results in

$$\frac{n_s}{n_{so}} = \frac{C_n f_r[(J_3/b) - (c/b^2)(bJ_3)^{1/2}] - k_{sr}(1 - f_r)}{C_n(1 - f_r)n_{so}}$$

$$= \exp\,[-(e/kT)(V_{sc} - V_{sc}^{o})] \qquad [13]$$

It will be next assumed that δV_H can be expressed, in terms of the extra charge on the surface level due to steady-state illumination by

$$\delta V_H = \gamma(f_o - f_r) \qquad [14]$$

where f_o is the fractional filling of the surface levels at equilibrium in the dark, and $\gamma = eN_r/C_H$ (C_H, the capacity of the Helmholtz layer).

We also assume that k_{vr} and k_{sr} both depend on δV_H through a Tafel relationship, with a symmetry factor $\beta = 1/2$. From Eq. [13], [14], and [4], and using the last assumption, the following equation for f_r (at an imposed V) is obtained

$$\frac{C_n f_r[(J_3/b) - (c/b^2)(bJ_3)^{1/2}] - k_{sr}^{o}(1 - f_r)\exp\,[(e\beta\gamma/kT)(f_o - f_r)]}{C_n(1 - f_r)n_{so}}$$

$$= \exp\,\{[-(e/kT)[V - \gamma(f_o - f_r)]\} \qquad [15]$$

k_{vr} (contained in b) is also expressed as $k_{vr}^{o}\exp\,[(\beta e\gamma/kT)(f_o - f_r)]$ k_{vr}^{o} and k_{sr}^{o} are the values of these rate constants in the dark, *i.e.*, in the absence of photocharging of the surface level.

Solution

The approach of Kelly and Memming (11) to the solution of an equation similar to Eq. [15] was to solve for "scanned" values of f_r. For each value of f_r assumed, δV_H can be calculated from Eq. [14], and k_{sr} and k_{vr} are next evaluated for assumed values of k_{vr}^{o} and k_{sr}^{o} (see below on the choice of values for k_{vr}^{o} and k_{sr}^{o}). Next P_s can be calculated from Eq. [11] or [12], and J_p can be then found from Eq. [2]. The ratio n_s/n_{so} follows from P_s according to Eq. [13], and can be used, in turn, to calculate V from Eq. [15]. The problem with this approach is the following. For many combinations of values for the parameters which appear in the above set of equations, including combinations which are of interest on physical grounds, f_r changes in a very narrow domain when the applied potential varies throughout the region of interest. Thus, for example, most of the details of the J *vs.* V curve, including the up sloping branch, may not be easily detected for some combinations of rate constants, because f_r happens to change only, *e.g.*, between 1 and 0.996. Realizing that this problem actually arises when trying to solve Eq. [15] in this manner (11) with the rate constants which seemed most relevant to our system (1), we set out to solve this equation in a way that mimics the experiment. For evenly spaced values of V, between V_{oc} (open-circuit photovoltage) and $V = 0$, f_r was solved from Eq. [15]. This was done by using a computer program[2] for the solution of the nonlinear equations, and employing double precision to take care of the very small variations of f_r and their very large influence on the final results evaluated. After f_r is obtained from Eq. [15], the rest of the solution is performed along the steps mentioned above, *i.e.*, first P_s and δV_H are calculated, and from their values J_p is obtained, while δV_H and the applied V determine V_{sc}, and, thus, J_n.

Results

Figure 2 shows the major features of the simulated current-voltage curve. The semiconductor sample considered has a bulk density of $n_o = 2.10^{16}\text{cm}^{-3}$ of majority carriers, and a dark current-voltage relationship (determined experimentally) which is characterized by $J_{no} = 3.10^{-8}$ Acm^{-2} (14) and an ideality factor $A = 2$ (15). It is assumed that the surface of the semiconductor is covered by $N_r = 6.10^{13}$ states cm^{-2}, which is a typical value for sulfide cov-

[2]A Tel-Aviv Library Program written by D. Sagin.

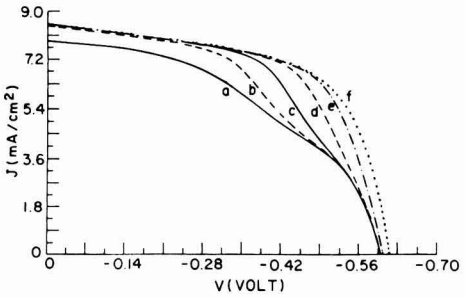


Fig. 2. Plots of J *vs.* V for the following parameters of the system: $N_r = 6 \times 10^{13}\ \text{cm}^{-2}$, $\sigma_n = \sigma_p = 10^{-15}\ \text{cm}^2$, $J_{no} = 3 \times 10^{-8}\ \text{Acm}^{-2}$, $A = 2$, $\tau_p = 1.25 \times 10^{-9}\text{s}^{-1}$, $\alpha = 1.4 \times 10^4\ \text{cm}^{-1}$ ($\lambda = 510$ nm) (1), $\phi_W = 0.05\ \text{Wcm}^{-2}$ (1.28×10^{17} photons $\text{cm}^{-2}\text{s}^{-1}$), $f_o = 1$, $n_o = 2 \times 10^{16}\ \text{cm}^{-3}$, $k_{vr}^{o} = 10^6\ \text{cms}^{-1}$. (a) $k_{sr}^{o} = 0$, (b) $k_{sr}^{o} = 10^2\text{s}^{-1}$, (c) $k_{sr}^{o} = 10^4\text{s}^{-1}$, (d) $k_{sr}^{o} = 10^5\text{s}^{-1}$, (e) $k_{sr}^{o} = 10^6\text{s}^{-1}$, (f) $k_{sr}^{o} = 10^8\text{s}^{-1}$

erages on CdS immersed in the electrolytes we employed (1). The surface states are characterized by equal capture cross sections for majority and minority carriers, of $\sigma_n = \sigma_p = 10^{-15}\ \text{cm}^2$. This combination of surface coverage and reactivity results in high capture velocities for both majority and minority carriers, and, thus, simulates a surface with high reactivity with respect to both carriers as suggested by the results of the photoluminescence decay experiments (1). Such a combination of surface coverage and reactivity results in surface capture velocities of $S_p = S_n = \sigma v_{th} N_r = 10^{-15} \cdot 10^7 \cdot 6.10^{13} = 6\ 10^5\ \text{cms}^{-1}$. It is also assumed that $V_{sc}^{o} = 0.7\text{V}$ (14), $C_H = 20\ \mu\text{F}$ (18). ϕ_W is assumed to be $0.05\ \text{Wcm}^{-2}$, which corresponds to a photon flux of $\phi = 1.3 \times 10^{17}\ \text{cm}^{-2}\text{s}^{-1}$.

It can be seen in Fig. 2 that even when k_{vr}^{o} is as large as $10^6\ \text{cms}^{-1}$, the shape of the J *vs.* V curve and the fill factor will be strongly influenced by the recombination activity at the surface as long as k_{sr}^{o} is very small. Under such conditions the curve has two plateaus, as shown also in Ref. (11). This shape is due to comparable rates of recombination and of charge transfer at intermediate photovoltages. The effect of increased k_{sr}^{o} in improving the fill factor (and, hence, the conversion efficiency), is seen by the clear difference between curve (a), where $k_{sr}^{o} = 0$ and curves (b)-(f), where k_{sr}^{o} is 10^3, 10^4, 10^5, 10^6, and $10^8\ \text{s}^{-1}$, respectively. The effect of k_{sr}^{o} is particularly significant with respect to the fill factor, which increases from 0.47 ($k_{sr}^{o} = 0$) to 0.58 ($k_{sr}^{o} = 10^6$-10^8s^{-1}). A slight increase in V_{oc} is also found. An important point to notice here is that the magnitude of the rate constant of $k_{sr}^{o} = 10^6\text{s}^{-1}$, which is seen to be sufficient to compete effectively with the surface recombination process, is actually quite modest. k_{sr}^{o} can be expressed as the number of "fruitful collisions" of acceptor (Red) ions with the semiconductor surface per unit time. Thus, k_{sr}^{o} is given by $k_{sr}^{o} = \sigma^{\text{ion}} \cdot v_{th}^{\text{ion}} \cdot C_{\text{Red}}$, where σ^{ion} is the cross section for the interfacial hole transfer reaction. A very reasonable maximum estimate for k_{sr}^{o} is obtained assuming $\sigma^{\text{ion}} = 10^{-15}\ \text{cm}^2$ (geometrical cross section), *i.e.*, $(k_{sr}^{o})_{\max} = 10^{-15} \cdot 10^4 \cdot 6 \cdot 10^{20} = 6 \cdot 10^9\text{s}^{-1}$, calculated for a redox system concentration level of 1M. A value of $k_{sr}^{o} = 10^6\text{s}^{-1}$ is thus seen to be 3-4 orders of magnitude lower than this estimate of a reasonable maximum. This is an important point, since it shows that a very conservative value for k_{sr}^{o} is enough for the surface to solution charge transfer process to compete efficiently with the process of recombination although the surface level is associated with high cross sections for interaction with both minorities and majorities. When $k_{sr}^{o} = 10^6\text{s}^{-1}$ and above, the active surface level is thus seen to be an effective charge transfer mediator. The capability to transfer the trapped minority carrier further on to the acceptor in solution must be the explanation of why the high capture reactivity with respect to majority carriers, as measured in the picosecond photoluminescence decay experiments, does not prevent high conversion efficiencies

from being obtained under normal continuous illumination conditions.

Figure 3 represents f_r *vs.* V for the same system described in Fig. 2. As can be seen, f_r depends both on the voltage and on the charge transfer rate constant k_{sr}^{o}. f_r increases as V increases toward V_{oc}. The filling of the surface states is higher when the charge transfer rate constant k_{sr}^{o} is higher. Indeed when k_{sr}^{o} is very high, ($10^6 s^{-1}$), f_r approaches 1 for all values of the photovoltage. This result demonstrates the advantage of the computational method employed here as compared to the method used by Kelly and Memming (11). The change in the potential drop in the Helmholtz layer due to photocharging of surface levels is maximum under short-circuit conditions (where f_r is minimum), while the change in the potential drop in the Helmholtz layer is minimum under open-circuit condition.

Figure 4 shows simulations for a situation as in Fig. 2, but with the surface capture velocities lowered by two orders of magnitude ($\sigma_n = \sigma_p = 10^{-17}$ cm^2), while k_{vr}^{o} is lowered at the same time by four orders of magnitude ($k_{vr}^{o} = 10^2$ cms^{-1}). It is clear that when the rate of direct charge transfer (valence band to solution) is very low, the conversion efficiencies are strongly influenced by the surface recombination velocity, even if the capture cross sections are quite small. In this case V_{oc} already shows strong lowering due to the surface recombination, but its full value for this level of photon flux, 1.3×10^{17} cm^{-2}, is practically restored when the process of hole transfer from surface state to solution is "switched on" with k_{sr}^{o} of $10^6 s^{-1}$. Under the same conditions, k_{sr}^{o} of $10^6 s^{-1}$ brings the fill factor up to 0.56.

Figure 5 shows an even worse situation, in that the ratio between the rate constants of surface capture and of the direct charge transfer process is further increased: $\sigma_n = \sigma_p = 10^{-15}$ cm^2 while $k_{vr}^{o} = 10^2$ cms^{-1}. However, even in such a case, a high but reasonable value of $k_{sr}^{o} = 10^8 s^{-1}$ ensures a high conversion efficiency. This last case clarifies that the interface can, in fact, operate practically exclusively through the surface mediated route for the minority carriers, and this route is capable of providing by itself high conversion efficiencies.

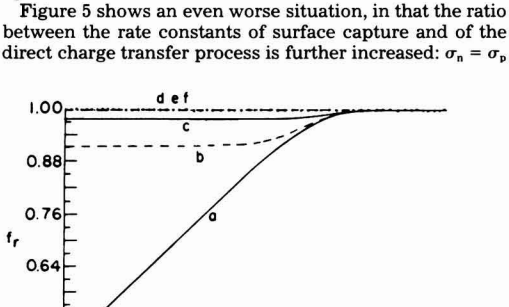


Fig. 3. Plots of the fractional filling, f_r of the surface state, *vs.* V for the parameters described in Fig. 2.

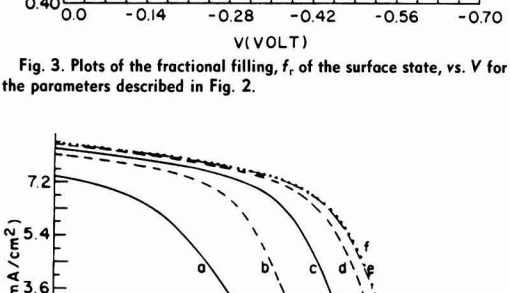


Fig. 4. Plots of J *vs.* V. The parameters are the same as in Fig. 2 but the cross sections for surface capture of electrons and holes are two order of magnitude smaller, $\sigma_n = \sigma_p = 10^{-17}$ cm^2, while k_{vr}^{o} is smaller by four orders of magnitude, $k_{vr}^{o} = 10^2$ cms^{-1}. (a) $k_{sr}^{o} = 0$, (b) $k_{sr}^{o} = 10^2 s^{-1}$, (c) $k_{sr}^{o} = 10^3 s^{1}$, (d) $k_{sr}^{o} = 10^4 s^{-1}$, (e) $k_{sr}^{o} = 10^5 s^{-1}$, (f) $k_{sr}^{o} = 10^8 s^{-1}$.

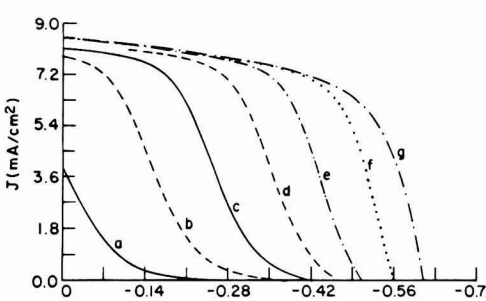


Fig. 5. Plots of J *vs.* V. Parameters as in Fig. 2 but the direct charge transfer rate is very low, $k_{vr}^{o} = 10^2$ cms^{-1}. (a) $k_{sr}^{o} = 0$, (b) $k_{sr}^{o} = 1$, (c) $k_{sr}^{o} = 10^2 s^{1}$, (d) $k_{sr}^{o} = 10^3 s^{-1}$, (e) $k_{sr}^{o} = 10^4 s^{-1}$, (f) $k_{sr}^{o} = 3 \times 10^5 s^{-1}$, and (g) $k_{sr}^{o} = 10^8 s^{-1}$.

The conversion efficiency η_c, is defined by Eq. [16] (19)

$$\eta_c = (J \times V)_{max}/\phi_W \qquad [16]$$

where ϕ_W is the total illumination power per unit area. Plots of η_c *vs.* the illumination intensity for several combinations of k_{vr}^{o} and k_{sr}^{o} are shown in Fig. 6. In these plots, two main groups are observed. In the lower group of curves, η_c is small since the charge transfer rate constant, k_{sr}^{o}, is quite low. In the upper group, k_{sr}^{o} and η_c values are both much higher. These results indicate that k_{sr}^{o} is a dominant factor in the conversion efficiency when the model for the interface considered here applies. At low levels of illumination all the curves coincide. The explanation for this phenomenon is the following. When the photovoltage is low, band bending is still significant, and the recombination processes, both in the SCR and at the surface, are slow. Therefore, most of the holes which have reached the SCR would be transferred to acceptors in solution. The overall efficiency is low, however, since the cathodic dark current does not depend on light intensity, and thus the photovoltage itself is low. When the illumination level is higher, recombination becomes more significant, and the

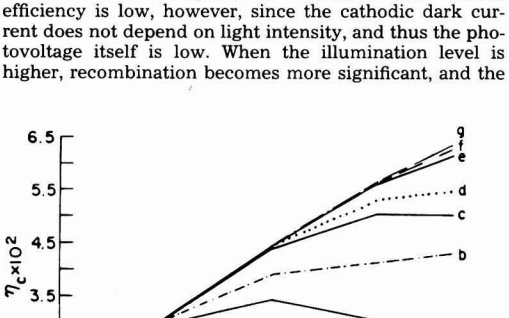


Fig. 6. The conversion efficiency η_c of the SC-electrolyte junction as a function of the irradiation intensity, ϕ_W, for the following combinations of k_{vr}^{o} and k_{sr}^{o}: (a) $k_{vr}^{o} = 10^2$ cms^{-1}, $k_{sr}^{o} = 10^2 s^{-1}$; (b) $k_{vr}^{o} = 10^6$ cms^{-1}, $k_{sr}^{o} = 10^2 s^{-1}$; (c) $k_{vr}^{o} = 10^2$ cms^{-1}, $k_{sr}^{o} = 10^4 s^{-1}$; (d) $k_{vr}^{o} = 10^6$ cms^{-1}, $k_{sr}^{o} = 10^4 s^{-1}$, (e) $k_{vr}^{o} = 10^2$ cms^{-1}, $k_{sr}^{o} = 10^6 s^{-1}$; (f) $k_{vr}^{o} = 10^6$ cms^{-1}, $k_{sr}^{o} = 10^6 s^{-1}$; (g) $k_{vr}^{o} = 10^2$ cms^{-1}, $k_{sr}^{o} = 10^8 s^{-1}$; (h) $k_{vr}^{o} = 10^6$ cms^{-1}, $k_{sr}^{o} = 10^8 s^{-1}$.

rates of the charge transfer processes become very important. Also, the overall efficiency may become much higher due to the increase in the photovoltage. When k_{sr}^{o} is very low (curve a) recombination processes will dominate at higher photovoltage and, thus, η_c decreases with the level of illumination.

In Fig. 7, η_c *vs.* the light intensity is plotted for the same system as shown in Fig. 6, except that δV_H is assumed to be zero. It can be observed that the η_c values are somewhat higher than those of the previous case, particularly when k_{sr}^{o} is small. During illumination δV_H is positive, and, thus, the charge transfer rate constants are expected to increase (typically by about a factor of 3-4) while the dark current is expected to decrease at a given voltage. From this point of view, η_c is expected to increase when δV_H increases. However, when δV_H is positive, the band bending is lower at a given applied voltage, and, hence, the recombination processes in the semiconductor phase are more effective, and the photocurrent decreases. Comparison of Fig. 6 and 7 demonstrates that the effect of surface state photocharging through the modification of δV_H is definitely noticeable, but is not a very dominant factor in the behavior of the junction, especially where k_{sr}^{o} is large.

Several assumptions made in the derivation of these simulated *J vs. V* curves deserve some comment. The first is the choice of the fractional filling of the active surface level at equilibrium as $f_o = 1$ in all cases, and the neglect of electron transfer from this level to the oxidized form of the redox couple in solution. A different selection, *i.e.*, $f_o < 1$, means appreciable rates of majority carrier (electron) transfer through the empty fraction of the surface level in the dark. This amounts to an additional parallel route for majority carrier transfer from the semiconductor to solution. Since an empirical dark current *vs.* voltage relationship has been included in the simulation, it has been assumed that this expression already includes all possible routes of majority carrier transfer across the interface. Hence, there is no place for an additional mechanism of majority carrier transfer in this model. An alternative presentation would be to describe the dark current as well in terms of two parallel routes, direct and surface mediated, where the sum of the two would result in the experimental overall dark current. We felt that this would complicate the treatment, without provision of better insight into the central problem. It follows from the above discussion that under illumination k_{sr}^{o} may be actually considered as the net rate of hole transfer from the surface level to solution, *i.e.*, hole transfer rate minus electron transfer rate.

The assumption of a Tafel relationship between δV_H and the charge transfer rate constants should also be briefly discussed. Other equations based on a Marcus-Levich type of relationship have been employed before (10, 11). Gratzel (20) showed that for photocharge transfer from the conduction band of TiO_2 to an acceptor in solution, variations in δV_H, brought about by variations of the pH, resulted in changes of the rate of charge transfer which conformed to a Tafel relationship. We chose the Tafel relationship because of its relative simplicity. While the exact nature of the dependence of charge-transfer rates on δV_H is a subject of great importance, it turns out to have only a small effect on the features of the photocurrent-voltage curve dealt with here (see Fig. 6 and 7). It is also worthwhile mentioning that the Tafel dependence may be regarded as a special case of the Marcus-Levich relationship, which applies for $\delta V_H << \lambda$, where λ is the energy barrier due to solvent reorganization required for charge transfer. Thus, the Tafel approximation should be satisfactory for f_o values close to f_{o}, as indeed found in many cases in the photovoltage region of interest (Fig. 3).

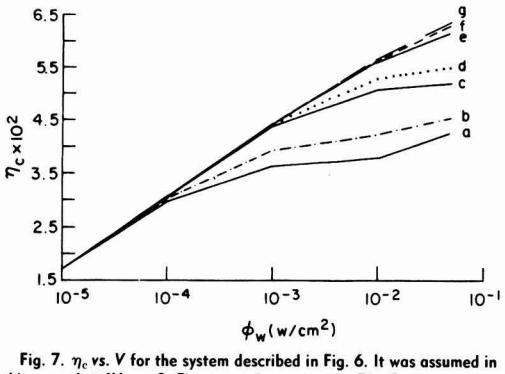


Fig. 7. η_c vs. V for the system described in Fig. 6. It was assumed in this case that $\delta V_H = 0$. Figure captions are as in Fig. 6.

Summary and Conclusions

The results obtained demonstrate that there is no contradiction between the high rate of carrier recombination at the surface under high injection conditions, as found in photoluminescence decay experiments (1), and the high conversion efficiencies obtained for the same semiconductor-electrolyte interface under steady-state normal level illumination. Furthermore, the combination of results obtained for the response of the same interface in the picosecond time domain and under steady state suggests a mechanism, where surface levels, generated by species adsorbed from the solution phase at the semiconductor surface, may act as effective photocharge transfer mediators. This mechanism for photocharge transfer may be written schematically in the following way, for sulfide ions as hole acceptors

$$p_s + S^{=}_{aq} \xrightarrow{k_{vr}} S^{-}_{aq} \qquad [17\text{-a}]$$

$$p_s + S^{=}_{ads} \xrightarrow{S_p} S^{-}_{ads} \qquad [17\text{-b}]$$

$$n_s + S^{-}_{ads} \xrightarrow{S_n} S^{=}_{ads} \qquad [17\text{-c}]$$

$$S^{-}_{ads} + S^{=}_{aq} \xrightarrow{k_{sr}} S^{=}_{ads} + S^{-}_{aq} \qquad [17\text{-d}]$$

The symbols S^{-}_{aq} and S^{-}_{ads} are used here to designate sulfide ions in solution and adsorbed at the surface, respectively, following the capture of a photohole. (S^{-}_{ads} is equivalent to an empty surface level and $S^{=}_{ads}$ to a filled surface level). Under conditions of high injection, $C_n n_{x=0} >> k_{sr}$, and the fate of the photogenerated minority carriers is determined by reactions [17-b] + [17-c], *i.e.*, by surface recombination. On the other hand, under conditions of normal illumination, $n_{x=0}$ is much smaller, being controlled by band bending. Therefore, under normal steady-state illumination the condition $k_{sr} >> C_n n_{x=0}$ may be easily obtained, considering a reasonable order of magnitude for k_{sr}^{o}. This last inequality ensures open-circuit voltages similar to those expected in the complete absence of recombination at the surface, and a fill factor of 0.6 or higher.

The modification of the semiconductor surface by chemisorbed species brings about, in the case under consideration, an enhancement of surface reactivity. The resulting high surface capture velocities have been shown by the simulations presented here to allow high ratios of charge transfer to recombination rates at the surface under normal illumination conditions, and thus to have an overall beneficial effect on the conversion efficiency. This example is contrary in a sense to the cases demonstrated previously (21, 22), where passivation of the surface with respect to recombinative reactivity resulted in an improved conversion efficiency. Obviously, there is an important difference between the last two systems (21, 22) and the one considered in this paper in that the chemisorbed species which rendered passivity to the SC surface was a metal ion (Ru^{+3} or Ag^{+}) with no significant redox activity. This is in contrast to the sulfide ions con-

sidered here which are known to be active in the photooxidative process at CdS. It thus seems that a beneficial surface modification could involve either a chemisorbed species which would lower the rate of surface recombination while being most probably inert in the process of charge transfer (21, 22), or it would involve a chemisorbed species with high surface capture cross sections, which may serve as an effective charge transfer mediator as seems to be the case for the $CdS/S^{=}$, $Sn^{=}$ system. Whether this model of photocharge mediation by adsorbed anions (or by other forms of surface states) is more or less general, should be verified by further similar measurements on other semiconductor-electrolyte interfaces.

Manuscript submitted April 22, 1985; revised manuscript received Oct. 28, 1985.

REFERENCES

1. M. Evenor, S. Gottesfeld, Z. Harzion, D. Huppert, and S. W. Feldberg, *J. Phys. Chem.*, **88,** 6213 (1984).
2. W. W. Gartner, *Phys. Rev.*, **116,** 84 (1959).
3. D. Canfield and S. R. Morrison, Report prepared for Lawrence Berkeley Laboratory, University of California (1982).
4. J. Reichman, *Appl. Phys. Lett.*, **36,** 574 (1980).
5. R. H. Wilson, *J. Appl. Phys.*, **48,** 4292 (1977).
6. F. El Gilbaly, K. Colbow, and B. L. Funt, *ibid.*, **52,** 3480 (1981).
7. F. El Gilbaly and K. Colbow, *ibid.*, **53,** 1737 (1982).
8. W. J. Albery, P. N. Bartlet, A. Hammett, and M. P. Dare-Edwards, *This Journal*, **128,** 1492 (1981).
9. D. Haneman and J. F. McCann, *Phys. Rev. B*, **25,** 1241 (1982).
10. P. Allongue, H. Cachet, and G. Horowitz, *This Journal*, **130,** 2352 (1983).
11. J. J. Kelly and R. Memming, *ibid.*, **129,** 730 (1982).
12. J. N. Chazalviel, *ibid.*, **129,** 963 (1982).
13. W. Shockley and W. T. Read, Jr., *Phys. Rev.*, **82,** 835 (1952).
14. Z. Harzion, Ph.D. Thesis, Tel-Aviv University (1983).
15. R. Tenne, *Ber. Bunsenges. Phys. Chem.*, **85,** 413 (1981).
16. C. T. Sah, R. N. Noyce, and W. Shockley, *Proc. IRE*, **45,** 1228 (1957).
17. C. H. Henry, R. A. Logan, and F. R. Merrit, *J. Appl. Phys.*, **49,** 3530 (1978).
18. R. H. Wilson, *This Journal*, **126,** 1187 (1979).
19. A. Rothwarf and K. W. Boer, in "Progress in Solid State Chemistry," Vol. 10, Part 2, p. 71 (1975).
20. M. Gratzel and A. J. Frank, *J. Phys. Chem.*, **86,** 2964 (1982).
21. R. J. Nelson, J. S. Williams, H. J. Leamy, B. Miller, H. C. Casey, B. A. Parkinson, and A. Heller, *Appl. Phys. Lett.*, **36,** 76 (1980).
22. A. Heller, H. J. Leamy, B. Miller, and W. D. Johnston, Jr., *J. Phys. Chem.*, **78,** 3239 (1983).

Polymer Films on Electrodes

XIX. Electrochemical Behavior at Polypyrrole-Nafion and Polypyrrole-Clay Thin Films on Glassy Carbon Electrodes

Fu-Ren F. Fan and Allen J. Bard*

Department of Chemistry, The University of Texas, Austin, Texas 78712

ABSTRACT

Biconductive films, involving the incorporation of an electronically conductive phase within an ionically conductive one, on glassy carbon electrode surfaces have been prepared by electropolymerization to form polypyrrole (PP) in matrices of Nafion and the clay, hectorite. These films display electronic conductivity and higher stability than films of PP alone. Electrochemical studies of several species at these electrodes ($Fe(CN)_6^{3-}$, $Ru(NH)_6^{2+}$, methyl viologen) are described. Freestanding PP/Nafion and PP/hectorite films have also been prepared.

Polymer-modified electrodes involving films of either ionically or electronically conductive materials have been investigated (1, 2). For example, the electronic conductor polypyrrole (PP) can be prepared by electrochemical oxidation of pyrrole and forms highly conductive films with good stability (2). However, the mechanical properties of these films are poor, and attempts have been made to improve these by electropolymerizing pyrrole in a poly(vinylchloride) matrix (3). We have also been interested in incorporation of an electronically conductive phase into ionically conductive polymer films to improve the charge transfer rates in such films and to grow unique conductive structures. Thus, tetrathiafulvalenium (TTF^{+}) was incorporated into Nafion (4, 5) and TTFBr structures formed by electrochemical cycling.

We report here an electrochemical method for producing flexible co-polymer films from ionically conductive Nafion and PP. These films have good electronic conductivity (*ca.* one order less than pure PP films) and a much higher cation exchange capacity as compared to $PP^{+}\ BF_4^{-}$ films. These films also possess high mechanical strength. Copolymerization of clay and pyrrole is also possible. The electrochemical responses at glassy carbon (GC) electrodes coated with these films in aqueous solutions containing various redox couples are also presented. Recently, Penner and Martin (6) have described the incorporation of PP into Nafion and Gore-tex-impregnated Nafion by electrochemical means.

* Electrochemical Society Active Member.

Experimental

All chemicals, if not otherwise mentioned, were reagent grade and were used without further purification. Pyrrole (Alfa Products) was purified by distilling from CaH_2 under N_2. Tetra-n-butylammonium fluoroborate ($TBABF_4$) was recrystallized twice from methanol. Cahectorite (SHCa-1, University of Missouri, Columbia, Missouri) was exchanged to the Na-form and dried by the standard method (7). N,N′-dimethyl-4,4′-bipyridinium (MV^{2+}) dichloride (Sigma Chemicals) was recrystallized from MeOH/acetone. Distilled water for all experiments was from a millipore water reagent system.

Electrode preparation.—$PP^{+}BF_4^{-}$ films were deposited electrochemically (2b) onto GC electrodes (Atomergic) (0.071 cm^2) from MeCN (spectrograde) solutions containing 0.2*M* $TBABF_4$ and 50 m*M* pyrrole by sweeping continuously between −0.6 and 1.0V *vs.* Ag until a total of *ca.* 42 mC/cm^2 of charge was consumed. The films were then thoroughly rinsed with MeCN. Na-hectorite films were prepared by dropping a known volume (50 μl) of aqueous clay colloid (2.5 g/l) onto the GC substrate. The films were dried under ambient conditions. Nafion films were prepared by dropping a known volume (50 μl) of an ethanolic Nafion (E.W. 1100, 2 g/l) (C.G. Processing, Incorporated, Rockland Delaware) solution onto the GC electrode. The films were dried in air at room temperature.

Hectorite-PP films were prepared by sweeping the potential of Na-hectorite-coated GC electrodes between −0.6

and 1.0V *vs.* Ag in MeCN solutions containing 0.2*M* $TBABF_4$ and 50 m*M* pyrrole until *ca.* 42 mC/cm² of charge was consumed. The films were then thoroughly rinsed with MeCN and dried under ambient conditions. Two different methods were employed to prepare Nafion-PP films. Type A films were prepared by the same procedure as used for PP deposition with Nafion-coated GC used as a substrate. Type B films were prepared by sweeping GC electrodes in 25 ml of mixed EtOH:MeCN (1:5 by volume) solutions containing 50 m*M* pyrrole and 10 meq. Nafion (E.W. 1100) over the potential range −0.8 to 1.0V *vs.* Ag until *ca.* 42 mC/cm² of charge was collected.

Instrumentation for electrochemical experiments consisted of a Princeton Applied Research (PAR) Model 173 potentiostat/galvanostat and PAR Model 179 digital coulometer. All electrochemical experiments were performed in an undivided three-electrode cell containing Pt counter- and Ag wire quasireference electrodes in nonaqueous solution and SCE reference electrode in aqueous solution. All experiments were performed in deoxygenated solutions and under nitrogen throughout the experiment, unless mentioned otherwise.

Results and Discussion

Film structure.—The deposition of PP involves oxidation of pyrrole to form cationic centers that polymerize with solution anions (*e.g.*, BF_4^-) as counterions (2). When Nafion is used as a substrate, the sulfonate groups attached to the polymer backbone play the role of anions, and, upon oxidation, the cationic PP polymer probably forms within the Nafion matrix with the expulsion of Na^+. We thus propose as the polymerization reaction (where ~ SO_3^- represents Nafion and P^+ oxidized pyrrole centers in PP)

$$(\sim SO_3^-Na^+)_x + xP - xe \rightarrow (\sim SO_3^- P^+\sim)_x + xNa^+ \quad [1]$$

Although the structure of the interwoven Nafion and PP chains has not yet been investigated, we assume that this dual chain structure of the copolymer is what leads to better mechanical stability, as discussed below. In a similar way, the anionic oxygen sites in the clay film probably play the role of the counterion in hectorite/PP films. The electrochemical behavior of these films was examined by cyclic voltammetry (CV) in aqueous 0.5*M* Na_2SO_4 solution in the absence and presence of additional redox couples.

Nafion-pyrrole films.—As shown in Fig. 1, both types of Nafion-PP thin films show the characteristic large background currents in the potential region where PP is not completely oxidized or reduced (−0.6 to 1.0V *vs.* SCE). These currents were smaller (by a factor of *ca.* 2 for an equivalent thickness) than those found with $PP^+BF_4^-$ films. The smaller background current of the Nafion-incorporated PP thin film paralleled a total lower conductivity (electronic and ionic) (*i.e.*, the conductance of a dry freestanding Nafion-PP film was about ten times smaller than the same thickness $PP^+BF_4^-$ film).[1] The incorporation of Nafion, as shown in Fig. 1, also affected the peak potentials for the reduction and reoxidation of the PP films, which on occasion were shifted by *ca.* ±100-200 mV.

The electrochemical activity of Nafion-PP thin film electrodes was examined in the presence of several one-electron reversible redox couples, which span a potential range from −0.68 to 0.22V *vs.* SCE and carry different kinds of charges. At a simple Nafion-coated GC electrode, $Fe(CN)_6^{3-/4-}$ is essentially electrochemically inactive, since penetration of the highly charged anion through the Nafion film *via* a membrane process is strongly hindered (Fig. 2a). However, reversible cyclic voltammograms are observed on both types of Nafion-PP electrodes (Fig. 2b). The voltammograms are consistent with a diffusion-controlled reaction ($i_p \propto v^{1/2}$), and

[1] Type B Nafion-PP films were found less conductive (*ca.* one order of magnitude) than $PP^+BF_4^-$ films. No attempt was made to measure the exact conductivities of those films.

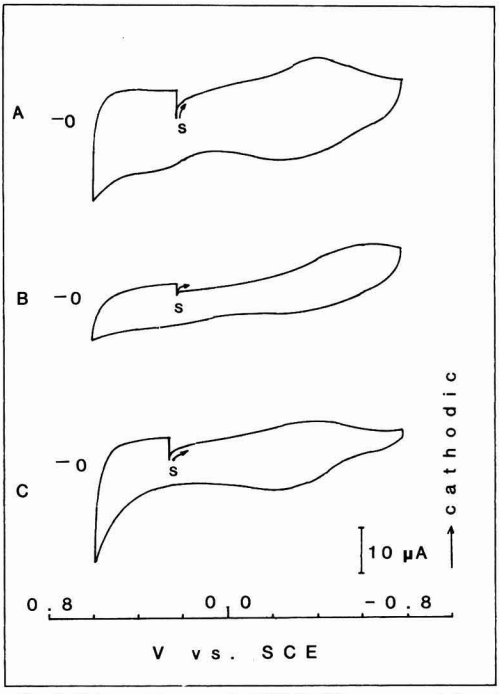


Fig. 1. Voltammetric curves in 0.5*M* Na_2SO_4 aqueous solution at scan rate 20 mV/s for (a) PP-coated GC electrode; (b) Type A Nafion-PP-coated GC electrode; (c) Type B Nafion-PP-coated GC electrode. PP deposition charge = 42 mC/cm².

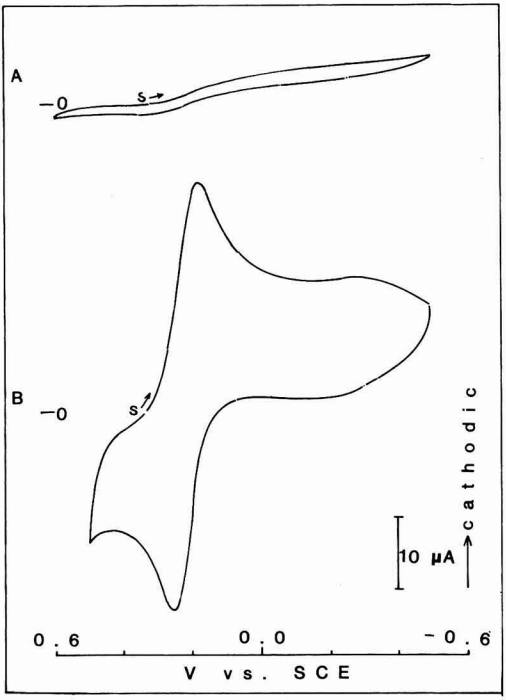


Fig. 2. Voltammetric curves in 0.5*M* Na_2SO_4 aqueous solution containing 10 m*M* $Fe(CN)_6^{3-}$ at scan rate 20 mV/s for (a) Nafion-coated GC electrode and (b) Type B Nafion-PP-coated GC electrode. PP deposition charge = 42 mC/cm².

there is no evidence of a specific interaction between films and the redox species (*e.g.*, as signaled by a change in the peak potentials). With couples, such as $Ru(NH_3)_6^{3+/2+}$, that carry positive charges and have redox potentials positive of the potential at which the film is completely reduced (*ca.* −0.5V *vs.* SCE), reversible cyclic voltammograms were obtained. However, the voltammograms, as shown in Fig. 3, were not purely diffusion-controlled (*e.g.*, peak current, i_p, was not proportional to the square root of scan rate, v) suggesting that some interaction occurs between the film and $Ru(NH_3)_6^{3+/2+}$. Higher peak currents and more symmetric cyclic voltammograms were observed at Nafion-PP electrodes, as compared with uncoated GC electrodes. After extensive cycling between −0.8 and 0.2V *vs.* SCE in a $Ru(NH_3)_6^{3+}$ solution, a Nafion-PP electrode, when transferred to 0.5*M* Na_2SO_4 alone, showed some current corresponding to the redox reaction of $Ru(NH_3)_6^{3+/2+}$ couple. Thus, some incorporation of $Ru(NH_3)_6^{3+/2+}$ (*ca.* 20-30% of that of a Nafion-coated GC electrode) into the film appears possible. For positively-charged redox species such as $MV^{2+/+}$ with redox potentials negative of −0.5V *vs.* SCE, the cathodic peak current was only about 5% of that obtained on bare GC electrodes on the first several scans (Fig. 4a). The low electrochemical activity of MV^{2+} on these electrodes indicates that the permeability of MV^{2+} through these polymer films is very low and is consistent with the nonconductive nature of PP in this potential region. Note that a single reduction wave of MV^{2+} is observed at a potential where the reduction of MV^{2+} is supposed to occur, but two reoxidation waves are observed. In addition to the normal reoxidation wave at *ca.* −0.6V *vs.* SCE, a second reoxidation wave is observed at a potential (−0.3 to −0.4 V *vs.* SCE) where PP is partially reoxidized and its conductivity is restored. The small reduction current demonstrates that the incorporation of MV^{2+} into these films is initially very low. However, extensive cycling of the Nafion-PP-film-coated GC electrodes between −0.9 and 0.3V *vs.* SCE in a 0.5*M* Na_2SO_4 solution containing 5 mM MV^{2+} increased substantially the amount of MV^{2+} incorporated (Fig. 4b). The incorporated MV^{2+} is held in these films when they are transferred to supporting electrolyte alone, as shown in Fig. 4c. The MV^{2+} diffusion coefficient in these Nafion/PP films has not yet been determined, because of the high background current and the uncertainty in the film concentration of MV^{2+}.

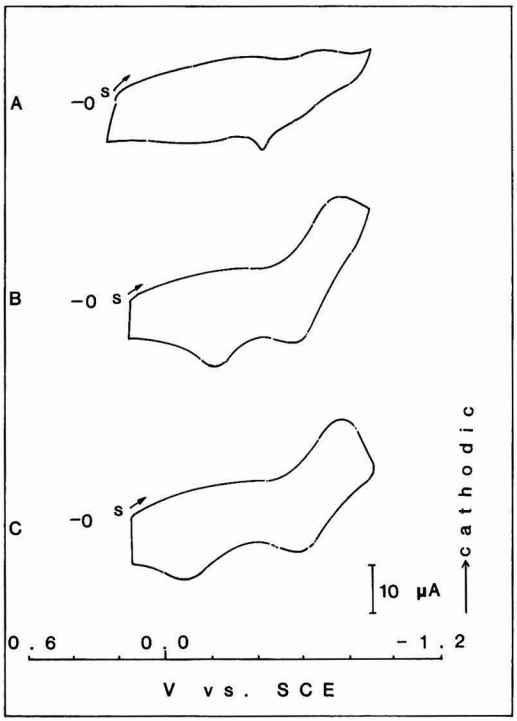


Fig. 4. Voltammetric curves at Type B Nafion-PP-coated GC electrode at scan rate 20 mV/s. (a) First several scans in 0.5M Na_2SO_4 solution containing 5 mM MV^{2+}; (b) the same electrode after sweeping at 20 mV/s between −0.9 and 0.3V vs. SCE in the same solution for 20 min; (c) the same electrode after (b) in 0.5M Na_2SO_4 solution but at scan rate 50 mV/s.

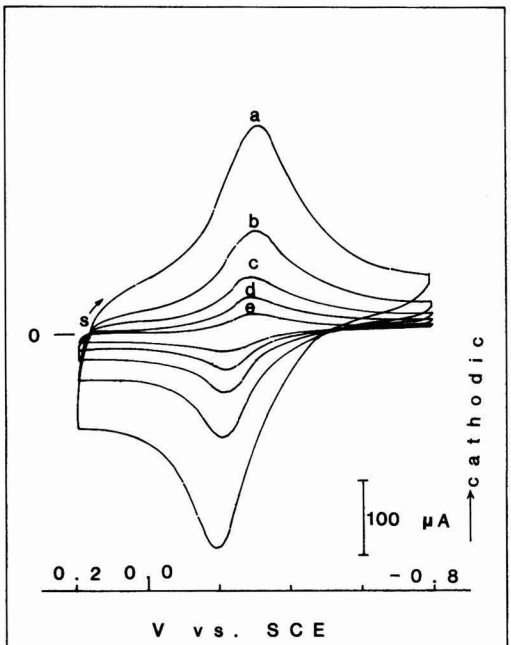


Fig. 3. Voltammetric curves in 0.5M Na_2SO_4 aqueous solution containing 5 mM $Ru(NH_3)_6^{3+}$ at Type B Nafion-PP-coated GC electrode at various scan rates: (a) 500, (b) 200, (c) 100, (d) 50, and (e) 20 mV/s PP deposition charge = 42 mC/cm².

Clay-pyrrole films.—Na-hectorite-coated GC electrodes in 0.5*M* Na_2SO_4 solution show a low flat background current over a potential region of −0.8 to 1.0V *vs.* SCE, so the electrode is suitable for studying various electrochemical reactions. These electrodes, after further coating with 42 mC/cm² of PP, show the characteristic large background current of a PP film. The shape (both magnitude and peak position) of the voltammograms, as with $PP^+BF_4^-$ films, varies with film thickness. The peak potential separation of the polymer redox reaction increased with film thickness.

The hectorite-PP film on a GC electrode is electronically conductive in the potential range where a large background is present (−0.6 to 1.0V *vs.* SCE in 0.5*M* Na_2SO_4 solution). The conductance of a dry freestanding clay-PP film was 10-100 times smaller than the same thickness $PP^+BF_4^-$ film. The film can be used as an electrode to drive various electrochemical reactions, as shown in Fig. 5. The hectorite-PP film behaves well for both negatively and positively charged species, and the redox peaks appear superimposed on the background current with redox potentials close to the values measured with a Pt electrode. In contrast to the hectorite-PP film, an unswollen Na-hectorite-coated GC electrode shows low electrochemical activity for $Fe(CN)_6^{4-/3-}$ (compare Fig. 5a and 5b); in this case, the anionic species penetrates the clay layer through small interparticle channels (7b). Electrochemical activity of clay-modified electrodes can be en-

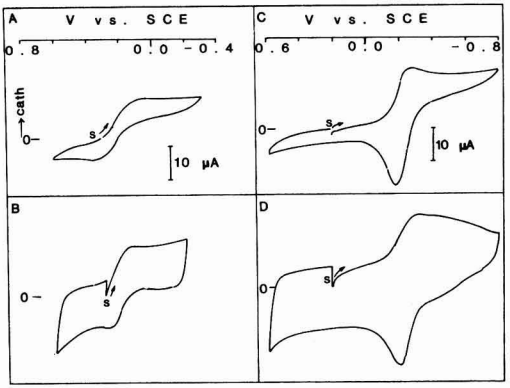


Fig. 5. Voltammetric curves at scan rate 20 mV/s. (a) At hectorite-coated GC electrode in 0.5M Na_2SO_4 solution containing 10 mM $Fe(CN)_6^{3-}$; (b) at hectorite-PP-coated GC electrode in the same solution; (c) at hectorite-coated GC electrode in 0.5M Na_2SO_4 solution containing 5 mM $Ru(NH_3)_6^{3+}$; (d) at hectorite-PP-coated GC electrode in 0.5M Na_2SO_4 solution with 5 mM $Ru(NH_3)_6^{3+}$.

hanced dramatically by swelling the clay film in aqueous solution (7b). Note that the peak current observed on a hectorite-PP electrode for $Fe(CN)_6^{3-}$ reduction is only about 1/2 of that found with a bare GC electrode, although hectorite-PP shows a smaller peak separation ($\Delta E_p \sim 100$ mV) compared to a GC electrode ($\Delta E_p \sim 150$ mV). This is very different from a Nafion-PP electrode which shows an active area for electrochemistry of a solution species that is the same as that of the GC electrode. This can be attributed to a poor swelling of the clay in acetonitrile[2] so that the deposition of PP occurs only at the grain boundaries of the clay particles; the molecularly homogeneous mixing that probably characterizes Nafion-PP does not occur with hectorite. For a positively charged species, such as $Ru(NH_3)_6^{3+/2+}$, there seems to be strong interaction between the clay film and the redox species, as manifested by the highly asymmetric shape of the voltammetric wave (Fig. 5c). The incorporation of PP into the clay film appears to reduce the extent of this interaction, and the voltammograms appear closer to those of a diffusion-controlled reaction (Fig. 5d).

The mechanical strength of a PP film is greatly enhanced by the incorporation of Nafion. A freestanding Nafion-PP film can be obtained by preparing the Nafion-PP film on a GC substrate (*ca.* 50 μm thick) and then peeling it from the GC with a razor blade. The resulting black film shows high flexibility. Clay-PP films are quite brittle. However, the mechanical strength of a clay-PP film might be improved, if a suitable solvent that is capable of swelling the clay and of dissolving pyrrole could be found, or if the clay is pillared (7c). Further research on the elucidation of the structure of these copolymers, and the application of such films as potential-controllable ion exchange membranes (8) are underway.

[2] A poorer swelling capability of clay in MeCN as compared in H_2O is manifested by the much lower rate of incorporation of redox species such as $Os(bpy)_3^{2+}$ into a clay film in MeCN. F.-R. F. Fan and A. J. Bard, Unpublished results.

Acknowledgment

The support of this research by grants from the National Science Foundation (CHE8402135) and IBM is gratefully acknowledged. We also thank R. Penner and C. R. Martin for a preprint of their manuscript.

Manuscript submitted July 15, 1985; revised manuscript received Aug. 30, 1985.

REFERENCES

1. (a) R. W. Murray, *Acc. Chem. Res.*, **13,** 135 (1980); (b) N. Oyama and F. C. Anson, *Anal. Chem.*, **52,** 1192 (1980); (c) P. J. Peerce and A. J. Bard, *J. Electroanal. Chem. Interfacial Electrochem.*, **112,** 97 (1980); (d) M. S. Wrighton, R. G. Austin, A. B. Bocarsly, J. M. Bolts, O. Haas, K. D. Legg, L. Nadjo, and M. C. Palazzotto, *J. Am. Chem. Soc.*, **100,** 1602 (1978).
2. (a) A. Dall'Olio, G. Dascola, V. Varacca, and V. Bocchi, *C.R.* **433,** 267C (1968); (b) A. F. Diaz and K. K. Kanazawa, *J. Chem. Soc., Chem. Commun.*, 635 (1979); (c) A. Diaz, J. M. Vasquez Vallejo, and A. Martinez Duran, *IBM J. Res. Develop.*, **25,** 42 (1981); (d) R. A. Bull, F.-R. F. Fan, and A. J. Bard, *This Journal*, **129,** 1009 (1982); (e) R. Noufi, A. J. Frank, and A. J. Nozik, *J. Am. Chem. Soc.*, **103,** 1849 (1981); (f) T. Skotheim, I. Lündstrom, and J. Prejza, *This Journal*, **128,** 1625 (1981); (g) C. R. Martin, I. Rubinstein, and A. J. Bard, *J. Am. Chem. Soc.*, **104,** 4817 (1982); (h) D. Buttry and F. C. Anson, *ibid.*, **105,** 685 (1983); (i) H. S. White, J. Leddy, and A. J. Bard, *ibid.*, **104,** 4811 (1982); (j) B. J. Feldman, P. Burgmayer, and R. W. Murray, *ibid.*, **107,** 872 (1985); (k) S. Feldberg, *ibid.*, **106,** 4671 (1984).
3. (a) M.-A. De Paoli, R. J. Waltman, A. F. Diaz, and J. Bargon, *J. Chem. Soc., Chem. Commun.*, 1015 (1984); (b) O. Niwa and T. Tamamura, *ibid.*, 817 (1984).
4. T. P. Henning, H. S. White, and A. J. Bard, *J. Am. Chem. Soc.*, **103,** 3937 (1981); T. P. Henning, H. S. White, and A. J. Bard, *ibid.*, **104,** 5862 (1982).
5. T. P. Henning and A. J. Bard, *This Journal*, **130,** 613 (1983).
6. R. M. Penner and C. R. Martin, Submitted to *This Journal*.
7. (a) P. K. Ghosh and A. J. Bard, *J. Am. Chem. Soc.*, **105,** 5691 (1983); (b) D. Ege, P. K. Ghosh, J. R. White, J. F. Equey, and A. J. Bard, *ibid.*, **107,** 5652 (1985); (c) T. J. Pinnavaia, M.-S. Tzou, S. D. Landau, and R. H. Raythatha, *J. Mol. Catal.*, **27,** 195 (1984), and references therein.
8. P. Burgmayer and R. W. Murray, *J. Phys. Chem.*, **88,** 2515 (1984),and references therein.

Effect of Counterions on the Formation of Ohmic Contact Between p-Si and Poly(pyrrole) Film

An AC Impedance Analysis

G. Nagasubramanian, S. DiStefano,* and J. Moacanin

Jet Propulsion Laboratory, California Institute of Technology, Pasadena, California 91109

ABSTRACT

Conditions under which, poly(pyrrole) (PP) films form ohmic contact with single-crystal p-Si are described. Counterions affect both the conductivity and flatband potential (V_{FB}) values of poly(pyrrole). While paratoluene-sulfonate-doped PP acts like a switch, the impedance behavior of PP films doped with ClO_4^-, BF_4^-, or PF_6^- allows evaluation of the V_{FB} of these films. The formation of "quasi-ohmic" and "non-ohmic" contacts respectively of PP (ClO_4) and PP films doped with other counterions, with p-Si, are explained in terms of conductivity of these films and V_{FB} of PP films with respect to that of p-Si. PP film seems to passivate or block intrinsic surface states present on p-Si surface.

Conducting organic polymers, in recent years, have generated wide-spread interest as potential choice materials for a variety of applications in different areas including solar energy conversion (photoelectrochemistry) (1, 2), batteries (3), electronics (4), and corrosion (5). Some of the well-characterized conducting polymers exhibit metallic conductivities (~500S cm^{-1}) (6), and there are speculations on the possible synthesis of polymers with conductivities larger than those of copper and silver (7). Their robust properties combined with metal-like conductivities prompted us to consider these polymers as possible replacement materials for metallic current collectors and back ohmic contacts and to explore the applicability of these materials as surface passivating agents in silicon solar cells. We report in this paper the preliminary results of our study (with a view to obtaining ohmic contacts) using ac impedance technique on the properties of p-Si PP interface and show that PP film not only forms a "quasi-ohmic" contact with p-Si, but also that it blocks the surface states present on p-Si surface. Poly(pyrrole) films were deposited electrochemically, in the dark, on p-Si. Few reports are available in the literature pertaining to the formation and properties of barriers between n-type semiconductors and conducting polymers (8, 9), and few data are available on the interfacial properties between p-Si and conducting polymers.

Experimental

Chemicals.—Polarographic grade, tetra-n-butyl ammonium perchlorate (TBAP) was dissolved and recrystallized from an acetone-ether mixture and dried under vacuum ($<10^{-5}$ torr) for two days, while the other supporting electrolytes $TBAPF_6$, $TBABF_4$, and tetra-n-ethyl paratoluene sulfonate (TEApTS) were dried under vacuum ($<10^{-5}$ torr) at 70°C for one day. The solvent acetonitrile (MeCN) was purified as previously described (10). Pyrrole was distilled in an inert atmosphere. All chemicals were stored inside an argon-filled (Vacuum/Atmospheres Corporation, LA; Hawthorne, CA.) glove box. Single-crystal p-Si (face III, source JPL) was ultrasonically cleaned prior to the formation of ohmic contact by electroplating gold-gallium alloy (SG-30, Transene Company Inc., MA, USA). A copper wire lead for electrical contact was attached to this side with silver epoxy (ACME Chemicals and Insulation Company, New Haven, CT) and was subsequently covered with five min epoxy. The assembly was mounted into 6 mm diameter glass tubing and was held in position with silicone rubber sealant (G.E., Waterford, NY) which also served as an effective seal against the seepage of electrolyte solution to the rear of the semiconductor electrode. The electrode area exposed to solution is ~0.16 cm^2. All measurements were made inside the glove box. For electrodeposition of PP film on p-Si, a two compartment (separated by a medium porosity glass frit) cell of ~15 ml capacity, con-

*Electrochemical Society Active Member.

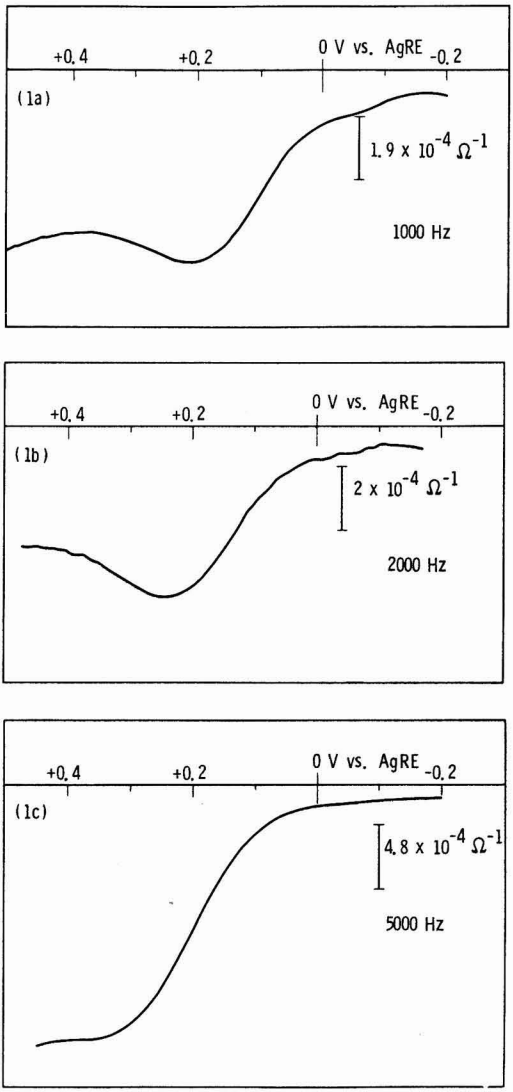


Fig. 1. G_p (equivalent-parallel conductance) *vs.* *V* plots in acetonitrile 0.1M TBAP solution, at three different frequencies for naked p-type single-crystal silicon electrode. Scan rate 2 mV/s.

taining a Pt counterelectrode in one of the compartments and the working (p-Si) and a quasi reference ("Ag wire") electrode in the other, was used. Pyrrole and supporting electrolyte were used at 1*M* and 0.1*M* concentrations, respectively. In a typical experiment, before the addition of pyrrole, the MeCN −0.1*M* supporting electrolyte solution was stirred with activated alumina (Woelm Neutral Alumina, activity Super I, Woelm pharma GmbH and Co., Eschevege, BRD) to remove any residual water present and was then placed in both the compartments. In the text below, poly(pyrrole) (PP) films doped with different counterions are denoted as follows: ClO_4^--doped PP-PP(ClO_4); BF_4^--doped PP-PP(BF_4); PF_6^--doped PP-PP(PF_6); and pTS-doped PP-PP(pTS). After deposition, the p-Si electrode was liberally rinsed with MeCN containing the appropriate supporting electrolyte to wash away any adhering pyrrole and then transferred to a single compartment cell of 25 ml capacity containing Pt counterelectrode (>40 cm²) and the quasi reference Ag wire, (hereafter referred to as AgRE electrode) for ac impedance measurements. At the conclusion of the experiments, both the cells were taken out of the glove box, and the potential of the AgRE was measured against the aqueous saturated calomel electrode (SCE). The potential of AgRE containing pyrrole is −250 mV, while that of the other used in ac impedance measurement is −200 mV *vs.* aqueous SCE. Current-potential behavior was obtained with a PAR Model 173 potentiostat with Model 179 digital coulometer plug-in whose frequency response was found to be satisfactory up to 7 kHz and Model 175 programmer (Princeton Applied Research, Princeton, NJ) and recorded with a Model 2000 X-Y recorder (Houston Instruments, Austin, TX). Poly(pyrrole) films were grown potentiostatically at +0.80V *vs.* AgRE, and the number of coulombs of charge passed was monitored with a digital coulometer.

AC impedance.—The lock-in technique (11, 12) was used to measure the ac impedance behavior as a function of applied potential. In this technique a small amplitude

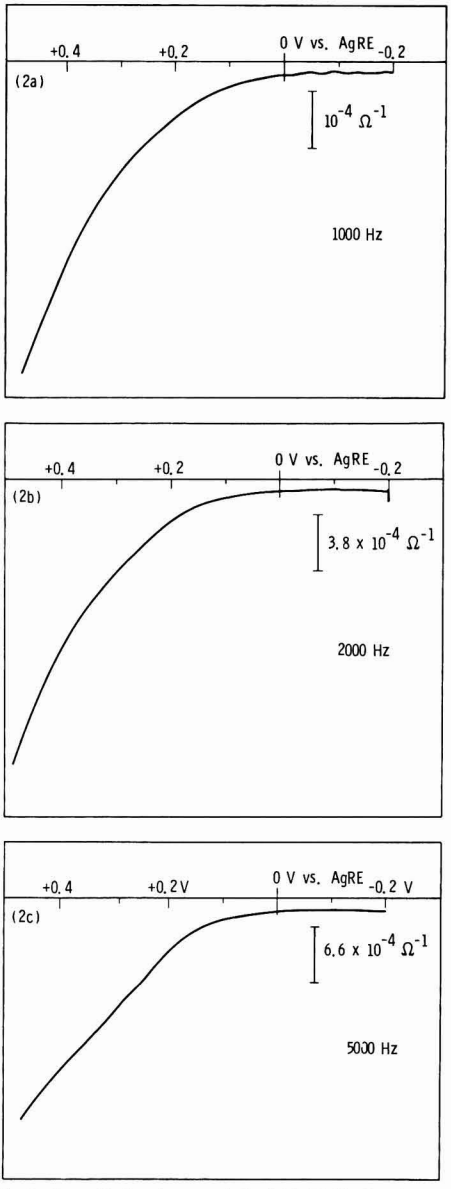
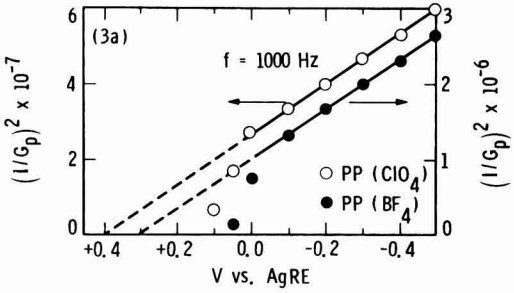


Fig. 2. G_p *vs.* *V* plots in acetonitrile 0.1*M* TBAP after depositing poly(pyrrole) on to p-Si. Counterion; ClO_4^-. Scan rate 2 mV/s.



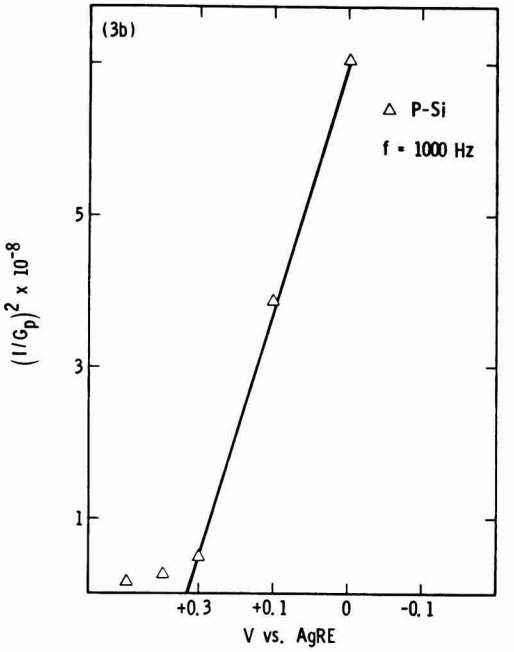


Fig. 3. $(1/G_p^2)$ *vs.* *V* plots in acetonitrile 0.1*M* TBAP or 0.1*M* $TBABF_4$ for (a) PP(ClO_4), PP(BF_4) electrochemically deposited on Au substrate and (b) p-Si. Thickness of PP film ~1-1.2 μm. Frequency 1 kHz.

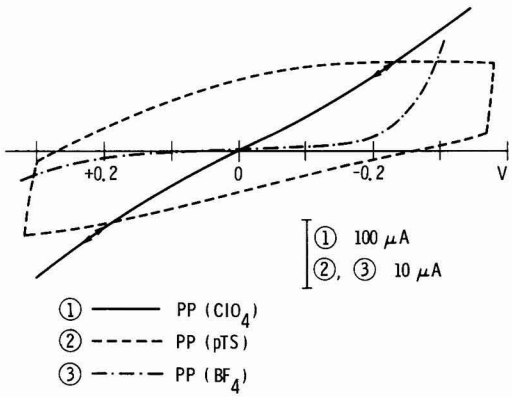


Fig. 4. *I-V* traces of p-Si PP interface for different counterions. *I-V* curves were recorded as follows: after depositing poly(pyrrole) onto p-Si (mounted as electrode; for description see Experimental)-surface, a Hg contact was made to the PP film after evaporating the solvent. While the copper lead was connected to both auxiliary and reference of the PAR potentiostat, the working through a Pt wire dipping in the Hg pool is connected to PP film. The potential was scanned at 20 mV/s, and output current was recorded as a function of potential.

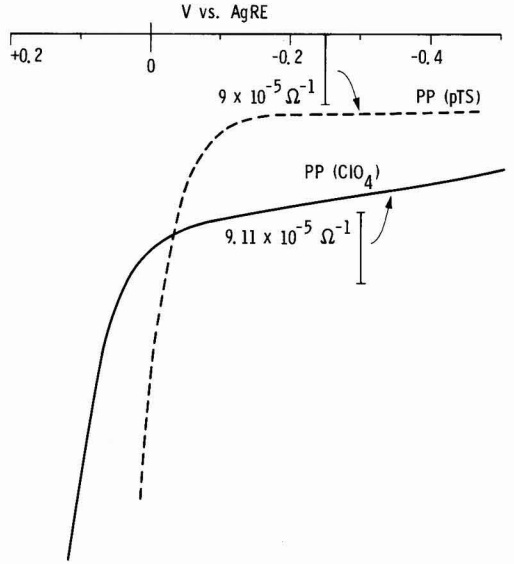


Fig. 5. Plots of G_p vs. V at 500 Hz, for PP films, on Au substrate, doped with (a) ClO_4^- and (b) pTS^- counterions. Scan rate 2 mV/s.

sine wave, 10 mVp-p from a wide-range oscillator (Wave Tek, Model 136, San Diego, CA) is superimposed on a slow (≤2 mV/s) dc ramp with the PAR universal programmer by the PAR potentiostat and applied to the cell. The output of the current follower of the potentiostat is input to a lock-in amplifier (PAR Model HR-8), which separates the signal into the components in and out of phase (90°) with the ac signal from the oscillator. These signals were calibrated by using an RC circuit comprised of a resistance substitution box and a precision decade capacitor (General Radio Company, Concord, MA). The in phase signal as a function of dc potential was plotted on the Houston Instruments X-Y recorder.

Results

PP films were grown potentiostatically in an electrochemical cell containing MeCN, 1*M* pyrrole, and 0.1*M* supporting electrolyte at +0.8V *vs.* AgRE. The charge passed in all cases, 20 mC, corresponds to a thickness of 1.0-1.2 μm taking, 1 mC/cm² = 120Å (2a). Films of this thickness were intentionally grown to minimize complications due to porosity. Bard *et al.* (13) have shown that PP films of thickness of the order of 0.2 μm are porous for at least some electrochemical reactions. Impedance measurements were made in the frequency range between 1 and 5 kHz. Typical plots of parallel equivalent conductance (G_p) *vs.* potential for naked p-Si electrodes in MeCN solution containing 0.1*M* TBAP at three different frequencies are shown in Fig. 1. In Fig. 2 are shown corresponding plots after depositing $PP(ClO_4)$. Plots in Fig. 2 exhibit an apparently improved behavior compared to their counterparts in Fig. 1. Such improved behavior is typical of the p-Si PP interface regardless of the counterion used, *i.e.*, BF_4^- or PF_6^- or pTS^-. In Fig. 3 are shown the plots of inverse square of conductance *vs.* voltage for $PP(ClO_4)$ and $PP(BF_4)$ deposited on Au substrate and for p-Si. Several authors have shown that V_{FB} can be culled from the plot of $1/G_p^2$ *vs.* V (14). An ohmic contact is characterized by (*i*) absence of photovoltaic effect and (*ii*) linear current-voltage characteristic. Because PP is a hole conductor and not an electron conductor, photovoltaic measurement was not performed on the p-Si PP interface, and in Fig. 4 are shown the current (I) *vs.* voltage (V) plots for the p-Si PP interface. While p-Si $PP(ClO_4)$ interface exhibits a "quasi-ohmic" behavior, as evidenced by a linear *I-V* plot, the interface doped with other counterions deviates from Ohm's law. This difference in the behavior can be explained in terms of the conductivity of the freestanding film and the flatband potential (V_{FB}) of the freestanding film compared to that of naked p-Si. Figure 5 shows the plots of G_p *vs.* V at 500 Hz for $PP(ClO_4)$ and PP(pTS) films deposited on Au substrate. To avoid redundancy, no electrochemical data are given on $PP(PF_6)$, since its behavior is similar to that of $PP(BF_4)$.

Discussion

As shown in Fig. 1, the G_p *vs.* V plots exhibit features with frequency dependent peak potential (V_p). In Fig. 6, the plot of V_p *vs.* frequency (f) is given. This type of shift in the peak potential with frequency toward flatband potential that is +0.35 *vs.* AgRE or +0.15 *vs.* SCE is due to the continuous distribution of surface states (15). The rationale for such a shift is the variation of time constant (RC) of surface states located in the bandgap of the semiconductor. Time constant, which is the rate of communication of charges between a surface state and one of the bands, is dependent upon the relative position of the surface states with respect to the band. This implies that surface states close to one of the bands are faster than those located toward the middle of the gap. Hence, as the surface is probed from the middle of the gap toward one of the bands, surface states, if present, can be identified at higher and higher frequencies. This causes the shift in peak potential toward V_{FB}. This type of behavior is typical and was also observed with other counterions, suggesting that these surface states do not originate due to adsorption of counterion species on the surface of p-Si. However, G_p *vs.* V plots after the deposition of poly(pyrrole) show an improved behavior. Although there are several effective possible representations of the semiconductor/liquid electrolyte junction, the equivalent circuit we chose is comprised of a series combination of surface-state resistance (R_{ss}) and capacitance (C_{ss}) connected in parallel to a parallel combination of space charge layer capacitance (C_{sc}) and resistance (R_{sc}). On the basis of this equivalent circuit representation, the improved behavior in Fig. 2 could be attributed to the passivation of surface states. This type of behavior has been previously observed where polymers have been shown to passivate surface states on layer-type semiconductor electrodes (16). Comparison of the *I-V* plots in Fig. 4 shows that the formation of an "ohmic" or "quasi-ohmic" interface between p-Si and PP film is a function of the counterion used and becomes less "ohmic" in the following order: $ClO_4^- > BF_4^- \simeq PF_6^- > pTS^-$. This is a rather intriguing observa-

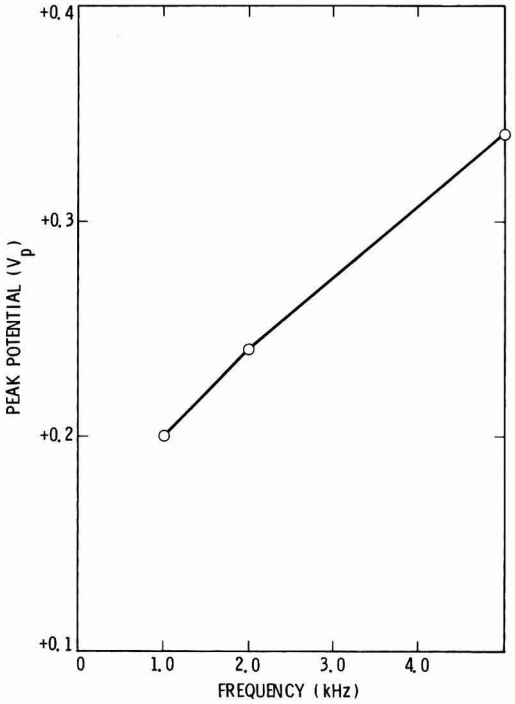
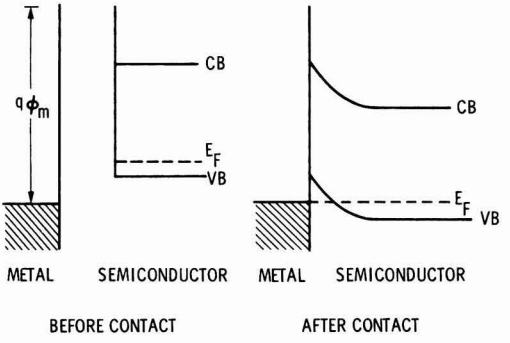


Fig. 6. Plot of peak potential *vs.* frequency. The peak potentials at different frequencies are culled from G_p *vs.* V plot for naked p-Si in MeCM, 0.1M TBAP solution.

tion, since the films were grown under identical conditions. Our observations as well as earlier reports show (17) that the room temperature conductivity (σ) of PP films is dependent on the counterion and decreases in the following order: $ClO_4^- > BF_4^- \simeq PF_6^- > pTS^-$. Both the sign and the linear dependence on temperature of thermoelectric power suggest that PP is a p-type metal, (17). Plots in Fig. 3a, however, indicate that PP is a p-type semiconductor. These two observations are consistent, in that PP is a p-type degenerate semiconductor, the reported bandgap of which is around 2.2 eV (18). The condition under which p-Si can form an ohmic contact with either a degenerate semiconductor or a metal is shown in Scheme I. This scheme suggests that the Fermi level of the contacting medium should be more positive, in an electrochemical potential scale, than the Fermi level of p-Si. Taking the cue from conductivity values, the Fermi levels corresponding to different counterion-doped PP film are shown in Fig. 7. Earlier, we showed that the V_{FB} of $PP(ClO_4)$ is around +0.19V *vs.* SCE and that that of $PP(BF_4)$ is around +0.11V *vs.* SCE, while for p-Si it is around +0.15V *vs.* SCE (Fig. 3), which is in accord with reported values (19). Although the values of V_{FB} are accurate only within ±0.1V, the salient feature of our observation is that $PP(ClO_4)$ is more likely to form an ohmic contact with p-Si than $PP(BF_4)$ film. Unfortunately, we could not determine the flatband potential of pTS-doped PP film, and the reason is given below. Compare and note the presence and absence of parabolic shapes in the G_p *vs.* V plots of $PP(ClO_4)$ and PP(pTS), respectively, in Fig. 5. For voltages more negative of 0.2 *vs.* AgRE, PP(pTS) is apparently an insulator with a constant resistance. More importantly, PP(pTS) films act like a switch. If the knee in the plot in Fig. 5 is any indication of V_{FB}, then it is apparent that the V_{FB} of PP(pTS) is more negative than that of $PP(ClO_4)$, and, hence, of all the four counterions investigated, it has the least chance of forming ohmic contact with p-Si. The above results apparently indicate that not only does the size of the counterion influence the electrochemical behavior of PP film, but that the switching characteristics do also, and they lead one to speculate that the bigger the counterion, the faster the switching speed.



Scheme I. Schematic representation of band positions of a p-type semiconductor and that of a metal for the formation ideal ohmic contact. (For example: see, A. L. Fahrenbruch and R. H. Bube, "Fundamentals of Solar Cells. Photovoltaic Solar Energy Conversion," p. 187, Academic Press, New York (1983).)

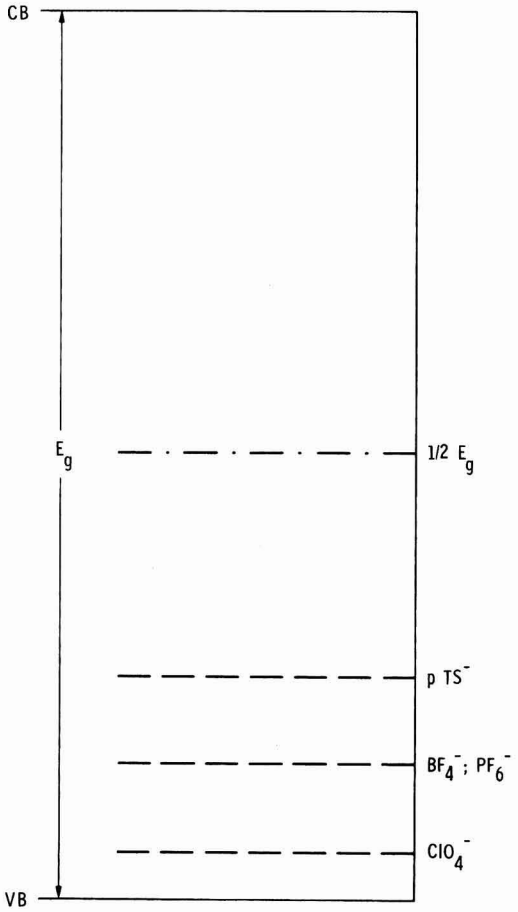


Fig. 7. Band positions of PP with different Fermi levels corresponding to films doped with different counterions. The chosen positions to Fermi level are arbitrary and intended only to show the relationship between conductivity (σ) and Fermi level and so by no means accurate.

Conclusions

We have shown that the counterions have profound influence on the flatband potential of PP films, with V_{FB} changing from more positive to less positive values in the following order: $ClO_4 > BF_4 \simeq PF_6 >$ pTS. This observation is in concurrence with the predictions from conductivity values. While PP(ClO_4) forms "quasi-ohmic" contact with p-Si, films grown with other counterions form barriers. V_{FB} of PP(pTS) on Au substrate could not be determined, since this film acts like a switch. However, the estimated value is negative of the V_{FB} of PP(ClO_4). PP film seems to passivate intrinsic surface states present on the p-Si surface. The results reported here are only preliminary, and more work is in progress in order to determine: (*i*) the effect of etching of the p-Si electrode and (*ii*) the effect of galvanostatically grown PP films, under various current densities, on the interfacial properties of p-Si PP interface.

Acknowledgment

The work described in this paper was carried out at the Jet Propulsion Laboratory, California Institute of Technology and was sponsored by U.S. Department of Energy, through an agreement with the National Aeronautics and Space Administration.

Manuscript submitted April 22, 1985; revised manuscript received Oct. 15, 1985.

The California Institute of Technology assisted in meeting the publication costs of this article.

REFERENCES

1. (a) F.-R. F. Fan, B. L. Wheeler, A. J. Bard, and R. N. Noufi, *This Journal*, **128**, 2042 (1981); (b) R. N. Noufi, A. J. Frank, and A. J. Nozik, *J. Am. Chem. Soc.*, **103**, 1849 (1981); (c) R. N. Noufi, A. J. Nozik, J. White, and L. F. Warren, *This Journal*, **129**, 2261 (1982).
2. (a) T. Skotheim, I. Lundstrom, and J. Prejza, *This Journal*, **128**, 1625 (1981); (b) R. A. Simon, A. J. Ricco, and M. S. Wrighton, *J. Am. Chem. Soc.*, **104**, 2031 (1982).
3. (a) K. Kaneto, M. Maxfield, D. P. Nairms, A. G. MacDiarmid, and A. J. Heeger, *J. Chem. Soc., Faraday Trans. 1*, **78**, 3417 (1982); (b) R. B. Kaner and A. G. MacDiarmid, *ibid.*, **80**, 2109 (1984); (c) "Conducting Polymers: Polymeric Organic Metals and Semiconductors." Course offered by the Institute in Materials Science, State University of New York (Nov. 12-14, 1984).
4. (a) "Polymers in Electronics," ACS Symposium Series 242, T. Davidson, Editor, ACS, Washington, DC (1984); (b) G. P. Kittlesen, H. S. White, and M. S. Wrighton, *J. Am. Chem. Soc.*, **106**, 7389 (1984); (c) J. H. Lai, S. A. Jenekhe, R. J. Jensen, and M. Royer, *Solid State Technol.*, **11**, 165 (1984); (d) R. H. Baughman, *Contemporary Topics in Polymer Science*, **5**, 321 (1984); (e) R. S. Potember and T. O. Poehler, *Polym. Mater. Electron. Appl.*, 233 (1982); (f) F. L. Carter, *J. Vac. Sci. Technol. B*, **1**, 959 (1983); (g) D. Baeriswyl, G. Harbeke, H. Keiss, and W. Meyer, in "Electronic Properties of Polymers," J. Mark and C. P. Fischer, Editors, John Wiley and Sons, New York (1982).
5. R. Noufi, D. Tench, and L. F. Warren, *This Journal*, **128**, 2596 (1981).
6. (a) K. J. Wynne and G. B. Street, *N.R. Reviews*, 38 (1981); (b) R. L. Greene and G. B. Street, *Science*, **226**, 651 (1984); (c) G. Wegner, *Angew. Chem. Int. Ed. Engl.*, **20**, 361 (1981); (d) K. K. Kanazawa, A. F. Diaz, R. H. Geiss, W. D. Gill, J. F. Kwak, J. A. Logan, J. F. Rabolt, and B. Street, *J. Chem. Soc., Chem. Commun.*, 894 (1979); (e) A. F. Diaz and B. Hall, *IBM. J. Res. Dev.*, **27**, 342 (1983).
7. J. H. Lai, S. A. Jenekhe, R. J. Jensen, and M. Royer, *Solid State Technol.*, **12**, 149 (1984).
8. (a) G. Horowitz, G. Tourillon, and F. Garnier, *This Journal*, **131**, 151 (1984); (b) K. Rageshwar, M. Kaneki, and A. Yamada, *ibid.*, **130**, 38 (1983).
9. (a) M. Ozaki, D. L. Peebles, B. R. Weinberger, C. K. Chiang, S. C. Gau, A. J. Heeger, and A. G. MacDiarmid, *Appl. Phys. Lett.*, **35**, 83 (1979); (b) O. Inganas, T. Skotheim, and I. Lundstrom, *J. Appl. Phys.*, **54**, 3636 (1983); (c) O. Inganas, T. Skotheim, and I. Lundstrom, *Phys. Scr.*, **25**, 863 (1982).
10. G. Nagasubramanian and A. J. Bard, *This Journal*, **128**, 1055 (1981).
11. G. Nagasubramanian, B. L. Wheeler, and A. J. Bard, *ibid.*, **130**, 385 (1983).
12. G. Nagasubramanian, B. L. Wheeler, and A. J. Bard, *ibid.*, **130**, 1680 (1983).
13. R. A. Bull, F.-R. F. Fan, and A. J. Bard, *ibid.*, **129**, 1009 (1982).
14. (a) F. Di Quarto and A. J. Bard, *J. Electroanal. Chem.*, **127**, 43 (1981); (b) V. A. Myamlin and Yu. V. Pleskov, in "Electrochemistry of Semiconductors," p. 323, Plenum Press, New York (1967); (c) E. C. Dutoit, R. L. Van Meirhaeghe, F. Cardon, and W. P. Gomes, *Ber. Bunsenges. Phys. Chem.*, **79**, 1206 (1975).
15. E. H. Nicollian and A. Goetzberger, *Bell Syst. Tech. J.*, **46**, 1055 (1967).
16. (a) H. S. White, H. D. Abruna, and A. J. Bard, *This Journal*, **129**, 265 (1982); (b) B. A. Parkinson, T. E. Furtak, D. Canfield, K. Kam, and G. Kline, *Discuss. Faraday Soc.*, **70**, 233 (1980); (c) D. Canfield and B. A. Parkinson, *J. Am. Chem. Soc.*, **103**, 1281 (1981).
17. (a) A. F. Diaz and K. K. Kanazawa, in "Extended Linear Chain Compounds," Vol. 3, J. S. Miller, Editor, p. 417, Plenum, New York (1982); (b) M. Salmon, A. F. Diaz, A. J. Logan, M. Krounbi, and J. Barbon, *Mol. Cryst. Liq. Cryst.*, **83**, 1297 (1982); (c) A. J. Frank, in "Energy Resources Through Photochemistry and Catalysis," M. Gratzel, Editor, p. 467, Academic Press, New York (1983).
18. T. Inoue and T. Yamase, *Bull. Chem. Soc. Jpn.*, **56**, 985 (1983).
19. (a) G. Nagasubramanian, B. L. Wheeler, F.-R. F. Fan, and A. J. Bard, *This Journal*, **129**, 1742 (1982); (b) G. Nagasubramanian, B. L. Wheeler, F.-R. F. Fan, and A. J. Bard, in "Photoelectrochemistry: Fundamental Processes and Measurement Techniques," W. L. Wallace, A. J. Nozik, S. K. Deb, and R. H. Wilson, Editors, p. 312, The Electrochemical Society Softbound Proceedings Series, Pennington, NJ (1982).

Electronically Conductive Composite Polymer Membranes

Reginald M. Penner and Charles R. Martin*

Department of Chemistry, Texas A&M University, College Station, Texas 77843

ABSTRACT

We have recently described the preparation and properties of ionically conductive Nafion-impregnated Gore-tex (NIGT) composite membranes (10). In this paper, we describe electronically conductive composite membranes prepared by electropolymerizing either pyrrole or thiophene within the ionically conductive NIGT membrane. These composites have the mechanical properties of the host membrane, yet the electronic conductivity of the NIGT/polypyrrole composite membrane is essentially identical to that of polypyrrole. For comparison, we have also attempted to electropolymerize pyrrole in Nafion membranes and films and in bare Gore-tex and poly(vinyl chloride)-impregnated Gore-tex.

A considerable amount of research effort is currently being devoted to studies of electronically conductive polymers (1-4). While a number of systems have been investigated, polymers based on heterocyclic monomers (*e.g.*, pyrrole) offer a number of important advantages (2-4). These polymers are more stable than, for example, polyacetylene, they can be very conductive, and they can be conveniently synthesized *via* electropolymerization (2-4). On the other hand, polypyrrole and its analogs are hard and brittle materials; these undesirable mechanical characteristics severely restrict the technological applications of these polymers (5).

Diaz *et al.* have recently prepared poly(vinyl chloride)-polypyrrole composite membranes by electropolymerizing pyrrole inside a poly(vinyl chloride) (PVC) film on an electrode surface (6, 7). These composites had the desirable mechanical properties of the PVC host, yet they retained the high conductivity of the polypyrrole (PP) dopant (6, 7). Because it is inherently neither porous nor ionically conductive, PVC is not the ideal host material for the preparation of conductive composites. This is evidenced by the long polymerization times required for the preparation of thin (less than 10 μm) PVC/PP composite films (6). The ideal host material would be mechanically stable, chemically inert, porous (to allow for impregnation by PP), and ionically conductive (to allow for quick ingress and egress of charge compensating ions). Furthermore, it would be advantageous for the host material to be a freestanding membrane (rather than a film cast on the electrode surface), so that the conductive composite could be easily removed, intact, from the electrode after doping.

We have recently prepared ionically conductive composite membranes by doping a host polytetrafluoroethylene membrane, Gore-tex (8), with a perfluorosulfonate ionomer, du Pont's Nafion (9, 10). Gore-tex (GT) is mechanically and chemically stable and has an open, porous structure. Because it is hydrophobic, GT is not wetted by water and, therefore, not ionically conductive when contacted with an aqueous electrolyte phase (10). We have shown, however, that when GT is impregnated with Nafion, the resulting composite is water-wetted and is an ionic conductor. Because GT has an open, porous structure, Nafion-impregnated Gore-tex (NIGT) is a better ionic conductor than Nafion itself (10).

The above discussion suggests that NIGT would be an ideal host material for the preparation of electronically conductive composite membranes. We have electropolymerized pyrrole and thiophene in NIGT and have examined the conductivities and electrochemical characteristics of the resulting composite membranes. For comparison, we have also attempted to grow PP in GT that does not contain Nafion, in Nafion (both as-received membrane and solution-cast film), and in PVC-impregnated GT (PVCIGT). The results of these studies are described here.

*Electrochemical Society Active Member.

Experimental

Materials.—Nafion 117 (1100 equivalent weight, proton form) and GT (3.0 μm mean pore diameter) membranes were generously donated by E.I. du Pont de Nemours and W. L. Gore Associates, respectively. Solutions of Nafion were prepared using the procedure of Martin *et al.* (11). Pyrrole and thiophene were obtained from Aldrich and distilled prior to use. Chromatographic grade PVC was obtained from Polysciences and used as received. Tetraethylammonium tetrafluoroborate was obtained from Aldrich and recrystallized from methanol. Burdick and Jackson acetonitrile was dried over molecular sieves prior to use. Pt foil (0.254 mm thick) was obtained from Aldrich. Other reagents were of highest commercial grades and were used without further purification.

Electrode preparation.—0.5 cm^2 disks were cut from the Pt foil, and Cu wires were soldered to one face. These disks were then sealed into 9 mm glass tubes using electron-microscopy-grade epoxy (Electron Microscopy Sciences). The exposed Pt faces were then polished, sequentially, with 600 grit carborundum, 1.0, 0.3, and 0.05 μm alumina on Texmet polishing cloth (all from Buehler). Electrodes were repolished between experiments with the 0.05 μm alumina. A GT membrane was stretched over the polished face and held in place with a sleeve of heat-shrinkable Teflon tubing (10).

The GT membrane was impregnated with Nafion by immersing the membrane-clad electrode into an ethanolic solution of Nafion (2 w/v %) and ultrasonicating for 20 min. The electrode was then removed from the impregnating solution, excess solution was wicked off, and the ethanol was allowed to evaporate for *ca.* 2h in air. These electrodes are referred to as Pt/NIGT electrodes. Pt/PVCIGT electrodes were prepared using the same procedure, only the Nafion solution was replaced with a 0.25 w/v % PVC solution in tetrahydrofuran.

Nafion film-modified electrodes were prepared by depositing 20 μl of a 4 w/v % Nafion solution (in 50/50 ethanol/water) onto the Pt disk electrode and allowing the solvent to evaporate. Film thickness was estimated assuming a density of 1.58 g-cm^{-3} (12). To study electropolymerization in as-received Nafion membranes, electrical contact must be made with the freestanding membrane (13). This was accomplished by depositing a 50 nm Pt film on one face of a Nafion disk (area = 0.5 cm^2) using a Technics Hummer argon plasma depositor. A Cu wire was attached to the Pt film with silver epoxy, and the resulting assembly was embedded into a 9 mm glass tube as described above.

Polymerization and polymer electrochemistry.—Electrochemical polymerizations and measurements were accomplished using a Bioanalytical Systems Incorporated CV-27 voltammograph in conjunction with a Houston Instruments 2000 X-Y recorder and a Perkin-Elmer strip chart recorder. An aqueous saturated calomel reference electrode (SCE), a Pt flag counterelectrode, and a single compartment electrochemical cell were used.

Polymerization solutions were 0.74*M* in pyrrole or 0.37*M* in thiophene, and 0.1*M* in tetraethylammonium tetrafluoroborate (Et_4NBF_4); acetonitrile was the solvent. To insure that the solvent and monomer had permeated the NIGT, PVCIGT, and bulk Nafion membranes, the membrane-coated electrodes were ultrasonicated briefly in supporting electrolyte and then equilibrated with the monomer solutions for 30 min prior to electrochemical polymerization. Pyrrole was polymerized as *per* Diaz *et al.* by stepping the potential of the Pt electrode to +0.80V *vs.* SCE (at the foot of the pyrrole oxidation wave) (8). In some experiments, pyrrole was polymerized by scanning the electrode potential through the oxidation wave (*e.g.*, Fig. 1). Thiophene was polymerized by stepping the potential to +1.90V or by scanning through the thiophene wave.

The NIGT membranes were 25 μm thick; the thicknesses of the PP films produced within these membranes were estimated by monitoring the charge consumed during polymerization and assuming that 24 mC cm^{-2} yielded a 0.1 μm film (14). While this is a crude assumption, it is of interest to note that according to this approximation, 6 C-cm^{-2} of charge should be required to grow PP completely through the GT membrane, and this is precisely what is observed experimentally. Pt/NIGT electrodes that have been impregnated with PP or polythiophene (PT) are referred to as Pt/NIGT/PP and Pt/NIGT/PT electrodes, respectively. Note, however, that the PP or PT grows from the Pt-NIGT interface towards the NIGT-solution interface. After polymerization, all membranes and films were extracted in dry, degassed acetonitrile for 30 min to remove unreacted monomer.

Conductivity measurements and scanning electron microscopy.—Electrical conductivity was measured using a conventional four-point conductivity meter (15), constructed in-house. Before the conductivity measurements were made, the membranes were removed from the electrode surface, Soxhlet extracted in acetonitrile for 4h, and then dried *in vacuo* for 30 min at ambient temperature. Scanning electron micrographs were obtained on a JEOL JSM-25SII at an accelerating voltage of 25 kV.

Results and Discussion

Electropolymerization at polymer-coated electrodes.—Pyrrole voltammograms at Pt/NIGT (Fig. 1, curve A) are qualitatively similar to pyrrole voltammograms at bare Pt (Fig. 1, curve B). Note, however, that the voltammetric wave at Pt/NIGT is shifted negatively by *ca.* 100 mV. The origins of this negative shift will be discussed below.

With continued scanning into the pyrrole oxidation wave, PP grows into the NIGT membrane, as evidenced by an increase in the capacitive currents (Fig. 2) and the darkening of the initially white NIGT. As indicated above, polymerization may be stopped before the PP film reaches the NIGT-solution interface; the electrode side of such a membrane is black, but the solution side is still white. Alternatively, the PP film may be grown all the way through the NIGT membrane, in which case both sides of the membrane are black. For a potential step to +0.80V, approximately one hour is required for the PP film to grow all the way through the 25 μm NIGT membrane.

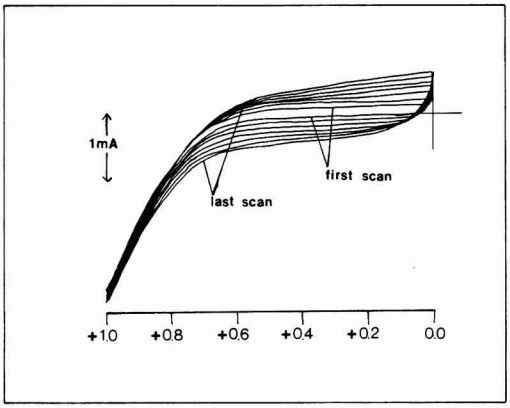


Fig. 2. Cyclic voltammograms (50 mV/s) for pyrrole at Pt/NIGT electrode showing the increase in capacitive currents as a result of PP deposition (solution as *per* Fig. 1).

The electrochemical characteristics of Pt electrodes covered with GT membranes (*i.e.*, no Nafion or PVC impregnation) were also studied. Pyrrole oxidation waves similar to those shown in Fig. 1 are observed at these Pt/GT electrodes, indicating that both electrolyte and pyrrole can permeate the bare GT membrane. However, PP does not grow through the membrane; instead, PP grows at the Pt-GT interface and seems to push the GT membrane away from this interface. This suggests that one of Nafion's roles in the Pt/NIGT system is as an adhesive to produce strong binding between the NIGT membrane and the electrode surface. Grot has also suggested that solution-cast Nafion can be used as an adhesive (16).

Electrochemical studies at Pt/PVCIGT corroborate the conclusion that a membrane/electrode adhesive is re-

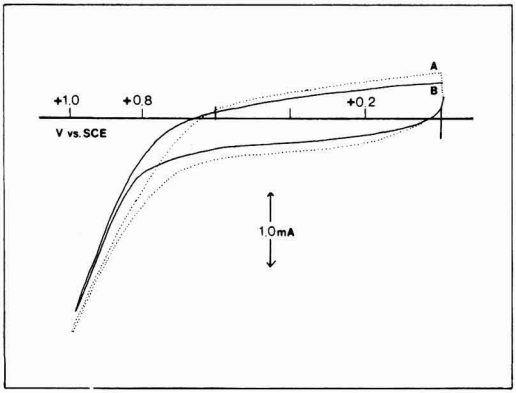


Fig. 1. Cyclic voltammograms (50 mV/s) for 0.74M pyrrole in 0.1M Et_4NBF_4, CH_3CN. A. Pt/NIGT electrode. B. Bare Pt electrode.

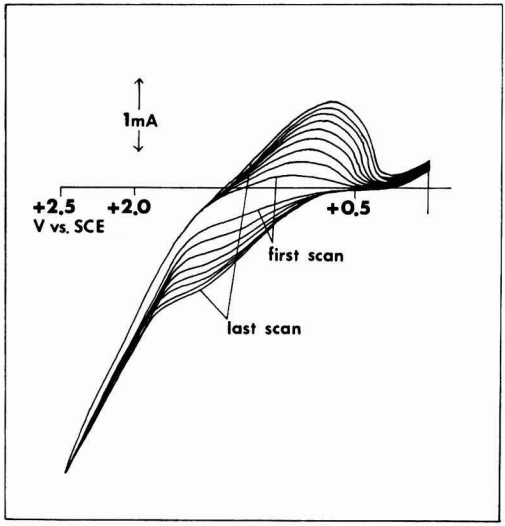


Fig. 3. Cyclic voltammograms (50 mV/s) for 0.37M thiophene in 0.1M Et_4NBF_4, CH_3CN at Pt/NIGT.

quired if PP is to be grown through the membrane. Because PVC is inert and nonionic, it would not be expected to promote permeation of either the monomer or the polymer through the GT membrane. In fact, since PVC-impregnation will lower the membrane void volume, PVC should lower the membrane permeability. While the rate of polymerization is lower at Pt/PVCIGT than at Pt/NIGT (see Fig. 8 and discussion below) PP grows all the way through the PVCIGT membrane. In a manner analogous to that of Nafion, solution-cast PVC acts as an electrode/membrane adhesive and, thus, also allows the PP to grow through the GT membrane.

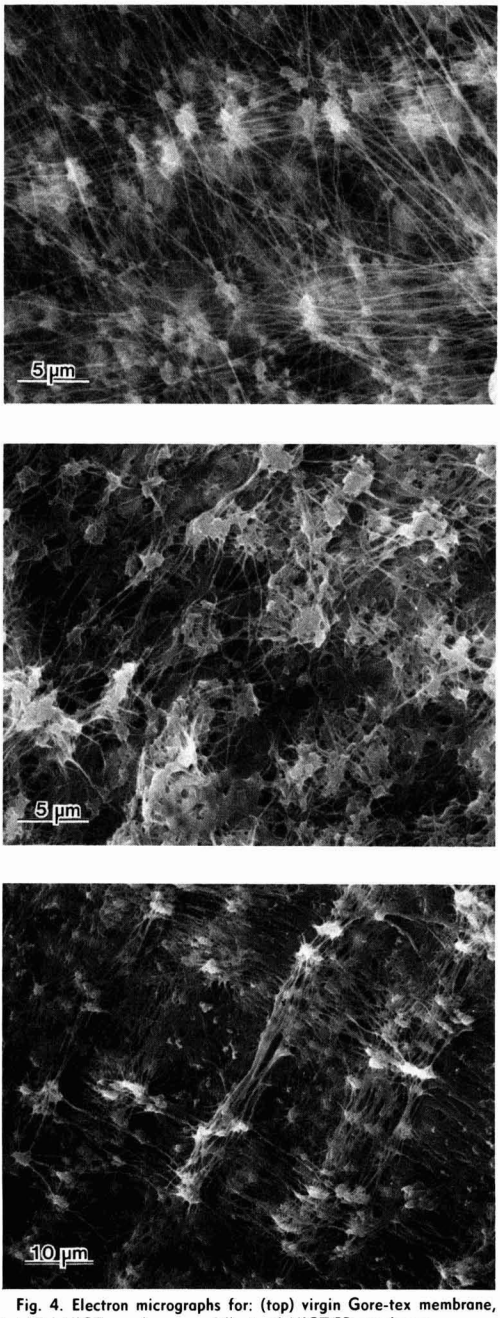


Fig. 4. Electron micrographs for: (top) virgin Gore-tex membrane, (middle) NIGT membrane, and (bottom) NIGT/PP membrane.

Finally, it was of interest to see if Nafion could serve as a host material for pyrrole polymerization. In agreement with the results of Fan and Bard, we have found that PP grows through solution-cast Nafion films on Pt electrode surfaces (17). In contrast, pyrrole electrochemistry is not observed at electrodes covered with bulk, as-received Nafion membranes, and no PP can be detected, either at the Pt surface or in the Nafion membrane, even after polymerization times as long as 12h. While the bulk membranes are somewhat thicker than the solution-cast films, the complete absence of pyrrole electrochemistry and PP indicates that the difference in thickness cannot account for these disparate results. Rather, these results corroborate Buttry and Anson's conclusion that solution-cast Nafion has a more open, porous structure than as-received Nafion membrane (18).

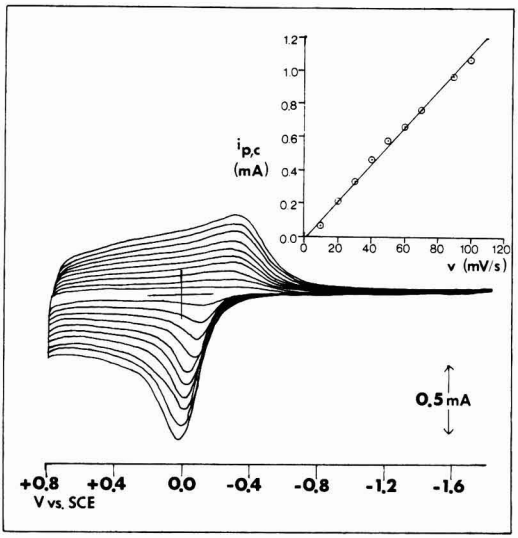
Figure 3 shows that thiophene is also oxidized at Pt/NIGT. These voltammetric waves are qualitatively similar to thiophene waves at bare Pt (19). As was the case with PP, PT is deposited within the NIGT membrane, as evidenced by the growth of the polymer redox wave (Fig. 3) and the darkening of the NIGT.

Scanning electron microscopy.—Electron micrographs (EM's) of bare GT (Fig. 4a) show a nodal structure with polytetrafluoroethylene fibers forming webs that extend from the nodes. EM's of NIGT (Fig. 4b) show that Nafion films collect in the polytetrafluoroethylene webs; higher magnification EM's show that Nafion also coats the individual fibers that make up the webs. Clearly, at this loading level (10 w/w % Nafion in the GT), only a small fraction of the available void volume is occupied by Nafion. This explains why ionic diffusion is faster in NIGT than in Nafion (10), and why PP is readily grown in the NIGT composite.

An EM for a NIGT/PP membrane is shown in Fig. 4c. The pyrrole polymerization time was adjusted such that the PP film just reached the membrane-solution interface, and the EM is of this interface. While some of the GT nodal structure can be seen at the surface, this EM indicates that the bulk of the GT void volume is completely filled by PP. This suggests that NIGT/PP should be much less permeable than NIGT, and this conclusion is borne out in experiments described below. Note that the EM's shown are of the surfaces of the various membranes; however, that both Nafion and PP are propogated all the way through the membrane is clearly indicated by the fact that both ions and electrons can pass from one surface, through the bulk, and to the other surface of the membrane.

Electrochemistry of Pt/NIGT/PP and Pt/NIGT/PT.—Figure 5a shows cyclic voltammograms for a Pt/NIGT/PP electrode that contains a *ca.* 0.4 μm PP film within the 25 μm NIGT membrane. These voltammograms are essentially identical to voltammograms obtained at thin PP films on Pt electrodes and show cathodic waves for the reduction of $[(\text{pyrrole})_n^+]$ to neutral PP and anodic waves for the corresponding reoxidation process (14). Peak currents are linearly related to scan rate, as is expected for a thin film redox couple (inset Fig. 5a). Figure 5b shows cyclic voltammograms for a Pt/NIGT/PT electrode. Again, the polymer electrochemistry is similar to the electrochemistry of Pt/PT (20).

The diminution in capacitive currents upon reduction (Fig. 5a) indicates that the PP within the NIGT membrane is an electronic conductor when oxidized and an insulator when reduced. An experiment originally described by Diaz *et al.* was used to prove this point (14). Because E^0 for ferrocene (Fc) is positive of E^0 for the reduction of $[(\text{pyrrole})_n^+]$ (the switching potential, *ca.* −0.22V), PP should be an electronic conductor in the potential region where Fc is oxidized. In contrast, E^0 for nitrobenzene (NB) is negative of the PP switching potential, and PP should be an insulator in the potential region where NB is reduced. Thus, Diaz *et al.* have shown that



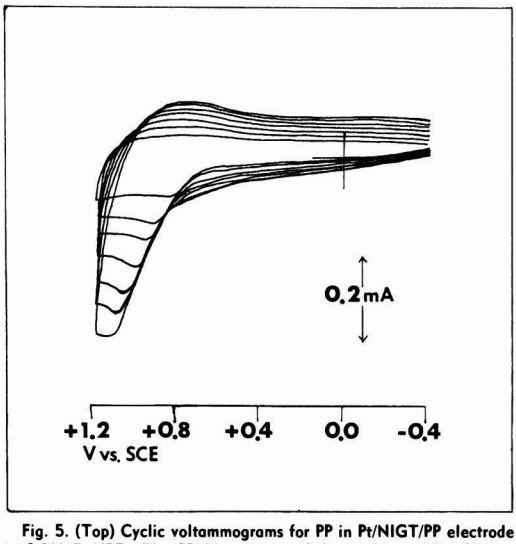


Fig. 5. (Top) Cyclic voltammograms for PP in Pt/NIGT/PP electrode in 0.1M Et_4NBF_4. The PP film was *ca.* 0.4 μm thick within 25 μm NIGT membrane. Scan rates = 10, 20, 30, 40, 50, 60, 70, 80, 90, 100 mV/s (smallest peak currents to largest peak currents, respectively). Inset: Cathodic peak current vs. scan rate for PP waves. (Bottom) Cyclic voltammograms for PT in Pt/NIGT/PT electrode (solution as in A). The PT film was *ca.* 0.2 μm thick. Scan rates = 20, 30, 40, 50, 60, 70, 80 mV/s (smallest peak currents to largest peak currents, respectively).

Fc is electrochemically active, whereas NB is electrochemically silent at Pt/PP (14). Because Pt/NIGT/PP shows identical electrochemistry (Fig. 6), the PP within the NIGT membrane also undergoes an electrochemically induced conductor/insulator transition.

It is of interest to note than when Pt/NIGT electrodes are exposed to CH_3CN solutions containing both Fc and NB (as *per* Fig. 6), redox waves for both couples are observed. This is not surprising, since NIGT is both wetted by CH_3CN and highly porous. The absence of NB electrochemistry at Pt/NIGT/PP shows, as anticipated from the EM's, that the PP completely fills the pores of the NIGT membrane.

Figure 7a shows $Fc^{+/0}$ voltammograms at Pt/NIGT/PP electrodes for various thicknesses of PP within the NIGT

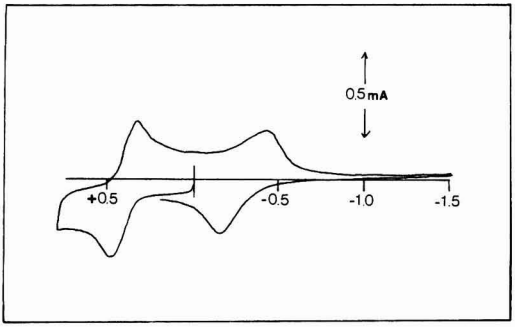


Fig. 6. Cyclic voltammetry (20 mV/s) at a Pt/NIGT/PP electrode in a solution 2.6 mM in ferrocene, 12.6 mM in nitrobenzene, and 0.1M in Et_4NBF_4, CH_3CN. The PP film was *ca.* 0.2 μm thick.

membrane. While the peak currents for the $Fc^{+/0}$ waves increase with PP film thickness, this increase is due to the superposition of a relatively constant faradaic signal on an increasing capacitive background current. This suggests that the area of the PP electrode that is accessible to the solution redox couple remains relatively constant, irrespective of the total PP film thickness. Since this observation has not been previously noted in the literature, we conducted analogous experiments at Pt/PP electrodes, and identical results were obtained (Fig. 7b). These data indicate that while small, charge compensating electrolyte ions can access the entire PP film, larger electroactive species can only access a constant outer fraction of the PP electrode.

Finally, the increase in peak splitting for the $Fc^{+/0}$ wave with PP film thickness (Fig. 7) is probably caused by uncompensated film resistance, the effects of which become more pronounced as the total current increases (21).

The effect of the medium on the electrochemistry of pyrrole.—As noted in Fig. 1, pyrrole oxidation occurs at less positive potentials at Pt/NIGT than at naked Pt (in both cases the supporting electrolyte was 0.1*M* Et_4NBF_4 in CH_3CN). There are several plausible explanations for this shift. First, it is at least in principle possible that this shift is caused by a junction potential created by the NIGT membrane. If this is the case, chemically similar redox couples might be expected to show similar positive shifts at Pt/NIGT (*i.e.*, similar redox couples should also be influenced by the junction potential). We have found, however, that $E^{o\prime}$ for Fc (which, like pyrrole, is oxidized from a neutral aromatic molecule to a cation radical) at Pt/NIGT is identical to Fc's $E^{o\prime}$ at naked Pt. This observation suggests that the shift observed is not the result of a junction potential.

The second possibility is that the oxidation of pyrrole is thermodynamically easier in NIGT than in solution. For example, the electrostatic interaction between the Nafion $-SO_3^-$ sites and the cationic center created upon oxidation of pyrrole could cause a negative shift in the pyrrole oxidation wave (22). While we do not have sufficient data to eliminate this possibility, it is of interest to note, again, that Fc oxidation, which also produces a cationic center, occurs at the same potential in NIGT as in CH_3CN solution. Because the electrostatic interaction is apparently not strong enough to produce a shift in the $E^{o\prime}$ value for $Fc^{+/0}$, it seems unlikely to us that electrostatics could produce the observed pyrrole shift.

Diaz *et al.* have shown that the rate-determining step in the pyrrole polymerization reaction is the coupling of two electrogenerated cation radicals (*e.g.*, dimerization) (23). It is possible that the positive shift in the pyrrole wave results from acceleration of these radical coupling reactions (24). We currently favor this explanation and are studying simple electroinitiated dimerization reactions in Nafion and NIGT to see if dimerization rates are faster in these media.

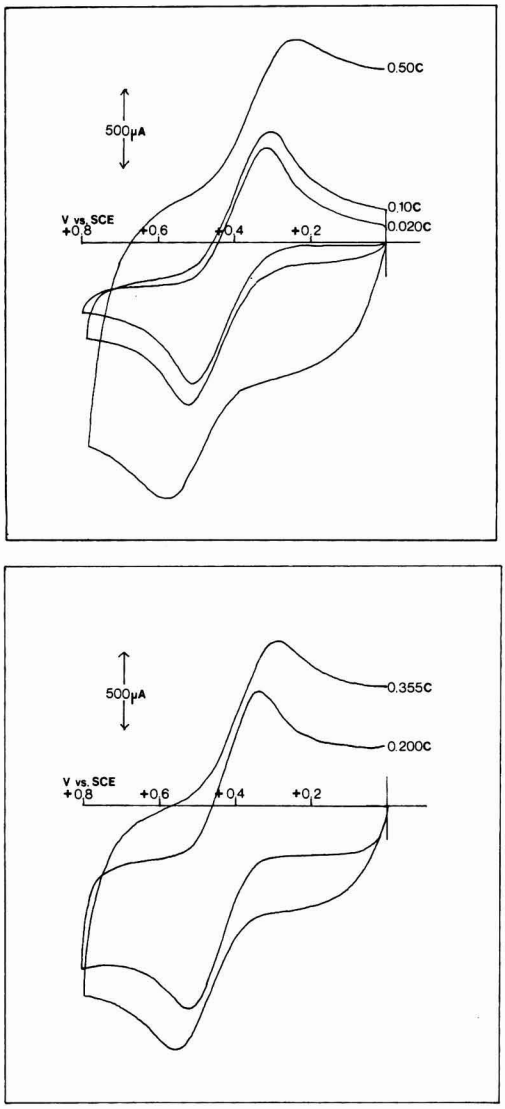


Fig. 7. Cyclic voltammograms (20 mV/s) for 10 mM ferrocene (0.1M Et_4NBF_4, CH_3CN): (top) at Pt/NIGT/PP electrodes having three different thicknesses of PP within the NIGT membrane; (bottom) at Pt/PP electrodes having two different PP film thicknesses. (The coulomb values associated with the voltammograms in this figure are charges passed during polymerization. For these electrodes, 12 mC = *ca.* 0.1 μm).

Whether dynamically or thermodynamically caused, the negative shift in the pyrrole oxidation wave in NIGT should cause current flow, at any potential, during the electropolymerization to be greater at Pt/NIGT than at bare Pt. Curves A, B, and C in Fig. 8 show pyrrole oxidation currents at naked Pt, Pt/PVCIGT, and Pt/NIGT, respectively, following a potential step from 0.0 to +0.8V. Currents at Pt/NIGT are, indeed, greater than currents at naked Pt and Pt/PVCIGT. The fact that polymerization is faster at Pt/NIGT than at Pt/PVCIGT suggests that Nafion is responsible for the observed current enhancement. To test this hypothesis, polymerization currents were monitored at Pt/(solution-cast Nafion) electrodes (Fig. 8, curve D). Polymerization currents at Pt/(solution-cast Nafion) are also much higher than at Pt or Pt/

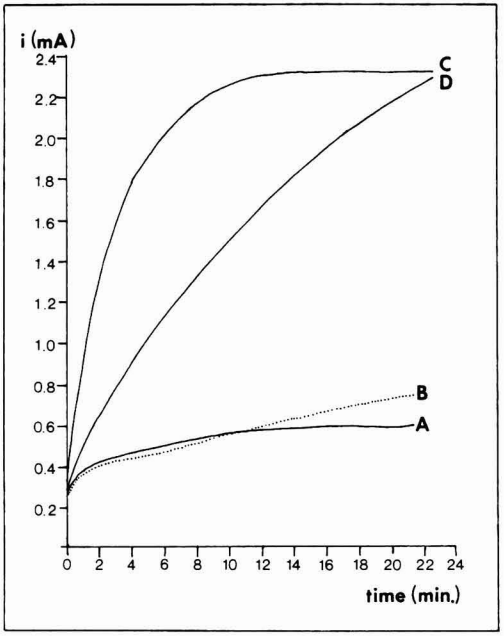


Fig. 8. Current during pyrrole polymerization *vs.* time following a potential step from 0.0 to +0.8V. A. Pt. B. Pt/PVCIGT. C. Pt/NIGT. D. Pt/(solution-cast Nafion). Solution as per Fig. 1.

PVCIGT. These data seem to confirm the conclusion that Nafion is the essential ingredient in the observed current enhancement.

An alternative explanation for the data in Fig. 8 is that the effective area of the growing PP electrode is greater when the PP is grown within the NIGT or Nafion membrane. To test this possibility, identical quantities of PP were grown at Pt and at Pt/NIGT, and cyclic voltammograms for Fc were then obtained at both electrodes. If the Pt/NIGT/PP had a larger effective PP electrode area, Fc oxidation currents at this electrode would be greater than at Pt/PP. Figure 9 shows that Fc oxidation currents are, in fact, slightly larger at Pt/PP than at Pt/NIGT/PP. These

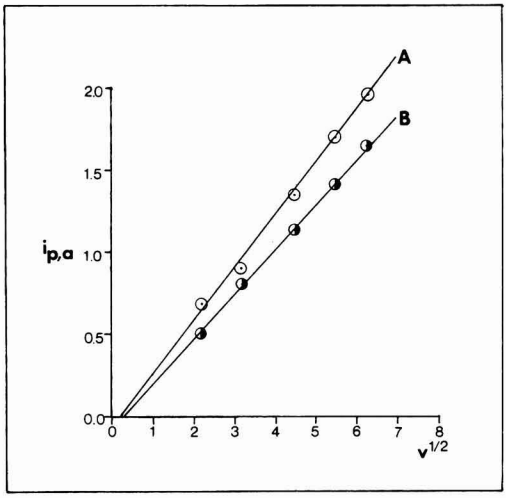


Fig. 9. Plots of anodic peak current for ferrocene oxidation *vs.* square root of scan rate at A. Pt. B. Pt/NIGT. Solution was 10 mM ferrocene, 0.1M Et_4NBF_4 in CH_3CN.

data show that the enhanced current at Pt/NIGT (Fig. 8) is not an artifact of the electrode area.

Conductivities.—NIGT/PP membranes were removed from the Pt electrodes, and the electrical conductivities of both the solution sides and the electrode sides of these membranes were measured. The electrode sides showed conductivities that varied between 20 and 50 S-cm^{-1}. If polymerization was interrupted before the PP film reached the NIGT-solution interface, the electronic conductivity of the solution face was essentially zero (*i.e.*, the electronic conductivity of NIGT). In contrast, when PP was grown all the way through the NIGT membrane, the conductivity of the solution face varied from 20 to 50 S-cm^{-1}. These conductivities compare favorably with conductivities for homogeneous PP films, which vary from 10 to 100 S-cm^{-1} (25).

Conclusions

We have shown that electronically conductive composite membranes can be prepared by electropolymerizing pyrrole within Nafion-impregnated Gore-tex. The electronic conductivity of the polypyrrole-doped NIGT membrane is essentially identical to the conductivity of polypyrrole (25). An interesting and potentially useful attribute of these composite membranes is that the conductive element (PP) can be grown to any desired thickness within the host material. Thus, membranes that conduct on one surface only, membranes that are conductive throughout, or even membranes that conduct, independently, on both surfaces but not in the bulk can be prepared.

We have also found that pyrrole oxidation occurs at less positive potentials at Pt/NIGT than at bare Pt. As a result of this negative shift, polymerization currents are higher at Pt/NIGT than at bare Pt. We are currently attempting to ascertain the causes of this shift in oxidation potential. Finally, we have found that Nafion can function as an adhesive to produce strong binding between a membrane and an electrode surface. This could prove to be a useful, general, method for adhering free-standing polymer, or other, membranes to electrode surfaces.

Acknowledgments

This work was supported by the Office of Naval Research and the Robert A. Welch Foundation. We wish to thank A. J. Bard and F. R. Fan of the University of Texas at Austin for providing a preprint of Ref. (17).

Manuscript submitted July 16, 1985; revised manuscript received Sept. 20, 1985.

The Office of Naval Research assisted in meeting the publication costs of this article.

REFERENCES

1. J. H. Kaufman, T.-C. Chung, and A. J. Heeger, *This Journal*, **131**, 2847 (1984).
2. S. Feldberg, *J. Am. Chem. Soc.*, **106**, 4671 (1984).
3. A. F. Diaz, J. I. Castillo, J. A. Logan, and W.-Y. Lee, *J. Electroanal. Chem.*, **129**, 115 (1981).
4. R. J. Waltman, A. F. Diaz, and J. Bargon, *This Journal*, **131**, 2847 (1984).
5. A. F. Diaz and B. Hall, *IBM J. Res. Dev.*, **27**, 342 (1983).
6. M.-A. De Paoli, R. J. Waltman, A. F. Diaz, and J. Bargon, *J. Chem. Soc., Chem. Commun.*, 1016 (1984).
7. M.-A. De Paoli, R. J. Waltman, A. F. Diaz, and J. Bargon, *J. Poly. Sci., Poly. Chem. Ed.*, **23**, 1687 (1985).
8. Gore-tex is a registered trademark of W. L. Gore & Associates, Inc.
9. Nafion is a registered trademark of E.I. du Pont de Nemours and Co.
10. R. M. Penner and C. R. Martin, *This Journal*, **132**, 514 (1985).
11. C. R. Martin, T. A. Rhoades, and J. A. Ferguson, *Anal. Chem.*, **54**, 1639 (1982).
12. C. R. Martin and K. A. Dollard, *J. Electroanal. Chem.*, **159**, 127 (1983).
13. C. M. Elliott and J. G. Redepenning, *ibid.*, **181**, 137 (1984).
14. A. F. Diaz and J. I. Castillo, *J. Chem. Soc., Chem. Commun.*, 397 (1980).
15. J. R. Reynolds, Ph.D. Dissertation, University of Massachusetts, Amherst, MA (1984).
16. W. G. Grot, U.S. Pat. 4,433,082 (1984).
17. F.-R. F. Fan and A. J. Bard, Submitted to *This Journal*.
18. D. A. Buttry and F. C. Anson, *J. Am. Chem. Soc.*, **104**, 4824 (1982).
19. R. M. Penner, Texas A&M University, Unpublished results, February 1985.
20. R. J. Waltman, J. Bargon, and A. F. Diaz, *J. Phys. Chem.*, **87**, 1459 (1983).
21. C. R. Martin, I. Rubinstein, and A. J. Bard, *J. Am. Chem. Soc.*, **104**, 4817 (1982).
22. M. N. Szentirmay, N. E. Prieto, and C. R. Martin, *J. Phys. Chem.*, **89**, 3017 (1985).
23. E. M. Genies, G. Bidan, and A. F. Diaz, *J. Electroanal. Chem.*, **149**, 101 (1983).
24. A. J. Bard and L. R. Faulkner, "Electrochemical Methods," Chap. 11, John Wiley and Sons, New York (1980).
25. A. F. Diaz, K. K. Kanazawa, and G. P. Gardini, *J. Chem. Soc., Chem. Commun.*, 635 (1979).

Phase Diagrams and Conductivity Characterization of Some PEO-LiX Electrolytes

C. D. Robitaille and D. Fauteux

Institut de Recherche d'Hydro-Québec, Varennes, Québec, Canada, J0L 2P0

ABSTRACT

PEO-LiX (X = $CF_3SO_3^-$, ClO_4^-, and AsF_6^-) systems have been characterized by x-ray diffraction and optical microscopy, and the resulting phase diagrams are taken into account for the interpretation of ac impedance measurements. Eutectic reactions and multiple-intermediate-compound formation are characteristic of most systems. Simple phenomenological models do not explain the overall conductivity behavior. The activation energy of ion transport is independent of the anion, and remains mainly constant at 0.7 eV over the concentration range studied for $T > 60°C$. Ion-pair formation seems to occur at low salt concentration.

Since the original work of Wright (1, 2) and Armand *et al.* (3) poly(ethylene oxide)-lithium salt (POE-LiX)-based electrolytes have been the focus of many characterization studies of their ion transport properties. Recently, their use in high-energy-density electrochemical batteries has been demonstrated (4, 5).

Three types of temperature dependence have been observed and discussed for electrolyte conductivity (3). First, for electrolytes with a high degree of crystallinity, this dependence is described by an Arrhenius-type relation

$$\sigma = A \exp(-Ea/RT) \quad [1]$$

even when a discontinuity is observed in the $\log_{10}(\sigma)$ *vs.* $1/T$ curve, in which case Eq. [1] applies to each segment. For an amorphous electrolyte, a Vogel-Tamman-Fulcher

(VTF) equation provides a better description

$$\sigma = A\sqrt{T}\exp(-Ea/(T-To)) \quad [2]$$

where To is a temperature which can be associated with the glass-transition temperature (T_g) of the electrolyte and Ea a pseudo-activation energy related to the configurational entropy of the polymer chain (6). The third type of electrolyte conductivity temperature dependence is a combination of the first two, namely, an Arrhenius type for temperatures below the transition temperature and a VTF for higher values.

Concurrently with research on the electrochemical applications of polymer electrolytes, James *et al.* (7) and Robitaille and Prud'homme (8) have characterized the interactions between PEO and sodium salts. The latter authors' work has enabled the phase diagram of the POE-NaSCN system to be established. This led the stoichiometry of the intermediate compound to be determined as $P(EO_3NaSCN)$, as recently confirmed by Hibma (9). Meanwhile, Gorecki (10), Berthier *et al.* (11), and Minier *et al.* (12) have shown for the PEO-NaI system that the stoichiometry of the intermediate compound is $P(EO_3NaI)$ whereas for the PEO-$LiCF_3SO_3$ system, the mole ratio of the intermediate compound appears to be 3.5. Also, Dupon *et al.* (13) have identified crystalline electrolytes having a composition $PEO_{3.4}LiBH_4$. Thus, contrary to what was generally admitted, by analogy with PEO_4-$HgCl_2$ (1, 14), the stoichiometry of intermediate compounds can be below the O/M mole ratio of 4.

Recently, Sorensen and Jacobsen (15), Gorecki (10), and Minier *et al.* (12) used phase diagrams to describe the interactions between PEO and $LiCF_3SO_3$ in an attempt to predict the variation in the total ionic conductivity with temperature and electrolyte composition. It is now generally accepted that these types of polymer electrolytes are not single-phase homogeneous materials in the ranges of temperature and composition of interest for electrochemical batteries. These binary systems can therefore be represented by phase diagrams and can sometimes reveal the presence of more than one definite compound (10, 16, 17). A number of these studies have also suggested that ion mobility is greatest in the amorphous phase.

In the study described here, PEO-LiX polymer electrolytes (X being $CF_3SO_3^-$, ClO_4^-, and AsF_6^-) were characterized by wide angle x-ray scattering (WAXS), polarized-light optical microscopy and ac conductivity and then described using the phase diagrams thus established. The dependence of the variation in $\log_{10}(\sigma)$ as a function of $(1/T)$ is discussed with reference to these diagrams. From the results presented here, it seems that simple phenomenological models do not provide a correct description of the variation in conductivity in terms of the different dependent parameters. A better understanding of the interactions between the solvating polymer and the lithium salts under study leads to a more accurate definition of the factors determining the ion transport mechanisms in such electrolytes.

Experimental

The high molecular weight (900 K) PEO was supplied by Aldrich. It was dried under partial vacuum, < 5 mm/Hg argon at 45°-50°C for ≃ 48h. The following lithium salts were recrystallized in acetonitrile then dried under partial vacuum for ≃ 48h at the temperatures specified: $LiCF_3SO_3$ (Pennwalt), 100°-110°C, $LiAsF_6$ (USS), 140°-150°C, $LiClO_4$ (Alfa), 100°-110°C.

All subsequent manipulations of these materials were carried out under an argon or helium anhydrous atmosphere. Thin films of electrolytes were obtained using a procedure described elsewhere (3, 18, 19). The latter, briefly, consists in dissolving predetermined amounts of PEO and lithium salts in acetonitrile (12-20% by vol) and casting these solutions on inert supports, then evaporating the solvent at 25°C. This yields films approximately 50 μm thick, which are then dried under partial vacuum at 95°-100°C for a minimum of 48h. Once dry and solvent-free, the electrolytes were stored in a glove box at 25°C and not used until crystallization was completed. Determination of the water content of the electrolyte materials by the Karl-Fischer technique revealed negligible values (< 25 ppm). The solvent used for the electrolyte preparations had previously been stored on a molecular sieve (H_2O < 20 ppm).

Microscopy.—The thermal behavior of the various electrolytes was studied by polarized-light optical microscopy using a Zeiss microscope and an in-house designed heating stage at an average heating rate of 2°C min^{-1}. The samples were mounted between two glass slides which were then sealed together with rapid-action epoxy glue in the glove box. Such a setup was sufficiently airtight to allow microscope observations in air.

X-ray diffraction.—Capillaries, 0.5 mm in diameter, were filled in the glove box with small pieces of electrolyte. The sealed capillaries were then exposed to nickel-filtered CuK_α radiation for 1.5h at ambient temperature. The diffraction patterns were recorded on Kodak AA5 film using a Debye-Scherrer camera (ϕ = 114.6 mm). The Bragg angle values were measured by means of a lighted glass plate fitted with a vernier with 1/20 mm graduations. The relative intensity of the diffraction lines was evaluated visually.

Conductivity.—The conductivity of the polymer electrolytes was determined by ac impedance measurements over a frequency range between 65 kHz and 1 Hz, with a Solartron 1250 frequency analyzer coupled to a HP-85 controller which handles all the digital-data acquisition and processing for the electrochemical cells under test. Two parallel symmetrical plane electrodes of stainless steel or lithium, 3.88 cm^2 in surface area, were used irrespectively although when lithium was used the surfaces were refreshed before being placed in contact with the electrolytes. The electrochemical cells were assembled at ambient temperature and were not preheated before the impedance measurements. They were kept under a mechanical pressure of approximately 2 kg cm^{-2}. A stabilization time of 1h was allowed for each of the ten or so temperature levels. All the conductivity curves of this work represented average values of σ for at least two different samples of each electrolyte. For the reported experimental conditions the conductivity behavior was quite reproducible; the σ values were within a few percent of the mean value.

Results and Discussion

Figure 1 gives the values of the various phase-transition temperatures published for the PEO-$LiCF_3SO_3$ system. The salt mass fractions are between 0.47 and 0.11, corresponding to mole ratios of O/Li = 4 and O/Li = 30, respectively. The values presented in Fig. 1 were obtained by NMR (12), by DTA or DSC (12, 18, 20), from ac conductivity measurements (12, 18), by optical microscopy (21) or by means of a conductivity-based model (15). The values determined by the authors of this work using optical microscopy and ac conductivity are also presented in the same figure. Gorecki (10), Berthier *et al.* (11), and Minier *et al.* (12) have proposed a 3.5:1 stoichiometry for the intermediate compound rather than the 4:1 stoichiometry usually accepted, basing their assumption on the NMR results and DSC analysis of the electrolytes, which characterize the electrolyte crystallinity and the salt concentration of the amorphous phase in terms of the temperature. Moreover the presence of a eutectic mixture at low salt concentrations is not unanimously accepted (10, 12, 15).

Figure 1 also presents a phase diagram for the POE-$LiCF_3SO_3$ system which was obtained from experimental results. This diagram is slightly different from the diagram of Minier *et al.* (12) although similar to the approximate diagram proposed by Sorensen and Jacobsen (15). The present authors' results suggest that the eutectic composition is somewhere around an O/Li mole ratio of 100. The melting of the eutectic mixture is easily detected by optical microscopy if the sample contains a large enough proportion of this eutectic mixture. This can be

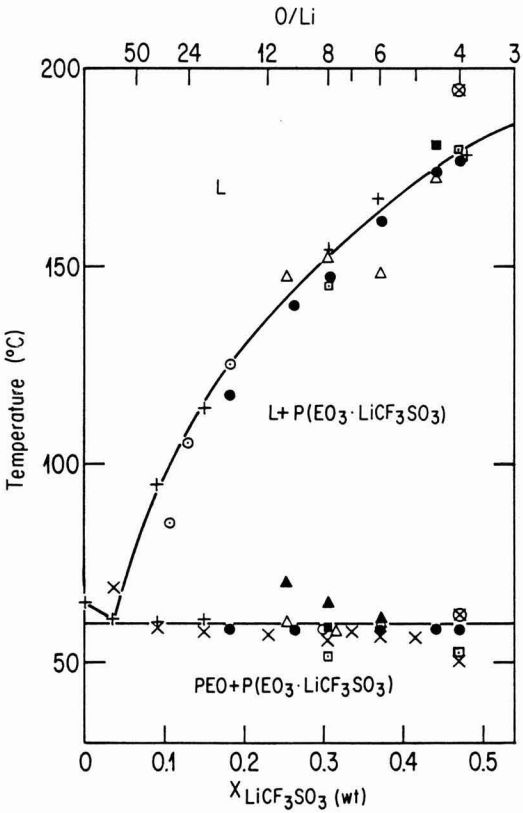


Fig. 1. Phase diagram of the PEO-$LiCF_3SO_3$ system. The transition temperatures were obtained using various experimental techniques: NMR ⊡ (12), DTA or DSC ● (12), △ (18), ⊗ (20), conductivity ○ (12), ▲ (18), optical microscopy ■ (21), and modeling ⊙ (15). This study: optical microscopy +; conductivity ×.

seen very clearly in Fig. 2 which presents a number of photomicrographs of the $POE_{36}LiCF_3SO_3$ mixture. The photos were taken at different increasing temperatures. The transmitted intensity does not decrease before 55°C but by 59°C, two-thirds of the sample has melted, although at this temperature its spherulitic morphology is preserved (Fig. 2a). One degree higher, around 60°C, almost all the sample has melted, leaving a liquid of eutectic composition in equilibrium with a small amount of the intermediate compound, whose spherulitic macrostructure is still conserved. The exposure time of the photo at 61°C (Fig. 2b) was about 30 times longer than for the previous one. The intensity transmitted by the small amount of intermediate compound then decreases gradually (Fig. 2c) to finally disappear at ≃ 95°C. The progressive dissolution of the small fraction of intermediate compound over such a wide temperature range would be hard to observe by DSC. Optical microscopy is therefore a suitable method for determining the liquidus line for compounds of near-eutectic composition, although it is less appropriate for detecting the presence of small amounts of eutectic mixtures in samples with a high salt concentration. The WAXS technique, as may be seen in Fig. 3, proves useful for this purpose. Debye-Scherrer patterns of PEO and $LiCF_3SO_3$ can be seen in Fig. 3a and 3c. The pattern of the $PEO_4LiC^{\neg}{}_3SO_3$ electrolyte in Fig. 3b does not show any lines characteristic of the pure salt. However, it cannot be concluded from this pattern that crystalline PEO is not present in this electrolyte, because two faint lines can be discerned corresponding to the two strongest reflections of PEO.

Histograms of the entire set of WAXS results for the PEO-$LiCF_3SO_3$ system are presented in Fig. 4. A slight addition of $LiCF_3SO_3$ to PEO produces several new diffraction lines, the two strongest being located at 2θ Bragg angles of 0.21 and 0.37 rad. The intensity of these new lines gradually increases, in proportion to the salt content of the mixtures, with an accompanying decrease in the intensity of the characteristic PEO lines. For the $PEO_4LiCF_3SO_3$ electrolyte, only very faint lines corresponding to PEO still can be distinguished. Furthermore the absence of all reflections at 0.34 and 0.58 rad, which are characteristic of salt, bears witness to the absence of free salt in this electrolyte. Thus, in agreement with the DSC and NMR results (10-12), the stoichiometry of the definite compound appears to be less than 4.

Figure 5 depicts the curves of $\log_{10}(\sigma)$ *vs.* $(1/T)$ for electrolytes with a mole ratio between 4 and 100. These total ion conductivity curves were obtained at increasing temperatures (from 25° to 130°C) for electrolytes that had reached their maximum degree of crystallinity and without preheating of the electrochemical cell. This differs from the usual procedure described by Armand *et al.* (3) and Weston and Steele (18, 19) among others, which consists in preheating the electrolyte under study, *in situ*, at a high temperature of 120°-150°C, usually under vacuum, for 16-24h. It was observed during the present work that long thermal cycles up to high temperatures have several effects on electrolytes, including: (i) substantial modifications in the geometry of the sample due to radial

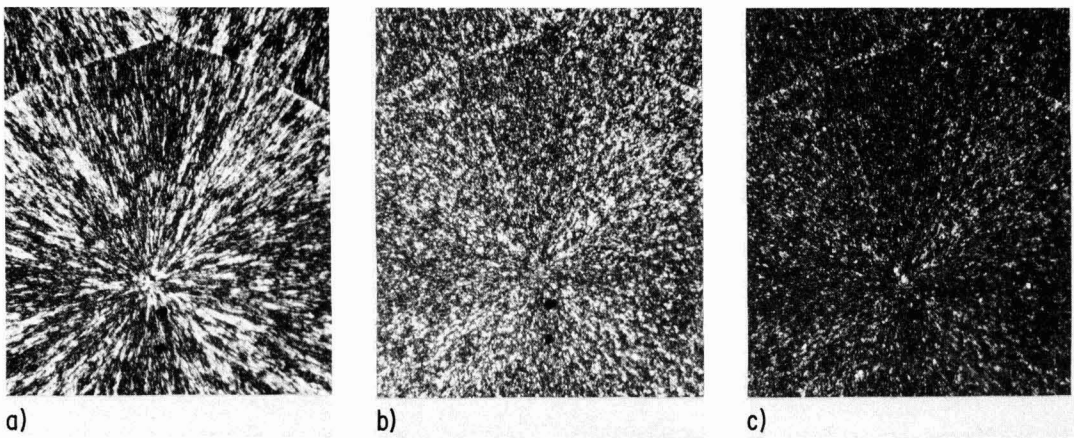


Fig. 2. Photomicrographs of the $PEO_{36}LiCF_3SO_3$ mixture: (a) T = 59°C, (b) T = 61°C, and (c) T = 81°C.

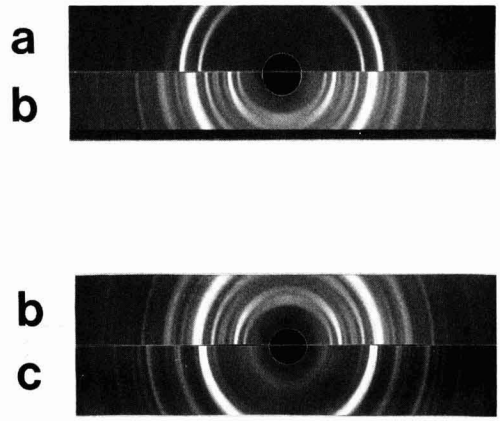


Fig. 3. X-ray diffraction patterns at T = 25°C: (a) PEO, (b) $PEO_4LiCF_3SO_3$ mixture, and (c) $LiCF_3SO_3$.

creeping of the electrolyte; (*ii*) VTF type conductivity behavior due to recrystallization kinetics, which can be very slow (several days, even weeks); (*iii*) modifications in the crystalline macrostructure of intermediate compounds and PEO when either of these are present (see phase diagrams).

For the experimental conditions used, the conductivity measurements therefore seem very representative of the materials characterized. All the curves in Fig. 5 show a knee and two regions of linear dependence of $\log_{10}(\sigma)$ with (1/T). Equation [1] provides an accurate description of these two regions. The temperatures observed for the discontinuities, plotted on Fig. 1, correspond to the eutectic melting temperature, the only exception being $PEO_{100}LiCF_3SO_3$, whose transition temperature was observed to be slightly higher.

It should be noted that the sharp variation in the conductivity observed at the transition temperature is relatively proportional to the mass fraction of the amorphous phase formed when the eutectic melts. Figure 6 contains

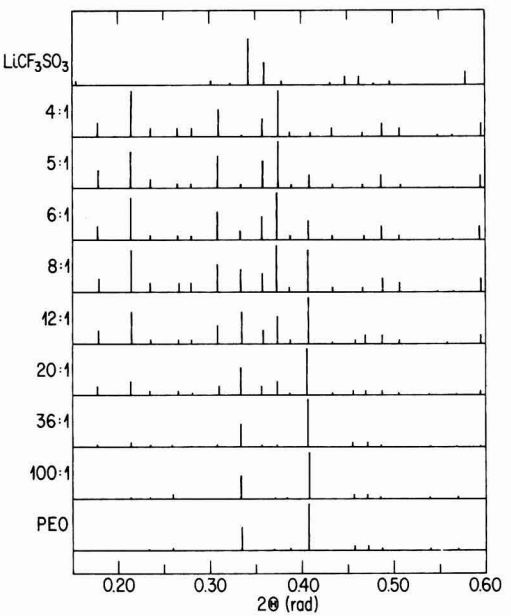


Fig. 4. Histograms of x-ray diffraction patterns for the PEO-$LiCF_3SO_3$ system.

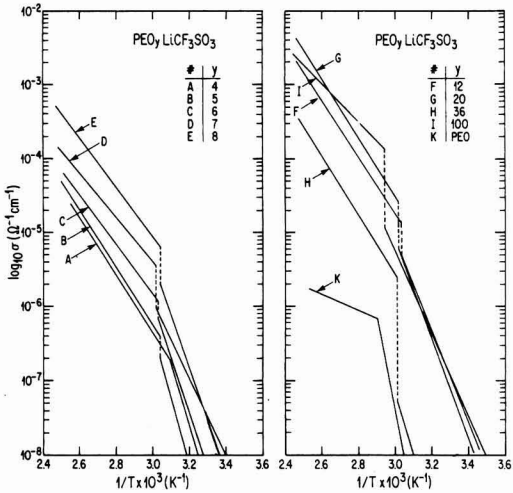


Fig. 5. Variation in total ion conductivity *vs.* inverse temperature for PEO-$LiCF_3SO_3$ based electrolytes with variable mole ratios O/Li(y).

plotted values of the activation energy of the ion conduction mechanism *vs.* the salt concentration for $T > 60$°C. Also included are values published by Berthier *et al.* (11) and Weston and Steele (18), for the same temperature range but under nonequivalent experimental conditions. Since all these systems are close to thermodynamic equilibrium, the activation energy values show good agreement. For PEO-$LiCF_3SO_3$ electrolytes with salt mass fractions of over $X \simeq 0.05$, a single ion transport mechanism seems to be determinant. Its activation energy is $\simeq 0.7$ eV. For temperatures below the transition temperatures, both the recrystallization kinetics and the different crystalline macrostructures can significantly influence the measured conductivity values and, consequently, the activation-energy values of the apparent conduction mechanisms.

Variations in $\log_{10}(\sigma)$ *vs.* the salt mass fraction in the electrolyte are plotted in Fig. 7 for different isotherms at $T > 60$°C. Two conductivity maxima are observed: one at $X \simeq 0.03$ (O/Li $\simeq$ 100), the other at $X \simeq 0.16$ (O/Li $\simeq$ 18). Two phenomenological models have been proposed (10, 12, 15) to describe and predict the conductivity variation of polymer electrolytes *vs.* temperature and salt content. Neither is able to describe the observed dependence (Fig. 7).

The ambiguity related to the conduction mechanism of the PEO-$LiCF_3SO_3$ system was pointed out by Gorecki (10). This system has a two-phase (crystalline and amorphous) composition at $T > 60$°C, with ion mobility occurring mainly in the amorphous phase. However, such electrolytes have an apparently Arrhenius type rather than a VTF behavior. Ratner (22) mentions that if the amorphous chains strong molecular movements are prevented, as in the case of very crystalline polymers, the dependence of configurational entropy on temperature is weak, giving rise to the Arrhenius type behavior observed. The phase diagram in Fig. 1 can be used to evaluate the relative proportions of the amorphous and crystalline phases present at $T > 60$°C. For $PEO_8LiCF_3SO_3$, for example, at least 50% (by wt) of the electrolyte is amorphous although after Ratner's discussion (22) this seems to represent a limiting case. Furthmore, according to Gorecki (10), Berthier *et al.* (11), and Minier *et al.* (12), the conductive amorphous-phase fraction ($L(T)$) is defined by the following equation

$$L(T) = 1/2[3A(T)-1] \quad [3]$$

where $A(T)$ is the amorphous-phase proportion evaluated from the phase diagram. Yet Eq. [3] is equal to zero when

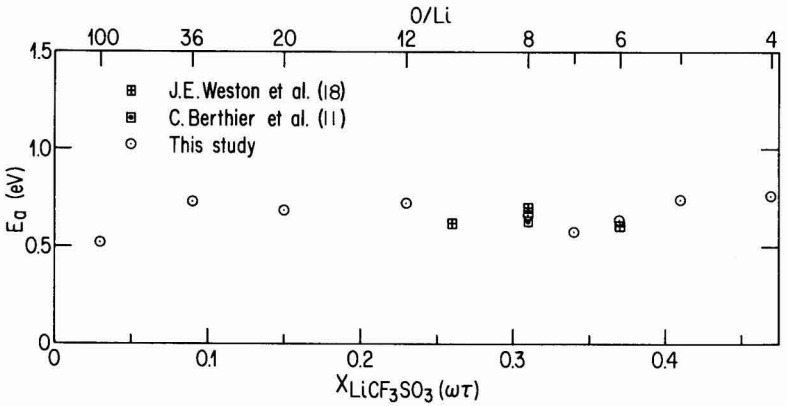


Fig. 6. Variation in activation energy of ion conduction mechanism vs. mass fraction of $LiCF_3SO_3$ in the electrolyte, for 60 < T < 130°C.

$A(T)$ is equal to 1/3 so that the proposed modeling equation

$$\sigma = L(T)N(T)/a(T)T \quad [4]$$

cannot apply to isotherms because temperature (T), scale factor ($a(T)$) and concentration ($N(T)$) are constant, making σ dependent only on $L(T)$, which varies between −0.5 and 1 over the entire concentration range. Sorensen and Jacobsen (15) proposed a model which, although simple, does not account for such significant parameters as variation in ion mobility *vs.* the salt concentration of the conductive amorphous phase. The activation energy of the conduction mechanism, calculated from Sorensen and Jacobsen's experimental results does depend on the salt concentration, contrary to previously reported results (18) and those of this study. The major influence of the amorphous phase on the ionic conductivity is the only point of convergence of the proposed models. A nonmodel-based study (23) suggests that anion mobility in PEO-LiX electrolytes depends on the viscosity of the amorphous phase. A similar conclusion was drawn from results for lithium salts in liquid organic solvents (24). However, such observations fail to take account of all the parameters governing the ion conductivity mechanism in PEO-$LiCF_3SO_3$ polymer electrolytes.

Figure 8 presents the WAXS results obtained at ambient temperature for PEO-$LiClO_4$ electrolytes. It shows very clearly that the addition of salt has two main effects. First it causes additional lines to appear, two of which, at 2θ = 0.18 and 0.29 rad, are very distinct from those for PEO; these can already be seen on the pattern of the $PEO_{20}LiClO_4$ mixture. Secondly, the intensity of two other lines at 2θ = 0.26 and 0.39 increases up to a salt concentration corresponding to that of the PEO_6LiClO_4 mixture. Note that at this stoichiometry there is no diffraction due to pure PEO. For salt concentrations higher than that of PEO_6LiClO_4, several new lines appear, the most intense

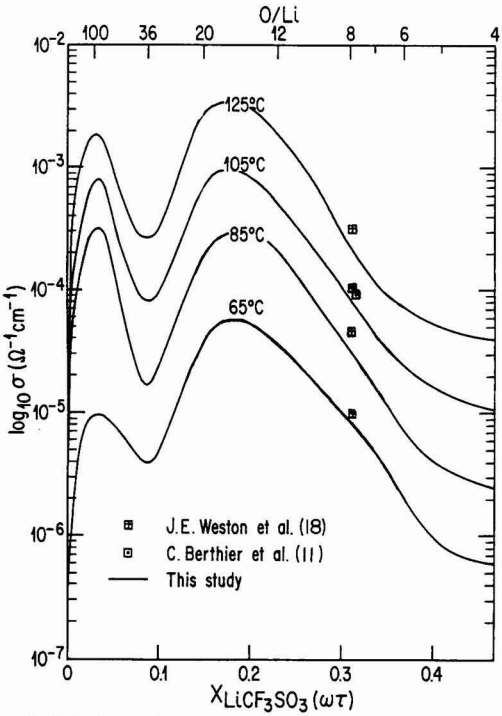


Fig. 7. Isotherms of ion conductivity *vs.* mass fraction of $LiCF_3SO_3$ in the electrolyte.

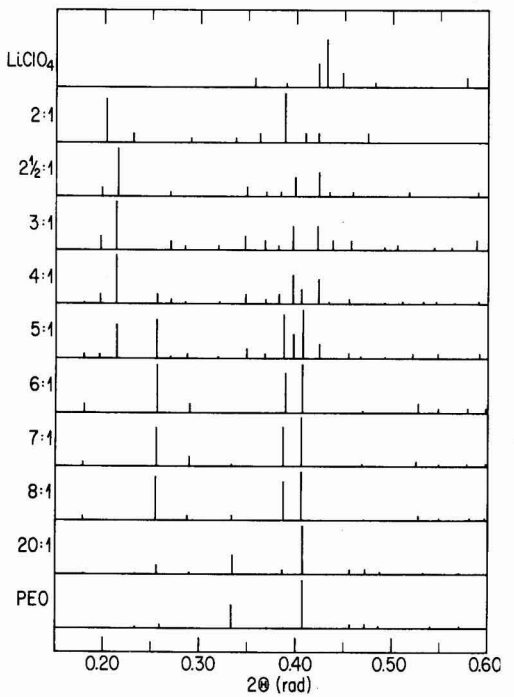


Fig. 8. Histograms of x-ray diffraction patterns for the PEO-$LiClO_4$ system.

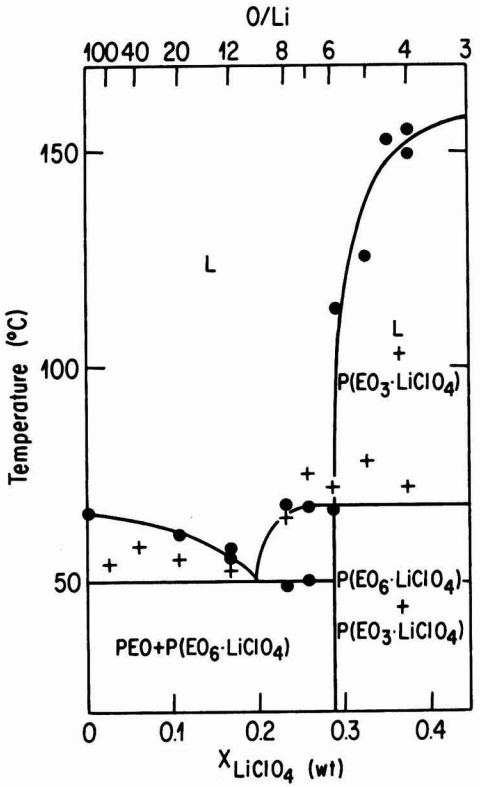


Fig. 9. Phase diagram of the PEO-$LiClO_4$ system: (●) transitions observed by microscopy, (+) transitions observed by conductivity measurements.

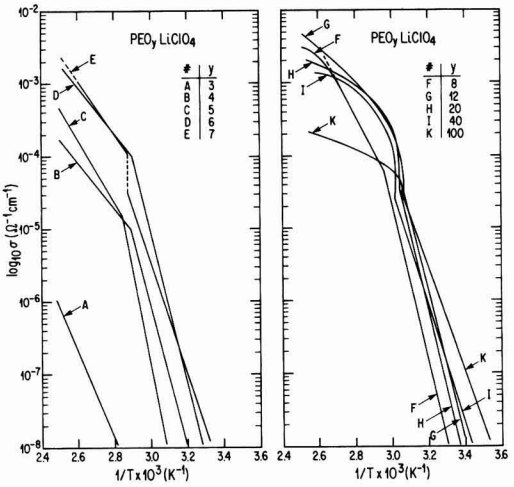


Fig. 10. Variations in total ion conductivity vs. inverse temperature for PEO-$LiClO_4$ based electrolytes with variable mole ratios O/Li(y).

around $2\theta = 0.21$, 0.40, and 0.42 rad. These do not correspond to the lines of lithium perchlorate, and the intensity of these lines increases in proportion to the salt concentration whereas that for the PEO_6LiClO_4 mixture are no longer observed.

The PEO-$LiClO_4$ system does not result in the formation of a intermediate compound with a mole ratio of 4 but in intermediate compounds with stoichiometries of $P(EO_3LiClO_4)$ and $P(EO_6LiClO_4)$, among others. Referring again to Fig. 8, it can be seen that the subsequent addition of salt to $P(EO_3LiClO_4)$ does not produce diffraction lines characteristic of pure lithium salt. As observed, the diffraction pattern of the PEO_2LiClO_4 mixture seems to indicate the presence of a new complex, whose most intense lines are located at $2\theta = 0.20$ and 0.39 rad. It therefore appears that the PEO-$LiClO_4$ system results in the formation of at least three intermediate compounds having different stoichiometries. After characterizing a PEO_8LiClO_4 mixture by DSC and NMR, Gorecki (10) raised the possible existence of two crystalline complexes with different $LiClO_4$ concentrations.

Figure 9 presents phase transitions observed by microscopy when various electrolytes of the PEO-$LiClO_4$ system were heated. These results suggest, in agreement with the WAXS results, the presence of an intermediate compound, $P(EO_6LiClO_4)$, melting at ≃ 65°C. This compound forms with PEO, a eutectic whose melting temperature is ≃ 50°C and whose composition is near $PEO_{10}LiClO_4$. However, no eutectic is observed between the intermediate compounds $P(EO_6LiClO_4)$ and $P(EO_3LiClO_4)$ but rather a monotectic, in other words the limit case where the eutectic composition is no longer distinguishable from the composition of one of the two constituents. The eutectic temperature, therefore, is the same as the melting temperature of $P(EO_6LiClO_4)$. The solubility curve of $P(EO_3LiClO_4)$ is relatively steep around this particular composition before finally reaching the melting temperature of $P(EO_3LiClO_4)$, namely, 160°C. Electrolytes with a salt concentration higher than that of $P(EO_3LiClO_4)$ have not been studied by microscopy.

As observed by optical microscopy and in agreement with the phase diagram in Fig. 9, most of the PEO_8LiClO_4 mixture melts at the eutectic temperature and then slowly dissolves the remaining $P(EO_6LiClO_4)$. This process reaches completion at ≃ 68°C. Weston and Steele (18, 19) report very different behavior for PEO_8LiClO_4 mixtures prepared in air with an anhydrous solvent compared to those prepared with solvents containing up to 2% water (by vol). However, infrared analysis reveals that anhydrous and BDH 99.7% acetonitriles have quasi equivalent water contents. Anhydrous $PEO_{8.2}LiClO_4$ has a reversible behavior in DSC during thermal cycling, which indicates fast recrystallization kinetics. According to DSC and conductivity measurements, this same electrolyte is similar in behavior to PEO-$LiCF_3SO_3$ electrolytes. The authors also report a transition temperature of 137°C for $PEO_{8.2}LiClO_4$, which is close to that obtained upon completion of the $PEO_8LiCF_3SO_3$ dissolution. Analysis of the DSC results reveals an equivalent end of dissolution temperature. It should be recalled that the samples used in the present work were prepared and stored under anhydrous conditions. The results reported here accurately describe the behavior of PEO-$LiClO_4$ electrolytes. Berthier *et al.* (11) have also reported that a PEO_8LiClO_4 mixture prepared under anhydrous conditions is totally amorphous at temperatures above the PEO melting temperature.

The PEO-$LiClO_4$ electrolytes were characterized by ac conductivity measurements. Curves of $\log_{10}(\sigma)$ *vs.* $(1/T)$ are presented in Fig. 10 for various compositions. These conductivity values were obtained during the first temperature rise. For temperatures below the transition temperature, the variation of $\log_{10}(\sigma)$ *vs.* $(1/T)$ shows a linear relationship, adequately described by Eq. [1], for all compositions investigated. The transition temperatures, given in Fig. 9, show agreement with the phase transitions predicted by the phase diagram. For temperatures above the transition temperatures, the variation in $\log_{10}(\sigma)$ *vs.* $(1/T)$ can be described by Eq. [1] for electrolytes with a salt content greater than that of PEO_8LiClO_4. For less concentrated electrolytes the experimental results show a VTF-type dependence but, in view of the restricted temperature range, these results can statistically be linearized in accordance with Eq. [1], with linearity coefficients close

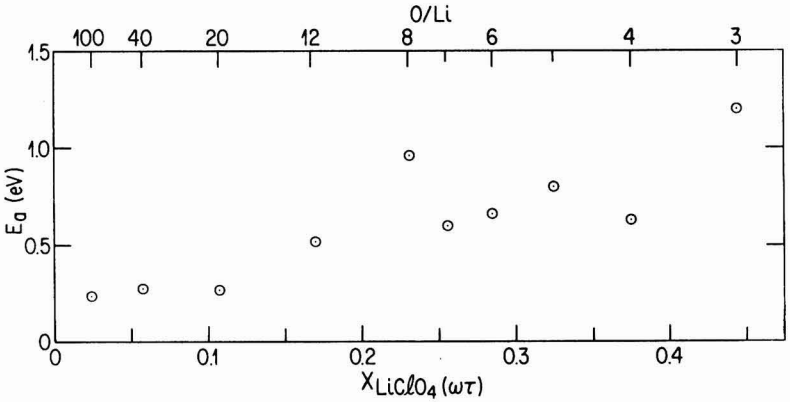


Fig. 11. Variations in activation energy of the ion conduction mechanism vs. mass fraction of $LiClO_4$ in the electrolyte, for $60 < T < 120$°C. For $X < 0.18$, the values were obtained by VTF curve linearization.

to 1 ($r > 0.95$), if account is taken of a jump in the conductivity value at the transition temperature. The calculated activation energies as a function of the salt mass fraction, are presented in Fig. 11. It can be seen that for high mass fractions the activation energy is approximately constant and equal to $\simeq 0.7$ eV whereas for diluted electrolytes, the value is nearer 0.3 eV.

Figure 12 depicts the variation in $\log_{10}(\sigma)$ *vs.* the mass fraction of $LiClO_4$ in the electrolyte for different isotherms at $T > 60$°C. PEO-$LiClO_4$ electrolytes, similar to those based on PEO-$LiCF_3SO_3$, have a high conductivity when diluted and likewise show a maximum for salt mass fractions of 0.18 (O/Li $\simeq$ 12). The latter agreement seems fortuitous, since PEO-$LiCF_3SO_3$ represents a two-phase system at $X \simeq 0.18$, over the temperature range from 65° to 125°C. For the PEO-$LiClO_4$ system at $X \simeq 0.18$, on the other hand, the electrolyte is single phase (amorphous) for the same temperature range. The same figure shows that the conductivity reaches a maximum near the P(EO_6LiClO_4) composition, which could be explained by a particular chain conformation, which is retained in the melted state, favoring the ion mobility. Raising the temperature to $T > 105$°C reduces this maximum quite considerably.

Another lithium salt widely used in lithium batteries is $LiAsF_6$, which is the reason the PEO-$LiAsF_6$ system was studied within the framework of this project. Figure 13 presents histograms of the WAXS diffraction patterns for this system over the range from pure PEO to the pure salt. Here again, the addition of salt causes several new lines to appear, different from those of the pure constituents. The three most intense are located at $2\theta = 0.25$, 0.38, and 0.395 rad, and their intensity increases at higher salt contents up to a mole ratio of 6-7. This is accompanied by a reduction in the intensity diffracted by the PEO, which

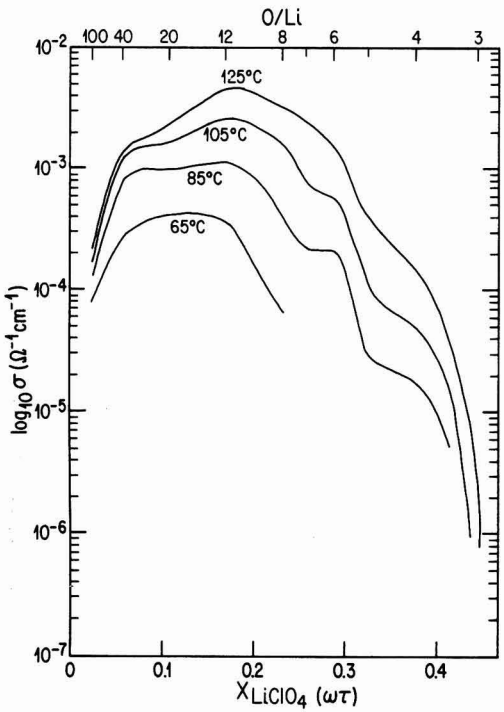


Fig. 12. Isotherms of ion conductivity vs. mass fraction of $LiClO_4$ in the electrolyte.

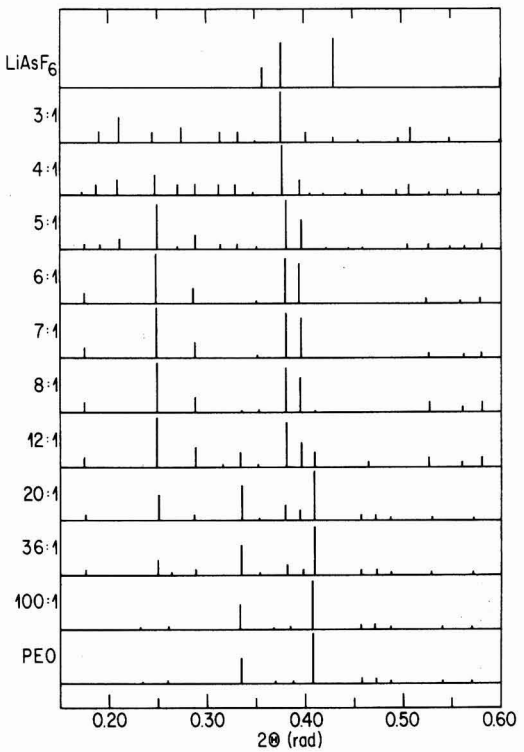


Fig. 13. Histograms of the x-ray diffraction patterns for the PEO-$LiAsF_6$ system.

from PEO_7LiAsF_6 onwards can no longer be detected. For salt concentrations higher than that of PEO_6LiAsF_6, new lines different from those of the $LiAsF_6$ salt appear. For PEO_3LiAsF_6 the characteristic lines of PEO_6LiAsF_6 are no longer observed. The PEO-$LiAsF_6$ system is therefore similar in behavior to the PEO-$LiClO_4$ system in that two intermediate compounds of stoichiometries $P(EO_6LiAsF_6)$ and $P(EO_3LiAsF_6)$ are formed.

Confirmation of the similarity between PEO-$LiAsF_6$ and PEO-$LiClO_4$ is provided by the isomorphism observed in one of their intermediate compounds. Figure 14, in fact, shows that the WAXS pattern of the intermediate compound $P(EO_6LiClO_4)$ is barely affected when the anion ClO_4^- is replaced by the anion AsF_6^-. This is an indication that (*i*) these two compounds are isomorphous, *i.e.*, have the same crystalline structure, and (*ii*) that their unit-cell parameters have very similar values. Actually, as seen in Fig. 14, these unit-cell values are slightly higher for $P(EO_6LiAsF_6)$, in agreement with the estimated volume of the AsF_6^- anion, which is also slightly larger. The difference in the scattering power of these two anions can explain the small variations observed in the relative intensity of the lines for the two intermediate compounds.

The thermal behavior of the PEO-$LiAsF_6$ mixtures corroborates the previous conclusions. As shown in Fig. 15, the different transitions observed by microscopy describe the formation of a eutectic between an intermediate compound, $P(EO_6LiAsF_6)$, and pure PEO. The eutectic temperature is around 55°C. The eutectic composition, approximately $PEO_{22}LiAsF_6$, has a higher salt concentration than the PEO-$LiCF_3SO_3$ system. As in the case of the PEO-$LiClO_4$ system, a sharp increase in the liquidus line of $P(EO_3LiAsF_6)$ is noted. It should be pointed out that the melting temperature of $P(EO_6LiAsF_6)$, *i.e.*, 136°C, is ≃ 70°C higher than that of $P(EO_6LiClO_4)$. Electrolytes with a higher salt content than PEO_3LiAsF_6 proved to be thermally unstable when observed microscopically and during conductivity measurements. The instability is worse in the presence of lithium electrodes and is observed even with electrolytes having a low salt concentration. It is characterized by a blackening of the electrolytes and an increase in conductivity *vs.* time at constant temperature when $T > 90$°C.

Figure 16 presents curves of $\log_{10}(\sigma)$ *vs.* $(1/T)$ for electrolytes with mole ratios between 4 and 100; these curves are described by Eq. [1]. The curve obtained for PEO_4LiAsF_6 is included only as an indication of conductivity values at higher salt concentration. The high apparent activation energy of this particular sample is at least partly due to its thermal degradation. The conductivity

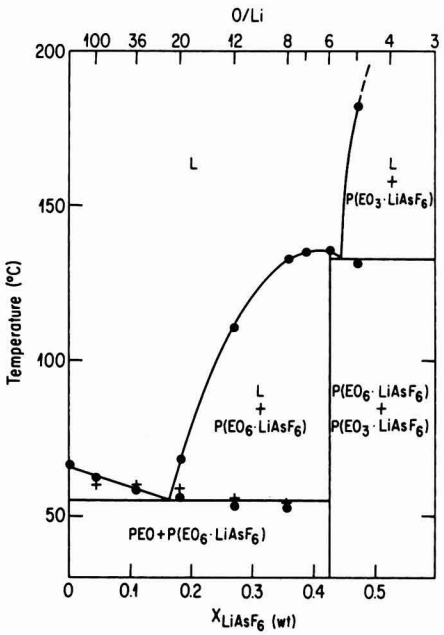


Fig. 15. Phase diagram of the PEO-$LiAsF_6$ system.: (●) transitions observed by microscopy, (+) transitions observed by conductivity measurements.

transition temperatures observed (Fig. 15) correspond to the melting temperatures of the eutectic for electrolytes with a salt concentration higher than that of $PEO_{22}LiAsF_6$, and to the end of dissolution temperature for less concentrated electrolytes. Note that in the case of the PEO-$LiAsF_6$ system as for the PEO-$LiCF_3SO_3$, the variation in conductivity at the transition temperature seems to be proportional to the amorphous-phase fraction formed.

Activation energy values obtained at temperatures higher than the conductivity transition temperatures observed are presented in Fig. 17 but only for electrolytes with a salt mass fraction lower than 0.35 (O/Li > 8). The above-mentioned instability of these electrolytes introduces a degree of nonreproducibility in the conductivity

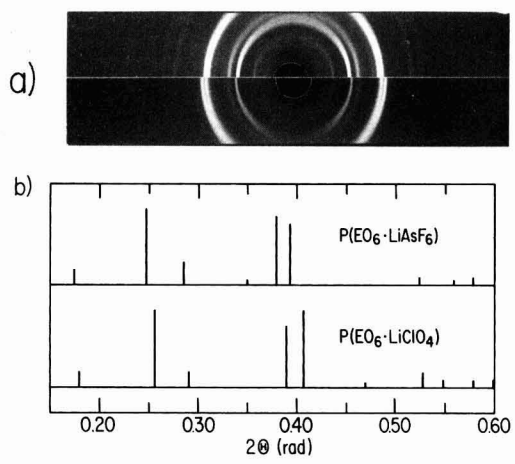


Fig. 14. X-ray diffraction patterns (a) and histogram (b) of the two isomorphous intermediate definite compounds, $P(EO_6LiAsF_6)$ and $P(EO_6LiClO_4)$.

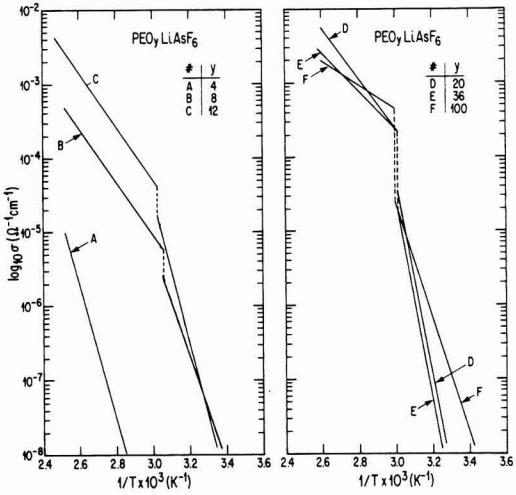


Fig. 16. Variations in total ion conductivity *vs.* inverse temperature for PEO-$LiAsF_6$ based electrolytes with variable mole ratios O/Li(y).

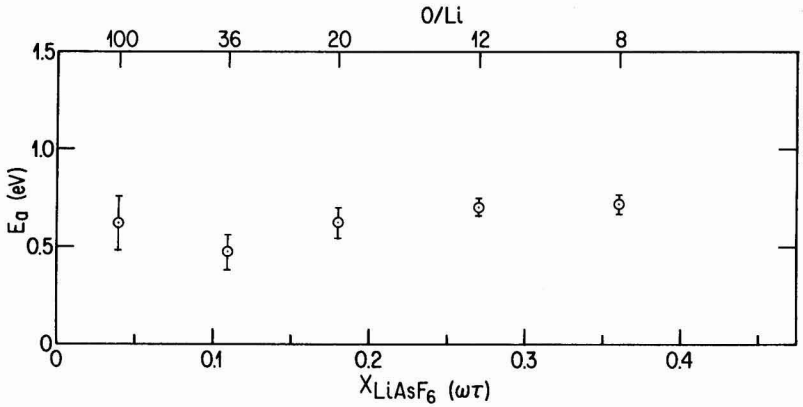


Fig. 17. Variations in the activation energy of the ion conduction mechanism vs. mass fraction of $LiAsF_6$ in the electrolyte, for $60 < T < 120$°C. For $X > 0.35$, the electrolytes are thermally unstable.

behavior, which explains the greater margin of uncertainty for the activation energy values of the PEO-$LiAsF_6$ system conduction mechanism. A more or less constant value of 0.6-0.7 eV can be taken as characteristic.

Figure 18 shows variations in $\log_{10}(\sigma)$ as a function of the salt mass fraction for different isotherms. Here again the conductivity reaches a maximum for diluted electrolytes. A second maximum is noted around $X = 0.18$, as in the case of the two previous systems. Unfortunately, the electrolyte instability makes it impossible to define the variation of $\log_{10}(\sigma)$ for $X > 0.35$ properly.

Discussion

It is known that the interactions between PEO and several organic compounds can be experimentally described by phase diagrams (25-29). Moreover, this seems to be a feature of macromolecular systems (30-35). For PEO-alkaline metal salts, however, the phase-diagram approach has only been applied to the following salts: NaSCN (8), $LiCF_3SO_3$ (10, 12, 15, 18), NaI (10), KSCN (36), NH_4SCN, and $NH_4CF_3SO_3$ (16), all of which are characterized by one or several eutectic reactions. A number of other salts are also known (3, 14, 17, 37, 38) to form intermediate compounds or complexes with PEO but their phase diagrams have not yet been established.

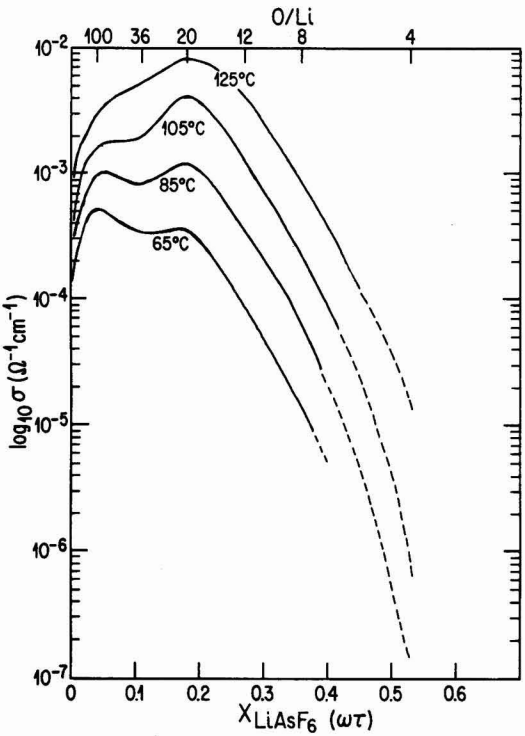


Fig. 18. Isotherms of the ion conductivity vs. mass fraction of $LiAsF_6$ in the electrolyte.

One of the characteristics of two of the systems covered by the present study is the formation of more than one intermediate compound or complex. The same characteristic has also been observed for other PEO-salt systems (10, 16, 17). The presence of several eutectic reactions has been noted for the PEO-$LiClO_4$ and PEO-$LiAsF_6$ systems whereas for the PEO-$LiCF_3SO_3$ system a simple eutectic reaction has been observed, although its salt concentration is far weaker than that of the other two systems. The former both have solubility curves which show that their intermediate compounds, $P(EO_3LiX)$, are not very soluble in molten $P(EO_6LiX)$. This shows up in the phase diagrams under the form of monotectics at a mole ratio of 6. This hexacoordination is kept in the amorphous state over quite wide temperature ranges, characteristic of each system. Only in the case of the PEO-$LiClO_4$ system is the hexacoordination such that the salt is solvated at the minimum temperature where the PEO can be considered as solvent ($T = 70$°C). In the case of the PEO-$LiAsF_6$ system it takes 25 oxygen monomer units to ensure total salt solvation at that temperature whereas at the other extreme some 100 units are needed for the PEO-$LiCF_3SO_3$ system.

The spherulitic growth rate is slow for both hexacoordinated intermediate compounds at equivalent undercooling values. This makes the organization of this crystalline structure a slow process, probably limited by the diffusion of macromolecular chains, as shown by conductivity measurements of these intermediate compounds which show no reduction in the mobility of the ionic species. On the contrary, the conductivity of $P(EO_6LiClO_4)$ shows a slight maximum for $60 < T < 105$°C (Fig. 12), which is consistent with the assumption that an intramolecular helix (6/1) is formed. This assumption agrees with the model proposed by Papke *et al.* (21) which corresponds to a macromolecular chain conformation of the $T_2GT_2\bar{G}$ type. Moreover, the isomorphism and quasi-equivalent unit cell parameters observed for the two $P(EO_6LiX)$ intermediate compounds seem to confirm the existence of a common polymer-cation/arrangement. These compounds together should form solid solutions.

As mentioned in the introduction, the formation of complexes of salt concentrations higher than a mole ratio of 4 has already been identified for lithium and sodium salts. A stoichiometry of 3 seems to be favored for such systems. In fact the experimental results obtained in the present study show that for the PEO-$LiClO_4$ and PEO-$LiAsF_6$ systems, the stoichiometry of at least one of the

intermediate compounds is 3; by analogy, an equivalent stoichiometry is proposed for the intermediate compound $P(EO_3LiCF_3SO_3)$.

When the variation in conductivity *vs.* the salt concentration in the electrolyte is presented in the form of isotherms, it is obvious that simple models cannot explain the conductivity dependence over the entire concentration range. The decrease in conductivity observed when the volume fraction of the crystalline phase increases can be modeled without taking all the determining parameters into account.

The experimental results of this work reveal that the activation energy of the ion conduction mechanism is constant, and consequently independent of the nature of the anion. The limiting step for conductivity is therefore dependent on the cation mobility in the amorphous phase. Supposing the conductivity is purely cationic, this should therefore result in equivalent conductivity values, from one amorphous system to another. But this is not what is observed experimentally and it may hence be deduced that the anionic interactions are not equivalent in each system (39-41). Graphic representations of the variations in equivalent conductance *vs.* concentration (Fig. 19) show a deviation from the expected linear behavior for dissociated 1:1 electrolytes (42). From the low dielectric constant of PEO, $\epsilon = 5$ (43), and the shape of the equivalent-conductance curves, there is reason to believe that ion pairs and/or triplets are formed in PEO-LiX solutions. Note, however, that the results presented here provide no information on anion mobility or their temperature- or concentration-dependence. The only way to determine the respective participation of ions is to make direct measurements of the cation and anion transport numbers.

Study of the variation in the conductivity of two-phase electrolytes calls for special consideration, particularly in the case of $PEO\text{-}LiCF_3SO_3$, which has a two-phase domain extending over wide temperature and concentration ranges. In this situation, two additional parameters may be identified, namely, (*i*) the nature of the nonconductive charges and their dielectric constant, and (*ii*) the effects of the interface between the amorphous and the crystalline phases which, in this specific case, presents very large surface/volume ratios.

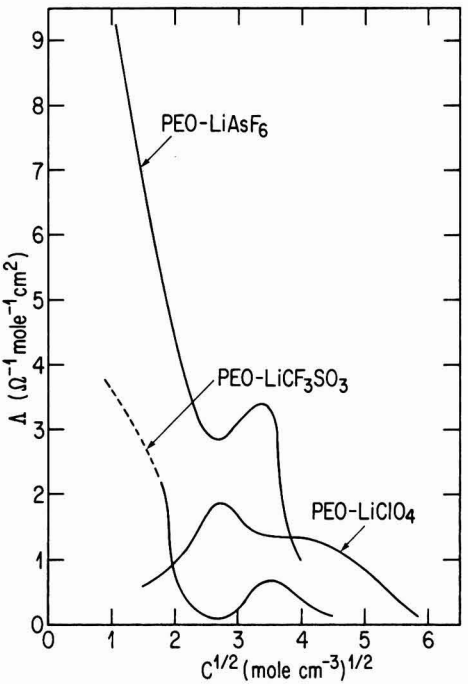


Fig. 19. Equivalent conductance *vs.* salt concentration in the electrolyte for the $PEO\text{-}LiCF_3SO_3$, $PEO\text{-}LiClO_4$, and $PEO\text{-}LiAsF_6$ systems at $T = 105°C$.

Conclusion

The PEO systems studied in this work are subject to the laws of classical thermodynamics and can therefore be described by phase diagrams. However, deviations can be induced by a number of particularities of the molecular nature of the solvent. For example, at temperatures below 60°C a fraction of the electrolyte remains in the amorphous state. PEO-LiX systems therefore can only be considered close to thermodynamic equilibrium in the two-phase or single-phase domain, which implies a liquid phase, as reflected by their conductivity behavior. Efforts to model the conductivity in terms of the various dependent parameters should therefore be based on precise data about the amorphous phase, *i.e.*, transport numbers and the ion pair/triplet formation constants. In the crystalline phase, other parameters such as the morphology or the crystalline macrostructure should be considered together with any deviations from thermodynamic equilibrium following the segregation of ionic species.

Acknowledgments

The authors would like to express their appreciation to Dr. M. Gauthier of IREQ and to Dr. M.B. Armand of the Laboratoire d'énergétique électrochimique of Grenoble, France, for valuable general discussions. The technical assistance of F. Brochu, D. Lebeuf, and R. Bellemare is also acknowledged.

Manuscript submitted May 8, 1985; revised manuscript received Oct. 18, 1985. This was Paper 312 presented at the Toronto, Ontario, Canada, Meeting of the Society, May 12-17, 1985.

Institut de Recherche d'Hydro-Québec assisted in meeting the publication costs of this article.

REFERENCES

1. D. E. Fenton, J. M. Parker, and P. V. Wright, *Polymer*, **14**, 589 (1973).
2. P. V. Wright, *Br. Polymer J.*, **7**, 319 (1975).
3. M. B. Armand, J. M. Chabagno, and M. J. Duclot, in "Fast Ion Transport in Solids," P. Vashishta, J. N. Mundy, and G. K. Shenoy, Editors, pp. 131-136, North-Holland, New York (1979).
4. A. Hooper and J. M. North, *Solid State Ionics*, **9 and 10**, 1161 (1983).
5. M. Gauthier, D. Fauteux, G. Vassort, A. Bélanger, M. Duval, P. Ricoux, J. M. Chabagno, D. Muller, P. Rigaud, M. B. Armand, and D. Deroo, Second International Meeting on Lithium Batteries, Paris, France, April 25-27, 1984.
6. B. L. Papke, M. A. Ratner, and D. F. Shriver, *This Journal*, **129**, 1694 (1982).
7. D. B. James, R. S. Stein, and W. J. Macknight, *Bull. Am. Phys. Soc.*, **24**, 479 (1979).
8. C. Robitaille and J. Prud'homme, 65th Canadian Chemical Congress, Toronto, May 1982, Abstract no. MA-10.
9. T. Hibma, *Solid State Ionics*, **9 and 10**, 1101 (1983).
10. W. Gorecki, Doctoral Thesis, Grenoble University, France (1984).
11. C. Berthier, W. Gorecki, M. Minier, M. B. Armand, J. M. Chabagno, and P. Rigaud, *Solid State Ionics*, **11**, 91 (1983).
12. M. Minier, C. Berthier, and W. Gorecki, *J. Phys.*, **45**, 739 (1984).
13. R. Dupon, B. L. Papke, M. A. Ratner, D. H. Whitmore, and D. F. Shriver, *J. Am. Chem. Soc.*, **104**, 6247 (1982).
14. A. A. Blumberg, S. S. Pollack, and C. A. J. Hoeve, *J. Polym. Sci. (A)*, **2**, 2499 (1964).
15. P. R. Sorensen and T. Jacobsen, *Polymer Bull.*, **9**, 47 (1983).
16. M. Stainer, L. C. Hardy, D. H. Whitmore, and D. F. Shriver, *This Journal*, **131**, 784 (1984).
17. M. Yakoyama, H. Ishihara, I. H. Iwamoto, and H. Tadokoro, *Macromolecules*, **2**, 184 (1969).

18. J. E. Weston and B. C. H. Steele, *Solid State Ionics*, **2**, 347 (1981).
19. J. E. Weston and B. C. H. Steele, *ibid.*, **7**, 81 (1982).
20. D. R. Payne and P. V. Wright, *Polymer*, **23**, 690 (1982).
21. B. L. Papke, M. A. Ratner, and D. F. Shriver, *This Journal*, **129**, 1434 (1982).
22. M. A. Ratner, *Acc. Chem. Res.*, **15**, 355 (1982).
23. D. Fauteux, J. Gauthier, A. Bélanger, and M. Gauthier, Abstract 711, p. 1140, The Electrochemical Society Extended Abstracts, Vol. 82-1, Montreal, Que., Canada, May 9-14, 1982.
24. J. M. Sullivan, D. C. Hanson, and R. Keller, This Journal, **117**, 779 (1970).
25. R. M. Myasnikova, *Vysokomol. soyad.*, **A19**, 564 (1977).
26. R. M. Myasnikova, E. F. Titova, and E. S. Obolonkova, *Polymer*, **21**, 403 (1980).
27. C. C. Gryte, H. Berghmans, and G. Smets, *J. Polym. Sci., Polym. Phys. Ed.*, **17**, 1295 (1979).
28. J. C. Wittmann and R. St. John Manley, *ibid.*, **15**, 2277 (1977).
29. R. E. Prud'homme, *ibid.*, **20**, 307 (1982).
30. P. Smith, G. O. R. Alberda van Ekenstein, and A. J. Pennings, *Br. Polymer J.*, **9**, 258 (1977).
31. A. M. Hodge, G. Kiss, B. Lotz, and J. C. Wittmann, *Polymer*, **23**, 985 (1982).
32. P. Smith and A. J. Pennings, *ibid.*, **15**, 413 (1974).
33. J. C. Wittmann and R. St. John Manley, *J. Polym. Sci., Polym. Phys. Ed.*, **15**, 1089 (1977).
34. P. Smith and A. J. Pennings, *ibid.*, **15**, 523 (1977).
35. M. Farina, G. Di Silvestro, and M. Grassi, *Makromol. Chem.*, **180**, 1041 (1979).
36. S. Marques, Master's Thesis, University of Montreal (1984).
37. D. F. Shriver, B. L. Papke, M. A. Ratner, R. Dupon, T. Wong, and M. Brodwin, *Solid State Ionics*, **5**, 83 (1981).
38. A. A. Brumberg and J. Wyatt, *J. Polym. Sci., Polymer Lett.*, **4**, 653 (1966).
39. H. Cheradame, A. Gandini, A. Killis, and J. F. LeNest, *J. Power Sources*, **9**, 389 (1983).
40. M. Mali, J. Roos, and D. Brinkmann, 22nd Ampere Colloquium, Zurich, Switzerland (1984).
41. S. Clancy and D. F. Shriver, Abstract 625, p. 911, The Electrochemical Society Extended Abstracts, Vol. 84-2, New Orleans, LA, Oct. 7-12, 1984.
42. R. M. Fuoss and F. Accascina, "Electrical Conductance of Electrolytes," Interscience, New York (1959).
43. N. G. McCrum, B. E. Read, and G. Williams, "Anelastic and Dielectric Effects in Polymeric Solids," John Wiley & Sons, New York (1967).

Aluminum Bromide-1-Methyl-3-Ethylimidazolium Bromide Ionic Liquids

I. Densities, Viscosities, Electrical Conductivities, and Phase Transitions

John R. Sanders, Edmund H. Ward, and Charles L. Hussey*

Department of Chemistry, University of Mississippi, University, Mississippi 38677

ABSTRACT

The solid-liquid phase diagram, experimental glass transition points, densities, viscosities, and electrical conductivities of the aluminum bromide-1-methyl-3-ethylimidazolium bromide ionic liquid are reported. Certain compositions of this two-component molten salt are liquid at room temperature. Density, viscosity, and conductivity data were collected over the range of aluminum bromide mole fractions from *ca.* 0.35 to 0.75 and over the range of temperatures from *ca.* 25° to 100°C. Equations are presented that describe both the composition and temperature dependence of the densities and transport properties. Both the viscosities and the conductivities display the non-Arrhenius temperature dependence typically associated with glass forming ionic liquids. Temperature-dependent activation energies are derived for these transport processes by using the Vogel-Tammann-Fulcher equation.

Certain mixtures of aluminum bromide ($AlBr_3$) and 1-methyl-3-ethylimidazolium bromide (MeEtimBr) are liquid at room temperature and display physical and chemical characteristics similar to binary aluminum chloride-organic chloride molten salt systems like aluminum chloride-1-butylpyridinium chloride ($AlCl_3$-BupyCl) and aluminum chloride-1-methyl-3-ethylimidazolium chloride ($AlCl_3$-MeEtimCl). In fact, the $AlBr_3$-MeEtimBr system is the bromide analog of the latter melt. All of these molten salts fall into the same general class of solvents that are known as room-temperature haloaluminate ionic liquids. Several reviews that discuss these haloaluminate melts are available (1-3).

$AlBr_3$-MeEtimBr molten salts may be useful solvents for electrochemical and spectroscopic investigations that are concerned with the chemistry of bromo complexes and related species since they are expected to display adjustable Lewis acid-base characteristics similar to those exhibited by the related chloroaluminate systems. However, the utilization of these melts as solvents presupposes knowledge of their physical properties and liquid range. The study reported herein was undertaken in an effort to obtain information about the densities, transport properties, and phase transitions of this new ionic solvent system. It is the first reported comprehensive investigation of the preparation and physical properties of a room-temperature bromoaluminate melt.

*Electrochemical Society Active Member.

Experimental

Melt preparation.—The preparation of melt samples and the loading of these samples into the apparatus described below were conducted in the nitrogen-filled dry-box system described previously (4). Anhydrous aluminum bromide (Fluka, 98%) was sublimed under vacuum in this dry box a minimum of three times before use. 1-Methyl-3-ethylimidazolium bromide was prepared by combining freshly distilled 1-methylimidazole (Aldrich, 99%) with an excess of ethyl bromide (Baker, reagent grade). The 1-methylimidazole was added dropwise to the chilled ethyl bromide in a flask fitted with a reflux condenser and balloon. (Caution: a rapid exothermic reaction takes place between these components.) The flask was cooled and the resulting white solid was recrystallized twice from anhydrous acetonitrile in Kontes Airless-ware. Great care was taken to avoid exposure of the salt to atmospheric moisture. The melting point of the purified product was 77°C. The aluminum bromide-1-methyl-3-ethylimidazolium bromide melts were prepared by combining precisely weighed quantities of the purified components inside the dry box. These melts appeared somewhat photosensitive and developed a yellow coloration due to the formation of free bromine after exposure to ordinary room light for several days. Appropriate precautions were taken to avoid unnecessary exposure of the $AlBr_3$-MeEtimBr melt to light, and no measurements were performed with highly discolored samples.

Phase transition measurements.—Melting points and glass transition points were determined in sealed quartz EPR tubes with the temperature-controlled apparatus described in a recent publication (5). The experimental methodology used for these experiments was similar to that described previously. In addition, some melting points were measured in melting-point capillaries with a MEL-TEMP apparatus (Laboratory Devices, Cambridge, Massachusetts).

Density measurements.—Densities were determined in a Pyrex dilatometer that was constructed from the bulb of a 10 ml pipette and a length of graduated capillary tubing. The diameter of the capillary tube bore was 1.74 mm, and etched graduations were provided every 1.00 mm on the capillary tube. One end of the capillary tube was attached to the pipette bulb, while a ROTAFLO TF6/13 Teflon vacuum stopcock was affixed to the other end. A similar stopcock was also attached to the remaining end of the pipette bulb. The dilatometer was weighed, filled, and sealed in the dry box, and then weighed again before being placed in an external water bath. The temperature of the water bath was controlled to ±0.1°C by means of either a Precision Scientific Number 66530 constant temperature bath controller or a B. Braun Model 1420 Thermomix immersion controller. The temperature of the bath was monitored with calibrated Brooklyn thermometers. The upper stopcock protruded above the surface of the water bath and was vented to the atmosphere through a drying tube each time the water bath temperature was changed. The dilatometer was calibrated over its entire working volume with distilled water. No corrections for thermal expansion of the apparatus were found necessary over the range of temperatures that was investigated. It was estimated that the density measurements could be reproduced with a precision of ±0.11%.

Viscosity measurements.—Viscosity measurements were made with a modified Cannon-Fenske Number 200 viscometer (Fisher Scientific). The viscometer was made airtight by cutting off both upright tubes horizontally just above the upper reference mark and then attaching the open ends of a U-shaped piece of large-bore Pyrex tubing to the ends of the severed tubes of the viscometer. A ROTOFLO TF6/18 vacuum stopcock was also attached to the viscometer. With these modifications, the viscometer could be filled and sealed in the dry box and then removed and evacuated prior to immersion in the water bath described above. The viscometer was mounted in the water bath on a vertical plate that could be manually rotated in order to recharge the viscometer. The bearings that supported this plate were fitted with a mechanism that stopped the rotation of the plate in a reproducible manner when the viscometer was exactly horizontal. The viscometer was calibrated with freshly distilled ethylene glycol over the appropriate range of temperatures. The viscometer was typically charged with 10.0 ml of sample. The efflux time of the sample in the viscometer was measured with a stopwatch to ±0.1s. The estimated reproducibility of a given measurement was ±2%.

Conductivity measurements.—Conductivity measurements were made with a Yellow Springs Instrument Company Number 3403 dip-type conductivity electrode equipped with platinized platinum-iridium electrodes. When in use, the electrode was sealed airtight with a Teflon bushing and Teflon encased o-ring into a cell

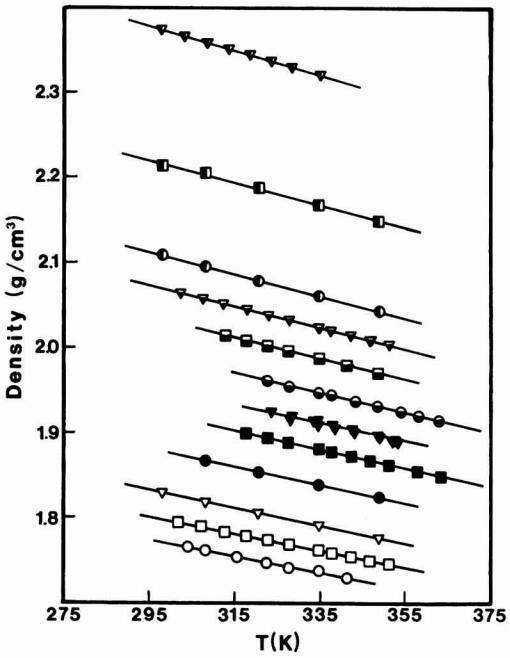


Fig. 2. Density data as a function of temperature for melts with the following mole fractions of $AlBr_3$: (○) 0.3496; (□) 0.3750; (▽) 0.4000; (●) 0.4444; (■) 0.4752; (▼) 0.4996; (◒) 0.5251; (◨) 0.5490 (▼) 0.5750; (◐) 0.6003; (◧) 0.6671; (▼) 0.7500.

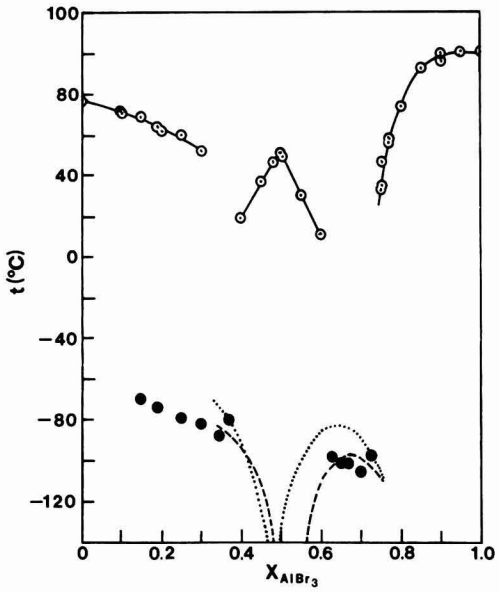


Fig. 1. Phase diagram for the $AlBr_3$-MeEtimBr molten salt system; (○) melting points; (●) experimental glass transition points; (...) T_0 derived from viscosity data; (— — —) T_0 derived from conductance data.

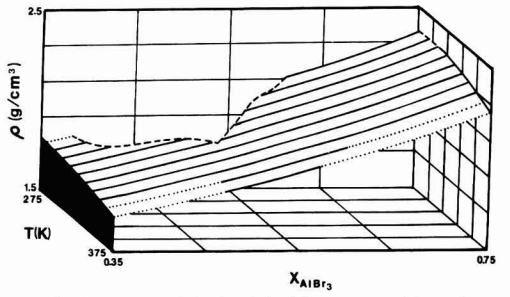


Fig. 3. Dependence of the fitted densities on composition and temperature; (— — —) limit defined by phase transitions; (...) projected data.

constructed by closing the end of a no. 15 Ace-Thred adapter tube. This cell was filled and sealed in the dry box before immersion in the water bath (*vide supra*). Resistance measurements were made at 1 kHz with a General Radio Type 1650-A impedance bridge. Resistance measurements taken at 5 kHz with this bridge and an auxiliary oscillator were identical to those made at 1 kHz. The conductivity cell was calibrated at 25°C with 0.001, 0.01, 0.1, and 1.0*M* solutions of KCl in freshly boiled, distilled, deionized water. The data given by Janz and Tompkins (6) were used to calculate the cell constant, which was *ca.* 1.0. No corrections for changes in the cell constant with temperature were found necessary over the range of temperatures examined in this study. It was determined that the resistance of a given solution at a fixed temperature could be reproduced to within ±0.31%.

Results and Discussion

Phase transitions.—A phase diagram for the $AlBr_3$-MeEtimBr melt system is shown in Fig. 1. Both melting points and glass transition points were obtained for some of the $AlBr_3$-MeEtimBr mixtures. In a few cases, it was not possible to induce the crystallization of certain melts, even at the temperature of liquid nitrogen. Only experimental glass transition points are reported for these liquids.

The phase diagram for the $AlBr_3$-MeEtimBr system is similar in general appearance to that for its chloroaluminate analog (5). However, there are some important temperature differences between the phase diagrams for the bromoaluminate and chloroaluminate systems. The solid-liquid phase transitions for the latter system are considerably lower than those for the former melts for mixtures in the range $0 < x < 0.60$, while the melting points for $AlBr_3$-MeEtimBr mixtures with $x >$ *ca.* 0.75 are lower than those for the corresponding $AlCl_3$-MeEtimCl mixtures. The lower melting points found in very acidic $AlBr_3$-MeEtimBr melts *vs.* those for the $AlCl_3$-MeEtimCl system probably reflect the lower melting point of $AlBr_3$ (Al_2Br_6) relative to that of $AlCl_3$ (Al_2Cl_6).

Densities.—Experimental density data for all of the melt compositions examined in this study are shown in Fig. 2. Experimental densities, ρ, were found to vary linearly with temperature. Data for each composition were fitted to linear equations of the form

$$\rho = a + bT \qquad [1]$$

The solid lines that appear in Fig. 2 were calculated for each composition from the values of a and b generated from these fits. It was found that the variation of the parameters a and b with x could be represented by polynominals of the type

$$a = a_0 + a_1x + a_2x^2 + a_3x^3 + \ldots . \qquad [2]$$

$$b = b_0 + b_1x + b_2x^2 + b_3x^3 + \ldots . \qquad [3]$$

A third-order polynominal was needed in order to adequately represent the variation of a and b with x in melts with compositions in the range $0.50 < x \leq 0.75$ (acidic melts), while a second-order polynominal was found to be sufficient for melts in the range $0.30 \leq x \leq 0.50$ (neutral and basic melts). The parameters obtained from nonlinear least squares fits of a and b as a function of x are collected in Table I. These parameters reproduced the experimental density data in acidic melts with a standard deviation, s, of 1.69×10^{-3} and in neutral and basic melts with $s = 1.81 \times 10^{-3}$. The standard deviations reported here and elsewhere (*vide infra*) were corrected for the total number of model parameters used to fit the experimental data in each case. Figure 3 shows a three-dimensional plot, produced from the constants in Table I with Eq. [1] to [3], which gives a perspective of the variation of density with composition and temperature and, in addition, delineates the range in which densities were determined.

Viscosity.—The experimental kinematic viscosities for $AlBr_3$-MeEtimBr mixtures were converted to absolute viscosities with the density data presented above. Arrhenius plots for the absolute viscosities, η, are shown in Fig. 4, and it can be seen that ln η does not vary linearly with $1/T$. Similar behavior was noted for the viscosities of the $AlCl_3$-MeEtimCl and related 1,3-dialkylimidazolium chloride-based chloroaluminate molten salts (5). This non-Arrhenius behavior is a characteristic of glass forming melts (7). Therefore, the logarithmic form of the three-pa-

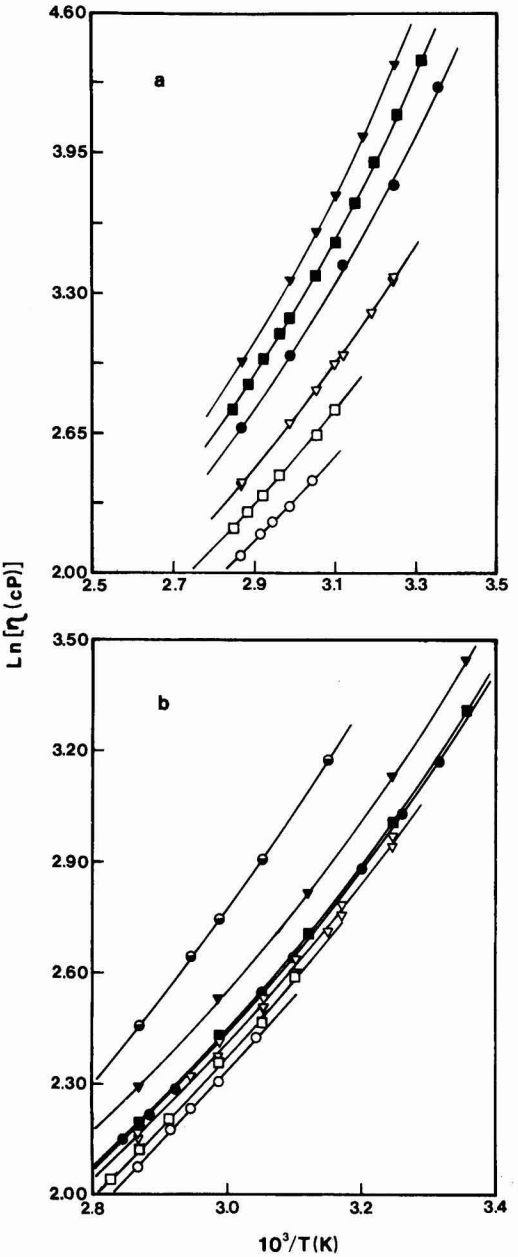


Fig. 4. Absolute viscosity data as a function of temperature for melts with the following mole fractions of $AlBr_3$: (a) (▼) 0.3496, (■) 0.3750, (●) 0.4000, (▽) 0.4450, (□) 0.4752, (○) 0.4998; (b) (○) 0.4998, (□) 0.5251, (▽) 0.5490, (●) 0.5750, (■) 0.6003, (▼) 0.6671, (◒) 0.7498.

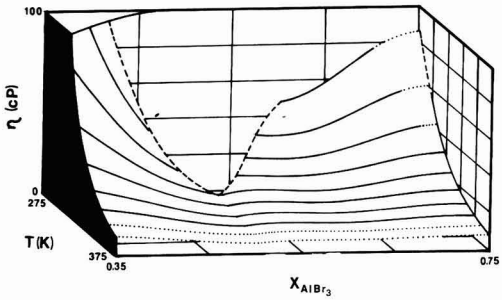


Fig. 5. Dependence of the fitted values of the absolute viscosities on composition and temperature; (— — —) limit defined by phase transitions; (...) projected data.

rameter Vogel-Tammann-Fulcher (VTF) equation (7) was used to represent the variation of the absolute viscosities as a function of the absolute temperature

$$\ln \eta = k_\eta/(T - T_0) + 1/2 \ln T + \ln A_\eta \quad [4]$$

where k_η, T_0, and $\ln A_\eta$ are constants in this equation. The product, $k_\eta R$, where R is the universal gas constant, is sometimes identified with the Arrhenius activation energy, and T_0, often designated as the "ideal" glass transition temperature, is given quasi-theroetical significance through the free volume theory of Cohen and Turnbull (8) and the configurational entropy approach of Adam and Gibbs (9). However, a detailed study of these parameters was not the goal of this investigation.

It was determined that each of the three parameters in Eq. [4] could be fitted as a function of x to cubic polynominal equations of the form

$$f(x) = c_0 + c_1x + c_2x^2 + c_3x^3 \quad [5]$$

in neutral and basic melts and to second order equations of the form

$$f(x) = c_0 + c_1/x + c_2/x^2 \quad [6]$$

in acidic melts. Values generated for the constants in these equations are collected in Tables II and III. Equations [4] and [5], with the appropriate parameters from Table II, reproduced the experimental viscosity data in neutral and basic melts with $s = 2.71 \times 10^{-2}$, while a value of $s = 4.63 \times 10^{-2}$ was obtained in acidic melts by using Eq. [4] and [6] and the parameters in Table III.

A three-dimensional plot of viscosity as a function of temperature and composition, which delineates the range over which viscosity was determined as a function of these two variables, is depicted in Fig. 5. Qualitatively, the viscosities of the melt rise from a poorly defined minimum at $x = 0.50$ as x is increased or decreased from this value. The irregular increase in the viscosity in acidic melt as x is increased was experimentally reproducible and did not appear to be the result of an artifact in the experimental method or the procedure used to fit the data. These results were somewhat different from those reported for the chloroaluminate analog (5) where the viscosity was found to decrease continuously with x.

Conductivity.—Experimental specific conductivity values, κ, were converted to equivalent conductivities by using the equation

$$\Lambda = \kappa M_E/\rho \quad [7]$$

where M_E is the equivalent weight of the molten mixture and is given by the equation

$$M_E = 191.08 + 266.71\, x/(1 - x) \quad [8]$$

This method for representing the molecular weight of a haloaluminate melt is advantageous because it takes into consideration the number of ions in the mixture (5, 10).

Arrhenius plots for the equivalent conductance of the $AlBr_3$-MeEtimBr melt are shown in Fig. 6. Like viscosity

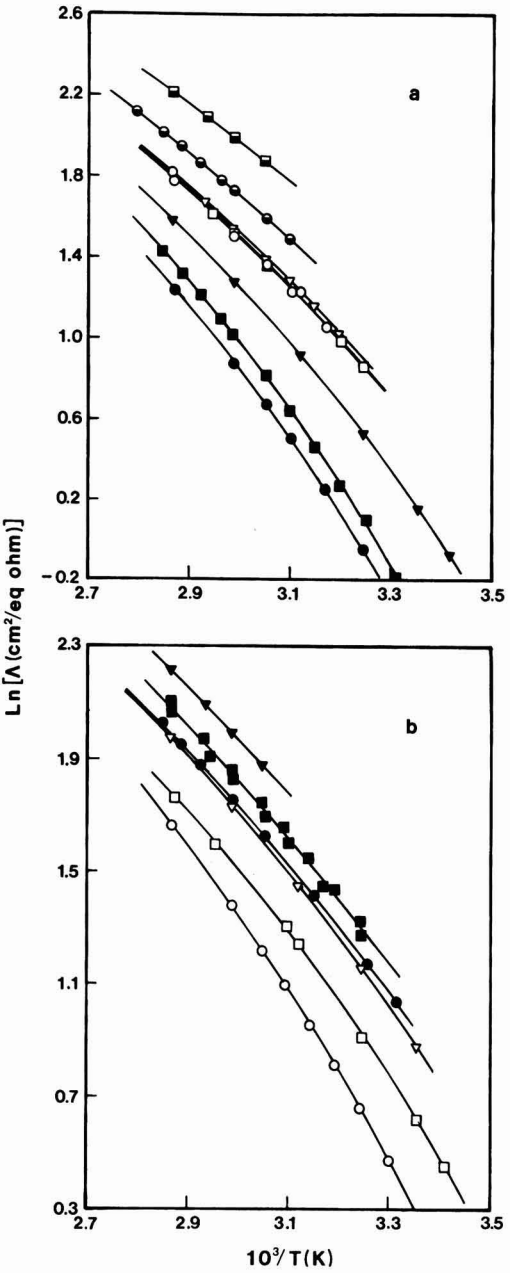


Fig. 6. Equivalent conductivity data as a function of temperature for melts with the following mole fractions of $AlBr_3$: (a) (●) 0.3493, (■) 0.3750, (▼) 0.4000, (○) 0.4444, (▽) 0.4450, (□) 0.4454, (◒) 0.4752, (◓) 0.4999; (b) (▼) 0.4999, (■) 0.5490, (●) 0.5750, (▽) 0.6003, (□) 0.6671, (○) 0.7500.

(*vide supra*), the equivalent conductance exhibits non-Arrhenius behavior. Therefore, the equivalent conductivities were fitted to the VTF equation for equivalent conductance (7)

$$\ln \Lambda = -k_\Lambda/(T - T_0) - (1/2) \ln T + \ln A_\Lambda \quad [9]$$

As for viscosity, the parameters in Eq. [9] were fitted as a function of x to Eq. [5] in basic and neutral melt and to Eq. [6] in acidic melt. The values of the constants that re-

Table I. Parameters for density, Eq. [1]-[3]

Range	a_0	a_1	a_2	a_3
$0.30 \le x \le 0.50$	1.0588	3.8594	−2.8945	0.00
$0.50 < x \le 0.75$	−5.8410	3.7009 × 10¹	−5.6629 × 10¹	3.0474 × 10¹

Range	b_0	b_1	b_2	b_3
$0.35 \le x \le 0.50$	1.2907×10^{-3}	-1.0448×10^{-2}	1.1519×10^{-2}	0.0
$0.50 < x \le 0.75$	1.7946×10^{-2}	-9.0089×10^{-2}	1.4121×10^{-1}	-7.4099×10^{-2}

Table II. Parameters for conductivity and viscosity in basic melt, $0.35 \le x \le 0.50$, Eq. [4], [5], and [9]

		c_0	c_1	c_2	c_3
Conductivity	T_0	-4.0191×10^1	1.9867×10^3	-4.5874×10^3	2.4562×10^3
	k_Λ	3.3582×10^3	-2.0888×10^4	4.8630×10^4	-3.3051×10^4
	$\ln A_\Lambda$	-2.8631×10^1	1.8526×10^2	-4.4919×10^2	3.4788×10^2
Viscosity	T_0	2.1405×10^3	-1.5128×10^4	3.9396×10^4	-3.4596×10^4
	k_η	-1.4147×10^4	1.1709×10^5	-3.0743×10^5	2.6769×10^5
	$\ln A_\eta$	-1.3581×10^1	1.8522×10^2	-5.1772×10^2	4.7652×10^2

Table III. Parameters for conductivity and viscosity in acidic melt, $0.50 < x \le 0.75$, Eq. [4], [6], and [9]

		c_0	c_1	c_2
Conductivity	T_0	-8.8020×10^2	1.3485×10^3	-4.2335×10^2
	k_Λ	9.3588×10^3	-1.1072×10^4	3.4117×10^3
	$\ln A_\Lambda$	-3.2068×10^2	3.5633×10^1	-1.0983×10^1
Viscosity	T_0	-3.8691×10^2	7.6383×10^2	-2.6176×10^2
	k_η	6.6201×10^3	-7.8145×10^3	-2.5214×10^3
	$\ln A_\eta$	2.5515×10^1	-2.2656×10^1	7.3019

sulted are collected in Tables II and III. These equations and the fitted model parameters reproduced the experimental data in acidic melts with $s = 4.58 \times 10^{-2}$ and in basic melt and neutral melts with $s = 5.13 \times 10^{-2}$.

A three-dimensional plot that delineates the range of composition and temperature over which conductance was studied is shown in Fig. 7. The maximum conductivity of the $AlBr_3$-MeEtimBr system occurs at exactly $x = 0.50$, and the conductivity decreases noticeably as x is increased or decreased from this composition. The organic cation has been determined to transport over 70% of the charge in the $AlBr_3$-MeEtimBr (11) and $AlCl_3$-MeEtimCl systems (4, 12, 13). In addition, the formation of ion pairs and larger aggregates between the organic cation and the anions in basic melt, especially bromide ion, has been shown to be important (14). Therefore, the decrease in equivalent conductance shown in Fig. 7 as x is decreased from 0.50 probably results from a decrease in the mobility of the organic cation as the relatively weak aggregates that involve $MeEtim^+ \ldots AlBr_4^-$ ion pairs are replaced by those containing the stronger $MeEtim^+ \ldots Br^-$ ion-pair interactions. The replacement of relatively weak aggregates by those with stronger anion-cation interactions may also account for the concomitant increase in viscosity that is found when x is decreased in basic melt. The decrease in the equivalent conductance and increase in viscosity with increasing x found in acidic melts cannot be explained in this fashion since ion-ion interactions are believed to become less important as x is increased in this composition region (14). The factors that might lead to this behavior are under investigation at the present time.

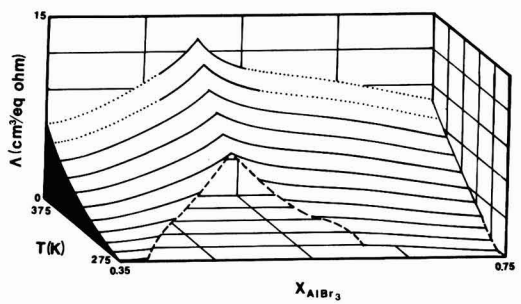


Fig. 7. Dependence of the fitted values of the equivalent conductivities on composition and temperature; (— — —) limit defined by phase transitions; (...) projected data.

Glass transitions.—The values of T_0 that resulted from the fits of Eq. [4] and [9] to the absolute viscosities and equivalent conductivities are shown in Fig.1. The composition range in which T_g and T_0 overlap in this figure is small, and the number of melt compositions examined was not sufficient to define the derived values of T_0 precisely. Therefore, it is difficult to draw detailed conclusions about the relationship between T_0 and T_g in this system. However, it can be seen that the T_0 values from viscosity and conductivity are in reasonable agreement with one another, vary with composition in a similar manner, and correspond in magnitude to the T_g values.

An interesting feature found in both of the plots of T_0 *vs.* x (Fig. 1) is the apparent minimum located proximate to $x = 0.50$. Easteal and Angell (15) reported a similar minimum in plots of T_0 *vs.* mole percent $ZnCl_2$ for the $ZnCl_2$-pyridinium chloride system at the composition that corresponds by stoichiometry to the $ZnCl_4^{2-}$ ion. Therefore, the minima that are suggested in Fig. 1 are probably associated with the formation of the $AlBr_4^-$ ion at $x = 0.50$.

Activation energies.—Temperature-dependent activation energies for the two transport processes discussed above can be obtained by performing partial differentiation of Eq. [4] and [9] with respect to T and noting that $E_{a,\eta} = RT^2(\partial \ln \eta/\partial T)$ and $E_{a,\Lambda} = RT^2(\partial \ln \Lambda/\partial T)$ (16). This operation yields the following expressions

$$E_{a,\eta} = -Rk_\eta T^2/(T - T_0)^2 + RT/2 \quad [10]$$

$$E_{a,\Lambda} = Rk_\Lambda T^2/(T - T_0)^2 - RT/2 \quad [11]$$

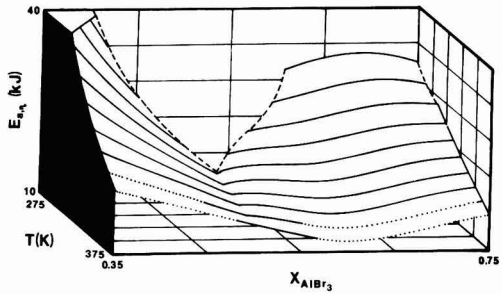


Fig. 8. Variation of the activation energy for viscous flow with composition and temperature; (— — —) limit defined by phase transitions; (...) projected data.

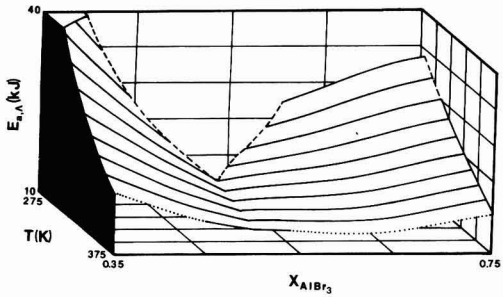


Fig. 9. Variation of the activation energy for electrical conduction with composition and temperature; (— — —) limit defined by phase transitions; (...) projected data.

Three-dimensional plots of $E_{a,\eta}$ and $E_{a,\Lambda}$ as a function of temperature and composition, constructed from the data in Tables II and III with Eq. [10] and [11], are shown in Fig. [8] and [9], respectively. The relatively close correspondence between the calculated values of $E_{a,\eta}$ and $E_{a,\Lambda}$ noted in these figures suggests that the energy barriers for viscous flow and electrical conduction are comparable in the $AlBr_3$-MeEtimBr melt system. Similar results have been reported for the chloroaluminate analog (5), several aluminum chloride-1-alkylpyridinium halide melts (10), and molten 1-methylpyridinium bromide and iodide (17).

Both activation energies exhibit an expected minimum with composition around $x = 0.50$ at low temperatures. Another less distinct minimum is also evident in acidic melt in the middle to upper portions of the temperature range (Fig. 8 and 9). It is also apparent that $E_{a,\eta}$ tends toward a maximum with x at low temperatures in acidic melt but transitions to a minimum at higher temperatures (Fig. 8). A similar maximum may also be present in the plot for $E_{a,\Lambda}$ at temperatures below those examined in this study. It can be speculated that this behavior may result from changes in the mechanisms for viscous flow and conduction with temperature.

Acknowledgments

The authors wish to express their gratitude to Dr. J. S. Wilkes and Dr. A. A. Fannin, Jr. of the F. J. Seiler Research Laboratory for helpful discussions about this work and for use of their facilities to obtain the phase transition data. We are indebted to Mr. K. G. Ray for verifying the experimental glass transition points. This work was supported by the National Science Foundation through Grant no. CHE 8412730.

Manuscript submitted July 10, 1985; revised manuscript received Nov. 6, 1985. This was Paper 488 presented at the Las Vegas, NV, Meeting of the Society, Oct. 13-18, 1985.

REFERENCES

1. H. L. Chum and R. A. Osteryoung, in "Ionic Liquids," D. Inman and D. G. Lovering, Editors, pp. 407-423, Plenum Press, New York (1981).
2. C. L. Hussey, *Adv. Molten Salt Chem.*, **5**, 185 (1983).
3. R. J. Gale and R. A. Osteryoung, in "Molten Salt Techniques," Vol. 1, D. G. Lovering and R. J. Gale, Editors, pp. 55-78, Plenum Press, New York (1983).
4. C. L. Hussey and H. A. Øye, *This Journal*, **131**, 1621 (1984).
5. A. A. Fannin, Jr., D. A. Floreani, L. A. King, J. S. Landers, B. J. Piersma, D. J. Stech, R. L. Vaughn, J. S. Wilkes, and J. L. Williams, *J. Phys. Chem.*, **88**, 2614 (1984).
6. G. J. Janz and R. P. T. Tompkins, *This Journal*, **124**, 55C (1977).
7. C. A. Angell and C. T. Moynihan, in "Molten Salts Characterization and Analysis," G. Mamantov, Editor, pp. 315-375, Marcel-Dekker, New York (1969).
8. M. H. Cohen and D. Turnbull, *J. Chem. Phys.*, **31**, 1164 (1959).
9. G. Adam and J. H. Gibbs, *ibid.*, **43**, 139 (1965).
10. R. A. Carpio, L. A. King, R. E. Lindstrom, J. C. Nardi, and C. L. Hussey, *This Journal*, **126**, 1644 (1979).
11. J. R. Sanders and C. L. Hussey, Unpublished data.
12. C. L. Hussey, J. R. Sanders, and H. A. Øye, *This Journal*, **132**, 2156 (1985).
13. C. J. Dymek, Jr., and L. A. King, *This Journal*, **132**, 1375 (1985).
14. J. S. Wilkes, C. L. Hussey, and J. R. Sanders, *Polyhedron*, In press.
15. A. J. Easteal and C. A. Angell, *J. Phys. Chem.*, **74**, 3987 (1970).
16. C. A. Angell, *ibid.*, **68**, 218 (1964).
17. D. S. Newman, R. T. Tillack, D. P. Morgan, and W.-C. Wan, *This Journal*, **124**, 856 (1977).

Electron Transfer at the WO_3-Electrolyte Interface under Controlled Mass Transfer Conditions

Jean Desilvestro* and Michael Grätzel

Institut de Chimie Physique, Ecole Polytechnique Fédérale de Lausanne, CH-1015 Lausanne, Switzerland

Tamás Pajkossy

Central Research Institute for Physics, Hungarian Academy of Sciences, H-1525 Budapest, POB 49, Hungary

ABSTRACT

The reduction of Fe^{3+} and Ce^{4+} at a polycrystalline n-WO_3 rotating disk electrode was studied in the dark as a function of potential, concentration of oxidized species, and rotation frequency. The measured current densities are shown to fit reasonably well to a model which involves electron transfer from the bulk of the semiconductor to the surface (rate constant K_1) and from the surface to the solution (K_2) and which involves transport of the oxidized species to the electrode surface (K_3). The dependence of K_1 and K_2 on electrode potential reveals that a significant portion of the potential drop occurs over the Helmholtz layer, indicating partial Fermi level pinning.

Photocatalysis and photosynthesis with powdered semiconductor particles might be a promising approach to detoxifying waste waters and to producing "useful" chemicals like H_2 at the same time (1). Recently, we started to investigate the local cell processes on these microelectrodes by modeling the particle suspensions with a single "macroelectrode" of the same material (2). We were able to show that the kinetics of photoreactions on particles of a typical diameter in the micron range is governed by light intensity, concentration of the redox species, pH, and mass transfer conditions in the same way as on illuminated electrodes under open-circuit conditions. From the local cell processes, it is obvious that for efficient photoreactions in heterogeneous media, the transfer of majority carriers from the semiconductor ("dark reaction") is as important as the transfer of photogenerated minority carriers ("photoreaction"). Thus, we became interested in the dark current characteristics of semiconductor electrodes in order to get a better understanding of the charge transfer mechanism between the conduction band and the solution.

Dark currents on semiconductor electrodes have been studied for a long time (3). Often the reported Tafel slopes were much higher than 59 mV/decade expected for a direct electron transfer from the semiconductor to the solution. Gomes *et al.* (4) observed that reduction currents on TiO_2 became more and more concentration independent with increasing concentration of the electron acceptor. They proposed a model in which the electron is transferred first in a concentration independent step from the conduction bandedge to an intermediate energy level on the surface ("surface state"), and then into the solution (Fig. 1). The rate constants for the two processes are k_1 and k_2. Gomes *et al.* also noticed that mass transfer does not influence the dark currents at high enough concentrations of the oxidized species. Salvador and Gutiérrez (5) could exclude mass transfer effects on cathodic currents at $SrTiO_3$ by strongly agitating the solution. Iwanski *et al.* (6) studied the reduction of $Fe(CN)_6^{3-}$ at a n-Fe_2O_3 rotating disk electrode (RDE) at just one rotation frequency (1800 rpm). They could estimate values for the rate constants k_1 and k_2. In a somewhat different approach, Chazalviel (7) assumed that the charge transfer occurs via a continuum of surface states between conduction and valence band.

In this work, we studied for the first time the transfer of majority carriers from a semiconductor to a redox system by systematically taking into account the mass transport to a RDE at different rotation frequencies ω. In a preliminary evaluation, we showed that Koutecky-Levich plots (j^{-1} *vs.* $\omega^{-1/2}$) and plots of reciprocal current densities *vs.* reciprocal bulk concentrations were reasonably linear and that quantities proportional to k_1 and k_2 could be obtained (8). In the following, we want to present a more rigorous procedure by taking into account the coupling of mass transport to the RDE and the electrode reaction. From studying the potential dependence of the rate constants, we expect information, not only regarding the reaction rates, but also regarding the potential drops in the semiconductor space charge layer and in the Helmholtz layer.

As a continuation of our previous studies (2a, 2c, 9), the n-WO_3/Fe^{3+} system (pH 2.0) was chosen. In addition, measurements were carried out at pH 0.0 and with another electron acceptor (Ce^{4+}).

Experimental

WO_3 (Johnson and Matthey, 99.998%), $Fe(NO_3)_3 \cdot 9H_2O$ (Fluka, > 99%), $Ce(SO_4)_2$ (Ventron, 99.9%), $HClO_4$ (70%, Fluka puriss.p.a.), KNO_3 (Merck, > 99%), were used as supplied. Deionized water was distilled twice. Titanium (grade 2) was obtained from Kobe Steel Limited via Sibner-Hegner (Zürich).

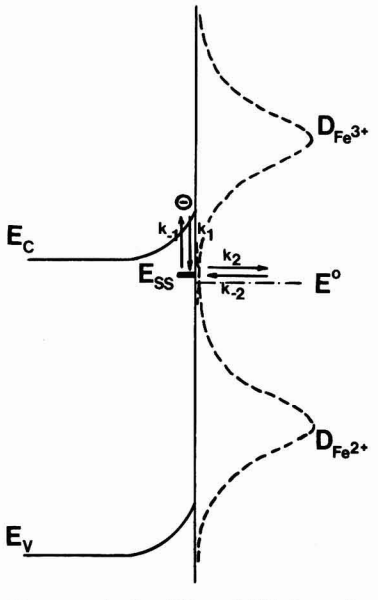


Fig. 1. Charge transfer from WO_3 to $Fe^{3+/2+}$ via a surface state of the energy E_{ss}. D: Density of acceptor and donor states.

*Electrochemical Society Student Member.

The preparation of polycrystalline n-WO_3 electrodes has been reported previously (2a, 9). A WO_3 layer of ~10 μm was deposited on a Ti rod of 4 mm diameter with a thread on one end. The electrode was embedded in a cylindrical piece of Teflon (diameter 15 mm) and connected to an Analytical Rotator "ASR" from Pine Instrument Company. The working electrode was positioned in the center of a 50 ml cell about 2 cm above the capillary of the saturated calomel electrode (SCE). The cylindrical Pt gauze counterelectrode (~150 cm²) was not separated from the working electrode by a membrane in order to partially reoxidize the reduced product during long runs. All solutions were prepared directly in the cell by adding the Fe-salt to 0.01N $HClO_4$ or 1.0N $HClO_4$ or $Ce(SO_4)_2$ to 1.0N H_2SO_4, and the electrolyte was deaerated with Ar before starting the experiments. The currents were measured quasistationarily at a scan rate of 0.5 mV/s by using a Wenking POS 73 potentiostat, at 4-5 concentrations and 5-6 angular frequencies. The potentials are quoted against SCE.

The polycrystalline WO_3 electrodes have been characterized by electron microscopy and photoelectrochemical measurements in previous reports (2a, 2c, 9, 10). A flatband potential of 0.26V (pH 0.0) and a slope of $\Delta E_{FB}/\Delta pH$ of −59 mV was determined from the onset of the photocurrents in different electrolytes (11). Electron micrographs and cyclic voltammetry of $Co(phen)_3^{3+}$ adsorbed on WO_3-electrodes (11) revealed a high surface roughness of approx. 100. A donor density of 10^{17} cm^{-3} has been estimated from impedance measurements after correcting for the real electrode surface area.

Theory

Our analysis is carried out in two steps: in the first we determine the rate constants (or quantities proportional to the rate constants) and in the second step we analyze the electrode potential dependence of these quantities. Some assumptions must be made concerning the processes described in Ref. (4) and illustrated in Fig. 1.

The rate of the processes is assumed as the sum of only one anodic and one cathodic process; the rate of the processes is regarded as proportional to the density or concentration of the reaction partners, *i.e.*, partial kinetic orders are taken to be invariably equal to 1. Thus, under steady-state conditions, the current density j is given by

$$j = -k_1 N_T(1 - f)\, en_s + k_{-1} N_T f e \qquad [1]$$

in which N_T is the surface-state density, e the elementary charge, f the occupancy of the surface states, and n_s the electron density at the conduction bandedge. On the other hand, the current density across the Helmholtz layer is expressed as

$$j = -k_2 c_{ox}{}^s N_T f \mathbf{F} z + k_{-2} c_{red}{}^s N_T (1 - f)\mathbf{F} z \qquad [2]$$

where c_{ox} and c_{red} denote the concentrations of the oxidizing (electron acceptor) and reducing (electron donor) agents. The superscript s refers to the surface concentration; $\mathbf{F}$ is the Faraday constant and z is the change of ion charge during the electrode reaction.

If the solution is free of any oxidizable species and the electrode potential is not too positive, the anodic terms can be neglected. As we mentioned in the introduction, the cathodic reaction, using easily reducible ions, depends on mass transport. The effect of the ion transport in the solution can be calculated easily by using a RDE. For a RDE, the cathodic current density is given by (12)

$$j = -0.62 z \mathbf{F} \omega^{1/2} D^{2/3} \nu^{-1/6} (c_{ox}{}^b - c_{ox}{}^s) \qquad [3]$$

where ν(cm/s) is the kinematic viscosity, D(cm²/s) is the diffusion coefficient of the oxidizing ion, ω(1/s) is the angular frequency of the RDE, and the superscript b refers to the bulk concentration. Using only the cathodic terms of Eq. [1] and [2], eliminating $c_{ox}{}^s$ and f we obtain from Eq. [1]-[3]

$$\frac{1}{j} = -\frac{1}{K_1}\left(1 + \frac{K_1/K_2}{c_{ox}{}^b + j/(K_3\omega^{1/2})}\right) \qquad [4]$$

where for sake of convenience, new parameters are applied

$$K_1 = k_1 N_T n_s e \qquad [5]$$

$$K_2 = k_2 N_T z \mathbf{F} \qquad [6]$$

$$K_3 = 0.62 z \mathbf{F} D^{2/3} \nu^{-1/6} \qquad [7]$$

Having measured the current density as a function of $c_{ox}{}^b$ and ω, and using an appropriate curve fitting procedure, the constants K_1 to K_3 can be determined. From our present point of view, the value of K_3 is of minor interest but the constants K_1 and K_2 will be further analyzed. This analysis is based on the following assumptions: (*i*) The potential difference between the two bulk phases is made up of two contributions: U_{sc}, the potential difference between the semiconductor bulk and surface, and U_H, the potential drop in the Helmholtz layer. In our present simplified view, the latter is the potential difference between the electrode surface and electrolyte bulk. Any change in the electrode potential causes a change of both potential differences. The electrode potential can therefore be written as

$$E = U_{sc} + U_H + E_{FB} + \text{const.} \qquad [8]$$

and

$$\Delta E = \Delta U_{sc} + \Delta U_H \qquad [9]$$

where E_{FB} is the flatband potential. (*ii*) K_1 depends on the electrode potential through n_s, which in turn depends on the band bending U_{sc}. n_s can be approximated by a Boltzmann distribution

$$n_s = n_b \exp(-eU_{sc}/kT) \qquad [10]$$

n_b is the bulk electron density in the conduction band, and the other symbols have their usual meaning. (*iii*) K_2 depends on the electrode potential through k_2. The dependence of k_2 on U_H is believed to be Volmerian, *i.e.*

$$k_2 = k_2{}^o \exp(-\alpha e U_H/kT) \qquad [11]$$

(*iv*) N_T and k_1 are assumed to be independent of the electrode potential. With these assumptions the following relations can be obtained: (*i*) Using Eq. [5] and [9]

$$K_1 = k_1 N_T e n_o \exp(-eU_{sc}/kT) \qquad [12]$$

Taking the logarithm of both sides of the equation, and differentiating with respect to the electrode potential, one obtains

$$\frac{d \ln K_1}{dE} = \frac{-e}{kT}\frac{dU_{sc}}{dE} \qquad [13]$$

which gives at room temperature

$$\frac{dU_{sc}}{dE} = -0.059\frac{d \log K_1}{dE} \qquad [14]$$

dU_{sc}/dE is important from a theoretical point of view: for a textbook semiconductor electrolyte contact in the depletion layer case its value should be one. However, the valve for a metal-like electrode, when the Fermi level is completely pinned, should be zero. (*ii*) A quasi-Tafel plot can be constructed by substituting Eq. [9] into the integrated form of Eq. [14]

$$U_H = E - \int_{E_{FB}}^{E} -0.059\frac{d \log K_1}{dE}\,dE + \text{const.} \qquad [15]$$

$$= E + 0.059 \log[K_1(E)/K_1(E_{FB})] + \text{const.} \qquad [16]$$

With Eq. [6] and [11]

$$\log K_2 = \frac{-\alpha}{0.059} \cdot [E + 0.059 \cdot \log K_1(E)] + \text{const.}' \qquad [17]$$

$$= \frac{-\alpha}{0.059} \cdot (U_H + \text{const.}'') \qquad [18]$$

Plotting $\log K_2$ *vs.* $E + 0.059 \cdot \log K_1$, a straight line is expected. From its slope, α can be obtained. If our model is adequate (or at least self-consistent), α should be close to 1/2.

Results

Figure 2 shows some representative $j - E$ curves for Fe^{3+} (0.01N $HClO_4$) and Ce^{4+} reduction (1.0N H_2SO_4) at different rotation speeds. Some of the j *vs.* c, j *vs.* $\omega^{1/2}$, j^{-1} *vs.*

c^{-1}, and j^{-1} *vs.* $\omega^{-1/2}$ plots have been reported previously (2c, 8). At low concentrations ($c_{ox} < \sim 10^{-3}M$) and rotation frequencies ($\omega < \sim 1600$ rpm), the reduction currents reach the mass transport controlled limit at potentials even more positive than the flatband potential, and increase linearly with c and $\omega^{1/2}$. However, at higher concentrations and stirring rates, the currents become increasingly independent of c and ω. The saturation of the reduction currents with increasing c and ω is especially pronounced at the more positive potentials ($E > 0.3$V).

In this work, we present the results in the form of $-K_1/j$ *vs.* $[K_1/K_2 \times 1/(c + j/K_3\omega^{1/2})]$ using the calculated K values. The parameters K_1, K_2, and K_3 were fitted to the measured data according to Eq. [4] using a nonlinear least squares procedure. The K_1 and K_3 values, as well as their standard deviations, are listed in Tables I-III. K_2 (E) is reported in the same tables as the heterogeneous rate constant $N_T k_2$, cf. Eq. [6]. In some cases, the parameter estimate is indefinite (the standard deviations are larger than the fitted values) because in the case of consecutive processes the rate constant of an extremely fast step can be determined only with large error.

The measured current densities, $j(c_{ox}{}^b, \omega)$, fit reasonably well to Eq. [4] for the reduction of Fe^{3+} at pH 2.0 and Ce^{4+} in 1*N* H_2SO_4. For the Fe^{3+} reduction at pH 0.0, the errors are much higher, therefore our conclusions are based mainly on the data from Tables I and III. Several attempts have been made to construct alternative kinetic models. Any simplification of the above model, however, yielded much worse fits, *i.e.*, no model with two processes/parameters/could produce the saturation of j with increasing $c_{ox}{}^b$ and ω. On the other hand, if further processes such as parallel direct electron transfer from the conduction band or anodic back reaction (cf. Eq. [1] and [2]) were taken into account, the rate constant of these processes could be determined only with very large error and without any marked improvement of the fit. Thus, we consider our model of three parameters to be the simplest one for reproducing the main features of the measured $j(c_{ox}{}^b, \omega)$ function.

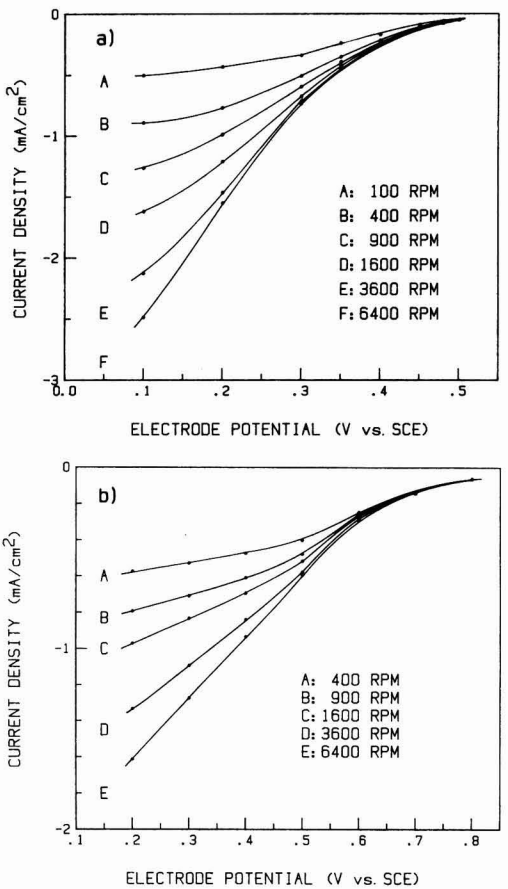


Fig. 2. Dark currents for reduction of Fe^{3+} (a) and Ce^{4+} (b) as a function of electrode potential and rotation frequency of a WO_3-RDE. Scan rate = 0.5 mV/s. a) 3.65 · 10^{-3}M $Fe(NO_3)_3 \cdot 9H_2O$ in 0.01*N* $HClO_4$, 3.57 · 10^{-3}M $Ce(SO_4)$ in 1*N* H_2SO_4.

According to Eq. [4], all data points can be plotted on a normalized plot, and all data points should lie on the line with unity slope and intercept (Fig. 3). Although some systematic deviations can be observed, the data are scattered around this line. Our further investigations are centered on evaluating K_1, K_2, and K_3. (*i*) The dependence of K_1 on the electrode potential is depicted as a plot of $-0.059\ d\ \log K_1/dE$ *vs.* E in Fig. 4. According to Eq. [13], the former quantity equals dU_{sc}/dE. Note that we obtained small standard deviations only for the reduction of Fe^{3+} at pH 2.0. However, it seems to be evident (also for the other two cases) that no data point is close to one, *i.e.*, the potential difference change in the semiconductor is always less than the electrode potential change. This tendency is especially pronounced for the more negative potentials in which the electrode is close to the flatband situation and behaves almost like a metal, indicating partial Fermi level pinning. (*ii*) The potential dependence of K_2 is seen in Fig. 5 for all systems studied. In order to check our model, a quasi-Tafel plot (Fig. 6) was constructed for the data of Fe^{3+} reduction in a pH 2.0 solution by reporting $\log K_2$ as a function of the potential drop through the Helmholtz layer U_H according to Eq. [15]-[18]. The majority of points lie on a straight line having a slope of 134 mV/decade. Thus, the transfer coefficient α is 0.44. Such a plot was not made for the reduction currents in 1*N* acid because of the lack of accurate K_1 data. However, we obtained additional information on the potential drop

Table I. Reduction of Fe^{3+} in 0.01*N* $HClO_4$

E *vs.* SCE (V)	K_1 10^{-3} A · cm^{-2}	$N_T k_2$ 10^{-3} cm · s^{-1}	K_3 10^{-2} Acm$^{-2}M^{-1}$ (radian/s)$^{-1/2}$
0.10	7.91 ± 0.23	18.8 ± 1.2	5.14 ± 0.09
0.20	3.83 ± 0.07	9.7 ± 0.5	4.63 ± 0.10
0.30	1.64 ± 0.05	3.7 ± 0.3	3.8 ± 0.3
0.35	1.04 ± 0.04	2.0 ± 0.2	3.6 ± 0.5
0.40	0.542 ± 0.015	1.11 ± 0.09	6 ± 2
0.45	0.22 ± 0.04	0.67 ± 0.05	3.4 ± 1.4
0.48	0.117 ± 0.022	0.47 ± 0.05	1.5 ± 0.6
0.50	0.065 ± 0.002	0.58 ± 0.2	0.3 ± 0.1

Table II. Reduction of Fe^{3+} in 1.0*N* $HClO_4$

E *vs.* SCE (V)	K_1 10^{-3} A · cm^{-2}	$N_T k_2$ 10^{-3} cm · s^{-1}	K_3 10^{-2} Acm$^{-2}M^{-1}$ (radian/s)$^{-1/2}$
0.22	5.1 ± 0.5	8.4 ± 1.4	3.5 ± 0.2
0.32	1.9 ± 0.2	4.8 ± 1.2	2.6 ± 0.3
0.42	0.74 ± 0.05	1.6 ± 0.3	1.5 ± 0.2
0.47	0.49 ± 0.04	0.86 ± 0.15	1.2 ± 0.2
0.52	indefinite	0.21 ± 0.04	0.9 ± 0.3
0.57	indefinite	0.08 ± 0.03	0.3 ± 0.1

Table III. Reduction of Ce^{4+} in 1.0*N* H_2SO_4

E *vs.* SCE (V)	K_1 10^{-3} A · cm^{-2}	$N_T k_2$ 10^{-3} cm · s^{-1}	K_3 10^{-2} Acm$^{-2}M^{-1}$ (radian/s)$^{-1/2}$
0.20	indefinite	21.0 ± 2.5	2.78 ± 0.14
0.30	indefinite	10.3 ± 1.3	2.74 ± 0.19
0.40	indefinite	4.82 ± 0.38	3.1 ± 0.3
0.50	indefinite	2.4 ± 0.4	3.2 ± 0.5
0.60	1.3 ± 0.2	1.31 ± 0.14	3.4 ± 0.9
0.70	0.70 ± 0.09	0.58 ± 0.05	indefinite
0.80	0.182 ± 0.013	0.291 ± 0.025	indefinite

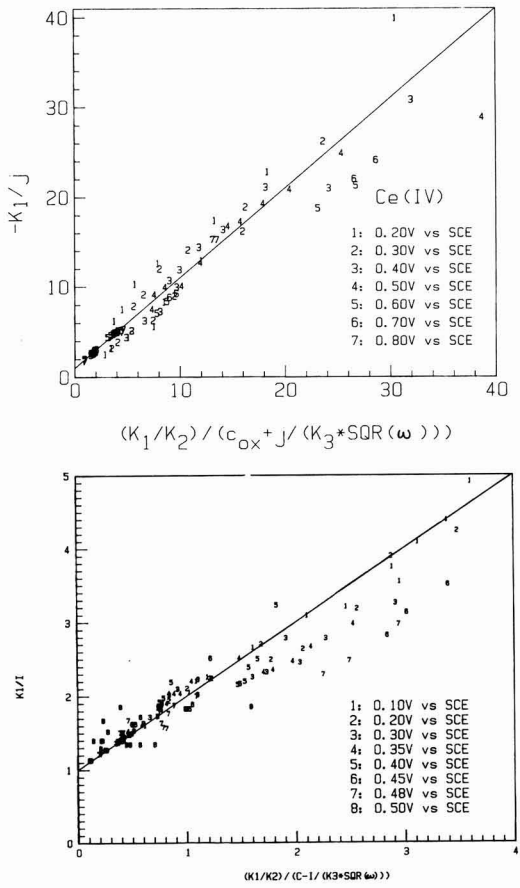


Fig. 3. j (c, ω) according to Eq. [4]. a, top. Ce^{4+} reduction in 1N H_2SO_4; Constants K_1 to K_3 are from Table III. b, bottom. Fe reduction in 0.01N $HClO_4$; Constants K_1 to K_3 are from Table I.

through the space charge and the Helmholtz layer from K_2 (E). As it is easy to show, the slope of the log K_2 *vs.* E line is $-0.059/(\alpha dU_H/dE)$. For Ce^{4+} reduction, we obtained a straight line with a slope of 325 mV/decade in the whole potential interval studied (Fig. 5). Assuming a value of $dU_{sc}/dE \sim 0.2$ (Fig. 4), one obtains $dU_H/dE \approx 0.8$ and $\alpha \approx 0.23$. Thus, the variation of electrode potential causes, in the case of Ce^{4+}, a significant change of the potential drop

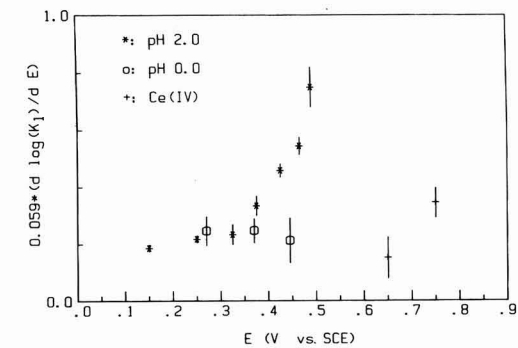


Fig. 4. Potential dependence of K_1 according to Eq. [13]. Reduction of Fe^{3+} (*, o) and Ce^{4+} (+). Error limits are indicated (|). K_1 data are from Tables I to III.

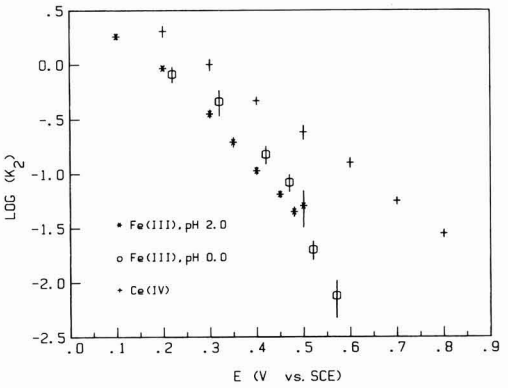


Fig. 5. Potential dependence of K_2 [$Acm^{-2}M^{-1}$]

in the Helmholtz layer, again indicating partial Fermi level pinning. (*iii*) K_3, being a parameter of ion transport, should be independent of the electrode potential, and its value can be calculated independently according to Eq. [7]. The fitted K_3 values for Ce^{4+} reduction reproduce the estimated value of 0.029 $Acm^{-2}M^{-1}s^{1/2}$ $radian^{-1/2}$ from $D(Ce^{4+}$ in 1N $H_2SO_4) = 3.4 \cdot 10^{-6}$ cm^2/s (14). The values for Fe^{3+} reduction differ from the calculated value (0.04 $Acm^{-2}M^{-1}s^{1/2}$ based on the diffusion coefficient of Fe^{3+} in 1N $HClO_4$ ($5.5 \cdot 10^{-6}$ cm^2/s (13)], especially at the anodic potential of the series. In our opinion, this discrepancy can be explained by taking into account the oxidation of the formed Fe^{2+} ions (cf. Eq. [1] and [2]), which is pronounced at potentials close to the redox potential of the Fe^{3+}/Fe^{2+} couple (+0.53V *vs.* SCE). The redox potential of the Ce^{4+}/Ce^{3+} couple, however, is much more anodic (1.22V *vs.* SCE), and therefore the anodic reaction of Ce^{3+} ion can safely be neglected.

Discussion

The above presented results show that the reduction currents at biased polycrystalline WO_3 tend to level off with increasing concentration of the oxidized species. This behavior could be described reasonably well by a two-step model for the electron transfer from the conduction band to the electrolyte (Fig. 1) and is in agreement with findings on other metal oxide electrodes (4-6).

K_1 values.—The K_1 values were extrapolated to the flatband potential. For the systems studied, taking into account the roughness factor of 100, $K_1(E_{FB})$ is in the order of magnitude of 10^{-4} A/cm^2. Since the electron density is

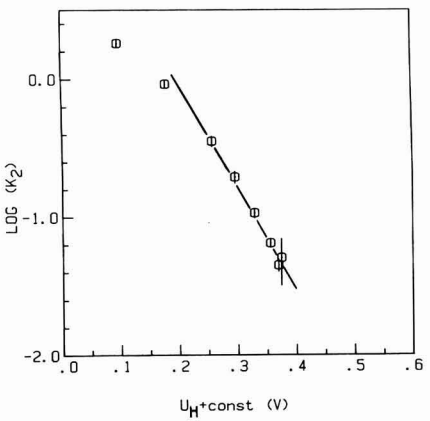


Fig. 6. Quasi Tafel plot constructed from K_1 and $N_T k_2$ values obtained from Table I.

equal to the donor density throughout the semiconductor at the flatband potential, *i.e.* $N_D = n_0 = n_s \approx 10^{17}$ cm^{-3}, then from Eq. [5] we can make the estimate $N_T k_1 \approx 6 \cdot 10^{-3}$ cm/s.

In comparison, Gomes *et al.* (4) reported saturation current densities ($= -K_1$) of -3 mA/cm^2 on n-$SrTiO_3$ single crystals at a potential 0.4V positive of the flatband potential by using different electron acceptors. The authors extrapolated to the flatband situation by assuming $d\Delta U_{sc}/dE = 1$ and obtained a high value of $N_T k_1 \approx 10^5$ cm/s. Similarly, they estimated $N_T k_1 = 4 \cdot 10^6$ cm/s for n-TiO_2 single crystals. Salvador *et al.* (5) concluded from their capacitance data on polycrystalline $SrTiO_3$ electrodes that dU_{sc}/dE is significantly lower than 1. They determined a saturation current density for $Fe(CN)_6^{3-}$ reduction of -0.6 mA/cm^2 at an effective band bending of 0.17V, which was corrected for the potential drop in the Helmholtz layer. The corresponding rate constant of $N_T k_1 = 0.29$ cm/s is similar in magnitude to our value. However, these authors assumed more than one set of surface states and that $N_T k_1$ values are potential dependent. Iwanski *et al.* (6) determined K_1 values of $2.5 \cdot 10^{-5}$ A/cm^2 for the reduction of $Fe(CN)_6^{3-}$ on polycrystalline Fe_2O_3 electrodes at potentials 0.7-0.8V positive of E_{FB}. Thus, we conclude from literature data and from our findings that relatively high dark currents of 10^{-5}-10^{-3} A/cm^2 at potentials of up to a few 100 mV positive of the flatband potential and partial Fermi level pinning can occur even at "high" bandgap semiconductors ($E_G \geq 2$ eV) like $SrTiO_3$ (4, 5), TiO_2 (4), Fe_2O_3 (6, 16), and WO_3. Furthermore, we are inclined to think that the $N_T k_1$ values are much higher for single crystalline electrodes than for polycrystals. The low value of dU_{sc}/dE may also be a consequence of the polycrystalline electrode structure.

Density of surface states.—For an ideal semiconductor, the capacity of the Helmholtz layer $C_H \approx 10$ μF/cm^2 (17) is large compared to the capacity of the depletion layer. Thus, the potential drop should occur mainly through the space charge layer. In our case, however, we observed that partial Fermi level pinning occurs. We can estimate a lower limit of the surface-state density by using the above C_H value. In the case of Fe^{3+} reduction at pH 2.0, we obtained ΔU_H values up to 0.3V (Fig. 6). Thus, we calculate an excess of surface charge of $\Delta Q_{ss} > C_H \Delta U_H = 3$ μC/cm^2 which corresponds to $2 \cdot 10^{13}$ elementary charges per cm^2 of real area. In comparison, a space charge of ~ 0.1 μC/cm^2 is estimated from Eq. [19] $\epsilon \approx 50$ (18) and $E - E_{FB} = 0.15$V. We conclude that the main

$$Q_{sc} = [2e\epsilon\epsilon_0 n_b(E - E_{FB} - kT/e)]^{1/2} \qquad [19]$$

contribution of the surface charge stems from charged surface states and not from the depletion layer charge, as in the case of heavily doped semiconductors (19). Thus, we estimate a high density of ionic surface states of $> 2 \cdot 10^{13}$ cm^{-2} for our WO_3 electrodes. This corresponds to $2 \cdot 10^{15}$/cm^2 of geometric area.

Salvador *et al.* (5) pointed out the difference in electrode kinetic behavior of metal oxides with empty (TiO_2, $SrTiO_2$) or partially filled (Fe_2O_3) d-bands and ZnO (d^{10}). Only the latter showed direct electron transfer from the conduction band into the solution. For TiO_2 and $SrTiO_3$, the authors proposed an interaction of unoccupied Ti:3d (t_{2g}) orbitals with occupied solvent orbitals creating energetic states below the conduction band. A similar mechanism could be responsible for the surface states in the case of WO_3.

$N_T k_2$ values.—It might be instructive to calculate the heterogeneous standard rate constants $N_T k_2^0$ for the three systems studied in this work (Table IV) and to compare them to values on metallic electrodes. The roughness factor of 100 was applied in the calculation. In $HClO_4$ electrolytes k^0 values of $2 \cdot 10^{-3}$ to 10^{-1} cm/s were reported for $Fe^{3+/2+}$ on Pt (15). The standard rate constants for the same reaction on carbon-paste electrodes are much lower [$7 \cdot 10^{-6}$-$5 \cdot 10^{-4}$ cm/s, (15)]. A value of $4.4 \cdot 10^{-4}$ cm/s was measured for the reduction of Ce^{4+} in 1N H_2SO_4 on Pt (20).

Table IV. Heterogeneous standard rate constants for the electron transfer through the Helmholtz layer of WO_3

Redox system	E^0 (V *vs.* SCE)	$N_T k_2^0$ (cm/s)
$Fe^{3+/2+}$ (0.01N $HClO_4$)	0.53	$3 \cdot 10^{-6}$
$Fe^{3+/2+}$ (1N $HClO_4$)	0.53	$2 \cdot 10^{-6}$
$Ce^{4+/3+}$ (1N H_2SO_4)	1.22	$1.5 \cdot 10^{-7}$

Galus and Adams (21) determined k^0 values of $3.7 \cdot 10^{-4}$ cm/s on Pt and $3.6 \cdot 10^{-4}$ cm/s on carbon. On gold, the currents depend on oxygen coverage. A value of $k^0 = 3 \cdot 10^{-4}$ cm/s has been reported in 2N H_2SO_4 on an Au electrode with 1-2 monolayers of oxide (22). Thus, the exchange rates through the Helmholtz layer of WO_3 are three to four orders of magnitude lower than those of metal electrodes.

In comparison, Iwanski *et al.* (6) obtained a $N_T k_2^0$ value of $\sim 1 \cdot 10^{-5}$ cm/s for the dark reduction of $Fe(CN)_6^{3-}$ on Fe_2O_3. The potential dependence of their rates $N_T k_2$ reveals also a significant potential drop through the Helmholtz layer.

Transfer coefficients.—The α value of 0.44 for Fe^{3+} reduction at pH 2.0 derived from Fig. 6 is close to $\alpha \approx 0.5$ reported for metallic electrodes (15). The low transfer coefficient $\alpha \approx 0.2$ for Ce^{4+} reduction is in good agreement with literature values obtained with metallic electrodes: $\alpha = 0.21$ on Pt (21), $\alpha = 0.28$ on carbon-paste (21), $\alpha = 0.25$ on Pt (20), $\alpha = 0.35$ on Au (22), and $\alpha = 0.29$-0.43 on Pt (14). These values, being close to the transfer coefficients on WO_3 electrodes, strongly support the adequacy of the model. We conclude that the surface states behave in a limited potential range phenomenologically like a very thin metallic electrode.

Rate limiting steps.—Our model involved 3 partial currents j_{sat} (Eq. [1]), $j_{Helmholtz}$ (Eq. [2]), and j_{Levich} (Eq. [3]). The data from Tables I-III and the theoretical K_3 values allow the prediction of different kinetic cases. If $c < 10^{-2}M$ and $E < 0.3$V the reduction currents depend on the concentration and the rotation frequency. If in addition, ω is low (<1600 rpm), the currents are limited by mass transport and increase linearly with c and $\omega^{1/2}$. On the other hand, j depends on c but hardly on ω if $c < 10^{-2}M$ and $E > 0.4$V because $j_{Helmholtz}$ becomes rate limiting in this case. Finally, the currents are determined mainly by j_{sat} over the whole potential range if $c > 10^{-2}M$ and $\omega > 1600$ rpm, when the charge transfer through the space-charge layer is the slowest step.

Conclusions

The electron transfer could be described by assuming an indirect electron transfer from the conduction band to the solute *via* an intermediate species on the electrode surface. The rotating disk electrode technique proved to be a straightforward method of extracting the rate constants K_1 and K_2 quite accurately by a least squares fit of the experimental data. $d\Delta U_{sc}/dE$ could be determined from the dependence of K_1 and K_2 on the electrode potential; the values differ significantly from either unity or zero, indicating partial Fermi level pinning. These findings indicate a high density of $>2 \cdot 10^{15}$ cm^{-2} surface states below the conduction band. The surface states limit the cathodic currents so that j becomes concentration independent. However, the currents do not decrease by a factor of 10 for $\Delta E = +59$ mV, but much slower, because the surface states get more and more positively (less negatively, respectively) charged under anodic polarization. Thus, a significant portion of the potential drop occurs through the Helmholtz layer.

Acknowledgments

This work was supported by the Swiss National Science Foundation. We are grateful to Dr. Pierre Infelta for his help in performing the calculations.

Manuscript submitted June 17, 1985; revised manuscript received Nov. 4, 1985.

REFERENCES

1. a) E. Borgarello, W. Erbs, M. Grätzel, and E. Pelizzetti, *Nouv. J. Chim.*, **7**, 195 (1983); b) N. Bühler, K. Meier, and J.-F. Reber, *J. Phys. Chem.*, **88**, 3261 (1984); c) T. Sakata and T. Kawai, in "Energy Resources through Photochemistry and Catalysis," M. Grätzel, Editor, Academic Press, New York (1983); d) M. Barbeni, E. Pramauro, E. Pelizzetti, E. Borgarello, M. Grätzel, and N. Serpone, *Nouv. J. Chim.*, **8**, 547 (1984); e) H. Hidaka, H. Kubota, M. Grätzel, N. Serpone, and E. Pelizzetti, *Nouv. J. Chim.*, **9**, 67 (1985).
2. a) W. Erbs, J. Desilvestro, E. Borgarello, and M. Grätzel, *J. Phys. Chem.*, **88**, 4001 (1984); b) M. Neumann-Spallart and O. Enea, *This Journal*, **131**, 2767 (1984); c) J. Desilvestro and M. Neumann-Spallart, *J. Phys. Chem.*, To be published.
3. Ref. 2-9 in (4).
4. J. Vandermolen, W. P. Gomes, and F. Cardon, *This Journal*, **127**, 324 (1980).
5. P. Salvador and C. Gutiérrez, *ibid.*, **131**, 326 (1984).
6. P. Iwanski, J. S. Curran, W. Gissler, and R. Memming, *ibid.*, **128**, 2128 (1981).
7. J.-N. Chazalviel, *ibid.*, **129**, 963 (1982).
8. J. Desilvestro and M. Grätzel, p. 191, International Society of Electrochemistry, Extended Abstracts, 35th Meeting, Berkeley, CA (1984).
9. J. Desilvestro and M. Grätzel, *J. Chem. Soc., Chem. Commun.*, 107 (1982).
10. a) J. Desilvestro and M. Grätzel, 4th International Conference on Photochemical Conversion and Storage of Solar Energy, Book of Abstracts, p. 53, Jerusalem (1982); b) M. Neumann-Spallart, *ibid.*, p. 73.
11. J. Desilvestro, PhD Thesis, Swiss Federal Institute of Technology, Lausanne, Switzerland (1985).
12. A. J. Bard and L. R. Faulkner, in "Electrochemical Methods," Chap. 8, John Wiley & Sons, New York (1980).
13. R. N. Adams, "Electrochemistry at Solid Electrodes," p. 220, Marcel Dekker, Inc., New York (1969).
14. R. Greef and H. Aulich, *J. Electroanal. Chem.*, **18**, 295 (1968).
15. K. E. Heusler, in A. J. Bard, Editor, "Encyclopedia of Electrochemistry of the Elements," Vol. IXA, p. 229, Marcel Dekker, Inc., New York (1982).
16. F. A. Benko, J. Longo, and F. P. Koffyberg, *This Journal*, **132**, 609 (1985).
17. A. J. Bard, A. B. Bocarsly, F.-R. F. Fan, E. G. Walton, and M. S. Wrighton, *J. Am. Chem. Soc.*, **102**, 367 (1980).
18. M. A. Butler, *J. Appl. Phys.*, **48**, 1914 (1977).
19. a) R. De Gruse, W. P. Gomes, F. Cardon, and J. Vennik, *This Journal*, **122**, 711 (1975); b) K. Uosaki and H. Kita, *ibid.*, **130**, 895 (1983).
20. K. J. Vetter, *Z. Phys. Chem.*, **196**, 360 (1950).
21. Z. Galus and R. N. Adams, *J. Phys. Chem.*, **67**, 866 (1963).
22. R. A. Bonewitz and G. M. Schmid, *This Journal*, **117**, 1367 (1970).

Electrochemical Behavior of Azide Ions on Platinum Electrodes

Hajime Miyama, Yoshio Nosaka, and Takashi Fukushima

Department of Chemistry, Technological University of Nagaoka, Kamitomioka, Nagaoka, 949-54, Japan

ABSTRACT

Reduction of azide ions on platinum electrodes in aqueous solution was investigated using cyclic voltammetry and rotating disk electrode methodologies. Azide ions are very strongly adsorbed on the platinum surface and produce NH_3 and N_2 via an adsorbed intermediate. A reaction mechanism characteristic of the platinum electrode is proposed.

Azide ion N_3^- is a typical pseudo-halide ion that produces ammonia by a photocatalytic reaction with water on a platinized TiO_2 surface in aqueous solution (1). Therefore, it is interesting to investigate the electrochemical behavior of N_3^- on a Pt electrode. Formation of N_2 by the anodic oxidation of azide ions on metal electrodes (2, 3), formation of AgN_3 on Ag electrodes (4), and the polarographic reduction on Hg electrodes (5-7) have been reported, but the reaction mechanism has not been clarified.

In this paper, we report on the electrochemical behavior of N_3^-, which we studied by utilizing cyclic voltammetry, single linear potential sweep (SLPS), and rotating disk electrodes (RDE). We propose a reaction mechanism that is consistent with the electrochemical result.

Experimental

Reagent grade chemicals were used in all experiments. For the preparation of the electrolyte solution, doubly distilled water was used. For the voltammetry, a working electrode of Pt wire of 15 mm length and 0.5 mm diam, a counterelectrode of Pt wire of 500 mm length and 0.5 mm diam, and an electrolytic cell of H type separated by a sintered filter glass were used. In order to obtain current-voltage curves, a homemade potentiostat and an X-Y recorder (Riken Denshi, F-3EP) were used. A saturated calomel electrode (SCE) was the reference electrode. Before the measurement, each electrode was cleaned by repeating the voltage sweep at the rate of 100 mV/s until a constant current-voltage curve was obtained.

For the SLPS measurements, the same apparatus used in the cyclic voltammetry was used. The measurements were carried out by keeping the electrode potential in the supporting electrolyte solution at −1.0V for a definite time, then adding NaN_3 solution, and sweeping the potential to the anodic side at the rate of 100 mV/s.

For RDE measurements, a Pt disk electrode of 6 mm diam, a Pt counterelectrode of 200 mm length and 1 mm diam, a simple cylindrical cell, an electrode rotating apparatus (Nikko Keisoku, RRDE-1), a motor speed controller (Nikko Keisoku, SC-5), a polarograph (Fuso Seisakusho, Model 31), and an X-Y recorder (Matsushita Tsushin, VP-6422A) were used. Before the measurements were made, the potential sweep was repeated from 0V to the H_2 generation potential at the rate of 5 mV/s until a reproducible curve was obtained.

Results and Discussion

Cyclic voltammograms measured in aqueous Na_2SO_4 solution without and with NaN_3 are shown in Fig. 1. For the positive-going potential sweep from 0V, the current in the solution with NaN_3 is more than two times larger than that for the solution without NaN_3, and the current in the former, 0.75V, rises earlier than that (1.15V) for the latter. The currents correspond to the formation of the adsorbed N_3 layer ($N_{3\,add}$), preceded by the discharge of N_3^- and the generation of N_2, respectively, as pointed out by Thomas (2). For the negative-going potential sweep from 0.95V in the solution with NaN_3, the reduction current appears at about −0.1V, continues to about −0.4V as a plateau current, then shows a maximum at about −0.7V (peak A), and, finally, decreases accompanied by H_2 generation at −0.95V. On the other hand, for the sweep in the solution without NaN_3, reduction current having a maximum at about −0.2V appears, and another reduction current appears at about −0.65V before H_2 generation. For the

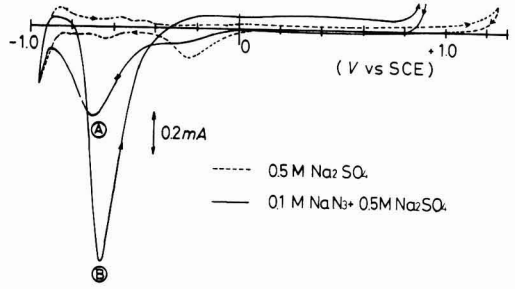


Fig. 1. Cyclic voltammograms for aqueous Na_2SO_4 without and with NaN_3. Pt electrode. Sweep rate 100 mV/s.

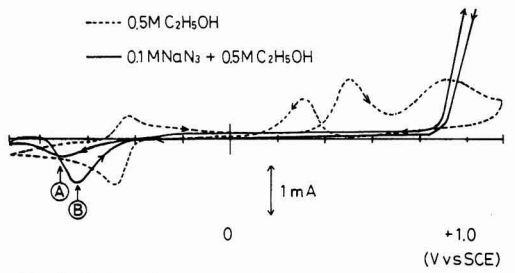


Fig. 2. Cyclic voltammograms for aqueous C_2H_5OH without and with NaN_3. Pt electrode. Sweep rate 100 mV/s.

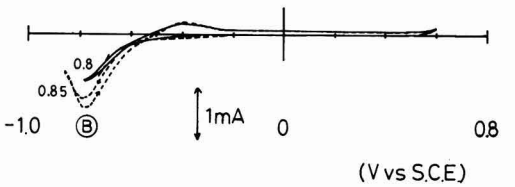


Fig. 3. Cyclic voltammograms for aqueous 1M NaOH + 0.1M NaN_3 solution where cathodic switching potentials are 0.8V (full line) and 0.85V (dotted line). Pt electrode. Sweep rate 100 mV/s.

positive-going potential sweep from −0.95V in the solution with NaN_3, a characteristic reduction current peak B appears at −0.63V, accompanied by N_2 generation and, then, by the oxidation current at −0.2V. The oxidation current was found to be due to the oxidation of NH_4^+, as indicated by an examination of current-voltage curves for various nitrogen compounds. The products formed by the long-period pulse electrolysis (from 0.5V to −0.6V and pulse frequency 0.5 Hz) of the NaN_3 + Na_2SO_4 solution were analyzed and found to be NH_3 and N_2. Also, the change of pH of the solution—from 11 to 13.6—shifted the H_2 generation voltage about 150 mV, the peak A about 80 mV, and the peak B about 120 mV, respectively, to the minus side. The shifts are considered to be characteristic of the reaction of protons.

In Fig. 2, voltammograms of aqueous C_2H_5OH with and without NaN_3 are shown. For the positive-going potential sweep in the solution without NaN_3 from 0V, two oxidation current peaks are observed. Also, for negative-going scans from O_2 generation, one oxidation peak appears. However, for the C_2H_5OH + NaN_3 solution, the oxidation peaks characteristic of C_2H_5OH disappear, while two reduction peaks A and B characteristic of N_3^- appear. It is known (8) that the anodic oxidation of C_2H_5OH occurs via the adsorption of C_2H_5OH on the Pt electrode (about 0.3V in Fig. 2). Therefore, the present result shows that the adsorption of N_3^- on the Pt electrode occurs at a potential below 0.3V, and that N_3^- is adsorbed strongly enough to inhibit the adsorption of C_2H_5OH on the Pt surface.

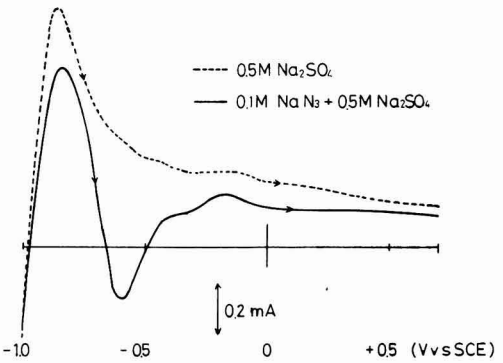


Fig. 4. Single-sweep voltammograms for aqueous Na_2SO_4 without and with NaN_3. Pt electrode. Sweep rate 100 mV/s.

Two voltammograms in aqueous 0.1*M* NaN_3 + 1*M* NaOH solution, where the negative switching potentials are −0.8V and −0.85V, are shown in Fig. 3. When the switching potential is higher than the potential of peak A (0.85V for the solution), peak B is not observed. However, when the switching potential is higher than that, peak B is observed. This indicates that the reaction at peak B is caused by the product of the reaction at peak A.

Current-voltage curves obtained by SLPS from −1.0V (H_2 generation potential) are shown in Fig. 4. Here, the curve for the aqueous NaN_3 + Na_2SO_4 solution is obtained by adding the NaN_3 solution to the Na_2SO_4 solution, keeping the potential at −1.0V, and by starting the sweep. For the Na_2SO_4 solution, an oxidation current peak due to the oxidation of the absorbed H_2 is observed at −0.85V, which is far larger than that shown in Fig. 1. This may be due to the larger amount of H_2 adsorbed in this case. For the aqueous NaN_3 + Na_2SO_4 solution, a similar oxidation peak is observed. However, its height is 25% less than that for the Na_2SO_4 solution. This indicates that the adsorption of N_3^- occurs even at these negative potentials. Also, a reduction current peak is observed that is shifted about 50 mV positive compared with peak B, shown in Fig. 1.

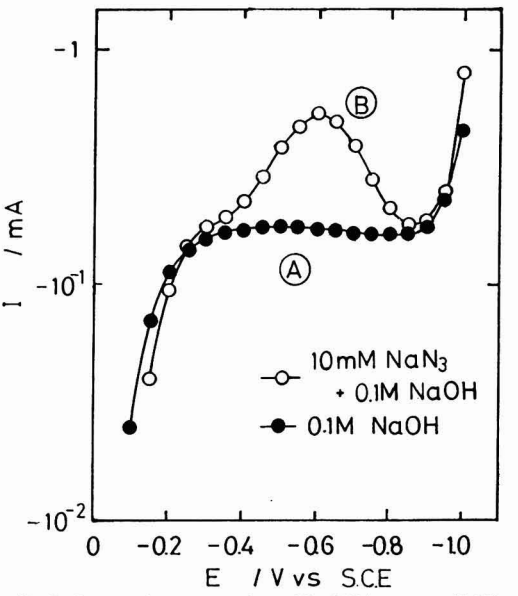


Fig. 5. Current-voltage curves obtained by RDE for aqueous NaOH without and with NaN_3. Rotating speed 500 rpm. Sweep rate 5 mV/s.

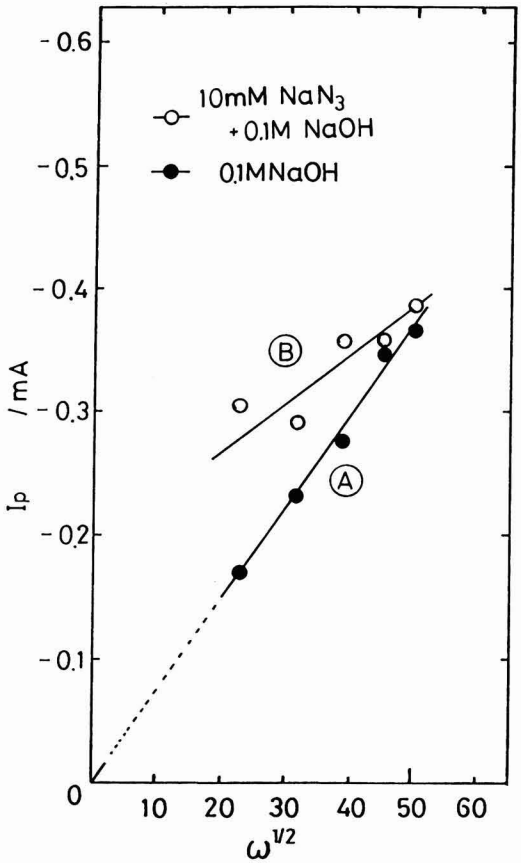


Fig. 6. Intensity of peak current at −0.6V against rotating speed of RDE for aqueous NaOH with and without NaN_3.

Therefore, it is considered that N_3^- is adsorbed on the platinum, even at −1.0V, and reduced at peak B.

Current-voltage curves in the aqueous NaOH solution (curve A) and the aqueous NaN_3 + NaOH solution (curve B), obtained by the RDE method, are shown in Fig. 5. In curve B, a reduction current peak is observed at −0.6V, and this peak varies with the number of sweeps but no longer changes after 3-5 sweeps. The value of the peak current at −0.6V is plotted against the square root of the rotation speed ($\omega^{1/2}$), as shown in Fig. 6. Linear plots are obtained for the NaOH (curve A) and the NaN_3 + NaOH solution (curve B). Plot A goes through the origin, which means that the current is produced by a convective diffusion-controlled reaction (9). On the other hand, the reaction rate at the peak in plot B is not so determined. This suggests a possibility of the reaction between $N_{3\text{-add}}$ and H_2O.

From the result shown in Fig. 1, reaction [1] is proposed for the adsorption of N_3^- on platinum

$$N_3^- \rightarrow Pt - N_{3\text{-add}} + e^- \qquad [1]$$

Since the shift of the peak A of about 80 mV due to the pH change 2.6 is roughly half of the shift of the H_2 generation potential of about 150 mV for the same pH change, approximately two protons may participate in the reduction at the peak A. Also, from the N_2 generation during the long-period electrolysis, the following reaction is proposed for the reduction of $Pt - N_{3\text{-add}}$

$$Pt - N_{3\text{-add}} + 2H^+ + e^- \rightarrow Pt = NH_{2\text{-add}}^+ + N_2 \qquad [2]$$

The result in Fig. 3 indicates that peak B is caused by the reaction product at peak A. The 120-m V shift of peak B due to the pH change of 2.6 suggests the participation of one proton in the reaction at peak B. From these results, together with the existence of the NH_4^+ oxidation peak at −0.2V in Fig. 1, the following reaction [3] is proposed for the reduction at the peak B

$$Pt = NH_{2\text{-add}}^+ + H^+ + 2e^- \rightarrow Pt + NH_3 \qquad [3]$$

The reaction scheme consisting of [1], [2], and [3] does not contradict the result in Fig. 5, namely, that the reduction current peak at −0.6V is not due to a diffusion-controlled reaction.

Acknowledgments

The authors are very grateful to Dr. T. Hinoue for allowing them to use the RDE apparatus. This study was supported financially by a Grant-in-Aid for Scientific Research from the Ministry of Education, Science, and Culture.

Manuscript submitted June 6, 1985; revised manuscript received Oct. 4, 1985.

Technological University of Nagaoka assisted in meeting the publication costs of this article.

REFERENCES

1. Y. Nosaka, Y. Ishizuka, K. Norimatsu, and H. Miyama, *Bull. Chem. Soc. Jpn.*, **57**, 3066 (1984).
2. J. G. N. Thomas, *Trans. Faraday Soc.*, **58**, 1412 (1962).
3. V. Plzak and H. Wendt, *Ber. Bunsenges. Phys. Chem.*, **83**, 481 (1979).
4. P. E. Kunz, J. G. Gordon II, M. R. Philpott, and A. Girlando, *J. Electroanal. Chem. Interfacial Electrochem.*, **112**, 391.
5. Z. P. Zagorski and A. Blum, *J. Electroanal. Chem. Interfacial Electrochem.*, **41**, 447 (1973).
6. J. Masek, *Coll. Czech. Chem. Commun.*, **25**, 3137 (1960).
7. C. V. D'Alkain, E. R. Gonzalez, and R. Parsons, *J. Electroanal. Chem. Interfacial Electrochem.*, **32**, 57 (1971).
8. I. Izumi and Y. Onishi, *Denki Kagaku*, **50**, 413 (1981).
9. V. G. Levich, "Physicochemical Hydrodynamics," p. 60, Prentice-Hall, Englewood Cliffs, New Jersey (1962).

Time-Resolved Photocurrent of WSe_2 Photoanode Studied with a Nanosecond Pulse Laser

T. Sakata,[1] E. Janata, W. Jaegermann, and H. Tributsch

Hahn-Meitner-Institut für Kernforschung, Berlin, Bereich Strahlenchemie, Berlin 39, Germany

ABSTRACT

Fast photocurrent transients were measured at single crystalline n-WSe_2 electrodes employing a nanosecond ruby laser as a light source. Dependence of the transients on laser intensity showed that the photocurrent intensity increased proportionally to the laser intensity below ~100 nJ/pulse. With more intense light, the photocurrent intensity showed a saturation, and the shape of the transient was deformed, being accompanied with a structure. The transient photocurrent due to the photocorrosion was suppressed by the addition of EDTA or Ag^+. Influence of redox reagents, such as I^-/I_2 and $K_3Fe(CN)_6/K_4Fe(CN)_6$, on the photocurrent transient was investigated. Dependence of decay time on bias voltage and load resistance showed that the decay time was determined by the RC time constant of the cell system. The flatband potential can easily be determined by this technique plotting τ^{-2} *vs.* V or by considering the onset of photocurrent, as disturbances are low due to the small absolute number of photogenerated carriers involved.

Photoelectrode processes in photoelectrochemical cells are essentially dynamic. Illumination of the semiconductor/electrode interface causes: (*i*) excitation of electrons in the valence band of the semiconductor, (*ii*) electron hole separation mainly in the space charge layer, (*iii*) trapping of electrons or holes by surface states or defects, (*iv*) charge transfer reaction at the interface. Understanding of such dynamic processes is important for improving the efficiency and stability of photoelectrochemical cells.

The use of transient techniques in investigating photoelectrochemical cells has been introduced recently, in order to evaluate kinetic parameters in the photoelectrode processes (1-12). The relaxation of an open-circuit photopotential was examined theoretically for the special case where there is no interfacial electron or hole transfer (13). Photopotential transients have been measured at TiO_2 and CdS electrodes with a "coulostatic flash" technique, in which the open-circuit potential change induced by a laser pulse of bandgap photons is measured (2-5). Also, a dye-sensitized system, SnO_2/rhodamine B, has been studied (6). Photocurrent transients obtained under short-circuit condition have also been studied (6-12). From the measured dependence of the decay time on the value of load resistance and additional capacitances, it has been shown that the photocurrent decay was controlled by the RC time constant of the cell (7, 9, 11). But sometimes also faster components could be observed, which have been attributed to alternative reaction paths involving recombination (6-9). Especially for oxygen evolving photoelectrodes, for which surface reactions are very important, a number of different decay times have been found independent of applied potential (10, 14).

Here, we report the results of fast transient measurements in photoelectrochemical cells of n-WSe_2, one of the transition metal dichalcogenides with layered structure, cells that have gained substantial interest due to their reasonably high solar energy conversion efficiency and good stability against photocorrosion (15, 16).

Experimental

The block diagram of the experimental setup for measuring the transient photocurrents is shown in Fig. 1. The measuring cell, a classical three electrode cell, was constructed to allow measurements on the nanosecond time scale—*i.e.*, the working electrode, the counterelectrode, and the cell holder were incorporated in a transmission line (50Ω) in order to reduce signal distortions caused by mismatches and parasitic inductances or capacitances. The counterelectrode is a short piece of protecting tube (15 mm long and 10 mm inner diameter) made of glassy carbon. The working electrode (crystal mount), a short piece of brass surrounded by a Teflon disk, fits into the counterelectrode and is kept in place by a short air-isolated transmission line (not shown) terminated by a GR connector. n-WSe_2 single crystals (E_g = 1.2 eV, very thin leaflet-like crystals with a typical area of 0.03-0.1 cm²), which were synthesized by chemical transportation methods, were used as photoanodes. The electrical contact between the semiconductor and the brass mount was made with silver epoxy. The brass mount was coated by a layer of epoxy so that only the van der Waals surface of the crystal was in contact with the electrolyte. The exposed area varied from crystal to crystal in the range of 0.01-0.05 cm². The transient photocurrent was registered as a voltage drop across the load resistor R_L (50Ω, in some measurements 5Ω) by a fast storage oscilloscope (7834 with 7AB and 7A92A plunge-in, Tektronix). The scope was connected to the cell holder by a 50Ω coaxial cable (2m, RG 58 U/A) with an additional outer shielding to reduce electrical noise generated by the laser. The potential of the photoanode was set by a dc power supply (Delta Electronica) connected to the counterelectrode *via* a voltage divider. The potential was measured with a high impedance digital voltmeter (HP 3478 A) between the reference electrode (SCE) and ground. The measurement introduces an error caused by the voltage drop of the dark current across the load resistor R_L, which in our experiments, was always small (<5 mV) and this could be neglected. However, this arrangement allows a convenient measurement of the anode potential (in cases where the dark current is excessive, it could be leached out (E. Janata, to be published)). A ruby laser (Korad K1 QDH) delivering pluses of 20 ns pulse width and 500 mJ of energy at 694 nm was used to illuminate the semiconductor in the measuring cell. The laser light was introduced through a small hole (diameter: ~1 mm) of a brass box in which the measuring cell was set. Neutral density filters were used to attenuate the laser intensity.

[1]Permanent address: Institute for Molecular Science, Myodaiji, Okazaki, 444, Japan

Results and Discussion

Dependence of photocurrent on light intensity.—Figure 2 shows the dependence of the peak value of the transient

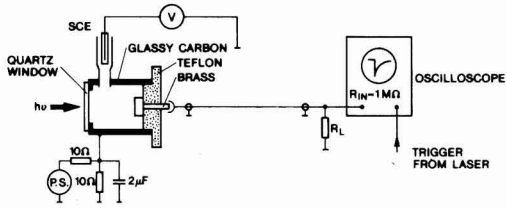


Fig. 1. A block diagram of the experimental system for measuring fast transients in photoelectrochemical cell. R_L is a load resistance. Typically, a 50Ω or 5Ω resistor is used. The input resistance of the oscilloscope is 50Ω.

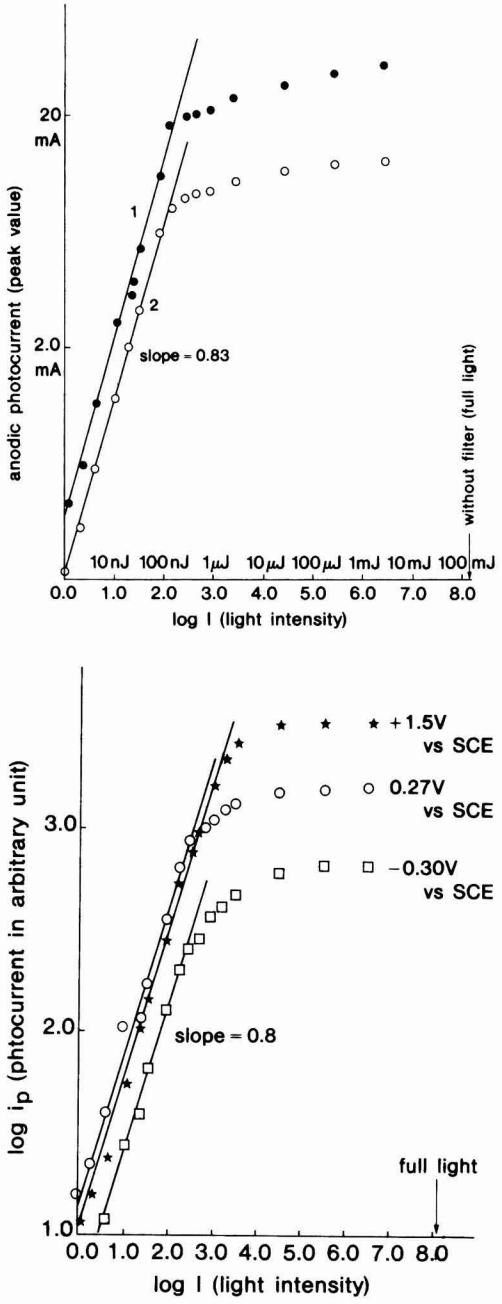


Fig. 2. (a, top) Dependence of transient photocurrent of n-WSe_2 on laser intensity.[2] Curve 1: $R_L = 5\Omega$. Curve 2: $R_L = 50\Omega$. Electrolyte: 2.0M KI. Electrode potential before irradiation: 0.50V *vs.* SCE. (b, bottom) Dependence of transient photocurrent of n-WSe_2 on laser intensity[2] at various potentials. Electrode potential before irradiation: 1.5V *vs.* SCE: 0.27V *vs.* SCE: −0.30V *vs.* SCE. Electrolyte: I_2(0.025M)/I^-(0.5M). $R_L = 50\Omega$.

[2]Since the laser light is introduced, through a small hole (diameter: 1 mm) of a brass box in which the measuring box is set, to a tiny WSE_2 single crystal electrode (surface area of WSe_2 crystals: 0.1-0.5 mm^2), the actual light intensity which hits the WSe_2 surface is estimated to be several times smaller than the values of the laser intensity indicated in the horizontal axis of this figure.

photocurrent on the light intensity for different R_L values (Fig. 2a) and for various electrode potentials (Fig. 2b). The light intensity of the horizontal axis indicates the light energy per laser pulse. As seen in these figures, photocurrent shows a saturation above 100 nJ/pulse. Below 100 nJ/pulse, the photocurrent is approximately proportional to the light intensity ($d \log i_p/d \log I = 0.83$). In this region, the decay of transient photocurrent is expressed approximately by a single exponent (Fig. 3, curve 1). In the saturation region, the rise and decay rates become slower with increase of the light intensity (Fig. 3, curve 2), and finally some structure begins to appear in the transient current with more intense light (Fig. 3, curve 3). When the photocurrent was integrated with time, a similar saturation was observed. Therefore, such a saturation phenomenon is considered an intrinsic one produced by the high density excitation of the semiconductor electrode. Since the photocurrent is nearly proportional to the light intensity below 100 nJ/pulse, the phenomena in this light intensity region are thought to be essentially the same as observed by experiments with a Xe lamp.

When n-WSe_2 was kept at 0.5V *vs.* SCE in 2*M* KI solution, the total charge, which was obtained by integrating the transient current, was 6.8×10^{-10} C. The intensity of laser pulse that hit the WSe_2 electrode was estimated to be 2-3 nJ. This corresponds to the quantum yield of 0.4-0.6. Figure 4 shows the dependence of decay rate of the transient photocurrent on the light intensity where the photocurrent intensity is linear to the light intensity (the electrode potential was kept constant at 0.27V *vs.* SCE). As is shown in this figure, the decay rate is not dependent on light intensity.

Current due to photocorrosion and effect of EDTA.—In K_2SO_4 solution, an anodic photocurrent was observed. In this case, the photocurrent can be related to photocorrosion of WSe_2, which is oxidized to WO_3 and SO_4^{2-} (15, 16). After anodic polarization to 1.8V *vs.* SCE of WSe_2 in 0.5*M*

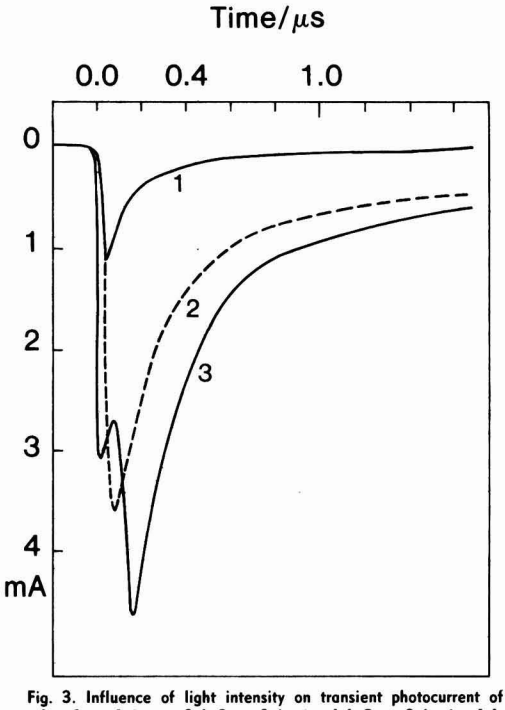


Fig. 3. Influence of light intensity on transient photocurrent of n-WSe_2. Curve 1: log *I* = 2.4. Curve 2: log *I* = 4.4. Curve 3: log *I* = 6.4. Here, the scale for light intensity (*I*) is the same as in Fig. 2. $R_L = 5\Omega$. Electrolyte: 2.0M KI. Electrode potential before irradiation: −0.3V *vs.* SCE.

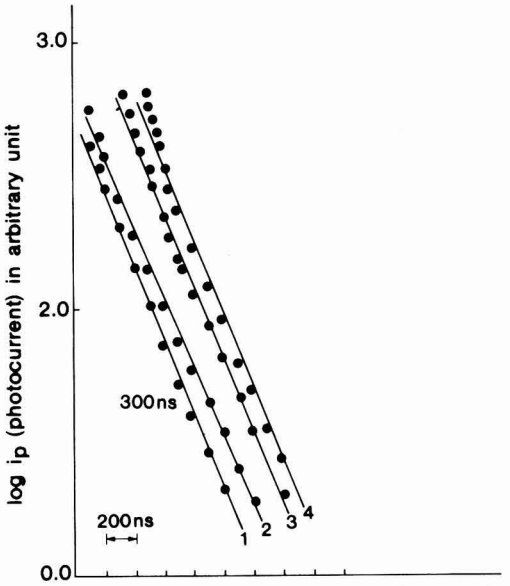


Fig. 4. Dependence of photocurrent decay time on laser intensity. Curve 1: log I = 0.6. Curve 2: log I = 1.3. Curve 3: log I = 2.2. Curve 4: log I = 3.4. The scale for light intensity (I) is the same as in Fig. 2. R_L = 50Ω. Electrolyte: I_3^-(0.025M)// I^-(0.5M). Electrode potential before irradiation: 0.27V vs. SCE.

K_2SO_4, the photocurrent is irreversibly increased. The longer the time of the strong polarization, the larger the irreversible increment grows. Under strong polarization, the van der Waals surface of WSe_2 is destroyed, and the number of lattice defects is increased irreversibly. The current of photocorrosion is thought to flow through these surface defects. Interestingly, EDTA or Ag^+ can suppress effectively this corrosion current. Figure 5a shows the effect of EDTA on the photocorrosion current. Curve 2 in Fig. 5a shows the photocurrent observed after 12h immersion of WSe_2 electrode in a 0.05*M* EDTA solution. This suppression effect was increased gradually with time. It took more than several hours to reach a constant value. It suggests that EDTA molecules are gradually adsorbed on the WSe_2 surface and form complexes with dangling bonds at the stepped surfaces protecting the surface from photocorrosion (17). After 12h immersion in the EDTA solution, the WSe_2 electrode was washed several times with distilled water to remove free EDTA molecules from the electrode surface and the photocurrent was measured in 0.5*M* K_2SO_4. The photocurrent was found to be still suppressed in the K_2SO_4 solution. This indicates that the complexation of EDTA with the surface defects is irreversible and prevents photocorrosion effectively and durably.

Effect of redox reagents on the transient photocurrent.—When the same electrode was used in solutions with redox couples, a strong effect on the photocurrent kinetics was observed. The result is shown in Fig. 5b and in Fig. 6. Interestingly, a remarkable effect was observed not only on the decay rate but also on the current intensity. The electrical charges that were obtained by integrating the transient photocurrents are shown in the same figure. As is shown in these figures, the electrical charge in 2.0*M* KI is increased nine times compared with that in 0.25*M* K_2SO_4 + 0.05*M* EDTA solution. This result indicates that this increment of the photocurrent is due to the oxidation of I^- at the WSe_2 photoelectrode. A similar effect was observed for $K_4Fe(CN)_6$. Figure 6b shows the dependence of the decay of the transient photocurrent on the concentration of $K_4Fe(CN)_6$. As is seen in Fig. 6, the decay rate is influenced strongly by the concentration of

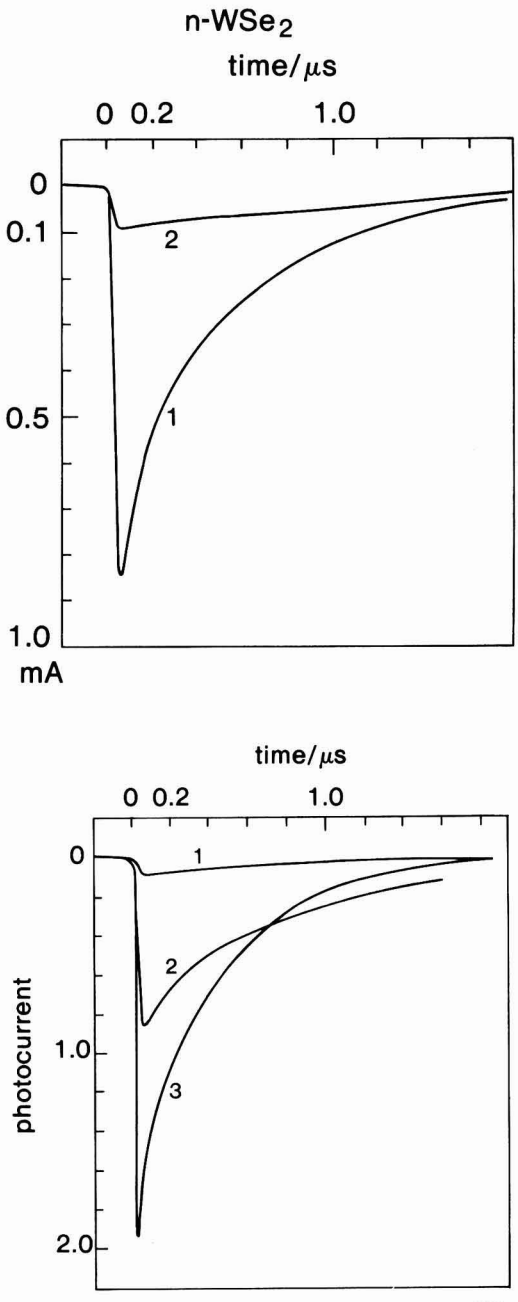


Fig. 5. (a, top) Effect of EDTA on photocurrent transient on n-WSe_2. Curve 1: 0.5M K_2SO_4. Electrode potential before irradiation: 0.0V vs. SCE. Curve 2: 0.25M K_2SO_4, 0.05M EDTA; the photocurrent measurement was carried out after the WSe_2 electrode was immersed in the electrolyte solution for 12h. Electrode potential before irradiation; 1.3V vs. SCE. Laser intensity: log I = 1.4. The scale for light intensity (I) is the same as in Fig. 2. R_L = 50Ω. (b, bottom) Effect of KI in photocurrent transients of n-WSe_2. Curve 1: 0.25M K_2SO_4, 0.05M EDTA. The photocurrent measurement was carried out after the n-WSe_2 electrode was immersed in the electrolyte solution for 12h. Curve 2: 0.2M KI. The photocurrent measurement was carried out after the measurement for curve 1 by replacing the electrolyte solution. Curve 3: 2.0M KI. Laser intensity: log I = 1.4. The scale for light intensity (I) is the same as in Fig. 2. R_L = 50Ω. Electrode potential before irradiation: 0.00V vs. SCE.

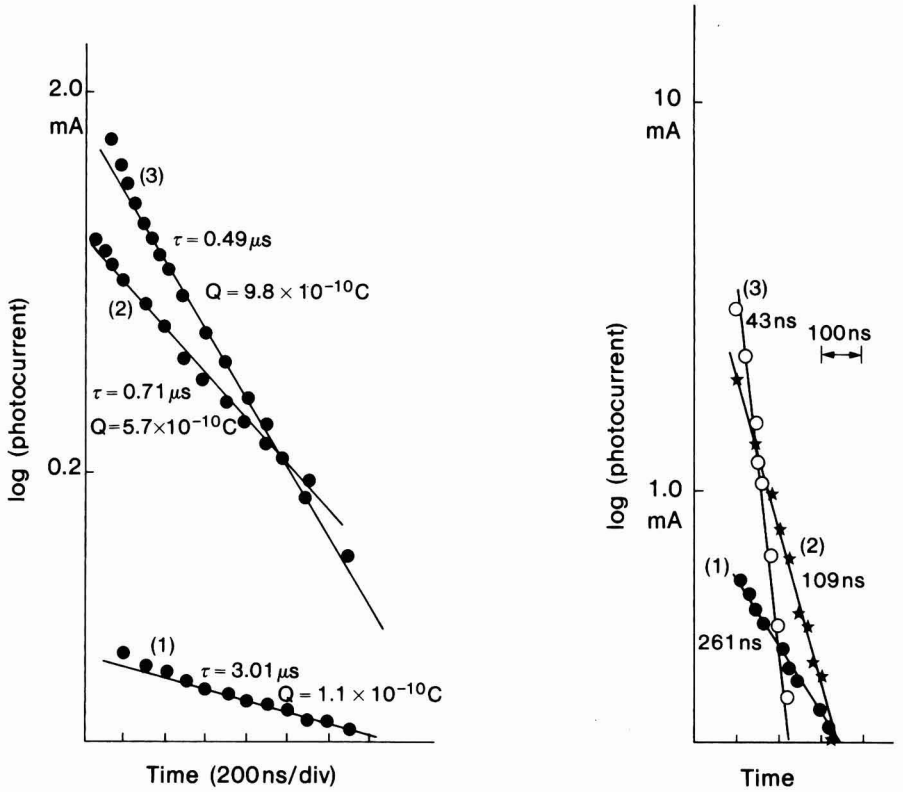


Fig. 6 (a, left) Effect of KI on the kinetics of photocurrent decay. Curve 1: 0.25M K_2SO_4, 0.05M EDTA. The photocurrent measurement was carried out after the n-WSe_2 electrode was immersed in the electrolyte solution for 12h. $\tau = 3.0$ μs. $Q = 1.1 \times 10^{-10}$C. Curve 2: 0.2M KI. $\tau = 0.71$ μs, $Q = 5.7 \times 10^{-10}$C. Curve 3: 2.0M KI. $\tau = 0.49$ μs, $Q = 9.8 \times 10^{-10}$C. Laser intensity: log $I = 1.4$. The scale for light intensity (I) is the same as in Fig. 2. $R_L = 50\Omega$. Electrode potential before irradiation: 0.0V vs. SCE. (b, right) Effect of $K_4Fe(CN)_6$ on the kinetics of photocurrent decay for n-WSe_2. Curve 1: 0.01M $K_4Fe(CN)_6$, 0.01M $K_3Fe(CN)_6$, 0.1M K_2SO_4. $\tau = 261$ ns. $Q = 1.75 \times 10^{-10}$C. Curve 2: 0.1M $K_4Fe(CN)_6$, 0.1M $K_3Fe(CN)_6$. $\tau = 109$ ns. $Q = 2.16 \times 10^{-10}$C. Curve 3: 0.5M $K_4Fe(CN)_6$, 0.1M $K_3Fe(CN)_6$. $\tau = 43$ ns. $Q = 2.23 \times 10^{-10}$C. Laser intensity: log $I = 1.4$. The scale for light intensity (I) is the same as in Fig. 2. $R_L = 5\Omega$. Electrode potential before irradiation: 0.210V vs. SCE.

the redox reagent, even though the electrode potential is kept constant.

Dependence of the transient photocurrent on the electrode potential.—The electrode potential was controlled by using a dc power supply, as shown in Fig. 1. Figure 7 shows the dependence of the photocurrent on the electrode potential for various concentrations of $K_4Fe(CN)_6$. The vertical axis shows the electrical charge, Q, that was obtained by integrating each transient anodic photocurrent against time. In this pulsed laser experiment, the expression by Q is more rational than that by the peak current, i_p, of the transient photocurrent, since the decay rate of the photocurrent depends on the electrode potential. Therefore, the Q-V curve in Fig. 7 corresponds to I-V curve in the steady-state experiment using a lamp. Interestingly, Q is increased with the increase of the concentration of the reducing agent, $K_4Fe(CN)_6$. This result seems to represent one of the characteristic features of this laser pulse method. In the present experiment one laser pulse irradiates the electrode surface with the photon density of $10^{10\text{-}11}$ photons/cm^2. Since the density of adsorbed molecules on the electrode surfaces is usually $10^{14\text{-}15}$ molecules/cm^2, this photon density is very small compared with the molecular density on the electrode surface. Therefore, only a small part of the surface molecules is involved in the electrode reactions per one pulse. Consequently, the influence of the diffusion processes of the reactants and products can be neglected in these experiments, which simplifies analysis of the results obtained by this method. This can be said to be a new aspect characteristic of this method. The result in Fig. 7 indicates that the concentration of the reducing agent on the electrode surface is related to the efficiency of the photoanodic reaction: the higher the concentration of $K_4Fe(CN)_6$, the larger the electrical charge passed. This result seems to be contradictory to the experimental results using a continuous light source like a Xe lamp, because the limiting photocurrent depends on the light intensity but not on the concentration of redox species under continuous irradiation. At the present stage of research, the reason for this phenomenon is not clear. One of the possible explanations is as follows: when the concentration of $K_4Fe(CN)_6$ is small, the main reaction is photocorrosion of WSe_2, in which SeO_4^{2-} and W^{6+} are produced (16). This photocorrosion consists of many reactions, because it is a multielectron transfer process. In a pulse laser experiment, we can observe this process dynamically. If we assume some of these reactions are much slower than the rate of RC time constant, it is possible that the contribution to Q from these slow processes is missed when the photocurrent is integrated, because of the small intensity. Although the integrated value is not negligible due to the slow rate, such a very slow process is possibly missed in a fast ac current measurement. Although the above reason is one of the possible explanations for the result of Fig. 7, further experiments are necessary to explain this phenomenon clearly.

General features of Q-V curves look like the I-V curves in the steady-state experiment with a lamp. However, a detailed examination revealed a clear difference in the on-

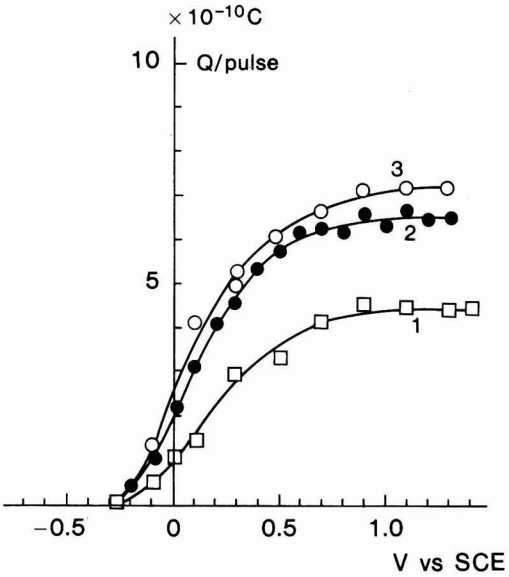


Fig. 7. The total charge, Q, which was obtained by integrating the photocurrent transient for n-WSe_2, vs. electrode potential. Curve 1: 0.01M $K_4Fe(CN)_6$, 0.01M $K_3Fe(CN)_6$, 0.1M K_2SO_4. Curve 2: 0.1M $K_4Fe(CN)_6$, 0.1M $K_3Fe(CN)_6$. Curve 3: 0.5M $K_4Fe(CN)_6$, 0.1M $K_3Fe(CN)_6$. Laser intensity: log I = 1.4. The scale for light intensity (I) is the same as in Fig. 2. R_L = 5Ω.

set potential of the photocurrent between this pulse method and the steady-state method. Figure 8 shows the potential dependence of the transient photocurrent by this pulse method and the steady-state photocurrent by a 500W Xe lamp. Since no reducing agent is added in 0.5M K_2SO_4, these photocurrents are due to the photocorrosion of WSe_2. As is shown in this figure, there is a big difference in the onset potential of photocurrents. In the case of the steady-state experiment, the oxidized species of reducing agents and the trapped holes on the semiconductor surface are thought to be accumulated at the electrode surface by the continuous supply of photogenerated holes (14). The potential drop across the Helmholtz layer would be influenced by those positive charges and the energy bands of the semiconductor would be shifted into positive direction. Since the oxidized species and trapped holes on the electrode surface can also work as electron acceptors, they can recombine again with electrons in the

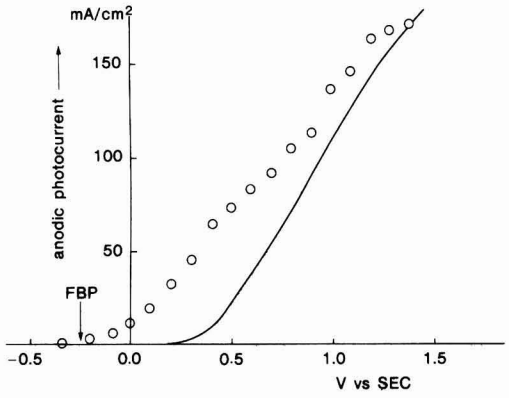


Fig. 8. Comparison of the photocurrent-voltage curve for n-WSe_2 in 0.5M K_2SO_4 solution. Line: steady-state experiment with a 500W Xe lamp. Circle: laser pulse experiment. log I = 1.4. The scale for light intensity (I) is the same as in Fig. 2. R_L = 5Ω.

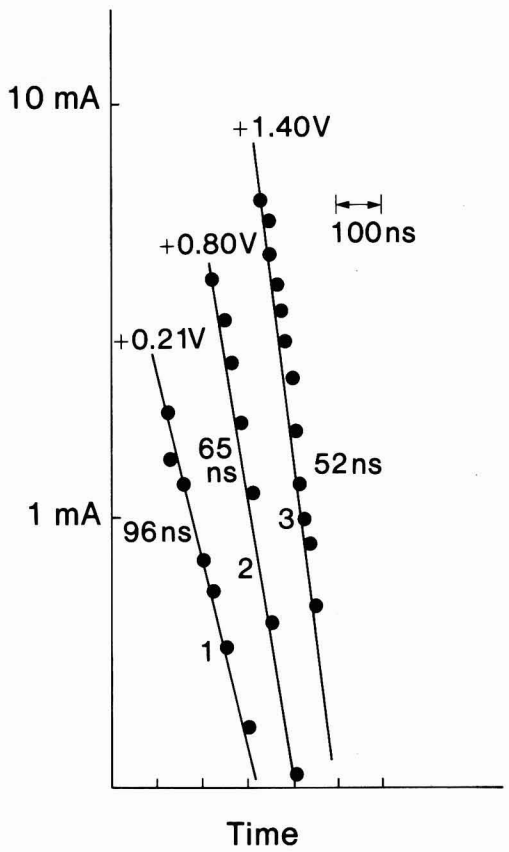


Fig. 9. Dependence of photocurrent decay time on the electrode potential. Electrode potential before irradiation: 0.21V vs. SCE for curve 1 (τ = 96 ns), 0.80V vs. SCE for curve 2 (τ = 65 ns), and 1.40V vs. SCE for curve 3 (τ = 52 ns). Laser intensity: log I = 1.4. The scale for light intensity (I) is the same as in Fig. 2. R_0 = 5Ω. Electrolyte: 0.1M $K_4Fe(CN)_6$, 0.1M $K_3Fe(CN)_6$.

conduction band at the electrode potential where the band bending is shallow. On the other hand, the number of holes generated by one laser pulse is very small ($10^{10\text{-}11}$/cm^2), as was already mentioned. Moreover, the repetition rate is very small (1 pulse/30s). Under these conditions, the accumulation of both the oxidized species and the trapped holes at the electrode surface would be negligibly small. As is seen in Fig. 8, the onset potential of the photocurrent for the laser pulse experiment agrees well with the flatband potential. This result suggests that the perturbation of the electrode surface produced by the laser pulse is quite small. This method appears to be an interesting new tool for determining the flatband potential of a semiconductor electrode.

Photocurrent transient decay kinetics.—As is shown in Fig. 9, the decay rate depends strongly on the electrode potential with a sorter decay at higher applied bias. In addition, it was found also to be dependent on the size of the semiconductor electrode and the magnitude of the load resistor, R_L. These facts suggest that the decay rate is determined by RC (19). Here R and C are the resistance and capacitance of the whole system. Figure 10a shows the dependence of τ^{-2} (τ: the lifetime of the exponential decay of the transient photocurrent) on the electrode potential. Near the flatband potential (V < 0.0V vs. SCE), a faster component precedes the RC-determined decay. In this case, only the RC component was considered. As is shown in this figure, τ^{-2} for each load resistance, R_L is on

a straight line. Since the capacitance of the whole system is approximated by that of the semiconductor electrode, it is expressed as

$$C = \frac{A}{\sqrt{V - V_0}} \quad [1]$$

Here $A = (\epsilon e N_d/8\pi)^{1/2}$ (ϵ: dielectric constant, e: electron charge, N_d: donor density) and $V_0 = V_{FB} + kt/e$ (V_{FB}: flat-band potential). By using this equation, τ^{-2} is expressed as

$$\tau^{-2} = (RC)^{-2} = \frac{V - V_0}{A^2R^2} \quad [2]$$

The solid lines (1) and (2) in Fig. 10a are the calculated ones with $A = 3.164 \times 10^{-9}\ F\ V$, $R_{int} = 22\Omega$, each value of R_L (5Ω for the solid line (1) and 50Ω for (2)), and $V_0 = -0.23$V *vs.* SCE.[3] From the intersection with x axis, -0.23V

[3]The total resistance R is calculated by the following equation

$$R = \Sigma R_i = \frac{1}{R_L^{-1} + 10^{-6}} + 5 + R_{int} \quad [3]$$

Here we took account of the fact that the load resistance R_L is in a parallel connection with the input resistance of the oscilloscope 1MΩ. 5Ω in the second term is the resistance in the potential control unit in Fig. 1, and R_{int} is the internal resistance of the photoelectrochemical cell (the total resistance of the semiconductor electrode, the electrolyte solution, and the counter-electrode.

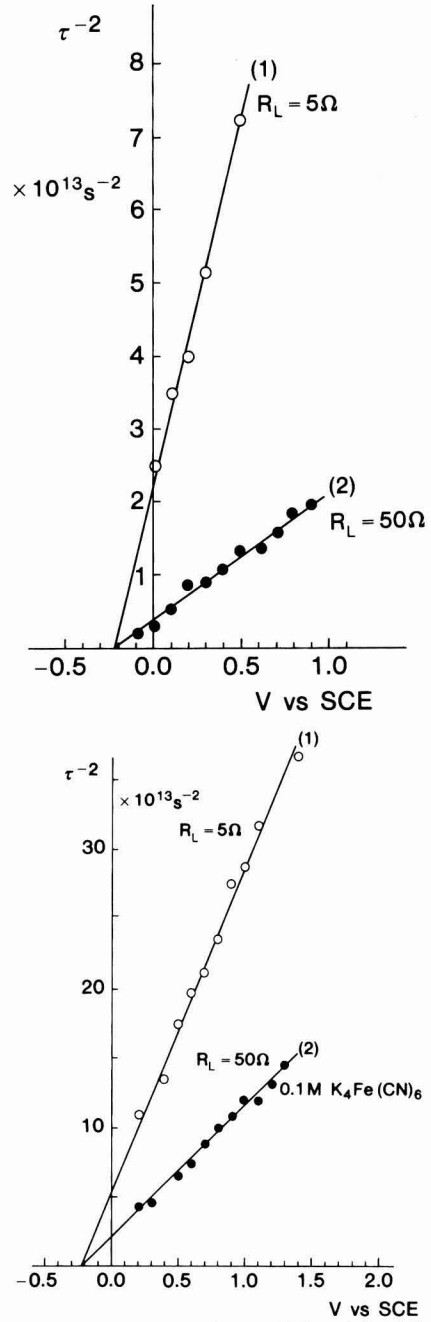


Fig. 10. (a, top) τ^{-2} *vs.* electrode potential. Curve 1: $R_L = 5\Omega$. Curve 2: $R_L = 50\Omega$. Electrolyte: 2.0M KI. Laser intensity: log $I = 1.4$. The scale for light intensity (I) is the same as in Fig. 2. (b, bottom) τ^{-2} *vs.* electrode potential. Curve 1: $R_0 = 5\Omega$. Curve 2: $R_0 = 50\Omega$. Electrolyte: 0.1M $K_4Fe(CN)_6$, 0.1M $K_3Fe(CN)_6$. Laser intensity: log $I = 1.4$. The scale for light intensity (I) is the same as in Fig. 2.

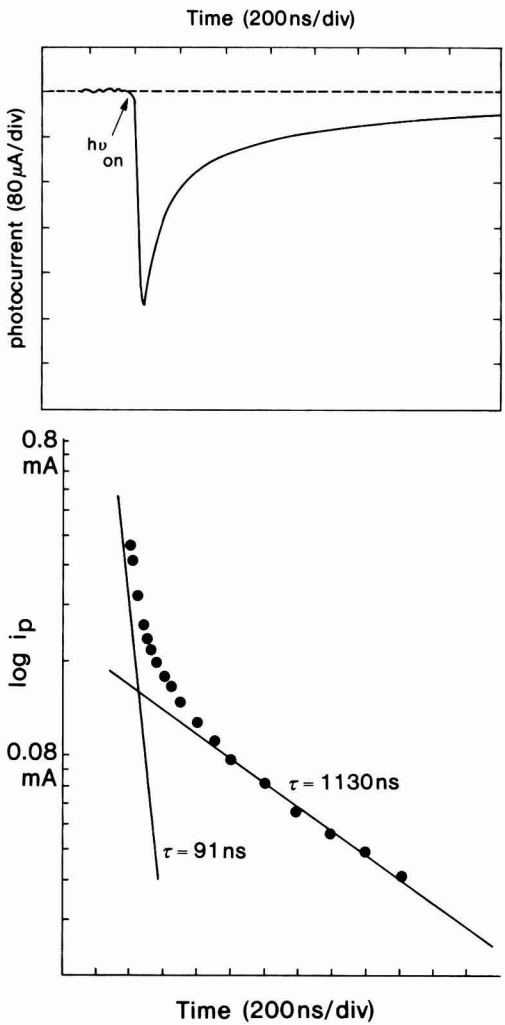


Fig. 11. The photocurrent transient of n-WSe_2 at -0.30V *vs.* SCE. Electrolyte: 2.0M KI. Laser intensity: log $I = 1.4$. The scale for light intensity (I) is the same as in Fig. 2. $R_L = 50\Omega$. (a, top) Photocurrent/time behavior. (b, bottom) log(photocurrent intensity)/time behavior.

vs. SCE, and a correction by kT/e, a value of -0.06V *vs.* NHE is obtained as the flatband potential. This value is close to the value obtained by capacity measurements ($+0.05$V *vs.* NHE, 98.4 MH_z, 0.5*M* K_2SO_4) and coincides with a flatband potential of -0.09V *vs.* NHE found by Nagasubramanian and Bard for n-WSe_2 in contact with an aqueous/electrolyte containing 0.5*M* Na_2SO_4 at *p*H 4.5/16.1 (18).

As is seen Fig. 10a, the agreement between the experiment and the calculation based on this simple model is good. Figure 10b shows the result for 0.1*M* $K_4Fe(CN)_6$. The solid lines in this figure are the calculated ones with $A = 8.729 \cdot 10^{-10}\ F\ V$, $R_{int} = 65.2\Omega$, each value for R_L and $V_{FB} = -0.29$V *vs.* SCE. Equation [2] can predict the lifetime at any potential for any R_L. For instance, $R_L = 0.5\Omega$, 83 ± 8 ns at 0.22V *vs.* SCE and 46 ± 5 ns at 1.30V *vs.* SCE were obtained experimentally for the same electrode in 0.1*M* $K_4Fe(CN)_6$. The calculated values obtained by Eq. [2] with numerical values for A, R_{int} and V_{FB} are 92 ns at 0.22V *vs.* SCE and 50 ns at 1.30V *vs.* SCE. They agree with the experimental ones. Differences obtained in the slope of the τ^{-2} *vs.* V plot for different redox electrolytes can be explained by different resistances of the electrolyte solution, thus influencing the overall R value.

As is shown in Fig. 6a and 6b, the decay rate is increased in the solution of KI or $K_4Fe(CN)_6$, even though the electrode potential is kept constant. At first sight, it would appear that the decay rate expresses the rate of oxidation of these reducing agents. However, as is analyzed in Fig. 10a and 10b, the decay rate was found to be determined by the RC time constant. The following explanations may be advanced for this interesting phenomenon: since the flatband potential is shifted into negative direction in the solution of KI or $K_4Fe(CN)_6$ (16), the band bending is increased at a fixed potential; then, the capacitance of the space charge layer is decreased according to Eq. [1]; simultaneously, the electron hole separation occurs more efficiently. The resistance change of electrolyte solution may be also responsible.

Another interesting result is that the transient photocurrent at the potential more negative than 0.0V *vs.* SCE is composed of two exponents. Figure 11(a) shows the typical example and Fig. 11b shows its logarithmic plot. As is seen in this plot, the lifetime of the fast component is 91 ns, and that of the slow component is 1130 ns. Because of the shifting of the potential into the cathodic direction, the slow component becomes slower, while the fast one becomes faster. The ratio of the fast component to the slow one is increased with increasing of the cathodic polarization. As already mentioned, the lifetime of the slow component can well be explained by RC. Since the fast component begins to appear near the flatband potential, it is thought to be related with the electron hole recombination. Similar behaviors were observed for other kinds of electrodes, such as CdSe (19). At low electrode potentials (more negative than -0.3V *vs.* SCE) also, a weak cathodic current following the anodic one has been observed. At more positive potentials, only anodic photocurrents have been observed. The cathodic current can be related to a back reaction of intermediates formed in the corrosion processes. It appears in the same voltage range where a back reaction can also be observed with intermittent light.

Acknowledgment

The authors would like to thank Professor E. Bucher, University of Konstanz, for supplying WSe_2 crystals.

Manuscript submitted Nov. 26, 1984; revised manuscript received Nov. 4, 1985.

The Institute for Molecular Science assisted in meeting the publication costs of this article.

REFERENCES

1. V. A. Mayamlin and Y. V. Pleskov, "The Electrochemistry of Semiconductors," Plenum Press, New York (1967).
2. S. P. Perone, J. H. Richardson, S. B. Deutscher, J. Rosenthal, and J. N. Ziemer, *This Journal*, **127**, 2580 (1980).
3. S. B. Deutscher, J. H. Richardson, S. P. Perone, J. Rosenthal, and J. Ziemer, *Faraday Discuss. Chem. Soc.*, **70**, 1 (1980).
4. J. H. Richardson, S. P. Perone, and S. B. Deutscher, *J. Phys. Chem.*, **85**, 341 (1981).
5. P. V. Kamat and M. A. Fox, *J. Phys. Chem.*, **87**, 59 (1983).
6. A. Frippiat, A. Kirsch-De Mesmaeker, and J. Nasielski, *This Journal*, **130**, 239 (1983).
7. T. Kawai, H. Tributsch, and T. Sakata, *Chem. Phys. Lett.*, **69**, 336 (1980).
8. Z. Harizon, N. Croitorn, and S. Gottesfeld, *This Journal*, **128**, 341 (1981).
9. S. Prybyla, W. S. Struve, and B. A. Parkinson, Submitted to *This Journal*.
10. Z. Harizon, D. Huppert, and S. Gottesfeld, *J. Electroanal. Chem.*, **150**, 571 (1983).
11. W. Jaegermann, *J. Phys. Chem.*, In press.
12. F. Willig, K. Bitterling, K. P. Charle, and F. Jecker, *Ber. Bunsenges, Phys. Chem.*, **88**, 374 (1984).
13. S. Gottesfeld and S. W. Feldberg, *J. Electroanal. Chem.*, **146**, 47 (1983).
14. W. Jaegermann, T. Sakata, E. Janata, and H. Tributsch, *ibid.*, **189**, 65 (1985).
15. H. Tributsch, *Shuct. Barding*, **49**, 127 (1982).
16. H. Tributsch, *Faraday Discuss. Chem. Soc.*, **70**, 190 (1980).
17. G. Razzini, L. Peraldo Bicelli, G. Pini, and B. Scorsati, *This Journal*, **128**, 2134 (1981).
18. G. Nagasubramanian and A. J. Bard, *ibid.*, **128**, 1055 (1984).
19. R. H. Wilson, T. Sakata, T. Kawai, and K. Hashimoto, *ibid.*, **132**, 1082 (1985).

A Platinized Titanium Anode for Chromium Electroplating

F. Hine*

Nagoya Institute of Technology, Gokiso-cho, Showa-ku, Nagoya 466, Japan

K. Takayasu

Showa Company, Limited, 2441 Kitatahara-cho, Ikoma, Nara 630-01, Japan

N. Koyanagi

Ishifuku Metal Industry Company, 1080 Aoyagi-cho, Soka, Saitama 340, Japan

There are two types of electrolyte for chromium electroplating: the Sergent bath and the chromate solution containing fluorine compound. The Sergent bath is an acidified chromate solution consisting of some 250 g/liter CrO_3, and easy to operate. However, the current efficiency for chromium deposition is low, about 10% or less. Metal deposition no longer takes place if the electric circuit is once interrupted. This is probably due to rapid passivation of the metal surface, and it is troublesome. Therefore, the Sergent bath is inadequate for some applications, such as the barrel plating.

Of the modified solutions containing fluorine compound, the fluosilicate bath, consisting of CrO_3, H_2SO_4, and sodium hexa-fluosilicate Na_2SiF_6, is most popular, although other electrolytic solutions, such as those containing fluoborate, for example, are also used. The current efficiency for metal deposition from the fluosilicate bath (FS bath, hereafter) is somewhat large compared to that from the Sergent bath because of the difference of the catalytic activity in both solutions. Metal deposition from the FS bath is able to continue even if the electric current is switched off during operation. It is of importance from the practical viewpoint.

A number of scientific papers on the chromium electroplating have been published since Müller proposed the mass transport through the oxide film formed on the cathode surface (1). However, the mechanism on the chromium electrodeposition has not yet been fully established.

Lead and its alloys, such as Pb-Sn and Pb-Sb, are employed as the anode in both the Sergent bath and the FS bath (2, 3). A lead dioxide layer formed on the surface prevents the anode from corrosion. At the open-circuit potential or at zero current, however, the oxide layer changes to lead chromate, and the cell voltage becomes high. This is caused by an extremely high resistance of the $PbCrO_4$ layer. The consecutive formation of PbO, $Pb(OH)_2$, $PbCrO_4$, and PbO_2 on the lead anode immersed in the chromium electroplating bath has been pointed out on the respective potentials before oxygen evolution, but no significant effect of addition of sulfuric acid to the chemical composition of the oxide layer has been found (4).

The corrosion rate of the Pb alloy anode in the Sergent bath is in the range 1-10 mg/Ah, depending on the alloy composition, the casting, and the operating conditions, but the anode consumption in the FS bath is great. According to the laboratory test, the corrosion rates of a Pb-2% Sn alloy anode in the Sergent bath and the FS bath were 5 and 12 mg/Ah, respectively, under normal conditions. With the plant experiences, the grain boundaries of alloy are attacked, fine particles go away into the solution, and a part of these solids precipitate on the cell bottom which is troublesome for the cell operation.

The lead alloy anode is consumed by two factors: the chemical attack and the physical degradation. The anode surface is dissolved gradually by electrolysis or by the faradaic current under operating conditions. The FS bath attacks the anode surface with a more serious effect than does the Sergent bath. Even so, the faradaic corrosion rate is relatively small, as shown above. The erosion loss by oxygen bubbles and the intergranular corrosion of the surface oxide of the alloy depend on the oxide layer and the alloy composition, as well as the solution composition.

In practice, however, the anode consumption and its cost evaluation are complicated because scrapings must be considered, and are great. For example, an electroplater consumed 24 anode strips for 3 years (or 888 days) of operation with the Sergent bath at 25 kAh/day. This corresponds to about six times of the faradaic loss, or more than 80% of the alloy was scraped, while the alloy could be recovered. Deformation of the anode plate is also a problem, and is dependent greatly on its manufacture.

As a result, any dimensionally stable anode like the DSA for chlor-alkali cells is looked for. Of course, such anodes should have a catalytic activity on the oxidation of chromic ions as well.

It is well known that existence of a certain amount of chromic ions in the chromium plating bath, composed of acidified chromate solution, is essential because without them chromium plating can no longer take place. A sound concentration of chromic ions is said to be in the range 1-5 g/liter. Chromic ions may form at the cathode as a side reaction of chromium plating, and hence an excess Cr^{3+} must be removed and/or converted into chromate to keep the Cr^{3+} concentration at a suitable level. Oxidation of Cr^{3+} to $Cr_2O_7^{2-}$ is an important role of the anode to be used, and the lead anode is capable of this action. Such characteristics are seldom seen at present with other materials. In practice, the area of the Pb anode to the cathode area is adjusted so as to control the Cr^{3+} concentration in the plating bath.

The laboratory experiment and the field test with a new anode material for chromium electroplating have been conducted. The time variations of the Cr^{3+} concentration in the electrolytic cell and degradation of the anode have been observed. The polarization characteristics of several anode materials in various solutions have been investigated to clarify the behavior of these anodes.

Experimental Procedure

Anode materials.—A new anode, MODE, is a platinized titanium sheet loaded with thermally deposited IrO_2 as catalyst. This material has been developed as an anode

*Electrochemical Society Active Member.

Table I. Electrolytes examined

	Composition (g/liter)		
	CrO_3	H_2SO_4	Na_2SiF_6
Sergent bath	250	2.5	—
Fluosilicate bath	250	1.5	5.0
Modified FS bath	250	0.5-2.5	0.1-15.0

for hypochlorite cell (5) while modified to some extent to meet chromium plating.

A platinized titanium sheet, referred to as Pt-Ti, without catalyst, was also prepared as reference.

A plain Pt sheet, pure Pb, Pb-Sn (5%) alloy, and a PbO_2-electrodeposited Ti mesh were examined in parallel.

Plating solutions.—The solution compositions of the Sergent bath, the FS bath, and the modified solutions examined, are listed in Table I. Although the fluosilicate concentration in the commercial bath was *ca.* 5 g/liter as Na_2SiF_6, it was varied in the range 0.1-15 g/liter to investigate the features and effectiveness of the MODE in the solutions containing fluosilicate.

Both the Sergent bath and the FS bath for the laboratory experiment were prepared with chemically pure CrO_3 and H_2SO_4. The Cr^{3+} concentration in the test solution was controlled by adding oxalic acid as the reducing agent. The time variation of the Cr^{3+} concentration was measured at a certain interval by means of the absorption spectrometry at a wavelength of 590 nm. The results varied somewhat due to formation of complex ions in various forms and other reasons, but the results obtained were useful for the purpose. Chromate was titrated by iodometry.

Polarization measurements.—The polarization measurements were conducted by the current interruption method to eliminate the IR-drop between the working electrode and the Luggin-Haber probe connected with the saturated calomel electrode through a salt bridge. Nickel was used as the counterelectrode in all experiments.

Field tests.—In a practical plant using the Sergent bath, a Fiberglas reinforced plastic (FRP) cell of *ca.* 5 m^3 in volume, equipped with a number of the MODE of 10 cm wide and 100 cm high, was operated for several months to investigate the corrosion resistance. Also, the MODE was employed as the auxiliary anode in the Sergent bath to ensure the uniform current distribution on the cathode to be plated.

In another plant where the FS bath was used, the MODE was tested as the principal anode. A modified solution containing less fluosilicate than in a common solution was tested at an experimental station of a chemical dealer.

The amperage and cell voltage were measured during operation. The Cr^{3+} concentration was measured at certain intervals. The surface morphology of the MODE was investigated occasionally.

Results and Discussion

Figure 1 shows the Cr^{3+} concentration in the Sergent bath in a laboratory cell as a function of the time of electrolysis. It is clear that the Cr^{3+} concentration in the cell equipped with the Pb and Pb-Sn alloy anodes is almost unchanged during electrolysis. Although chromate ions are reduced to chromic ions at the cathode as a side reaction, the Pb anode can oxidize chromic ions into chromate ions in this case. Of course, the oxidation rate of Cr^{3+} at the anode differs from the formation rate of Cr^{3+} at the cathode, so that the ratio of the anode area to the cathode area is adjusted in plating shops with skill to keep the solution composition at an adequate level.

On the other hand, the Cr^{3+} concentration increased greatly with time when the Pt anode was used. No significant effect of the IrO_2 catalyst was found in the Sergent bath.

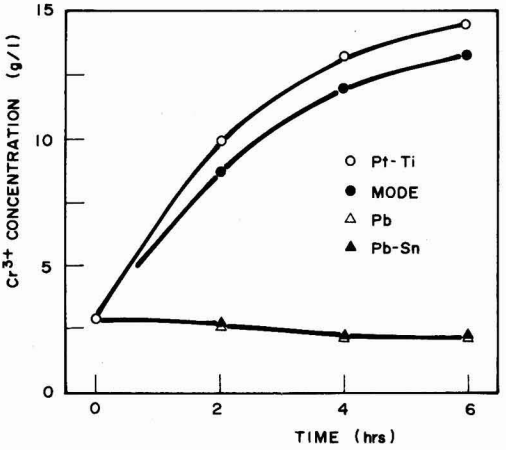


Fig. 1. Cr^{3+} concentration in the Sergent bath as a function of the time on line. Total current = 5A. Solution volume = 150 ml. Temperature = 54°-62°C.

Latimer states that it is difficult to oxidize chromic ions to chromate at a platinum anode, while the oxidation is highly efficient at a lead anode probably due to the association of the Pb^{2+}/PbO_2 couple with the mechanism of oxidation reaction (6).

The Cr^{3+} concentration *vs.* time curves obtained with a conventional FS bath is illustrated in Fig. 2. The Cr^{3+} concentration in a cell equipped with the Pb alloy anode was kept constant, as observed in the Sergent bath. It is interesting that the electrodeposited PbO_2 anode (7) worked well as well as plain Pb. Chromic ions are not oxidized by the Pt anode also in this solution. However, note that the Cr^{3+} concentration in the FS bath equipped with the MODE is unchanged. Thus, experiments were conducted by changing the fluosilicate concentration in the range 0.1-15 g/liter. The MODE could oxidize Cr^{3+} to chromate when the solution contained a small amount of fluosilicate ions.

Figure 3 illustrates the polarization curves of a plain Pt anode in the Sergent bath containing *ca.* 9 g/liter Cr^{3+}. A polarization curve of a Pt anode obtained in the Sergent bath free of Cr^{3+} is also plotted as reference (curve 4). The Pt working electrode was polarized cathodically at 1.0V *vs.* SCE for about 1h prior to the experiment to reduce the

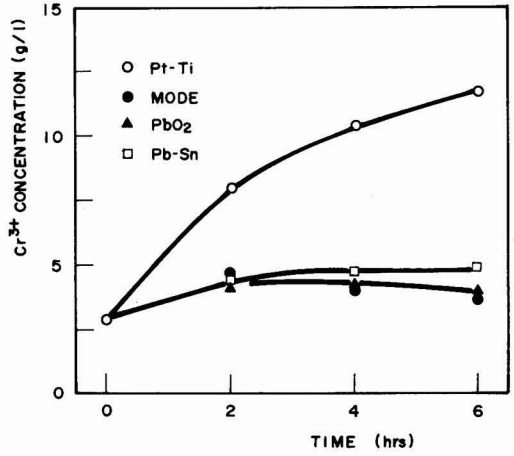


Fig. 2. Cr^{3+} concentration in a fluosilicate bath as a function of the time on line. Total current = 5A. Solution composition = 250 g/liter CrO_3 + 5 g/liter Na_2SiF_6 + 1.5 g/liter H_2SO_4. Solution volume = 150 ml. Temperature = 40°-44°C.

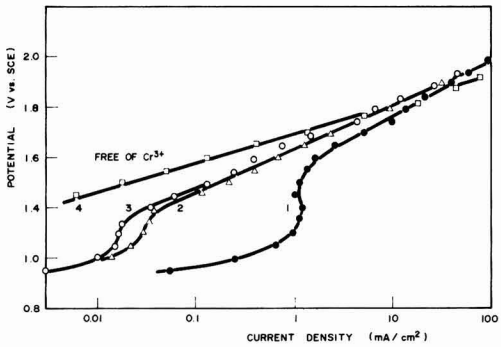


Fig. 3. Polarization curves of a plain Pt anode in the Sergent bath at 50°C. Solution composition = 250 g/liter CrO_3 + 2.5 g/liter H_2SO_4 + *ca.* 9 g/liter Cr^{3+}.

surface oxide. Such a Pt anode showed very low overvoltage at low current densities (curve 1). The potential rose to *ca.* 1.2V *vs.* SCE quickly probably because of the oxidation of the Pt surface. Oxygen formation took place simultaneously. The potential *vs.* current density curve did not follow curve 1 when the polarization current was decreased from the highest current density (curve 2). The potential came down by *ca.* 0.2V when the current density was decreased to 0.02 mA/cm², and tended to the static potential. The polarization curve of the electrode with current increasing (curve 3) was almost the same as of curve 2, while the limiting current moved slightly to the left. Curve 4 shows the polarization curve of oxygen evolution at the Pt anode in the solution free of Cr^{3+}. No other parallel reaction may take place. The Tafel slope of this polarization curve is *ca.* 100 mV/decade and is smaller than those of curves 2 and 3 because it is expected that the anodic oxidation of chromic ions takes place to some extent in parallel with oxygen evolution at the anode in the Sergent bath containing Cr^{3+}. Schuldiner *et al.* studied the characteristics of a Pt electrode in sulfuric acid in the potential range from hydrogen evolution to the oxygen evolution (8). The cathodically polarized Pt electrode is charged with hydrogen which depolarizes the electrode during anodic polarization until all of the dissolved hydrogen is oxidized.

The polarization behavior of the Pb anode differs greatly from that of the Pt anode as shown in Fig. 4 and 5. As is shown in Fig. 4, the potential of a fresh Pb anode moved extensively by *ca.* 0.5V (curve 1), and the anode surface was oxidized. The anode potential was almost unchanged thereafter, until the current density reached at 10 mA/cm². Finally, the potential rose to the positive direction with the increase in current density. The polarization curve, with the decrease in current density (curve 2),

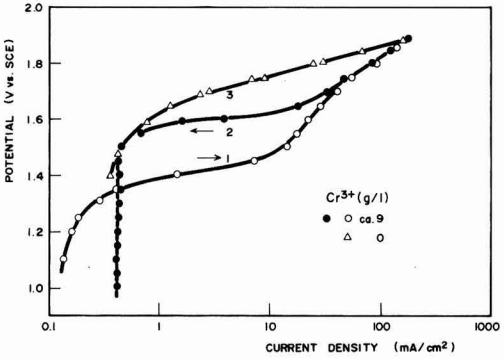


Fig. 4. Polarization curves of a pure Pb anode in the Sergent bath at 50°C. Solution composition = 250 g/liter CrO_3 + 2.5 g/liter H_2SO_4.

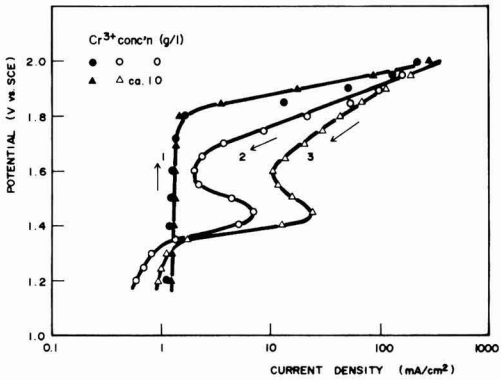


Fig. 5. Polarization curves of a pure Pb anode in a fluosilicate bath at 40°C. Solution composition = 250 g/liter CrO_3 + 5 g/liter Na_2SiF_6 + 1.5 g/liter H_2SO_4.

resembles curve 1 in shape, while the potential of the plateau is *ca.* 0.2V more positive than that of curve 1. This is caused by an oxide layer formed on the anode surface.

Polarization curve 3 was obtained in a solution free of Cr^{3+}. It shows the polarization behavior of oxygen formation at a Pb anode in the Sergent bath. Of course, the anode surface is already covered with a PbO_2 layer.

In the FS bath, on the other hand, the polarization potential of a fresh anode jumped up from 1.2V *vs.* SCE to 1.8V, and the potential moved to the positive direction with the increase in current density. The anode surface was covered by a brown PbO_2 layer. With the decrease of the current density, the anode potential moved monotonously to *ca.* 1.6V *vs.* SCE, then dropped to *ca.* 1.4V, with some increase and decrease of the current density probably due to the change of the surface oxide layer on the anode. Note that the polarization curve with the decrease in current density is affected greatly by the existence of Cr^{3+}; a similar effect was found in the Sergent bath as shown in Fig. 4.

It is clear that the polarization behavior of a MODE in the Sergent bath is not affected by the presence of Cr^{3+}, as shown in Fig. 6.

Figures 7 and 8 show the polarization curves of the MODE in solutions containing various amounts of Na_2SiF_6 with and without Cr^{3+}, respectively. There is no significant influence of chromic ions on the polarization curves at low current densities. However, the polarization curves at the current densities of more than 10 mA/cm² are affected by the Cr^{3+} concentration, *i.e.*, the higher the Cr^{3+} concentration, the higher the potential. Fluosilicate ions might be adsorbed by the active sites on the working electrode, resulting in a disturbance of oxygen evolution. The anodic reaction consists of an oxygen formation and oxidation of chromic ions. From the thermodynamic viewpoint, both processes can occur in a whole range of the current density shown in Fig. 3-8. In fact, Cr^{3+} is oxi-

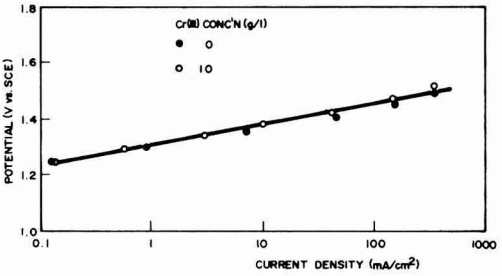


Fig. 6. Polarization curve of a MODE in the Sergent bath at 40°C. Solution composition = 250 g/liter CrO_3 + 2.5 g/liter H_2SO_4.

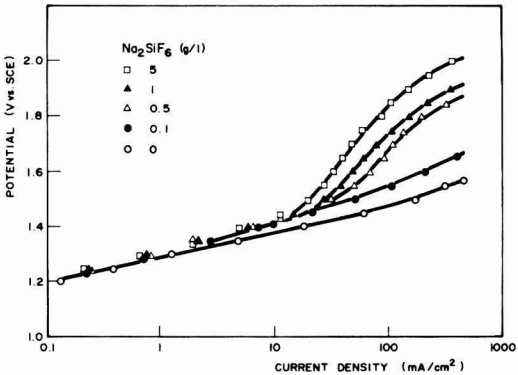


Fig. 7. Polarization curves of the MODE in the Cr electroplating bath containing different amounts of fluosilicate at 40°C. Cr^{3+} concentration = 10 g/liter.

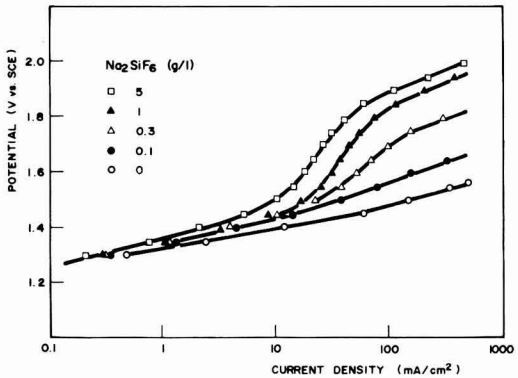


Fig. 8. Polarization curves of the MODE in the Cr electroplating bath containing different amounts of fluosilicate at 40°C. Solution is free of Cr^{3+}.

dized efficiently on the Pb anode in both the Sergent and the FS baths. With the MODE, oxidation of Cr^{3+} is stimulated by fluosilicate ions, but oxygen bubbles evolve at the Pt anode preferentially with no significant oxidation of chromic ions. In Fig. 3 and 4, the oxygen overvoltage of a fresh Pt anode is relatively low in comparison with a Pb anode, but the Pt anode is oxidized gradually to form the Pt-O layer (9). Such a Pt anode is polarized greatly (curves 2-4 in Fig. 3). The difference of curves 2 and 3 from curve 4 is attributed to the oxidation of Cr^{3+} on the Pt anode, as stated above. One can consider that the oxidized Pt anode is able to convert Cr^{3+} into CrO_4^{2-} because the anode potential is sufficiently high, but that differs from the results shown in Fig. 1 and 2. The different reaction sequence on the MODE from that on the Pt anode is attributed to the electrochemical catalysis of IrO_2, loaded on a porous platinum layer on the MODE surface, while the reaction mechanism and the role of IrO_2 have not been clarified in detail.

As described above, the field tests for applicability of the MODE as the anode for chromium electroplating are being conducted in two locations, using the Sergent bath and the FS bath. Figure 9 illustrates an example of the MODE for the chromium plating. The frame is made of the Ti-cladded steel of *ca.* 10 cm wide and 1m long, and the triangular crossbars are of solid titanium. Such a structure enables one to remove oxygen bubbles quickly, thus resulting in stimulation of mass transfer and oxidation of chromic ions at the anode surface. Uniform current distribution along the anode surface is anticipated as well.

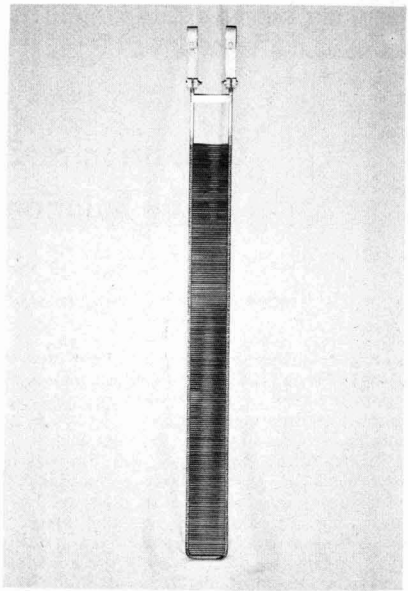


Fig. 9. An example of the MODE for Cr electroplating

Use of the Ti-clad steel is not only for reducing the cost, but for keeping the electrical conduction in the electrode structure. An appropriate weight of the anode is also of importance in the plating shop since otherwise electric contact of the anode hanger with the busbar becomes insufficient.

In conclusion, applicability of a platinized titanium anode, loaded with IrO_2 catalyst as a candidate of the anode for chromium electroplating, was investigated. This anode material, named MODE, was resistant to corrosion, but the ability of oxidation of chromic ions to chromate was weak in a fresh solution of the Sergent bath. On the other hand, chromic ions in the plating bath containing fluosilicate, to some extent, are oxidized efficiently on the MODE surface. This is caused by the catalytic behavior of IrO_2. The anodic polarization curve of the MODE was also affected greatly by the fluosilicate ions in the range of current density higher than 10 mA/cm².

The field tests of the MODE are being conducted at two locations without serious troubles.

Acknowledgments

The authors wish to express many thanks to Dr. M. Yasuda and Y. Kondo for their great efforts in laboratory work. Also we thank the Shinsei Denka Kogyo Company, Nagoya, and Uemura Kogyo Company, Osaka, who gave the opportunities for the field tests.

Manuscript submitted June 17, 1985; revised manuscript received Sept. 26, 1985. This was Paper 425 presented at the Toronto, Ontario, Canada, Meeting of the Society, May 12-17, 1985.

Ishifuku Metal Industry Company assisted in meeting the publication costs of this article.

REFERENCES

1. E. Müller, *Z. Elektrochem.*, **5**, 469 (1899).
2. G. Dubpernell, "Electrodeposition of Chromium from Chromic Acid Solutions," p. 21, Pergamon Press, New York (1977).
3. R. Weiner, "Die galvanische Verchromung," p. 134, Eugen G. Leuze Verlag, Saulgau/Wurtt (1974).
4. T. M. H. Saber and A. M. Shams El Din, *Electrochim. Acta*, **13**, 937 (1968).
5. T. Asaki, Y. Kamegaya, and K. Takayasu, *This Journal*, **132**, 1895 (1985).
6. W. M. Latimer, "The Oxidation States of the Elements

and Their Potentials in Aqueous Solutions," p. 250, Prentice-Hall, Englewood Cliffs, NJ (1961).
7. F. Hine, M. Yasuda, T. Iida, Y. Ogata, and K. Hara, *Electrochim. Acta*, **29**, 1447 (1984).
8. M. Rosen, S. Schuldiner, and D. R. Flinn, *This Journal*, **119**, 412 (1972).
9. J. P. Hoare, "The Electrochemistry of Oxygen, p. 81, Interscience Publ., New York (1968).

Deposition of Zinc Selenide Thin Films by Solution Growth Technique

P. Pramanik and S. Biswas

Department of Chemistry, Indian Institute of Technology, Kharagpur 721302, India

Solution growth techniques for the deposition of thin films of lead selenide (1-3) and bismuth selenide (4) have been reported earlier. Various well-known processes for the formation of zinc selenide thin films have been cited in the literature (5-6). However, the chemical deposition method for the formation of ZnSe thin film has not yet been reported. The present brief communication describes the authors' successful attempt for the deposition of ZnSe thin films by solution growth technique.

A 0.4M sodium selenosulfate solution was prepared by refluxing 8g selenium powder with 25 gm anhydrous sodium sulfite in 140 ml of distilled water for 8h. It was cooled and kept overnight, since on cooling, a little selenium separated out from the solution. It was then filtered to obtain a clear solution and made up to 200 ml with distilled water.

For the deposition of ZnSe thin films, 2.5 ml of 1*M* zinc chloride solution was taken in a 50 ml beaker and to it, 10 ml of 7.4*M* triethanolamine (TEA), 2.5 ml of 7.5*M* sodium hydroxide solution, and 12.5 ml of 14*M* ammonia solution were added in order to form, with continuous stirring, a clear homogeneous solution. Then 0.8 ml of hydrazine hydrate (80%) was added, followed by another 6.3 ml of about 0.4*M* sodium selenosulfate solution and the volume consisted of about 50 ml of distilled water. The solution was then poured into another beaker containing a scrupulously cleaned glass slide, clamped vertically; finally the container was placed into an oil bath at around 100°C. After 1h, the slide was covered with a light yellowish deposit, which very slowly changed to a light reddish color, was taken out, washed with distilled water, and dried in a dessicator. The ZnSe film thicknesses were in the range of 0.05 to 0.12 micron. It is worth mentioning that the absence of hydrazine hydrate in the respective solutions does not produce any film or precipitate of ZnSe.

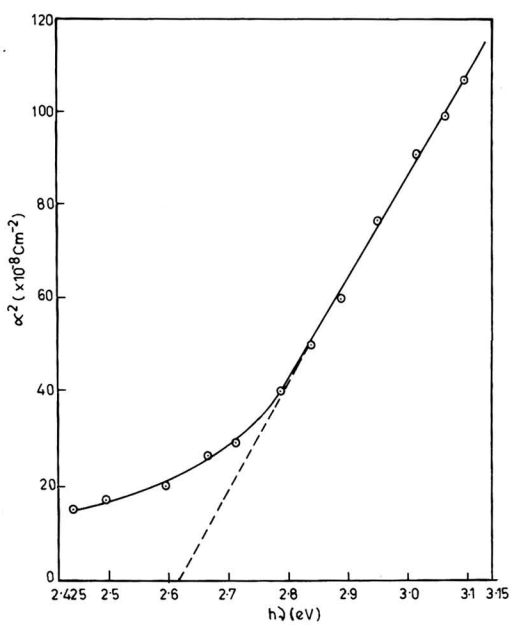


Fig. 1. Optical absorption spectrum of ZnSe thin film deposited on glass substrate at 100°C.

Table I. X-ray data of ZnSe films prepared by the present method

Observed *d* values (Å) for ZnSe	Possible identification with standard *d* (Å)
3.40	(100) 3.43
3.28	(002) 3.25
3.08	(101) 3.05
2.39	(102) 2.368
1.98	(110) 1.997
1.81	(103) 1.84
1.71	(112) 1.703
1.55	(202) 1.527
1.34	(203) 1.353
1.293	(120) 1.308
1.24	(105) 1.222
1.148	(300) 1.153
1.105	(213) 1.119
1.06	(302) 1.087

X-ray diffraction data reveal that the films prepared by the present method are polycrystalline in nature and their observed 'd' values are in good agreement with the standard 'd' values taken from the ASTM Diffraction Data File, which is shown in Table I.

The optical densities of ZnSe thin films, measured at various wavelengths by a Cary 17D spectrophotometer, were used to determine the absorption coefficient α for the samples at various photon energies. A plot of α^2 *vs.* $h\nu$ for ZnSe film is shown in Fig. 1. Extrapolation of the linear portion of the curve to $\alpha^2 = 0$ gives the optical bandgap, which is about 2.63 eV. This value is in good agreement with the standard bandgap (7) of 2.6 eV.

By thermoelectric probe method it has been observed that the present films are *n* type in nature. Their conductivities lie in the order of $\sim 10^{-4}$ S cm^{-1}, as measured by the four probe method at room temperature (30°C). The films are found to be photoconductive in nature. More detailed studies are in progress.

Manuscript received Sept. 5, 1985.

REFERENCES

1. T. S. Moss, *Proc. IRE*, **43**, 1869 (1955).
2. J. Bolem, *Appl. Sci. Res.*, **6B**, 92 (1956).
3. D. H. Roberts and J. E. Baines, *J. Phys. Chem. Solids*, **6**, 184 (1958).
4. P. Pramanik, R. N. Bhattacharya, and A. Mondal, *This Journal*, **127**, 1857 (1980).
5. W. E. Johnson and L. A. Schlie, *Appl. Phys. Lett.*, **40(9)**, 798 (1982).
6. A. Yoshikawa, K. Tanaka, S. Yamoga, and H. Kasai, *Jpn. J. Appl. Phys.*, Part 2, **23(6)**, 424 (1984).
7. R. H. Bube, in "Photoconductivity of Solids," p. 233, John Wiley and Sons, New York (1960).

A 12% Efficient Photoelectrochemical Cell Based on Polycrystalline n-$CuInSe_2$ Electrodes

G. Razzini and L. Peraldo Bicelli*

Centro Studio Processi Elettrodici del CNR, Dipartimento di Chimica Fisica Appicata, Politecnico di Milano, Milan, Italy

B. Scrosati*

Dipartimento di Chimica, Universitá di Roma "La Sapienza," Rome, Italy

L. Zanotti

MASPEC CNR, Parma, Italy

Photoelectrochemical cells are important devices for the conversion of solar energy. However, the development of these cells has been so far somewhat hindered by the relatively low conversion efficiency and the poor stability offered by the most common semiconductor/electrolyte systems.

Recently, there has been a renewed interest in the field, due to the characterization of highly stable semiconductor electrodes selected among the class of ternary chalcogenides of the chalcopyrite or spinel type.

The most promising material of this class is undoubtedly copper indium diselenide, $CuInSe_2$. This ternary semiconductor has an optimal value of bandgap (around 1 eV) and offers a very promising photoelectrochemical behavior, as shown by the recent results reported by Cahen and co-workers (1-3) and by Lewerenz and coworkers (4-7).

All these results show that the photoelectrochemical response of $CuInSe_2$ electrodes is greatly influenced by the nature and the composition of the electrolyte solution. If the electrolyte composition is properly selected, high efficiencies and long stabilities may be obtained from $CuInSe_2$-based photoelectrochemical cells (4-7).

Effectively, using a typical polysulfide electrolyte, an efficiency of 5.2% has been reported (1). However, this value may be greatly enhanced when the surface of the semiconductor electrode is protected by an indium oxide film (3) and a polyiodide electrolyte with suitable additions of Cu^+ and In^{3+} ions and of HI, is used (5, 7, 8). Under these conditions, efficiencies of 11.7% (3) and of 9.5% (5), have been reached with photoelectrochemical cells using n-$CuInSe_2$ single-crystal electrodes.

These are impressive values which make the $CuInSe_2$ photoelectrochemical cells worthy of consideration for practical applications. However, to successfully achieve this goal, one must necessarily consider the use of low-cost, easily prepared, polycrystalline electrodes.

Lewerenz *et al.* (4) have synthesized polycrystalline p-$CuInSe_2$ samples and tested them in cells using the V^{2+}/V^{3+} redox electrolyte. However, the performance of these cells is very poor and their efficiency remains below 1%.

More encouraging results have been very recently obtained by Haneman and Szot (9) who have considered polycrystalline boules of n-$CuInSe_2$. By using selected samples of polycrystalline $CuInSe_2$ and the electrolyte recommended by Menezes (5, 8), these authors have obtained photoelectrochemical cells with efficiencies of about 5-6%.

Therefore, it has appeared to us of interest to carry out a careful synthesis of n-$CuInSe_2$ polycrystalline material, in order to evaluate if optimization in uniformity and grain size could result in an improved behavior and in better cell efficiencies.

Experimental

Due to their tendency of being easily oxidized, chalcogenides like $CuInSe_2$ must be synthesized in vacuum or in a protective atmosphere. Consequently, we have performed a direct synthesis from the melt using stoichiometric amounts (about 30g) of 6*N* pure constituent elements in an evacuated (10^{-5} torr) round bottom quartz ampul, 20 mm in diameter and 150 mm in length.

The melting was carried out in a homemade vertical Bridgman furnace, supplied with a temperature controller and a programmer, in order to keep the ampul under a suitable thermal gradient. Since indium reacts exothermally with selenium leading to the generation of unreacted selenium vapor, the ampul was initially kept at 200°C for about 10h and then heated slowly (4°-5°C/h) to melting. A complete homogenization was obtained keeping the melt at 1050°C for about 20h. Then the furnace was cooled gradually (20°C/h) to avoid ampul cracking due to thermal expansion of the melt on solidification.

Following this procedure we obtained very homogeneous polycrystalline ingots in which the average grain size was in the 1-2 mm range. X-ray powder analysis, carried out in different regions of the ingots, confirmed that only a single phase (chalcopyrite type) was present in the whole boule. The polycrystalline $CuInSe_2$ material so obtained is of n type and has a resistivity of 2.6 Ω-cm.

Slices of about 1 mm thickness were cut from the ingots and fracture pieces of these slices were mounted on a Teflon holder, polished, and etched with a Br_2-MeOH (2%) solution. The samples were then polarized at −1V (*vs.* SCE) for 5 min in aqueous solution of 1 m*M* $In_2(SO_4)_3$ and 1*M* Na_2SO_4, to electrodeposit an In film of about 50Å thickness on the surface of the semiconductor. The film was then oxidized to indium oxide by annealing at 130°C for 3h. Observations at the scanning electron microscope (SEM) showed that the film uniformly covered the semiconductor surface.

The $CuInSe_2$ electrodes so prepared were then assembled in the photoelectrochemical cell, following a procedure described in detail elsewhere (10).

The electrolyte used was generally similar to that recommended by Menezes (5, 8), *i.e.*, an aqueous solution of 2*M* KI, 20 m*M* I_2, 20 m*M* CuI, 20 m*M* $In_2(SO_4)_3$, and 2*M* HI. This solution is here generally indicated as the polyiodide electrolyte. The current-voltage curves of the $CuInSe_2$/polyiodide electrolyte cell were obtained under a xenon lamp of 100 mW/cm² illumination. To avoid oxidation of the electrolyte, the photoelectrochemical measurements were carried out under a nitrogen atmosphere.

Results and Discussion

Similar to what is reported for single-crystal electrodes (3, 5, 7), the performance of the polycrystalline samples described here are greatly influenced by surface treatments and electrolyte compositions. The power output characteristic illustrated in Fig. 1 has been typically obtained with our polycrystalline $CuInSe_2$/polyiodide photoelectrochemical cell. Under the best operative conditions and with an AM1 illumination by an unfiltered xenon lamp, a conversion efficiency of 12% is shown by this cell, which we believe is the highest value ever obtained with a photoelectrochemical cell using polycrystalline

* Electrochemical Society Active Member.

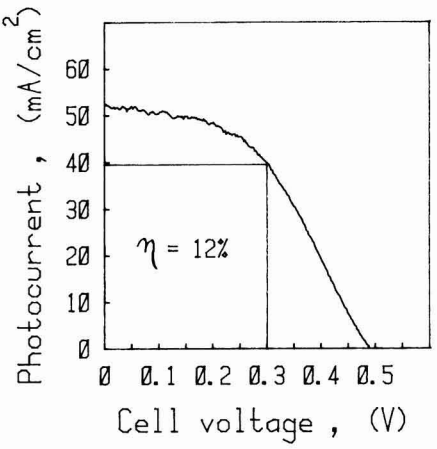


Fig. 1. Output power characteristics of the polycrystalline n-$CuInSe_2$/polyiodide electrolyte/Pt photoelectrochemical cell. Illumination: 100 mW/cm^2. Cell stirred under nitrogen.

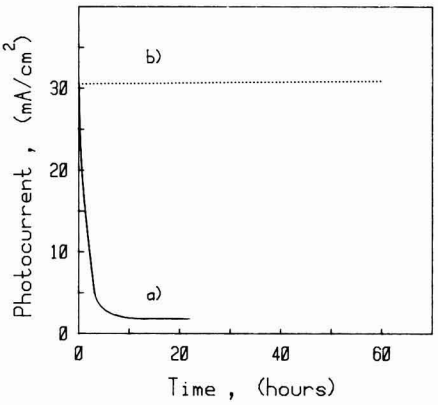


Fig. 2. Output photocurrent under continuous illumination of a polycrystalline n-$CuInSe_2$ photoelectrochemical cell. (a) 2M KI, 20 mM I_2 solution; (b) indium oxide coated semiconductor electrode and addition of 20 mM CuI, 20 mM $In_2(SO_4)_3$, and 2M HI (polyiodide electrolyte). Cell stirred under nitrogen.

semiconductor electrodes. Under direct solar illumination, efficiencies around 10% were typically obtained.

These values appear even more interesting if one considers that the cell was not optimized in terms of electrode separation and of light reflectivity.

The impressive behavior shown by the characteristic of Fig. 1 is, in our opinion, the result of various combined effects which include an accurate synthesis of the polycrystalline semiconductor samples, a suitable modification of their surface, and a convenient selection of the composition of the electrolyte.

The homogeneity of the polycrystalline ingots and the large dimension of the grains are certainly main factors in determining the observed high efficiencies. However, also the electrode treatments, such as the passivation of its surface by the deposition of the indium oxide layer, and the selection of the proper electrolyte composition, are undoubtedly of dramatic importance, this confirming the observations of Cahen and co-workers (3) and of Menezes and co-workers (5, 8) in the case of single-crystal $CuInSe_2$ cells.

At this stage it is not completely clear to us as to which is the specific role of HI in the selected electrolyte composition. In fact, while the effect of the Cu^+ and of the In^{3+} ions is likely that of reducing the rate of the reaction of the photocorrosion of the semiconductor, it remains difficult to explain the beneficial action of HI, which could be tentatively attributed to the adsorption of proton and/or iodide ions on the semiconductor surface. Work is in progress in our laboratories to clarify this point.

Figure 2 shows the trend of the ouput photocurrent under continuous illumination for a cell without (curve a) and with (curve b) addition of CuI, $In_2(SO_4)_3$, and HI to the I_3^-/I^- couple in solution. In the latter case, the photoelectrochemical cell performance remained unchanged for over 60h, corresponding to 6.7 kC/cm^2 photocharge passed. Examination under the SEM of the electrode surface at the end of the stability test did not show evidence of surface modifications. Obviously, more detailed and prolonged tests are necessary to establish the effective stability of the polycrystalline n-$CuInSe_2$ electrodes. However, the results of Fig. 2 are certainly encouraging in this respect.

Acknowledgments

The authors are grateful to Miss L. Tenti for a part of the experimental measurements. This work was carried out with the financial support of the Consiglio Nazionale delle Ricerche, PFE 2, Sottoprogetto Carbone e Idrogeno.

Manuscript submitted May 20, 1985; revised manuscript received Oct. 1, 1985.

Universitá di Roma "La Sapienza" assisted in meeting the publication costs of this article.

REFERENCES

1. Y. Mirovski and D. Cahen, *Appl. Phys. Lett.*, **40,** 727 (1982).
2. Y. Mirovski, G. Demjal, and D. Cahen, *Nuovo Cimento*, **2D,** 2039 (1983).
3. D. Cahen and Y.-W. Chen, *Appl. Phys. Lett.*, **45,** 746 (1983).
4. H. J. Lewerenz, H. Goslowsky, and F. A. Thiel, *Solar Energy Mater.*, **9,** 160 (1983).
5. S. Menezes, H. J. Lewerenz, and K. J. Bachmann, *Nature*, **305,** 615 (1983).
6. S. Menezes, H. J. Lewerenz, G. Betz, K. J. Bachmann, and R. Kotz, *This Journal*, **131,** 3030 (1984).
7. K. J. Bachmann, S. Menezes, R. Kotz, M. Fearheil, and H. J. Lewerenz, *Surf. Sci.*, **138,** 475 (1984).
8. S. Menezes, *Appl. Phys. Lett.*, **45,** 148 (1984).
9. D. Haneman and J. Szot, *ibid.*, **46,** 778 (1985).
10. B. Scrosati, L. Fornarini, G. Razzini, and L. Peraldo Bicelli, *This Journal*, **132,** 593 (1985).

Polythiophene/PolyTHF: A Multicomponent Electrically Conducting Polymer

Mark A. Druy*

GTE Laboratories, Incorporated, Waltham, Massachusetts 02254

Electrically conducting polymers have been plagued in the past by problems associated with environmental stability and/or poor mechanical properties. Polyacetylene, the prototype conducting polymer, was successfully blended with elastomers (1) and thermoplastic elastomers (2). As a result its mechanical properties were dramatically improved. Blending, however, had no major impact on stability (1). Soluble processible conducting polymer precursors such as polyphenylene and polyphenylene sulfide have been doped in solution and conducting films of these materials could be cast from the solution (3). Unfortunately, once doped, polyphenylene and polyphenylene sulfide are quite reactive in air (4, 5).

Polyheterocycles such as polythiophene and polypyrrole are polymers which have exhibited dramatic improvements in oxidative stability (6). Recent work by several investigators has enhanced the mechanical properties of polypyrrole by forming composites with polyvinyl alcohol and polyvinyl chloride (7).

Polythiophene, however, has rather poor mechanical properties. In fact it is very difficult to synthesize polythiophene as a free-standing film (>10 microns thick). Most attempts to electrochemically synthesize polythiophene result in intractable powders which are deposited on the surface of an electrode (8, 9). Only by keeping the current density at 10 $\mu A/cm^2$ is it possible to peel off a fragile free-standing film (9). Since the conductivity of polythiophene is rather stable in air, attempts to improve its mechanical properties and processibility are warranted. Furthermore our research is aimed at obtaining structural modification and control of the morphology of polymers via electrochemical means. This communication describes a successful electrochemical approach to the improvement of the mechanical properties and processibility of polythiophene. Recent work by Frommer *et al.* suggests that polythiophene can be chemically polymerized in solution and conducting films can be cast (10). In another laboratory, free-standing films of polythiophene were grown electrochemically using large applied potentials (>10V) (11). Because of these high potentials, other reactions such as ring opening may occur and thus the material may contain species other than polythiophene.

Experimental

A three compartment electrochemical cell was used for the electrochemical synthesis of a polythiophene/polyTHF multicomponent system. Figure 1 shows this cell. A Ag/Ag^+ reference electrode (+0.3V *vs.* SCE) was used to monitor the working electrode potential during the galvanostatic synthetic process. The working electrode was a 4 cm × 2.5 cm platinum working electrode, and a nickel mesh counterelectrode was used. The cell was filled with 50 ml of a 1*M* lithium perchlorate in tetrahydrofuran solution. The lithium perchlorate (G. F. Smith Company) had been previously dried at 110°C in dynamic vacuum for 36h, and then melted and allowed to cool under dynamic vacuum. The tetrahydrofuran (Fisher HPLC) was refluxed over lithium aluminum hydride, collected, and transferred under nitrogen flow to a flask containing benzophenone and sodium metal. The THF was degassed using free-thaw cycles on a vacuum system. THF was transferred, using vacuum distillation techniques, from this container to another flask which could be brought into a dry box. The cell was assembled in the dry box and the platinum electrode was made the anode during a controlled current process. The solution in the working electrode compartment was stirred continuously. A current of 0.8 mA/cm^2 was passed for a duration of 30C. During this time, oxidation of THF occurred at the platinum electrode and the solution became more viscous. Figure 2(a) is an infrared spectrum of the material formed during this oxidation process. It compares well to the infrared spectrum of polyTHF (12).

After the passage of 30C, the cell was turned off and 0.1g of bithiophene was added to the working electrode compartment. The bithiophene (Eastman) was previously sublimed under vacuum. The working electrode was again made the anode for an additional 30-50C passed at a current density of 0.8 mA/cm^2. During this time the working electrode potential was monitored and was found to be 0.7V *vs.* Ag/Ag^+, indicative of bithiophene oxidation and polymerization (9). A dark green film formed on the electrode during this second electrolysis. After the second electrolysis period the electrode was removed from the cell and was scraped with a knife in order to remove excess polyTHF. The electrode was immersed in a beaker containing THF. This was done in order to dissolve any residual polyTHF on the surface of the electrode. The electrode was then removed from the dry box and a flexible free-standing film 40-120 microns thick was peeled off the electrode. These films were washed a second time in THF and then dried under vacuum.

The conductivity of the films at room temperature and at elevated temperatures was measured using a 4-probe pressure contact. Scanning electron micrographs of a film before and after extraction with THF were obtained. Extraction of the polyTHF component was accomplished in a soxhlet extractor. Films were extracted for 4h and the weight percent (by weight loss) of polyTHF in the multicomponent system was determined.

All electrochemical measurements and syntheses were carried out with a PAR Model 174 signal programmer, 173/179 potentiostat/galvanostat/coulometer, and a Houston Instruments X-Y recorder.

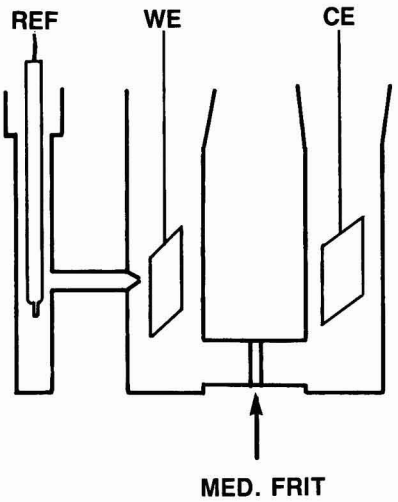


Fig. 1. Electrochemical cell for the polymerization of bithiophene and THF.

*Electrochemical Society Active Member.

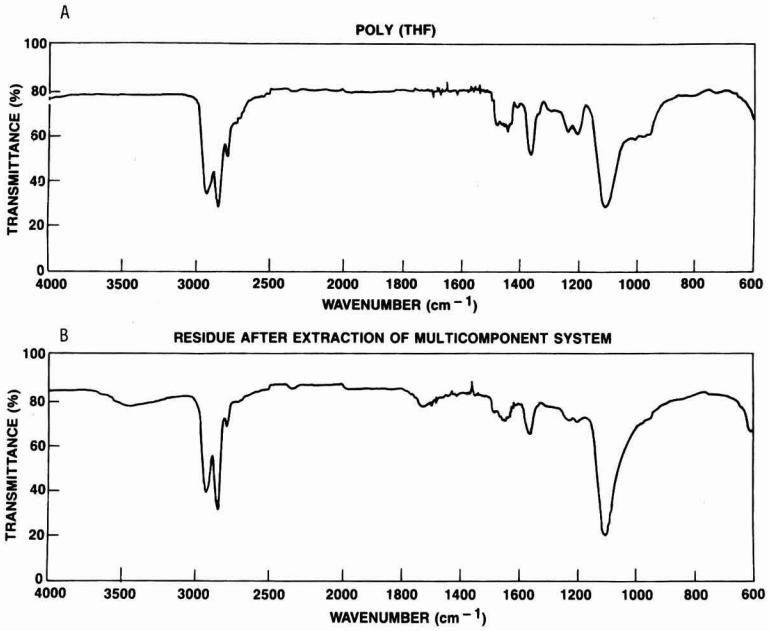


Fig. 2. (a) Infrared spectrum of electrochemically polymerized polyTHF. (b) Infrared spectrum of residue after extraction of polythiophene/polyTHF system.

Results and Discussion

It was previously determined by other investigators that THF is capable of undergoing electrochemical polymerization (13). A cyclic voltammogram of a 1*M* lithium perchlorate/THF solution at a platinum electrode indicated that the onset of THF oxidation occurred at 0.65V *vs.* Ag/Ag^+. At potentials more positive than 0.70V *vs.* Ag/Ag^+, bithiophene also undergoes oxidation and subsequent polymerization. Thus, the oxidation and polymerization of bithiophene and THF occur spontaneously. The observation that the THF solution in the working electrode compartment became more viscous during the electrochemical polymerization of bithiophene supports the above conclusion. The oxidation of bithiophene leads to a cation radical species which results in a polymer with an oxidized conjugated backbone (14). Oxidation of THF results in the formation of the oxonium ion with a subsequent ring opening polymerization occurring (13).

The conductivities of the films made in the above manner were in the range of 0.01-1 $(\Omega\text{-cm})^{-1}$. The conductivity of polythiophene can vary by two orders of magnitude depending on the morphology and the current density during the electrochemical polymerization (9). Incorporating an insulator such as polyTHF into the multicomponent system should also affect the conductivity depending on the distribution of polyTHF. There did not seem to be a dependence of conductivity on the polymerization time of THF before bithiophene was added to the cell. The films grown in this manner were of more uniform appearance than polythiophene grown from acetonitrile solutions. The scanning electron micrograph in Fig. 3 revealed large continuous nodular-like growths on the surface of the film. After extraction in THF, the surface of the film revealed discontinuous nodules. The film was flexible before extraction and brittle after extraction. Presumably the polyTHF component may serve to interconnect these nodules. Since the scanning electron microscopy examines the surface of the sample, one cannot determine from this experiment if the polyTHF resides in the bulk of the sample. One can say, however, that the polythiophene forms a continuous phase such that electronic conduction still occurs. The weight loss after extraction was 18%. An infrared spectrum of the residue isolated from the extraction experiment is shown in Fig. 2b and is identical to the spectrum of polyTHF. This confirms the presence of polyTHF in the film.

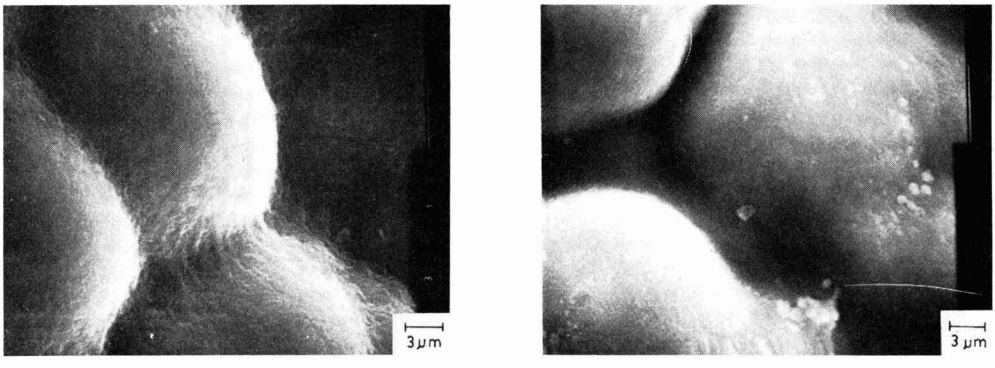


Fig. 3. Scanning electron micrograph of polythiophene/polyTHF multicomponent system; (a) before extraction with THF, (b) after extration with THF.

Table I. Conductivity of PT/PTHF and PT before and after heating in air for 900 min

	Temp. °C	Before (S/cm)	After (S/cm)
PT/PTHF	55	0.07	0.1
PT/PTHF	76	0.2	0.2
PT/PTHF	76	0.06	0.08
PT/PTHF	76	0.7	0.8
PT/PTHF	110	1.1	0.46
PT/PTHF	110	0.02	0.03
PT	110	0.02	0.02
PT	110	0.02	0.02

PT/PTHF = Polythiophene/PolyTHF
PT = Polythiophene

The behavior of the conductivity of the polythiophene/polyTHF multicomponent system before and after heating in air for 900 min is shown in Table I. The conductivities were measured at room temperature and for comparison the conductivity of polythiophene before and after heating at 110°C is also shown.

The stability of the conductivities of polythiophene and the polythiophene/polyTHF multicomponent system are comparable. There is a trend towards a decrease in conductivity for the multicomponent system when heated in air above 90°C for an extended period of time. Studies involving the determination of the kinetics of the degradation process are in progress and will be discussed in a future paper.

In conclusion, we have shown that flexible freestanding films of a polythiophene/polyTHF multicomponent system can be grown using electrochemical techniques. These films are electrically conducting and are thermally stable in air to 90°C for extended periods of time. The techniques are adaptable to other electrochemical polymerizations and this represents a new means of modifying the properties of conducting polymer systems.

Acknowledgment

The authors would like to acknowledge Mr. Michael Salmon for his assistance in obtaining the scanning electron micrographs, Mr. Andrew Coleman for sample preparation, and Dr. Sukant Tripathy and Dr. Mrinal Thakur and Mr. Michael Rubner for their critical review of the manuscript.

Manuscript submitted April 25, 1985; revised manuscript received Oct. 8, 1985. This was Paper 617 presented at the New Orleans, Louisiana, Meeting of the Society, Oct. 7-12, 1984.

GTE Laboratories, Incorporated assisted in meeting the publication costs of this article.

REFERENCES

1. M. F. Rubner, S. K. Tripathy, J. Georger, Jr., and P. Cholewa, *Macromolecules*, **16**, 870 (1983).
2. K. I. Lee and H. Jopson, *Makromol. Chem., Rapid Commun.*, **4**, 375 (1983).
3. J. E. Frommer, R. L. Elsenbaumer, and R. R. Chance, ACS Symposium Series No. 242, T. Davidson, Editor, p. 447 (1984).
4. D. M. Ivory, G. G. Miller, J. M. Sowa, L. W. Shackette, R. R. Chance, and R. H. Baughman, *J. Chem. Phys.*, **78**, 5656 (1983).
5. M. F. Rubner, Unpublished results.
6. K. K. Kanazawa, A. F. Diaz, R. H. Geiss, W. D. Gill, J. F. Kwak, J. A. Logan, J. F. Raboldt, and G. B. Street, *J.C.S. Chem. Comm.*, 854 (1979); G. Tourillon and F. Garnier, *This Journal*, **130**, 2042 (1983).
7. M. A. DePaoli, R. J. Waltman, A. F. Diaz, and J. Bargon, *J. Chem. Soc., Chem. Commun.*, 1015 (1984); O. Niwa and T. Tamamura, *J. Chem. Soc., Chem. Commun.*, 817 (1984); G. B. Street, International Conference on Synthetic Metals, Abano Terme, Italy, June 1984.
8. G. Tourillon and F. Garnier, *J. Polym. Sci. Polym. Phys. Ed.*, **23**, 33 (1984).
9. M. A. Druy, R. J. Seymour, and S. K. Tripathy, ACS Symposium Series No. 242, T. Davidson, Editor, p. 473 (1984).
10. J. E. Frommer, Paper presented at ACS National Meeting, August 1984, Philadelphia, PA.
11. K. Kaneto, Y. Kohno, K. Yoshino, and Y. Inuishi, *J. Chem. Soc., Chem. Comm.*, 382 (1983).
12. P. Dreyfuss and M. P. Dreyfuss, *Adv. Polymer Sci.*, **4**, 528 (1967).
13. A. N. Dey and E. J. Rudd, *This Journal*, **130**, 1294 (1974) and references therein.
14. R. J. Waltman, J. Bargon, and A. F. Diaz, *J. Phys. Chem.*, **87**, 1459 (1983).

Time-Dependent Degradation in Sodium-Beta" Alumina Solid Electrolytes

David C. Hitchcock[1]

Materials and Molecular Research Division, Lawrence Berkeley Laboratory, University of California, Berkeley, California 94720

Lutgard C. De Jonghe

Department of Materials Science and Mineral Engineering, University of California, Berkeley, California 94720

During the operation of sodium/sodium or sodium/sulfur electrochemical cells utilizing sodium beta- or beta"-alumina solid electrolytes, various forms of electrochemical degradation may occur. The most significant form of degradation involves the rapid propagation of a sodium metal-filled crack, driven by the Poiseuille pressure of sodium cathodically plated in it, leading to an electronic short circuit (1-5). This form of degradation, Mode I, starts from a pre-existing surface flaw when a critical current density is exceeded. A possible, separate slow mode of degradation, Mode II, was discussed by De Jonghe (6, 7), and can occur when sodium is electrolyzed through a solid electrolyte that contains a gradient in the transport number ratios of the electrons and the ions. Such a gradient could result from the slow reduction of the electrolyte in contact with the metallic sodium electrode and thus provide a mechanism for delayed failure. The conditions for the initiation of this type of delayed failure appear to require overvoltages that are not normally encountered in the operation of cells, unless impurities or significant electrode polarization are present. It is, however, also possible that a slow crack-growth phase is associated with Mode I degradation. Such subcritical crack growth should be expected on the basis of the Richmann and Tennenhouse (RT) model (10). The model presumes a dissolution at the electrolyte crack tip as a consequence of current flow opposed by capillary redeposition. Direct experimental evidence to support the various assumptions of the RT model has not yet been reported. The current work investigates one aspect of the RT model: the possibility of slow, subcritical crack growth.

[1] Present address: InterNorth Inc., Omaha, Nebraska.

Materials

Sodium beta″-alumina disks were prepared by Ceramatec, Incorporated, Salt Lake City, Utah, by a method described by Miller *et al.* (8), except that the disks were formed by cold-die pressing before sintering. The microstructures and the composition were similar to those described earlier (9). Certified ACS sodium from Fisher Scientific Company, Santa Clara, California, was used in Na/Na cells made with these electrolytes.

Experimental

To detect the onset of Mode I degradation, acoustic emission testing was used. The method has been described in detail earlier (9). In the present work, disk-shaped rather than tubular electrolytes were used. Sealing was accomplished with SBW sealing glass, Schott America, New York. The cells were preheated to 350°C for 30 min to promote the wetting of the electrolytes and were tested at 300°C. A molybdenum electrode was inserted in the cell, making direct contact with the electrolyte, and Na was plated on it at a very low current density to form the working electrode. Filling the inside of the cell in this way minimized impurity contamination. The plating process was monitored with the acoustic emission system to eliminate specimens in which Mode I degradation had been initiated during cell filling. The electrolytes were tested by passing an increasing ionic current and recording the moment at which acoustic activity commenced or became continuous. To assess the possible presence of slow crack growth, a number of electrolytes were tested with two different rates of current increase. The current ramp was generated with a programmer and galvanostat such that the current through the cell started at zero and increased linearly with time. The acoustic activity during this test was recorded.

Results and Discussion

Initiation of Mode I degradation depends on the statistical distributions of pre-existing surface flaws and current densities. The Mode I initiation is a phenomenon that is governed by extreme value statistics, and Weibull statistics should be expected to be suitable for their description. Since the electrodes were of a finite shape, the current distribution was not uniform. It is possible to calculate the actual current distribution on the electrode when the exchange current densities are known. This allows the failure probability to be expressed as a function of an equivalent uniform current density rather than as a function of the average macroscopic current density. The equivalent uniform current density is slightly higher than the average macroscopic one. It has been shown (9) that the survival probability P_s (uniform), at an equivalent uniform electrode current density equal to the average macroscopic one, is related to the measured survival probability, P_s, by

$$P_s(\text{uniform}) = P_s^{1/C}$$

where C is a function of the electrode current density distribution and of the Weibull modulus, n. The value of C was found to be 1.33. Both P_s and P_s (uniform) have been shown in Fig. 1-3. The statistical methods, the determination of the secondary current distribution, and the determination of C have been described in detail before by Buechele *et al.* (9).

Na/Na cells were subjected to currents increasing at a rate of 1 mA/cm² s and of 10 mA/cm² s. Figures 1, 2, and 3 show that the critical current density for initial acoustic emission, for continuous acoustic emission, and for a drop in cell resistance all increased when the rate of increase of the current density was higher. The dashed lines give P_s, while the solid lines give P_s (uniform). Each datum point in these graphs represents the result of a separate test. The initial acoustic emissions were somewhat difficult to distinguish at the 10 mA/s ramping rate and only one reliable datum point could be obtained. The results are summarized in Table I. The effect was greater for the initial than for the continuous emission, and it was least for the drop in cell resistance. The results indicate that the time dependence for the initiation of Mode I degradation is greater than that for the propagation of the Mode I cracks, showing that the crack velocity is high once the critical current density has been exceeded.

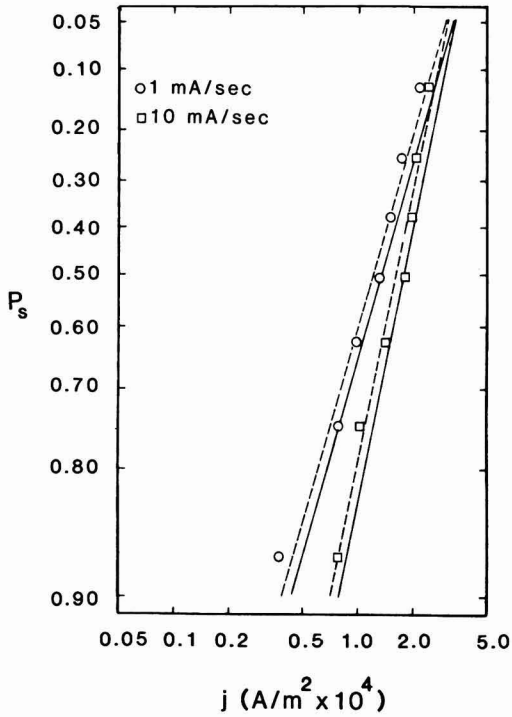


Fig. 1. Weibull plot of the first acoustic activity as a function of the average current density at 1 mA/s and at 10 mA/s. The solid lines show P_s (uniform) while the dashed lines show P_s.

The increase of the average current density for Mode I failure initiation with higher rates of current increase demonstrates clearly that time dependent, electrochemically assisted crack growth can be active at subcritical current densities.

Since mechanical, stress-assisted slow crack growth does not appear to be significant (3, 11), it is reasonable to assume that, during slow growth, the crack tip velocity would be determined by the current density at the crack tip only. This current, I_{tip}, is proportional to the crack length over the crack opening displacement, c/r, and to the macroscopic current density, I. (6) Assuming that the crack opening displacement does not vary strongly with crack length allows one to make an estimate at the dependence of the crack extension rate on time and current density. This assumption will overestimate I_{tip}. The crack tip velocity, c, can then be expressed to a first approximation, as

$$\dot{c} = A\, I^m\, c^m \qquad [1]$$

where A is a proportionality constant. At some point, when the stress intensity at the tip exceeds the critical stress intensity (12), the crack will reach the critical size, c_c, and propagate catastrophically, driven by Poiseuille

Table I. Acoustic emission testing results

I_0	Onset	I_c (μA/cm²) Continuous	Voltage drop
1 mA/s	153	60	1300
10 mA/s	(310)	1205	1580

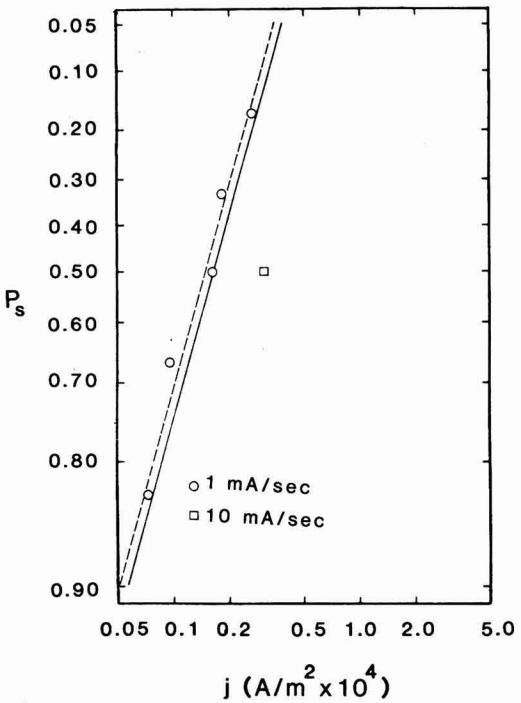


Fig. 2. Weibull plot of the onset of sustained acoustic activity as a function of average current density at 1 mA/s and at 10 mA/s. The solid lines are for P_s (uniform); the dashed lines are for P_s.

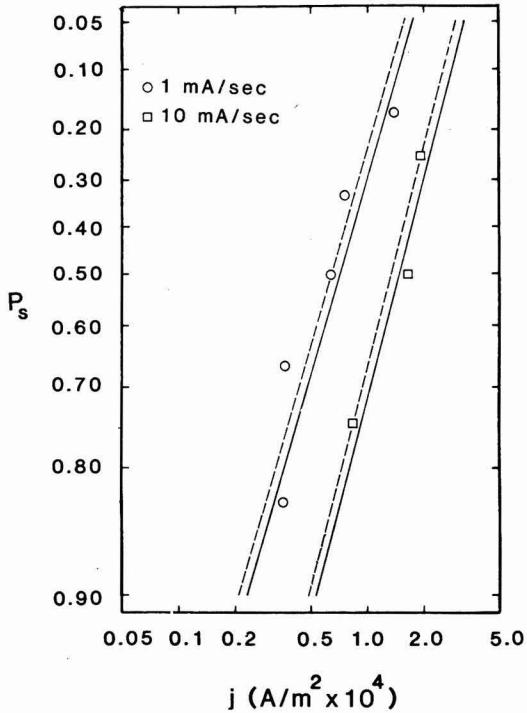


Fig. 3. Weibull plot of the first all resistance drop as a function of average current density at 1 mA/s and at 10 mA/s. The solid lines show P_s (uniform), while the dashed lines show P_s.

pressure. In the present experiments, the current is increasing at a constant rate, $\dot{I}_o$, so that

$$I = \dot{I}_o t \qquad [2]$$

If it is assumed that the critical crack size, c_c, is large compared to the initial crack size, c_i, when the stress intensity at the crack tip, caused by Poiseuille pressure, has reached the critical value, then [1] may be integrated to give

$$t_f = [m\, c_i^{(1-m)}/(m-1)A\, \dot{I}_o^m]^{1/(m+1)} \qquad [3]$$

The value of the exponent m then follows from a comparison of observed times to catastrophic crack propagation, t_f, at the two different values of $\dot{I}_o$, from

$$t_{f1}/t_{f2} = [\dot{I}_{o2}^m/\dot{I}_{o1}]^{m/(m+1)} \qquad [4]$$

From the data listed in Table I, m is found to be

$$m \approx 2.25$$

An approximate value of A in [1] can be determined if some assumption is made about the size of the initial crack, c_i. It has been demonstrated previously that failure initiates preferentially at the grain boundaries of large grains (13). The large grains are typically on the order of 50 to 100 μm in this electrolyte. Assuming c_i to be about 50 μm leads to

$$A \approx 1.3 \times 10^{-11} \text{ m/s } ((\text{mA/s})\mu\text{m})^{-m} \qquad [5]$$

The values of m and A can be used to estimate the time to catastrophic crack propagation for actual cell condition, where the electrolyte operates at a constant current density of about 100 mA/cm^2 during its charging cycle. At constant current density, integration of [1] gives a time to catastrophic crack propagation equal to

$$t_f = c_i^{(1-m)}/A(m-1)\, I^m \qquad [6]$$

Using the approximate values of A and m and a minimum initial crack size c_i of 10 μm, one can predict from [6] an upper boundary on the failure time of about 1×10^5 s, or a little over one day.

Thus, subcritical crack growth, if simply extrapolated from the rate measurements to normal electrolyte operating conditions, will account only for early electrolyte failures, since a critical size would be reached rapidly, even if failure initiating cracks were as small as 10 μm. While the experiments clearly demonstrate the existence of subcritical crack growth for Mode I failure, experience of sodium/sulfur cell developers has demonstrated that sodium beta"-alumina solid electrolytes can support current for very extended periods, with no evidence of Mode I failure initiation. The two observations can be reconciled only if a threshold crack size exists below which slow crack growth does not occur. Such a threshold may arise for certain types of electrochemical crack tip reactions. One such reaction, the destructive reduction of the electrolyte as a consequence of oxygen depletion at the crack tip during electrolysis, leads to a critical flaw size for slow degradation and has been discussed in detail elsewhere (15).

Acknowledgments

This work was supported by the Division of Materials Sciences, Office of Basic Energy Sciences, U.S. Department of Energy, under Contract No. DE-AC03-76SF0098.

Manuscript submitted March 11, 1985; revised manuscript received Oct. 15, 1985.

REFERENCES

1. R. D. Armstrong, T. Dickinson, and I. Turner, *Electrochim. Acta*, **19**, 187 (1974).
2. L. C. De Jonghe, L. Feldman, and A. Buechele, *J. Mater. Sci.*, **16**, 780 (1981).
3. D. H. Shetty, A. V. Virkar, and R. S. Gordon, in "Fracture Mechanics of Ceramics," Vol. 4, Proceedings of an International Symposium on Fracture Mechanics of Ceramics, R. C. Bradt, *et al.*, Editors, pp. 651-665 (1977).
4. A. Virkar and L. Viswanathan, in "Fracture Mechanics

of Ceramics," Vol. 62, Proceedings of an International Symposium on Fracture Mechanics of Ceramics, R. C. Bradt, *et al.*, Editors, p. 528 (1979).
5. L. Feldman and L. C. De Jonghe, *J. Mater. Sci.*, **17**, 885 (1982).
6. L. C. De Jonghe, *This Journal*, **129**, 752 (1982).
7. L. C. De Jonghe, *Solid State Ionics*, **1**, 61 (1982).
8. M. L. Miller, B. J. McEntire, G. R. Miller, and R. S. Gordon, *Am. Ceram. Soc. Bull.*, **58**, 522 (1979).
9. A. C. Buchele, L. C. De Jonghe, and D. Hitchcock, *This Journal*, **130**, 1042 (1983).
10. R. H. Richmann and G. J. Tennenhouse, *J. Am. Ceram. Soc.*, **58**, 63 (1975).
11. L. Feldman and P. Millett, *Mater. Res. Bull.*, **14**, 589 (1979).
12. R. W. Davidge, G. Tappin, J. R. McLaren, and G. J. May, *Am. Ceram. Soc. Bull.*, **58**, 771 (1979).
13. B. R. Lawn and T. R. Wilshaw, "Fracture of Brittle Solids," Cambridge University Press, Cambridge, England 1975.
14. L. C. De Jonghe, A. Buechele, and K. H. Yoon, *Adv. Ceram.*, **7**, 220 (1983).
15. D. Hitchcock and L. C. De Jonghe, Submitted to *This Journal*.

Semiconductor Electrodes

LX. Photoelectrochemistry of p-ReS_2 and p-$ReSe_2$ in Aqueous Solutions

Bob L. Wheeler, Jonathan K. Leland,* and Allen J. Bard**

Department of Chemistry, The University of Texas, Austin, Texas 78712

Since the first work of Tributsch on layer-type semiconductors (1), this class of compounds has received considerable attention. Some of the more extensively studied compounds, MoS_2, $MoSe_2$, WS_2, and WSe_2, are quite stable under illumination in a photoelectrochemical (PEC) cell (2). Interest in these compounds is based on several factors. As originally discussed by Tributsch, both the conduction and valence bands have mainly metal d orbital character. Hence, absorbed light produces an electron-hole pair but does not result in the breaking of a bond (3). In principle, this should promote stability of the semiconductor lattice against decomposition, although photocorrosion of n-type layer materials still occurs when reactions that take place at very positive potentials (*e.g.*, oxygen evolution) are attempted. A second advantage of layer-type compounds is that fresh surfaces, often with a low density of surface states, can be prepared by peeling a layer of material from the surface ($\perp$C-axis). When edge planes are exposed, they can sometimes be passivated. The adsorption of I_3^- is sometimes beneficial in the operation of PEC cells (4, 5). Finally, small single crystals of many of the layer compounds are readily prepared by vapor transport methods (6). The transport agents employed are an important factor in determining the type of majority carrier in the crystal produced (n or p). For example, transport of WSe_2 with Br_2 produces n-type crystals, while I_2 transport produces p-type crystals (7).

Marzik *et al.* recently reported the growth and PEC properties of ReS_2 and $ReSe_2$ (8). The compounds were produced with Br_2 as the transport agent, and n-type single crystals were described; this is the only report of the use of ReS_2 and $ReSe_2$ in PEC cells. While earlier reports of the semiconducting nature of ReS_2 and $ReSe_2$ can be found (9, 10), to our knowledge, p-type crystals of these compounds have not been described. Our interest in p-type crystals of these compounds derives from their possible application in PEC photovoltaic (or regenerative) cells. Moreover, p-type materials can be useful in photosynthetic applications, *e.g.*, for the reduction of CO_2 (11). Generally, a catalyst is required on the surface of a semiconductor to carry out a kinetically complex photoreduction. Since rhenium and its compounds have been used as catalysts (12, 13), p-ReS_2 and p-$ReSe_2$ might find application in photoelectrosynthesis. While a change in the majority carrier can be accomplished by choice of dopant in most semiconductors, by analogy to WSe_2, we grew p-type crystals by using I_2 as the transport agent. This paper describes our first studies of the growth and PEC behavior in aqueous solutions of p-ReS_2 and p-$ReSe_2$.

Experimental

Crystal growth and electrode preparation—Crystals of ReS_2 and $ReSe_2$ were prepared from rhenium (4N7 purity, Johnson Matthey, Incorporated, Seabrook, New Hampshire), sulfur (precipitated, Alfa, Danvers, Massachusetts), and selenium (3N purity, Johnson Matthey). The quartz ampuls used for growing the single crystals were rinsed successively with HF, HCl-HNO_3 (50%-50% by volume), HF, and finally, distilled water. The tubes were dried and then evacuated to *ca.* 10^{-5} torr. The procedure of Marzik *et al.* (8) for preparation of the compounds was followed with minor changes. The Re was heated at 950°C in a stream of H_2 to remove any oxides and then heated at 350°C in a dynamic vacuum to remove adsorbed H_2. The chalcogens were freshly sublimed in vacuum. Stoichiometric amounts of the elements, enough to make *ca.* 3g of compound, were ground together with an agate mortar and pestle and placed in a quartz tube that measured 15 cm long by 1.5 cm diameter. The tube was evacuated for 15 min and then filled with He. Triply sublimed I_2 (5 mg/cm^3) was quickly added and the tube was cooled in liquid N_2, evacuated, and then sealed. The temperatures and times used for growing the crystals were the same as those reported previously (8). A three-zone furnace (Lindberg, Watertown, Wisconsin) was used. At the conclusion of the experiment, the ampul was opened and the products rinsed several times with CCl_4. There were many small (4 × 5 mm) crystals, many of which were twinned, and much polycrystalline powder. X-ray powder diffraction patterns of the products matched those of ReS_2 and $ReSe_2$ (ASTM card no. 27-502 for ReS_2, no. 18-1086 for $ReSe_2$). The single crystals were quite thin (*ca.* 100 μm) and easily bent; great care was needed to prepare a flat, edge-free, surface for an electrode. After a crystal had been selected, the back of the crystal was attached to a copper wire with a drop of silver paint (Acme Chemicals and Insulation, New Haven, Connecticut) and this connection was covered with 5 min epoxy cement (Devcon, Danvers, Massachusetts). The copper wire was placed through a 6 mm diameter glass tube and held in place with epoxy cement. All surfaces except the front surface of the crystal were then covered with silicone sealant (Dow-Corning Corporation, Midland, Michigan).

Photoelectrochemical experiments.—A standard one-compartment electrochemical cell, with optically flat windows for illumination of the semiconductor electrodes, was used. The counterelectrode was a large (>40 cm^2) Pt gauze and the reference electrode was a saturated calomel electrode (SCE). A potentiostat [Princeton Applied Research (PAR) Model 173, Princeton, New Jersey] and programmer (PAR Model 175) were used for current-voltage measurements, recorded on an XYY recorder (Soltec Model 6432, Sun Valley, California). Capacitance measurements were performed with the preceding plus a PAR 5204 lock-in amplifier and HP200CD wide range oscillator (Hewlett-Packard, Palo Alto, California) by previously reported procedures (14).

*Electrochemical Society Student Member.
**Electrochemical Society Active Member.

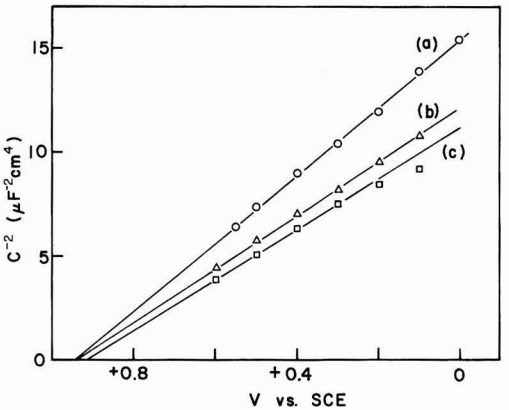


Fig. 1. Mott-Schottky plot of p-$ReSe_2$ in 0.1M $(NH_4)_2SO_4$, 0.1M Na_2SO_4, 50 mM $Ru(NH_3)_6Cl_3$ (pH ≠5) at frequencies of (a) 2000, (b) 1000, (c) 500 Hz.

White light illumination of the electrode was by a 450W Xe arc lamp (Oriel Corporation, Stamford, Connecticut). Monochromatic illumination was provided by a 2500W Xe arc lamp (Schoeffel Instrument Company, Westwood, New Jersey) and monochromator (Oriel Model 7240).

Results

Capacitance measurements.—Mott-Schottky (M-S) plots ($1/C^2$ *vs.* *V*), where *C* is capacitance and *V* is potential *vs.* SCE, for $ReSe_2$ in 0.1*M* $(NH_4)_2SO_4$, 0.1*M* Na_2SO_4, 50 m*M* $Ru(NH_3)_6Cl_3$ are shown in Fig. 1. Although there was some frequency dispersion in the plots, estimates of the flat-band potential (V_{FB}) and doping level can be obtained. The intercept with the potential axis gives a value of $V_{FB} = 0.9 \pm 0.1$V *vs.* SCE. With the assumption that the dielectric constant for $ReSe_2$ is close to that of ReS_2 ($\epsilon = 7.8$) (9), the slope of the Mott-Schottky plot gives a value for the doping density of $N_A = 1.3 \pm 0.3 \times 10^{18}$ cm^{-3} (15). A value of the effective density of states in the valence conduction band, N_v, of 2.5×10^{19} cm^{-3} can be calculated by taking the effective mass of holes in $ReSe_2$ to be the same as that in WSe_2 ($m_h^* = m_e$) (16). With these values, ΔE_F, the difference in energy between the valence band energy and the Fermi level is calculated to be 0.08 eV.

The ReS_2 crystals showed quite different $1/C^2$ *vs.* *V* behavior. The resistance of these crystals was quite high and the capacitance varied little with bias. Mott-Schottky plots did not intercept the potential axis until quite positive potentials. In addition, the frequency dependence of these plots was such that values for V_{FB} and the doping density could not be obtained from those measurements.

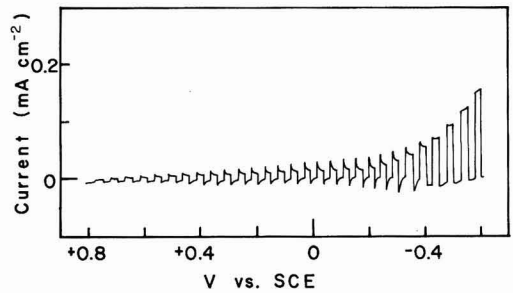


Fig. 3. Photocurrent-voltage curve for p-ReS_2 with chopped white light (*ca.* 50 mW/cm^2) in 0.1M MV^{2+} in 1M KCl.

PEC behavior.—The photocurrent (i_{ph})-potential behavior of a p-ReS_2 electrode is shown in Fig. 2 for Fe(II)EDTA/Fe(III)EDTA, and in Fig. 3, for methyl viologen (MV^{2+}) solutions. The behavior in the iron solution was clearly that of a p-type semiconductor and no photo-oxidation of Fe(II)EDTA or dark reduction of Fe(III)EDTA was observed. The onset of the photocurrent was just positive of +0.6V *vs.* SCE, but the current rose slowly and saturated only near the reversible potential for the couple, V_{redox} (−0.12V *vs.* SCE). In MV^{2+} solutions (Fig. 3), only small photoeffects were seen as far positive as +0.8V *vs.* SCE, but net reduction current was seen only at potentials negative of +0.6V *vs.* SCE. Notice that the i_{ph}-*V* curve, obtained with chopped irradiation, consisted of a series of current spikes, both cathodic as the light was turned on, and anodic as the light was turned off, unlike the Fe(II/III)EDTA solution. Moreover, i_{ph} did not attain a saturation value. A two-electrode cell (p-ReS_2 and Pt) in the Fe(II/III)EDTA solution, illuminated with 50 mW/cm^2 white light, gave an open-circuit photovoltage (V_{oc}) of about 400 mV. Plots of $(\phi h\nu)^{1/2}$ *vs.* $h\nu$ (Fig. 4), where ϕ = quantum efficiency of photocurrent and $h\nu$ is photon energy, gave a value of 1.31 ± 0.01 eV for the indirect gap. This value agrees with that of Marzik *et al.* (8), who used the absorption coefficient to obtain a value of 1.32 eV for the indirect gap for n-ReS_2. Short-circuit quantum efficiencies of > 10% at 600 nm were obtained (without correction of reflective losses from the mirror-like surfaces of the crystal).

The i_{ph}-*V* behavior of p-$ReSe_2$ in the Fe(II/III)EDTA solution was similar to that for p-ReS_2 (Fig. 5). No oxidation current in the dark, or under irradiation over the potential region +0.6 to −0.2V was observed. The onset for i_{ph} was +0.4V *vs.* SCE, about 0.2V more negative than for p-ReS_2. The photocurrent rose much more sharply and saturated close to 0 V *vs.* SCE. A two-electrode cell with this solution gave a V_{oc} of *ca.* 430 mV. A plot of $(\phi h\nu)^{1/2}$ *vs.* $h\nu$

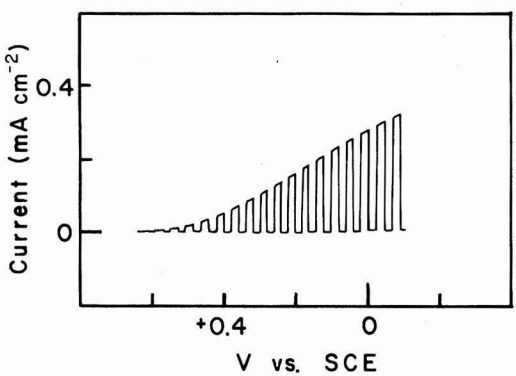


Fig. 2. Photocurrent-potential curve for p-ReS_2 with chopped white light (*ca.* 50 mW/cm^2). Solution was 50 mM Fe(II)EDTA, 50 mM Fe(III)EDTA, 0.2M Na_2SO_4 adjusted to *p*H 5.

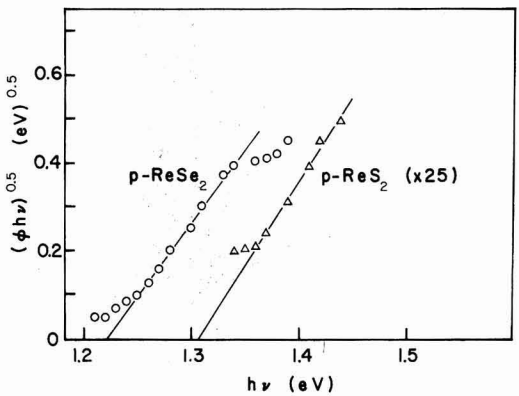


Fig. 4. Photocurrent *vs.* frequency (as $(\phi h\nu)^{1/2}$ *vs.* $h\nu$) for (a) p-ReS_2 and (b) p-$ReSe_2$; solution as in Fig. 2.

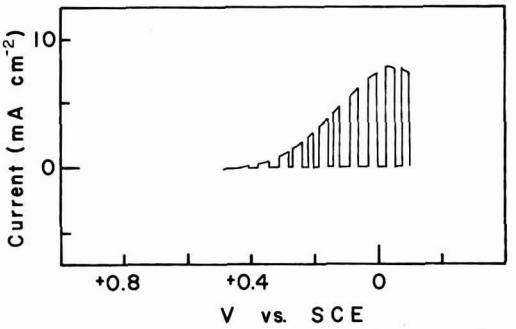


Fig. 5. Photocurrent-potential curve for p-$ReSe_2$ with chopped white light (*ca.* 50 mW/cm^2) with same solution as in Fig. 2.

(Fig. 4) gave a value of 1.22 ± 0.01 eV for the indirect gap, compared with 1.17 eV reported by Marzik *et al.* (for n-$ReSe_2$). Short-circuit quantum efficiencies of about 50% were obtained at 800 nm (without correction for electrode reflectance).

Discussion

Knowledge of V_{FB}, E_g, and ΔE_F allows calculation of the energy levels of the conduction and valence bands. This information is useful in the determination of proper redox couples for solar-to-electrical or chemical energy conversion. For our p-$ReSe_2$ crystal, V_{FB} = 0.9V *vs.* SCE and the valence bandedge, E_V, is about 1.0V *vs.* SCE. Since E_g was 1.2 eV, the conduction bandedge (E_c) will be near −0.2V *vs.* SCE. Marzik *et al.* (8) found V_{FB} for n-$ReSe_2$ to be −0.2V *vs.* SCE in a solution of 0.05*M* NaI, 2 m*M* I_2, 0.05*M* H_2SO_4. With their reported value of the donor density ($N_0 = 7 \times 10^{16}$ cm^{-3}) and the same assumption we used, *i.e.*, that the effective mass of electrons is the same as that for holes, ΔE_F for n-$ReSe_2$ is 0.15 eV. Thus, for Marzik *et al.*, the conduction bandedge should be −0.35V *vs.* SCE. Layer type compounds usually do not show shifts of the bandedge energies with different redox couples or with solution pH (14), although adsorption of I_3^-, with a resultant negative shift of the bands, has been noted (4, 6). Within the uncertainties of the measurements and assumptions, the values for band energies found for n- and p-type are essentially the same.

No shift was observed in the photocurrent onset potential for either p-ReS_2 or p-$ReSe_2$ after soaking the electrodes in a 1*M* KI, 50 m*M* I_2 solution, rinsing, and replacing the electrodes in Fe(II/III)EDTA or MV^{2+} solutions. The photocurrent onset for p-$ReSe_2$ occurs at potentials more negative than the V_{FB} determined from capacitance measurements and would be equivalent to E_V = 0.7V and E_c = −0.5V *vs.* SCE. However, photocurrent onsets may not be reliable for estimates of band-edge energies, *e.g.*, because of recombination effects or because filling of surface states by electrons while the electrode is under illumination can cause the bandedges to shift to more negative values (3, 17). The estimated band-edge potentials for p-$ReSe_2$, along with the potentials of several redox couples, are given in Fig. 6. Note that E_c is positive of the redox potential for MV^{2+} (−0.68V *vs.* SCE), and no photoeffect should be observed. The small spiked photocurrents that are seen with this couple might be explained by a shift of the bands in a negative direction under illumination through the formation of an inversion layer at the surface (17-19) until electrons can reduce the solution species. The back (anodic) spike can be explained as reoxidation of MV^+, as the conduction band in the dark again becomes positive of the redox potential.

The much slower rise to saturation for p-ReS_2 in the i_{ph}−V curves, the small quantum efficiencies, and the deviation of the C-V curves from the M-S equation can probably be attributed to the high resistivity of these crystals, although other factors may also be important. If the photocurrent onset (0.45V *vs.* SCE) is taken as V_{FB}, the

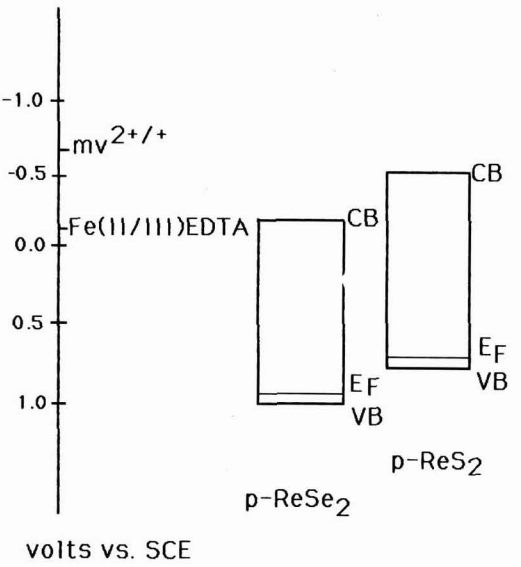


Fig. 6. Schematic diagram of the band positions of p-$ReSe_2$ and p-ReS_2. Note that there is considerable uncertainty about the band positions of p-ReS_2.

valence and conduction bands are located near 0.6V *vs.* SCE and −0.7V *vs.* SCE, respectively. Marzik *et al.* (8) report V_{FB} for n-ReS_2 as being positive of n-$ReSe_2$. With the slightly larger bandgap energy, the valence band probably would be more positive for the sulfide than for the selenide, as evidenced by other sulfide and selenide compound semiconductors (20, 21). In this case, V_{redox} for MV^{2+} is again negative of the conduction band minimum and poor photocurrent-voltage behavior is expected (as observed). The positions of the bands for p-ReS_2, taking $V_{FB} \approx 0.5$V, are shown in Fig. 6. Note, however, that V_{FB} for p-ReS_2 is probably positive of the potential for the onset of photocurrent because of the high resistance in the semiconductor crystals.

Conclusions

p-ReS_2 and p-$ReSe_2$ can be grown by following the procedure for growing n-ReS_2 and n-$ReSe_2$ by substituting I_2 for Br_2 as the transport agent. The reason for the change from donor to acceptor doping is unclear, but is also seen with other systems. The bandgaps of the compounds determined in this work agreed well with previously determined values for the n-type compounds. Open-circuit photovoltage values of *ca.* 400 mV were obtained from both crystals in Fe(II/III)EDTA solution. Unfortunately, the conduction bandedges are too positive to photoreduce CO_2, but might be able to produce H_2 with a suitable catalyst. Work is currently under way in our laboratory to vary the conditions of crystal growth and add dopants to lower the resistivity of p-ReS_2. Studies of the behavior of these compounds in nonaqueous solvents are also being undertaken.

Acknowledgment

The support of this research by the National Science Foundation (CHE8304666) is gratefully acknowledged.

Manuscript submitted Aug. 19, 1985; revised manuscript received Oct. 22, 1985.

The University of Texas assisted in meeting the publication costs of this article.

REFERENCES

1. H. Tributsch, *Ber. Bunsenges. Phys. Chem.*, **81**, 361 (1977).

2. K. Rajeshwar, *J. Appl. Electrochem.*, **15,** 1 (1985).
3. H. Tributsch, *Ber. Bunsenges. Phys. Chem.* **82,** 169 (1978).
4. W. Kautek and H. Gerischer, *Electrochim. Acta*, **26,** 1771 (1981).
5. R. Memming, in "Comprehensive Treatise of Electrochemistry," Vol. 7, B. E. Conway *et al.*, Editors, p. 529, Plenum Press, New York (1983).
6. G. Nagasubramanian, B. L. Wheeler, G. A. Hope, and A. J. Bard, *This Journal,* **130,** 385 (1983).
7. L. C. Upadhyayula, J. L. Loferski, A. Wold, W. Giriat, and R. Kershaw, *J. Appl. Phys.*, **39,** 4736 (1968).
8. J. V. Marzik, R. Kershaw, K. Dwight, and A. Wold, *J. Solid State Chem.*, **51,** 170 (1984).
9. J. Lagrenaudie, *J. Phys. Radium*, **15,** 299 (1954).
10. J. C. Wildervanck and F. Jellinek, *J. Less-Common Met.*, **24,** 73 (1971).
11. M. S. Wrighton, *J. Vac. Sci. Technol. A.*, **2,** 795 (1984).
12. B. D. McNicol, *J. Catal.*, **46,** 438 (1977).
13. E. Aharon-Shalom and A. Heller, *This Journal,* **129,** 2865 (1982).
14. S. Nagasubramanian, B. L. Wheeler, and A. J. Bard, *ibid.*, **130,** 1680 (1983).
15. S. M. Sze, in "Physics of Semiconductor Devices," 2nd ed., p. 249, John Wiley and Sons, New York (1981).
16. B. L. Evans and P. A. Young, *Proc. R. Soc., London, Ser. A*, **284,** 402 (1965).
17. S. Cooper, J. A. Turner, B. A. Parkinson, and A. J. Nozik, *J. Appl. Phys.*, **54,** 6463 (1983).
18. W. Kautek and H. Gerischer, *Ber. Bunsenges. Phys. Chem.*, **84,** 645 (1980).
19. C. D. Jaeger, H. Gerischer, and W. Kautek, *Ber. Bunsenges Phys. Chem.*, **86,** 20 (1982).
20. H. Tributsch, *This Journal*, **125,** 1086 (1978).
21. R. N. Noufi, P. A. Kohl, J. W. Rogers, Jr., J. M. White, and A. J. Bard, *ibid.*, **126,** 949 (1979).

JOURNAL OF THE ELECTROCHEMICAL SOCIETY

SOLID-STATE SCIENCE AND TECHNOLOGY

FEBRUARY 1986

Analysis of Corrosion on Aluminum Double-Layer Metallization

T. Wada, H. Higuchi, and T. Ajiki

QA Centre Semiconductor Group, Matsushita Electronics Corporation, 1, Kotari-yakemachi, Nagaokakyo-shi Kyoto-Fu 617, Japan

ABSTRACT

Aluminum double-layer metallization is a very important technology for VLSI circuits. Aluminum corrosion and electrolytic leakage current of double-layer metallization have been studied using mainly an unsaturated pressure cooker test (USPCT). Major results were that (*i*) a vertical electrolytic leakage current through the inter-layer between top and lower metals is a main factor, (*ii*) the plasma-deposited silicon nitride (SiN) is an excellent dielectric layer for moisture prevention, and (*iii*) the combination of SiN passivation and SiN inter-layer is a strong structure to mechanical stress.

The level of integration of semiconductor devices has risen progressively, and the electric field between electrodes has increased. For high density LSI circuits, multilayer metallization structure is essential.

Plastic encapsulation is widely used in the semiconductor industry (1). However, plastics are neither hermetic nor free from impurities, and thus there is considerable uncertainty as to the reliability of plastic encapsulated IC's in moist environments (2).

A humidity test of double-layer metallization was done using two-level aluminum metallization test elements. It was found that a vertical leakage current between lower and top metals is a main factor.

Experimental

Samples.—The test vehicle used for our humidity test contained a group of two-level aluminum metallization test elements. The layout of the test chip is shown in Fig. 1. Starting from the bottom, they consisted of the Si-substrate, SiO_2, lower level metal (lower metal), intermediate dielectric layer (inter-layer), top level metal (top metal), and passivation dielectric layer (passivation). Figure 2 indicates pin connections and dimensions. Four combinations of passivation and inter-layer were prepared, as shown in Table I. Where NSG is nondoped silicate glass (CVD 420°C), PSG is phosphorus-silicate glass (CVD 420°C, P_2O_5 4 weight percent), LP-PSG is low pressure chemical vapor-deposited phospho-silicate glass (420°C, P_2O_5 4 w/o), and SiN is plasma-deposited silicon nitride (380°C). The thickness of the dielectric layer was inter-layer 1.0 μm and passivation 0.8 μm. The lower metal was 0.8 μm (Al/Si 1%), and the top metal was 2.0 μm (pure Al). Both metals were produced by standard photolithographic methods, and chips were mounted on a 16-lead DIP leadframe, wired with gold ball bonding, and molded with standard epoxy novolac plastic package.

Test conditions.—Two tests, with bias (bias test) and without bias (storage test), were done in two humidity ambient conditions of 85°C/85% RH and 121°C/85% RH. To detect corrosion, the resistance of the Al line was measured at room temperature. The criterion for Al corrosion failure was 100% change of the resistance. Leakage measurements were also done between metals, with 30V applied.

Table I. Combinations of passivation and inter-layer

No.	Inter-layer	Passivation
I	LP-PSG	NSG + PSG + NSG
II	SiN	NSG + PSG + NSG
III	SiN	SiN
IV	SiN	Bare

Results

Al corrosion.—Figure 3 gives the cumulative failure of Al corrosion as a function of test time under ambient conditions of 85°C/85% RH at 30V. The top metal (5, 8 pins) is biased 0 V, and the lower metal (6 pin) is biased 30V. The results show that the median corrosion lifetime of samples I, II, IV, and III are 900h, 2700h, 5000h, and more than 10,000h, respectively. The median lifetime is affected by the materials of the dielectric layer. It is found that the SiN passivation/SiN inter-layer (SiN/SiN) is the best combination of passivation and inter-layer. For samples II and IV in Table I, which have the same inter-layers (SiN) but different passivation layers (II:NSG + PSG + NSG, IV: Bare), the median lifetime of sample IV is longer than that of sample II. A possible reason for this result is a micro-crack in the inter-layer caused by the mechanical stress due to the difference of thermal expansion of the multi-layer structure (Si substrate — lower metal — inter-layer — top metal — passivation). The coefficients of thermal expansion for these layers are, for plastic, 2.2 ×

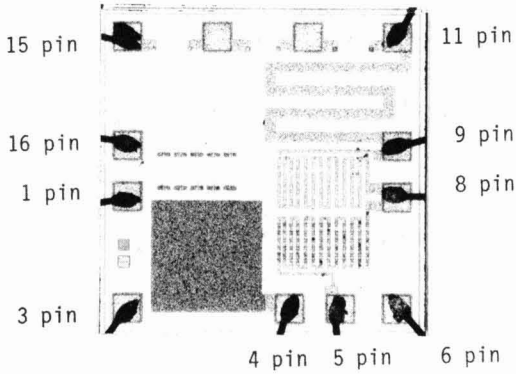


Fig. 1. The test chip

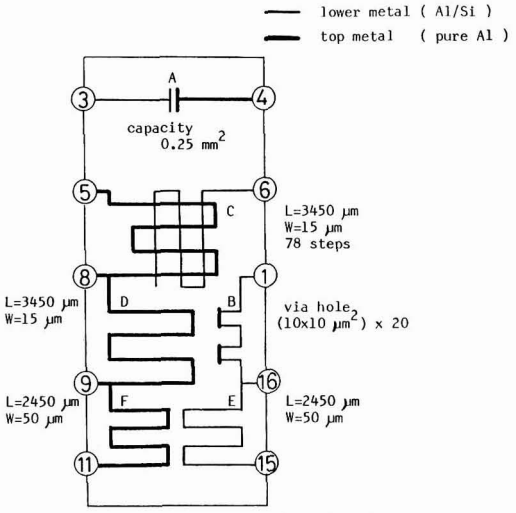


Fig. 2. Pin connection and dimensions of sample

10^{-5}/°C, SiN 2.5-3.0 × 10^{-6}/°C, SiO_2 6.0-9.0 × 10^{-7}/°C, Al 2.5 × 10^{-5}/°C, and Si 2.3 × 10^{-6}/°C, respectively. The matching of material in the multi-layer structure is essential for micro-cracks caused by this mechanical stress. In sample III (SiN/SiN), the SiN does not absorb moisture and, in addition, the material matching is better than that for other combinations.

Al corrosion occurred at the cathodic metal, as shown in Fig. 4a. Figure 4b indicates the example of corrosion in reverse bias of Fig. 4a, top metal is biased 30V and lower metal is biased 0V. In this case, the corrosion is observed on lower metal. These are the typical cathodic corrosion, independent of whether the level is upper or lower. If we were to assume the time for diffusion of absorbed moisture, it would be expected that corrosion at top metal would be severer than at lower metal, and that, at the side of chip, the corrosion would be severer than center of chip. However, the obtained results do not support the assumption. The corrosion always occurred at cathode aluminum and was not dependent on the distance from the source of moisture.

Electrolytic leakage current.—In order to check moisture absorption in detail, the electrolytic leakage current was measured after accelerated life tests in a moist atmosphere (121°C/85% RH). A moist atmosphere with a relative humidity of 85% RH at 121°C was established by unsaturated pressure cooker test equipment (USPCT) (3, 4). The autoclave used for USPCT has two heaters: one in the outer wall adjacent to samples (heater A) and another

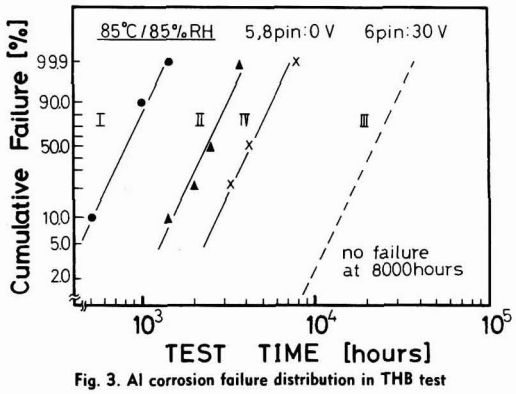
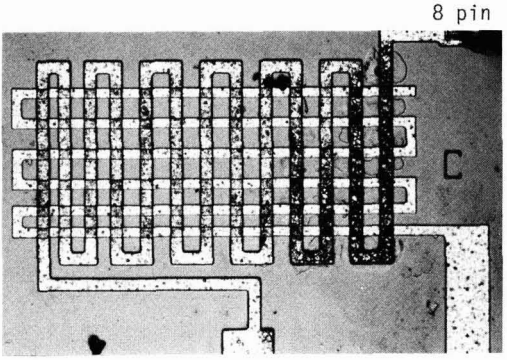
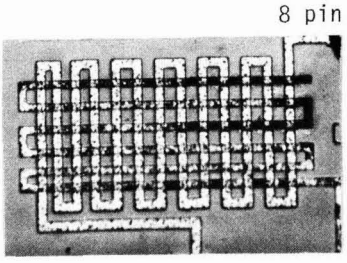


Fig. 3. Al corrosion failure distribution in THB test



5,8 pin (top metal)=0 V
6 pin (lower metal)=30 V

FIG. 4a



5,8 pin (top metal)=30 V
6 pin (lower metal)=0 V

FIG. 4b

Fig. 4. (a) Cathodic corrosion for sample I (6 pin = 30V, 5,8 pin = 0 V). (b) Cathodic corrosion for sample I (6 pin = 0 V, 5,8 pin = 30V).

in the water (heater B). Heater A is always set higher in temperature than heater B. As a result, independent control of humidity and temperature is possible. Figure 5 shows an example of life tests on bipolar IC's in a DIP 18 package. From this figure, we derived an activation energy of 0.9 eV.

The influence of dielectric layer.—Figure 6 gives the average leakage current (5, 8 pins — 6 pin) as a function of test time for samples I, III, and IV. The leakage current of sample I (NSG + PSG + NSG/LP − PSG) already reaches 100 pA at 50h and reaches the order of 1 nA at 300h. On the other hand, the leakage current of sample III (SiN/SiN) does not reach 1 pA at 300h. It is obvious that SiN is a remarkably better passivation than NSG + PSG + NSG. SiN does not absorb moisture, and electrolytic leakage current remains very low. The leakage current on sample IV (Bare/SiN) is about 1 pA until 200h, but the leakage current suddenly increases after 200h and reaches about 100 pA at 300h. This delay of increase of leakage current explains the delay of Al corrosion in Fig. 3.

Lateral leakage current and vertical leakage current.—Figure 7 shows the leakage current at 100, 200, 300, and

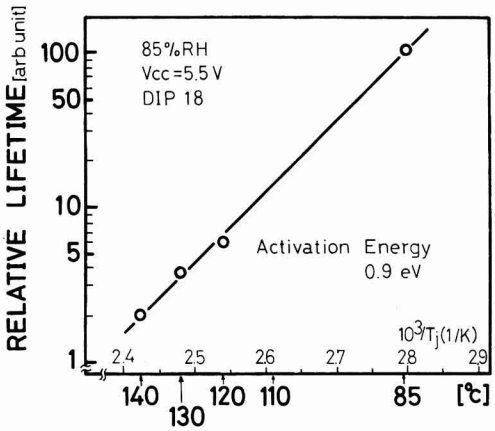


Fig. 5. Example of test result using a highly accelerated test (USPCT).

400h of exposure to the 121°C/85% RH ambient for sample I (NSG + PSG + NSG/LP − PSG). The results show that the leakage current through inter-layer of 3 pin-4 pin, 5 pin-6 pin, and 9 pin-16 pin is larger than that of other patterns. From these results, in double-layer metallization, it is found that the vertical leakage current through inter-layer is more important than the lateral leakage current between the same layer metals. Comparing between 3 pin-4 pin and 5, 8 pins-6 pin, when the facing areas of top and lower metals are large, one finds that the leakage current does not readily reach a saturation value, and the saturated value is larger.

Figure 8 shows the leakage current as a function of test time for samples III (SiN/SiN) and IV (Bare/SiN). In sample III, the leakage current is about 0.4 pA, and the difference of the three patterns is not found. On the other hand, for sample IV, the leakage currents of 3 pin-4 pin and 9 pin-16 pin are about 1 pA, but 5, 8 pins-6 pin are increasing after 200h. The current increases at the meander

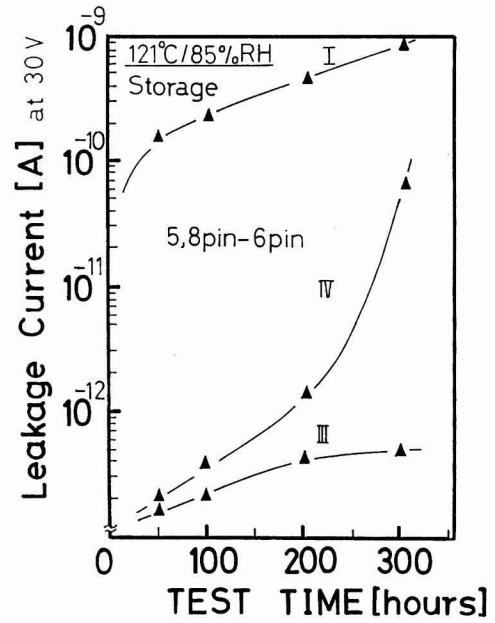


Fig. 6. The leakage current between top and lower as a function of test time.

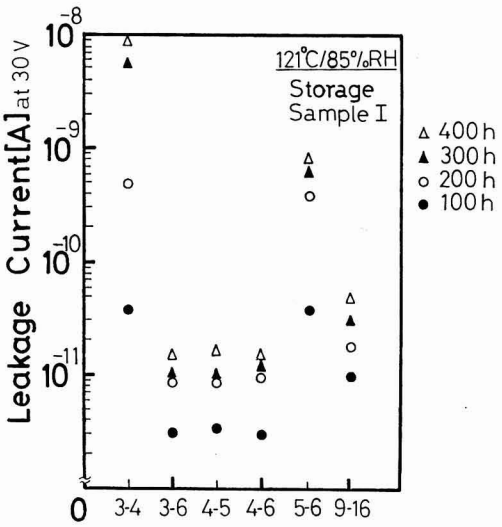


Fig. 7. Al pattern dependence of leakage current for sample I

pattern (5 pin-6 pin) after 200h but does not increase at the large area capacitor (3 pin-4 pin). It is supposed that this failure is due to micro-cracks of the SiN inter-layer at steps.

Discussion

From investigation of Al corrosion and leakage current in double-layer metallization, it is seen that the increase of the leakage current is the main reason of Al corrosion. In double-layer metallization, it was found that the vertical leakage current between top and lower metals is a main factor, because the thickness of the inter-layer is 1 μm and the electric field between lower and top metals is

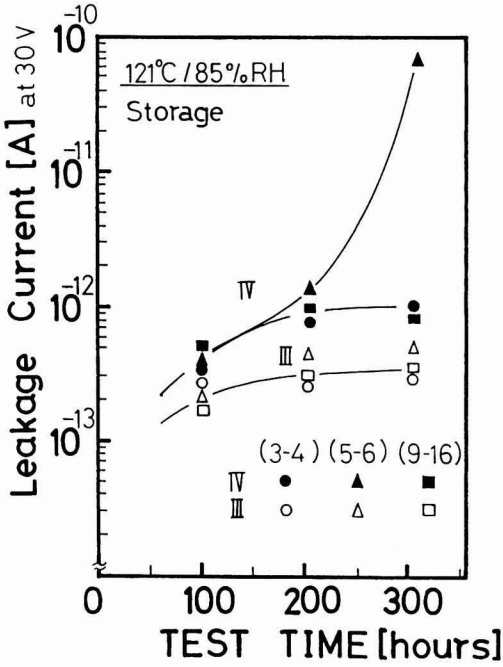


Fig. 8. The Al pattern dependence of leakage current between top and lower metals for samples III and IV.

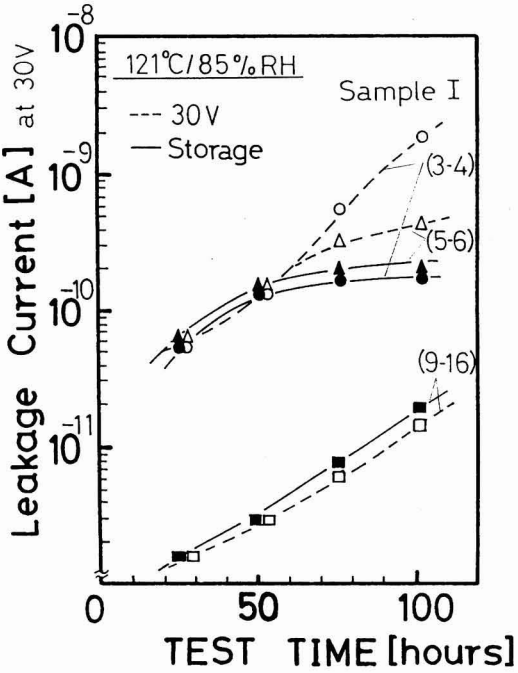


Fig. 9. The influence of bias for leakage current

larger than that between the same layer metals. Generally, for step coverage and via hole, it is difficult to increase the thickness of the inter-layer.

Figure 9 indicates the leakage current as a function of the test time for sample I (NSG + PSG + NSG/LP – PSG) with and without bias. In this figure, the solid line shows the results without voltage, and the dotted line shows the results with voltage. The increase of the leakage current by applied voltage for 3 pin-4 pin is larger than that of 5, 8 pins-6 pin. On the other hand, in the case of 9 pin-16 pin, the increase of the leakage current by applied voltage was not observed. It is found that the leakage current increases by applied voltage, and this effect is larger in pattern when a facing area is large. This bias effect may be explained by the additional cracks in the inter-layer induced by the Al corrosion. Moisture penetrates into the package through the bulk of the plastic and via the interface plastic-metal leads. Then, an electrolyte is formed and corrosion of Al metallization occurs. Since the corrosion products have a large volume, additional cracks are formed and the leakage current increases. The bias effect can be explained by this volume expansion induced by corrosive oxidation.

Figure 10a gives a photograph of Al corrosion for 3 pin-4 pin of sample I under the condition of lower metal 30V and top metal 0 V. At first, the corrosion was observed on the edge, and then Al corrosion invaded the center, as shown in Fig. 10b. The results in Fig. 10a and 10b show that Al corrosion around a chip is not predominant, because Al corrosion is early observed on center part in chip. It is found that moisture penetrates from edge of the pattern, and diffuses inside of the pattern.

The increase of leakage current is regarded as a function of water and phosphorus in the inter-layer. After absorption of moisture, phosphorous oxide makes the water content acidic. The increased hydrogen ion leads the leakage current increase. The large leakage current of 3 pin-4 pin appears to be due to the facing area. The ratio of the facing area is 3 pin-4 pin: 5, 8 pins-6 pin = 14: 1, and the leakage currents are 3 pin-4 pin = 10 nA and 5, 8 pins-6 pin = 1 nA. From only these results, it seems that leakage current is in proportion to facing areas.

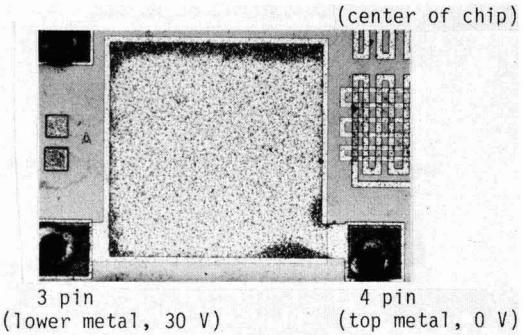


FIG. 10a

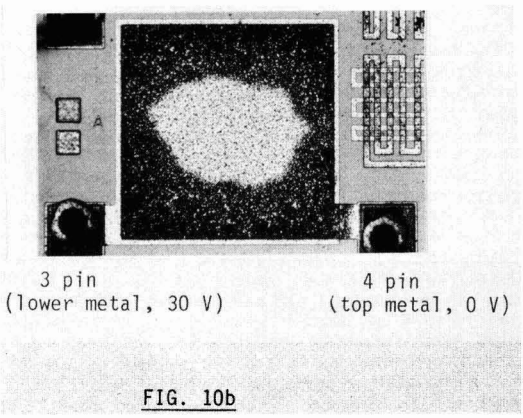


FIG. 10b

Fig. 10. (a) Cathodic corrosion of sample I at 1000h (lower metal = 30V, top metal = 0 V). (b) Cathodic corrosion of sample I at 3000h (lower metal = 30V, top metal = 0 V).

Conclusion

Investigation of aluminum corrosion and leakage current in double-layer metallization shows the following results:

1. The combination of SiN/SiN is excellent as compared with four combinations of passivation/inter-layer. Because SiN does not absorb moisture and SiN/SiN is strong structure for mechanical stress.
2. In double-layer metallization, a vertical leakage current through the inter-layer between the top and lower metals is predominant. This is because the inter-layer is thin and the electric field between top and lower metals is larger than that between the same layer metals.
3. Aluminum corrosion always occurs at cathodic metals, regardless of whether the metal is top or lower and regardless of whether the metal is located at the side or the center of the chip.
4. Leakage current is increased by applied bias. This may be explained by the additional cracks in the inter-layer induced by aluminum corrosion.

Acknowledgment

We would like to thank S. Sugimoto for his advice.

Manuscript submitted Sept. 27, 1984; revised manuscript received Aug. 9, 1985.

The Matsushita Electronics Corporation assisted in meeting the publication costs of this article.

REFERENCES

1. M. J. Fox, *Microelectron. Reliab.*, **16**, 251 (1977).

2. F. Neighbour and B. R. White, *ibid.*, **16,** 161 (1977).
3. K. Ogawa, J. Suzuki, and K. Sano, Proceedings of the International Symposium for Testing and Failure Analysis, 75 (1981).
4. J. E. Gunn, S. K. Malik, and P. M. Mazumdar, *Proc. Int. Reliability Phys. Symp.*, **19,** 48 (1981).
5. E. P. van de Ven and H. Kolemans, *This Journal*, **123,** 143 (1976).

CVD Growth and Properties of "Phoslon" Dielectric Films

P. C. Li and L. C. Hsia*

IBM General Technology Division, East Fishkill Facility, Hopewell Junction, New York 12533

ABSTRACT

"Phoslon" is a coined name for a new dielectric family ($P_xN_yO_z$) prepared by either the conventional CVD or PECVD techniques. While it contains no Si component, it consists of phosphor, nitrogen, and oxygen with phosphorus nitride as an extreme. The dielectrics thus formed are very stable, inert to almost all chemicals commonly used in semiconductor industry, and have dielectric constants comparable to Si_3N_4. The dielectric breakdown strength of phoslon is in the order of 10^7 V/cm, which is far better than that of the Si_3N_4 films grown by CVD.

The formation of dielectric films containing phosphorus, nitrogen, and oxygen by the thermal condensation of phosphoryl triamide $PO(NH_2)_3$ has been previously reported (1). In the past decade, the thin film growth technology has been tremendously advanced. Amorphous phosphorus-nitrogen-oxygen films (PNO) can now be prepared by either chemical vapor deposition (CVD) or plasma enhanced chemical vapor deposition (PECVD) (2, 3). Inert phospham dielectric films (10) can be readily formed by PECVD from a gas mixture of PH_3, H_2, and N_2. The increasing use of reactive ion etch or plasma etch in the microelectronics industry has made the study of PN and PNO dielectrics much more important because of their potential applications as encapsulant, insulator for multilayered metallurgy, gate dielectric, etch mask, and protective coating. Hirota *et al.* (4) reported the use of CVD formed P_3N_5 as a gate insulator for InP MISFET devices; and Furukawa *et al.* (5) have studied other PN films as gate insulators.

Amorphous phosphorus nitride has been investigated by Veprek *et al.* (3). It seems nitrogen can be alloyed with phosphorus in any stoichiometric ratio up to P_3N_5. The addition of a gaseous source in the reaction gases to bring an oxygen component to the phosphorus-nitrogen composition will likely enhance adhesion in coating. The properties of PNO system will be discussed in detail in the following sections.

Known PN compounds reported in the early work (6) include P_3N_5, P_2N_3, $(PN)_z$, and PON. Their general properties are summarized in Table I. In the preparation of the P_3N_5 compound, phospham, PHN_2 usually forms as an intermediate (Eq. [1], [2])

$$PCl_5 + 4NH_3 \rightarrow PHN_2 + 2NH_4Cl + 3HCl \qquad [1]$$

$$3PHN_2 \xrightarrow[\text{Vacuum}]{400°C} NH_3 + P_3N_5 \qquad [2]$$

Table I. Known simple P-N or P-N-O compounds

Compound	Density	Decomposition temp, °C	Remarks
P_3N_5	2.79[3] 5.57, 2.58 2.51	670, 800, 1100	
P_3N_{5-x}[3]			
P_2N_3	—	Stable up to 750	
P_3N_{21}	—	Explosive	Oily liquid
PON	—	Melt at red heat	
$P_3(N_3)_5$	—	Decomposes to form $P(N_3)_3$	
$(PN)_z$	—	(Stable above 730) Decomposes above 800°C	Enflames when heated in O_2

Upon heating in vacuum at 730°C, P_3N_5 is converted into $(PN)_z$ polymer

$$P_3N_5 \xrightarrow[\text{Vacuum}]{730°C} (PN)_z \qquad [3]$$

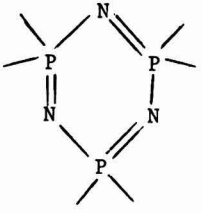
Further heating $(PN)_z$ in a NH_3 atmosphere at 800°C results in forming two different $(P_3N_5)_x$ polymers—the red and yellow forms; the red form is stable in cold sulfuric acid but not in hot sulfuric acid, and the yellow form is attacked by cold sulfuric acid.

Hirota *et al.* (4) reported the formation of P_3N_5 vapor at temperatures above 860°C from a NH_3 and PH_3 mixture and the deposition of the film on InP substrates at 600°C by condensation in a three-zone temperature gradient reactor system.

Using the plasma enhanced low pressure deposition technique, Veprek *et al.* (3) have successfully synthesized the P_3N_5 compound from P and N_2 at a much lower temperature (300°C), and $P_3N_5H_x$ compounds from PH_3 and H_2. The structure of the amorphous P_3N_5 has been discussed by Veprek *et al.* (3). The ideal P_3N_5 consists of two kinds of even number rings or chains containing

$$-N=P-N= \quad \text{and} \quad \rangle N-P-N\langle$$

groups, respectively. Further consideration of the plausible constraint, such as nature of the bonds and the bond angles, results in the suggestion that the 6-numbered rings containing double bonds represent the most probable structured unit as shown below



At present, the structure of phoslon ($P_xN_yO_z$) is not known. It is reasonable to assume that it is closely related to the P_3N_5 structure. This paper deals with the preparation and properties of the phoslon and its structure will not be discussed.

Preparation and Composition Characterization of Phoslon

The system used for phoslon deposition is schematically illustrated in Fig. 1. The apparatus includes a fused quartz reactor tube having a rectangular cross section of approximately 4¼ in. × 1¾ in. Surrounding the reactor

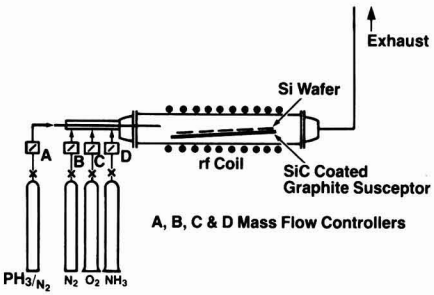


Fig. 1. Schematic drawing of phoslon CVD System

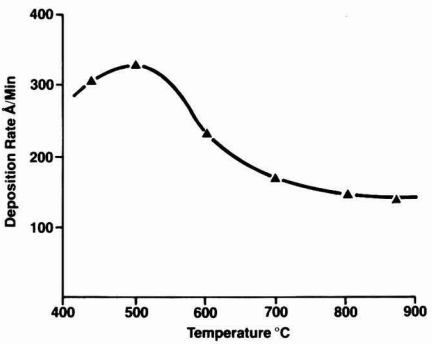


Fig. 3. Phoslon growth rate vs. deposition temperature (based on the film buildup at 4 in. away from the gas mixture inlet in the reactor. The total gas flow rate is 11 liters/min with PH_3 content 0.02-0.08%, NH_3 2-7%, O_2 0.5-2%, balance N_2).

wall is an induction heating coil. Within the reactor is a graphite susceptor which is enclosed in a fused quartz envelope. Wafers are positioned over the graphite susceptor. The temperature of the substrates are raised by RF induction heating until the substrate temperature is between about 400°-900°C. The reaction gases containing phosphine, nitrogen, ammonia, and oxygen sources then pass through the chamber where the deposition of the amorphous phoslon films occurs over the susceptor where the wafers set. Approximately 0.5% PH_3 in N_2 was fed into the reactor with various amounts of O_2, NH_3, and N_2.

The buildup along the reactor generally varies from the gas inlet to the outlet. Figure 2 illustrates the formation region of some phoslon composition over the deposition temperature about 400°-900°C for a specified position in the reactor. This will be discussed in detail later. The oxygen concentration in the feed gaseous mixture varies from 0.01 to about 98%, excluding the ammonia and phosphine. It is interesting to note that almost no deposition occurs in the absence of oxygen in the CVD process. Some possible explanations for this phenomena will be given later. However, the mechanism of oxygen promotion of deposition is not clear at this time. All data points illustrated indicate where good, adhering, and stable coatings were formed. Figure 3 shows the deposition rate of the phoslon as a function of temperature. In this figure, the deposition rates were measured at a 4 in. distance away from the gas inlet in the reactor, where the maximum deposition rate occurs. At each temperature there is an optimum gas flow rate for proper uniform film buildup along the susceptor. For the film processed at 435°C, because of lower thermal energy available at this temperature, the maximum film buildup was somehow shifted to 5¼ in. location with a growth rate of 390 Å/min, about 100Å higher than at the 4 in. position. At 860°C the film growth rate decreases to 123 Å/min, possibly resulting from sublimation or decomposition. The lowest temperature at which to start a measurable deposition is about 350°C. However, the deposits are unstable in air or water. Below 350°C no chemical reaction at the surface was observed over a few hours of deposition. Thus, it is kinetically not feasible for the film growth in a flow reactor system at this temperature.

The mechanism of phoslon formation is necessarily a complex one. There may exist many competitive reactions. The overall reaction and film growth mechanism are suggested as follows. Some compounds containing N, H, and P, such as phospham, P_2NH, and phosphorus amide imide, $P(NH)NH_2$ are also, like phoslon, inert, insoluble, and highly polymerized (6). When phospham is heated to 500°C, network rearrangement occurs with gradual elimination of H to give P_3N_5, which itself changes to P_3N_3 at high temperature

$$PN(NH) \rightarrow P_3N_5 \rightarrow (PN)_n \quad [4]$$

In light of this analysis, the most probable reactions during the phoslon CVD film formation can be suggested as follows

$$PH_3 + O_2 + NH_3 + N_2 \rightarrow OP(NH_2)_3$$
$$\rightarrow P_xN_yO_z + N_2 + H_2 + \text{unidentified products} \quad [5]$$

The network rearrangement also occurs at about 500°C with the elimination of H from $OP(NH_2)_3$ to give $P_xN_yO_z$. This suggestion is supported by the fact that the relative high deposition rate occurs at about 500°C (Fig. 3). At higher temperatures, the outgassing of hydrogen serves

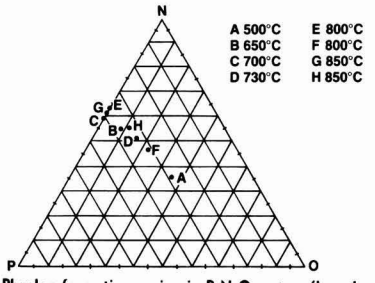


Fig. 2. Phoslon formation region in P-N-O system (based on nuclear backscattering analyses).

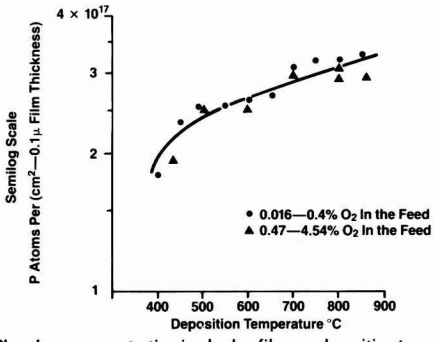


Fig. 4. Phosphorus concentration in phoslon films vs. deposition temperature (by x-ray fluorescence analysis).

as a buffer, somewhat hindering the deposition rate. At temperatures higher than 900°C, decomposition of PN network may occur. It has been established that P_3N_5 decomposes according to the following steps (4)

$$P_3N_5 \xrightarrow{750°C} 3PN\ (g) + N_2 \quad [6]$$

$$PN \xrightarrow{800°C} P + N \quad [7]$$

The decomposition of phoslon ($P_xN_yO_z$) may follow the similar steps

$$P_xN_yO_z \rightarrow PN + N_2 + O_2 \xrightarrow{(PN \rightarrow P + N)} P_2P_5 + N_2 \quad [8]$$

And PN further decomposes into P and N, and finally P and O form P_2O_5. Thus, at higher temperatures, simultaneous growth and decomposition compete with each other, partially accounting for the complicated and abnormal dependence of deposition rate on the process temperature.

An important competitive reaction may take place, with P_2O_5 serving as an intermediate

$$PH_3 + O_2 \rightarrow P_2O_5 \quad [9]$$

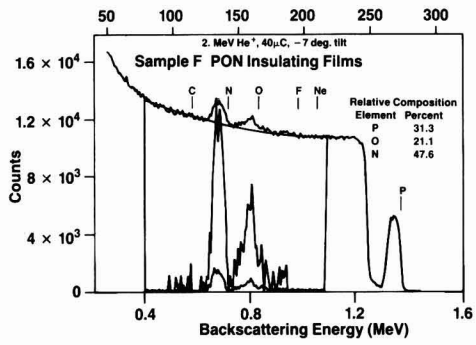
$$P_2O_5 + NH_3 \rightarrow P_xN_y \quad [10]$$

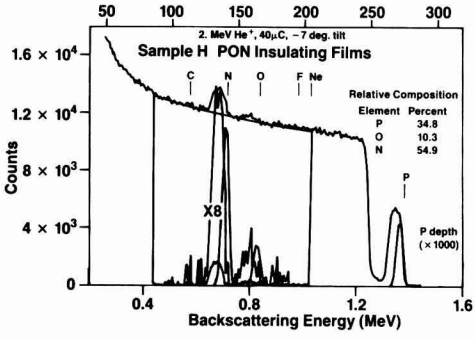
In this reaction, the inclusion of oxygen is necessary even though the deposited film does not contain a detectable amount of oxygen. Data obtained in this work strongly indicate that at some deposition temperatures, with proper gas mixture in the feed, the films contain almost no oxygen. Therefore, it is possible that at these temperatures, P_xN_y compounds form through the above reaction, thus explaining the necessity of the inclusion of oxygen in the deposition process. A comparison with the results of Hirota *et al.* (4) (deposition temperature 860°C/600°C, deposition rate 800 Å/h at 600°C substrate temperature), reveals that the inclusion of oxygen in the feed gas mixture gives rise to the following effects: (i) expanding the film deposition temperature range, and (ii) increasing the deposition rate from about 800 Å/h to approximately 13,700 Å/h at 600°C from this work.

Veprek *et al.* (3) lowered the deposition temperature to 300°C and yet obtained a growth rate of about 13 μ/h using a low pressure RF glow discharge deposition technique from P and N_2 sources.

In order to characterize the composition of phoslon films, the films were studied for the composition using x-ray fluorescence (XRF), nuclear backscattering, and microprobe techniques. Among these analytical techniques, the nuclear backscattering analysis provides the most reliable compositional data; the microprobe and x-ray fluorescence techniques, because of their limitation in sensitivity, can only provide partial composition information. Figure 4 shows the results of the XRF analysis for the phosphorus content for samples deposited from 400° to 900°C with various amounts of oxygen content, up to 4.56% in the feed gas mixture. The samples were compared to the standard of P in a CVD PSG film prepared from N_2, $SiBr_4$, PH_3, and O_2 at 900°C. This figure shows a trend of increasing P content in the film as the deposition temperature rises from 400° to 900°C and an independence of oxygen content in the gaseous feed mixture. This is possibly due to the higher volatility of PNO compounds relative to PN compounds co-deposited on the substrate, thus making the films phosphorus rich at higher deposition temperatures. Another possible explanation could be that the increase of reactivity among PH_3, NH_3, N_2, and P_2O_5 leads to the formation of materials much richer in P content.

Table II contains the nuclear backscattering data for some phoslon materials. It can be observed that the oxygen content in the film is correlated to the oxygen partial pressure in the feed gas mixture. The maximum oxygen content in the film occurs at 500°C, which coincides





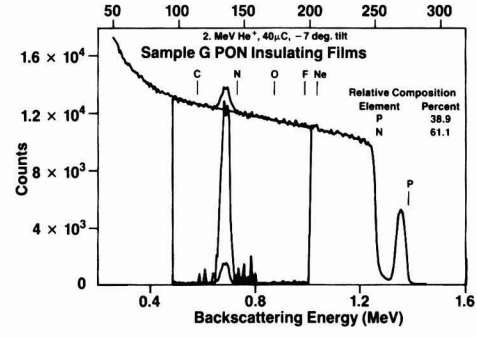


Fig. 5. (a, above left), (b, above right), and (c, left) nuclear backscattering spectra of some typical phoslon films.

Table II. Composition of phoslon by nuclear backscattering analysis

Sample	Deposition temp, °C	Feed gas composition m/o (Bal N_2) O_2	NH_3	PH_3	Refractive index n	Thickness t, (Å)	Film composition a/o N	O	P
A	500	0.023	2.30	0.024	1.769	4860	34	36.3	29.7
B	650	0.016	1.58	0.017	1.877	1047	54.2	9.3	36.5
C	700	0.021	1.07	0.011	1.961	5064	59.7	—	40.3
D	730	0.927	1.79	0.020	1.810	7105	50.4	15.9	33.7
E	800	0.048	0.97	0.010	1.908	4538	62.1	—	37.9
F	800	24.16	0.94	0.010	1.825	0161	47.6	21.1	31.3
G	850	0.037	0.47	0.010	1.942	792	61.1	—	38.9
H	850	0.241	0.96	0.010	1.942	1053	54.9	10.3	34.8

Table III. Composition of phoslon by microprobe analysis

Sample	Deposition temp, °C	Feed gas composition m/o (Bal N_2) O_2	NH_3	PH_3	Film composition a/o N	O	P
1	650	0.041	1.36	0.14	47.9 ± 0.51	21.13 ± 0.54	31.93 ± 0.25
2	650	0.340	1.36	0.14	43.11 ± 1.29	25.87 ± 2.21	31.00 ± 1.02
3	650	23.36	1.87	0.020	41.98 ± 0.66	26.49 ± 0.85	31.51 ± 0.67
4	650	46.73	1.87	0.020	42.08 ± 1.77	26.67 ± 2.16	31.23 ± 0.55
5	650	87.72	3.51	0.037	36.53 ± 0.46	32.82 ± 0.59	30.63 ± 0.65

with the relatively high deposition rate at that temperature. The comparison of C and D, E and F, and G and H, grown at the same temperature, respectively, reveals that at higher temperatures, low oxygen content in the feed results in no oxygen presence in the films. Some of the observations will be further discussed.

Figure 5 shows the nuclear backscattering spectra for samples F, H, and G, deposited at about 800°C. The relative intensities for P, O, and N yield the relative film composition. The mole percent of oxygen in the feed for the deposition is 24, 0.241, and 0.037, respectively. The resulting oxygen atomic % in the film is 21.1 [Fig. 5(a)], 10.3 [Fig. 5(b)], and 0 [Fig. 5(c)], respectively. It is possible that a small amount of hydrogen might be incorporated into the film. However, hydrogen cannot be detected by this technique.

The composition of the phoslon was also analyzed by the microprobe technique. Table III contains the compositions of the films grown at 650°C with various feed gas mixtures. As compared to the nuclear backscattering analysis, this technique appears to indicate a higher oxygen content in the films. It is apparent that at this temperature the oxygen content in the film is independent of that in the feed, with the exception of films 1 and 5, which were formed with an extremely large amount of oxygen in the gas mixture. For film 3 and film 4, the oxygen content shows almost no change. However, when oxygen content in the feed increases from 46.73 to 87.72 m/o, the oxygen content in the film increases by 23%. It can also be observed that the N and P contents do not vary much with the feed gas composition, with the exception of films 1 and 5. Films grown at other temperatures may not have the same behavior, but there is no data available at this moment.

Properties of phoslon

Some of the preliminary studies on the properties of phoslon are reported in this section. Phoslon films grown in this work are extremely inert and are not attacked by the chemicals commonly used in the microcircuit fabrication. The films are also amorphous and lack any crystallinity shown by the TEM study. The films demonstrate attractive properties as a dielectric. The refractive indexes of the phoslon films, as measured by the ellipsometry technique, vary from 1.61 to 2.0, depending on the deposition temperature. The dependence is shown in Fig. 6. For comparison, the indexes of refraction for both the as-deposited Si_3N_4 films and the Si_4N_4 films annealed in a N_2 environment at 1000°C for 20h are also included in Fig. 7. It can be observed that the phoslon films have indexes of refraction higher than or comparable to those of the Si_3N_4 films prepared in the same temperature range as shown in Fig. 7 (by the authors of this work).

The apparent dielectric constants of the phoslon films, as calculated from the capacitance measurements, vary from 6 to 8, as shown in Fig. 8. A minimum occurs at 600°C. The abnormally high dielectric constants of low temperature phoslon are probably resulting from relatively high H content in the films due to the residual intermediate phospham.

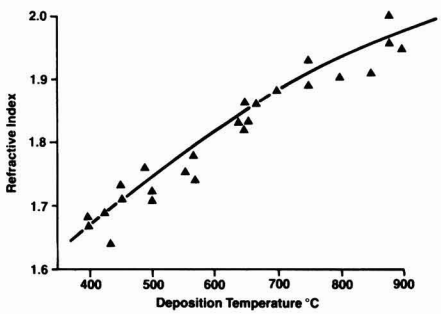


Fig. 6. Refractive index of phoslon films vs. deposition temperatures

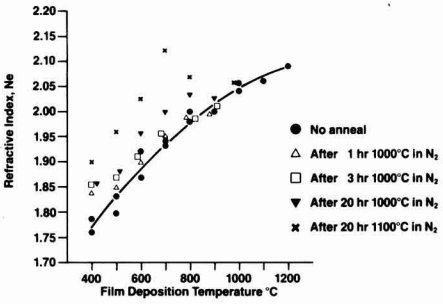


Fig. 7. Refractive index of CVD silicon nitride films from the $SiBr_4$-NH_3-N_2 process.

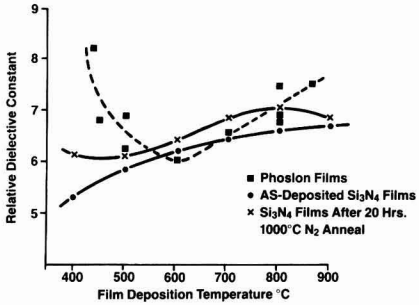


Fig. 8. Relative dielectric constant of phoslon films vs. deposition temperature.

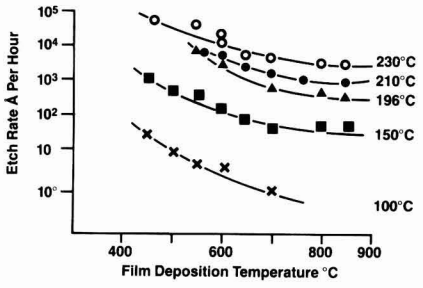


Fig. 10. Wet etch rate of phoslon films in 96% sulfuric acid at bath temperature from 100° to 230°C vs. film deposition temperature.

The dielectric breakdown strength (accumulation mode) of the phoslon films was also measured. As shown in Fig. 9 for the films deposited above 500°C, breakdown strength is higher than 10×10^6 V/cm, which is better than that of CVD or PECVD Si_3N_4 (based on the equivalent normalized oxide thickness). In Table IV the dielectric breakdown strength of some metal-phoslon-oxide-silicon (MPOS) structures is shown. With a phoslon/oxide ratio greater than 1:1, the breakdown strength is close to 20×10^6 V/cm.

Phoslon deposited in this work was found to be inert to many chemicals, including warm H_2SO_4 solution. However, at elevated temperatures, phoslon can be etched by a 96% H_2SO_4 solution. Figure 10 shows the etch rate of phoslon at various etchant temperatures, with respect to the film deposition temperature. At all etchant temperatures, the etch rate decreases rapidly as the deposition temperature increases. At 100°C etchant bath, the films made above 700°C show undetectable etch rate. The increase of the etchant temperature will definitely increase the etch rate. Figure 11 shows the etch rate of the phoslon film deposited at 800°C in a 96% H_2SO_4 solution at 196°C, as a function of the oxygen content in the feed. It is interesting to note that for higher oxygen content in the feed, the etch rate is also higher. From Table II, it is known that for higher oxygen content in the feed, the oxygen content in the films is higher too. Thus, it is believed that the etch rate is correlated to the oxygen content in the film.

The phoslon films can be etched by the $CF_4 + O_2$ plasma. Table V contains the etch rate obtained using a DRIE 100 plasma system. The pressure was set at 0.18 torr, with 110 sccm CF_4 and 11 sccm O_2. The RF power was 700W and the substrate temperature was kept at 60°C. The etch rate of phoslon films is comparable to that of the PECVD nitride (320°C), about 4000 A/min. An abnormality was found for the etch rate of the film deposited at 500°C. An etch rate of 84 A/min seems rather low. Also, the film made at 850°C with low O_2/PH_3 ratio has an abnormally high etch rate. Compositions of these particular samples need to be analyzed for possible explanation.

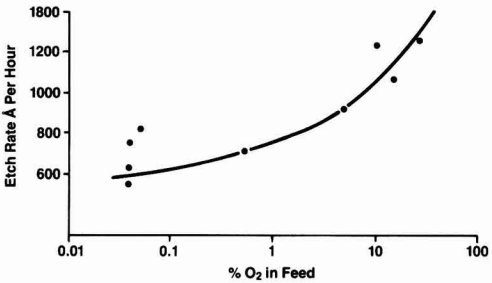


Fig. 11. Wet etch rate of 800° phoslon films in 96% sulfuric acid at 196°C vs. O_2% in the feed gas mixture.

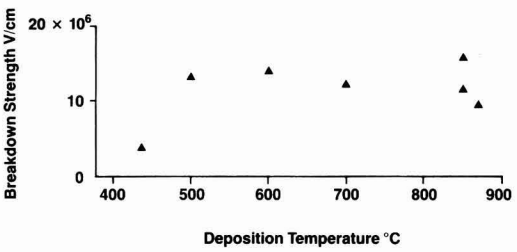


Fig. 9. Dielectric breakdown strength of phoslon films deposited on P-Si wafer (accumulation mode).

Table IV. Dielectric breakdown strength of phoslon/SiO_2 dielectrics

Run no.	Temp	Phoslon/SiO_2 (thickness in Å)	10^6 V/cm
408-1	850°C	600/200 (P-Si)	19.0
409-3	850°C	350/200 (N-Si)	18.1
319-5	650°C	170/200 (P-Si)	11.7

Table V. Plasma etch rate of phoslon

Sample	Dep. temp	O_2/PH_3 ratio	n	Plasma etch rate Å/min*
1	850	23.5	1.938	5800
2	850	4.8	1.940	30360
3	800	4.7	1.918	7296
4	800	1420	1.877	4380
5	800	2368	1.820	5796
6	800	4.7	1.919	7680
7	900	23.0	1.957	2496
8	700	1.9	1.870	4884
9	550	0.95	1.715	5556
10	500	0.91	1.706	84

* Etch rate was tested in DRIE 100 at 0.18 torr/110 sccm CF_4 11 sccm O_2, RF power 700W, and substrate temp 60°C. Under the same conditions, the etch rate of PECVD silicon nitride (320°C) is 4000 Å/min.

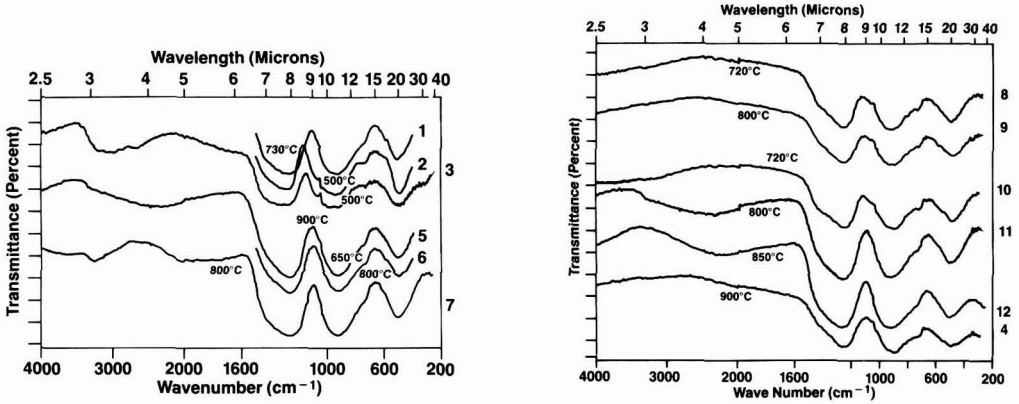


Fig. 12. IR spectra of phoslon films deposited at various temperatures

IR Spectra and Discussion

There are relatively few detailed studies of the structure of nonsilicate dielectrics containing phosphorus. Infrared spectroscopic investigations of phosphorus nitride and amorphous $P_3N_2H_x$ were conducted by Steger *et al.* (1), Rajeis *et al.* (2), and Veprek *et al.* (3, 7). Their data indicate the presence of single and double phosphorus-nitrogen bonds. The purpose of using the IR spectroscopic study in this work is to compare its results with their results.

A series of IR measurements was made using a Perkin Elmer Model 521 spectrometer on the phoslon films deposited at various temperatures. The results are shown in Fig. 12. The preparation conditions of phoslon film for IR study are detailed in Table VI. Three broad absorption bands at 500, 920, and 1260 cm^{-1} were found in all samples. These three strong absorption bands were reported previously and understood to be due to the single and double P-N bonds. Their positions, shapes, and relative intensities are almost independent of the preparation conditions.

According to Rejeis *et al.* (3), the positions, as well as the widths of the bands at 920 and 1230 cm^{-1}, suggest that they are due to predominantly stretching-type lattice vibrations of the amorphous phosphorus nitride network. The relative sharp antiresonnance-like minimum at 1100 cm^{-1} and the apparent asymmetry of the bands indicate a strong anharmonic coupling between these modes. This asymmetry becomes more conspicuous for the samples deposited at lower temperatures (spectrum 3). Spectrum 2 was obtained from the same sample as spectrum 3, annealed at 860°C for 0.5h. It shows even a stronger anharmonic coupling between these two modes, possibly resulting from densification.

Table VI. Infrared spectra samples

Spectrum	Deposition temp, °C	Composition of feed gas mixture m/o (Bal. N_2) O_2	NH_3	PH_3
1	730	0.93	1.78	0.020
2	500 (1/2h 860°C N_2, anneal)	Trace	4.44	0.028
3	500	Trace	4.44	0.028
4	900	0.47	1.86	0.020
5	650	Trace	3.53	0.010
6	800	0.93	1.85	0.020
7	800	Trace	4.44	0.028
8	720	15.75	1.57	0.017
9	800	15.75	1.57	0.017
10	720	15.75	1.57	0.017
11	800	0.93	1.85	0.020
12	850	0.47	1.86	0.200

The band at 500 cm^{-1} may be due to a deformation mode (bending) of the PN network.

A weak absorption band located at 720 cm^{-1} was also found in all the samples. Compared with the results obtained by Steger *et al.* (1), this band can be attributed to a POP vibrational mode. It is important to notice that the intensity of this mode has a definite correlation with the oxygen content in the feed, and thus the oxygen content in the film (Table II). This point can be well illustrated by comparing spectra 7, 4, and 10, where the oxygen content ranges from none to high. Spectrum 7, obtained for a sample containing almost no oxygen, shows very weak absorption at this band. As the oxygen content increases, the mode intensity becomes stronger, as shown by spectra 4 and 10. Thus, it is very reasonable to attribute this absorption band to the POP vibration mode.

The spectra show some very interesting features in the ranges from 1700 to 4000 cm^{-1}. Depending on the oxygen content in the film, the spectrum may show one broad band, or no absorption band at all. Spectrum 10 is an example of samples with very high oxygen content. No absorption can be observed from the spectrum. From spectrum 11, obtained for an oxygen-deficient sample, a broad band from 1700 to 3500 cm^{-1} can be observed. This may be caused by incorporating hydrogen into the PN network, and thus broadening the mode (or modes) by the presence of oxygen. However, there is no direct confirmation of the H presence. Spectra 3, 5, and 7, obtained for samples with very high oxygen deficiency, show more complex band structures. For spectra 3, the broad absorption between 2500 and 3500 cm^{-1} is due to the overlapping of the OH stretching mode of absorbed moisture (a maximum at 3300 cm^{-1}) and to the NH stretching mode at the lower frequency side.

Conclusion

Amorphous phoslon ($P_xN_yO_z$) films have been successfully prepared at temperatures from 400° to 900°C using the CVD process. Oxygen is essential to the deposition. Both O_2 partial pressure of the gaseous feed mixture and substrate temperature are important to the resulting film composition and reactivity. The films thus formed, in general, are quite inert, durable, yet can be etched by the plasma process.

The IR spectra show that the CVD process has successfully eliminated H from the PN network. Results from other authors (3) may suggest that the growth of phoslon type films could be further improved using plasma enhanced chemical vapor deposition from suitable source materials.

Although the material has not been extensively incorporated in device fabrication, the potential applications

make the phoslon an extremely interesting subject for further extensive investigation.

Acknowledgments

The authors are deeply grateful to P. Saunders, E. Vishnesky, S. Cvikevich, L. Plaushin, and D. Kirby for their assistance in this work.

Manuscript submitted May 10, 1985; revised manuscript received Sept. 25, 1985.

IBM Corporation assisted in meeting the publication costs of this article.

REFERENCES

1. E. Steger and G. Milder, *Z. Anorg. Allg. Chem.*, **332**, 5 (1964).
2. U.S. Pat. 4,172,158, 1980, and *IBM Tech. Disclosure Bull.*, **26** (3A), Aug. 1983.
3. S. Veprek, Z. Igbal, J. Brunner, and M. Scharli, *Philos. Mag.*, **B 43**, 527 (1981).
4. Y. Hirota and T. Kobayashi, *J. Appl. Phys.*, **53**, 5037 (1982).
5. Y. Furukawa, O. Mikami, M. Okamura, and Y. Hirota, Paper 169 presented at The Electrochemical Society Meeting, Las Vegas, NV, Oct. 13-18, 1985.
6. D. Corbridge, "Studies in Inorganic Chemistry 2," 2nd ed., Elsevier Scientific Publishing Co., Amsterdam (1980).
7. M. Rejeis, L. Rejeis, and T. Miller, *Latv. PSR Zinat. Akad. Vestis. Kim. Ser.*, 261 (1976).
8. L. Rejeis, 5th Konferencia Molodych Nauchnich Raboth; kov. Institut Neorgitcheskoj Khimii, Riga, 20 (1976).
9. S. Veprek and J. Roos, *J. Phys. Chem. Solids*, **37**, 554 (1976).
10. M. E. Cowher and A. J. Shuskus, Abstract 379, p. 537, The Electrochemical Society Extended Abstracts, Vol. 84-2, Fall Meeting, New Orleans, LA, Oct. 7-12, 1984.

The Effect of Bulk Traps on the InP Accumulation-Type MISFET

L. G. Meiners

Department of Electrical Engineering and Computer Sciences, University of California, San Diego, La Jolla, California 92093

ABSTRACT

Calculations of the effect of bulk traps on the time dependence of the channel current in InP accumulation-type MISFET's are reported. It is shown that a uniform density of deep acceptors in the bulk material gives rise to a decay in the channel current, which decays approximately linearly as a function of the logarithm of time. If capture of the electrons is assumed to occur by a nonradiative multiphonon emission process, then the temperature dependence that is obtained agrees with experimental results.

Indium phosphide (InP) is an attractive material for the fabrication of metal-insulator-semiconductor (MIS) field-effect transistor (FET) because of its large saturated drift velocity for electrons and the favorable conditions present at its oxide-semiconductor interface. While efforts to construct MISFETs on gallium arsenide were unsuccessful due to the large interface-state density on this material (1, 2), progress has been much more rapid in the case of InP. Interface-state densities between deposited layers of silicon dioxide (SiO_2) and InP have been calculated to be as low as 2×10^{11} $cm^{-2}eV^{-1}$ based on capacitance-voltage measurements on MIS diodes (3, 4, 5). A type of MISFET that has been labeled the accumulation-type device has been realized on InP (6). Construction of this device begins with the formation of two heavily doped (n^+) ohmic contacts for the source and drain regions on a wafer of semi-insulating (SI) InP. The wafer is then coated with a thin insulating layer, overlapping gate electrodes are evaporated on top of the insulator, and windows are etched through the insulator for connection to the source-drain electrodes. A cross-sectional view of the device is shown in Fig. 1. This device was originally proposed and fabricated because the reduced capacitance between the conducting channel and the substrate was expected to lead to a better high frequency response than that of similar devices constructed on p-type substrate material. Indeed, this was found to be the case.

A remaining problem to be solved before the device is perfected is a long-term drift in the drain current that is observed when a constant voltage is applied between the gate and source electrodes (7, 8). Several models have been proposed that attempt to explain the origin of the drift by tunneling currents between states in the insulator and the conduction band of the semiconductor (9, 10, 11). I feel that these models have serious shortcomings and that, although they give substantially correct mathematical expressions for the current drift, they have errors in their formulation. This is further discussed in the paper.

A first-order model for the I-V behavior of the accumulation-type transistor, based on the gradual channel approximation, has been formulated by Wieder (12). His model assumed that the substrate (the SI InP) could be treated as an ideal insulator.

In this paper, I present calculations for the time-dependent behavior of the accumulation-type transistor that take into account the fact that the conducting channel of the device is on the surface of a semiconductor that contains both shallow donors (due to native defects) and deep acceptors (introduced by iron doping). The time dependence of the device is calculated by assuming that the capture and emission of electrons by the bulk impurity states is governed by a Shockley-Read type of recombination process. Poisson's equation has been solved numerically to obtain the time development.

Background

The key features that must be explained by any proposed model for drift of the channel current in the accumulation-type transistor are illustrated in data published by Lile *et al.* (7), which are reproduced in Fig. 2. The channel current decays linearly as a function of the logarithm of time and the capture process "freezes out" at low temperature. Clearly, a tunneling process, as described by Heiman and Warfield (13), cannot explain such data, since there would be no temperature dependence if electrons were to tunnel from conduction band states to oxide trap levels at the same energy.

One of the proposed models for explaining the current drift in the accumulation-type transistor, as presented by

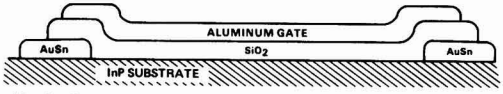


Fig. 1. Cross sectional view of accumulation-type MISFET on InP

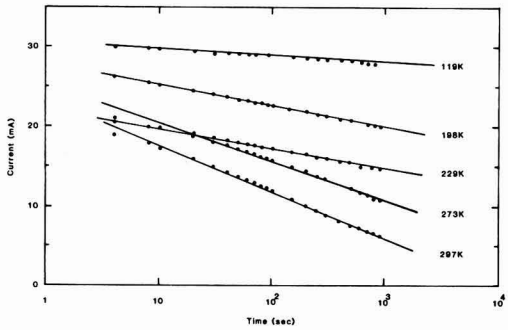


Fig. 2. Channel current as a function of time for an accumulation-type MISFET on InP, after Lile *et al.* (7). Channel length 4 μm, channel width 400 μm, oxide thickness 100 nm, gate voltage 4V, drain voltage 2V.

Goodnick *et al.* (9), is attractive, because it is based on physical evidence that the interface of InP coated with deposited SiO_2 consists of multiple layers, as shown in Fig. 3a. They proposed that the layer immediately adjacent to the InP consists of relatively large bandgap material ($InPO_4$) that is covered with lower bandgap material (In_2O_3), which in turn is covered with SiO_2. They also proposed that, when a positive voltage is applied to the gate of the device to form the conducting channel in the SI InP, a thermally assisted tunneling current flows from the semiconductor to states in the In_2O_3. Their solution for the channel current (I_d) as a function of time gives a linear dependence of I_d on log t. The temperature dependence is obtained in their model from the experimentally measured conduction band offset between the InP and the In_2O_3. Wager *et al.* (14) concluded from photoemission (XPS, UPS) and electron loss spectroscopy (ELS) measurements of deposited SiO_2 layers on InP that the conduction band minimum in the native oxide In_2O_3 is 0.1-0.2 eV higher than in InP. In the Goodnick *et al.* thermally assisted tunneling model, the electrons can tunnel from the InP to the In_2O_3 only if their kinetic energy is greater than the energy barrier step from the InP to the In_2O_3. As the temperature is reduced, fewer electrons are able to surmount this barrier, and the drift effect decreases. However, this model fails to take into account the fact that, with a positive voltage on the gate electrode, there will be a voltage drop across the $InPO_4$ layer and a lowering of the conduction band of the In_2O_3, as shown in Fig. 3b. Once the conduction band of the In_2O_3 is below the conduction band of the InP, all the temperature dependence of the I_d *vs.* t curves would disappear. For a 40Å layer of $InPO_4$, as assumed in their calculation, this requires a gate voltage of $V_g \simeq .2(d_{SiO_2} + d_{InPO_4})/d_{InPO_4} = 5.2V$. In this very rough estimate, d_i represents the thickness of the $InPO_4$ and SiO_2 layers, the dielectric constants of the two layers have been assumed equal, and the amount of conduction band offset has been assumed to be, as an upper limit, 0.2V. The temperature dependence of the drift current should then disappear for gate voltages larger than about 5V. This is contrary to the experimental evidence. At low temperature, the current drift disappears for all values of gate voltage. One could attempt to salvage this model by reducing the thickness of the $InPO_4$ layer so as to minimize the voltage drop across it. However, this would at the same time eliminate the tunneling barrier and eliminate the log t dependence of I_d. Alternatively, one could assume a lower resistivity of the $InPO_4$ layer so that the voltage drop across it would be less, but this would again eliminate the tunneling behavior needed to get the proper time dependence.

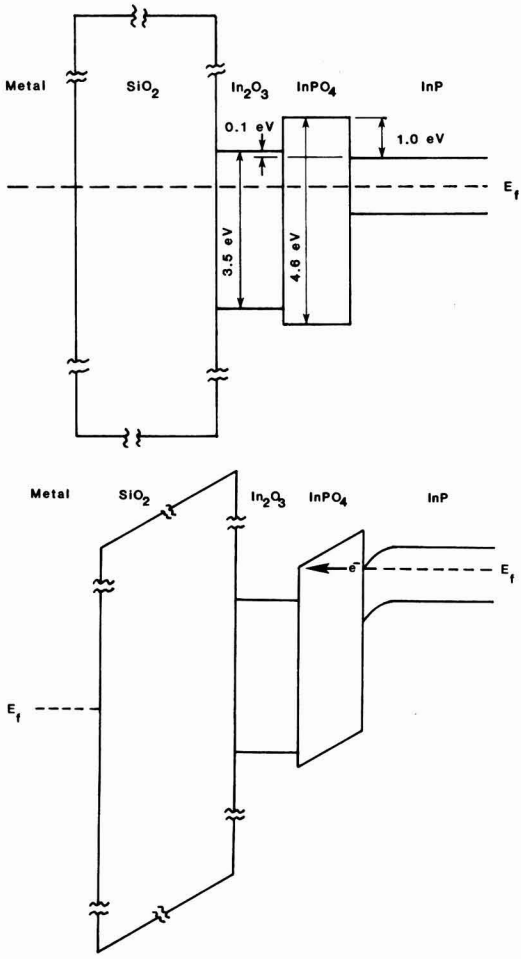


Fig. 3. (a, top) Energy band diagram for the native oxide on InP as proposed by Goodnick *et al.* (9) with gate voltage equal to zero. (b, bottom) Energy band diagram for the native oxides on InP with a positive gate voltage.

Okamura and Kobayashi (10) have proposed that the current drift in the accumulation-type device can be explained by thermally assisted tunneling from the conduction band of the InP into a pair of electron trap levels in the insulator. The energy band diagram relevant to their scheme is shown in Fig. 4. They base their calculation on a model originally proposed by Koelmans and DeGraaff

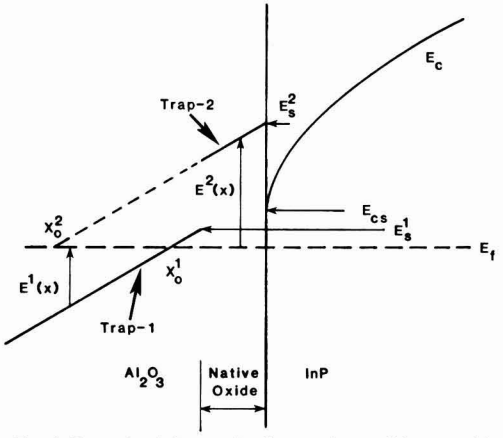


Fig. 4. Energy band diagram for the tunneling model proposed by Okamura and Kobayashi (10).

(15). This model begins by assuming that the charge flow into the oxide trap can be represented by a Shockley-Read (16) type of recombination rate equation, *viz.*

$$\frac{dn_{tr}}{dt} = S(x)\bar{v}[n_s(N_{tr} - n_{tr}) - n_1 n_{tr}] \quad [1]$$

where n_s is the electron concentration at the interface, n_{tr} is the density of filled traps, $\bar{v}$ is the average thermal velocity of the electrons, and N_{tr} is the total trap density. The quantity n_1, is given by the equation

$$n_1 = N_c e^{-(E_{cs} - E(x))/kT} \quad [2]$$

where N_c is the effective density of states for the conduction band, k is Boltzmann's constant, T is the absolute temperature, and E_{cs} and $E(x)$ are energies defined in Fig. 4. This particular value of n_1 must be used if the principle of detailed balance is to be maintained. That is, at thermal equilibrium

$$\frac{dn_{tr}}{dt} = 0 \quad [3]$$

which then implies that

$$n_1 = \frac{n_s(N_{tr} - n_{tr})}{n_{tr}} \quad [4]$$

Since

$$n_s = N_c e^{(E_{cs})/kT} \quad [5]$$

and

$$\frac{N_{tr} - n_{tr}}{n_{tr}} = e^{E(x)/kT} \quad [6]$$

Analogous to the equation for the ratio of ionized donors to nonionized donors for an impurity state in a semiconductor (17), one is forced to choose Eq. [2] to represent n_1 in order to satisfy the detailed balance requirement. The tunneling current is modeled by assuming that the charge flow into the oxide traps can be accounted for by a capture cross section that is an exponential function of distance into the oxide, *i.e.*

$$S(x) = S_0 e^{-ax} \quad [7]$$

where $1/a$ represents a tunneling length. In this picture, the probability that an electron at the surface will tunnel into an oxide trap is represented by the product of the electron density at the surface, the thermal velocity, the number of empty traps at distance x into the oxide, and the distance-dependent capture cross section. Koelmans and DeGraaff solve this equation to obtain an equation for the total trapped charge density, ($N_e(t)$, as a function of time (t), which is of the form

$$N_e(t) = \frac{N_{tr}}{a} \ln (t/t_0) \quad [8]$$

where t_0 is a constant. The original model, as formulated by Koelmans and DeGraaff, gives no temperature dependence to the tunneling current.

The modification of this model proposed by Okamura and Kobayashi includes a trap level in the oxide that is placed above the conduction band of the InP by an energy ($E_s^{(2)} - E_{cs}$). They reasoned that only the more energetic conduction band electrons would be able to be captured by these traps and that the capture rate would be reduced by a factor $e^{-(E_s^{(2)} - E_{cs})/kT}$. If the Shockley-Read equation is solved using their capture cross section, then the charge trapped by this level is given by

$$N_e = \frac{N_{tr}^{(2)}}{a^{(2)}} e^{-E_s^{(2)}/kT} \ln (t/t_0) \quad [9]$$

However, their derivation neglects the constraint that detailed balance imposes on the formulation of the Shockley-Read rate equation. If the rate equation must satisfy the requirement that

$$\frac{dn_{tr}^{(2)}}{dt} = 0 \quad [10]$$

at thermal equilibrium, then the term $n_1^{(2)}$ in the emission rate expression must be changed to

$$n_1^{(2)} = N_c e^{-(E_s^{(2)} - E_{cs})/kT} e^{-(E_{cs} - E(x))/kT}$$

$$= N_c e^{-(E_s^{(2)} - E(x))/kT} \quad [11]$$

This is mathematically equivalent to assuming a smaller capture cross section for the trap. When the rate equation is solved with this reformulation, there is again no temperature dependence of the trapped charge density. This is consistent with the paper of Koelmans and DeGraaff (15), since they formulated their model assuming that the trap level was placed at an arbitrary position in the forbidden energy gap and obtain the generalized result that the trapping of electrons in the oxide is not temperature-dependent. The question of whether or not one is justified in neglecting the detailed balance requirement will be addressed later in the paper.

Yamaguchi *et al.* (11) have calculated the tunneling current into the oxide using a model similar to the original Koelmans and DeGraaff model. Although they employ a different calculation scheme, their model, like the Koelmans and DeGraaff model, contains no element for predicting the experimentally observed temperature dependence of the drift current.

Given the problems that have been encountered in devising a model that simultaneously gives the correct time and temperature of the drift current in the accumulation-type transistor when the charge trapping mechanism is placed in the insulator, it is interesting to consider an alternate approach that places the charge trapping mechanism in the semiconductor. How do we know that the charge is being trapped in the insulator? The answer is that we do not. The extant published data do not rule out the possibility that the charge trapping may occur in the semiconductor. The next point to consider is that the accumulation-type device has as its basis an electric-field-induced layer of electrons on the surface of an InP SI crystal. The InP substrate material has a background concentration of unintentionally introduced hydrogenic donors that are located 7-10 meV below the conduction band minimum (E_c) (18) and have a density that is of the order of 2×10^{15} cm^{-3}. In the near-surface region, phosphorus vacancies may also exist. These are thought to give rise to an energy level 0.1 eV below E_c (19). In these calculations, E_d was placed 0.1 eV below E_c, although the results were not particularly sensitive to the value used for this parameter. The origin of these native donors is, at the present time, unknown. During the growth of the crystal, iron is added to the melt to produce deep compensating acceptors, which are located approximately 0.68 eV above the valence band maximum (E_v). As long as the deep acceptor density is greater than the background concentration of native donors, the material will be semi-insulating. At the present time, commercially available SI InP with clearly specified upper limits to the amount of iron that may be present is not sold. Consider now Fig. 5, which illustrates the energy band diagram of an SI InP substrate biased so that the surface is accumulated. If the material is fully compensated and the bands are flat, then, at thermal equilibrium, nearly all the donors ($N_{di} \simeq N_d$) will be ionized, but only a fraction ($N_{ai} \simeq N_d$) of the acceptors will be ionized. The ionized donor density will be given by

$$N_{di} = \frac{N_d}{1 + g_d e^{(E_F - E_d)/kT}} \quad [12]$$

the ionized acceptor density will be given by

$$N_{ai} = \frac{N_a}{1 + 1/g_a e^{(E_a - E_F)/kT}} \quad [13]$$

the electron density will be given by

$$n = N_c e^{-(E_c - E_F)/kT} \quad [14]$$

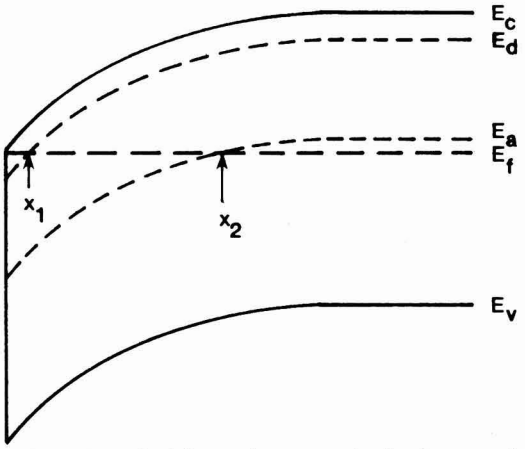


Fig. 5. Energy band diagram for an accumulated surface on semi-insulating InP.

and the hole density will be given by

$$p = N_v e^{-(E_F - E_v)/kT} \quad [15]$$

In these equations, $g_{d,a}$ represents the degeneracy of states for donors and acceptors respectively, E_F represents the position of the Fermi level with respect to E_v in the neutral bulk material, $E_{d,a}$ represents the energy of the donor and acceptor levels, respectively, as measured with respect to E_v, N_c represents the effective density of states at $E = E_c$ for electrons, and N_v represents the effective density of states at $E = E_v$ for the holes. The position of the Fermi level can be readily calculated by numerically solving the equation

$$\rho = -n + p + N_{di} - N_{ai} = 0 \quad [16]$$

for E_F and using Eq. [12], [13], [14], and [15] to solve for the desired quantities. If N_a is greater than several times N_d, and E_d is greater than E_v by several kT, then, to a good approximation

$$E_F = E_A - \frac{kT}{q} \ln \frac{2(N_a - N_d)}{N_d} \quad [17]$$

When a positive voltage is applied to the gate electrode of a MOS device on SI InP, the energy bands will bend downward, as shown in Fig. 5. Notice that acceptor states near the surface that were formerly above the Fermi level are now pushed downward by electric field. As this happens, electrons will fill the empty acceptor states, causing them to be completely ionized in the near-surface region. If the gate voltage is held constant, then the electric field, which now terminates on the additionally ionized acceptors, will clearly cause a reduction in the mobile channel charge. This process would lead to a reduction of the channel current of an FET over time and could easily be mistaken for interfacial charging. The remainder of this paper presents numerical calculations of the time dependence of this drift effect under various conditions.

Theory

The first step in the formulation of this model is the assumption that n^+ ohmic contacts are present on the surface of the semiconductor and that the gate electrode partially overlaps these contacts. This is the typical state of affairs for the accumulation-type MISFET. This assumption is essential from a physical standpoint, because the n^+ contact provides for easy transfer of electrons in and out of conduction band states and is essential for the formulation of the model because it permits the electron density to be described by an equilibrium Fermi level. The generation recombination processes were assumed to be characterized by the Shockley-Read rate equations (16)

$$\frac{dN_{di}(x)}{dt} = C_d[-N_{di}(x) n_b e^{q\psi/kT} + \frac{N_c}{2} e^{(E_d - E_c)/kT}(N_d - N_{di}(x))] \quad [18]$$

and

$$\frac{dN_{ai}(x)}{dt} = C_a[(N_a - N_{ai}(x)) n_b e^{q\psi/kT} - \frac{N_c}{2} e^{(E_a - E_c)/kT} N_{ai}(x)] \quad [19]$$

where C_d and C_a represent capture coefficients given by $\bar{v}\sigma_d$ and $\bar{v}\sigma_a$, respectively, n_b represents the electron density in the bulk material, ψ is the static potential, and σ_d and σ_a represent the capture cross sections for the donors and acceptors, respectively. Both the donor and acceptor impurity states were assumed to be doubly degenerate. The boundary conditions were as follows: it is assumed that the fixed interfacial charge is equal to zero and that the work function difference between the metal and the semiconductor is equal to zero. A gate voltage $V_g = 0$ is applied for $t \leq 0$, and a fixed positive gate voltage is applied for $t \geq 0$. With these boundary conditions

$$N_{di}(x)|_{t=0} \cong N_d \text{ and } N_{ai}(x)|_{t=0} \cong N_d \quad [20]$$

The value of the surface potential at $t = 0^+$ was obtained by solving the equation

$$V_g = \psi_s + \frac{Q_s + Q_{ss}}{C_{ox}} = \psi_s + \frac{\epsilon_s E_s}{C_{ox}} + \frac{Q_{ss}}{C_{ox}} \quad [21]$$

where Q_s and E_s are, respectively, the total charge on the semiconductor and the surface electric field, Q_{ss} is the charge in surface states, and C_{ox} is the oxide capacitance per unit area. For the calculated results presented herein, it has been assumed that $Q_{ss} = 0$. The effect of a nonzero threshold voltage (V_{th}) can be obtained in this model by assuming a nonzero fixed value of Q_{ss}. The boundary condition V_g = constant would then be replaced with the boundary condition $V_g = Q_{ss}/C_{ox}$ = constant. At $t = 0^+$, the ionized donor and acceptor densities were assumed not to have changed from their values for $t \leq 0$. The equation for the surface electric field as shown below (20)

$$E = -\frac{d\psi}{dx} = \left(\frac{2kT}{\epsilon_s}\right)^{1/2} [n_b(e^{q\psi/kT} - 1) + N_d \ln\left[\frac{2 + e^{(-q\psi + E_c - E_d - E_F)/kT}}{2 + e^{(E_c - E_d - E_f)/kT}}\right] + N_a \ln\left[\frac{2 + e^{(E_f - E_a - E_v - q\psi)/kT}}{2 + e^{(E_f - E_a - E_v)/kT}}\right] + p_b(e^{-q\psi/kT} - 1)]^{1/2} \quad [22]$$

reduces to

$$E = -\frac{d\psi}{dx} \simeq \left(\frac{2kT\, n_b}{\epsilon_s}\right)^{1/2} e^{q\psi/2kT} \quad [23]$$

for $q\psi >> kT$; p_b, $n_b << N_a$, N_d, and $N_{di} \simeq N_{ai}$.

The charge density distribution at $t = 0^+$ can be obtained explicitly by simultaneously solving Eq. [21] and [23]. Similarly the charge density distribution at $t = \infty$ can be obtained by simultaneously solving Eq. [21] and [22]. A graphical solution of these equations is indicated in Fig. 6 and 7. The E_s *vs.* ψ_s curves at $t = 0^+$ and $t = \infty$ were calculated for specific donor and acceptor impurity densities. The intersection of these curves with a particular curve of constant V_g as formulated by Eq. [21] represents a particular solution. The area between the E_s *vs.* ψ_s curves at $t = 0^+$ and $t = \infty$ represents the field of possible solutions for the time-dependent problem. The decrease in the conducting channel carrier density can be obtained by noting the solution for ψ_s as indicated in Fig. 6 and 7. At $t = 0^+$, the total

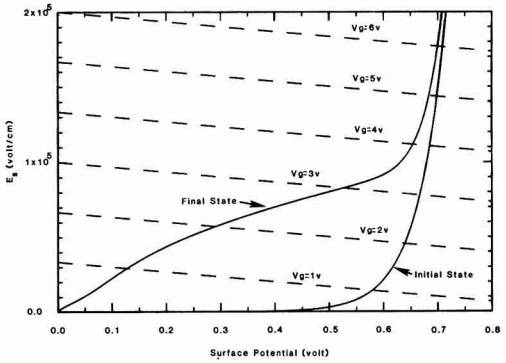


Fig. 6. Surface electric field vs. surface potential at $t = 0$ and $t = \infty$ for InP with $N_a = 5 \times 10$ cm^{-3}, $N_d = 1 \times 10^{16}$ cm^{-3}, and $T = 300$ K. The dashed lines represent the boundary condition, $V_g = \psi_s + \epsilon_s E_s / C_{ox}$ = constant, for various values of the gate voltage, V_g. As time increases from $t = 0$, the solution for the system will move along a line of constant gate voltage from the curve representing the initial state to the curve representing the final state.

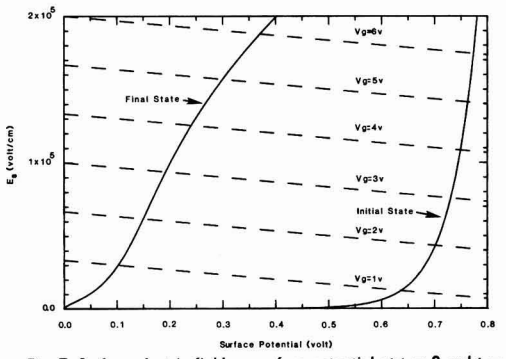


Fig. 7. Surface electric field vs. surface potential at $t = 0$ and $t = \infty$ for InP with $N_a = 5 \times 10$ (17) cm^{-3}, $N_d = 1 \times 10^{16}$, and $T = 300$ K.

charge due to conduction band electrons is given to a good approximation by

$$Q_n \simeq \epsilon_s E_s \simeq (2kT\epsilon_s n_b)^{1/2} e^{q\psi_s/2kT} \quad [24]$$

At $t = \infty$, the mobile electron charge can be obtained by numerically integrating the equation

$$Q_n = q\int_0^\infty n(x)dx \quad [25]$$

or its equivalent

$$Q_n = q\int_{\psi_s}^0 \frac{n_b e^{q\psi/kT} d\psi}{(d\psi/dx)} \quad [26]$$

where $d\psi/dx$ is given by Eq. [22] and ψ_s is obtained from Fig. 6 or 7. Although Fig. 6 seemingly indicates that the solutions differ very little for large V_g, this is not quite the case. The solutions for ψ_s do differ by a small amount, but since the mobile electron density depends exponentially on ψ_s, the difference in electron density can be large. The reduction in channel current for a range of acceptor concentrations is indicated in Fig. 8. It is instructive to consider calculated plots of the surface potential and electric field in Fig. 9 as a function of distance into the crystal. An unobvious point is that the electric field penetrates an extremely large distance ($w \simeq 2$ mm) into the material when the gate voltage is initially applied. This is because, initially, only a small fraction of the acceptors are ionized, and there are few charged centers on which the electric

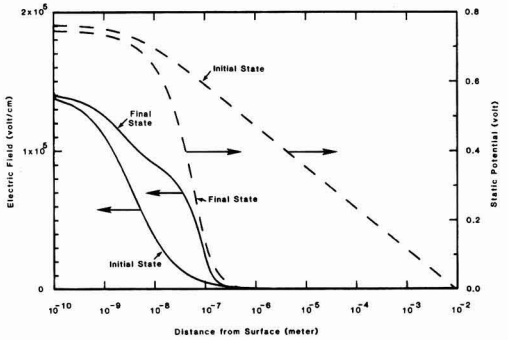


Fig. 8. Plots of electric field and surface potential vs. distance from the semiconductor surface at $t = 0$ and $t = \infty$. N_d is 1×10^{15} cm^{-3}, N_a is 5×10^{16} cm^{-3}, and T is 300 K.

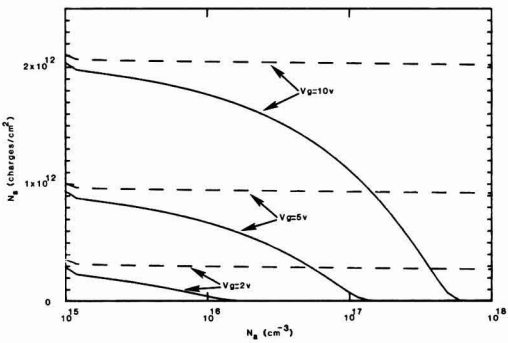


Fig. 9. Dependence of initial and first values of the charge in the conducting channel of an accumulation-type MISFET on the deep acceptor doping. The dashed lines represent initial values and the solid lines represent final values. The dielectric thickness is 100 nm, the relative dielectric constant is 4, N_d is 10^{15} cm^{-3}, and T is 300 K.

field lines can terminate. If a small-geometry FET were being considered, the entire surrounding area of the FET would be affected by the field. Only after the deep acceptor levels near the surface have filled with electrons does the accumulation layer width shrink to device dimensions. The calculations presented here, being one-dimensional in nature, do not take into account such two-dimensional geometry effects, since the InP crystal has been assumed to be semi-infinite.

Solution of the time dependence of this problem begins by evaluating Eq. [22] at $\psi = \psi_s$, inserting this into Eq. [21], and solving the result iteratively using Newton's method to obtain ψ_s. The variation of ψ with position at $t = 0^+$ was obtained by integrating Eq. [23]

$$\int_0^x dx = -\left(\frac{\epsilon_s}{2kTn_b}\right)^{1/2} \int_{\psi_s}^{\psi(x)} e^{-q\psi kT} d\psi \quad [27]$$

which yields

$$x = \left(\frac{2\epsilon_s kT}{n_b q^2}\right)^{1/2} (e^{-q\psi(x)/2kT} - e^{-q\psi_s/2kT}) \quad [28]$$

which can be solved for $\psi(x)$ to give

$$\psi(x) = -\frac{2kT}{q} \ln\left[e^{-q\psi_s/2kT} + \left(\frac{n_b q^2}{2\epsilon_s kT}\right) x\right] \quad [29]$$

The carrier density at $t = 0^+$ is then obtained by inserting Eq. [29] into

$$n(x) = n_b e^{q\psi(x)/kT} \quad [30]$$

The above equations were used to solve for the values of $\psi(x)$ and $n(x)$ on an array of points x_i with a variable spac-

ing selected with the algorithm $x_0 = 0$, $x_1 = 10^{-10}m$, $\Delta x_1 = 10^{-10}m$, $x_{i+1} = x_i + \Delta x$; $\Delta x_{i+1} = \Delta x$; if $n(x_{i+1}) \geq 1.1\ n(x_i)$ and $\Delta x_{i+1} = 1.1\ \Delta x$; if $n(x_{i+1}) \leq 1.1\ n(x)$. The variable spacing is required in order to have closely spaced points near the surface, where the carrier density drops rapidly, and widely spaced points in the interior, where the carrier density drops slowly.

Given initial values for $n(x)$, $N_{dl}(x)$, and $N_{al}(x)$, the time development of the trapped charge was approximated by using Eq. [18] and [19] to obtain

$$N_{dl}(x, t + \delta t) \simeq N_{dl}(x, t) + \frac{dN_{dl}(x, t)}{dt}\delta t \qquad [31]$$

and

$$N_{al}(x, t + \delta t) \simeq N_{al}(x, t) + \frac{dN_{al}(x, t)}{dt}\delta t \qquad [32]$$

With these new values of ionized impurity density, Poisson's equation

$$\frac{d^2\psi}{dx^2} = -\rho/\epsilon_s \qquad [33]$$

can be solved numerically using a fourth-order Runge-Kutta method (21), given that the charge density is

$$\rho = q(-n + N_{dl}(x, t + \delta t) - N_{al}(x, t + \delta t)) \qquad [34]$$

where

$$n = n_B e^{q\psi(x)/kT} \qquad [35]$$

The second-order differential equation can be reduced to the pair of coupled first-order equations given by

$$\frac{dE}{dx} = \rho/\epsilon_s \qquad [36]$$

and

$$\frac{d\psi}{dx} = -E \qquad [37]$$

In the solution of Eq. [32] for a new value of time, say $t = t + \delta t$, the first trial value of $\psi_s(t + \delta t)$ was set to $\psi_s(t)$. This value of ψ_s was used in Eq. [20] to solve for the trial value of $E_s(t + \delta t)$. These starting values of ψ_s and E_s were used in the Runge-Kutta procedure to solve for $\psi(x, t + \delta t)$ and $E(x, t + \delta t)$ from the surface inwards. If $\psi(x, t + \delta t)$ and $E(x, t + \delta t)$ reached zero simultaneously, then ψ_s and E_s represent a solution. If $\psi(x, t + \delta t)$ reached zero before $E(x, t + \delta t)$, then ψ_s was too small, and if $E(x, t + \delta t)$ reached zero before $\psi(x, t + \delta t)$ then ψ_s was too large. A new value of ψ_s was chosen that was known to lie between values of ψ_s that had been calculated to be either too large or too small, and the process was repeated until a solution was obtained.

Calculated results for the charge in conduction band states (N_s) as a function of time are shown in Fig. 10. The charge is nearly constant for very short times and then exhibits a decay that is nearly linear in log t. The time dependence of the calculated results is very similar to the data presented by Yamaguchi, *et al.* (8) and by Lile *et al.* (7). However, the temperature dependence is not as strong as observed in the measurements by Taylor *et al.* The temperature dependence in the model just described is due to the reduction in the Debye length

$$L_D = \left[\frac{2kT\epsilon_s}{q^2 n_B}\right]^{1/2} \qquad [38]$$

as the temperature is lowered. At low temperature, the electrons crowd closer together at the surface, and the electron density in the far-surface region is reduced. This has the effect of reducing the magnitude of the terms due to electron capture in Eq. [17] and [18]. In order for a model based on trapping by bulk impurities to give the temperature dependence observed experimentally, it is

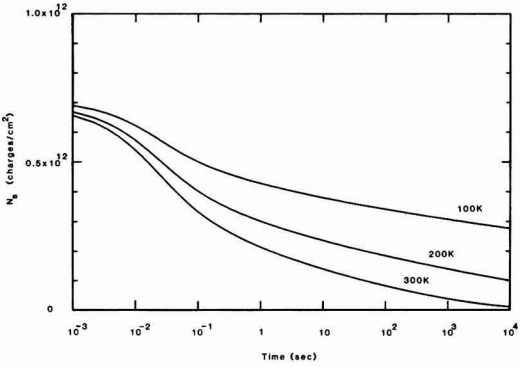


Fig. 10. Time dependence of the channel current for an accumulation-type MISFET assuming a Shockley-Read type of rate equation. V_g is 4V, the dielectric thickness is 100 nm, the relative dielectric constant is 4, σ_n (donor states) is 1.25×10^{-26} cm^2, and σ_p (acceptor states) is 1.25×10^{-26} cm^2.

necessary to introduce an energy barrier for electron capture. Clearly, a model based on Fig. 5 cannot give the required temperature dependence. In this simplest formulation, the capture rate of electrons is given, for example, by

$$R_e = \bar{v}\sigma n N_{an} \qquad [39]$$

which is mathematically equivalent to a statement that all that is required for an electron and a neutral acceptor to recombine is that they be in sufficiently close proximity to each other.

A model for nonradiative transitions in a crystal, which can perhaps explain the observed behavior on SI InP, was first proposed by Huang and Rhys (22) and expanded on by Kubo and Toyozawa (23) and by Rickayzen (24). In this model, it is assumed that the capture of an electron by a deep level impurity is accompanied by a local relaxation of the crystal lattice. In Fig. 11, the upper curve represents the total potential energy of the lattice plus free electron as a function of a generalized lattice coordinate Q. The curve represents schematically a hyper surface in 4-space. The lower curve represents the total potential energy of the lattice plus that of a trapped electron. The minima of the two curves are displaced due to

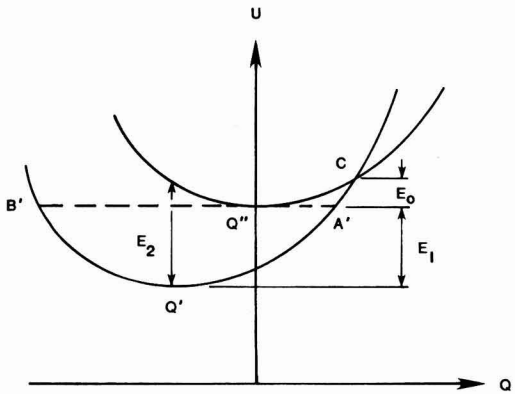


Fig. 11. Configuration coordinate diagram for a deep level trap. The energy (U) of the total system of the lattice plus one electron is plotted as a function of a generalized lattice coordinate (Q) and is plotted for the case in which the electron is free (upper curve) and for the case in which the electron is trapped (lower curve). E_0 represents the energy barrier for electron capture, and E_1 represents the energy for electron emission. The energy for optical emission from the minimum energy, Q', of the system to the conduction band when the electron is trapped is given by E_2.

the lattice relaxation that occurs when the electron is trapped. There are two processes by which an electron can transfer from the free to the trapped state. Classically, it can undergo a transition if the lattice vibrations are large enough to cause the energy to cross point C on the upper curve. Since the system could be in either state and have the same value of energy and lattice coordinate, there is finite probability that the electron will transfer from the free to the bound state. The activation energy for this process will be E_o. At low temperature, when the transition probability *via* this path becomes small, the relative probability of direct tunneling from state Q'' to A' and the subsequent emission of one or more phonons becomes larger. At $T = 0$, the optical transition energy would be E_o. The thermal activation energy for transition from the bound to free state is indicated by E_1. The applicability of this model for interpreting measurements on GaAs and GaSb has been discussed by Henry and Lang (25).

Seemingly, an immediate consequence of proposing this model for the electron trap is that one is forced to abandon the concept that the principle of detailed balance will determine the relationship between the capture and emission rates at steady state with no electric field applied. I hesitate to use the phrase thermal equilibrium to describe this condition because it seems as if this type of trap would not be in thermal equilibrium with the conduction band electrons. The relative magnitudes of the capture and emission coefficients would determine the density of occupied traps at steady state, and the ratio of filled traps to the total number of traps can be used to define a quasi-Fermi level for the electrons in the traps. That this result would be the case can be argued by imagining that the energy E_o of the trap is increased as E_1 is held constant. The capture rate would then decrease while the emission rate remained constant, and the density of occupied traps would decrease. Since the Fermi energy for the electrons in conduction band states would be independent of the details of the trap configuration, the only way out, apparently, is to describe the trap by a different quasi-Fermi level even in the steady-state condition. The rate equation describing the dynamic behavior of this trap then becomes

$$\frac{dN_{at}(x)}{dt} = C_a e^{-E_o/kT}(N_a - N_{at}(x))n_b e^{q\psi/kT} - e_a N_c e^{-E_1/kT} N_{at}(x) \qquad [40]$$

where the functional form of the emission rate as proposed by Kubo (26) has been employed.

The calculation of the time dependence of the channel current for the accumulation MISFET was repeated using Eq. [35] for the dynamics of the electron capture by the deep acceptors and Eq. [17] for the capture dynamics of the shallow donors. For comparison, the data of Lile *et al.* (7) are presented, with the results as calculated above, in Fig. 12. The essential features of the data seem to be adequately represented by this model.

The 300 K current drift behavior of the accumulation MISFET was calculated, using the above model, for a series of different deep acceptor concentrations, as shown in Fig. 13. As can be observed from this figure, the maximum permissible acceptor concentration for current drift that does not exceed 5% of the initial current value is about 2×10^{15} cm^{-3}.

Conclusion

The crucial question, which can only be answered by further experimental work, concerns the amount of time required for the deep acceptor levels to come to equilibrium after the application of a gate pulse. If the process occurs in less than a nanosecond, then the filling of deep levels by electrons is clearly not causing the drift in channel current that has been observed. On the other hand, if the process takes several days (not very plausible), it is also not of much technological interest. Only if the capture cross sections are such as to make the effect observable over a time interval from about 10^{-8} to 10^{4}s will the effect be important to circuit designers. In the present calculations, the capture cross section has been treated as a curve fitting parameter — no independent measurements of capture cross sections for these deep levels are available. Clearly, it is important to obtain such data. The values of the impurity capture cross sections used in these calculations are considerably smaller than those quoted by Henry and Lang (25) for GaAs and GaSb. Until we have such data for InP, it will be difficult to determine whether or not the values used for the present calculations are realistic.

The alert reader will have noted that early in the paper I made the point that the calculations of Okamura and Kobayashi give the correct temperature dependence of the current drift only if they neglect the principle of detailed balance in their formulation of the rate equation to describe the capture and emission of electrons from traps in the oxide. Then, at a later stage, I have invoked essentially the same mathematical formalism to describe the capture of electrons by deep levels in the semiconductor through a multiphonon emission process. How do we know where the charge trapping is occurring? Is it in the insulator or in the semiconductor? Given the available data, the possibility of drift due to traps in the oxide cannot be eliminated; however, it can be argued that at least some of the observed drift is due to traps in the semiconductor. At very low temperatures (77 K), we see no drift on any time scale. If the semiconductor traps were charg-

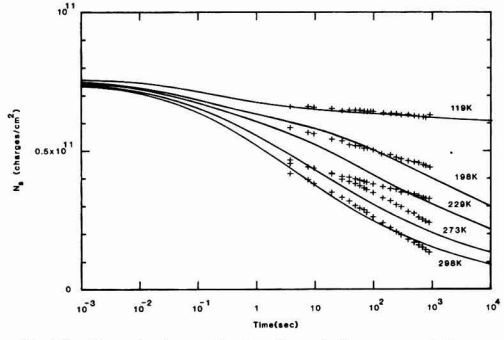


Fig. 12. Charge in the conducting channel of an accumulation-type MISFET as a function of time, assuming that electron capture by the deep acceptor takes place *via* a multiphonon emission process. The crosses represent data taken by Lile *et al.* (7). N_d is 1.1×10^{17} cm^{-3}, σ_n (donor) is 1.25×10^{-26} cm^2, σ_p (acceptor) is 1.25×10^{-30} cm^2, and $\mu_{fe} = 1230$ cm^2 V^{-1}s^{-1}.

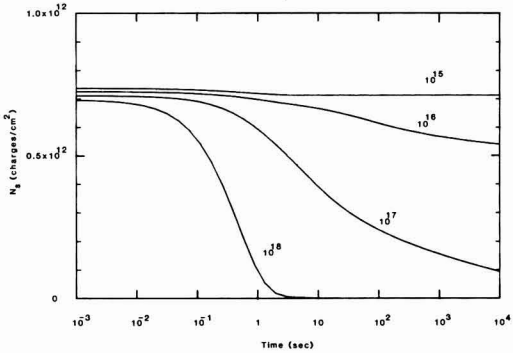


Fig. 13. Charge in the conducting channel of an accumulation-type MISFET as a function of time for deep acceptor concentrations between 10^{15} cm^{-3} and 10^{18} cm^{-3}, assuming that the electron capture takes place *via* a multiphonon emission process. N_d is 10^{15} cm^{-3}, and T is 300 K.

ing too rapidly to be observed at 300 K, we should at least see some evidence of their existence as the sample is cooled. Instead, we see nothing — no drift. The calculations presented in this paper have shown that, for deep acceptor densities in the range of 10^{16} cm^{-3} (a lower limit for the current materials technology), the effects of deep level charging are easily observable. Therefore, at least some of the charging effects that are seen from 77 K upward must be due to charging of states in the semiconductor.

In the present calculations, only the effects of uniform impurity densities have been considered. If greater densities of deep levels are caused near the interface due to processing-induced damage, then even stronger effects than those predicted from estimates of the bulk iron density would result. Such results would also be observed if the processing were to induce the pile-up of iron near the surface.

Obviously, there is a need for those people working on InP devices to begin to evaluate carefully the acceptor and donor densities in semi-insulating starting material before trying to draw conclusions on the efficacy of various surface preparation and insulator growth procedures in producing improved InP accumulation-type transistors. Such measurements are, at the moment, time consuming and tedious, and vendors of InP cannot be relied upon to provide such information. However, there seems to be no alternative if we are to make further progress in developing this device.

Acknowledgments

I wish to express my gratitude for financial support for this work from the Naval Research Laboratory under grant no. N00014-82-K-2032. I also wish to thank H. H. Wieder for several useful suggestions during this effort.

Manuscript submitted May 13, 1985; revised manuscript received Aug. 20, 1985. This was Paper 167 presented at the Las Vegas, Nevada, Meeting of the Society, Oct. 13-18, 1985.

REFERENCES

1. L. G. Meiners, *J. Vac. Sci. Technol.*, **15,** 1402 (1978).
2. G. Weimann, *Thin Solid Films*, **56,** 173 (1979).
3. L. G. Meiners, *J. Vac. Sci. Technol.*, **19,** 373 (1981).
4. D. L. Lile and D. A. Collins, *Thin Solid Films*, **56,** 225 (1979).
5. K. P. Pande and D. Gubierrez, *Appl. Phys. Lett.*, **46,** 416 (1985).
6. L. G. Meiners, D. L. Lile, and D. A. Collins, *Electron. Lett.*, **15,** 578 (1979).
7. D. L. Lile, M. Taylor, and L. Meiners, *Jpn. J. Appl. Phys.*, **22,** 389 (1982).
8. D. L. Lile and M. J. Taylor, *J. Appl. Phys.*, **54,** 260 (1983).
9. S. M. Goodnick, T. Hwang, and C. W. Wilmsen, *Appl. Phys. Lett.*, **44,** 453 (1984).
10. M. Okamura and T. Kobayashi, *Jpn. J. Appl. Phys.*, **19,** 2143 (1980).
11. E. Yamaguchi, M. Minakata, and Y. Furukawa, *ibid.*, **23,** L49 (1984).
12. H. H. Wieder, *IEEE Electron. Device Lett.*, **edl-4,** 108 (1983).
13. F. P. Heiman and G. Warfield, *Trans. Electron. Devices*, **ed-12,** 167 (1965).
14. J. F. Wager, K. Geib, C. W. Wilmsen, and L. L. Kazmerski, *J. Vac. Sci. Technol.*, **B1,** 778 (1983).
15. H. Koelmans and H. C. DeGraaff, *Solid-State Electron.*, **10,** 497 (1967).
16. W. Shockley and W. T. Read, *Phys. Rev.*, **87,** 835 (1952).
17. J. S. Blakemore, "Semiconductor Statistics," p. 118, Pergamon Press, New York (1962).
18. E. W. Williams, W. Elder, M. G. Astles, M. Webb, J. B. Mullin, B. Straughan, and P. J. Tufton, *This Journal*, **120,** 1741 (1973).
19. R. Schachter, D. J. Olego, J. A. Baumann, L. A. Bunz, P. M. Raccah, and W. E. Spicer, *Appl. Phys. Lett.*, **47,** 272 (1985).
20. R. Siewatz and M. Green, *J. Appl. Phys.*, **29,** 1034 (1958).
21. S. D. Conte and C. deBoor, "Elementary Numerical Analysis: An Algorithmic Approach," p. 365, McGraw Hill, New York (1972).
22. K. Huang and A. Rhys, *Proc. R. Soc., London*, **Ser. A, 204,** 406 (1951).
23. R. Kubo and Y. Toyozawa, *Prog. Theor. Phys.*, **13,** 160 (1955).
24. G. Rickayzen, *Proc. R. Soc., London*, **Ser. A, 204,** 480 (1957).
25. C. V. Henry and D. V. Lang, *Phys. Rev. B*, **15,** 989 (1977).
26. R. Kubo, *Phys. Rev.*, **86,** 929 (1952).

Selective Growth of Polysilicon

Y. Furumura, F. Mieno, T. Nishizawa, and M. Maeda

IC Development Department, Fujitsu, Limited, 1015 Kamikodanaka, Nakahara-ku, Kawasaki 211, Japan

ABSTRACT

A chemical vapor deposition (CVD) technique for selective growth of polysilicon has been developed. This technique makes it possible to grow polysilicon only on the exposed silicon without a Si nucleus on the SiO_2 or Si_3N_4 mask. Perfect selectivity over the whole wafer surface was obtained in a $SiHCl_3$-H_2 system in the temperature range of 900°-1000°C under a pressure of 100 Pa at a significantly high line velocity. These conditions provide a perfectly selective silicon epitaxy technique, while addition of trichloroethylene as a gas that causes extreme deterioration of the crystallinity produced the selective polysilicon technique without a degradation of selectivity. A SEM observation showed that the grain size of the grown film was about 0.3 μm. SIMS analysis indicated that the concentration of carbon atoms incorporated in the film was on the order of 10^{20} cm^{-3}. X-ray rocking curve analysis derived a smaller lattice parameter of 5.425A, due to incorporated carbon atoms.

With the increase in integration of IC's, submicron and multi-layered wiring in VLSI and ULSI is now facing many serious problems related to planarization. For example, the sharp steps at contact holes sometimes break the thin aluminum wiring material. The simplest solution for this kind of problem would be to fill the contact holes with a conductive material. Selective silicon epitaxial growth (1) is one filling technique that has been well-known for a long time. Even if the contact holes are successfully filled with Si by using this technique, another problem associated with the combination of aluminum and silicon still remains (2). Substitute materials that can be grown selectively may include tungsten (3). It is, however, still difficult to grow tungsten selectively to a thickness of about 1 μm as required for the IC process. On the other hand, polysilicon is a good material to fill the contact holes, if it can be grown selectively. It seems, however, that no technique for selective growth of polysilicon has been reported so far.

A technique of selective polysilicon growth is reported herein. This technique has been developed on the basis of the selective epitaxy technique. A perfectly selective epitaxy, *i.e.*, no nucleation on mask, has been achieved at a line velocity figure as high as 400 cm/s under a low pressure of 100 Pa in the temperature range of 900°-1000°C with trichlorosilane ($SiHCl_3$) and H_2 gas. The perfectly se-

lective polysilicon growth has been performed merely by introduction of an additional gas that causes extreme deterioration of the crystallinity. As such a gas, nitrogen, oxygen, ammonia, trichloroethylene (C_2HCl_3), and methane (CH_4) were studied. Of these gases, the result with C_2HCl_3 is reported below. The results for the other gases will be reported in other articles.

Experimental

A cold-wall-type reactor was employed for the growth. A substrate wafer was placed on a SiC-coated carbon susceptor, which was heated inductively at 8 kHz in the temperature range of 900°-1000°C. The temperature was measured by a pyrometer within an estimated error of ±30°C. A pumping system, which was a combination of a rotary pump and a mechanical booster pump with different combined pumping speeds, was connected to the reactor, producing the required line velocity. The line velocity figure, defined here as a parameter characterizing a flow condition, was derived by simple calculation from reactor tube diameter and pumping speed, entirely ignoring influences of susceptor and wafer arrangement.

This line velocity figure was changed in the range of 200-400 cm/s by replacing the pump system. The pressure was measured by a Baratron pressure gauge (MKS-221A) and kept to 100 ± 15 Pa. $SiHCl_3$ bubbled with H_2 was employed as the Si source gas, a part of which was put into the reactor through a mass flow controller. The temperature of the $SiHCl_3$ bubbler container, which did not change appreciably, was not controlled by any special means. To maintain the bubbling rate of $SiHCl_3$ mostly at a rate of 3.0 g/min, a Tylan Source V controller was used. The above conditions yielded selective epitaxy, while the input of an additional gas that greatly causes deterioration of the epitaxial quality produced the selective polysilicon technique. Trichloroethylene (C_2HCl_3) was chosen as such a deteriorating gas and introduced into the reactor by being bubbled with H_2. The rate of introduction was controlled by regulating the bubbling gas H_2 with a mass flow controller. However, the absolute quantity of C_2HCl_3 introduced could not be determined easily, due to a lack of bubbling data of C_2HCl_3. So, characteristics associated with carbon atoms incorporated in the grown polysilicon were evaluated not by C_2HCl_3 quantity introduced, but by a carbon concentration determined by SIMS (secondary ion mass spectroscopy) measurement.

A (111) oriented 4 in. silicon wafer with a resistivity of 10 Ωcm served as a substrate. The polysilicon film grown was evaluated by using this substrate in various forms.

Selectivity was evaluated by using a substrate with 1000Å-thick thermal SiO_2 film on the half surface side and a substrate having windows with different sizes and shapes through 6000Å thermal SiO_2. A bare substrate served for SIMS and x-ray analysis. In order to obtain a good reproducibility of selective growth, these substrates were loaded after a rinse with diluted HF, and the prebaking procedure shown in Fig. 1 was adopted.

Thickness of the selectively grown polysilicon was measured by Talystep with the SiO_2 half surface as a reference level, on which there was no Si nucleus for the benefit of selectivity. For low magnification observation of the surface features, an optical microscope was used, while for detailed observation of a window filling, a SEM was used.

The determination of carbon concentration of a grown film was carried out by SIMS measurement, which was performed by an outside analysis company. X-ray rocking curves, measurement of which was also done by an outside analysis company, were analyzed to investigate the orientation of grains and lattice parameters of the films.

Results

The selective polysilicon technique described in this article is based on a technique of selective silicon epitaxy, which was established in advance. Therefore, data related to the selective epitaxy technique must be presented first. A representative view of selective epitaxy is shown

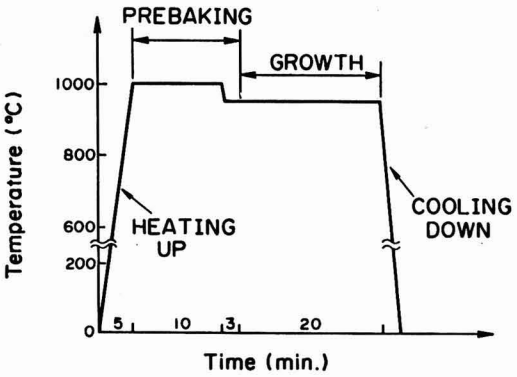


Fig. 1. Temperature program of selective polysilicon growth

in Fig. 2. No Si nuclei at all were found on the SiO_2 mask on the right half side, while a silicon epitaxial layer grew selectively to a thickness of about 1 μm on the silicon surface on the other half side.

A growth rate of 400 Å/min was obtained at 1000°C at a $SiHCl_3$ flow rate of 0.5 l/min and a H_2 flow rate of 6 l/min. Although the temperature was varied in the range of 900°-1000°C and the flow rates of $SiHCl_3$ and H_2 were varied in the range of 0.2-0.75 l/min and 5-10 l/min, respectively, perfect selectivity was maintained as long as the line velocity figure defined above was kept to 400 cm/s, while the growth rate and the pressure changed correspondingly. A perfect selectivity was also obtained with the use of phosphosilicate glass (PSG) or silicon nitride (Si_3Ni_4) as a mask material as well as SiO_2 with the same results.

Selective polysilicon growth was achieved merely by introducing C_2HCl_3 into the reactor. A representative view of selectively grown polysilicon is shown in Fig. 3. As can be seen from this figure, perfectly selective growth of polysilicon was achieved without a nucleus on a SiO_2 mask on the right half side. A low magnitude microphotograph and a SEM image of the grown polysilicon selectively filling the fine holes are shown in Fig. 4 and 5, respectively. A good selectivity and a good filling property can be seen from these figures. The depth profiles of carbon concentration about two representative samples are shown in Fig. 6. In the case of sample (a), C_2HCl_3 was introduced at a fixed rate, while in the case of (b), an increased amount of C_2HCl_3 was introduced in the initial stage of the growth for about 3 min, in order to enhance the transition to polycrystalline effectively. The peak in

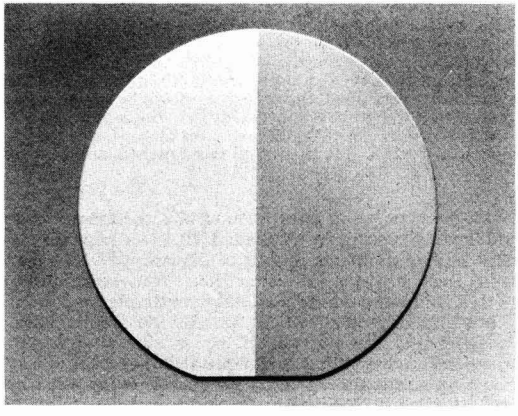


Fig. 2. Photograph of epitaxial silicon grown selectively at 1000°C and 100 Pa in a H_2-$SiHCl_3$ system to a thickness of about 1 μm. There is no nucleus on the right half side SiO_2 mask.

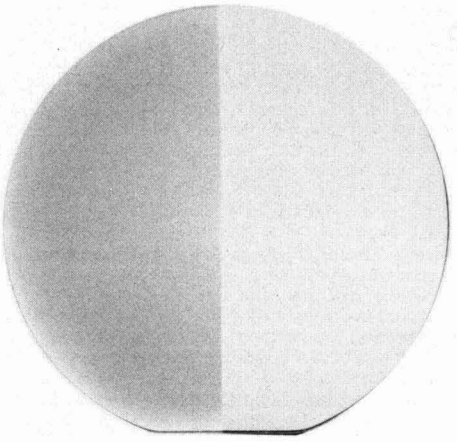


Fig. 3. Photograph of polysilicon grown selectively by introducing an additional deteriorating gas C_2HCl_3 under conditions that are otherwise the same as those of selective epitaxy.

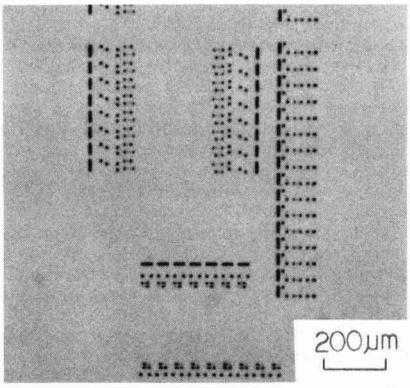


Fig. 4. Microphotograph showing polysilicon selectively filling the SiO_2 windows.

the profile (b) (at a depth of about 1.3 μm) corresponds to this increase. The difference in carbon concentration between (a) and (b) at a substrate depth of more than 2 μm is probably due to the measurement error factor of about two. It is seen from these profiles that the carbon concentrations were on the order of 10^{20} cm^{-3} at the flat portion, the value of which corresponds to the order of 1

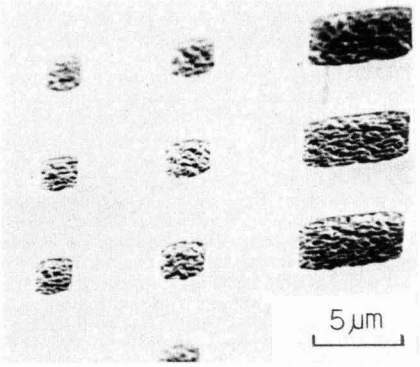


Fig. 5. SEM image showing polysilicon selectively filling the SiO_2 windows.

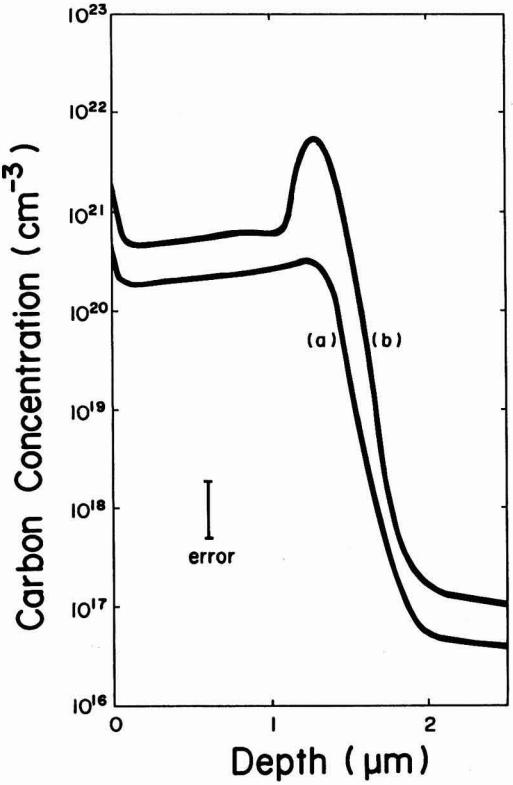


Fig. 6. Depth profiles of carbon concentration measured by SIMS. A deteriorating gas C_2HCl_3 was introduced into the reactor (a) at a constant rate and (b) at an increased rate only at the initial stage of growth.

a/o for Si. In order to know the influence of incorporated carbon atoms on a change in the lattice parameter and grain orientation of the grown polysilicon, the x-ray rocking curves were measured. For comparison, similar measurements were made on reference specimens, including (111) single silicon substrate, silicon powder as an ideal polysilicon, and a conventional polysilicon film that was deposited at 600°C to about 1 μm thickness on a silicon substrate. The peak in the curves obtained are shown as histograms in Fig. 7. The indexes of the diffraction appearing for sample (b) correspond well to those for the silicon powder, clearly indicating that the film obtained is polysilicon. Table I summarizes the main indexes of diffraction peaks and values of the lattice parameters derived from analysis of the rocking curves for samples (a) and (b) with the corresponding values for the reference silicon substrate. As can be seen from Table I, there are appreciable reductions in lattice parameters in selectively grown polysilicon films.

Discussion

The technique of selective polysilicon growth is based on a selective epitaxial technique. Therefore, before dis-

Table I. Lattice parameters derived from x-ray rocking curve analysis together with diffraction indexes and carbon concentrations

Sample	Carbon concentration (atoms/cm^3)	Lattice parameter (Å)	Diffraction indexes of main peaks
Substrate	5×10^{16}	5.430	(111)
(a)	2×10^{20}	5.426	(111), (222)
(b)	5×10^{20}	5.425	(111), (220), (311), (422), (440)

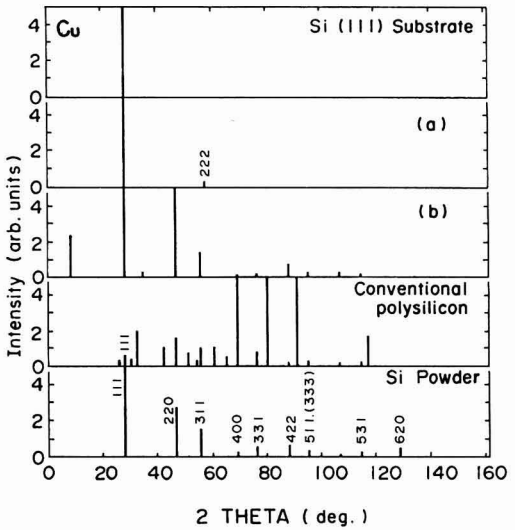


Fig. 7. Histogram representations of x-ray rocking curves

cussion of the selective polysilicon technique, the selective epitaxy technique should be discussed. Historically, there have been various methods of selective silicon epitaxy, including hydrogen reduction of chlorosilane $SiCl_4$ (4-8), $SiHCl_3$ (9, 10), or SiH_2Cl_2 (11, 12), the thermal decomposition of SiH_4 (13) at a higher temperature. A transport method using an I_2 (14) is also known to produce a good selectivity. In spite of its long history, the selective epitaxial technique still appears to be immature in practical use, probably because layers in sharp shapes suited for IC fabrication are difficult to grow due to growth rate anisotropy (15), and also because undesired nuclei are generated on the SiO_2 mask due to an area effect. At minimum, perfect selectivity must always be maintained for any applications to be possible.

Perfect selectivity was achieved in this experiment by the combination of $SiHCl_3$ use and a high line velocity. Therefore, it is necessary to refer to the correlation between the selectivity and this combination. According to research using infrared spectroscopy (16) and mass spectrometry (17-20) on molecular species contributing to the growth at atmospheric pressure in a chlorosilane-H_2 system, species $SiCl_4$, $SiHCl_3$, SiH_2Cl_2, $SiCl_2$, and HCl have been observed. The partial pressure of each specie changes, depending on the growth conditions. Aoyama, Inoue, and Suzuki (20) reported that, in a $SiCl_4$-H_2 system, the $SiCl_4$ specie contributes greatly to growth when the line velocity is high, as does $SiCl_2$ when the line velocity is low. The line velocity figure defined in this experiment is as high as 400 cm/s, which is a value higher by one order or more than those used in usual low pressure silicon epitaxy. A comparison with Ref. (20) may suggest that the $SiHCl_3$ specie, rather than $SiCl_2$, is dominant under this line velocity. This line velocity dependence of the dominant specie can be understood qualitatively from the changes of the gas temperature distribution. The equilibrium partial pressures of $SiHCl_3$ and $SiCl_2$ in the Si-H-Cl system, for example, are given in Ref. (21), indicating that under a fully equilibrium reaction at a temperature above 1000°C, $SiCl_2$ is expected to be a dominant specie in the reaction. But, under a high line velocity, the high temperature region may be restricted approximately in a stagnant layer. This restriction would decrease substantially the contribution of $SiCl_2$ specie. Therefore, aside from differences in temperature and pressure, $SiHCl_3$ may be considered as a dominant specie in this growth. The fact that a good selectivity has been obtained in this growth indicates that a higher $SiHCl_3$ partial pressure relative to $SiCl_2$ in the growth contributing region is a key point of good selectivity. In order to verify this physics view, the growth parameters affecting $SiHCl_3$ partial pressure were intentionally changed in the decreasing direction. It was found as a result that, with the changes shown below from (*i*) to (*iv*), selectivity was degraded, as seen from the way that polysilicon grew on the SiO_2 mask around the edge of a wafer placed downstream of the flow. (*i*) The growth temperature increased from 1000° to 1100°C. (*ii*) H_2 flow rate increased from 6 l/min to 50 l/min. (*iii*) The line velocity decreased from 400 cm/s to 200 cm/s. (*iv*) $SiHCl_3$ was replaced with SiH_2Cl_2. From these experimental results, it was verified that a higher $SiHCl_3$ partial pressure relative to SiH_2Cl_2 or $SiCl_2$ leads to a good selectivity. In order to understand the selectivity difference between $SiHCl_3$ and $SiCl_2$ species, the research on nucleation in the SiH_4-HCl-H_2 and SiH_2Cl_2-H_2-N_2 systems by Classen and Bloem (21-23) is very helpful.

According to this research, $SiCl_2$ plays an important role in nucleation at temperatures above 925°C. The presence of two unbonded electrons in the $SiCl_2$ specie, which can make bonds with electrons of surface atoms, produces an adsorption energy higher than that of the SiH_2Cl_2 specie. A higher adsorption energy will cause a longer residence time with an increased possibility of nucleation. Taking into account the reactive property of the $SiCl_2$ specie can help us understand that the selectivity degradation with the parameter changes listed above was caused by the relative increase in $SiCl_2$ partial pressure. A good selectivity might require a smaller partial pressure of the reactive specie $SiCl_2$. Since this work was not intended for quantitative study of the selectivity, further experiments related to selective epitaxy were not made. As the next step, experiments of selective polysilicon growth were made as follows on the basis of the established selective epitaxial technique.

Figures 3-5 show the features of polysilicon that were selectively grown by introducing C_2HCl_3 into the reactor. The grain size of about 0.3 μm estimated from Fig. 5 is not satisfactory. A finer size may be required in practical applications. However, no remarkable changes in grain size were observed when the growth temperature was varied in the range of 900°-1000°C. The amount of carbon introduced into the reactor is a most promising factor for producing a fine grain size, because a smaller amount of introduced C_2HCl_3 resulted in a larger grain size. As a matter of fact, introduction of a large amount of carbon, which was realized with CH_4 gas instead of C_2HCl_3, owing to its control facility, produced a grain size below 0.1 μm. The results will be reported in detail elsewhere.

Table I summarizes the main indexes of diffraction and lattice parameters obtained by analysis of x-ray rocking curves about the grown polysilicons. As can be seen from this table, sample (a) has indexes (111) and (222). The index (111) indicates that the orientation of the grown polysilicon is still strongly affected by the (111) substrate. The index (222), which would not appear for Si crystals under the extinction rule, was observed weakly. This fact indicates that carbon atoms replaced partly with silicon atoms in (111) planes defy the extinction rule. Sample (b), which has an increased carbon concentration in the beginning layer of the grown polysilicon, has many different diffraction indexes that correspond very well to those for silicon powder shown in Fig. 7, excluding the intensity. Therefore, it was verified that the grown film of sample (b) was polysilicon. The lattice parameter 5.425Å of sample (b) was smaller by 0.005Å than the value 5.430Å of the silicon substrate. This difference can be interpreted from the detected carbon concentration of 5×10^{20} cm^{-3}. Assuming a qualitative holding of Vegard's law, the carbon concentration 5×10^{20} cm^{-3} gives a reduction in lattice parameter of about 0.01Å, which is not much different from the measured reduction of 0.005Å. For a more precise relationship between carbon concentration and lattice parameter change in the covalent Si – C system, detailed experiments will be required.

Conclusion

It was found that silicon epitaxial growth with a perfect selectivity on the whole wafer surface was made possible by a low pressure CVD using $SiHCl_3$ under a high line velocity figure of 400 cm/s and that introduction of C_2HCl_3 achieved a perfectly selective growth of polysilicon. The polysilicon grown selectively has a smaller lattice parameter value of 5.425Å and x-ray main diffraction peaks of (111), (220), (311), (422), and (440). It was also found that this technique could fill polysilicon selectively into the SiO_2 windows.

Acknowledgment

We express our sincere thanks to H. Ino for his unstinting encouragement and advice.

Manuscript submitted June 17, 1985; revised manuscript received Nov. 4, 1985. This was Paper 277 presented at the Toronto, Ontario, Canada, Meeting of the Society, May 12-17, 1985.

Fujitsu, Limited, assisted in meeting the publication costs of this article.

REFERENCES

1. B. D. Joyce and J. A. Baldrey, *Nature*, **195,** 485 (1962).
2. M. Mori, *IEEE Trans. Electron. Devices*, **ed-30,** 81 (1983).
3. N. E. Miller and I. Beinglass, *Solid State Technol.*, **25,** 85 (1982).
4. H. Ogawa, T. Nishinaga, M. Kasuga, and T. Arizumi, *Jpn. J. Appl. Phys.*, **10,** 1675 (1971).
5. P. Rai-Choudhury and K. K. Schroder, *This Journal.*, **120,** 664 (1973).
6. G. L. Schnable, W. J. Hillegas, Jr., and C. G. Thornton, *Electrochem. Technol.*, **4,** 485 (1966).
7. B. D. Joyce, N. P. Formigoni, C. C. Roe, and F. Schliesing, *ibid.*, **4,** 482 (1966).
8. W. J. Oldham and R. Holmstom, *This Journal*, **114,** 381 (1967).
9. K. E. Bean, *Thin Solid Films*, **83,** 173 (1981).
10. R. K. Smeltzer, *This Journal*, **122,** 1666 (1975).
11. K. Tanno, N. Endo, H. Kitajima, Y. Kurogi, and H. Tsuya, *Jpn. J. Appl. Phys.*, **21,** L564 (1982).
12. W. A. P. Claassen and J. Bloem, *J. Cryst. Growth*, **50,** 807 (1980).
13. P. Rai-Choudhury and K. K. Schroder, *This Journal*, **118,** 107 (1971).
14. P. D. Braun and W. Kosak, *J. Cryst. Growth*, **45,** 118 (1978).
15. R. J. Jaccodine, *This Journal*, **110,** 524 (1963).
16. J. Nishizawa and H. Nihira, *J. Cryst. Growth*, **45,** 82 (1978).
17. V. S. Ban and S. L. Gilbert, *This Journal*, **122,** 1382 (1975).
18. V. S. Ban, *ibid.*, **122,** 1389 (1975).
19. V. S. Ban and S. L. Gilbert, *J. Cryst. Growth*, **31,** 284 (1975).
20. T. Aoyama, Y. Inoue, and T. Suzuki, *This Journal*, **130,** 203 (1983).
21. W. A. P. Claassen and J. Bloem, *ibid.*, **127,** 1836 (1980).
22. W. A. P. Claassen and J. Bloem, *ibid.*, **128,** 1353 (1981).
23. W. A. P. Claassen and J. Bloem, *ibid.*, **127,** 194 (1980).

Deep Melting of Silicon Wafers

Lynn O. Wilson, G. K. Celler,* and L. E. Trimble

AT&T Bell Laboratories, Murray Hill, New Jersey 07974

ABSTRACT

A one-dimensional analytical solution is derived for melt propagation in silicon wafers uniformly heated with lamp radiation from one side and radiatively cooled from both sides. Only the case of deep melting is considered, beyond the power threshold required for elimination of all solid inclusions at the irradiated surface. The solutions for bulk silicon and for silicon with a buried oxide layer are in reasonable agreement with the experimental data. The results are relevant to formation of single crystalline silicon films on SiO_2 by crystallization from the melt.

Single crystalline silicon films on insulating substrates are attractive for electronic applications. In particular, Si films of 10-100 μm thickness on oxidized Si wafers are needed for dielectrically isolated high voltage integrated circuits. Such films can be formed by radiative melting of deposited polysilicon and controlled recrystallization (1, 2). In this paper, we solve analytically propagation of the melt front in a one-dimensional configuration. A two-dimensional numerical model of melting and recrystallization in Si-SiO_2 structures is described elsewhere (2).

Silicon irradiated with a stationary radiative heater from one side and radiatively cooled from all sides initially melts on the irradiated surface by breaking up into coexisting solid and liquid regions. The spacing is dependent upon the incident flux, thermal parameters, and the crystalline properties of the sample, all of which profoundly affect the transfer of energy and rate of melting (3-5). The coexisting regions occur when the power P from the lamp furnace is such that $P_1 < P < P_2$, where

$$P_1 = (1 + \epsilon_B/\epsilon_S)\sigma\, T_m^4 \qquad [1]$$

$$P_2 = (1 + \epsilon_B/\epsilon_L)\sigma\, T_m^4 \qquad [2]$$

Here σ is the Stefan-Boltzmann constant, T_m is the melting temperature of Si, and ϵ_S, ϵ_L, and ϵ_B are the emissivities of a fully solid top surface, a fully liquid top surface, and the bottom surface, respectively.

*Electrochemical Society Active Member.

When $P \geq P_2$, a fully molten surface can be supported. Power in excess of P_2 will be used to melt the silicon more deeply. This paper is concerned with the deep melting regime.

Formulation

Rough estimates, based on typical parameter values, indicate that heat transport within the wafer is predominantly due to conduction. To describe the temperature distribution $T(y, t)$, we use the thermal diffusion equation

$$\rho C \frac{\partial T}{\partial t} = \frac{\partial}{\partial y}\left(K \frac{\partial T}{\partial y}\right) \qquad [3]$$

Any flow of the molten silicon and consequent convective transport of heat is neglected, as are density differences between liquid and solid silicon. Radiative transport of heat across the oxide layer (if present) is negligible compared to the conductive transport of heat. Heat input will be modeled through coupling at the wafer surface of the power $P(t)$ from the lamps, rather than as a source term in the diffusion equation, since the skin depth is $\lesssim 1$ μm (6), small by comparison with typical melt depths.

The model is one-dimensional, so effects due to wafer edges or to nonuniformities in heat input, for example, are ignored. Any effects due to crystalline anisotropy are also not included.

In the above equation, ρ is an average density, C is the specific heat, and T is the temperature. The thermal con-

ductivity K is assumed to take on constant values K_S, K_L, and K_0 in the solid Si, liquid Si, and oxide, respectively. Distance y is measured from the wafer bottom, with $y = D$ denoting the wafer top.

At temperatures close to the melting temperature T_m of Si, the dominant mechanism for heat loss at the wafer surfaces is radiative cooling. Accordingly, we take as boundary conditions for the heat flux

$$K_L \frac{\partial T}{\partial y} = \epsilon_L[P(t) - \sigma T^4] \text{ at } y = D \text{ (top surface)} \quad [4]$$

$$K_S \frac{\partial T}{\partial y} = \epsilon_B \sigma T^4 \text{ at } y = 0 \text{ (bottom surface)} \quad [5]$$

The motion of the front $y_f(t)$ is governed by the Stefan equation

$$\rho L \frac{dy_f}{dt} = K_S \left.\frac{\partial T}{\partial y}\right|_{y_f^-} - K_L \left.\frac{\partial T}{\partial y}\right|_{y_f^+} \quad [6]$$

The fluxes are evaluated on both sides of the solid-liquid interface y_f, given by

$$T(y_f, t) = T_m \quad [7]$$

L denotes the latent heat of Si.

To complete the mathematical formulation, we assume that initially the front is at a position y_0

$$y_f(0) = y_0 \quad [8]$$

Typical physical parameter values are (7, 8)

$T_m = 1685$ K

$\sigma = 5.672 \times 10^{-12} \frac{\text{J}}{\text{s-cm}^2\text{ K}^4}$

$\epsilon_L = 0.58$, $\epsilon_S = 0.84$, $\epsilon_B = 0.62$

$K_S = 0.216$W/(cm K), $K_L = 0.64$W/(cm K), $K_0 = 0.02$W/(cm K)

$\rho = 2.41$ g/cm^3

$L = 1810$ J/g

$C = 1.04$ J/(g K)

$D = 500$-700 μm [9]

The emissivity ϵ_B is that for a rough solid Si surface (5). The emissivity ϵ_S, used to calculate the initial melting threshold P_1, but not needed in the deep melting model, is that for a rough solid Si surface near T_m, encapsulated with a SiO_2 layer (5). It is obtained by using a theory due to Yablonovitch (9). The emissivity ϵ_L of such a surface after melting decreases relatively little, since the roughness is preserved by the solid SiO_2 capping layer.

The density ρ is taken to be the average of the densities $\rho_S = 2.33$ g/cm^3 and $\rho_L = 2.49$ g/cm^3 for solid and liquid Si (8).

It is fruitful to write the governing equations [3]-[8] in a dimensionless form. A bar is placed on the dimensional quantities T, $K(=K_S, K_L, K_0)$, P, D, t, y_f, and y, so they can be distinguished from their dimensionless counterparts, to be used subsequently.

Let $\tilde{d} = 10$ μm, $\tau = 1$s, $\tilde{K} = 0.1$W/(cm K), and $\tilde{P} = \sigma T_m^4$ be a characteristic length, time, thermal conductivity, and power normalization, respectively. Experimentally, power is applied to the surface for a few seconds or tens of seconds and the typical melt front velocity is approximately 10 μm/s.

Define the Péclet number Pe, the Stefan number S, and the radiation number R by (10)

$$\text{Pe} = \frac{\rho C \tilde{d}^2}{\tilde{K}\tau} \approx 2.5 \times 10^{-5} \quad [10]$$

$$\text{S} = \frac{L}{CT_m} \approx 1.03 \quad [11]$$

$$R = \frac{\sigma \tilde{d} T_m^3}{\tilde{K}} \approx 2.7 \times 10^{-4} \quad [12]$$

Also, form other dimensionless quantities as follows

$$y = \bar{y}/\tilde{d},\ t = \bar{t}/\tau,\ D = \bar{D}/\tilde{d} \quad [13]$$

$$K = \bar{K}/\tilde{K} \quad [14]$$

$$P(t) = \bar{P}(\bar{t})/\tilde{P} \quad [15]$$

$$\bar{T} = T_m(1 + RT) \quad [16]$$

Then the dimensionless counterparts to [3]-[8] are

$$\text{Pe} \frac{\partial T}{\partial t} = \frac{\partial}{\partial y}\left(K \frac{\partial T}{\partial y}\right) \quad [17]$$

$$K_L \frac{\partial T}{\partial y} = \epsilon_L [P(t) - (1 + RT)^4] \text{ at } y = D \quad [18]$$

$$K_S \frac{\partial T}{\partial y} = \epsilon_B (1 + RT)^4 \text{ at } y = 0 \quad [19]$$

$$\frac{dy_f}{dt} = \frac{R}{\text{Pe S}}\left[K_S \left.\frac{\partial T}{\partial y}\right|_{y_f^-} - K_L \left.\frac{\partial T}{\partial y}\right|_{y_f^+}\right] \quad [20]$$

at the solid-liquid interface y_f where

$$T(y_f, t) = 0 \quad [21]$$

and

$$y_f(0) = y_0 \quad [22]$$

This system of two partial differential equations, plus the associated boundary conditions and initial condition, constitutes a one-dimensional Stefan problem for the unknown temperature distribution $T(y, t)$ and the position y_f of the melt or solidification front. It is nonlinear because of (*i*) the coupling between t and y_f, (*ii*) different material properties in solid Si, liquid Si, and SiO_2, and (*iii*) the fourth power dependence in the radiation boundary conditions.

Since the Péclet number Pe << 1, it is entirely reasonable to neglect the left-hand side of [17] and use

$$\frac{d}{dy}\left(K \frac{dT}{dy}\right) = 0 \quad [23]$$

This means that the time for the wafer to reach thermal equilibrium is small compared to the time scale (seconds) typical for decribing motion of the front.

This mathematical technique partially decouples the governing equations. An analogous technique was used earlier by Deal and Grove (11) in deriving a relationship for the thermal oxidation of Si.

Henceforth, all quantities in the text will be in dimensionless form; graphical results will be in dimensional form.

Lowest Order Solution: Silicon Wafer

Consider now a silicon wafer with no buried oxide layer. In this section, as a consequence of the fact that the temperature difference across the entire wafer thickness is only a few degrees, we neglect the nonlinear contribution to the radiation boundary conditions

$$(1 + RT)^4 \approx 1 \quad [24]$$

To justify this, suppose that the wafer surface is barely melted. Then $T(D) \approx 0$ and, by [23], $dT/dy = \epsilon_B/K_S$ throughout almost the entire wafer, so that $T(0) \approx -(\epsilon_B/K_S)D$. With $R = 2.7 \times 10^{-4}$, $D = \bar{D}/d = 70$, and $\epsilon_B/K_S = 0.29$, we find that $(1 + RT)^4 \approx 1$ at the wafer top and ≈ 1.02 at the wafer bottom, a 2% difference. We will reconsider and refine this assumption later, in the section on radiative loss due to wafer heating.

Equation [23], subject to the boundary conditions [18], [19], and [21], and the approximation [24] then has the solution

$$T(y) = (\epsilon_B/K_S)(y - y_f) \qquad 0 \leq y \leq y_f$$
$$= (\epsilon_L/K_L)[P(t) - 1](y - y_f) \qquad y_f \leq y \leq D \qquad [25]$$

Apply this result to the flux Eq. [20] governing the motion of the melt or solidification front to obtain

$$\frac{dy_f}{dt} = \frac{R}{\text{Pe S}}\{\epsilon_L[P(t) - 1] - \epsilon_B\} \qquad [26]$$

A natural way to normalize the lamp power $P(t)$ is with respect to the (dimensionless) threshold P_2 for deep melting

$$P(t) = P_2[1 + p(t)] \qquad [27]$$

$$P_2 = 1 + \epsilon_B/\epsilon_L \qquad [28]$$

so that melting (solidification) occurs when $p(t)$ is positive (negative). Equation [26] with initial condition [22] then has a solution

$$y_f(t) = y_0 - \beta \int_0^t p(t')dt' \qquad [29]$$

with

$$\beta = (\epsilon_L + \epsilon_B)\frac{R}{\text{Pe S}} \qquad [30]$$

Consider now a specific irradiation profile $p(t)$: starting with $t = 0$ when the deep melting threshold is reached, ramp the power up linearly with time, hold it constant for a while, and then ramp it down linearly with time until the lamps are off. Thus

$$p(t) = \frac{p_{max}t}{\Delta_1} \qquad 0 \leq t \leq \Delta_1$$
$$= p_{max} \qquad \Delta_1 \leq t \leq \Delta_1 + \Delta_2$$
$$= p_{max} - \frac{[t - (\Delta_1 + \Delta_2)](1 + p_{max})}{\Delta_3}$$
$$\Delta_1 + \Delta_2 \leq t \leq \Delta_1 + \Delta_2 + \Delta_3$$
$$= -1 \qquad \text{otherwise} \qquad [31]$$

With this irradiation profile, we find that

$$y_f(t) = y_0 - \frac{\beta p_{max}t^2}{2\Delta_1} \qquad 0 \leq t \leq \Delta_1$$
$$= y_0 - \frac{1}{2}\beta p_{max}\Delta_1 - \beta p_{max}(t - \Delta_1)\,\Delta_1 \leq t \leq \Delta_1 + \Delta_2$$
$$= y_0 - \frac{1}{2}\beta p_{max}\Delta_1 - \beta p_{max}\Delta_2 - \beta p_{max}[t - (\Delta_1 + \Delta_2)]$$
$$+ \frac{\beta(1 + p_{max})[t - (\Delta_1 + \Delta_2)]^2}{2\Delta_2}$$
$$\Delta_1 + \Delta_2 \leq t \leq \Delta_1 + \Delta_2 + \Delta_3 \qquad [32]$$

Consequently, the melt depth increases parabolically during the initial ramping up stage and linearly during the constant power stage, then decreases parabolically during the ramping down stage, as depicted in Fig. 1 for representative parameter values.

The maximum melt depth δ_m is achieved at

$$t_m = \Delta_1 + \Delta_2 + \frac{\Delta_3 p_{max}}{1 + p_{max}}, \text{ when } p(t_m) = 0 \qquad [33]$$

and is given by

$$\delta_m = D - y_f(t_m)$$
$$= D - y_0 - \beta p_{max}\left[\frac{1}{2}\Delta_1 + \Delta_2 + \frac{\Delta_3 p_{max}}{2(1 + p_{max})}\right] \qquad [34]$$

Experimentally, the maximum power used is typically a few percent larger than P_2, so $p_{max} << 1$. Consequently, the maximum melt depth varies linearly with the time Δ_2 at maximum incident power and approximately linearly with the excess power p_{max}.

Complete solidification is achieved at a time t_S, such that $y_f(t_S) = D$. Unless Δ_3 is extraordinarily short, this is given by

$$t_S = \Delta_1 + \Delta_2 + \frac{\Delta_3 p_{max}}{1 + p_{max}}\left\{1 + \left[1 + \frac{1 + p_{max}}{\Delta_3 p_{max}}\left(\Delta_1 + 2\Delta_2 + \frac{2(D - y_0)}{\beta p_{max}}\right)\right]^{1/2}\right\} \qquad [35]$$

Notice also, from [25], that the temperature gradient in the solid Si is constant, both in space and in time. That in

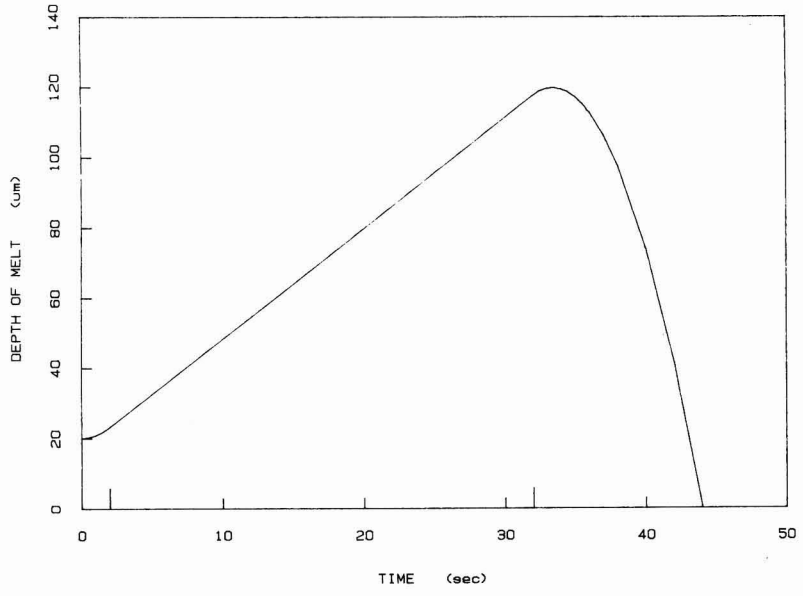


Fig. 1. Melt depth as a function of time, with y_0 = 20 μm, Δ_1 = 2s, Δ_2 = 30s, Δ_3 = 60s.

the liquid Si is uniform spatially, but varies with time. If $P(t)$ is reasonably close to the threshold P_2 for a fully molten surface, the temperature gradient in the solid Si exceeds that in the liquid by a factor of approximately $K_L/K_S \approx 3$. The temperature changes by ~1.2° over 100 μm of solid Si, ~0.4° over 100 μm of liquid Si.

Experimental Results

Bulk Si wafers of 100 mm diameter were used for determination of the depth of melt. Their front surface was sandblasted to produce a uniform matte finish and then a 2 μm layer of SiO_2 was deposited by low pressure CVD. Sandblasting was necessary in order to introduce a high density of extended defects at the irradiated surface. This eliminates faceted melting (3) and provides a well defined planar melt front. Capping of the surface was not necessary but it increased the surface emissivity and also made easier comparisons with results obtained for wafers with buried oxide layers. Such wafers require an oxide cap to prevent balling up of the molten Si film.

The melting experiments were carried out in a lamp furnace described in detail previously (12). A bank of tungsten halogen lamps provided uniform irradiation of the top side of each sample. Radiative cooling occurred from all sides. The melt threshold P_1 is easily detected with a pyrometer that monitors the temperature of the back side of the sample. For the bulk sandblasted Si wafers this threshold is at 49% of full input power to the lamps and corresponds to about 80 W/cm².

It was not possible to observe directly the depth of melt *vs.* time. Instead, a series of wafers was irradiated with the same power ramping profile but with a different value of the maximum power for each wafer. Each run started with 5 min at 47% of full power in order to preheat the furnace, and in particular the quartz window separating the samples from the lamps. This preheating cycle minimized thermal drifts of the sample, of particular importance in comparing results for different lengths of time at maximum power.

Melted and recrystallized wafers were cleaved at three places and briefly etched with a Schimmel defect solution. This delineated the heavily doped recrystallized region. For very deep melts some redistribution of silicon occurred so the depth of melt was measured with reference to the back surface.

In Fig. 2 the maximum depth of melt is plotted *vs.* the incident power. It is difficult to obtain absolute calibration of the incident power because of some uncertainty in the value of the emissivity. The three curves represent three locations on the wafers. One side of each wafer melted consistently more deeply than the opposite side, with the difference across the wafer being equivalent to about 2% change in flux. Below the second threshold P_2, which is located approximately at the knee of each curve, melting is only superficial. This is consistent with the co-

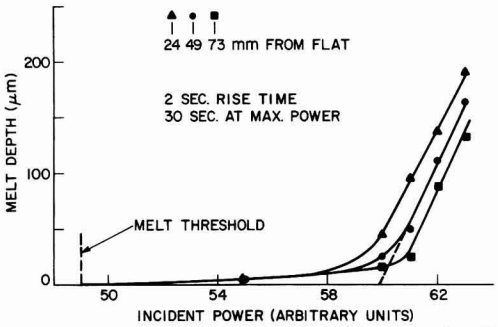


Fig. 2. Maximum melt depth *vs.* incident power for crystalline Si with a sandblasted surface covered by a 2 μm SiO_2 layer. Curves represent three locations on the wafers. The intersection of the dashed line with the power axis indicates the approximate value of P_2 for the middle curve. Melt threshold $P_1 \approx 80$ W/cm² and $P_2 \approx 97$ W/cm².

existence of microscopic solid and liquid regions for incident powers below P_2 (5).

Above P_2, which is approximately 97 W/cm², the melt depth is a linear function of the input power, in agreement with Eq. [34]. The slope of the experimental curves is, however, about 20% less than the calculated slope.

In Fig. 3, the depth of melt is plotted as a function of time Δ_2 at the maximum power. At a power setting of 60, there is almost no dependence of the melt depth on Δ_2, as expected from the steady-state model for $P < P_2$. At the setting of 62, there are three separate curves that effectively correspond to 61.5, 62, and 62.5 for the reason explained above. The dependence on time is sublinear for the two lower powers and linear for the highest power setting. The slope of the linear curve is again about 20% less than the value calculated from Eq. [34].

Increased Radiative Loss due to Wafer Heating

Experimentally, the maximum melt depth δ_m is a sublinear function of the constant irradiation time Δ_2. This indicates that the melt front slows down as it proceeds more deeply into the wafer. As the wafer heats up during the melting process, more power is lost from both surfaces due to the T^4 effect. This radiative effect is small here, since the wafer temperature is elevated only slightly. However, the maximum power input is typically only a few percent above the threshold P_2 for complete surface melting, so the driving force for advancement of the front is also small. Can the increased radiative loss account for the sublinearity of δ_m with Δ_2?

We return to the theory of the sections of formulation and lowest order solution and retain another term in the approximations for the radiative heat loss from the wafer surfaces. Replace [18] and [19] by

$$K_L \frac{dT}{dy} = \epsilon_L[P(t) - 1 - 4RT] \text{ at } y = D \qquad [36]$$

$$K_S \frac{dT}{dy} = \epsilon_B(1 + 4RT) \text{ at } y = 0 \qquad [37]$$

Then [23], with [21], [36], and [37], has the solution

$$T(y) = (\epsilon_B/K_S)[1 + 4RT(0)](y - y_f) \qquad 0 \leq y \leq y_f$$
$$= (\epsilon_L/K_L[P(t) - 1 - 4RT(D)](y - y_f) \qquad y_f \leq y \leq D \qquad [38]$$

Neglecting terms of order $(4RD)^2$, we find, using [20], that

$$\frac{dy_f}{dt} = \frac{R}{\text{Pe S}}\{-\epsilon_L[P(t) - 1 - 4RT(D)] + \epsilon_B[1 + 4RT(0)]\}$$
$$\approx \frac{R}{\text{Pe S}}\left\{-\epsilon_L(P(t) - 1)\left(1 - 4\frac{\epsilon_L}{K_L}RD\right)\right.$$
$$\left. + \epsilon_B - 4Ry_f\left[\epsilon_L\frac{\epsilon_L}{K_L}(P(t) - 1) + \epsilon_B\frac{\epsilon_B}{K_S}\right]\right\} \qquad [39]$$

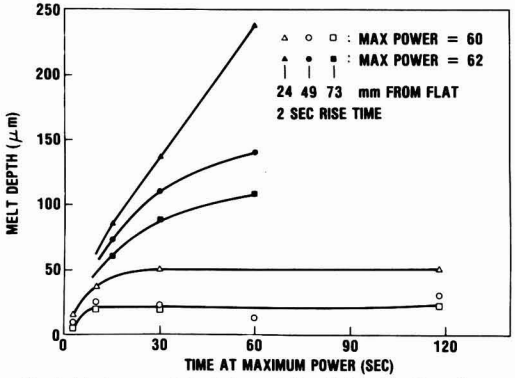


Fig. 3. Maximum melt depth in crystalline Si from Fig. 3 *vs.* time at the maximum power. The risetime was measured from a power setting ~5% below P_1.

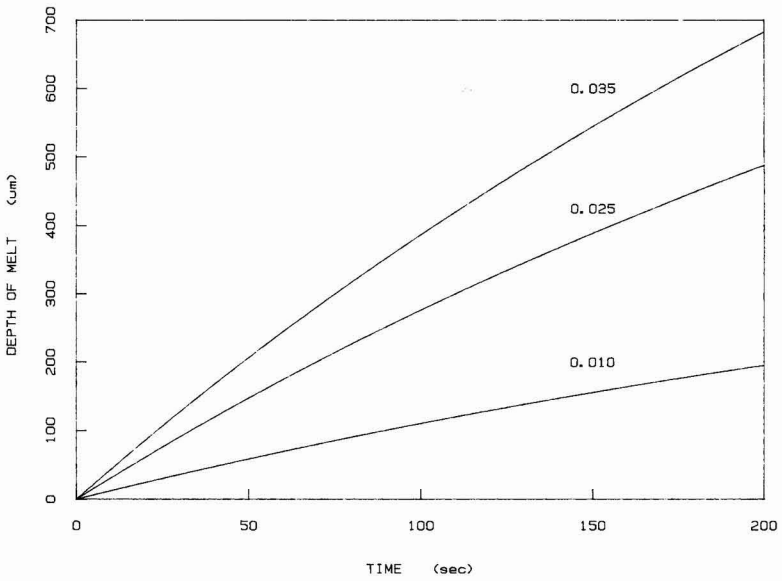


Fig. 4. Melt depth as a function of time for $\delta_0 = 0$. Irradiation is a constant at the dimensionless values of $\tilde{p}_{max}$ indicated. The quantity $\tilde{p}_{max}$ represents the power in excess of the threshold for a fully molten surface, normalized by that threshold.

This time, normalize $P(t)$ with respect to a refined version of the threshold for a fully molten surface

$$P(t) = \left[1 + \frac{\epsilon_B}{\epsilon_L}\left(1 - 4RD\,\frac{\epsilon_B}{K_S}\right)\right][1 + \tilde{p}(t)] \qquad [40]$$

Then after also neglecting terms of order $4RD\,\tilde{p}_{max}$, we find that

$$\frac{dy_f}{dt} = \frac{R}{\text{Pe S}}\left[-(\epsilon_L + \epsilon_B)\tilde{p}(t) + 4\epsilon_B R(D - y_f)\left(\frac{\epsilon_L}{K_L} + \frac{\epsilon_B}{K_S}\right)\right] \qquad [41]$$

It is more instructive at this point to think in terms of the melt depth

$$\delta_f(t) = D - y_f(t) \qquad [42]$$

We have

$$\frac{d\delta_f}{dt} = \beta\tilde{p}(t) - \gamma\delta_f \qquad [43]$$

with

$$\beta = (\epsilon_L + \epsilon_B)\frac{R}{\text{Pe S}} = \frac{(\epsilon_L + \epsilon_B)\sigma T_m^4}{\rho L d} \approx 12.6$$

$$\gamma = 4\beta R\left(\frac{\epsilon_B}{\epsilon_L + \epsilon_B}\right)\left(\frac{\epsilon_L}{K_L} + \frac{\epsilon_B}{K_S}\right)$$

$$= 4\epsilon_B\left(\frac{\epsilon_L}{K_L} + \frac{\epsilon_B}{K_S}\right)\frac{(\sigma T_m^4)^2}{\rho L\, T_m} \approx 2.7 \times 10^{-3} \qquad [44]$$

where the parameter values of the formulation section were used.

If we now consider only constant irradiation, $\tilde{p}(t) \equiv p_{max}$, Eq. [43], subject to the initial condition $\delta_f(0) = \delta_0$, has a solution

$$\delta_f(t) = \frac{\beta\tilde{p}_{max}}{\gamma} + \left(\delta_0 - \frac{\beta\tilde{p}_{max}}{\gamma}\right)e^{-\gamma t} \qquad [45]$$

As expected, for small γt this reduces to

$$\delta_f(t) \approx \delta_0 + \beta\tilde{p}_{max}t \qquad [46]$$

which is equivalent to the linear growth portion of [32].

Curves for the melt depth δ_f as a function of time are shown in Fig. 4 for $\delta_0 = 0$ and several values of $\tilde{p}_{max}$. Recall that the dimensionless quantity $\tilde{p}_{max}$ represents the power in excess of the threshold for a fully molten surface, normalized by that threshold. Although the functional form of the curves agrees qualitatively with the experimental data of the experimental results section, the curves tend toward their asymptotes much less rapidly than the experimentally obtained curves do. We must conclude that increased radiative loss due to wafer heat only partially accounts for the sublinear dependence of the melt depth on time.

Buried Oxide

Suppose now that the silicon wafer contains a buried oxide layer. How does this affect the temperature profile and the motion of the melt or solidification front?

Assume that the substrate occupies the region $0 \leq y \leq d_1$, the SiO_2 is in the region $d_1 \leq y \leq d_1 + d_2$, and an additional layer of Si is in $d_1 + d_2 \leq y \leq d_1 + d_2 + d_3 \equiv D$, as is illustrated in Fig. 5. Typical dimensions for a technologic-

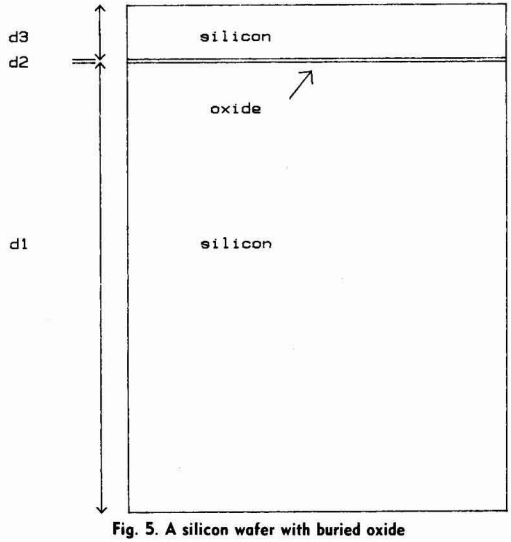


Fig. 5. A silicon wafer with buried oxide

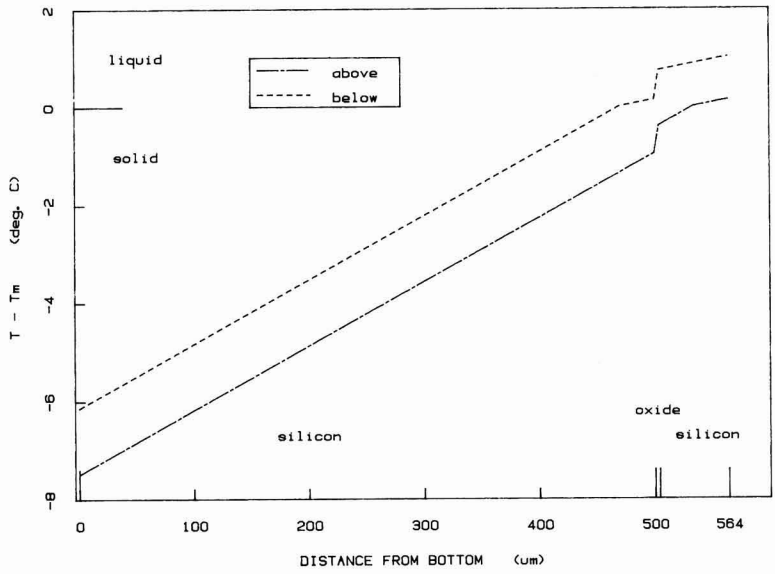


Fig. 6. Typical temperature profiles in a wafer with buried oxide, with the melt front 30 μm above or below the oxide layer: d_1 = 50 μm, d_2 = 4 μm, d_3 = 500 μm, p_{max} = 0.025.

ally important process are d_1 = 500 μm, d_2 = 4 μm, d_3 = 60 μm.

We return to using the zeroth order approximation [24] to the radiation boundary conditions and to using the appropriate power normalization [27]. The solution to the quasi-static diffusion equation and associated boundary conditions again yields a piecewise linear temperature profile. The form of the profile is different, depending on whether the melt/solidification front y_f is above or below the oxide layer.

For a front above the oxide, we have

$$\begin{aligned} T(y) &= (\epsilon_B/K_S)\{(y - y_f) - d_2[(K_S/K_O) - 1]\} \\ &\qquad 0 \le y \le d_1 \qquad \text{below oxide} \\ &= (\epsilon_B/K_O)\{y - (K_O/K_S)y_f - (d_2 + d_3)[1 - (K_O/K_S)]\} \\ &\qquad d_1 \le y \le d_1 + d_2 \qquad \text{in oxide} \\ &= (\epsilon_B/K_S)(y - y_f) \\ &\qquad d_1 + d_2 \le y \le y_f \qquad \text{below front, above oxide} \\ &= (1/K_L)[\epsilon_B + (\epsilon_L + \epsilon_B)p(t)](y - y_f) \\ &\qquad y_f \le y \le D \qquad \text{above front, above oxide} \end{aligned} \quad [47]$$

On the other hand, if the front is below the oxide layer

$$\begin{aligned} &T(y) \\ &= (\epsilon_B/K_S)(y - y_f) \\ &\qquad 0 \le y \le y_f \qquad \text{below front, below oxide} \\ &= (1/K_L)[\epsilon_B + (\epsilon_L + \epsilon_B)p(t)](y - y_f) \\ &\qquad y_f \le y \le d_1 \qquad \text{above front, below oxide} \\ &= (1/K_O)\{y - d_3[1 - (K_O/K_L)] - (K_O/K_L)y_f\}[\epsilon_B + (\epsilon_L + \epsilon_B)p(t)] \\ &\qquad d_1 \le y \le d_1 + d_2 \qquad \text{in oxide} \\ &= (1/K_L)\{y - y_f + d_2[(K_L/K_O) - 1]\}[\epsilon_B + (\epsilon_L + \epsilon_B)p(t)] \\ &\qquad d_1 + d_2 \le y \le D \qquad \text{above oxide} \end{aligned} \quad [48]$$

Typical theoretical temperature profiles are shown in Fig. 6. These are obtained from [47] and [48], using the parameter values of [9] and those indicated in the figure caption. As before, the temperature gradient in the solid Si is constant, both in space and in time. That in the liquid Si and the SiO_2 is uniform spatially. The gradient varies with time in the liquid Si, and also in the SiO_2 layer when the front lies below it. However, the time variation is small if $p(t) << 1$. Notice also the steep gradient across the oxide because of its low thermal conductivity.

Using [20] and [47] or [48], we find that to this order of approximation, the motion of the melt front is again given by

$$\frac{dy_f}{dt} = -\beta p(t), \beta = (\epsilon_L + \epsilon_B)\frac{R}{\text{Pe S}} \quad [49]$$

independent of whether the front is above or below the oxide.

Consequently we might expect melting and solidification behavior similar in many respects to that of a Si wafer containing no buried oxide layer. When melting is taking place and the front is above the oxide layer, Eq. [29] should be directly applicable. When the melt isotherm passes through the oxide layer, no latent heat is absorbed, since the SiO_2 does not melt. The isotherm passes through the layer extremely rapidly, on a time scale which is short compared to that (seconds) used for this quasi-static analysis. In a corresponding fashion, if Si below the SiO_2 is molten and solidification is taking place, the freezing isotherm will pass through the oxide layer extremely rapidly.

In theory, then, melting and solidification proceed according to [29] applied region by region (Si above SiO_2, Si below SiO_2, Si above SiO_2 again

$$y_f(t) = y(t_i) - \beta \int_{t_i}^{t} p(t')dt' \quad [50]$$

with the initial times t_i and positions $y(t_i)$ adjusted so that there are jump discontinuities in the positions of the melt/solidification front at the times it passes through the oxide layer. There are corresponding jump discontinuities in the temperature distribution across the wafer.

In practice it is difficult to make any meaningful measurements of the depth of melt under a continuous buried oxide. The problem is similar to the one encountered in melting the surface of a defect-free single crystal: there is a nucleation barrier for melting and silicon becomes superheated. Melting that follows is spatially irregular as it originates at randomly located nucleation sites. A planar melt front develops eventually, but only at a depth of 150-200 μm under the SiO_2.

To avoid the nucleation problems, we used SiO_2 with a pattern of slit-shaped openings of the type used for seeded lateral crystallization over the SiO_2 (1). This configuration requires a two-dimensional model for a complete description of melting in the vicinity of the windows (2). Here we are interested only in matching the data to the one-dimensional solution that should be correct away from the windows and for deep melts. In Fig. 7, the depth of melt is plotted *vs.* incident power for wafers with 80 μm of polysilicon on 4 μm of buried patterned oxide. A capping oxide layer, 2 μm thick, covered the front and also the back surface.

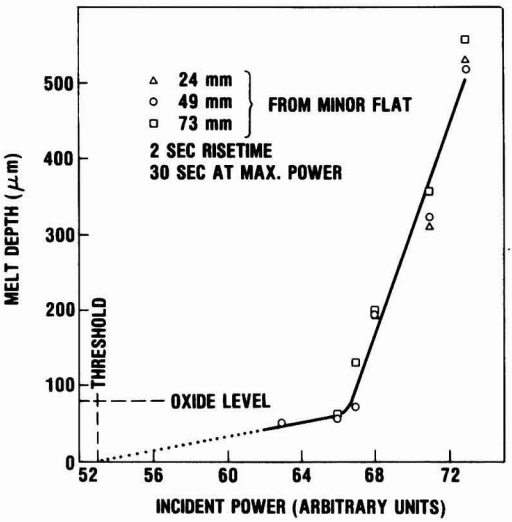


Fig. 7. Maximum melt depth vs. incident power for Si with a patterned SiO_2 layer buried 80 μm below a rough encapsulated surface.

The front surface emissivities ϵ_S and ϵ_L should be quite similar to the values for bulk Si wafers in Fig. 2. In both cases the surfaces were rough, although the roughness in the crystalline Si was produced mechanically, while that in the polysilicon occurred naturally during deposition. The emissivity of the back sides was higher, ~0.72 as compared to 0.6 for bare Si (5). This explains why the thresholds P_1 and P_2 are shifted from 49 and 60 to 53 and 65.5, in agreement with Eq. [1] and [2]. The data scatter in Fig. 7 is less than in Fig. 2, so only one curve is plotted.

In Fig. 7, the melt-depth curve has a non-zero slope even below P_2. It is not clear if this effect has any physical significance or is only a reflection of the uncertainty of measurement within the polycrystalline Si and the melt shape distortion by the openings in the SiO_2. The slope of the second segment, for $P > P_2$, is greater than in Fig. 2, consistent with the increased ϵ_B. But this slope is also slightly less than expected from Eq. [34].

Conclusions

We derived a one-dimensional solution to the problem of melting of Si with a radiative flux. The solution is applicable above the power threshold for deep melting P_2. It predicts the melt depth increasing parabolically during the initial ramping up stage and linearly during the constant power stage, with a parabolic decrease when the input power is ramped down linearly. These results provide the foundation for understanding and controlling the kinetics of melting of thick Si layers heated by extended radiant heaters. The experimental data for the maximum melt depth are in qualitative agreement with the calculated values.

Manuscript submitted May 27, 1985; revised manuscript received Oct. 10, 1985.

AT&T Bell Laboratories assisted in meeting the publication costs of this article.

REFERENCES

1. G. K. Celler, McD. Robinson, L. E. Trimble, and D. J. Lischner, *This Journal*, **132,** 211 (1985).
2. L. O. Wilson and G. K. Celler, *ibid.*, **132,** 2748 (1985).
3. G. K. Celler, McD. Robinson, L. E. Trimble, and D. J. Lischner, *Appl. Phys. Lett.*, **43,** 868 (1984).
4. G. K. Celler, K. A. Jackson, L. E. Trimble, McD. Robinson, and D. J. Lischner, *Mater. Res. Soc. Symp. Proc.*, **23,** 409 (1984).
5. G. K. Celler, L. E. Trimble, and L. O. Wilson, *Mater. Res. Soc. Symp. Proc.*, **35,** 635 (1985).
6. G. E. Jellison and F. A. Modine, *Appl. Phys. Lett.*, **41,** 180 (1982).
7. A. Bell, *RCA Rev.*, **40,** 295 (1979).
8. M. E. Glicksman and P. Voorhees, *J. Electron. Mater.*, **12,** 161 (1983).
9. E. Yablonovitch, *J. Opt. Soc. Am.*, **72,** 899 (1982).
10. H. M. Ettouney and R. A. Brown, *J. Comput. Phys.*, **49,** 118 (1983).
11. B. E. Deal and A. S. Grove, *J. Appl. Phys.*, **36,** 3770 (1965).
12. D. J. Lischner and G. K. Celler, *Mater. Res. Soc. Symp. Proc.*, **4,** 759 (1982).

Sidewall Spacer Technology for MOS and Bipolar Devices

Sang H. Dhong* and Edward J. Petrillo

IBM Thomas J. Watson Research Center, Yorktown Heights, New York 10598

ABSTRACT

Chemical-vapor-deposited (CVD) oxide or nitride sidewall spacers formed at the edges of polysilicon lines by reactive ion etching (RIE) have important applications in both MOS and bipolar technology. In this paper, we present processing parameters that have to be understood and monitored for any successful sidewall spacer process and also report some of the inherent limitations of the spacer technology, an angular dependence of etch rate in reactive ion etching, and a new interpretation of RIE selectivity. The processing parameters that we studied experimentally are oxide etch uniformity, oxide-to-silicon selectivity; conformality, uniformity, and thickness of CVD deposition. The effects of these parameters on the shape of the spacers were noted and compared with computer simulation done by using the SAMPLE program. Good agreement between the experiments and computer modeling was only obtained when an angular dependence of etch rate in RIE was included in the computer model. The analytic and anisotropic etch models were inadequate in predicting the exact spacer shape but provided a sufficiently accurate first-order approximation. Experiments also showed that oxide-to-silicon selectivity is a strong function of time that, as etching continues, asymptotically reaches the selectivity values previously reported in literature.

Chemical-vapor-deposited (CVD) oxide or nitride sidewall spacers formed at the edges of polysilicon lines have many important applications in both MOS and bipolar technologies. In a bipolar transistor with a self-aligned emitter, such as the one reported by Tang (1), the oxide spacers formed at the edges of the polysilicon base electrode isolate electrically the base from the self-aligned emitter. The width and shape of the spacers determine the emitter opening size in this application.

More extensive applications of spacers can be found in MOS technology. In the lightly doped drain-source (LDD) FET structure, spacers are used as an ion-implant mask to achieve a double-diffused structure that shows significant improvements in breakdown voltages, hot-electron

*Electrochemical Society Active Member.

effects, and short-channel effects (2, 16). The spacers are also widely used in the self-aligned silicide technology (3, 4) to prevent bridging between the gate and source/drain during the silicide formation. In this paper, we are concerned with the understanding, characterization, and computer modeling of oxide and nitride spacer technology and also report some of the inherent limitations of the spacer technology within the context of the aforementioned applications.

In the next section, we describe experiments carried out to form sidewall spacers at the polysilicon edges and to observe the conformality of CVD film deposition. The processing tools used in the experiments are also discussed. We then derive models for sidewall spacers. The analytic model for a spacer as a function of processing parameters is derived. Computer modeling using simulation and modeling of profiles in lithography and etching (SAMPLE) (8) and the tacit assumptions made in the program are discussed. Next, we treat in detail each of the parameters: the slope of polysilicon lines, the conformality, uniformity, and thickness of a CVD film, the oxide etch uniformity, and the oxide-to-silicon selectivity. The individual effects of these parameters on the spacers are characterized and analyzed by experiments and by computer simulation using SAMPLE. Finally, the limitations imposed on the spacers due to the mutually interrelated effects of the processing parameters and their implications in IC technology are discussed.

Experimental

The first step in the fabrication of sidewall-spacer experiment samples was deposition of a 300 nm polysilicon layer on a 22.5 nm thermally grown oxide. These values were chosen to simulate 1.25 μm MOS technology as closely as possible. The polysilicon was patterned by an optical stepper and was reactive-ion-etched (RIE) using CCl_2F_2 in a flexible diode system to make polysilicon lines with vertical edges (5). After oxide films of various thicknesses had been deposited by CVD, sidewall spacers were formed by etching the layer in a mixture of CF_4 and hydrogen in an RIE mode (see Fig. 1 (a) and (b)). In case of silicon nitride spacers, LPCVD nitride was deposited in lieu of the oxide. The spacers thus formed usually had a wedge shape whose base was only a few hundred nanometers wide at best and were difficult to observe under SEM. The difficulty was circumvented by first oxidizing the wafers to grow a 22.5 nm oxide, which helped to delineate the top of the polysilicon step. A polysilicon layer approximately 300 nm thick was deposited as an overcoat before the wafers were cleaved. Then, the spacers were etched in BHF for oxide and in HF for nitride in order to decorate them for SEM observation, as shown in Fig. 1 (c).

The profiles of CVD oxide and nitride films covering the polysilicon lines were found by decorating the layer by two different methods for SEM inspection. In one method, which is shown in Fig. 1 (d), the CVD layer was covered by an overcoat of polysilicon before cleaving and was etched in HF. The other method of etching the polysilicon and leaving the CVD oxide for SEM observation is schematically shown in Fig. 1 (e) and was used to decorate the samples for Fig. 4. In this method, polysilicon was selectively etched while leaving the oxide unetched in a CF_4 plasma at a few hundred millitorr.

Sidewall spacers of three different materials, *i.e.*, nitride, low temperature oxide (LTO), and tetraethyl orthosilicate (TEOS) oxide, are studied in this paper. Silicon nitride was chemically deposited at 450 mtorr at 820°C by reacting dichlorosilane and ammonia. Tetraethyl orthosilicate was decomposed in an LPCVD reactor at approximately 725°C to deposit TEOS oxide. Low temperature oxide was deposited by reacting silane with oxygen at 400°C in an LPCVD reactor. Nitride and TEOS oxide were deposited at higher temperatures than LTO, and, consequently, these films were more conformal than LTO films. The consequence of film conformality is studied in the section entitled "Processing Parameters and Their Effects."

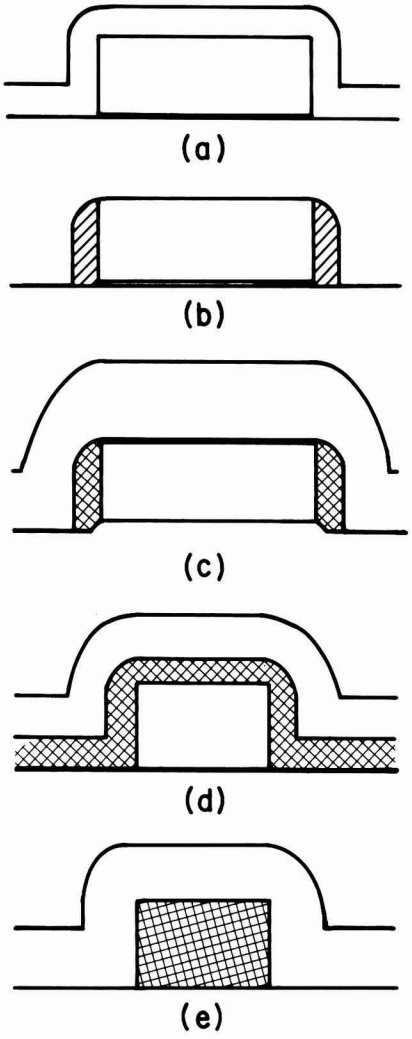


Fig. 1. Spacer formation: (a) CVD deposition over a polysilicon line; (b) spacer formation by RIE; (c) the spacers etched in HF appear dark under SEM; (d) the CVD layer etched in HF appears dark under SEM; (e) the polysilicon line etched in a plasma appears dark under SEM.

The polysilicon lines were etched in a CCl_2F_2 plasma at 30 mtorr in a flexible diode system, which is described in detail elsewhere (5). The sidewall profile of the polysilicon lines is shown in Fig. 2 and has a small foot near the bottom. Though not completely vertical, it was adequate for our study. The sidewall spacers were formed by reactive ion etching oxide or nitride using an approximately 40% mixture of hydrogen in CF_4 at 25 mtorr with a power density of 0.16 mW/cm^2 and an approximate self-induced dc bias of 400V. Endpoint detection was done by using a laser interferometer (6, 7).

Analytic Model for Sidewall Spacers

An analytic model for the thickness and apex of a spacer can be found with the simplifying assumptions that the CVD film deposition is completely conformal and that the RIE used to form spacers is purely anisotropic with an infinitely high selectivity to the substrate and polysilicon lines. Assume a sidewall process where an oxide or nitride film of thickness t_f (see inset of Fig. 3) is de-

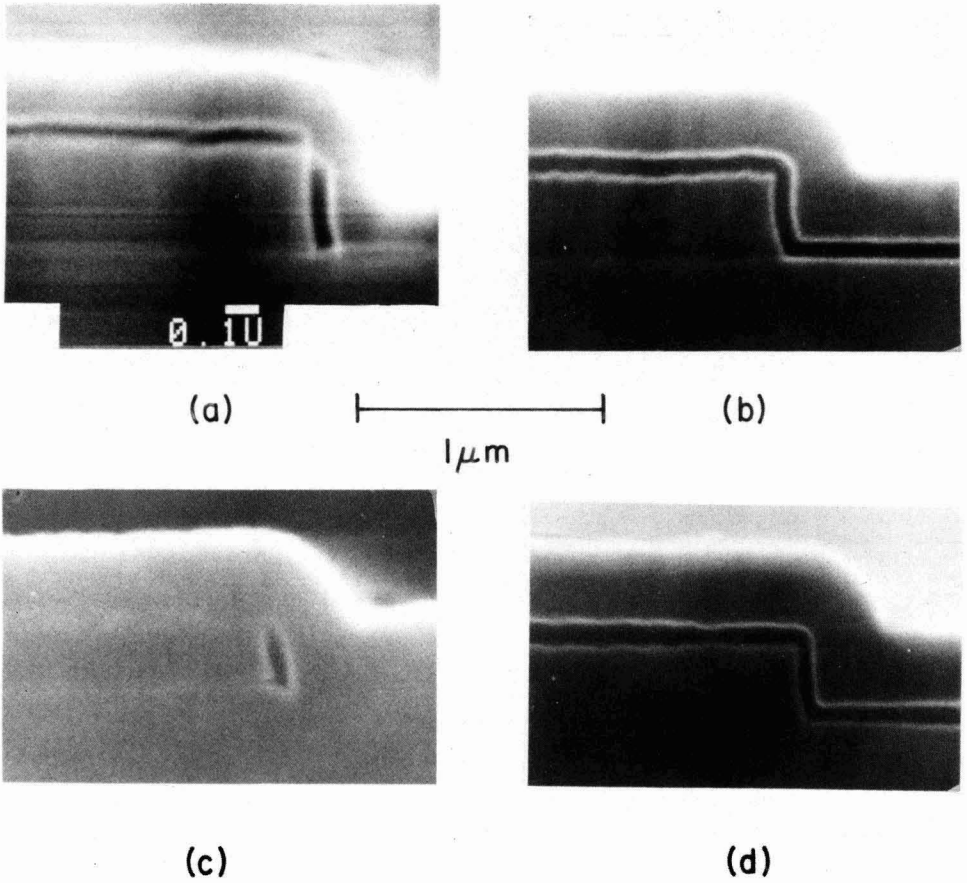


Fig. 2. (a) Nitride spacer: t = 300 nm, t_f = 100 nm, δ = 10%; (b) CVD nitride film (100 nm thick); (c) TEOS spacer; t = 300 nm, t_f = 100 nm, δ = 10%; (d) CVD TEOS film (100 nm thick).

posited by CVD over a polysilicon line with a step height of t and is reactive-ion-etched to form a spacer of width w

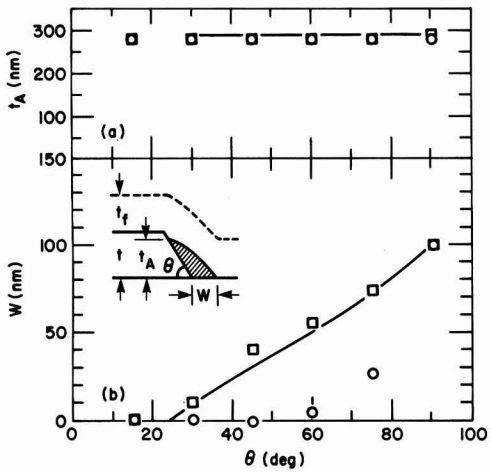


Fig. 3. (a) Spacer height vs. polysilicon step slope, and (b) spacer width vs. polysilicon step slope. Solid line: analytic expression; circles: simulation points with the angular dependence with 5.2249, −5.5914, and 1.3665 for *A*, *B*, and *C*, respectively; squares: simulation points with the anisotropic etch model.

with its apex lying at t_A above the substrate. The RIE step requires some overetching in order to completely clear the film. Let δ be the ratio of the overetched thickness to the film thickness t_f. Then, the following relationships can be found for the spacer width w by extending the analysis done by Tsang (16, 17)

(i) For a CVD film with $\dfrac{t}{1-\cos\theta} \le t_f$,

$$w = t\sqrt{\left(\frac{t_f}{t}\right)^2 - \left\{(1+\delta)\frac{t_f}{t} - 1\right\}^2} - t\cot\theta \quad [1]$$

(ii) If $t\,\dfrac{\cot\theta}{\sin\theta} \le t_f \le \dfrac{t}{1-\cos\theta}$,

$$w = t_f\left(\tan\frac{\theta}{2} - \delta\cot\theta\right) \text{ for } 0 \le \delta \le \frac{t}{t_f} + \cos\theta - 1 \quad [2]$$

$$w = t\sqrt{\left(\frac{t_f}{t}\right)^2 - \left\{(1+\delta)\frac{t_f}{t} - 1\right\}^2} - t\cot\theta \text{ for } \frac{t}{t_f} + \cos\theta - 1 \le \delta \quad [3]$$

(iii) For $0 \le t_f \le t\,\dfrac{\cot\theta}{\sin\theta}$,

$$w = t_f\left(\tan\frac{\theta}{2} - \delta\cot\theta\right) \quad [4]$$

The apex t_A of the spacer is found by solving a quadratic equation that finds the intersections between a circle and a straight line. For all values of t_f

$$t_A = t\left[1 - \frac{t_f}{t}(1+\delta)\sin\theta\left\{\sin\theta - \sqrt{\frac{1}{(1+\delta)^2} - \cos^2\theta}\right\}\right] \quad [5]$$

The expression for t_A reduces to $t_A = t$ if the overetching amount δ is 0 or to $t_A = t - \delta t_f$ for $\theta = 90°$.

The above formulas can be normalized with respect to the polysilicon step height t, and the ratio t_f/t becomes the single most important factor that characterizes the spacers and will be called the normalized thickness. Even though the validity of the equations is limited by the idealizing assumptions, they give us clear guidance in understanding the effects of individual processing parameters on the spacers in the next section.

Computer Modeling Using SAMPLE

Computer modeling was done by using the SAMPLE program (8). The program employs the string-model algorithm (14) and allows an etching step to be modeled in two ways, either as an adjustable mixture of isotropic and anisotropic etching component or as a directional etching with angular dependent variables (8, 15). A CVD deposition is modeled as reverse etching with only an isotropic component, which results in a completely conformal deposition profile. Reactive ion etching of oxide in a mixture of CF_4 and hydrogen is extremely anisotropic, with a selectivity of larger than 10:1 to silicon. We simulated the RIE step as being completely anisotropic etching with a zero substrate etch rate. This model does not take into consideration any angular dependence of the etch rate during the RIE step and had poor agreement with the experiment.

In the other method, which has mainly been used for ion milling or sputtering simulation, the etch rate is modeled according to the sputtering yield

$$S(\theta) = S_0\left[\frac{\phi}{\rho}\right](A\cos\theta + B\cos^2\theta + C\cos^4\theta) \quad [6]$$

where S_0, A, B, and C characterize the sputtering yield of the material to be etched, ρ is the atomic layer density, and ϕ is the current density of the ion flux. This model gave us a better agreement with the experiments with properly chosen A, B, and C, as will be further discussed in the next section. All the SAMPLE computer runs were repeated using the two different etching models, and the results are compared whenever possible.

Processing Parameters and Their Effects

Spacer formation can be divided into three major processing steps: (i) delineation of polysilicon lines; (ii) deposition of a CVD film; and (iii) reactive ion etching to form spacers. Each step has its unique effect on the spacers and is examined in detail in four separate subsections.

Delineation of polysilicon lines and sidewall slope.— Sidewall spacers are formed at the edges of polysilicon lines as shown in Fig. 2. The profile and thickness of the polysilicon lines are the two most important parameters in this step. The effect of the slope of the polysilicon lines is examined analytically and by computer simulation, because making polysilicon lines with various sidewall

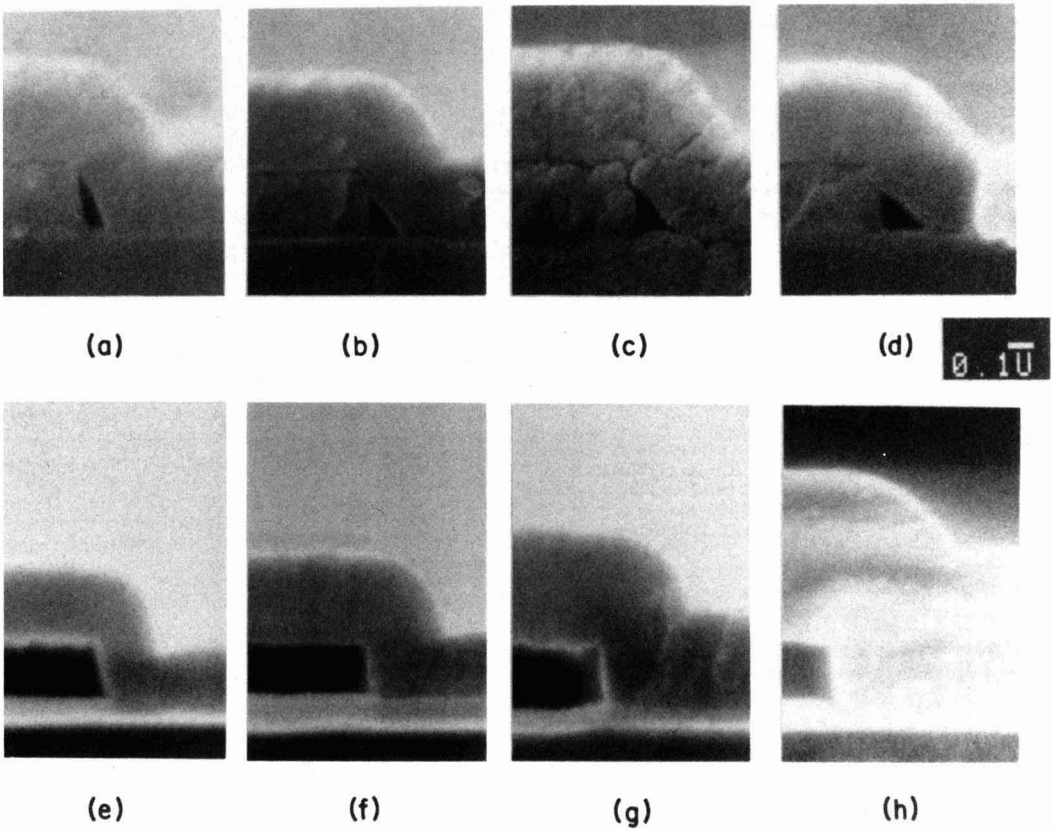


Fig. 4. Top row: TEOS spacers; bottom row: TEOS films over polysilicon steps. t = 300 nm, δ = 20%, t_f = 200 nm for (a) and (e), 300 nm for (b) and (f), 400 nm for (c) and (g), and 600 nm for (d) and (h).

slopes in a controlled manner goes beyond the scope of this paper, even though we did one experiment to see the effect.

The sidewall spacers shown in Fig. 2 were formed on a 300 nm polysilicon step by depositing 100 nm oxide and etching the film with 10% overetching. Computer simulation using SAMPLE was done in order to see the effect of the slope on a similar spacer shown in the figure, and the simulation results for the width of the spacer and the height of the apex are shown in Fig. 3 along with the analytical data obtained from Eq. [4] and [5]. For the first set of simulation results shown as squares in Fig. 3, the etching was modeled as anisotropic. The agreement with the analytic expressions, which is shown as the solid line in the figure, is excellent. As the slope of the step is decreased from 90°, the spacer width decreases quite rapidly, and, at a slope of approximately 50°, the spacer width becomes half of the width at 90°. This trend is not at all surprising, because if a spacer is formed at a steeper step, less of its side portion is exposed to etching due to the anisotropicity of RIE.

The second set of simulations was done using the etching model with the angular dependence shown by curve (c) in Fig. 11, and the results are plotted as circles in Fig. 3. The calculated spacer width is much narrower than the previous one, except for the one formed at a vertical polysilicon step. In one experiment, we obtained polysilicon lines with a sidewall slope between approximately 45° and 55° by changing the slope of the photoresist mask used in defining the polysilicon lines and proceeded to form spacers. However, we could not observe any spacers on the polysilicon line edges. This tends to support the results from the second set of simulations. The effect of the variation of the polysilicon thickness is inversely related to changing the CVD film thickness, because the spacers can be characterized in terms of the normalized thickness, as described in the next subsection.

CVD film: uniformity, conformality, and thickness.—In this processing step, oxide or nitride is deposited over the polysilicon lines in an LPCVD reactor. The processing parameters particularly important to sidewall spacers are the thickness, uniformity, and conformality of the CVD film. The effect of changing the thickness of the CVD film on the shape of the spacers is experimentally studied and is shown in Fig. 4. The TEOS oxide thickness was changed from 200 nm to 600 nm in four steps, which corresponds to changing the normalized thickness t_f/t from 0.6 to 2.0. Varying the normalized thickness from 0.3 to 2.0 causes the slope of sidewall spacers to change from near 90° to 35° along with a change in the spacer width (see Fig. 1 and the top row of Fig. 4). Increasing the thickness of the CVD film makes the spacers not only wider but also more sloped. This can be understood by checking the profiles of TEOS film over the polysilicon lines in the bottom row of Fig. 4. The slope of the oxide directly above the polysilicon step becomes gentler as the normalized thickness increases. The spacer, which copies the slope of the CVD film during RIE, has, consequently, a gentler slope.

SAMPLE simulation was done to understand the effect of oxide or nitride thickness with parameters chosen as closely to the experiments as possible. An isotropic deposition of 200 nm to 600 nm of oxide over a 300 nm step of polysilicon with a sidewall slope of 80° was followed by etching with 20% overetching. The results with the anisotropic etch model are shown in Fig. 5 and are plotted as X's in Fig. 7. The analytic expressions are shown as solid lines in Fig. 7 and agree very well with the simulation results with the anisotropic etch model. Somewhat different results are obtained if the angular dependent etch model is used and the results are shown in Fig. 6 and are plotted in Fig. 7 as squares. The experimental data are shown as circles in Fig. 7. The simulation results with the angular-dependent model give steeper spacer profiles with narrower spacer widths, and their agreement with the experiments is quite good, especially for thicker oxide films. The shapes of computer simulated spacers are very similar to those of the experiments except for the spacer with a normalized thickness of 0.67 shown in Fig. 4 (a). Both models are quite accurate in predicting t_A. The discrepancy of the actual shape from the simulation results is believed to be due to two factors: (*i*) inadequacy of modeling of the TEOS deposition, which is obviously not 100% conformal; and (*ii*) incomplete modeling of the RIE process. We believe that this discrepancy will be minimized when more accurate models for CVD deposition and RIE become available in the future.

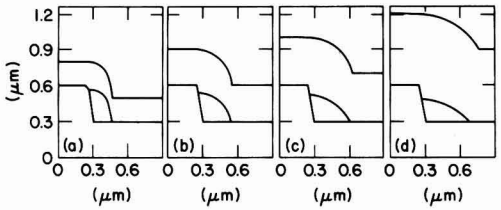


Fig. 5. SAMPLE simulation results with the anisotropic etch model. Each frame shows the CVD profile and resulting spacer at the polysilicon step. t = 300 nm, θ = 80°, δ = 20%, and t_f = 200 nm for (a), 300 nm for (b), 400 nm for (c), and 600 nm for (d).

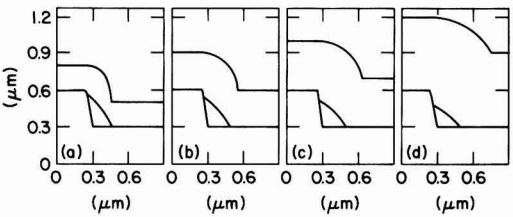


Fig. 6. SAMPLE simulation results with the angular dependence with 5.2249, −5.5914, and 1.3665 for *A*, *B*, and *C*, respectively. Each frame shows the CVD profile and resulting spacer at the polysilicon step. t = 300 nm, θ = 80°, δ = 20%, and t_f = 200 nm for (a), 300 nm for (b), 400 nm for (c), and 600 nm for (d).

The profile of an oxide or nitride film affects the shape of the spacers, and the conformality of the film may be expected to be an important factor influencing the spacer. An LTO film that was deposited at a lower temperature than a TEOS film is less conformal. Figure 8 shows

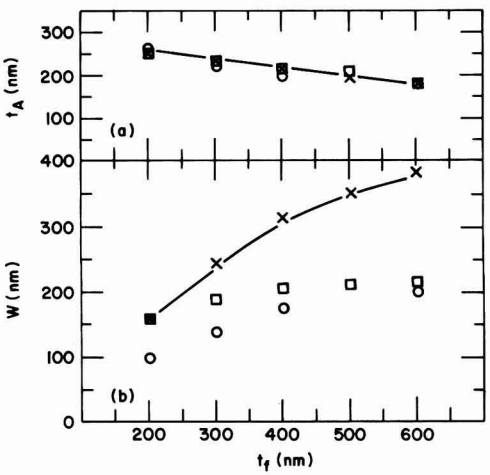


Fig. 7. (a) Spacer height *vs.* CVD oxide layer thickness, and (b) spacer width *vs.* CVD oxide layer thickness. Solid line: analytic expression; squares: simulation points with the angular dependence with 5.2249, −5.5914, and 1.3665 for *A*, *B*, and *C*, respectively; X's: simulation points with the anisotropic etch model; circles: experiment.

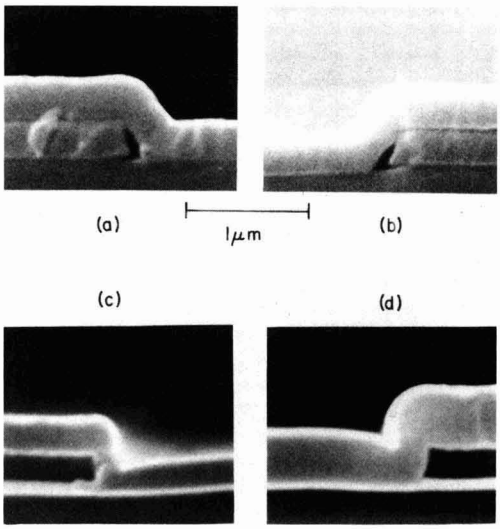


Fig. 8. (a) LTO spacer: t = 300 nm, t_f = 200 nm, and δ = 20%; (b) LTO spacer: t = 300 nm, t_f = 400 nm, and δ = 20%; (c) LTO film (200 nm thick); (d) LTO film (400 nm thick).

LTO spacers and profiles of LTO films, which can be compared with those in Fig. 4 to see the difference between the two kinds of spacer. Notching of the LTO films near the root of the polysilicon step is somewhat more prominent than that of the TEOS films. However, the difference in the profiles of these two films is not significant enough to make any big difference in the shape of spacers, as long as polysilicon steps are not too closely spaced compared to their heights so that notching does not become too severe.

Uniformity of CVD films is usually within ±5% for a film a few hundred nanometers thick. The variation in the thickness should be taken into consideration when calculating the amount of overetching needed during the etching and is discussed in conjunction with the RIE process.

RIE of CVD film, overetching and selectivity.—The oxide or nitride film deposited over the polysilicon steps was etched in a mixture of CF_4 and H_2 at an approximate etch rate of 30 nm per minute. The etching was very anisotropic and was highly selective for silicon nitride and oxide over silicon with a reported selectivity over 20 (9). The etching mechanism is treated by Kushner (10). Only etching uniformity and selectivity to silicon are treated here, because of their importance in spacer technology.

Uniformity of oxide etching was found as follows. The oxide thicknesses at nine points on each of the seven wafers that comprise a batch were measured before and after the etching using a film thickness analyzer. The differences were normalized with respect to the average etched depth and were plotted as a function of their positions on the cathode, as shown in Fig. 9 (a). Figure 9 (b) is a plot of the normalized etch rates along three major axes of the cathode and clearly indicates that the etch rate decreases toward the center of the cathode and also toward the centers of wafers, confirming the "bull's-eye" effect reported earlier (11). Even though the etch uniformities of single wafers were as good as a few percent, the batch uniformity, which is defined as the difference between the maximum and minimum etched depth divided by two times the average etched depth, was approximately 12%, with a few percent run-to-run variation. The necessary overetching required to form spacers is the sum of the nonuniformities of the CVD film and RIE for the worst case analysis. A somewhat different expression is found if three standard deviation (3σ) values are used in calculating uniformity. Typical CVD film nonuniformity

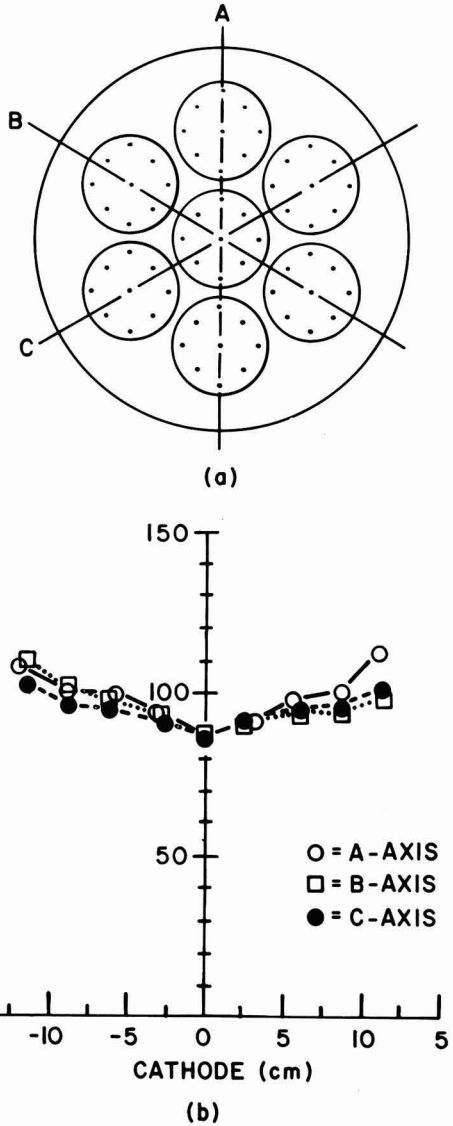


Fig. 9. (a) Measurement points on the cathode; the seven circles represent wafers. (b) Normalized etch rate along the three axes A, B, and C shown in (a).

is about 5%, and the required overetching was about 20% for our case.

The effect of overetching is seen in Fig. 4 in two different ways: a depression of the apex of the spacer below the top of the polysilicon line, and etching of the silicon substrate. The overetching specified for the worst case completely compensates for the nonuniformities of the CVD film and of etching and leaves the apex of the worst case spacer at the same height as the polysilicon step. A nominal spacer has its apex below the step by the overetching amount, which is given as a percentage of the CVD film. Consequently, a spacer formed from a CVD film with a larger normalized thickness should have its apex lower than the one formed from a film with a smaller normalized thickness. This trend can be clearly seen from experiments and simulation (Fig. 4, 5, 6, and 7).

Etching of the silicon substrate due to the overetching is unavoidable and can only be minimized by improving

the etch selectivity of oxide to the substrate. A previous work with the same gas mixture reported a selectivity of over 20. In this work, we achieved a selectivity of approximately 10 on a more routine basis, even though a higher selectivity can be achieved by increasing the hydrogen concentration closer to the "polymer point," where polymer formation causes cessation of etching with a subsequently narrower processing widow.

For a 600 nm thick CVD film, calculations suggest that approximately 12 nm of silicon would be consumed with 20% overetching. However, the experimental data suggest a somewhat higher consumption of silicon, even though the exact amount is difficult to find. This suspicion led us to a study of the selectivity as a function of etching time, the results of which are shown in Fig. 10. In the experiment, oxide and polysilicon wafers were measured before and after etching, and the etched thicknesses are plotted as a function of time. The selectivity, the ratio between the etched depth in oxide and polysilicon, is superimposed on the same plot. The selectivity is initially very low and increases to reach a value close to 10 after 3 or 4 min.

This unexpected result can be qualitatively explained as follows. Initially, the silicon is consumed almost as fast as silicon oxide in a plasma until a polymer layer forms on the silicon surface; after that, the polymer-protected silicon etches at a more constant rate compatible with the higher selectivity. The fluctuation in the selectivity values in the plot is not thought to be significant and can be attributed to the inaccuracy in finding the etched polysilicon thickness, where two big numbers (polysilicon thicknesses before and after etching) were subtracted to yield a small number (etched polysilicon thickness).

RIE of CVD film, angular dependence of etch rate.— The difference in the spacer shapes between the experiments and the simulation results with the anisotropic etch model, which can be seen by comparing Fig. 4 and 5, is too large to be caused only by the nonconformality of a CVD film. The actual spacers are much steeper and more wedge-shaped than predicted by the simulation results, suggesting an angular dependence of the etch rate during the etching. The angular dependence of the etch rate is quite well-known in sputter etching or in ion milling, where the substrate is tilted relative to the ion beam to achieve a higher milling rate. A similar effect during reactive ion etching has been proposed only recently by Nagy (12) as an explanation for sidewall tapering observed during silicon and oxide etching using a photoresist mask in a hexode-type etching system. The experimental relative yield curve as a function of angle of incidence is extremely difficult to obtain for an RIE process and is not yet available in the literature. However, reactive ion oxide etching in a mixture of CF_4 and hydrogen is done in a plasma discharge deficient in fluorine and requires ion bombardment of the etching surface. Some similarity in angular etch rate dependence to ion milling can be expected, even though their exact etching mechanisms are different.

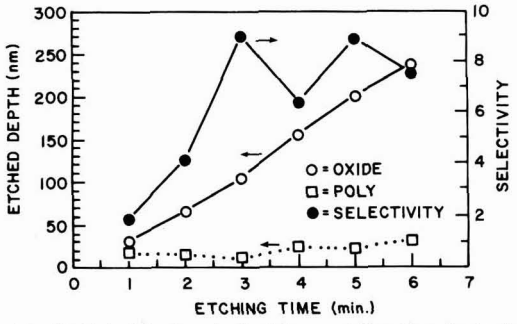


Fig. 10. Etched depth and selectivity vs. etching time. Empty circles: oxide; solid circles: selectivity; squares: polysilicon.

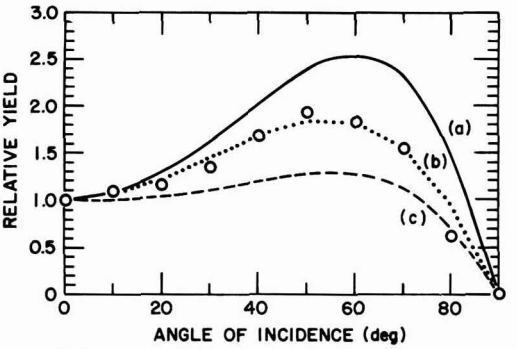


Fig. 11. Relative yield vs. angle of incidence. A, B, and C in Eq. [6] are: 10.7, −11.7, and 2.00 for (a); 6.50, −5.80, and 0.3 for (b); 5.2249, −5.5914, and 1.3665 for (c). Circles: data from Ref. (13).

To simulate the effect, we first took the relative sputtering yield data for SiO_2 provided in the SAMPLE program as the default values and did a SAMPLE computer run for the spacer formed from depositing a 600 nm layer over a 300 nm step. The default values give the yield data curve shown as (a) in Fig. 11, which has a maximum of 2.55 at an incident angle of 60°. For this curve, A, B, and C in Eq. [6] are 10.7, −11.7, and 2.0, respectively. The simulation result is shown in Fig. 12 (a) at various etching times. The initial CVD profile degrades too rapidly and no sidewall-spacer forms. For the next try, we used the published data on the angular dependence of SiO_2 for Ar ion beam ion milling (13) to repeat the computer run. The curve (b) in Fig. 11 is the approximation used to fit the ion milling data, which are shown as circles in the figure; it has a maximum of 1.8 at 55° with $A = 6.50$, $B = -5.8$, and $C = 0.3$. The simulation result with the angular dependence is shown in Fig. 12 (b) and shows no spacer formation. These two results led us to conclude that the angular dependence of the etch rate in RIE is much smaller than that of sputter etching or of ion milling. Better agreement between the simulation and experiment was produced when we chose the curve (c) in Fig. 11, which has a maximum of 1.3 at an incident angle of 60° with 5.2249,

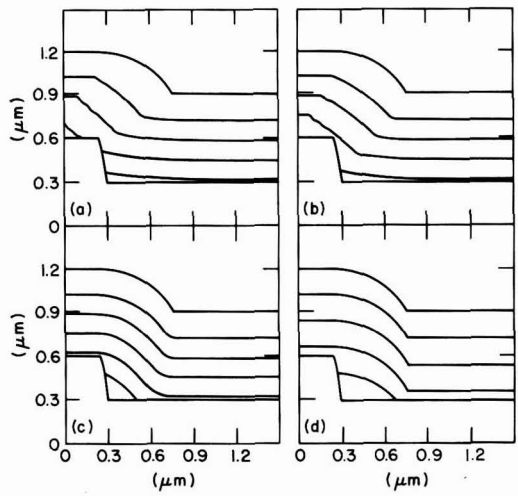


Fig. 12. Simulation of spacer formation at various time steps: t = 300 nm, θ = 80°, δ = 20%, and t_f = 600 nm. (a) Simulation with the angular dependence of curve (a) in Fig. 11; (b) simulation with the angular dependence of curve (b) in Fig. 11; (c) simulation with the angular dependence of curve (c) in Fig. 11; (d) simulation with the anisotropic etch model.

−5.5914, and 1.3665 as A, B, and C, respectively. The simulation result is shown in Fig. 12 (c) and agreed very well with the experiment. One surprising fact is that, even though the directional etch model with the angular dependence whose maximum is only 1.3 is not very different from the anisotropic etch model with no angular dependence, the resulting spacers are very much different, as can be seen in Fig. 5 and 6.

Comparing Fig. 4, 5, and 6, one can see that the inclusion of the angular dependence in the simulation improves the agreement between the experiments and simulation noticeably for the spacers formed from a CVD film with a larger normalized thickness. However, the difficulty of analyzing SEM photos of spacers and of sorting out all the interrelated parameters prevents us from making any definite conclusion on the physical mechanisms involved, even though we strongly believe the angular dependence of etch rate plays a very significant role.

One important aspect of RIE that has not been mentioned yet is the isotropic component of RIE. An isotropic component would make spacers thinner. The degree of thinning would be related to the ratio between the isotropic and anisotropic component. Unlike polysilicon RIE, oxide RIE almost always requires ion bombardment of the surface to be etched (10) and, consequently, is very anisotropic. Thus, the effect on spacers is believed to be very small, and no further study is attempted. However, it should be remembered that this only applies to oxide or nitride spacers and that, if polysilicon spacers are in question, the isotropic component has to be dealt with.

Limitations of Sidewall Spacers

All the parameters we mentioned in the last section play different, but significant, roles in forming spacers and, consequently, put certain limitations on the spacer shape. Some of their implications are discussed below.

(i) The normalized thickness of the CVD films with respect to the step height almost uniquely determines the shape of spacers.—For example, doubling the thickness of the film in order to get a spacer of the same shape with its width doubled is not practical. The width may double but the shape will change to a wedge with a gentler slope. This relationship between the width and slope should be taken into consideration when the spacers are used in the LDD structure or in self-aligned silicide applications, where the shape, as well as width of the spacer, influences the performance of devices.

(ii) The apex of a spacer is always lower than the top of the step by an amount determined by the thickness of the CVD film because of the overetching needed to clear the film.—The thicker the film is, the lower the apex lies, due to the larger overetching required. This has an important bearing when the spacer is used for an isolation between two electrodes, such as the base and emitter in a bipolar transistor (1). Spacers alone cannot provide the necessary isolation. An additional insulating layer and a tight control of the overetching are needed for a successful application of spacers.

Conclusions

In this paper, CVD sidewall spacers formed at the edges of polysilicon lines are studied in detail. We derived analytic expressions for describing a spacer in an ideal situation and verified the effects of various processing parameters on the spacers by experiments and computer simulation. Those parameters that we studied and found important are: (*i*) sidewall slope of polysilicon lines, (*ii*) conformality, thickness, and uniformity of a CVD film, and (*iii*) uniformity, selectivity, and overetching during an RIE step. We reconfirmed the presence of the "bull's-eye" effect and also found the time dependence of selectivity during an RIE, which, we think, was never mentioned in the literature before. We also propose an angular dependence of etch rate in reactive ion oxide etching, whose dependence is not as large as the one observed in ion milling or in sputter etching but is large enough that it must be considered in order to obtain any meaningful agreement between simulation and experiments. Finally, we discussed some inherent limitations of spacers and their implications for device applications. These findings, which are in some sense rather obvious, have been frequently overlooked, leading to a disappointing device performance. Understanding the basic mechanism of spacer formation and optimizing the processing parameters discussed in the paper are necessary in formulating a sidewall-spacer technology with an acceptable device performance.

Acknowledgment

The authors would like to thank J. Malinowski for doing some of the experiments, T. Ross for SEM support, S. Barbee for TEOS deposition, and Yorktown Silicon Facility for processing the samples. Special thanks go to Dr. T. Y. Chiu at the Bell Laboratories, who first suggested how to decorate the sidewall spacers for SEM observation.

Manuscript submitted July 10, 1985; revised manuscript received Oct. 12, 1985.

The IBM Corporation assisted in meeting the publication costs of this article.

REFERENCES

1. D. D. Tang, P. M. Solomon, T. H. Ning, R. D. Isaac, and R. C. Burger, *IEEE J. Solid-State Circuits*, **sc-17,** 925 (1982).
2. S. Ogura, P. J. Tsang, W. W. Walker, D. L. Critchlow, and J. F. Shepard, *IEEE Trans. Electron. Devices*, **ed-27,** 1359 (1980).
3. T. Yamaguchi, S. Morimoto, H. K. Park, and G. C. Eiden, *IEEE J. Solid-State Circuits*, **sc-20,** 104 (1985).
4. Y. Taur, G. J. Hu, R. H. Dennard, L. M. Terman, C. Y. Ting, and K. E. Petrillo, *IEEE J. Solid-State Circuits*, **sc-20,** 123 (1985).
5. L. M. Ephrath, *IEEE Trans. Electron. Devices*, **ed-28,** 1315 (1981).
6. M. Sternheim, W. van Gelder, and A. W. Hartman, *This Journal*, **130,** 655 (1983).
7. P. Marcoux and P. Foo, *Solid State Technol.*, **24,** 115 (1981).
8. J. L. Reynolds and A. R. Neureuther, *J. Vac. Sci. Technol.*, **16,** 1772 (1979).
9. L. M. Ephrath, *This Journal*, **126,** 1419 (1979).
10. M. J. Kushner, *J. Appl. Phys.*, **53,** 2939 (1982).
11. A. G. Nagy, *This Journal*, **131,** 1871 (1984).
12. A. G. Nagy, *ibid.*, **132,** 689 (1985).
13. D. J. Elliott, "Integrated Circuit Fabrication Technology," p. 279, McGraw-Hill, New York (1982).
14. "SAMPLE User Guide," ERL, Univ. of Calif., Berkeley (1983).
15. Y. Sakai, J. L. Reynolds, and A. R. Neureuther, *This Journal*, **131,** 627 (1984).
16. P. J. Tsang, S. Ogura, W. W. Walker, J. F. Shepard, and D. L. Critchlow, *IEEE Trans. Electron. Devices*, **ed-29,** 590 (1982).
17. P. J. Tsang, J. F. Shepard, S. Ogura, and J. Riseman, Abstract 233, p. 373, The Electrochemical Society Extended Abstracts, Vol. 82-2, Detroit, Michigan, October 17-21, 1982.

Analytical Model for Phosphorus Diffusion in Silicon

Kjell O. Jeppson and Dan Anderson

Department of Electrical and Computer Engineering, Chalmers University of Technology, S-412 96 Göteborg, Sweden

ABSTRACT

The problem of diffusion of phosphorus in silicon is investigated using an analytical approach based on similarity methods. The analysis results in simple explicit solutions, which accurately describe all relevant features of the phosphorus diffusion profiles including the properties of the surface region, the kink, and the tail region.

It is well known (1-4), that at high concentrations, the diffusion of phosphorus in silicon gives rise to impurity profiles that deviate significantly from the standard profiles (gaussian and erfc functions) of linear diffusion theory. Phosphorus exhibits some rather complex features, which have not previously been given a consistent analytical description, cf. (1-5). The diffusion profiles generally consist of an almost flat, high concentration surface region with a rather steep descent which abruptly turns into a broad tail region at lower concentrations. This feature gives the impurity profile its characteristic kink. Evaluation of the diffusion profiles, using the Boltzmann-Matano analysis, has revealed a strongly nonlinear, concentration dependent, diffusion coefficient in the surface region. This has been explained by Fair and Tsai (3) in terms of phosphorus-vacancy pair diffusion, involving the doubly negative charged vacancies, $V^{=}$, in the silicon. When the electron concentration drops below a certain concentration, n_e, the phosphorus diffusivity is increased as a result of phosphorus-vacancy pair dissociation. This dissociation creates excess negative charged V^{-} vacancies which enhance the diffusivity. As shown in Fig. 1, the diffusivity increases in the transition region as the electron concentration drops until the kink concentration, n_k, is reached. For lower electron concentrations in the tail region, the diffusivity assumes a constant value, D_{tail}, which is much larger than the nonlinear diffusivity at the kink concentration. However, even if the nonlinearity of the diffusion coefficient has been fairly well established experimentally, there is still a discussion about the physical correctness of the Fair and Tsai diffusion model. Today, this model is widely regarded as an empirical model.

In this paper, we present an analytical model for phosphorus diffusion at high electron concentrations. The surface and the tail regions are treated separately with a discontinuous diffusion coefficient, while the transition region ($n_k < n < n_e$) is neglected. The diffusion coefficient in the two regions is given by

$$D = \begin{cases} D_0 \left(\dfrac{n}{n_i}\right)^2 & n > n_k \\ D_{tail} & n < n_k \end{cases} \qquad [1]$$

where n_i is the intrinsic concentration, $D_0 = hD_i^{=}$ where $h \approx 2$ is the self electric-field enhancement factor, and $D_i^{=}$ is the intrinsic diffusivity of the phosphorus negative charged vacancy pairs. The electron concentration is related to the phosphorus concentration, C, according to

$$n = \frac{C}{2}\left(1 + \sqrt{1 + \left(\frac{2n_i}{C}\right)^2}\right) \qquad [2]$$

which in the nonlinear regime ($C >> 2n_i$) implies $n \simeq C$. D_{tail} denotes the linear diffusion constant in the tail region. Since we neglect the transition region where $n_k < n < n_e$, the diffusion constant makes a discontinuous "jump" at the kink concentration (see Fig. 1). This approximation is justified by the narrow width of the transition region, which is caused by the small difference between n_e and n_k in combination with the very steep descent of the impurity profile in this region.

The purpose of this paper is to present an analytical model for phosphorus diffusion that is based on the experimentally observed nonlinear diffusion coefficient. Our approach avoids the "flat region" simplification (1) and is more complete than the "arsenic model" that has recently been applied to the phosphorus surface region (5). As far as we know, our model is the only analytical model that is attractively simple while covering both the surface and the tail regions. We will also give comparisons with experimental data that show excellent agreement between theory and experiments. This agreement is good even for very high surface concentrations, when the diffusion is retarded due to misfit-induced strain which causes a bandgap narrowing in the silicon.

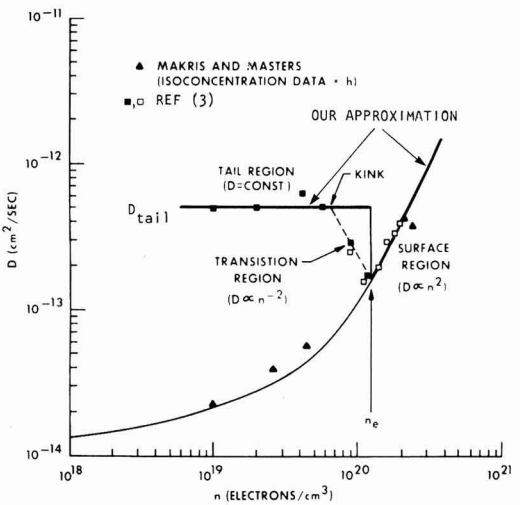


Fig. 1. Phosphorus diffusivity vs. electron concentration in silicon at 1000°. Our approximation of diffusivity is shown as the thick solid line. This figure is from Fair and Tsai (3).

Analysis

The fundamental diffusion equation determining the evolution of the phosphorus impurity profile is

$$\frac{\partial C}{\partial t} = \frac{\partial}{\partial x}\left(D\frac{\partial C}{\partial x}\right) \qquad [3]$$

where $C(x, t)$ is the phosphorus concentration, x and t are the space and time variables respectively, and D is the diffusion constant given by Eq. [1].

In two previous papers (6, 7), we have investigated Eq. [3] in the case of concentration dependent diffusion constants, $D \sim C^{\gamma}$. The analysis relies on similarity methods, and simple explicit solutions are found for two-step diffusion processes involving redistributive drive-in diffusion of an initially shallow implantation profile. Comparison with experimental arsenic profiles showed very good agreement with analytical predictions.

Since the similarity approach was elaborated in some detail in Ref. (6, 7), it is sufficient here to give the main

steps of the analysis and to concentrate on the new features which characterize the diffusion of phosphorus.

If the diffusion is performed under the condition of constant surface concentration, C_s, the proper similarity variable is the Boltzmann variable $\xi = x/\sqrt{t}$ and writing $C(x, t) = \phi(x/\sqrt{t})$ we find the following equation for $\phi(\xi)$

$$-\frac{1}{2}\xi\frac{d\phi}{d\xi} = \frac{d}{d\xi}\left(D(\phi)\frac{d\phi}{d\xi}\right) \quad [4]$$

The conditions on ϕ are: $\phi(0) = C_s$ and $\phi(\xi) \to 0$ as $\xi \to \infty$. In the nonlinear region we obtain ($\tilde{\phi} = \phi/C_s$, $\tilde{\xi} = n_i\xi/C_s\sqrt{D_0}$)

$$-\frac{1}{2}\tilde{\xi}\frac{d\tilde{\phi}}{d\tilde{\xi}} = \frac{d}{d\xi}\left(\tilde{\phi}^2\frac{d\tilde{\phi}}{d\tilde{\xi}}\right) \quad [5]$$

An exact solution of Eq. [5] is not possible, but a good approximation is, cf. (8)

$$\tilde{\phi} = \tilde{\phi}_B(\tilde{\xi}) \simeq (1 - \tilde{\xi}/\tilde{\xi}_0 + \tilde{\xi}^3/(12\tilde{\xi}_0))^{1/3} \quad [6]$$

where $\tilde{\xi}_0^2 = 8/9$. This curve is plotted in Fig. 2 together with erfc and gaussian functions characteristic of linear diffusion and the profile of implanted phosphorus to be discussed later. However, the solution given by Eq. [6] is only valid up to the location of the kink, *i.e.*, for $\tilde{\xi} \le \tilde{\xi}_k$ where $\tilde{\xi}_k$ is determined by the kink condition

$$\tilde{\phi}(\tilde{\xi}_k) = \tilde{\phi}_k \equiv \frac{C_k}{C_s} \quad [7]$$

where C_k is the phosphorus kink concentration.

The steep descent of the impurity profile given by Eq. [6] together with the fact that $C_k/C_s << 1$ imply that $\tilde{\xi}_k$ can be determined from $\tilde{\phi}(\tilde{\xi}_k) \simeq 0$. The corresponding solution is easily found to be

$$\tilde{\xi}_k \simeq 1.035 \quad [8]$$

i.e., the location of the kink, $x_k(t)$, as a function of time is determined by

$$x_k(t) \simeq 1.035\frac{C_s}{n_i}(D_0 t)^{1/2} \quad [9]$$

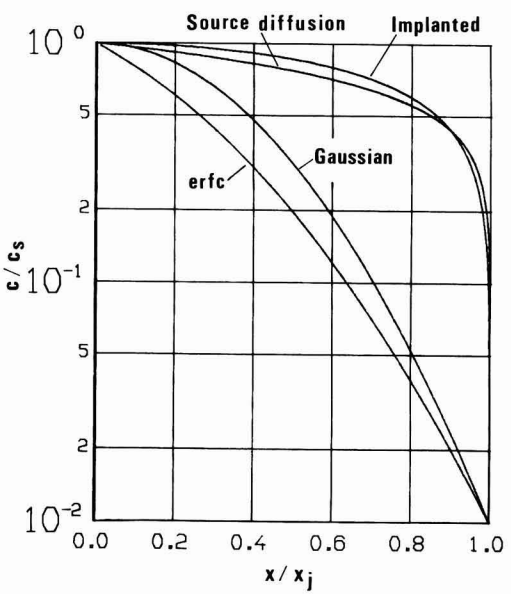


Fig. 2. Normalized impurity profiles for the phosphorus surface region for the case of source diffusion with constant surface concentration and implanted phosphorus after redistributive diffusion, respectively. The Gaussian and erfc profiles are given for comparison.

For concentrations $C < C_k$ the diffusion equation becomes linear, viz.

$$-\frac{1}{2}\xi\frac{d\phi}{d\xi} = D_{tail}\frac{d^2\phi}{d\xi^2} \quad [10]$$

for which the initial condition is $\phi(\xi_k) = \phi_k$. The corresponding solution is ($\bar{\xi} = \xi/2\sqrt{D_{tail}}$)

$$\phi = \phi_T(\bar{\xi}) = C_k\frac{\mathrm{erfc}(\bar{\xi})}{\mathrm{erfc}(\bar{\xi}_k)} \quad [11]$$

Summing up the solutions in the two domains we find

$$C \simeq \begin{cases} C_s(1 - \tilde{\xi}/\tilde{\xi}_0 + \tilde{\xi}^3/(12\tilde{\xi}_0))^{1/3} & \tilde{\xi} < \tilde{\xi}_k \\ C_k\dfrac{\mathrm{erfc}(\bar{\xi})}{\mathrm{erfc}(\bar{\xi}_k)} & \bar{\xi} > \bar{\xi}_k \end{cases} \quad [12]$$

where $\tilde{\xi} = n_i x/(C_s\sqrt{D_0 t})$, $\tilde{\xi}_0 = \sqrt{8/9}$, $\tilde{\xi}_k \simeq 1.035$, $\bar{\xi} = x/\sqrt{4D_{tail}t}$, and $\bar{\xi}_k = 1.035(C_s/2n_i)\sqrt{D_0/D_{tail}}$.

We now turn to investigate the drive-in diffusion of a predeposited impurity profile, which implies diffusion under the condition of constant dose. The similarity solution in this case, assuming $D = D_0(C/n_i)^2$ and an initially very narrow profile, is (6)

$$C(x, t) = C_s(t)\left(1 - \frac{x^2}{x_j^2(t)}\right)^{1/4} \quad [13]$$

where the surface concentration, $C_s(t)$, and the position of the diffusion front, $x_j(t)$, are given by

$$C_s(t) = \left(\frac{4}{\pi^2}\frac{Q_0^2 n_i^2}{D_0 t}\right)^{1/4}$$

$$x_j(t) = \left(\frac{64}{\pi^2}\frac{Q_0^2 D_0 t}{n_i^2}\right)^{1/4} \quad [14]$$

and Q_0 is the total number of impurities. This impurity profile is also included in Fig. 2.

However, the solution given by Eq. [13]-[14] is only valid for concentrations $C > C_k$ and the solution must be complemented by a linear solution for $C < C_k$. Unfortunately, the similarity solutions involve different similarity variables for $C > C_k$ ($\xi = x/t^{1/4}$) and $C < C_k$ ($\xi = x/t^{1/2}$), respectively.

This excludes a simple solution in the whole domain although approximate solutions can be given which make use of the different characteristic time scales for the respective diffusion process. Nevertheless we will not pursue this idea, but will simply emphasize the result that the kink position $x_k(t)$ can be approximately identified with the position of the diffusion front, *i.e.*

$$x_k(t) \simeq x_j(t) \cong \left(\frac{Q_0^2 D_0 t}{n_i}\right)^{1/4} \quad [15]$$

Discussion and Comparison with Experiments

In this section we intend to discuss the results of our analytical analysis and to compare the theoretical predictions with experimental data. First of all, we emphasize the fact that the presently obtained nonlinear impurity profiles will consist of a very flat surface region with a steep descent which abruptly, at the kink concentration, turns into a broad tail region. This is qualitatively in very good agreement with observed profiles, cf. (1-4). This emerges naturally as a consequence of the assumed diffusion coefficient.

In the surface region, the diffusivity is given by Eq. [1], where $D_i^= = 44.2\exp(-4.37/kT)$ cm²/s is the intrinsic diffusivity of the phosphorus-vacancy pairs and kT is the thermal energy in eV. The depth of the surface region or equivalently, the kink depth, is given by Eq. [9] as

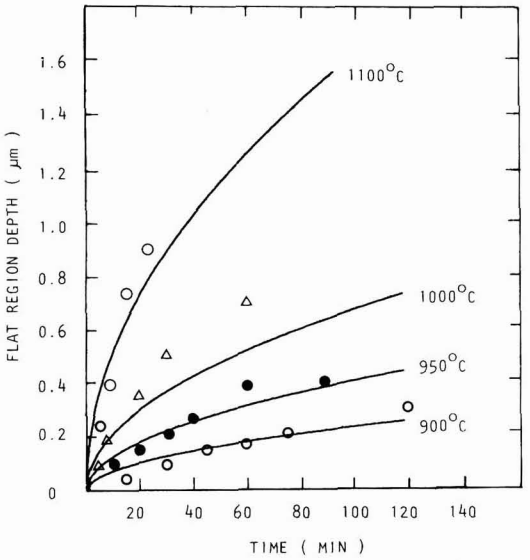


Fig. 3. The depth of the surface region plotted vs. diffusion time. The solid lines are the theoretical values from Eq. [16] and the dots are experimental values from Ref. (1, 3).

$$x_k = 1.035\ (C_s/n_i)\sqrt{2D_i^- t} \qquad [16]$$

This depth is plotted for different temperatures in Fig. 3 and compared to experimental data given by Tsai (1) and Fair (4). Excellent agreement between theory and experiments is shown, except at 1000°C.

When the electron concentration drops below n_e, the phosphorus diffusivity is increased as a result of the phosphorus-vacancy pair dissociation when the Fermi level drops 0.11 eV below the conduction band. This dissociation creates excess V^- vacancies which enhance the diffusivity. The diffusivity increases (as $1/n^2$) until the kink concentration $n_k \approx C_k$ is reached when the tail diffusivity assumes a constant value. In our model, the transition region between n_e and n_k is neglected and we instead assume a step change in the diffusivity at the kink concentration. This enhanced tail diffusivity is given by Fair and Tsai (3) as

$$D_{tail} = \frac{n_s^3}{n_e^2 n_i}[1 + \exp(0.3/kT)]$$

$$4.44 \exp(-4.0/kT)\ \text{cm}^2/\text{s} \qquad [17]$$

where the electron concentration n_e is given by $n_e = 4.65 \cdot 10^{21} \exp(-0.39/kT)\ \text{cm}^{-3}$. The kink concentration, n_k,

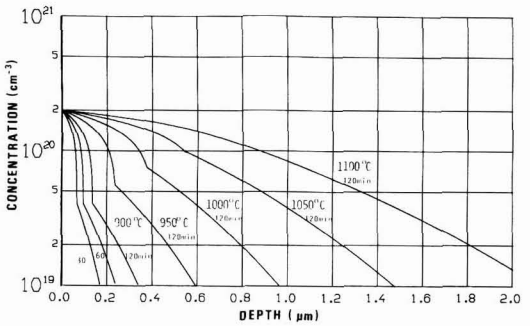


Fig. 4. Theoretical impurity profiles at five different temperatures. Note that the kink that is predominant at lower temperatures has disappeared at 1100°.

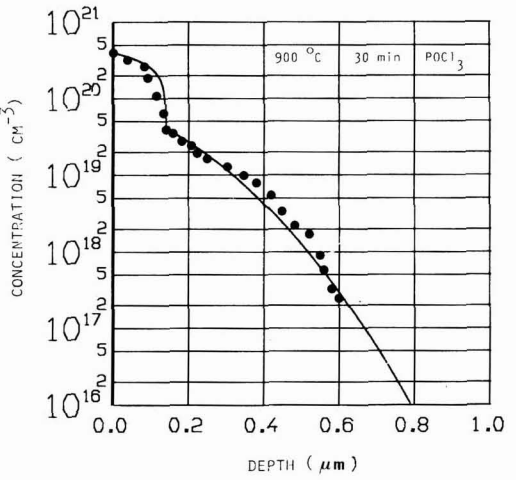


Fig. 5. Calculated and measured (3) total phosphorus profiles in silicon after 30 min of $POCl_3$ diffusion at 900°C.

where the diffusivity changes, is given by $n_k = 1.0 \cdot 10^{23} \exp(-0.79/kT)\ \text{cm}^{-3}$. Both of these two values are derived from Fair and Tsai (3).

In Fig. 4, the theoretical phosphorus impurity profile after 30 min of diffusion at different temperatures is shown for a surface concentration of $C_s = 2 \cdot 10^{20}\ \text{cm}^{-3}$. As expected, the kink is most evident at low diffusion temperatures and has almost disappeared at 1100°C.

In Fig. 5, the calculated and measured (3) total phosphorus concentration profiles in silicon are shown for a 30 min, $POCl_3$ source, diffusion at 900°C. Excellent agreement between theory and experiments is found, in both the surface and the tail regions. The theory is shown to be accurate enough also for junction depth determination in the tail region.

Yoshida *et al.* (9) and Fair and Tsai (3) have shown that the Boltzmann variable, $x/\sqrt{t}$, is the proper variable, since for constant surface concentration, phosphorus diffusion profiles obtained at different diffusion times and temperatures practically fall on top of each other when

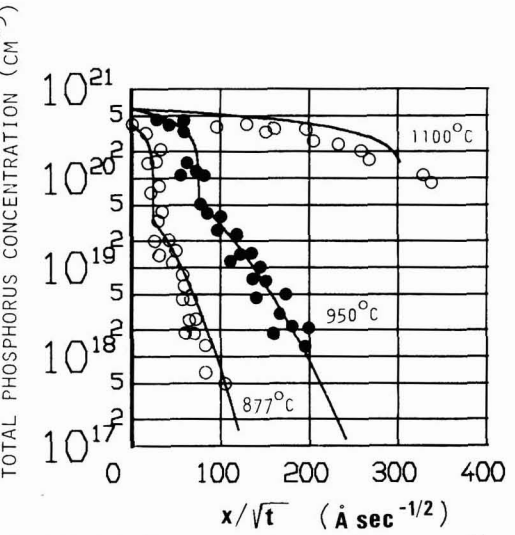


Fig. 6. Total phosphorus concentration vs. the Boltzmann-variable, $x/\sqrt{t}$, for three different temperatures. Experimental data from Fair and Tsai (3).

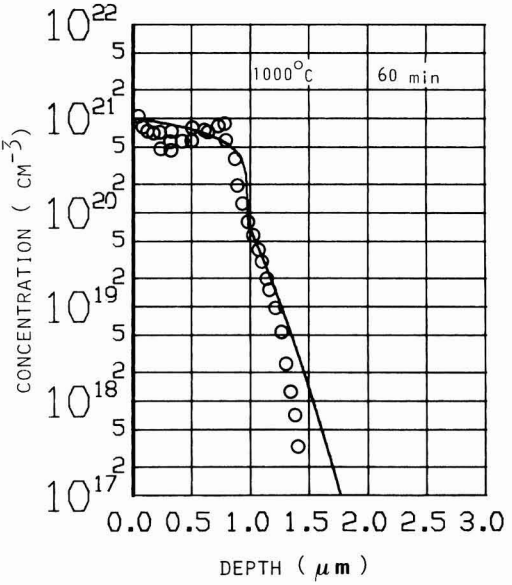


Fig. 7. Calculated and measured (10) total phosphorus profiles in silicon after 60 min of $POCl_3$ diffusion at 1000°C. The effect of strain-induced bandgap narrowing ($\Delta E_G = -0.08$ eV) is included.

plotted in this scale. This is shown in Fig. 6, where the experimental data supplied by Fair and Tsai (3) are plotted together with our theoretical curves. As shown, there is excellent agreement between theory and experiment.

For surface concentrations above 4-5 · 10^{20} cm^{-3}, Fair (10) has shown that both the nonlinear and the tail diffusivities are retarded. This has been explained by a misfit-induced lattice strain which changes slowly in depth compared to the phosphorus diffusion length. Strain induced by tensile stress causes a bandgap narrowing which will reduce the nonlinear diffusivity according to

$$D_o^s = D_o \exp(\Delta E_G/kT) \quad [18]$$

and the tail diffusivity according to

$$D_{tail}^s = D_{tail} \exp(3\Delta E_G/kT) \quad [19]$$

where the s superscript indicates the diffusion coefficients due to strain and ΔE_G is the bandgap narrowing at the surface. The effect of bandgap narrowing makes the analytical expressions, derived under no stress, applicable also under stress at high surface concentrations, when the number of electrons, n, begin to deviate from the total phosphorus concentration, C. In Fig. 6, the 950° and 1100°C-curves have been plotted with $\Delta E_G = -0.025$ eV.

In Fig. 7, an experimental (10) high surface concentration impurity profile obtained after 60 min of, $POCl_3$ source, diffusion at 1000°C is shown. Our theoretical curve has been plotted with a bandgap narrowing of −0.08 eV, retarding the nonlinear diffusivity according to Eq. [18] and giving a tail diffusivity, $D_{tail} = 2.45 \cdot 10^{-13}$ cm^2/s, according to Eq. [19]. These values agree exceptionally well with those found by Fair (10).

Conclusions

An analytical model describing the nonlinear and tail diffusion of phosphorus has been presented. This model fits the experimental data of the nonlinear impurity profile in the surface region and its depth extremely well. The physical background of the model makes it clearly superior to the "flat region" model (1) and the "arsenic model" that has recently been applied to phosphorus (5).

Even though the tail region has been approximated with a single erfc-function, and the transition region has been neglected, the model gives an excellent description of the tail. Also, at very high surface concentrations close to the solid solubility limit, this analytical model is applicable with excellent results if the effect of reduced diffusivity due to the bandgap narrowing under lattice strain is included.

Manuscript submitted June 10, 1985; revised manuscript received Nov. 4, 1985.

Chalmers University of Technology assisted in meeting the publication costs of this article.

REFERENCES

1. J. C. C. Tsai, *Proc. IEEE*, **57,** 1499 (1969).
2. F. N. Schwettmann and D. L. Kendall, *Appl. Phys. Lett.*, **21,** 2 (1972).
3. R. B. Fair and J. C. C. Tsai, *This Journal*, **124,** 1107 (1977).
4. R. B. Fair, *ibid.*, **125,** 323 (1978).
5. W.-S. Wang and Y.-H. Lo, *IEEE Trans. Electron Devices*, **ed-30,** 1828 (1983).
6. D. Anderson and K. O. Jeppson, *This Journal*, **131,** 2675 (1984).
7. D. Anderson and K. O. Jeppson, *ibid.*, **132,** 1409 (1985).
8. D. Anderson and M. Lisak, *Phys. Rev. A.*, **22,** 2761 (1980).
9. M. Yoshida, E. Arai, H. Nakamura, and Y. Terunuma, *J. Appl. Phys.*, **45,** 1498 (1974).
10. R. B. Fair, *ibid.*, **50,** 860 (1979).

Fabrication of Highly Reliable Tungsten Gate MOS VLSI's

N. Yamamoto, H. Kume, S. Iwata, K. Yagi, and N. Kobayashi

Central Research Laboratory, Hitachi, Limited, Kokubunji-shi, Tokyo 185, Japan

N. Mori and H. Miyazaki

Nippon Mining Company, Limited, 2-10 Toranomon Minato-ku, Tokyo 105, Japan

ABSTRACT

Recently, refractory metals, such as W and Mo, with low resistivity and a high melting point have received keen interest as materials for gate electrodes and interconnects for MOS VLSI's. However, it is commonly believed that MOS devices with refractory metal gates have low reliability due to mobile ion contamination. In this work, it was clarified that W gates with commercially available W sputtering targets introduced high level mobile charges into the gate oxide. It was also found that the rates of degradation of W gate MOS transistors due to hot carriers were higher than those of poly-Si gates, and the internal stresses in W gates increased the degradation rates. Therefore, the authors developed a high purity W sputtering target fabrication technique through the use of electron melting. A W gate annealing technique was developed to reduce the internal stress in W films. Through these techniques, the above-mentioned problems can be eliminated, and W gate devices that have characteristics comparable to those of poly-Si gates can be produced.

The minimum feature size of very large-scale integrated circuits (VLSI's) has been reduced to one micrometer or even less, while at the same time the number of elements per chip continues to increase. Under the present D-RAM developmental situation, a 256kb D-RAM has reached the stage of practical use, and 1Mb D-RAM prototypes have been examined and tested by a number of LSI makers (1-3). These developments have imposed severe demands on the materials and interconnects in MOS VLSI's.

The technical and material outlook for gate electrodes and interconnects of future generation MOS VLSI's is shown in Fig. 1. Polycrystalline silicon is widely used in MOS VLSI's. However, its high resistivity causes degradation in circuit speed due to R-C delay time. If poly-Si is used as a word line of a 256kb or 1Mb D-RAM, the delay time at the word line increases at a rapid rate.

Gate electrodes and interconnects made of silicides of refractory metals (4) or their "polycides"[1] (5, 6) have attracted more and more interest over the past few years.

However, it is apparent that the signal delay caused by the resistance they exhibit will become a serious problem in Mb-level VLSI's, even in silicide gates. Thus, pure metals such as Mo and W are being considered as materials for MOS gates. A new process for W gate MOS has been developed (7-9), which makes W attractive for VLSI application. For practical applications, the process using W must be reliable and the MOS characteristics must be stable over a long period of time. In this paper, problems with regard to fabrication processes or MOS characteristic reliability are discussed, and the solutions to the problems are presented.

Major Problems of Tungsten Gates

Refractory metals, such as W and Mo, as alternative materials for low resistance gate electrodes, have been considered many times over the past years. However, many important problems have been left unsolved. The first of these is that W films peel off SiO_2 during the patterning processes for gate electrodes and interconnects. The second problem is that these metals cannot withstand high temperature oxidizing ambients during IC fabrication. The third problem is that films such as W and Mo cannot block implanting ions during the formation of self-aligned junctions. This formation technique is used in conventional poly-Si gate MOS technology. The fourth problem is instability or degradation caused by mobile charges and hot carriers. The first, second, and third problems degrade process reliability, and the fourth problem reduces the reliability of MOS characteristics. Techniques for solving the second and third problems have already been described in previous papers (7, 9). The purpose of this study is to reveal the performance of W gate MOS devices, which hitherto have lacked reliability, and to develop a fabrication technique for highly reliable W gate MOS VLSI's.

[1]Silicide/poly-Si structure.

Experimental

Device fabrication.—A p-type silicon wafer with (100) orientation and 10 Ω · cm resistivity was used as the substrate for fabrication of MOS devices with 10-20 nm thick gate oxide.

Tungsten films were deposited on the wafer by a dc planar magnetron sputtering device. Cathodes (targets) were bonded to a Cu backing plate and were water-cooled through the plate.

The W targets used in this study were (*i*) commercially available sintered target of 99.95% purity and (*ii*) high purity target made by using the electron beam melting method.

After evacuating the chamber down to 2×10^{-5} Pa and heating the substrates to 300°C, Ar gas of 99.995% purity was introduced into the vacuum chamber. The working pressure of Ar was kept between 0.13 Pa and 3.0 Pa. The internal stress in the W film was controlled with Ar pressure. This stress influences the adhesion of W film to SiO_2 (7). The thickness of the W films was 350 nm. The films were then etched to pattern the gates using a parallel plate plasma reactor containing SF_6 gas.

Heat-treatment for fabrication of MOS devices after the deposition of the metals was carried out in an appropriate ambient, *e.g.*, O_2-free N_2, H_2, or H_2 containing H_2O. In conventional silicon gate technology, self-aligned junctions are generally produced by implantation through the gate oxide, with the poly-Si gate acting as an ion implantation mask. However, the W gate could not completely block As^+ ions from being implanted in the Si substrate due to

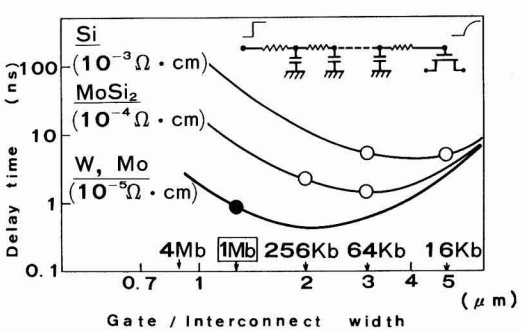


Fig. 1. Technical and material outlook for gate electrodes and interconnects of future generation MOS VLSI's.

channeling (7, 8). Therefore, the W was coated with phospho-silicate glass (PSG) to prevent channeling. PSG was also used as an insulator between W and Al interconnect layers in MOS VLSI's.

Analysis of impurities in W.—The impurity densities in the W targets and films were quantitatively analyzed, as follows. A flameless atomic absorption (FLAA) spectrophotometer was used for obtaining Na and K concentration. The U impurity concentration determined by using a (solid) fluorescence spectrometer and by a solid spark mass spectrograph method was applied to determine the concentration of other impurities. The lower limits of detection for Na, K, and U were 10 ppb, 20 ppb, and 2 ppb, respectively.

Results and Discussion

Almost all MOS devices with refractory metal gates, such as W and Mo, have been thought to have low reliability. The factors that have degraded the reliability of W gate devices and fabrication process W gates were evaluated, and prevention techniques for the problems were developed.

Process reliability.—The SiO_2 films around W gate electrodes may be damaged or contaminated during patterning and implantation. Thus, the dielectric integrity of the SiO_2 can become severely degraded.

In conventional poly-Si gate technology, these SiO_2 films are usually regrown in an O_2 ambient after removal. However, similar techniques have not been developed for refractory metal gate technologies, because refractory metals have poor resistance in an oxidizing ambient.

In this work, a novel heat-treatment has been developed where Si can be oxidized in the presence of W without oxidizing the W. This technique is called wet hydrogen (WH) heat-treatment, because an H_2 atmosphere containing an appropriate amount of H_2O is used. With regard to this technique, other papers (7, 8) published by the authors are available for reference.

Next, adhesion of W to SiO_2 will be discussed. It is important that refractory metals such as W and Mo have good adhesion to SiO_2. Tungsten was chosen because its reaction with SiO_2 was minimal (7, 9). However, good adhesion to SiO_2 was not always obtained. After comparing the adhesion and internal stress in W, it was found that W did not peel off SiO_2 when the internal stress was less than 5×10^9 dyne/cm^2 (tensile). This was accomplished by controlling the Ar pressure during W sputtering, as shown in Fig. 2. The results for Mo are also shown in this figure. Molybdenum films indeed tended to peel off SiO_2 after patterning, which is in agreement with the results shown in Fig. 2. The dependence of internal stress in W films on Ar pressure showed results similar to those obtained by Wagner (10). In general, it is said that the internal stress of deposited films by sputtering becomes tensile for films with fewer trapped impurities, while it becomes compressive for films with highly trapped impurities (11). However, the results of this study showed that the resistivity of films with compressive internal stresses ($\sigma = -10^{10}$ dyne/cm^2, $\rho = 11\ \mu\Omega \cdot$ cm) were lower than that of films with tensile internal stresses ($\sigma = +1 \times 10^9$ dyne/cm^2, $\rho = 16\ \mu\Omega \cdot$ cm), which was consistent with Wagner's results.[2]

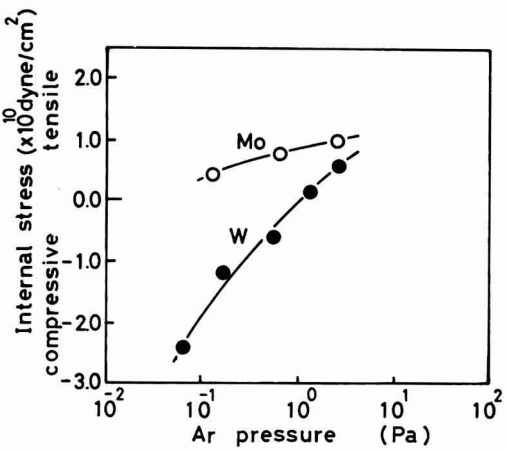


Fig. 2. Variation of W and Mo film stress with Ar pressure during sputtering. Power: 2.5 kW, substrate temperature: 300°C.

Reliability of MOS Characteristics

Charges in SiO_2.—X-rays, electrons, and photons are the radiation damage sources that can generate charges in the gate oxides (12). Therefore, the charges produced in SiO_2 during W deposition by magnetron sputtering were evaluated (a comparison of radiation damage that occurred during electron beam evaporation and magnetron sputtering for metallization is discussed in the Appendix).

The midgap surface-state densities (N_{ss}) at the SiO_2/Si substrate interfaces were determined by quasi-static and high frequency C-V measurements and an MIS conductance method. The N_{ss} of MOS capacitors before any heat-treatment were $1 \sim 3 \times 10^{11}$ cm^{-2} eV^{-1}. After annealing in nitrogen at 900° ~ 1000°C for 30 min, N_{ss} was reduced to $\leq 2.5 \times 10^{10}$ cm^{-2} eV^{-1}. This is comparable to the $\leq 2 \times 10^{10}$ cm^{-2} eV^{-1}, N_{ss} of poly-Si gate MOS capacitors.

Solomon (13) determined the charges in SiO_2 near the SiO_2/Si substrates from hysteresis of the Fowler-Nordheim current (I-V characteristics), which was induced by electron injection into SiO_2 from a Si substrate. In this work, the Fowler-Nordheim injection technique of Solomon was applied to determine the charges near the W-gate/SiO_2 interfaces. The substrate temperatures (preheating temperature for samples before W deposition), T_{sub}, were 25° and 300°C, and the deposition rate was 2.5 nm/s. Following the deposition, W films were annealed out in flowing N_2 gas at 1000°C for 30 min. The I-V curves, the ramp voltages of which were applied to the samples, were measured using p-type wafers with a negative gate polarity. The ramp rate was 0.3 V/s. Ramp voltages were continuously applied twice to the same sample. No ledge-like characteristics were seen and no hysteresis appeared between the initial and second ramp I-V curves, as shown in Fig. 3. It was considered that the trap centers at the W-gate/SiO_2 interfaces were $\leq 5 \times 10^{10}$ cm^{-2} (this value was the detection limit of our system), and this value was comparable to that of poly-Si gate MOS capacitors.

Next, flatband voltages (V_{FB}) were obtained from C-V measurements at a frequency of 1 MH$_z$ on capacitors with various gate oxide thicknesses (t_{ox}). The physical contribution to V_{FB} may be the result of the work-function difference between the gate electrode material and silicon (Φ_{ms}), as well as the fixed surface charge density (Q_{ss})

$$V_{FB} = \Phi_{ms} - \epsilon_{ox} Q_{ss} t_{ox} \qquad [1]$$

ϵ_{ox}: permittivity of gate oxide (F/cm).

The V_{FB} of W gate capacitors is shown as a function of t_{ox} in Fig. 4. The Q_{ss} was calculated from the slope of the curve. The slopes are usually negative for poly-Si and Al gates, which means that Q_{ss} values are positive charges. However, the slope of V_{FB}-t_{ox} characteristics of W gate capacitors before high temperature annealing (1000°C) in nitrogen was positive, showing Q_{ss} to be negative with a value of 2.6×10^{11}/cm^2 obtained from Fig. 4. The mechanism of negative charge generation was not clear from the results of this experiment, but we estimated that these charges were produced by the damage incurred during W deposition or W dry etching. After high temperature an-

[2]He indicated that the amount of oxygen incorporated in the W films with tensile stress was more than that of compressive stress films. However, the impurities in W films (O, Ar, N) were lower than the detection limits of Auger electron spectroscopy and mass spectroscopy.

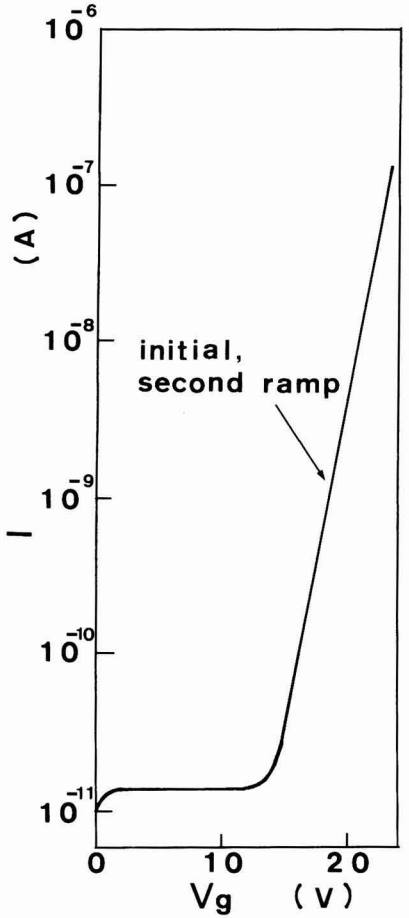


Fig. 3. Sequential ramp I-V characteristic of W gate MOS capacitor made of W film deposited using dc magnetron sputtering. The first ramp voltages rose to 16V and the second ramp voltages followed immediately afterward. The capacitor was annealed N_2 at 1000°C for 30 min. Ramp rate = 0.3 V/s, SiO_2 = 20 nm.

nealing, the slope changed to negative. Therefore, Q_{ss} was positive, and its density was decreased to $2 \times 10^{10}/cm^2$. This value was comparable to that of a poly-Si gate capacitor ($\leq 4 \times 10^{10}/cm^2$).

From the experiments described above, it appeared that the damage inflicted on the MOS devices during W deposition by magnetron sputtering was reduced by N_2 high temperature annealing, and the characteristics of W gate MOS devices related to the charges in SiO_2 were comparable to those of poly-Si gates.

Breakdown voltage of gate oxides.—The breakdown voltages of gate oxides (SiO_2) 10 and 20 nm thick with rectangular-shaped gate electrodes were compared for W gate and poly-Si gate MOS capacitors (Fig. 5). The breakdown voltages of the W gate MOS capacitors were higher than those of poly-Si gate capacitors. The difference observed is considered to be due to the following factors.

(i) *Difference between their work functions.*—Their work functions were evaluated from the C-V measurements shown in Fig. 4. The work functions of W and poly-Si gates were 4.7 ± 0.1 eV and 4.1 ± 0.1 eV, respectively. The breakdown voltage was taken to be the gate voltage at which I_{leak} = 10 nA. The leak current in insulators flows according to the Fowler-Nordheim equation at the current level. Therefore, the breakdown voltage depends on the work function of the gate electrode. Thus, the breakdown voltages of W gate capacitors appear higher than those of poly-Si.

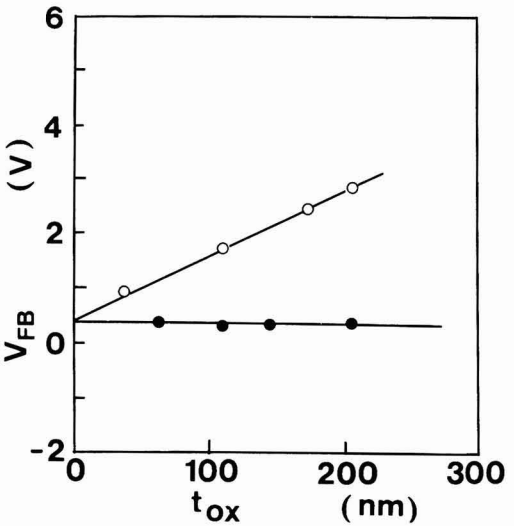


Fig. 4. Flatband voltage (V_{FB}) as a function of gate oxide thickness (t_{ox}). Open circle: before N_2 annealing; Closed circle: after N_2 annealing at 1000°C for 30 min.

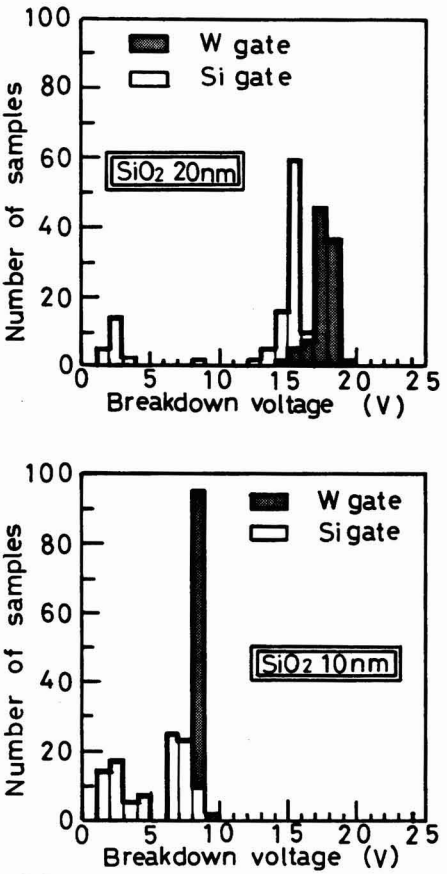


Fig. 5. Comparison of breakdown voltages for W gate and poly-Si gate MOS capacitors.

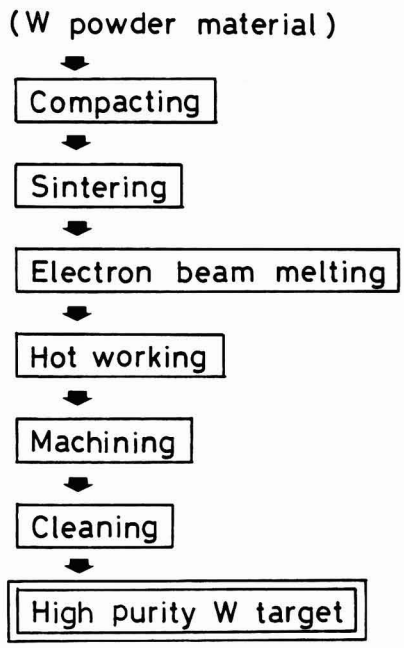


Fig. 6. Process flow for fabrication of high purity W targets

(ii) *Reaction between gate electrode and SiO_2.*—No reaction at the W/SiO_2 interface was observed, even at 1200°C, a result in agreement with thermodynamic considerations. The free energy of SiO_2 formation, ΔG at 1100°C, is −3.44 eV and is more negative than that of W oxides (WO_2 = −1.92 eV, WO_3 = −1.73 eV) (14). On the other hand, poly-Si gates reduced SiO_2 by a heat-treatment at 1000° ~ 1200°C (15).

(iii) *Diffusion of phosphorus.*—The penetration of phosphorus from a poly-Si gate into SiO_2 may degrade the gate oxide. However, this was not clarified in the present work.

Mobile ion contamination.—Reducing the mobile ions in a gate oxide is necessary to obtain highly reliable MOS devices.

In the case of metal gate MOS devices, the mobile charge is mainly introduced by impurities such as Na or K in the metal. When a W gate was not coated with PSG during annealing, the V_{FB} of the MOS capacitors was shifted by the bias-temperature stress test (3 MV/cm, 200°C, 30 min). The mobile ion density was estimated to be higher than 5×10^{11} cm^2.

However, for a W gate coated with PSG, in the carefully fabricated MOS, capacitors were equal to or less than 5×10^{10} cm^{-2}. However, this value is low enough to obtain highly reliable MOS VLSI's. For example, the V_{FB} of a poly-Si gate capacitor was not shifted by the bias-temperature stress test. The above results were values for W gate MOS devices made using a 99.95% (3*N*) purity W sputtering target. This purity is the highest grade among commercially available W targets.

Attempts, therefore, were made to obtain W targets of higher purity. The process-flow of the production of high purity targets is shown on Fig. 6. The most important process in this technology is electron beam melting. In the case of W, the W ingot was heated up to about 4500°C. All processes were carried out using extremely clean equipment. A comparison of the impurity concentration of this new high purity target with that of a commercially available target is shown in Table I. The Na or K impurity concentration in the new target was reduced to two or three orders of magnitude below that in the commercially available W target. This new target was obtained from W powder with a purity of 99.95% by using the processes shown

Table I. Comparison of impurities for a new high purity W target and a commercially available 99.95% pure W target

W target	Impurity (ppb) Na	K	U
New high purity target	10 ~ 20	20 ~ 50	5 ~ 7
Commercially available target	10,000 ~ 100,000	[a]	[a]

[a] Not analyzed.

Table II. Impurities in W films formed using a new high purity W target and a commercially available W target

W film	Impurity (ppb) Na	K	U
Sample I (new target)	<10	44	<2
Sample II (new target)	<10	20	<2
Sample III (commercially available target)	170	720	5

in Fig. 6. These processes are similar to that for obtaining high purity Mo targets, as described by Amazawa *et al.* (16), except for the initial processes for obtaining the high purity Mo powder that was included.

The impurities in W films were quantitatively analyzed, as represented by Table II. Samples I and II were W films deposited using the new high purity target shown in Table I. The commercially available target with the highest purity level was used for the preparation of

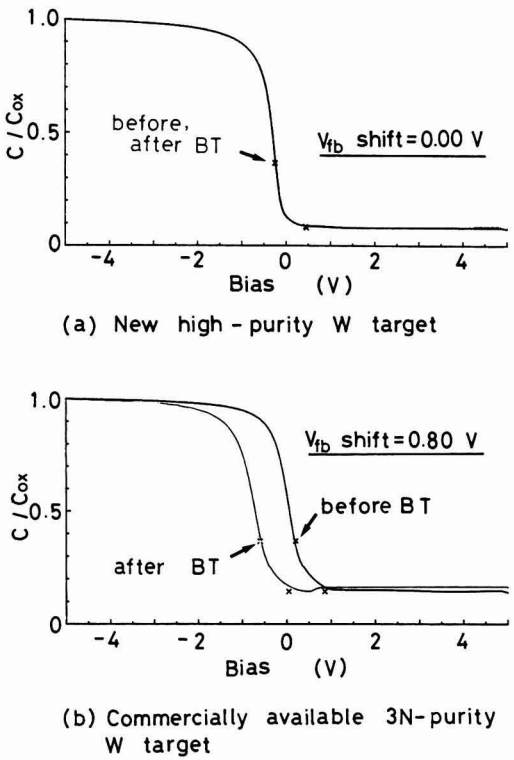


Fig. 7. C-V characteristics before and after bias-temperature stress testing. Bias = 3 MV/cm, temperature = 200°C, time = 30 min.

sample III. Generally speaking, the impurities in the films were reduced from those in the W targets.

In Fig. 7, the C-V characteristics before and after the bias-temperature stress test were measured for the MOS capacitors with W films, as shown in Table II. The V_{FB} shifts of the samples with new high purity W targets were not detectable. On the other hand, the V_{FB} shifts of the capacitors fabricated by the commercially available W targets were distributed in the range of −0.8 to −3V.

Soft error caused by radioactive impurities is another important problem of MOS VLSI's. The U impurities in W films formed from the new high purity target were less than 2 ppb, the lower limit of detection (Table II). Thus, it is believed that this new target is effective for prevention of soft error in MOS VLSI's.

Hot carrier effects.—Hot carrier injection into the gate oxide of narrow channel MOS transistors is another important problem facing MOS VLSI's.

In the various mechanisms already reported, the injection of hot holes into SiO_2 causes the most significant degradation of the threshold voltage (V_{th}) and the transconductance (g_m) of MOS transistors (17, 18).

The hot holes are generated by avalanche multiplication in the high field near the MOS transistor drain.

The degradations of g_m due to hot holes were evaluated, and a comparison between W gate and poly-Si gate narrow channel MOS transistors is shown in Fig. 8.

Lifetime (τ) is defined as the time it takes g_m to be reduced 10% from the initial transconductance (g_{mo}). The horizontal axis of the figure shows the substrate current (I_{SUB}). The substrate current is proportional to the number of electro-hole pairs generated due to avalanche multiplication in the region near the drain. The measurement was carried out at the gate voltage (V_{GS}) and source/drain voltage (V_{DS}) condition, in which the substrate current was at its maximum ($I_{SUB(max)}$). The substrate current as a function of the gate voltage is shown in Fig. 9. The MOS transistors had an abrupt junction with a single-drain structure. The lifetimes of the transistors fabricated using our conventional W gate process (9) (sample A) were

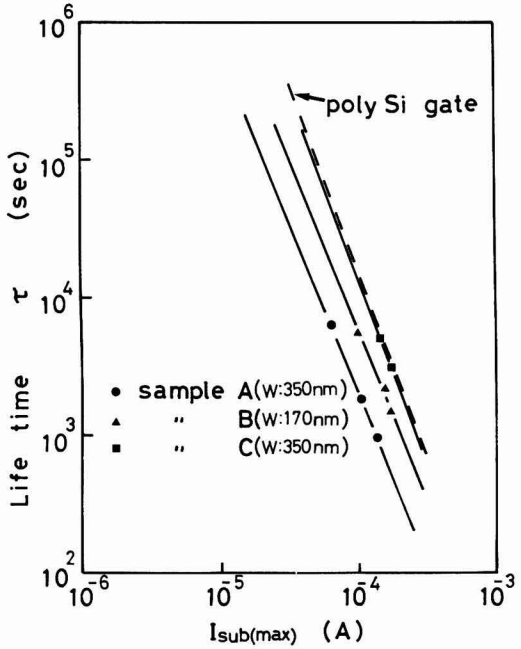


Fig. 8. Degradation characteristics of the transconductance of a narrow channel MOS transistor due to hot carriers. At $\Delta g_m/g_{mo} = 10\%$, $L_{eff} = 0.9m$, $W_D = 10m$, $SiO_2 = 20$ nm.

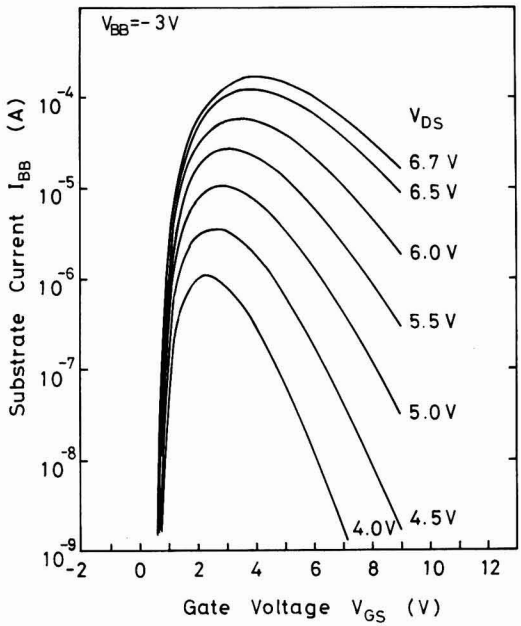


Fig. 9. Substrate current as a function of gate voltage with source-drain voltage as a parameter.

shorter than those of poly-Si gate devices by about one order of magnitude.

The injection of hot hole and electron pairs into SiO_2 is said to generate fast surface states (N_{ss}) at the SiO_2/Si substrate interface (17). The degradation due to this mechanism is considered to be caused mainly by the generation of N_{ss} (17). Therefore, N_{ss} was obtained with the quasi-static C-V characteristics or the I_{DS}-V_{DS} characteristics.

The results were given in the previous section. These values were nearly equal to those determined for a poly-Si gate. The rate of degradation of the transconductance is found to be proportional to the rate of increase of the surface-state density (17, 18).

$$\frac{\Delta g_m}{g_{mo}} \propto \frac{\Delta N_{ss}}{N_{sso}} \qquad [2]$$

The index "o" corresponds to an unstressed case. The same relationship was obtained for W gate and poly-Si gate MOS transistors, as shown in Fig. 10. The $\Delta N_{ss}/N_{sso}$

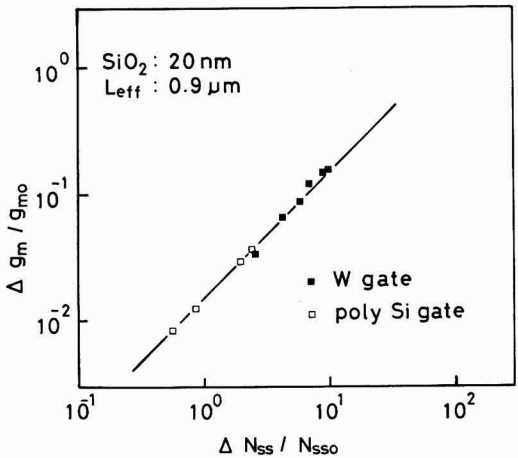


Fig. 10. Relationship between the rate of degradation of transconductance and the rate of increasing of surface-state density.

of W gate devices is greater than that of poly-Si gate devices, as evident from Fig. 10. Whether the gate materials directly influence the rate is questionable. We estimated that the gate material indirectly influences $\Delta N_{ss}/N_{sso}$ via the internal stress values in W films from the following study. The W films of the above experimental samples had strong compressive internal stress values of about 1.5 $\times$ 10^{10} dyne/cm^2.[3]

However, the internal stress of poly-Si films (gates) was a weak internal stress ($\leq 2 \times 10^9$ dyne/cm^2, tensile or compressive). Therefore, it appears that the effect of the force applied to gate oxides or Si substrates by the internal stress in gate electrodes is sensitive to the degradation rates of MOS transistors due to hot carriers. The following experiments were performed according to this hypothesis. Sample B, the gate electrode of which was made of a W film of about half the thicknesses of that in sample A, was fabricated, so that the force applied to the active region of the MOS transistor was reduced to half that of sample A. The lifetime of sample B was improved to about three times as long as that of sample A, as shown in Fig. 8. Many defects that were induced by the internal stresses in W gates were obtained at the active regions in Si substrates under gate electrodes of long-channel and wide-width MOS transistors. The number of defects in sample A was more than twice that in sample B. On the basis of these experiments, a new technique to prevent degradation due to hot carriers on W gate devices was developed. Its key point is the annealing process following W deposition added to our conventional W gate process (9). It was found that annealing at a temperature of 900°C or higher in a N_2, H_2, or H_2 + H_2O atmosphere decreased the internal stress in W films to about 2×10^9 dyne/cm^2 tensile stress. By applying the new technique, it was possible to eliminate the defects that appeared at the active region of the MOS transistors, and the degradation due to hot carriers was reduced. The internal stress in the W gate of sample C after W deposition was comparable to that of sample A. Following W deposition, the new technique was applied to sample C. Annealing was carried out at 950°C for 30 min in N_2. The $\tau - I_{SUB(max)}$ characteristics of sample C were also shown in Fig. 8. The characteristics were improved to the same level as those of poly-Si gate MOS transistors. This type of result regarding degradation of MOS transistors due to internal stresses in the gate electrodes may be anticipated on the basis of elementary physics. However, important questions still remain unsolved. What kind of defects are caused by the W film stress? Where are the defects produced? How do the defects affect the trapping of hot carriers?

Available data and analyses of degradation due to hot carriers in W gate MOS devices are not yet adequate. Further studies in this area are now being carried out (19).

Conclusions

To enable W gates to be applied in MOS VLSI's, the reliability of W gate fabrication processes and electrical characteristics were evaluated. It was clarified that ionic contamination penetrating into the gate oxides (SiO_2) from W gates formed by using commercially available W targets shifted the flatband voltage. It was also found that the degradation rate of W gate MOS transistors due to hot carriers was higher than that of poly-Si gates, and that it may be caused by internal stress in W films.

Therefore, a W gate fabrication technique for solving these problems was developed. The technique consists of (*i*) applying the high purity W sputtering target fabrication technique to reduce contamination, (*ii*) annealing following W deposition to eliminate the defects in Si substrate and prevent the degradation of MOS transistors due to hot carriers, and (*iii*) oxidizing Si without oxidizing W, in order to improve the breakdown voltage of gate oxides and eliminate the contamination introduced during ion implantation and dry etching. Through these techniques, W gate devices that have characteristics comparable to those of poly-Si gate devices may be produced.

[3]At the fabrication stage for a 1 Mb D-RAM TEG, W was deposited at an Ar pressure lower than 5×10^{-1} Pa. To put it another way, the internal stress in W films was limited to compressive stress by strict pressure control. The fact that the interconnects made of W films off-deposited at higher pressures were broken off at the device steps is the reason the etching rate of W films at the steps was higher than that of W films on the flat field.

Acknowledgments

The authors would like to thank Dr. Shoojirou Asai for his encouragement and suggestions during the course of this work. Numerous members of the VLSI Center, Hitachi Central Research Laboratory, have contributed to refractory metal gate process development. The authors are also grateful to Dr. Yasuo Wada and Dr. Tomoyuki Terada of Hitachi VLSI Engineering Company, Limited, for their discussions and support, which aided in the development of device processes. Special acknowledgment is due to Dr. Yasushi Nakamura of Nippon Mining Company, Limited, for analysis of the impurities in W. We are also thankful to Dr. Hideo Oikawa and Dr. Takao Amazawa of Atsugi Electrical Communication Laboratory, Nippon Telegraph and Telephone Company for their encouragement and comments.

Manuscript submitted July 19, 1985.

Hitachi, Limited, assisted in meeting the publication costs of this article.

APPENDIX

The following is a summary of a comparative study on the effects of refractory metal deposition by electron beam (EB) evaporation and dc magnetron sputtering (sputtering) on the characteristics of MOS devices. It appears that sputtering is effective in fabricating MOS devices with low trap densities at the metal/SiO_2 interfaces. Molybdenum gate MOS capacitors were used for this purpose. The reason why the evaporation of W by EB was difficult was because of the very high melting point (3350°C) of W. The values of N_{ss} and Q_{ss} were compared for Mo gate MOS capacitors, the Mo films of which were formed by the above two types of deposition devices. These values after N_2 annealing were comparable to those of poly-Si gate capacitors, as shown in Table A-I. Therefore, it was estimated that radiation damage to the characteristics at the interface or vicinity of SiO_2/Si substrate incurred during Mo deposition could be nearly eliminated by the annealing. On the other hand, some differences were obtained between the charges produced in the Mo/SiO_2 interfaces during EB evaporation and those produced during sputtering. Ledge-like characteristics were seen in the initial I-V curves (first ramp) of the capacitor made of Mo deposited by EB at T_{sub} = 300°C, as represented in Fig. A-1 (the samples with Mo deposited at 25°C showed similar I-V curves). The second ramp I-V curves shifted to 1.2 MV/cm higher than the first ramp I-V curves and showed no ledge curve. When positive charge trap centers exist at the gate electrode/SiO_2 interface, electrons injected into the SiO_2 from the electrode will be caught by the centers resulting in neutralization. The ledge in the first ramp I-V curve in Fig. A-1 was caused by electron trapping in the SiO_2. The shift in the applied voltages indicated charge density of 2.1 $\times$ 10^{12} cm^{-2} (by a

Table A-I. N_{ss} and Q_{ss} of Mo gate MOS capacitors using Mo films deposited by EB evaporation and dc planar magnetron sputtering

	Heat-treatment	Magnetron sputtering	EB evaporation
N_{ss} (cm^{-2} · eV^{-1})	Before N_2 annealing	$1 \sim 2 \times 10^{11}$	$2 \sim 5 \times 10^{11}$
	After N_2 annealing	$\leq 3 \times 10^{10}$	$\leq 5 \times 10^{10}$
Q_{ss} (cm^{-2})	After N_2 annealing	$\leq 2 \times 10^{10}$	$5 \sim 7 \times 10^{10}$

N_2 annealing: 1000°C, 30 min.

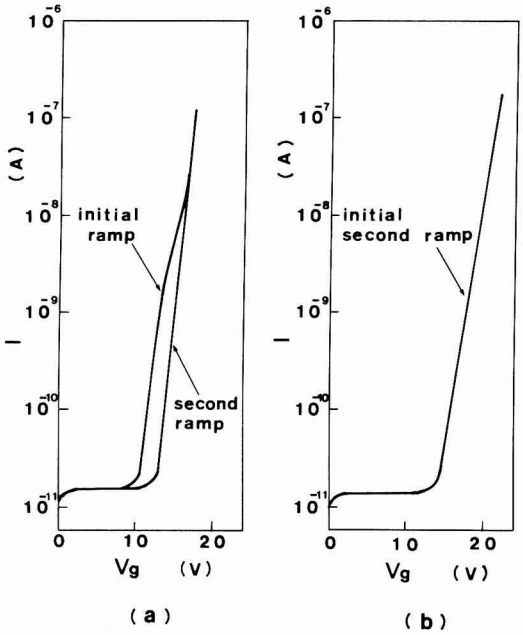


Fig. A-1. Comparison of the sequential ramp I-V characteristics of MOS capacitors made of Mo films by (a) EB evaporation, and (b) magnetron sputtering. The first ramp voltages rose to 16V and the second ramp voltages followed immediately afterward. N_2 annealing: 1000°C, 30 min. Ramp rate = 0.3 V/s, SiO_2 = 20 nm.

simple first-order estimation). However, the ledge-like and the hysteresis I-V curves did not appear in the case of capacitors with Mo deposited by sputtering. These results indicate that there were few trap centers at the Mo/SiO_2 interfaces. It is considered that trap centers at the interfaces of the capacitors made of Mo deposited by EB evaporation were introduced by (*i*) the reaction between Mo and SiO_2 (9) (it including the penetration of metals into SiO_2 (20)), (*ii*) ionic impurities such as Na or K penetrating into the SiO_2 from Mo films, (*iii*) the Mo oxide or carbide formed by the segregation of oxygen or carbon impurities in Mo at Mo/SiO_2 interfaces, and (*iv*) the charges produced by radiation damage during Mo evaporation.[4] However, the mechanism of the generation has not yet been clarified in our study.

[4]Ning (21) showed that the centers at SiO_2 substrates caused by x-ray or scattered electrons disappeared by annealing at 500° ~ 600°C. However, he did not describe radiation damage at the metal/SiO_2 interface. His experiments were only carried out for the case of Al evaporation, and the effect of annealing temperature on the disappearance of radiation damage due to various energy levels has not yet been demonstrated in any paper.

REFERENCES

1. K. Itoh, R. Hori, J. Etoh, S. Asai, N. Hashimoto, K. Yagi, and H. Sunami, *Digest Tech. Papers ISSCC*, 284 (1984).
2. M. Taguchi, S. Ando, S. Hijiya, T. Nakamura, S. Economo, and T. Yabe, *ibid.*, 100 (1984).
3. S. Suzuki, M. Nakao, T. Takeshima, and M. Yoshida, *ibid.*, 106 (1984).
4. Y. Mizutani, K. Maeguchi, T. Mochizuki, M. Kimura, M. Isobe, Y. Uchida, and H. Tango, "Proceedings of the 12th Conference on Solid State Devices," p. 55, Japan Society of Applied Physics, Tokyo (1980).
5. M. Y. Tsai, F. M. d'Heurle, C. S. Petersson, and R. W. Johnson, *J. Appl. Phys.*, **52,** 5350 (1981).
6. S. P. Muraruka, D. B. Fraser, A. K. Sinha, and H. J. Levinstein, *IEEE Trans. Electron. Devices*, **ed-27,** 1409 (1980).
7. N. Yamamoto, S. Iwata, N. Kobayashi, and T. Terada, "Extended Abstracts of the 15th Conference on Solid State Devices and Materials," p. 217, Tokyo (1983); N. Yamamoto, S. Iwata, N. Kobayashi, K. Yagi, and Y. Wada, in "VLSI Science and Technology 1984," K. E. Bean and G. A. Rozgonyi, Editors, p. 361, The Electrochemical Society Softbound Proceeding Series, Pennington, NJ (1984).
8. N. Kobayashi, S. Iwata, N. Yamamoto, and T. Terada, in "Digest of the 1983 Symposium of VLSI Technology," p. 94, IEEE and Japan Society of Applied Physics, Hawaii (1983).
9. S. Iwata, N. Yamamoto, N. Kobayashi, T. Tereda, and T. Mizutani, *IEEE Trans. Electron. Devices*, **ed-31,** 1174 (1984).
10. R. S. Wagner, A. K. Sinha, T. T. Sheng, H. J. Levinstein, and F. B. Alexander, *J. Vac. Sci. Technol.*, **11,** 582 (1974).
11. "Handbook of Thin Film Technology," L. I. Maissel and R. Glang, Editors, Chap. 12, McGraw-Hill, New York (1970).
12. C. W. Gwyn, *J. Appl. Phys.*, **40,** 4886 (1969).
13. P. Solomon, *ibid.*, **48,** 3843 (1977).
14. O. Kubaschewski and C. B. Alock, "Metallurgical Thermochemistry (5th), p. 378, Pergamon Press, Oxford (1979).
15. N. Kobayashi, S. Iwata, and N. Yamamoto, "Abstracts for Fall Meeting, Japan Society of Applied Physics," p. 389 (1983).
16. T. Amazawa, H. Oikawa, N. Shiono, and N. Honma, 1984 International Conference on Solid State Devices and Materials, Kobe, Aug. 1984.
17. H. Gesch, J-P. Leburton, and G. E. Dorda, *IEEE Trans. Electron. Devices*, **ed-29,** 913 (1982).
18. R. B. Fair and R. C. Sun, *ibid.*, **ed-28,** 83 (1981).
19. H. Kume and N. Yamamoto, Submitted to *Electron Device Lett.*
20. T. Amazawa and H. Oikawa, "Extended Abstracts of the 15th Conference on Solid State Devices and Materials," p. 229, Tokyo (1983).
21. T. H. Ning, *J. Appl. Phys.*, **49,** 4077 (1978).

Characterization and Control of Silicon Surface Modification Produced by CCl_4 Reactive Ion Etching

A. Rohatgi[1] and P. Rai-Choudhury*

Westinghouse Research and Development Center, Pittsburgh, Pennsylvania 15235

S. J. Fonash,* P. Lester, and Ranbir Singh

Engineering Science Program, The Pennsylvania State University, University Park, Pennsylvania 16802

P. J. Caplan and E. H. Poindexter

United States Army Electronics Technology and Devices Laboratory (ERADCOM), Fort Monmouth, New Jersey 07703

ABSTRACT

The work constitutes a survey of CCl_4-based reactive-ion-etching-induced surface modification in silicon. The damage produced during reactive ion etching (RIE) is studied using a diverse set of techniques, such as spreading resistance, metal-semiconductor contacts, electron spin resonance, and reflected high energy electron diffraction. The surface chemistry was also investigated through the use of Auger electron spectroscopy. Among the possible effects that could be produced by RIE (structural damage, impurity and etching ion permeation, and coating residue or film formation), the bulk of the evidence points to structural (bonding) damage with its associated positive charge, as being the dominant surface modification caused by CCl_4 or CCl_4 + He etching for the process parameters used in this study. The evolution of this damage with varying etching parameters is also examined. Further, a survey of various dry processes that can be used to overcome or reverse the surface modification occurring during RIE is made. Specifically, we show that hydrogen passivation, low temperature (~600°C for times ≳ 1h) furnace anneals, or rapid thermal anneals (1100°C for 10s) can be used to restore the properties of the RIE-damaged silicon surface. A criterion for the efficacy of rapid thermal annealing in restoring surface properties after RIE involving other gases is postulated.

It is well established that there are deleterious effects that can occur at semiconductor surfaces as a result of using dry etching. These may be categorized as: (*i*) bonding or structural damage (1-5), (*ii*) impurity and etching-ion permeation (1, 2, 6), and (*iii*) coating residue or film formation (1, 2, 6, 7). The last two of these effects can, in principle, be eliminated, or at least strongly reduced, by careful design of the etching system and by careful selection of the etching chemistry. Unfortunately, there is evidence, (1-5), which we augment in this report, that the first of these effects, structural damage, is inherent in anisotropic dry etching techniques that are based on directed ion bombardment (viz., ion etching, reactive ion etching (RIE), ion beam etching (IBE), and reactive ion beam etching).

The three deleterious effects of dry etching can result in a number of problems. For example, it has been demonstrated that thermal oxides grown on reactive-ion-etched (RIE) or ion-beam-etched (IBE) silicon yield MOS structures with high interface state densities and degraded minority carrier generation time (6). Metal/silicon contacts on RIE- or IBE-exposed surfaces also exhibit modified behavior, *i.e.*, the current-voltage (I-V) characteristics of contacts made on IBE or RIE silicon are radically different from the I-V characteristics of contacts made to wet chemically etched silicon (2-6, 8-11). In addition, it has recently been shown that the kinetics of silicide formation, at least in the case of low temperature Pd_2Si, are different on dry-etched Si surfaces and it has been demonstrated that the act of forming the low temperature Pd_2Si does not fully restore the I-V characteristics for n-type silicon to those expected for Pd_2Si formed on chemically etched material (12). Further, damage of the type that can occur in anisotropic etching has also recently been shown to be related to Al contact penetration in silicon (13).

In this paper, we present a survey of our characterization of the modifications produced at a silicon surface by CCl_4 or CCl_4 + He RIE and a survey of three approaches to restoring the near-surface-layer properties. Reactive ion etching based on CCl_4 is very common in silicon processing, and hence a comprehensive characterization of its effects on the near-surface layer of an etched silicon surface is important. A survey of the efficacy of various restoration techniques for CCl_4-etched Si is equally important, both because of its impact on CCl_4 RIE and because of its pertinence to other dry etching processing.

The characterization of the CCl_4 or CCl_4 + He RIE silicon is undertaken using reflected high energy electron diffraction (RHEED) and electron spin resonance (ESR) for structural characterization, Auger electron spectroscopy (AES) for chemical characterization, and spreading resistance and current-voltage (I-V) behavior of Au/semiconductor contacts for electrical characterization. From the RHEED and ESR data, we show that CCl_4 or CCl_4 + He RIE produces a modified near-surface layer in the etched silicon that has many of the structural damage features previously seen for inert gas, ion beam etching (2-5, 8). Using the AES data, we demonstrate that contamination (chlorine) is also present at surfaces etched by CCl_4 RIE, although there is no strong evidence from AES for the presence of a carbonaceous residue layer after CCl_4 RIE. From the electrical characterization, we show that CCl_4 or CCl_4 + He RIE produces the same electrical modifications previously established for inert gas IBE-exposed Si (2-5, 8) and for NF_3 RIE-exposed Si (9, 10), viz., CCl_4 and CCl_4 + He RIE results in barrier reduction on n-type Si and barrier enhancement on p-type Si. Because (*i*) these same electrical modifications are seen for inert and chemically active gases, (*ii*) AES does not detect the presence of a surface residue layer in the case of our CCl_4-based RIE, and (*iii*) hydrogen passivation of the electrical modifications is demonstrated to occur reversibly (*i.e.*, the modifications reappear if the hydrogen is driven out), we argue that the modified electrical properties of the etched surfaces are due principally to structural damage.

We conclude by surveying three approaches for reversing the near-surface modifications produced by CCl_4 RIE, viz., defect passivation, furnace annealing, and rapid thermal annealing. Defect passivation using low energy hydrogen beams is found to restore the electrical properties of the surface; however, hydrogen can evolve out of the damaged regions if subsequent processing temperatures exceed 400°C. Our results show that furnace annealing at temperatures ≳ 600°C for times ≳ 60 min can also produce surface recovery. We also show that a rapid

*Electrochemical Society Active Member.

[1]Present address: School of Electrical Engineering, Georgia Institute of Technology, Atlanta, Georgia 30332

thermal anneal at 1100°C for 10s can achieve a substantial degree of restoration of the near-surface damage.

Experimental

All the RIE done in this study was performed in an Anelva 503 reactor, such as that seen in Fig. 1. The spacing between the cathode and anode in this system was 60 mm; the pressure, power, gas mixture, and flow rates were all automatically controlled by a microprocessor built into the etching station. The silicon wafers to be etched (p- and n-type, 1-10 Ω-cm (100) Cz for the spreading resistance mapping of etching damage; p- and n-type, 4-8 Ω-cm (100) Cz or Fz for the RHEED and Au/Si contact evaluation; and p-type, 50-70 Ω-cm (100) Cz for the ESR evaluation) were placed on the water-cooled, stainless steel cathode, and the perforated anode was held at ground. In all cases, the wafers used in this study were given a blanket etch with CCl_4 or CCl_4 + He mixtures. Pressure was kept in the 20-100μ range, and RF power varied between 100-600W. Pressure, power, and peak cathode voltage (approximately equal to the energy of the ions impinging on the Si) were monitored in all etching runs.

Samples to be used for electrical evaluation were given a standard preclean prior to placement into the etching station; samples to be used for ESR were prepared as described elsewhere (2, 3). After RIE, either spreading resistance samples were given an HF dip (5s in 1:20::HF:H_2O) just prior to measurement, or wet chemical treatment was completely omitted. Spreading resistance measurements, using a single point technique, were performed after the RIE treatments on partially masked (with silicon) samples to map the surface damage. To minimize penetration, a probe loading on only 5g was used, which resulted in a probe "footprint" of ~5 μm. After RIE exposure, Si to be used for Au/Si contacts was dipped for 5s in 1:20::HF:H_2O or given a HF vapor etch, followed by a DI water rinse and Au metallization through a (15 or 30 mil diameter) shadow mask. For samples used in all the electrical evaluation, back contacts were established either by sandblasting followed by Ti/Pd/Ag evaporations or by a simple, resistive-heating Al evaporation.

In the case of the structural characterization (RHEED and ESR), all chemical treatment after RIE was omitted. The samples used for RHEED were also examined for surface contamination using AES; hence, the AES studies were done on samples that were not exposed to chemical treatment after RIE. Since the energetic particle bombardment of RIE results in property modifications that are significant in a shallow (≲100Å) near-surface region, two AES scans at different depths and a surface scan were made. We note here that interpretation of depth profiles obtained using sputtering techniques (such as in-depth profiling by AES) is difficult. In this case, knock-on implantation during the depth profiling can drive in impurities to the same depths to which they can permeate during RIE. Nevertheless, we use the AES data to demonstrate the presence or absence of contamination by comparing the AES data for RIE-exposed samples to that of unexposed samples.

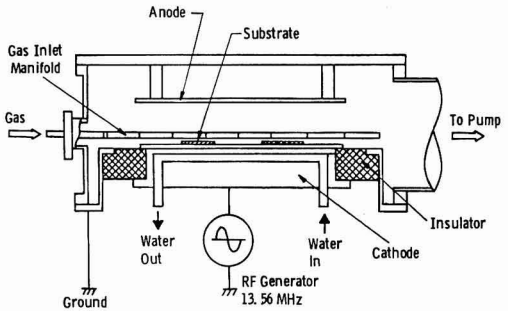


Fig. 1. Schematic diagram of Anelva 503 reactor

In examining the control of surface modifications caused by CCl_4 RIE, both surface restoration and passivation approaches were considered. In the study of furnace annealing for the restoration of surface properties, isochronal (one hour) anneals in N_2 in the temperature range of 200°-800°C were explored. All annealing was done after RIE and prior to front contact (Au) and ohmic back contact deposition. Furnace-annealed samples were chemically etched using a mild HF treatment (similar to the one used for evaluating the Si immediately after RIE-exposure) after the anneal but before the front metal deposition. The study of rapid thermal annealing (RTA) for the restoration of surface properties was done using 10s, tungsten halogen lamp RTA exposures in N_2 for the temperature range 500°-1100°C. In this case also, all annealing was done after RIE and prior to contact depositions. Both the use and omission of the HF procedure after RTA but prior to deposition were examined. Hydrogen ion implantation for the passivation of dry etching damage has previously been shown to be effective for controlling IBE damage and RIE damage (4). We continue that work in this report, again using a Kaufman ion source to generate the hydrogen ion beam. In this study, the beam energy was 0.4 keV, the implant time was 5 min, and all H^+ implants were done after RIE. A mild HF etch was used in the passivation procedure after the H^+ implant but prior to contact deposition. For all three approaches, the degree of recovery of surface properties following RIE exposure was evaluated from the I-V characteristics of Au-Si contacts; in some cases, restoration was also evaluated using RHEED and AES.

Characterization of Surface Modification

Spreading resistance measurements.—Spreading resistance is an attractive tool for determining if RIE modifies

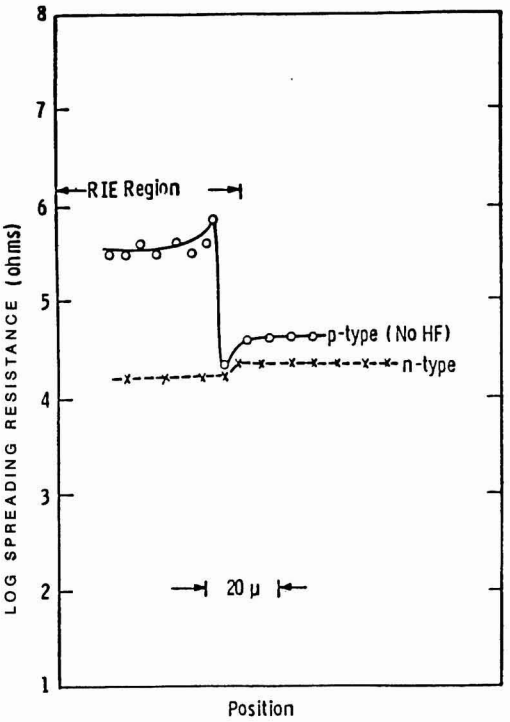


Fig. 2. Spreading resistance map on reactive-ion-etched silicon: etching conditions were: gas CCl_4, power 600W, pressure 60μ, and etch time of 1.5 min.

the electrical properties at the surface of etched silicon. This measurement yields a resistance that is the series combination of the metal probe/silicon surface contact resistance and the constriction resistance in the silicon beneath the probe.

Figure 2 shows two typical spreading resistance maps. One has been obtained by stepping the probe from the unetched to the RIE region on n-type Si, and the other has been obtained by stepping the probe from the unetched to the RIE region on p-type Si. As may be noted from the figure, the spreading resistance was found to be higher in RIE regions on p-type Si and lower in RIE regions on n-type Si. This observation suggests RIE-induced positive charge on the silicon surface, because positive charge on p-silicon will deplete the adjacent silicon region, resulting in higher spreading resistance, but the positive charge will accumulate n-Si underneath, causing a reduction in the spreading resistance. The use or omission of the HF dip procedure prior to measurements was found to have no significant effect on this trend.

Figure 2 demonstrates that spreading resistance measurements can be used to detect RIE modification to silicon surfaces. However, because of the nature of the measurement, it cannot be determined if it is the contact characteristics or the constriction resistance that is being modified in the RIE regions. By going to larger deposited metal/silicon contacts, constriction resistance can be suppressed, and the current-voltage measurements can focus on the electrical characteristics of the metal/Si contact itself.

RHEED and AES characterization.—Reflected high energy diffraction can be used to monitor the structure of the near-surface region of a silicon wafer. Figure 3a shows the diffraction pattern obtained for a control sample that did not undergo any RIE. The spot pattern and the Kikuchi lines are clearly indicative of an ordered silicon surface. After exposing the Si wafer to the CCl_4 plasma (600 W/20μ) for 5 min, the diffraction pattern changes, as seen in Fig. 3b, from that of a crystalline surface to a ring-like pattern representative of a polycrystalline surface. Inspection shows that Fig. 3b contains a ring pattern corresponding to polycrystalline silicon. We have seen similar ring RHEED patterns indicative of the formation of polycrystalline silicon for inert gas IBE. Ohira has also used RHEED to characterize inert gas ion etching (14). In that case, a ring pattern was not observed; rather, the pattern was hazy, which is indicative of an amorphous layer. Polycrystalline Si may be present in the RIE samples of this study, due to redeposition or regrowth or, perhaps, due to a combination of both. This is a point that needs further exploration.

The status of the silicon surfaces after CCl_4 RIE was also examined using AES scans, as shown in Fig. 4. Comparing Fig. 4a (control) and Fig. 4b (after RIE), one can see that the only significant difference between the two sets of AES data is the presence of chlorine after RIE. Silicon is seen at the surface of both the control and the RIE

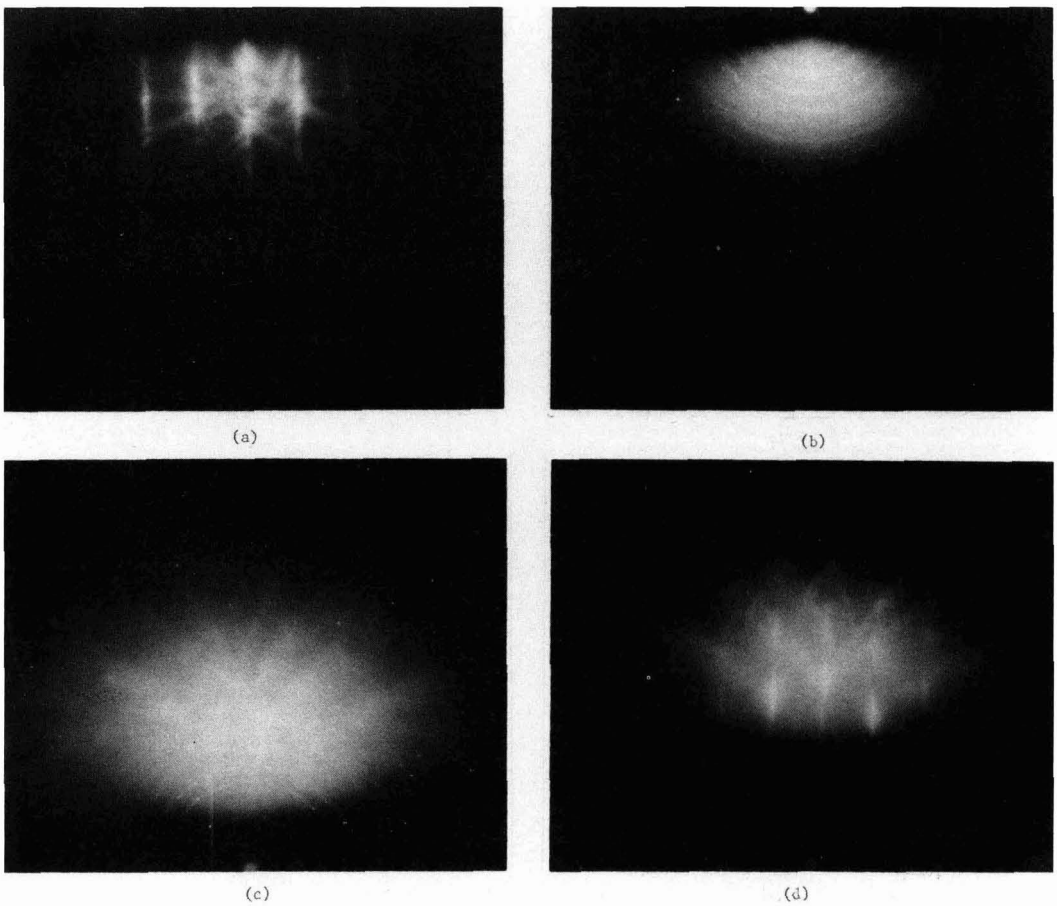


Fig. 3. Reflection electron diffraction pattern of silicon: (a) untreated control water, (b) after RIE, (c) after RIE and 800°C/10s rapid thermal anneal, and (d) after RIE and 1100°C/10s rapid thermal anneal.

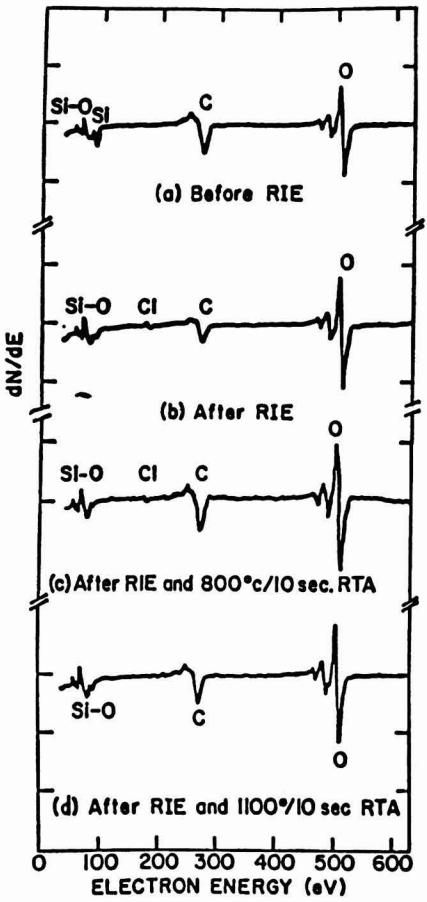


Fig. 4. AES scans of the silicon wafers whose RHEED characterization is shown in Fig. 3.

samples; carbon is present to about the same extent in both cases. The chlorine peak disappears after sputter etching approximately 30Å of the silicon surface, indicating that any permeation by the chlorine in this CCl_4 RIE is restricted to within ≳30Å. Closer examination of Fig. 3b suggests the presence of an extremely faint ring in the RHEED pattern than cannot be attributed to Si. Since the intensity of this ring is extremely low and AES data show no carbonaceous deposits, we conclude that a primarily non-Si residue layer does not cover the surface for the etching parameters of this study.

When residue layers are present—as they are for some RIE chemistries (1, 15)—they can dominate the electrical characterization of metal-semiconductor contacts to etched Si surfaces. Phenomenologically, they appear, both for n- and p-type Si, as a resistance in series with the contact; this resistance can overshadow electrical property changes occurring in the silicon near-surface regions (14). As we will see, the barrier height changes arising in the near-surface region are clearly observable for CCl_4-etched surfaces, and there is no discernable series resistance caused by the RIE exposure. This lends further support to the AES evidence that a substantial residue layer is not formed for the CCl_4 RIE parameters used in this study. As we will also discuss, we believe the success of rapid thermal annealing achieved in this study is attributable to the apparent absence of a residue layer.

Au/Si contact I-V characteristics.—We now examine current-voltage (I-V) characteristics of metal-semiconductor contacts to monitor the electrical properties of the

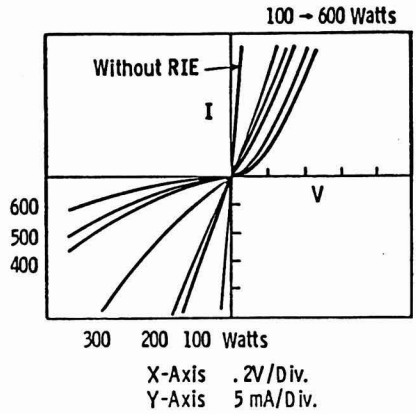


Fig. 5. Effect of RIE power on I-V characteristics of Au/p-Si contacts: Au contacts were deposited after RIE; the etching conditions were CCl_4/He etching gas, 100μ pressure, and 1.5 min etching time. Flow rate was 500 sccm CCl_4 + 50 sccm He.

near-surface region of CCl_4 reactive ion-etched Si. In general, examination of these characteristics shows that dry etching of Si using CCl_4-based gases causes apparent barrier lowering, when compared to controls on chemically etched n-type Si, for contacts between nonreactive metals and dry-etched n-type Si. Further, compared to controls made on chemically etched p-type Si, contacts between nonreactive metals and dry etched p-type Si yield higher barriers. This phenomenon has also been observed in the case of IBE with H, Ne, Ar, and Kr (2-6, 9), and for RIE with NF_3 (9, 10).

This barrier-shifting phenomenon is shown in Fig. 5 and 6 for Si samples reactive-ion-etched in CCl_4 or CCl_4 +

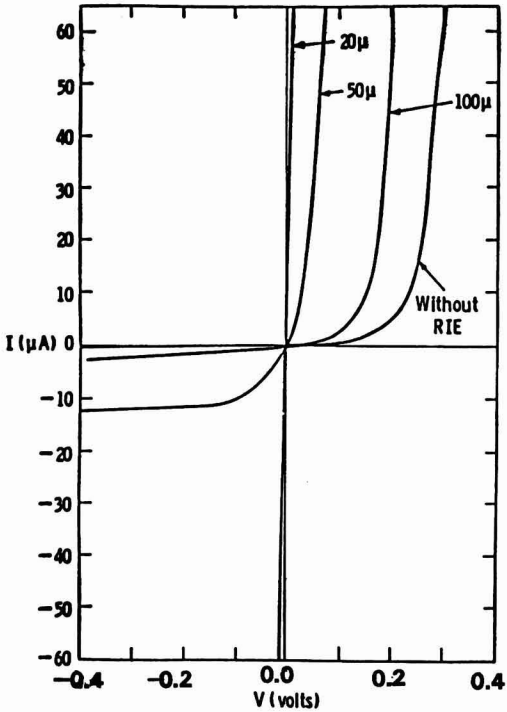


Fig. 6. Effect of RIE pressure on I-V characteristics of Au/n-Si contacts: Au contacts were deposited after RIE; etching conditions were CCl_4 etching gas, 300W power, and 1.5 min etching time.

He mixtures. Figure 5 shows the current-voltage (I-V) characteristics for Au/p-Si contacts fabricated on material subjected to various RF power levels but to the same pressure in CCl_4 + He RIE. Ohmic-like (very low barrier height) characteristics are seen, as expected, for the contact on the chemically etched (without RIE) p-Si. However, a barrier is seen to be present for Au contacts on the RIE p-Si, and this barrier is more pronounced with increasing RF power during RIE for a constant pressure (100μ), constant etching time (1.5 min), and constant gas flow rate (50 sccm CCl_4 + 50 sccm He).

The effect of varying the gas pressure during RIE on electrical properties is shown in Fig. 6. In this case, n-type Si was reactively ion-etched using CCl_4 for 1.5 min at a constant power level (300W) a gas flow rate (40 sccm). As indicated in the figure, the pressure was held constant during each run at values that varied between 20 μm and 100 μm. The evolution of the I-V characteristics of gold/silicon contacts to these etched surfaces points to a direct relationship between the degree of rectification and gas pressure, *i.e.*, the barrier degrades monotonically on the n-type Si as the gas pressure is reduced.

Figures 5 and 6 show that CCl_4-based RIE exposure does not simply introduce damage that serves only to shunt any barrier present at the surface. If this were the case, the barrier height of Au/Si contacts would appear to be reduced after the RIE for both n-type and p-type silicon. Instead, reduction is observed on n-type and enhancement on p-type silicon. Further, the data show that these changes in the Au/Si I-V characteristics caused by CCl_4-based RIE cannot be attributed to an insulating (series resistance) layer resulting from coating residue or film formation. This barrier evolution seen here for CCl_4-based RIE and seen previously for inert gas-based IBE and NF_3-based RIE is also difficult to attribute to the formation of a heterojunction, since it would be extremely fortuitous if inert gas IBE, NF_3 RIE, and CCl_4 RIE all gave heterojunctions with low barriers on n-type Si and high barriers on p-type Si. Similarly, it is difficult to argue that this barrier evolution is due to impurity doping in the surface layer (*i.e.*, homojunction formation), since the same barrier change trends have been seen for a variety of etching species, including mass-analyzed Ar ion beams, and a variety of etching systems (1, 16).

However, the barrier evolution observed with CCl_4-based RIE is consistent with the model (2-5, 8-10) that IBE and RIE create structural damage (as we have seen for CCl_4 RIE using RHEED) and concomitant localized gap states in a modified near-surface layer. These localized states contain positive charge, which, for Au/Si contacts, reduces the band bending in the bulk n-type silicon below the damaged layer (*i.e.*, there is sharp band bending in the damaged layer) causing a change in the effective barrier height of an Au/n-Si contact, whereas it induces enhanced band bending in the bulk p-type Si below the damaged layer increasing the barrier height of an Au/p-Si contact. Both the spreading resistance data mentioned previously and the I-V measurements presented here for deposited contacts support this model of the formation of positive charge at CCl_4 and CCl_4 + He RIE-damaged silicon surfaces. Further, Fig. 5 and 6 show that this damage modifying the barrier increases with a higher RF power level and lower gas pressure during RIE. This dependence of the damage on process variables can be explained by the data of Fig. 7, which show that the cathode voltage, a measure of the ion energy, decreases with increasing pressure and also with decreasing RF power. According to this model, higher ion energy creates more structural damage which, in turn, causes a greater barrier modification. This leads to the power and pressure dependencies seen in Fig. 5 and 6. The data of Fig. 7 were measured in the Anelva etching station under the conditions indicated.

Electron spin resonance measurements.—We have presented data that show that CCl_4 and CCl_4 + He RIE produces a near-surface layer with modified structure, some

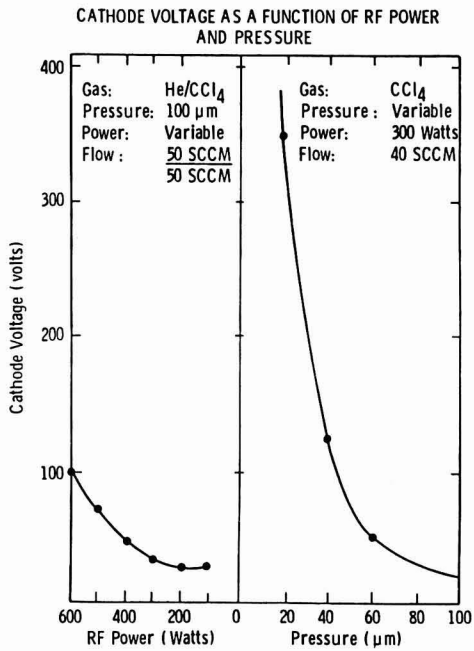


Fig. 7. Cathode voltage as a function of power and pressure in Anelva 503 reactor.

Cl contamination, and modified electrical properties. In this section, we present evidence that directly demonstrates that Si bonding damage is part of the structural modification produced by RIE; to make that determination, we used ESR measurements. We have previously shown, using ESR, that silicon bonding damage (in the form of a type of trivalently bonded silicon defect) is present in IBE silicon (2, 3). The etching ion energies used in this RIE study were lower [see Fig. 7 and Ref. (2 and 3)] than those employed in the IBE investigation. In anticipation of lower levels of damage, we increased the signal strength for the ESR characterization of RIE damage by placing five identically prepared Si samples simultaneously in the ESR cavity. Figure 8 shows the ESR signature of these five specimens prior to RIE; this figure gives the ESR spectrum for the magnetic field H_0 perpendicular to the surface of these samples and for H_0 parallel to the surface of the sample. As discussed elsewhere, the signature seen in these spectra is that of the so-called P_b defect center, which has been established to be a trivalently bonded Si defect existing at an SiO_2/Si interface. The P_b defect, present as a nascent oxide begins to grow, has spectra that are seen in Fig. 8 to be definitely anisotropic (*i.e.*, signal strength and g-value are a function of magnetic field orientation). This is a result of there being a preferred orientation for the disrupted bond at the SiO_2/Si interface (18-20).

Figure 9 shows the ESR signature of these same five specimens after RIE exposure. The spectrum is seen to be isotropic now and essentially the same as the damage resonance obtained previously for IBE silicon (3). There is also an indication in Fig. 9 of small, lingering P_b resonance. Comparison of Fig. 8 and 9 makes the point that RIE does modify the silicon surface and results in silicon bonding damage. This bonding damage is similar to that previously seen for IBE Si, *i.e.*, a type of trivalently bonded silicon defect.

Approaches to Controlling Surface Modification

In this section, three techniques for recovering the surface properties of CCl_4 or CCl_4 + He RIE Si are surveyed. Two of them strive to achieve restoration of the near-sur-

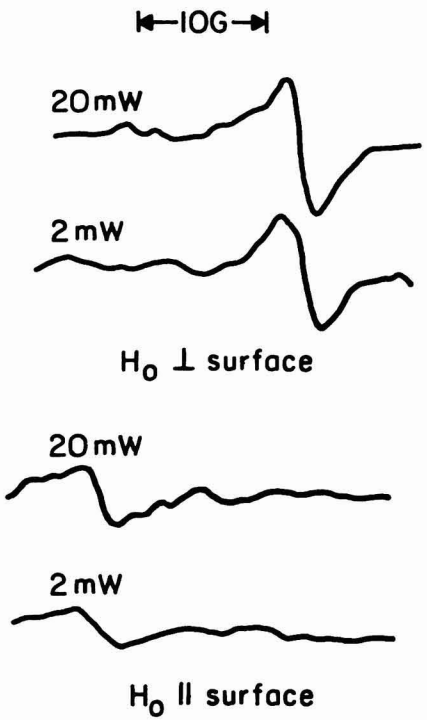


Fig. 8. ESR spectra from base line silicon samples prior to RIE. Anisotropic signature of the P_b defect center arising from the growth of nascent oxide on the sample is seen by comparing the spectrum for magnetic field H_0 perpendicular to the surface with that for the magnetic field parallel to the surface. There were five samples in the cavity. Data for two microwave power levels are shown.

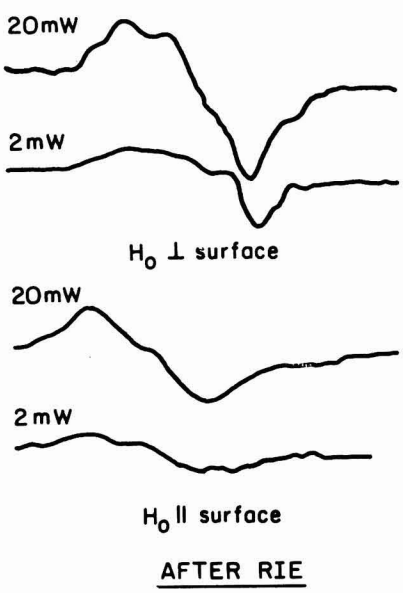
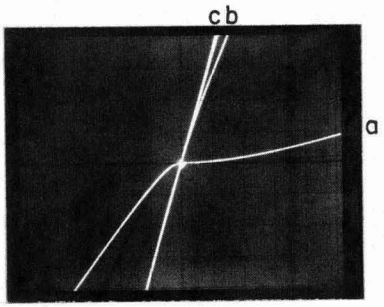


Fig. 9. ESR spectra from the silicon samples of Fig. 7 after RIE. Presence of isotropic damage signal resulting from RIE is seen. The five samples of Fig. 7 were simultaneously in the cavity.

ANNEALING OF REACTIVE ION ETCHING INDUCED SURFACE DAMAGE ON p-SILICON



Etching Conditions: CCl_4, 600 W, 60 μm, 1 1/2 min

a) After RIE Treatment

b) RIE + 500°C Anneal in N_2 for 1 Hr.

c) RIE + 600°C Anneal in N_2 for 1 Hr.

Fig. 10. Furnace annealing of RIE-induced surface damage on p-silicon: I-V characteristics after (a) RIE, (b) RIE + 500°C/1h anneal in N_2, and (c) RIE + 600°C/1h anneal in N_2; etching conditions were CCl_4, 600W, 60μ, and 1.5 min.

face structure; one strives to achieve passivation. The degree of restoration or passivation is assessed by evaluating the I-V behavior of Au/Si contacts on etched surfaces.

Furnace thermal annealing.—Figure 10 shows the I-V characteristics of several Au/Si contacts fabricated on p-type silicon. In each case, the silicon has been reactively ion-etched using CCl_4 with a power of 600W, a pressure of 60μ, and an etching time of 1.0-0.5 min. For the sample yielding curve (a), the Au contact was deposited after RIE exposure. However, the sample that yielded curve (b) was annealed after RIE for 1h at 500°C in N_2, and the sample that yielded curve (c) was annealed after RIE for 1h at 600°C in N_2. Higher temperature anneals yielded the same result as that shown in curve (c). We note that whenever annealing was done, Au contacts were deposited after the anneals.

The data of Fig. 10 show that the CCl_4 RIE-exposed p-type Si is only partially restored after the 500°C/1h anneal; a 600°C/1h anneal is required for full recovery. Similar studies on n-type Si also showed that $T \gtrsim 600$°C and times $\gtrsim$ 1h were also required for restoration of the I-V characteristics of Au/n-Si contacts.

The use of 600°C/h anneal for devices and for fabrication may become a matter of concern in the future; therefore, the use of rapid thermal anneals was investigated.

Rapid thermal annealing.—We survey here attempts made to restore RIE damage by rapid thermal annealing (RTA) using tungsten halogen lamps (AG Associates, Model 210). Anneals were done in an N_2 ambient for 10s in the temperature range of 600°-1100°C. In this experiment, n- and p-type, 4-8 Ω-cm float-zone silicon wafers were subjected to RIE in CCl_4 for 5 min at a power level of 600W and a pressure of 20μ. The above RIE conditions were selected to maximize RIE damage (see Fig. 5 and 6). Au contacts were evaporated after the anneals, and I-V characteristics were measured to evaluate the damage recovery (Fig. 11).

Curve (a) (no RIE) and curve (b) (after RIE) in Fig. 11 show that RIE damage converts the Au/p-Si ohmic contact into a rectifying one, as we expect. Curve (c) (RIE +

800°C RTA) shows that an 800°C/10s rapid anneal is not enough to restore this RIE-damaged layer, because the contact remains rectifying. An 1100°C/10s rapid anneal after RIE (curve (d)), though, is able to cause a gold contact to CCl_4 RIE-exposed p-Si to exhibit ohmic behavior. Although p-type CCl_4 RIE-exposed Si recovers to an ohmic I-V characteristic after this 1100°C/10s RTA, a complete recovery is not seen for n-type material when using these same RTA parameters. Figure 12 demonstrates that the barrier height does increase after the RTA for RIE-exposed n-type material, which corresponds to the observed barrier height decrease after RTA seen in Fig. 11 for p-type silicon. However, the leakage currents (and, hence, effective barrier height) seen in Fig. 12 fall short of those observed for the control Au/n-Si contacts.

We explain this difference in the RTA response of CCl_4 RIE-exposed p-type and n-type silicon as follows: we believe that the 1100°C/10s RTA reduces the positive charge resulting from the CCl_4 RIE damage in both the case of the p-type and of the n-type material. Reduction of the positive charge in the surface layer lowers the barrier on p-type Si and raises the barrier on n-type Si, *i.e.*, barrier height recovery takes place for both p- and n-type material. However, additional (perhaps neutral) damage still remains after the RTA. This residual damage can affect charge transport by acting as a barrier shunting current path. For p-type material, the current flowing via this shunting residual damage is masked by the large over-the-barrier current of the recovered, low barrier p-Si contact. For n-type material the current flowing via this shunting residual damage is significant compared to the over-the-barrier current of the recovered, high barrier n-Si contact. Consequently, this shunting current controls the leakage current and gives the appearance of a somewhat reduced barrier height. To remove this barrier-shunting damage observable for n-type Si, it is clear that RTA procedures with higher temperature or longer time, or both, are required.

To correlate the electrical recovery seen in Fig. 11 and 12 following an 1100°C/10s RTA with the recovery of near-surface structure, RHEED was used to characterize the RTA-treated samples. As we have seen in Fig. 3a and 3b, CCl_4 RIE exposure causes the RHEED pattern of a silicon wafer to change from a single-crystal diffraction pattern to a ring pattern indicative of a polycrystalline layer. After an 800°C/10s rapid thermal anneal, only a partial recovery of this disorder is indicated by RHEED pattern in Fig. 3c. Full recovery of the crystalline order after 1100°C/10s RTA can be seen by the restoration of the single-crystal diffraction pattern in Fig. 3d. However, because of our Au/Si contact electrical measurements on n-type Si, we know that some barrier-shunting residual defects still remain, even after this anneal.

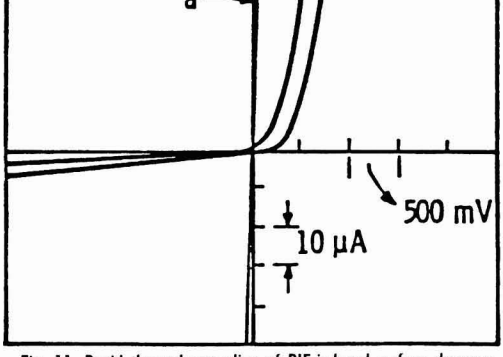


Fig. 11. Rapid thermal annealing of RIE-induced surface damage: I-V characteristics of Au/p-Si contacts after (a) no RIE (control), (b) RIE, (c) RIE + 800°C/10s RTA, and (d) RIE + 1100°C/10s RTA; etching conditions were CCl_4, 600W, 20μ, and 5 min.

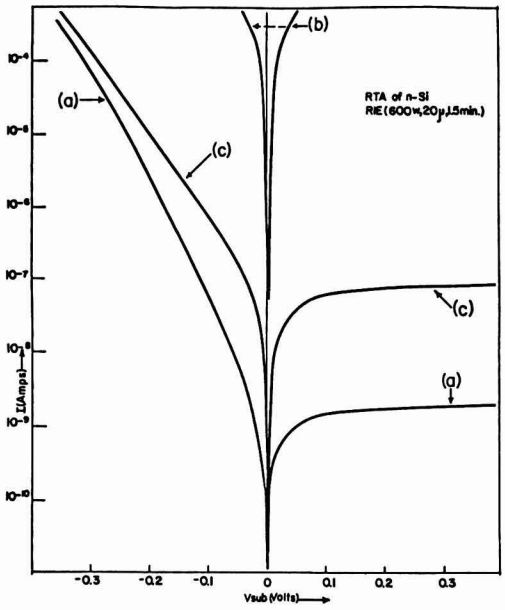


Fig. 12. Rapid thermal annealing of RIE-induced surface damage. I-V characteristics of Au/n-Si after (a) no RIE, (b) after RIE, and (c) 1100°C/10s RIE.

Auger electron spectroscopy scans were also taken following RTA; these are shown in Fig. 4c and 4d. It is interesting to note that Fig. 4c (800°C/10s RTA) still shows the presence of chlorine at the surface. Only after the 1100°C/10s RTA does this peak disappear from the surface (Fig. 4d). This suggests that the presence or absence of chlorine at the surface is related to the ordering of the surface. Indeed, in studies on ion-implantation using BF_2^+, it has been found that fluorine tends to accumulate at regions where, following annealing, residual damage still persists (21).

Low-energy hydrogen ion implants.—It has been established that the modified electrical properties produced by CCl_4-based RIE and detected by Au/Si contacts arise from a layer that has been found to contain silicon bonding defects. Hydrogen might be expected to exercise its well-known ability to tie up dangling Si bonds if introduced into these damaged layers. Further, if these dangling bonds are related to the anomalous electrical properties, hydrogen passivation should restore RIE-damaged Si to a state where Au/Si contacts exhibit normal (*i.e.*, the same as seen on chemically etched Si) behavior.

We found that the hydrogen implants are able to do just what is expected, *i.e.*, they can passivate the modified layer produced by RIE as seen in Fig. 13. These results have been discussed elsewhere in detail (2, 4, 22) and are reviewed here for completeness. In those reports, we have shown that low energy hydrogen implants can also produce an insulating film on the surface of the Si (Fig. 13d) that must be removed for complete recovery (curve (c)). However, as has been demonstrated (2, 4, 22), it is clear that removal of this hydrogen-modified layer by the HF treatment is not the cause of surface restoration, *i.e.*, it is the tying up of dangling Si bonds by hydrogen that causes passivation. The only disadvantage of this technique is that hydrogen may come out if the device is given a greater than 400°C heat-treatment after passivation.

Conclusions

Reactive ion etching with CCl_4 or CCl_4 + He modifies the near-surface region of silicon. The deleterious effects

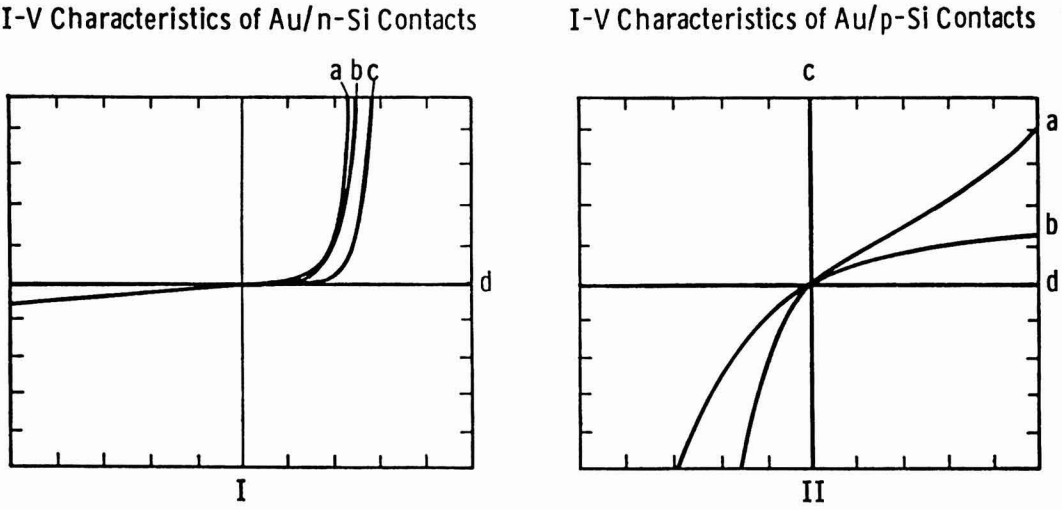


Fig. 13. Passivation of RIE damage by hydrogen ion implantation: I-V characteristics of Au/p-Si contacts after (a) RIE + HF vapor etch, (b) RIE only, (c) RIE + 0.4 keV H^+ + HF vapor etch, and (d) RIE + 0.4 keV H^+.

produced in the near-surface layer by this RIE procedure are structural changes, some chlorine contamination, and electrical property modifications. There is no evidence that blanket CCl_4 RIE of Si, for the parameters used in this study, produces any substantial carbonaceous residue layer. To develop this model, techniques as diverse as spreading resistance measurements, Au/Si contact I-V characteristics, ESR, RHEED, and AES were employed. Among the possible deleterious effects that are produced by CCl_4-based RIE, structural damage and concomitant positive charge dominate for the etching parameters used in this study.

Electrical characterization of Au contacts to these CCl_4 or CCl_4 + He RIE Si surfaces, while not detecting the presence of any series resistance from a residue layer, does show the presence of a surface layer containing a positive charge that causes a shift in the barrier height of Au contacts to the RIE silicon. The barrier height of an Au/n-Si contact is reduced, while the barrier height of an Au/p-Si contact is increased by the positive-charge-induced downward bending of silicon bands. This same observation, that the modified layer caused by dry etching contains positive charge for Au/Si contacts, has been made for inert gas IBE and NF_3 (an obvious non-halocarbon) RIE of silicon, indicating the ubiquitous nature of this phenomenon in silicon for dry etching techniques based on directed ion bombardment. Further, studies of the evolution of Au/Si barrier shift on an RIE surface, as a function of power or pressure in this investigation, supports the hypothesis that the degree of barrier shift is controlled by the energy of the etching ions as they impact the silicon surface.

The surface modifications produced by CCl_4-based RIE can be controlled by subsequent dry processing. As we established earlier, hydrogen can passivate CCl_4 RIE-caused damage. Further, the damage caused by CCl_4 RIE, for the etching parameters used in this study, can be annealed out by furnace annealing. We also demonstrated that it can, to a great extent, be annealed out by 1100°C/10s rapid thermal annealing. Although this approach has been recently reported to be completely unsuccessful for other etching gases (23), we believe that RTA is successful here, due to the absence of a substantial residue layer. Also, since impurities may be present after RIE, it is important to have a situation where these impurities evolve out of the regrowing layer during the heat pulse provided by RTA. For etching procedures that satisfy these two criteria, RTA is a very attractive approach to removing the structural and barrier-modifying damage of RIE. Its use for the removal of dry etching damage appears highly compatible with the drive towards strict dimensional control.

Acknowledgments

The authors would like to thank M. R. Chin, L. G. Stampahar, and M. J. Testa for help in the RIE, J. G. Gigante for the RTA, S. Karako for the I-V measurements, and L. Rathbun for the AES data. The authors wish to thank John Thomas of RCA for first pointing out the significance of the ring spacing in our RHEED patterns. The group at The Pennsylvania State University would like to thank Dr. Robert Mazur of Solid State Measurement for assistance in the spreading resistance measurement. This group would also like to acknowledge the support of the National Science Foundation through grant number ESC-8305646 and through providing access to the National Research and Resource Facility for Submicron Structures of Cornell University. The support of the Department of the Army through contract number DAAK 20-84-K-0456 is also acknowledged.

Manuscript submitted Jan. 28, 1985; revised manuscript received July 5, 1985. This was Paper 320 presented at the Washington, DC, Meeting of the Society, Oct. 9-14, 1983.

The Westinghouse Research and Development Center, assisted in meeting the publication costs of this article.

REFERENCES

1. S. J. Fonash, *Solid State Technol.*, **28,** 150 (1985).
2. R. Singh, S. J. Fonash, S. Ashok, P. J. Caplan, J. Shappirio, M. Hage-Ali, and J. P. Ponpon, *J. Vac. Sci. Technol.*, **A1,** 334 (1983).
3. R. Singh, S. J. Fonash, P. J. Caplan, and E. H. Poindexter, *Appl. Phys. Lett.*, **43,** 502 (1983).
4. J.-S. Wang, S. J. Fonash, and S. Ashok, *Electron. Device Lett.*, **edl-4,** 432 (1983).
5. R. J. Davis, R. Singh, S. J. Fonash, P. J. Caplan, and E. H. Poindexter, in "Proceedings of the Symposium on Thin Films and Interfaces," pp. 607-618, Vol. 25 of the Materials Research Society Symposia Proceedings (1984).
6. S. W. Pang, *Solid State Technol.*, **27,** 249 (1984).
7. J. S. Chang, *ibid.*, **27,** 214 (1984).
8. S. J. Fonash, S. Ashok, and R. Singh, *Thin Solid Films*, **90,** 231 (1982).
9. S. Ashok, T. P. Chow, and B. J. Baliga, *Appl. Phys. Lett.*, **42,** 687 (1983).

10. T. P. Chow, S. Ashok, B. J. Baliga, and W. Katz, *This Journal*, **131**, 156 (1984).
11. A. Rohatgi, M. R. Chin, P. Rai-Choudhury, P. Lester, R. Singh, and S. J. Fonash, Abstract, 320, p. 508, The Electrochemical Society Extended Abstracts, Vol. 83-2, Washington, DC, Oct. 9-14, 1983.
12. A. Climent and S. J. Fonash, *J. Appl. Phys.*, **56**, 1063 (1984).
13. L. J. Brillson, M. L. Slade, A. D. Katnani, M. Kelly, and G. Margaritondo, *Appl. Phys. Lett.*, **44**, 110 (1984).
14. F. Ohira, *This Journal*, **130**, 1201 (1983).
15. S. J. Fonash, *Solid State Technol.*, **28**, 201 (1985).
16. S. Ashok and A. Mogro-Campero, *IEEE Electron. Device Lett.*, **edl-5**, 48 (1984).
17. S. J. Fonash, R. Singh, A. Rohatgi, P. Rai-Choudhury, P. J. Caplan, and E. H. Poindexter, *J. Appl. Phys.*, **58**, 862 (1985).
18. P. J. Caplan, E. H. Poindexter, B. E. Deal, and R. R. Razouk, *J. Appl. Phys.*, **50**, 5847 (1979).
19. E. H. Poindexter, P. J. Caplan, B. E. Deal, and R. R. Razouk, *ibid.*, **52**, 879 (1981).
20. P. J. Caplan, E. H. Poindexter, and S. R. Morrison, *ibid.*, **53**, 541 (1982).
21. M. Y. Tsai, D. S. Day, B. G. Streetman, P. Williams, and C. A. Evans, Jr., *ibid.*, **50**, 188 (1979).
22. A. Climent, J.-S. Wang, and S. J. Fonash, in "Proceedings of the Symposium on Thin Films and Interfaces," pp. 613-618, Vol. 25 of the Materials Research Society Symposia Proceedings (1984).
23. C. M. Ransom, T. Sedgwick, S. K. Chicokta, S. Cohen, and T. I. Chappell, Abstract 407, p. 587, The Electrochemical Society Extended Abstracts, Vol. 84-2, New Orleans, LA, Oct. 7-12, 1984.

Highly Sensitive Impurity Analysis of GaAs Using SIMS and Chemical Preparation

T. Tanaka and S. Kurosawa*

NTT Musashino Electrical Communication Laboratories, Musashino-shi, Tokyo, 180, Japan

ABSTRACT

This paper describes a newly formulated secondary ion mass spectrometry (SIMS) method for ultra-trace impurity analysis in GaAs. Elements of analysis are separated from GaAs crystals, concentrated into a salt film, and analyzed by SIMS. To successfully formulate this method, the separation of impurities from GaAs, the residual film formation and the quantitative method were studied in detail. This new method was ascertained to have a sensitivity 1000 times higher than direct SIMS analysis for such impurities as Zn. Furthermore, it is clear that this method provides more accurate data than do other quantitative methods through a comparison of the quantitative data concerning impurities in GaAs.

GaAs crystals are used for LSI fabrication. In such crystal, residual impurities seriously affect the GaAs LSI electronic properties. Consequently, the amount of impurities must be evaluated and then controlled. Liquid-encapsulated Czochralski-(LEC) grown GaAs crystals contain less than 10 ppb impurities by weight. A sufficiently high sensitivity has been required in quantitative methods to analyze undoped GaAs crystals.

Techniques usually used to obtain such high sensitivity are secondary ion mass spectrometry (SIMS) (1), spark source mass spectrometry (SSMS) (2), flameless atomic absorption analysis (FLAA) (3), and inductively coupled plasma emission analysis (ICP) (4). Although mass spectrometry methods (SIMS and SSMS) have relatively high sensitivities, their detection limits are thought to be 10 ppb at best, since they exhibit a small background noise level in instruments. In addition, their complex ionization mechanisms often make quantitative analyses difficult. FLAA and ICP can provide quantitative analysis data because they are supported by chemical preparation using standards. However, their detection limits are 0.1-10 ppm, which are not low enough for GaAs impurity analysis.

We have, therefore, proposed a new highly sensitive, extremely accurate SIMS method (5) (a chemical SIMS method). The chemical SIMS method can basically be divided into three processes. The first is chemical separation. A GaAs crystal is dissolved with an acid mixture ($HCl:HNO_3:H_2O$ = 6:1:6), and its residual impurities are separated from the GaAs matrix and concentrated into a drop. The second is residual film formation, where the drops are mixed with a salt to accentuate film formation and then heated until dry with an infrared (IR) lamp. The sensitivity is elevated to the extent that the matrix volume is reduced from the GaAs crystal to the residual film. In addition, the choice of salts has the potential of elevating the sensitivity, since particular chemical states of the salts will enhance the ionization of the impurities by varying degrees. The third is SIMS analysis, where the formed film is analyzed and the concentration of impurities are evaluated using standard materials, such as stable isotopes and internal standard elements. High accuracy can be achieved by adding a known concentration of such materials.

Only a few reports exist on the chemical separation of impurities in GaAs. The method (6) that employs the distillation of As followed by the extraction of Ga with ether seems to be the most reasonable. However, there are serious problems with respect to the separation of volatile impurities. In addition, the HCl-form anion-exchange method (7) has the potential of systematic separation of B, Al, Cr, Cu, and Zn in GaAs in the microgram range. These elements in particular are continually encountered in practical analyses. Furthermore, we applied this separation method to the nanogram range of these impurities.

We also developed a residue film formation technique, which is necessary for use with the SIMS analysis of the separated trace elements. We then determined the highly sensitive analytical conditions. This was followed by an examination of isotope dilution and internal standard methods for accurate analysis.

Experimental

Chemical separation.—A 1.2 cm × 30 cm quartz column was used to prevent samples from being contaminated. Teflon PFA jars were used as solution stock vessels for the same purpose. The anion-exchange resin Dowex 2-X8 was used in commercial grade because almost no impurities were found in its rinsed-out solution. Commercial-grade HCl and HNO_3 contain small amounts of impurities. Accordingly, they were purified by three separate distillations, using a quartz apparatus.

* Electrochemical Society Active Member.

A representative example of the chemical separation process involves several steps. A 4-ml solution of 4 GaAs was dropped into an ion column and then mixed first with a 6*N* HCl solution, and finally with a dilute HNO_3 solution (*ca.* 2*N*). The eluted solutions were collected 3 ml at a time. All of the fractions were then analyzed by FLAA or ICP if microgram level separation occurred, or by the chemical SIMS method if nanogram level separation occurred.

Residual film formation.—All of the micropipettes used were made of Teflon ware. The Si wafer was chosen as the film substrate because of its high purity and resistance to HCl and HNO_3. The wafer was cut into 5 mm × 5 mm pieces and etched with conc HF to remove the hydrophilic oxide layer.

The typical residual film formation procedure is presented in Fig. 1. A 50 μl solution of 0.04% inorganic salt was added into the solution obtained from chemical separation. The mixture was concentrated to about 10 μl, dropped onto the Si wafer, and dried with an IR ramp.

SIMS analysis.—All of the stable isotopes were imported from the Oak Ridge National Laboratory, Tennessee. The oxides of ^{50}Cr, ^{65}Cu, and ^{68}Zn were dissolved with HCl and then stocked in 0.2% solutions (spike solution). ^{50}Cr was also used as the internal standard element of Mn and Al because of its similar chemical behavior.

The Hitachi IMA-2 was used as the secondary ion mass spectrometer. Ar^+, accelerated to 10 kV, was used as a primary ion with a beam current of 1.5 μA and a diameter of 1 mm. To compensate for the primary ion charging of an insulant salt film, a 0.3A electron beam was irradiated toward the particular charge-up locations on the film. The pressure in the chamber was 1×10^{-7} torr.

Results and Discussion

Chemical separation.—The anion exchange method has been reported to be selective with respect to the possible separations involving metal complexes. A method using 6*N* HCl as a solvent in particular achieves Ga separation from the other elements, such as Al (7). In this section, this HCl-form anion exchange method was applied to the separation of Cr, Mn, Cu, Zn, and Se from the GaAs matrix.

These elements can be divided into three groups by their adsorption behaviors. One group includes Cr, Mn, As, and Se, another Cu and Ga, and the other Zn. The amounts of Ga and As are at least about 10^6 times larger than impurities found in practical analyses. Accordingly, it is important, although difficult, to separate the elements among the same groups. For Zn, its separation becomes difficult because the amount of residual Ga cannot be neglected. The separation of Cr, Mn, and Se from As, that of Cu from Ga, and that of Zn from Ga were the primary focal points of this work. These separation methods were applied to the nanogram level separation that is necessary for practical analysis using the chemical SIMS method.

Separation of Cr, Mn, and Se.—Initially, typical adsorption behavior of Ga and As as well as impurities were examined, using a 10-cm-length column. The elution curves are shown in Fig. 2, where C/C_{max} means the concentration divided by the maximum concentration of the element in the eluted solution. Cr, Mn, As, and Se are slightly adsorbed and soon elute in 6*N* HCl (6), whereas Cu, Zn, and Ga exhibit strong adsorption. The separations among this group are difficult under the same condition (Fig. 3a), because the amount of As is about 10^6 times larger than the impurities found in practical analyses. However, the elution of As is slightly delayed compared with Cr, Mn, and Se. This demonstrates that the increased resin amount enables the perfect separation of Cr and Mn from As, because a slight adsorption difference between Cr (Mn) and As has accumulated. The elution curves using a 25-cm-length column are given in Fig 3b. Using the long column, the elution of As is so delayed that separation of Cr and Mn can be achieved.

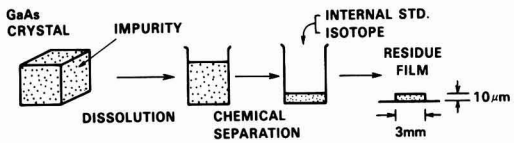


Fig. 1. Chemical preparation and residual film formation

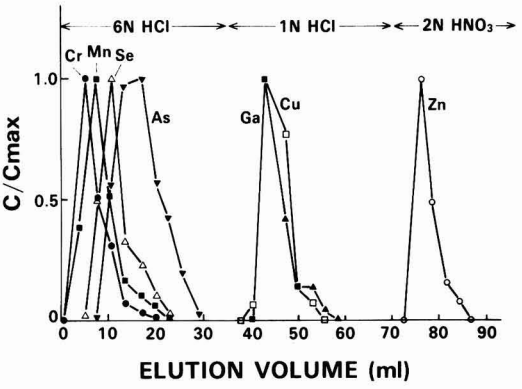


Fig. 2. Anion-exchange separation of Cr, Mn, Cu, Zn, Ga, As, and Se; Cr, Mn, and Cu 1 μg, Zn and Se 20 μg, and Ga and As 20 mg, with 10 cm × 1 cm² column (Dowex 2-X8).

The adsorption behaviors of Cr and Mn at 160 ng and As at 80 mg are presented in Fig. 4. The Cr and Mn elution curve peaks are almost completely separated from that of As, although the tails of both are slightly superimposed. However, the As amount in this overlapping part is about 100 μg, which corresponds to only 0.1% of the total As amount. On the other hand, Ga is not detected when it is added (*ca.* 80 mg), which shows that Ga and As can be removed at the same time with this method, even during the nanogram level separation of Cr and Mn.

The adsorption behavior of Se is quite similar to that of As. When Se is separated from As, the column used seems to be longer than that used in the separation of Cr and Mn. However, further investigation has not yet been done in relation to this.

Separation of Cu.—Cu does not pass through the anion-exchange resin in 6*N* HCl as well as Ga does (Fig. 2). When the amount of Ga increases, the separation of Cu is difficult to accomplish only by anion exchange. To achieve the separation, ether extraction (8) is thought to be available after the removal of As through the anion exchange method. This ether extraction was carried out three times, and these ether solutions, along with aqueous solution, were analyzed by the chemical SIMS method.

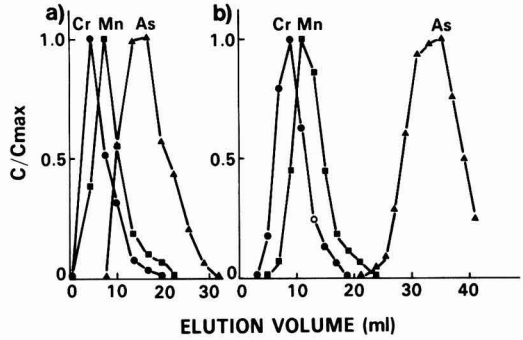


Fig. 3. Separation of Cr, Mn, and As; Cr and Mn 1 μg and As 20 mg, (a) with 10 cm × 1 cm² column, and (b) with 25 cm × 1 cm² column.

The Ga in aqueous solutions decreases dramatically according to the extraction time. Through three extractions, Ga was found to be reducible to 0.01% of the total added Ga weight. No As is detected in the solutions treated with this combination method. Thus, this separation method is found to be useful for Cu separation.

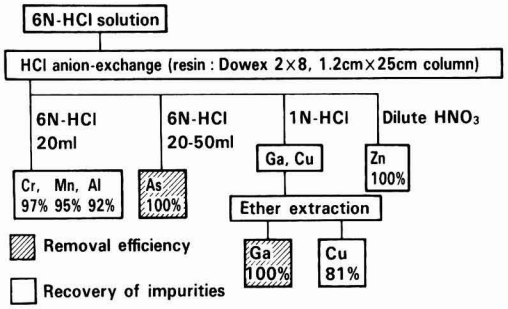
Separation of Zn.—Zn exhibits excellent adsorption, even in a dilute HCl solution, whereas Ga elutes in 1*N* HCl (Fig. 2). Zn can be eluted by adding dilute HNO_3. During nanogram level separation, Zn can also be recovered without loss. Here, the small amount of Ga that was mixed in was less than 0.1%. As this is not such a serious problem, verification can be made as to whether or not this separation method can be applied to this chemical SIMS method.

Recovery and removal.—The chemical separation procedures are summarized in Fig. 5. Cr, Mn, and Zn can only be separated from GaAs using an anion-exchange resin. Cu can be separated by the combination of anion exchange and extraction. From the GaAs removal efficiency viewpoint, the combination of removing As by distillation and Ga by ether extraction is more useful for recovering metal impurities like Cu than in the present systematic method. However, this method exhibits the potential for separating volatile impurities, although a problem exists in the recovery of such impurities during the removal of As by distillation. Furthermore, the overall procedure is easier with this method than with the distillation method.

The recoveries and removal efficiencies of Ga and As are also given in Fig. 5. Satisfactory impurity recoveries, as well as removal efficiencies, are obtained by this separation method. The impurity recoveries range is from 80 to 100%, that is, Cr 97%, Mn 95%, Cu 81%, and Zn 100%. With this method, recovery is not necessarily 100%, because cancellation or compensation is possible in the recoveries by adding an internal standard material before separation. The removal efficiencies of Ga and As are almost 100%. GaAs left in an impurity solution interferes with analyses only if it is comparable to or larger than 100 μg, which is the amount of a salt necessary for residual film formation (see next section).

Residue film formation.—Procedure.—A GaAs crystal is dissolved with an acid mixture. An internal standard solution (or a spike solution), and a salt solution (*ca.* 2%) for residual film formation are added to this GaAs solution. The mixture is next concentrated to about 10 μl and dropped onto a Si wafer substrate using a 5 μl micropipette. It is then heated until dry with an IR ramp to obtain a residual film.

The uniformity in the residual film is thought to affect the accuracy and precision in the chemical SIMS method. In addition, the secondary ion emission process of impurity elements depends on the chemical nature of its surroundings. Consequently, the chemical nature of the selected salt is thought to affect the secondary ion intensity. That is, the choice of salt is very important to the sensitivity of the chemical SIMS method.



GaAs SEPARATION PROCESS

Fig. 5. Block diagram of chemical separation for impurities in GaAs

Accuracy and precision.—Various salts for obtaining uniform films were investigated. Chlorides and nitrates of alkali metals and alkali earth metals, as well as Ga and Bi, were found to give relatively uniform films. The typical film diameter obtained was 3 mm. Estimation of these films by SIMS showed that the variation in secondary ion intensities of matrices fell into the 30% range. No serious precision problems were apparent from these results. No difference existed between the elements in any one film, and the secondary ion intensity ratios were almost completely constant between the two elements. This indicates that high accuracy is expected in quantitative analyses using standards for these chloride or nitrate films.

Sensitivity.—Secondary ion intensity dependence on the chemical nature of salts was investigated for the anion and cation chemical states for several films. First, The anion effect was examined using the electronegativity of the anions in the salts as a parameter. Changes in the secondary ion intensity of Ti, Cr, Mn, Fe, Cu, and Zn (500 ng for each) *vs.* the anion electronegativity of bismuth salts are indicated in Fig. 6. As the electronegativity in these

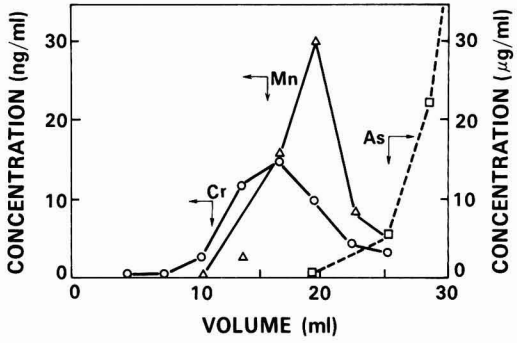


Fig. 4. Nanogram-level separation of Cr, Mn, and As; Cr and Mn 50 ng and As 80 mg, with 25 cm × 1 cm² column.

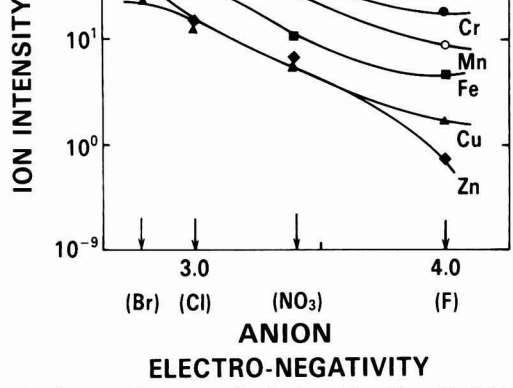


Fig. 6. Anion effect on secondary ion intensities of impurities in bismuth salts; impurities 500 ng and bismuth salts 100 μg.

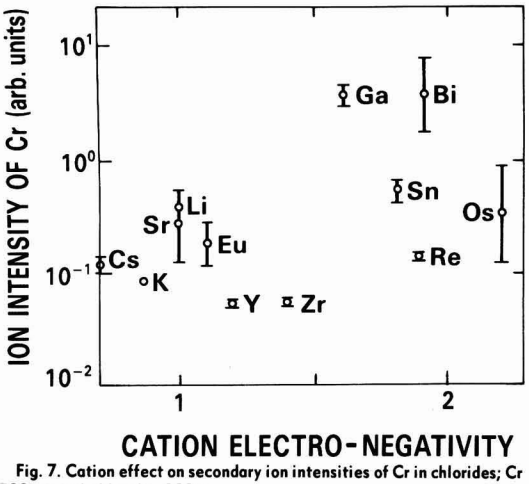


Fig. 7. Cation effect on secondary ion intensities of Cr in chlorides; Cr 500 ng and chlorides 100 μg.

salts increases, the ion intensities of the impurities decrease. It is clear that the chloride and bromide give relatively high intensities. The charging of these insulating salts should be one of the reasons for this dependence on salts, but more detailed studies are needed to explain it. However, from the precision and accuracy standpoints, the chloride seems to be the most suitable for residue films.

The cation effect was also examined using the cation electronegativity for the chlorides that give uniform film. The dependence of Cr secondary ion intensities on the cation electronegativities is plotted in Fig. 7. For bismuth chloride, the Cr ion intensities are higher, while they are lower for cesium and potassium chlorides. From these results, bismuth chloride is thought to be the best salt to use in the new SIMS method.

SIMS analysis.—For quantitative analysis of our method, the isotope dilution method was used for Cr, Cu, and Zn, which have more than two stable isotopes, while the internal standard method was used for Al and Mn, which have only one stable isotope. The principal focus was on their accuracy and precision.

Isotope dilution method.—In the chemical method, two points essential to achieving high accuracy must be considered. One is good recovery during chemical separation, and the other is the small secondary ion intensity variation occurring throughout the residue film. However, using the isotope dilution method, losses during separation are canceled out because the chemical behavior is the same between the two stable isotopes. The variation in the ion intensity is also canceled out, as it is mainly attributed to the elemental distribution across the film, that is, the chemical behavior. Consequently, high accuracy is expected in the isotope dilution methods.

One analysis example, that of Cr, is given in Table I. The sample contains 12 ng of Cr, and its stable isotope is ^{50}Cr, having a known concentration. The maximum deviation from the true value (added Cr values) is 0.8 ng, which corresponds to 6.7% of the true value. This demonstrates that isotope dilution methods have rather high accuracies. The CV (coefficient of variation) is within 3.9%, which indicates that they also exhibit good precision (repeatability).

Table I. Analysis of Cr by isotope dilution method using ^{50}Cr as a standard (Cr; 12 ng)

Run no.	Cr found ng	Deviation ng	Deviation %
1	11.5	−0.5	−4.2
2	12.1	+0.1	+0.8
3	12.1	+0.1	+0.8
4	12.3	+0.3	+2.5
5	11.2	−0.8	−6.7

RSD = 4.2%.

The isotope dilution methods were also applied to Cu and Zn, where ^{65}Cu and ^{68}Zn were chosen as the standards of Cu and Zn. There maximum deviations from the true value were at most 10%, and the CV values were within 5%. The chemical SIMS method using isotope dilution methods ensures an accuracy and precision higher than other quantitative analysis methods, such as FLAA and ICP.

Internal standard method.—For the internal standard method, the two problems mentioned above become severe and adversely affect the accuracy and precision of the analysis. Mn has an adsorption behavior similar to Cr, while its recovery is the same as that of Cr. Thus, ^{50}Cr was used as a standard. The secondary ion intensity ratios of Mn to ^{50}Cr were examined in $BiCl_3$ and $Bi(NO_3)_3$. The intensity ratios were found not to vary in these salts. The relationship between the amount and the intensity ratio of Mn to ^{50}Cr in $BiCl_3$ is plotted in Fig. 8. A good linear relationship was obtained over the wide range of 1 ng to 1000 ng. In addition, the repeatability of this slope was within 10% of the CV value. This implies that the method using ^{50}Cr is very useful for Mn quantitative analysis. ^{50}Cr can be used as the standard for achieving the quantitative analysis of Al.

Application limits.—The quantitative methods, their accuracies and detection limits are summarized in Table II. The detection limits of GaAs were calculated from the detection limit concentrations of the elements in solutions by assuming that the amount of treated GaAs was 200 mg. These detection limits are restricted by the sensitivity, as well as by the contamination in the new method. The former is dependent on the effective concentration degree following chemical separation, as well as on the ionization efficiency of elements due to the ionization potential and the chemical state of the residual film. The latter mainly originates from the reagents, apparatuses, and surroundings present during the analysis procedures.

Al, Cr, and Mn exhibit inherently higher sensitivities with the direct SIMS method. Consequently, the sensi-

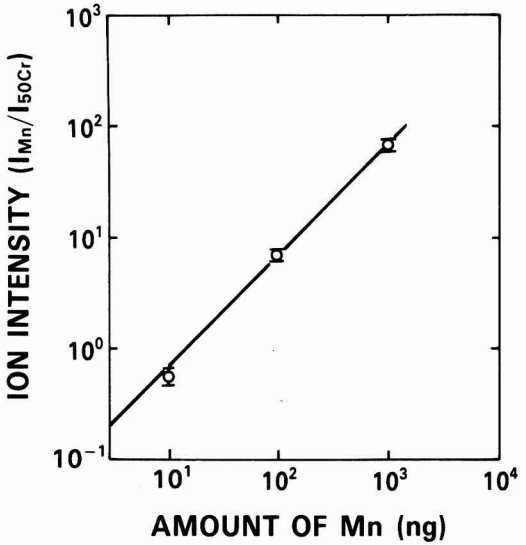


Fig. 8. Relationship between Mn amount and secondary ion intensity ratio of Mn to ^{50}Cr; ^{50}Cr 10 ng and $BiCl_3$ 100 μg.

Table II. Detection limit in GaAs[a] and precision of chemical SIMS method compared with direct SIMS method

Element	Chemical SIMS			Direct SIMS	
	Analytical method	Precision (RSD%)	Detection limit (ppb)	Precision (RSD%)	Detection limit (ppb)
Cr	Isotope[b]	5	3	10	7
Mn	Internal[c]	5-10	0.5	10	5
Cu	Isotope	5	5	10	350
Zn	Isotope	5	5	10	5000
Al	Internal	5-10	50	10	1

[a] Detection limits in GaAs were calculated by assuming the amount of the treated GaAs was 200 mg.
[b] Isotope dilution method.
[c] Internal standard method.

tivities of Cr and Mn increase at the most to an extent of 10 times those from the direct analysis. However, the Cu and Zn analyses from the chemical SIMS method exhibit sensitivities 10^2-10^3 times higher than those from the direct method, in which the sensitivities of Cu and Zn are very low due to their high ionization potentials.

In particular, the chemical SIMS method is useful for Cu and Zn analyses. For Cr, Mn, Cu, and Zn, their sensitivities increase mainly by elevating the effective concentration degrees. In Al analysis, however, its sensitivity decreases dynamically up to 10^{-3} times, due to contamination. This shows that contamination during chemical preparation is an important factor in deciding the detection limits.

Application.—Analyses of impurities in GaAs were conducted using the new method. The analytical results for Cr, Mn, Cu, and Zn are summarized in Table III, together with those from other methods. The quantitative results from the new method demonstrate good agreement with those from the other methods. It should be noted that more than two effective numbers exist for each datum. Therefore, the new method has been proven to lend itself to analysis that is potentially high in terms of accuracy and sensitivity.

Summary

This paper has reported the development of a highly sensitive impurity analysis method for GaAs using SIMS in conjunction with chemical preparation. The method involves specifically for quantitative sensitivity of up to 10^2-10^3 higher than conventional SIMS analysis. The method should be widely applicable to trace analysis relative to semiconductors.

Table III. Analysis of impurities in GaAs crystal (ppm)

Element	Chemical SIMS	FLAA	SSMS	Direct SIMS
Cr	0.62 ± 0.02	0.7 ± 0.2	1.3 ± 0.2	0.65 ± 0.05
Mn	6.0 ± 0.5	7 ± 2	15 ± 2	—
Cu	1.45 ± 0.04	0.9 ± 0.3	1.2 ± 0.3	n.d.
Zn	13.1 ± 0.4	—	18 ± 3	n.d.

Acknowledgments

The authors would like to thank S. Hattori, N. Honma, and Y. Homma, of Musashino Electrical Communication Laboratory, for their support through discussions on this work. We also wish to thank to K. Kobayashi of Ibaraki Electrical Communication Laboratory, and J. Osaka of Atsugi Electrical Communication Laboratory for their valuable suggestions on this work.

Manuscript submitted June 10, 1985; revised manuscript received Oct. 14, 1985. This was Paper 453 presented at the New Orleans, Louisiana, Meeting of the Society, Oct. 7-12, 1984.

NTT Musashino Electrical Communication Laboratories assisted in meeting the publication costs of this article.

REFERENCES

1. Y. Homma and Y. Ishii, *J. Appl. Phys.*, **56,** 1892 (1984).
2. M. R. Brozel, J. B. Clegg, and R. C. Newman, *J. Phys. D: Appl. Phys.*, **11,** 1331 (1978).
3. T. Hadeishi and H. Kimura, *This Journal*, **126,** 1988 (1979).
4. S. Kurosawa, Y. Homma, T. Tanaka, and M. Yamawaki, "Secondary Ion Mass Spectrometry SIMS IV," p. 107, A. Benninghoven, J. Okano, R. Shimizu, and H. W. Werner, Editors, Springer-Verlag, Berlin, Heidelberg, New York, Tokyo (1984).
5. N. Honma, S. Kurosawa, and I. Kawashima, Rev. Electr. Commun. Lab., **30,** 503 (1982).
6. W. F. Hillebrand, G. E. F. Lundel, H. A. Bright, and J. I. Hoffmann, "Applied Inorganic Analysis," p. 259, John Wiley and Sons, Inc., New York (1955).
7. K. A. Kraus and G. W. Smith, *J. Phys. Chem.*, **58,** 11 (1954).
8. H. Onishi and E. B. Sandel, *Anal. Chim. Acta*, **13,** 159 (1955).

Thermodynamics of the Silicon-Chlorine-Hydrogen System: Chemical Potential for Homogeneous Nucleation

Kenneth D. Allen* and Herbert H. Sawin**

Department of Chemical Engineering, Massachusetts Institute of Technology, Cambridge, Massachusetts 02139

ABSTRACT

The equilibrium deposition efficiency and the chemical potential driving force for nucleation and/or deposition of silicon from the gaseous Si-Cl-H system are presented for a wide range of compositions and temperatures. Chlorine addition lowers the thermodynamic potential for nucleation, as well as the equilibrium deposition efficiency. In addition, a chemical buffering effect is observed, which potentially could be exploited to improve the uniformity of CVD processes. Possible applications of these results to thin film deposition and polysilicon production in free-space and fluidized bed reactors are discussed.

Homogeneous nucleation of silicon from the vapor is an important phenomena in several industrial processes. In chemical vapor deposition (CVD) of thin silicon films for microelectronic devices, the formation of fine particles by homogeneous nucleation results in poor film quality and limits the deposition rate achievable in CVD processes. Control of nucleation is also vital to the success of proposed free-space reactor and fluidized bed reactor processes for the production of solar-grade polysilicon. The potential economic advantages of these processes over the conventional Siemen's technology are well documented (1-3). Consequently, the dependence of nucleation on processing conditions (temperature and composition) is of great practical importance.

A priori prediction of homogeneous nucleation rates is not presently possible. The two most commonly cited nucleation theories (classical and statistical mechanical) are based on thermodynamic arguments. Unfortunately, they predict nucleation rates differing by over 15 orders of magnitude, although each has shown reasonable agreement with experiment for certain chemical systems (4). Also, these theories are directly applicable only to the case of nucleation by physical condensation (*e.g.*, the nucleation of water droplets from water vapor). In the Si--Cl-H system, nucleation may occur through two mechanisms: physical condensation of atomic silicon and CVD reaction involving silicon-bearing species. Katz and Donohue have extended nucleation theory to include simultaneous deposition via chemical reaction through a kinetic formulation, and demonstrated the dramatic influence of CVD reactions on homogeneous nucleation rates in silica condensation (5). Although the surface reaction rates and sticking coefficients required for implementation of this theory are currently unavailable for the Si-Cl-H system, reasonable estimates might be used to examine trends in nucleation rate with processing conditions. In the present work, however, we consider the thermodynamic approach in light of its simplicity and popularity.

Physical nucleation occurs via a series of reversible "reactions." In each step, an atom of the condensing species adds to a previously formed cluster of atoms; evaporation of an atom from the cluster constitutes the reverse reaction. Condensation is driven by the difference in energy states between the two systems: (*i*) vapor equilibrium in the absence of solid, and (*ii*) gas-solid equilibrium. At constant temperature and pressure, this corresponds to the change in the Gibbs energy of the system upon addition of one atom of vapor to the cluster phase. In some processes (constant temperature and volume) it is more correct to consider the Helmholtz energy change, although either representation specifies the chemical potential differences between an atom in the vapor and an atom in the growing cluster as the pertinent driving force.

For deposition to occur on a cluster, a sufficient driving force is required to overcome the retarding energy barrier due to increasing cluster surface area. This energy barrier is most significant in small clusters. The cluster growth rate is determined by the magnitude of the chemical potential driving force relative to the surface energy barrier; this ratio increases with cluster size. Growth of small clusters is not energetically favorable due to the large surface energy (resulting from the small radius of curvature) and the large incremental surface area increase per deposited atom; however, there is a statistically finite probability that a small cluster will grow. When a cluster reaches a critical size of j atoms, further growth becomes energetically favorable. In the classical theory, formation of the critical cluster (or nuclei) is considered the rate-limiting step. The nuclei concentrations are determined using a Boltzmann distribution based on the driving and retarding forces. For nucleation of atomic silicon from the vapor, the classical nucleation rate I is proportional to

$$I \alpha\ p_g{}^2/T^2 \exp[-(j\Delta\mu + \sigma A_j)/kT] \qquad [1]$$

Here, p_g is the atomic silicon partial pressure, T is the absolute temperature, σ is the surface energy, k is Boltzmann's constant, and A_j is the surface area of a critical cluster. The driving force term, $\Delta\mu$, is the difference between the chemical potentials of atomic silicon in the pure vapor equilibrium state, $\mu_g{}^o$, and bulk solid silicon in the gas-solid equilibrium state, $\mu_s{}^e$. For systems where ideal gas behavior can be assumed, the driving force is often expressed in terms of the supersaturation ratio S

$$\Delta\mu \equiv \mu_s{}^e - \mu_g{}^o = -kT \ln S \qquad [2]$$

where the supersaturation is defined as the ratio $p_g{}^o/p_g{}^e$, the atomic silicon partial pressure in the vapor equilibrium system relative to that in the gas-solid equilibrium system. Note that a system in gas-solid equilibrium has $\Delta\mu = 0$, and that the driving force for nucleation of a supersaturated system is negative. Conversely, if $\Delta\mu$ is positive, solid will not deposit from the vapor.

The concept of $\Delta\mu$ as the only driving force is not completely correct for a chemically reacting system. Solid silicon can be deposited by CVD reactions as well as by physical condensation of gaseous atomic silicon. For example, there is considerable evidence that silicon deposition in the presence of chlorine proceeds via $SiCl_2$ adsorption on the surface and subsequent reaction with H_2 (6). Whereas the Gibbs energy change of the system upon physical condensation of an atom of atomic silicon is $\Delta\mu$, the Gibbs energy change upon CVD reaction depends on the Gibbs energy of the reaction, ΔG_r. In other words, there is also an effective supersaturation for species which can react to form solid silicon. The chemical potential of these species are related to $\Delta\mu$ as follows: if $\Delta\mu = 0$ all CVD reactions are also in thermodynamic equilibrium, while if $\Delta\mu < 0$, CVD processes are energetically favorable and deposition can occur by chemical, as well as physical, processes.

In the calculation described below, we have also assumed that the quasi-equilibrium approach is valid, *i.e.*, that vapor equilibrium is established quickly relative to

*Electrochemical Society Student Member.

*Electrochemical Society Active Member.

the nucleation onset time. This assumption may be in error for the Si-Cl-H system if gas-phase reactions are rate limiting, thereby influencing the vapor composition during nucleation. To correctly model nucleation, kinetic rates for all gas phase and deposition reactions must be included. However, the thermodynamic approach is merited as a zeroth-order description of nucleation in the Si-Cl-H system because of the lack of kinetic data available, and because it is consistent with the prevailing nucleation theories.

The rate of homogeneous nucleation is strongly dependent on the driving force, as is evident in Eq. [1]. Knowledge of the driving force therefore allows semi-quantitative prediction of nucleation behavior in a chemically reacting system. The driving force for deposition also influences the rate of CVD reactions, although the relationship may not be known. In the present work, the chemical potential driving force of the Si-Cl-H system (at 1 atm total pressure) was calculated over a wide range of compositions. Previous workers primarily concerned with equilibrium species distributions have performed calculations for the gas-solid Si-Cl-H system (7, 8). The results of such calculations are in satisfactory agreement with experiment (9).

Results

Equilibrium calculations were performed using the reactor series method, chosen for its excellent convergence properties and computational flexibility (10). Seventeen chemical species (see Table I) were included in the calculations. The specific chemical reactions used in the equilibrium calculations were generated by Gauss-Jordan elimination of the set of species formation reactions, using major species as the pivots to minimize the required computation time. The results reported here are considered computationally accurate within 0.001%, but are sensitive to the accuracy of the thermodynamic data, as discussed later.

We calculated $\Delta\mu$ for a range of temperature (700°-1200°C), elemental chlorine/silicon ratio (0-4), and elemental chlorine/hydrogen ratio (0-10). In addition, we obtained some results for the SiH_4-H_2 system. The equilibrium silicon deposition efficiency ξ was also calculated. We define ξ as the moles solid silicon deposited from the vapor during equilibration, per mole of total elemental silicon in the system. Previous workers have performed similar calculations of equilibrium composition and equilibrium deposition efficiency over more restricted ranges [*e.g.*, Ref. (12)], but have not reported chemical potential driving forces.

Contours of constant $\Delta\mu$ were generated by linear regression to a polynomial expression, for a matrix of conditions. These results are presented as a function of Cl/Si ratio and Cl/H ratio at temperatures of 800°C (Fig. 1) and 1000°C (Fig. 2). Contours of ξ at 800° and 1000°C are shown in Fig. 3 and 4, respectively. Hydrogen dilution effects in several important chemical systems (SiH_4 + HCl, SiH_2Cl_2, $SiHCl_3$, and $SiCl_4$) are easily examined by following vertical lines at the noted Cl/Si ratios. For example, hydrogen addition to $SiHCl_3$ is represented graphically by moving down the page at Cl/Si ratio of 3.

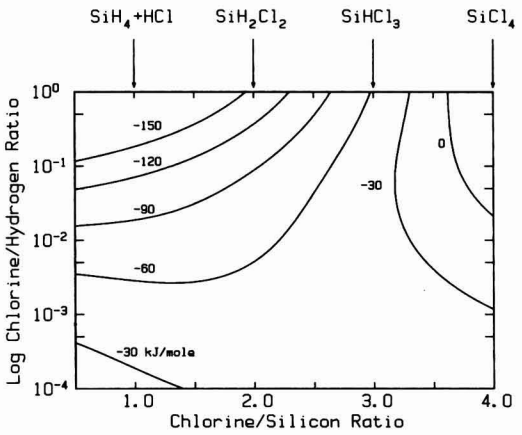


Fig. 1. Contour plot of chemical potential driving force $\Delta\mu$, in kJ/mole, at 800°C. More negative values of $\Delta\mu$ indicate a greater driving force for nucleation and deposition.

The general trends seen in Fig. 1-4 can be explained using the calculated equilibrium species distributions, which have also been presented elsewhere [*e.g.*, Ref. (7)]. Since the partial pressure of silicon increases with either decreasing Cl/Si or increasing Cl/H ratio, the driving force for deposition increases (*i.e.*, $\Delta\mu$ becomes more negative) as we move up or to the left on the figures. The deposition efficiency ξ increases as either Cl/Si or Cl/H decreases because a lesser fraction of the silicon is tied up in chlorinated species. The opposite responses of $-\Delta\mu$ and ξ to changes in Cl/H result from the shift of chlorine from SiH_xCl_y species to HCl as Cl/H decreases. For example, the addition of SiH_2Cl_2 to a SiH_2Cl_2/H_2 mixture causes the partial pressure of silicon (and consequently the chemical potential driving force) to increase due to increased silicon loading, but the fraction of silicon tied up (at equilibrium) in chlorinated species (rather than as solid) also increases, causing the deposition efficiency to decline.

Recall that the driving force, and hence the nucleation rate, is large when $\Delta\mu$ is very negative; the sharp increase in $\Delta\mu$ with increasing Cl/Si is therefore in agreement with experimental evidence that chlorine addition inhibits nu-

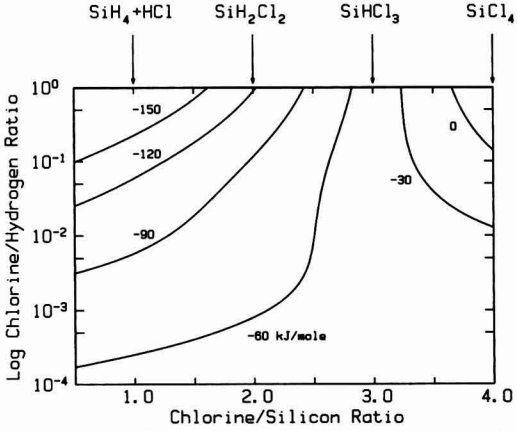


Fig. 2. Contour plot of chemical potential driving force $\Delta\mu$, in kJ/mole, at 1000°C.

Table I.

Species	Reference for thermo. data
H_2	(7)
Cl_2	(7)
Si(s)	(7)
HCl	(7)
SiH_4	(7)
SiCl	(7)
$SiCl_2$	(7)
$SiCl_3$	(7)
$SiCl_4$	(7)
SiH	(7)
Cl	(7)
H	(7)
Si_2Cl_6	(7)
Si(g)	(7)
SiH_3Cl	(11)
SiH_2Cl_2	(11)
$SiHCl_3$	(11)

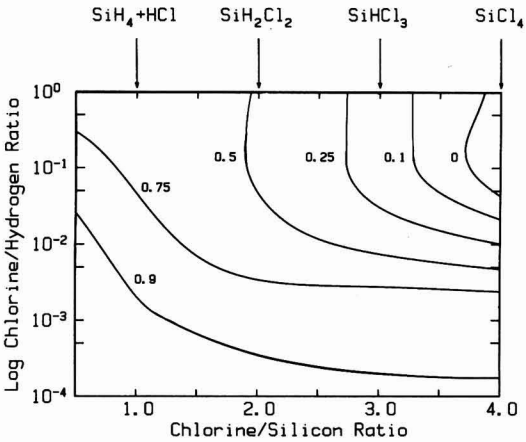


Fig. 3. Contour plot of equilibrium deposition efficiency ξ at 800°C

cleation (13). This effect is partially kinetic in nature, but the point is underscored by the thermodynamic results. Examination of the species distribution reveals that silicon is increasingly tied up in highly chlorinated species such as $SiCl_2$ as Cl/Si is increased, presumably resulting in a great decrease in the rate of nucleation by physical condensation. At high (>2) Cl/Si_2 ratios, $SiCl_2$ is generally a major silicon-bearing species. Note also that at low Cl/H ratios (dilute mixtures of chlorosilane in hydrogen), $\Delta\mu$ is relatively constant with Cl/Si. For Cl/Si>3, $\Delta\mu$ is relatively insensitive to the Cl/H ratio, as indicated by the nearly vertical contour lines. Consequently, increasing the mole fraction of $SiHCl_3$ in hydrogen has little effect on the energetics of nucleation. However, the condensation rate should increase with chlorosilane loading due to the increased partial pressure of atomic silicon. For lower Cl/Si ratios, $\Delta\mu$ is strongly dependent on Cl/H. We note that a large driving force is not necessary for chemical vapor deposition, as seen in the $SiCl_4$-H_2 system wherein silicon deposits at low Cl/H ratios and etches at higher Cl/H ratios (14).

For Cl/H greater than 10^{-3}, $\Delta\mu$ generally decreases with increasing temperature, more rapidly in highly chlorinated systems. This trend is difficult to see in the contour plots, but was clear in the numerical results. Therefore, the rate homogeneous nucleation should increase more rapidly with temperature for $SiHCl_3$ than for SiH_2Cl_2. Similar calculations for SiH_4-H_2 mixtures show that $\Delta\mu$ decreases rapidly with increasing temperature due to atomic silicon production by silane decomposition. We therefore expect that the nucleation rate would be very sensitive to temperature, since both the kinetics and the thermodynamic driving force increase with temperature. The predicted rapid increase in nucleation rate with temperature (manifested as a reduction in the critical SiH_4 concentration) has been observed experimentally (15). In a more recent study, a similar temperature dependence was observed in the nucleation of SiH_2Cl_2 (16).

Contours of equilibrium deposition efficiency at 800° and 1000°C are displayed in Fig. 3 and 4, respectively. Note the region at high Cl/Si and high Cl/H (upper right corner). Here $\Delta\mu$>0, so silicon deposition is not energetically favorable, hence silicon etching occurs. The slight differences between the $\Delta\mu = 0$ contours in Fig. 1 and 2 and the $\xi = 0$ contours in Fig. 3 and 4 result from fitting errors of the polynomials used in the contour plotting. Note that chlorine addition at fixed Cl/Si (corresponding to increasing chlorosilane concentration in hydrogen) rapidly decreases ξ for low Cl/H ratios. However, ξ is relatively constant for high (>10% in H_2) SiH_2Cl_2 or $SiHCl_3$ loading, as evidenced by the near vertical contour lines for these gases at high Cl/H ratios. Previous workers [*e.g.*, Ref. (12)] concerned only with epitaxial growth have not investigated chlorosilane concentrations (in hydrogen) of more than a few percent.

The important implication here is that ξ is relatively independent of chlorosilane mole fraction X_{CS}; therefore, the achievable throughput (per unit volume of gas feed) of a deposition process is approximately linear in X_{CS} for concentrated mixtures. This is an equilibrium result, and is not meant to suggest that silicon deposition rates are linear in X_{CS}. In fact, CVD rates from dichlorosilane are roughly linear in composition up to about 10% SiH_2Cl_2 in hydrogen (17-21). However, extension of the linear dependence to higher X_{CS} is questionable since the rate-limiting step may change with increasing surface coverage, and also because the reaction rate is dependent on hydrogen concentration. As Cl/Si increases, the deposition rate becomes sublinear in X_{CS}, even at low Cl/H ratios (22). Since deposition rate data for concentrated chlorosilane systems is not presently available, operating conditions must be optimized experimentally.

As a crude measure of the reliability of the thermodynamic results, the sensitivity of the results to the thermodynamic parameters used in the calculations was examined. Thermodynamic data for stable species such as $SiHCl_3$ and $SiCl_4$ should be accurate within a few percent. For example, Farber and Srivastava report uncertainties in chlorosilane enthalpies of formation (ΔH_f) as 2-5% (11). However, important unstable radical species such as $SiCl_2$ may not be as well characterized, and 10% error is possible. In Table II the sensitivities of $\Delta\mu$ and ξ to the thermodynamic data are demonstrated by calculations using ΔH_f at the extremes of the stated uncertainty ranges for three major species. Trichlorosilane and tetrachlorosilane enthalpies of formation were varied ±5% from the base value in accordance with published uncertainties, and ΔH_f of $SiCl_2$ was varied by ±10%. Similar results to those shown in Table II were obtained at other temperatures and compositions, although the sensitivities vary somewhat with conditions.

The results are quite sensitive to relatively small changes in the heats of formation. As seen in Table II, a 5% change in the enthalpy of formation of a major species can change $\Delta\mu$ and ξ by factors of two. Generally, deposition efficiency decreases as a silicon-bearing species is made more stable (by making ΔH_f more negative), since more silicon is tied up in the vapor phase. The effect on chemical potential driving force is similar; as $SiHCl_3$ or $SiCl_2$ are made more stable, the driving force decreases (becomes more positive) as atomic silicon is consumed in favor of chlorinated species. However, the response of the system to changes in ΔH_f of $SiCl_4$ is less obvious. As $SiCl_4$ is made more stable the mole fraction of $SiCl_4$ increases, but less chlorine is available for formation of other chlorinated silicon-bearing species. The net effect is an in-

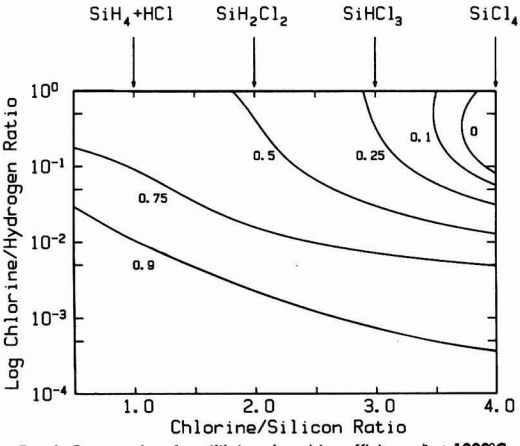


Fig. 4. Contour plot of equilibrium deposition efficiency ξ at 1000°C

Table II. Sensitivity of calculations to thermodynamic data at Cl/Si = 3.0 and Cl/H = 0.158 (10% $SiHCl_3$ in H_2), T = 1000°C

ΔH_f, $SiHCl_3$ (kJ/mol)	ΔH_f, $SiCl_4$ (kJ/mol)	ΔH_f, $SiCl_2$ (kJ/mol)	$\Delta\mu$ (kJ/mol)	ξ
−119.3*	−156.7*	−38.2*	−10.06	0.215
−125.3	−156.7*	−38.2*	−9.84	0.077
−113.6	−156.7*	−38.2*	−10.94	0.309
−119.3*	−164.5	−38.2*	−17.27	0.277
−119.3*	−149.2	−38.2*	−6.84	0.135
−119.3*	−156.7*	−42.0	−4.89	0.156
−119.3*	−156.7*	−34.7	−13.20	0.229

* Indicates published data, used as base value.

crease in both the deposition efficiency and the chemical potential driving force for deposition.

Discussion

These results have important implications to polysilicon production in free-space reactors (FSR). Briefly, a FSR is a tubular reactor through which the reactant gases (*e.g.*, SiH_4 and H_2) are flowed. The reactor can be seeded with small silicon particles which grow by CVD as they pass through the reactor. Silicon throughput in a FSR is considerably higher than in the Siemen process due to the large surface area available for deposition, and the elimination of mass transfer limitations.

The goal is to grow a large diameter, monodisperse silicon powder, both to facilitate handling and to minimize surface contamination. Homogeneous nucleation results in an aerosol of a wider size distribution; the fines produced present problems in further processing. Process optimization involves a trade-off between high particle growth rates and suppression of nucleation. One approach to reducing the nucleation is to seed the reactor with a high number density of small silicon particles. Since the heterogeneous deposition is fast compared to homogeneous nucleation, the nucleation between particles can be minimized. If the interparticle distance is less than the clearance volume, defined as the distance over which a particle depletes the gas of atomic silicon, homogeneous nucleation is suppressed (23). Acceptably monodisperse silicon powders have been produced from SiH_4 by this technique (24). However, the maximum particle size is limited by the particle number density, *i.e.*, each particle can only collect silicon from a volume defined by a sphere with a radius of roughly one-half the interparticle distance. Increasing the clearance volume decreases the required particle number density, thereby increasing the interparticle distance and the maximum particle size. Using classical nucleation theory, the clearance volume ρ^3 of a particle is related to the thermodynamic properties of the system by (25)

$$\rho^3 \propto \sigma^3/(\ln S_\infty)^3(kT_\infty)^2 p_{m\infty} \quad [3]$$

where S_∞ is the supersaturation at a point outside the range of influence of the particle. T_∞ and $p_{m\infty}$ are the temperature and monomer partial pressure far away from the particle, respectively. Note that the clearance volume decreases with supersaturation, so a large particle density is required to suppress nucleation in a highly supersaturated system, thereby limiting the maximum particle size.

Chlorine addition results in increased clearance volume by reducing the propensity of the system to nucleate. Consequently, the seed particle density required to prevent nucleation will be lowered and the maximum particle size increased. As an example, consider the following cases: (*i*) 1% SiH_4 in H_2 at 650°C [typical FSR operating conditions from Ref. (26)], and (*ii*) pure SiH_2Cl_2 at 1000°C. The chemical potential driving forces in these two systems are within 10 kJ/mole, and the atomic silicon partial pressures are the same order of magnitude; therefore, the calculated clearance volumes are indistinguishable and similar particle number densities will be required for prevention of incipient nucleation. However, the mass of silicon available for deposition is about 50 times larger in the SiH_2Cl_2 system than in the SiH_4 system since ξ is about 0.5 in SiH_2Cl_2 (see Fig. 4) and 1.0 in SiH_4. Since the maximum (equilibrium) particle size varies as the cube root of the available silicon loading, a factor of 4 in particle diameter is gained in the SiH_2Cl_2 system. In this simple analysis it is implicitly assumed that chlorine addition does not alter the surface energy of the growing clusters, which may be incorrect since chlorine is known to absorb strongly on silicon (27). Small changes in cluster stability due to chlorine adsorption could significantly affect the nucleation rate. Also, we have again used only thermodynamic arguments here; the kinetics of nucleation in the presence of chlorine have not been considered.

In addition, more uniform deposition in CVD reactors should be possible since the Si-Cl-H system acts to chemically buffer the chemical potential of gaseous silicon; *i.e.*, chlorosilane species react so as to maintain a relatively constant chemical potential as silicon is consumed by deposition. In high deposition rate epitaxial CVD, the primary concerns are film quality and uniformity of the film thickness over the entire distance between the entrance and exit of the reactor. Chlorine addition to silane processes not only suppresses nucleation (permitting higher gas loadings), but may improve the uniformity as well. For Cl/Si < 3, the deposition driving force is not a strong function of gas phase composition, *i.e.*, the contour lines are spaced broadly with respect to variation of the Cl/Si ratio. For example, at Cl/H = 5×10^{-3}, $\Delta\mu$ is not far from −60 kJ/mole for 0.5 < Cl/Si < 3. Therefore, the deposition driving force does not change appreciably for a factor of six change in vapor-phase silicon loading, *i.e.*, as silicon is deposited from the vapor. This is in contrast to the SiH_4 system, where the nearly complete dissociation to gaseous silicon results in a deposition driving force which scales directly with the vapor-phase silicon loading; as the vapor is depleted of silicon by deposition, the driving force for further deposition similarly declines.

The equilibrium deposition efficiencies of the Si-Cl-H system, although lower than in the SiH_4/H_2 system, should be sufficiently high for commercial use. If high concentrations of chlorosilane are used as feed gas (rather than silane), the smaller reactant conversions will not significantly deplete the gas, and the deposition rate should remain more constant with distance down the reactor. The uniformity requirements in high deposition rate epitaxy may be satisfied by this technique, reducing the need for temperature ramping or susceptor tilting.

Of course, there are several disadvantages to chlorine addition. For heavily chlorinated systems, the equilibrium deposition efficiency becomes small and maximum throughput is lowered. Also, silicon CVD rates are lower in chlorinated systems than in SiH_4, resulting in longer residence times for a specified particle size. However, the increased gas loading possible in the chlorinated systems may compensate for this. In addition, the added design costs due to corrosiveness of chlorine must be considered.

The chemical potential driving force results given in the present work are helpful for the qualitative comparison of nucleation rates with varying conditions. As regards the quantitative prediction of nucleation rates, it should be noted that the surface energetics of small silicon clusters are not well understood, particularly when strongly adsorbed species (*e.g.*, Cl) are present. Given the uncertainty in the surface energetics of the Si-Cl-H system and the ongoing controvesy over the validity of the classical theory, predicted nucleation rates should be interpreted with care. Much further work, both experimental and theoretical, is required to increase the understanding of homogeneous nucleation in this system.

Summary

Although nucleation is a kinetic phenomenon, the chemical potential driving force for nucleation follows ex-

perimental trends in nucleation rate with temperature and composition. An important property of the Si-Cl-H system is that the equilibrium deposition efficiency is independent of Cl/H ratio for concentrated mixtures of chlorosilane in hydrogen, implying that free-space reactor throughput increases linearly with chlorosilane loading of the feed. This observation, combined with the inhibiting effect of chlorine on nucleation in the Si-Cl-H system, suggests that addition of chlorine to free-space reactors may yield more efficient polysilicon production. However, in light of the sensitivity to the thermodynamic data, the results of these calculations should be interpreted carefully. The general trends with composition and temperature are most likely valid, but the absolute values may be in error due to incorrect thermodynamic data.

Manuscript submitted April 4, 1985; revised manuscript received Oct. 20, 1985.

Massachusetts Institute of Technology assisted in meeting the publication costs of this article.

REFERENCES

1. C. L. Yaws, K. Y. Li, J. R. Hopper, Y. S. Fang, and K. C. Hansen, JPL Final Report no. NASA-Cr-164009 (1981).
2. J. R. Lay and S. K. Iya, 15th IEEE Photovoltaic Specialists Conference, p. 565 (1981).
3. R. Lutwack, in Third European Communities Photovoltaic Solar Energy Conference, W. Palz, Editor, p. 220, Reidel Publishing, (1980).
4. G. S. Springer, *Adv. Heat Transfer*, **14**, 281 (1978).
5. J. L. Katz and M. D. Donohue, *J. Colloid Interface Sci.*, **85**, 267 (1982).
6. J. Bloem and L. J. Giling, in "Current Topics in Materials Science," Vol. I, E. Kaldis, Editor, p. 147, North-Holland, Amsterdam (1978).
7. L. P. Hunt and E. Sirtl, *This Journal*, **119**, 1741 (1972).
8. C. S. Herrick and R. A. Sanchez-Martinez, *ibid.*, **131**, 455 (1984).
9. D. W. Woodruff and R. A. Sanchez-Martinez, *ibid.*, **132**, 706 (1985).
10. H. P. Meissner, C. L. Kusik, and W. H. Dalzell, *Ind. Eng. Chem., Fundam.*, **8**, 659 (1969).
11. M. Farber and R. D. Srivastava, *J. Chem. Thermodyn.*, **11**, 939 (1979).
12. K. R. Sarma and M. J. Rice, *This Journal*, **128**, 2647 (1981).
13. T. U. M. S. Murthy, N. Miyamoto, M. Shimbo, and J. Nishizawa, *J. Cryst. Growth*, **33**, 1 (1976).
14. P. Van der Putte, L. J. Giling, and J. Bloem, *ibid.*, **31**, 299 (1975).
15. F. C. Eversteijn, *Philips Res. Rep.*, **26**, 134 (1971).
16. C. S. Herrick and D. W. Woodruff, *This Journal*, **131**, 2417 (1984).
17. C. E. Morosanu, D. Iosif, and E. Segal, *J. Cryst. Growth*, **61**, 102 (1983).
18. J. Delong, *Solid State Technol.*, **15**, 29 (October 1972).
19. A. Lekholm, *This Journal*, **119**, 1122 (1972).
20. P. H. Robinson and N. Goldsmith, *J. Electron. Mater.*, **4**, 313 (1975).
21. Y. S. Chiang, *RCA Rev.*, **38**, 500 (1977).
22. J. Bloem, *J. Cryst. Growth*, **18**, 70 (1973).
23. A. J. Pesthy, R. C. Flagan, and J. H. Seinfeld, *J. Colloid Int. Sci.*, **82**, 465 (1981).
24. M. K. Alam and R. C. Flagan, *Aerosol Sci. Technol.*, **2**, 271 (1983).
25. M. K. Alam and R. C. Flagan, *J. Colloid Interface Sci.*, **97**, 232 (1984).
26. M. K. Alam, PhD Thesis, California Institute of Technology, Pasadena, CA (1984).
27. A. A. Chernov and M. P. Rusaikin, *J. Cryst. Growth*, **45**, 73 (1978).

Thermochemical Stability of β- and β''-Alumina Electrolytes in Na/S Cells

I. The Activities of Na_2O and Al_2O_3

N. S. Choudhury*,[1]

General Electric Corporate Research and Development, Schenectady, New York 12301

ABSTRACT

The Na_2O activity in certain compositions of β-, β''-alumina ceramic electrolytes was determined by open-circuit emf measurements. The Al_2O_3 activity was estimated with the assumptions that the β-, and β''-alumina phases may be treated as line compounds belonging to the pseudobinary Na_2O-Al_2O_3 system. These thermochemical parameters are utilized in Part II to assess the stability of the electrolytes in Na/S cells.

The degradation behavior of β- and β''-alumina electrolytes in Na/S cells has been studied by several investigators, and various mechanisms have been proposed. Notable among these mechanisms are impurity diffusion (1-4), dendritic penetration of metallic sodium during charge (5-15), and electron injection (16). However, little attention has been paid to the thermodynamic stability of these electrolytes in Na/S cells. The lack of attention may be partly due to the absence of all the pertinent thermochemical data for the various phases in the Na_2O-Al_2O_3 system. This series of papers addresses the issue of the thermochemical stability of the solid electrolytes. Part I of the series is concerned with the determination and estimation of the activities of Na_2O and Al_2O_3 in β-, β''-alumina electrolytes. These results are used in Part II to assess the thermochemical stability of the electrolytes in the environment of the Na/S cells.

* Electrochemical Society Active Member.
[1] Present address: General Electric/Knolls Atomic Power Laboratory, Schenectady, New York 12301

Review of Pertinent Thermochemical Data

The ceramic electrolytes of various compositions used in the Na/S cells are mainly composed of β''-alumina and β-alumina phases. In addition to Na_2O and Al_2O_3, these compositions also contain a few weight percent of dopants, *e.g.*, Li_2O, MgO, etc. However, at 600 K (the cell operating temperature) the dopants are most likely to be "frozen-in," and thus the β''- and β-alumina electrolytes may be considered to belong to the pseudo binary Na_2O-Al_2O_3 system, in which α-Al_2O_3, β-alumina, β''-alumina, and $NaAlO_2$ are the consecutive phases with increasing Na_2O content (17). The occurrence of other soda-rich phases, *e.g.*, Na_5AlO_4, $Na_7Al_3O_8$ (18), etc., have been reported. However, these phases are not germane to the present analysis.

The thermochemical data on Al_2O_3, Na_2O, and $NaAlO_2$ may be obtained from various compilations, *e.g.*, by Barin, Knacke, and Kubaschewski (19). The only other thermochemical information for the Na_2O-Al_2O_3 system

Table I. Thermochemical data for $NaAlO_2$, β''-alumina and β-alumina at 600 K

Phase, j	x_j	c_j, (kcal/mol) = $RT \ln (a_{Na_2O} \cdot a^{x_j}{}_{Al_2O_3})$	Na_2O-rich coexistent phase	Al_2O_3-rich coexistent phase	$RT \ln a_{Na_2O}$ limits (kcal/mol) Upper	Lower	$RT \ln a_{Al_2O_3}$ limits (kcal/mol) Lower	Upper	Reference
$NaAlO_2$	1	−43.281	$Na_7Al_3O_8$	β''-alumina	—	—	—	—	(19)
β''-alumina	≈5	—	$NaAlO_2$	β-alumina	—	—	—	—	—
β-alumina	≈9	−80.5	β''-alumina	α-Al_2O_3	—	−80.5	—	0	(20)
		−65.15			—	−65.15	—	0	(21, 22)
		−52.65			—	−52.65	—	0	(23)

reported in the literature is the Na_2O activity for α-Al_2O_3, β-alumina coexistence, as given in Table I.

The chemical potential of any composition, Na_2O xAl_2O_3 in the pseudobinary system (where x varies from 0 to infinity) may be represented by

$$\mu^\circ_{Na_2O \cdot xAl_2O_3} = \mu^\circ_{Na_2O} + x\mu^\circ_{Al_2O_3} + RT \ln a_{Na_2O} + xRT \ln a_{Al_2O_3} \quad [1]$$

where $\mu^\circ_{Na_2O}$ and $\mu^\circ_{Al_2O_3}$ are the chemical potentials of Na_2O and Al_2O_3 in the standard states and a_{Na_2O} and $a_{Al_2O_3}$ are the prevailing Na_2O and Al_2O_3 activities at that composition. If for a given phase, j, with composition $Na_2O \cdot x_j Al_2O_3$, x_j can be treated as a constant, or in other words, if the phase has a limited stoichiometry, Eq. [1] may be modified as follows

$$RT \ln a_{Na_2O} + x_j RT \ln a_{Al_2O_3} = c_j \quad [2]$$

where $c_j = (\mu^\circ_{Na_2O \cdot x_jAl_2O_3} - \mu^\circ_{Na_2O} - x_j\mu^\circ_{Al_2O_3})$ and is a constant for that phase. The ranges of $RT \ln a_{Na_2O}$ and $RT \ln a_{Al_2O_3}$ in Eq. [2] for the phase, j, are given by the equilibrium values fixed by the two-phase coexistence at both sides of the single-phase field. The β-, β''-alumina and $NaAlO_2$ phase fields are quite narrow (17) and, therefore, Eq. [2] should be valid for each of these intermediate phases. Table I lists the values of x_j and the available thermochemical information in terms of Eq. [2]. It is apparent from the table that additional information on either the a_{Na_2O} or $a_{Al_2O_3}$ for any one pair of coexistent phases (*e.g.*, a_{Na_2O} in β-, β''-alumina) is sufficient to estimate the activities of Na_2O and Al_2O_3 for all the pairs of coexistent phases (*e.g.*, $a_{Al_2O_3}$ in β-, β''-alumina; a_{Na_2O} and $a_{Al_2O_3}$ in β''-alumina, $NaAlO_2$) between $NaAlO_2$ and α-Al_2O_3, with the aid of Eq. [2]. The Na_2O activity in electrolytes, composed mainly of β- and β''-alumina phases, was determined to provide the necessary information.

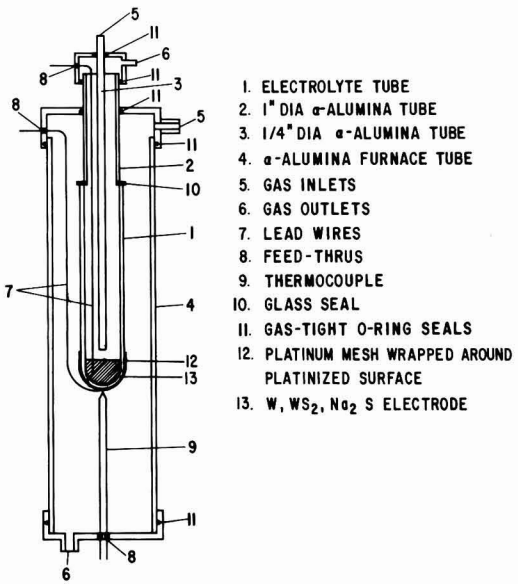


Fig. 1. Schematic of the cells used to determine Na_2O activity between 1020 and 1220 K.

Experimental Methods for Na_2O Activity Determination

The Na_2O activity was determined from open-circuit emf's of two types of cells operating at 1020-1220 K and at ~623 K.

Cell arrangement for emf measurements at 1020-1220 K.—The cell: W, WS_2, Na_2S/electrolyte/p_{O_2} was employed for the higher temperature measurements. The cell arrangement is shown in Fig. 1. The electrolyte was in the form of a closed end, 33 mm diam, ~18 in. long tube. The open end of the electrolyte tube was sealed to a 1 in. diam α-alumina tube with a sealing glass. The cell was positioned inside an α-alumina furnace tube with appropriate gas-tight seal made on the side of the 1 in. diam α-alumina tube. The arrangement enabled the outside gas (O_2 or 90 ppm O_2 + argon mixture fixing the p_{O_2}) passing through the furnace tube to be isolated from the inside of the electrolyte. A mixture of W, WS_2, Na_2S (1:1:4 molar) was placed inside the electrolyte tube and served to establish the Na chemical potential at the inner electrode. A cover gas of argon (purified by passing through titanium chips held at 675 K) was admitted through the 1/4 in. diam α-alumina tube. The bottom end of the 1/4 in. α-alumina tube was positioned about 1/2 in. above the electrode mixture by the gas-tight sealing arrangement at the open end of the 1 in. diam α-alumina tube.

The outer surface of the electrolyte tube at the closed end was platinized and electrical contact with the platinum lead wire was established by wrapping the outer platinized surface with a platinum mesh spot welded to the lead wire. A tungsten lead wire embedded in the W, WS_2, Na_2S mixture provided electrical contact to the inner electrode. The thermocouple emf's between the W and Pt lead wires were separately determined in the operating temperature range of the cell and appropriate corrections to the observed cell emf's were made.

The cell emf's were monitored with a digital electrometer (input impedance 10^{14} Ω) and were recorded after waiting for at least 1/2h at each temperature. The attainment of equilibration was indicated by the reproducibility of the recorded emf's on cycling the cell temperature within the range of measurements.

Cell arrangements for emf measurements at ~623 K.—The open-circuit emf's between the reference electrode (Na) and test electrodes (Hg or In) in a molten $NaNO_3$ bath operating at ~623 K were used to compute the Na_2O activity at 623 K. A schematic diagram showing the

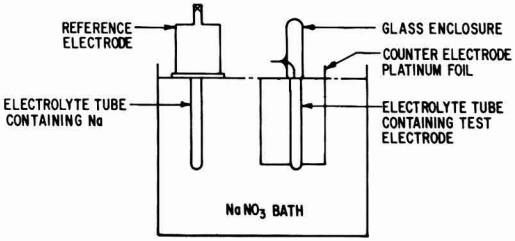


Fig. 2. Schematic of the cells used to determine Na_2O activity at ~623 K.

Table II. List of ceramic electrolyte compositions used for Na_2O-activity determination

Composition code	Nominal composition, w/o				Phases, % (~)		Starting α-Al_2O_3 powder	
	Na_2O	MgO	Li_2O	Al_2O_3	β″	β	Source	Estimated total oxide impurity, w/o
CSPL 2/8	8	2	—	90	50	50	Alcoa A16SG	0.206
G8	9	1	0.3	89.7	70	30	Alcoa A17	0.146
G8B	9	1	0.3	89.7	70	30	Baikowski Type AS2	0.021
Ceramatec	8.85	—	0.75	90.4	99	Tr.	Baikowski* Type AS2	0.021

* The starting powder used by Ceramatec, Incorporated (supplier) is believed to be Baikowski Type AS2 or of similar purity.

local arrangement of the test half-cell, reference electrode and a counterelectrode in the $NaNO_3$ bath is shown in Fig. 2. The test half-cells were produced from closed end, 10 mm diam β, β″-alumina electrolyte tubes of appropriate compositions. The open end of the electrolyte tube was sealed to an open-ended glass tube (FN glass), which had a Rodar alloy feed-thru (to make electronic contact with the test electrode) sealed through the wall. An appropriate amount of either Hg or In (in small chunks) was placed inside the half-cell and the cell was evacuated by a mechanical pump for about an hour and then the top of the glass tube was sealed off. The primary purpose of this cell arrangement was to investigate the anodic degradation of the ceramic electrolytes at Hg and In electrodes; details will be published in separate reports (24).

Various electrolyte compositions were investigated. Table II lists the nominal compositions, amounts of different phases (β″-alumina, β-alumina) estimated by x-ray diffraction, and source and purity of α-alumina starting powder used in the manufacture of the electrolytes. The densities of the electrolyte tubes were between 3.25 and 3.26 g/cm³ (≥99% theoretical).

Results and Discussions

Na_2O activity in β″-β-alumina.—Results from emf measurements at 1020-1220K.—Stable and reproducible emf's were obtained for the W, WS_2, Na_2S/electrolyte/p_{O_2} cells with the CSPL 2/8 electrolyte tubes. Tables III and IV list the emf data (corrected for the W/Pt thermocouple emf) together with the calculated $RT \ln a_{Na_2O}$ for two cells. $RT \ln a_{Na_2O}$ was calculated from the following equation, appropriate for the cell.

$$RT \ln a_{Na_2O} = \Delta G^\circ_{Na_2S} - 1/2\ \Delta G^\circ_{WS_2} - \Delta G^\circ_{Na_2O} + 1/2\ RT \ln p_{O_2} - 2FE \quad [3]$$

Table III. Open-circuit emf data for W, WS_2, Na_2S/CSPL 2/8 electrolyte/p_{O_2} cell no. 1

Temp, K	p_{O_2}, atm	EMF, V (corrected)	$RT \ln a_{Na_2O}$, kcal/mol
1019	1	1.290	−46.752
1053	1	1.264	−46.307
1094	1	1.230	−45.649
1120	1	1.198	−44.750
1137	1	1.192	−44.851
1172	1	1.164	−44.336
1200	1	1.139	−43.804

Table IV. Open-circuit emf data for W, WS_2, Na_2S/CSPL 2/8 electrolyte/p_{O_2} cell no. 2

Temp, K	p_{O_2}, atm	EMF, V (corrected)	$RT \ln a_{Na_2O}$, kcal/mol
1108	90×10^{-6}	0.996	−45.422
1136	90×10^{-6}	0.954	−44.366
1169	90×10^{-6}	0.929	−44.251
1176	90×10^{-6}	0.924	−44.240
1198	1	1.135	−43.575
1218	1	1.128	−43.696

Elrefaie and Smeltzer (21) used the W, WS_2, Na_2S electrode for the a_{Na_2O} determination in electrolytes composed of β- and α-alumina phases. Substituting the data for $\Delta G^\circ_{Na_2S}$, $\Delta G^\circ_{WS_2}$, and $\Delta G^\circ_{Na_2O}$ tabulated in their paper, Eq. [3] reduces to

$$RT \ln a_{Na_2O} = (35{,}351 - 22.189T + 1/2\ RT \ln p_{O_2} - 2FE)\ \text{cal/mole} \quad [4]$$

The least squares best fit of the $RT \ln a_{Na_2O}$ *vs.* T data in Tables III and IV gives the following equation

$$RT \ln a_{Na_2O} = (-63.551 + 0.0165T)\ \text{kcal/mole} \quad [5]$$

with a correlation coefficient of 0.9791. The $RT \ln a_{Na_2O}$ value extrapolated to 600 K is −53.65 kcal/mole.

Results from emf measurements at ~623 K.—Open-circuit emf's at ~623 K with the Hg electrode, after a few anodic sweeps (to ~3.0V), were in the range of 2.79-2.85V, and were most likely controlled by the following reaction

$$[Na_2O] + Hg = HgO + 2Na^+ + 2e \quad [6]$$

where $[Na_2O]$ represents Na_2O in the electrolyte at the prevailing activity. However, the initial open-circuit emf's, before the anodic sweeps, were between 2.2 and 2.4V and are believed to be mixed potentials; the cathodic reaction may be the amalgamation reaction

$$Na^+ + e = [Na]_{Hg} \quad [7]$$

Fluctuations of ~50 mV were observed on the open-circuit emf's and are believed to be caused by rapid observed convection of Hg within the electrolyte/glass enclosure assembly (Fig. 2). Thus, the open-circuit emf data for the Hg electrode (after anodic sweeps) presented in Table V represent the mean observed emf's. Table V also shows the corresponding $RT \ln a_{Na_2O}$ values. The appropriate thermodynamic data used in the computation (and also that for the In electrode) were estimated by linear interpolation at 623 K from the compilations of Barin, Knacke, and Kubaschewski (19).

Table V. Open-circuit emf data for Na/electrolyte/Hg cells

Electrolyte composition	Temp, K	EMF, V	$RT \ln a_{Na_2O}$, kcal/mol
G8	623	2.85	−57.473
G8	625	2.85	−57.473
G8B	623	2.79	−54.706
Ceramatec	623	2.80	−55.167
Ceramatec	624	2.79	−54.706

Table VI. Open-circuit emf data for Na/electrolyte/In cells

Electrolyte composition	Temp, K	EMF, V	$RT \ln a_{Na_2O}$, kcal/mol
G8	620	1.647	−54.215
G8	622	1.605	−52.278

Table VII. Estimates of Na_2O and Al_2O_3 activities for coexistent phases at 600 K

Coexistent phases	$RT \ln a_{Na_2O}$ kcal/mol	a_{Na_2O} (log mean)	$RT \ln a_{Al_2O_3}$ kcal/mol	$a_{Al_2O_3}$ (log mean)
$NaAlO_2$, β''-alumina	−38.198 ± 1.540	1.21×10^{-14}	−5.083 ± 1.540	0.014
β''-alumina, β-alumina	−55.559 ± 0.798	5.75×10^{-21}	−1.870 ± 0.990	0.208
β-alumina, α-alumina	−80.5[1] −65.15[2]	4.72×10^{-30} 1.84×10^{-24}	0 0	1 1

[1] Ref. (20).
[2] Ref. (21, 22).

The open-circuit emf data at ~623 K with the In electrode are listed in Table VI; the $RT \ln a_{Na_2O}$ values were calculated on the basis of the following reaction

$$3[Na_2O] + 2In = In_2O_3 + 6Na^+ + 6e \quad [8]$$

It is apparent from Tables V and VI that the Na_2O activities of various electrolytes at ~623 K are in reasonable agreement with each other and with that of the CSPL 2/8 electrolyte extrapolated to 623 K using Eq. [5]. The least squares best fit of the $RT \ln a_{Na_2O}$ *vs.* T data pooled from Tables III through VI gives the following equation

$$RT \ln a_{Na_2O} = (-67.556 + 0.0200T) \text{ kcal/mole} \quad [9]$$

with a correlation coefficient of 0.9790. Equation [9] is graphically illustrated in Fig. 3, which also shows the maximum likelihood estimates for the 95% confidence band. The 95% confidence range at 600 K is −54.761 to −56.357 kcal/mole. The regression analyses were performed with the GE STATPAC computer program (25).

The above results indicate that the purity, composition, and changes in the phase content of the ceramic electrolytes do not have significant effect on the Na_2O activity at ~600 K, *i.e.*, the various electrolytes appear to belong to a pseudobinary, two-phase (β''- and β-alumina) system with the impurities and dopants "frozen-in."

Estimates of the Na_2O and Al_2O_3 activities.—In order to estimate the Al_2O_3 activity for β''-alumina, β-alumina coexistence from the present result of Na_2O activity for β''-alumina, β-alumina, and the Na_2O activity for β-alumina, α-alumina coexistence (see Table I); thermochemical consideration requires that $RT \ln \alpha_{Na_2O}$ for β-alumina, β''-alumina coexistence be greater than the RT in α_{Na_2O} for β-alumina, α-alumina coexistence. This precludes the possibility of using the data of Ref. (23) in conjunction with the present results for the estimate of the Al_2O_3 activity for β''-alumina, β-alumina coexistence. Although the reason for the discrepancy between Choudhury's (20) results ($RT \ln a_{Na_2O} = -80.5$ kcal/mole and those of Elrefaie and Smeltzer (21) and Rog *et al.* (22) ($RT \ln a_{Na_2O} = -65.15$ kcal/mole) for β-alumina, α-alumina coexistence is not known, both of these values are used to estimate the Al_2O_3 activity for β''-alumina, β-alumina coexistence and the Na_2O and the Al_2O_3 activities for $NaAlO_2$, β''-alumina coexistence, as discussed below.

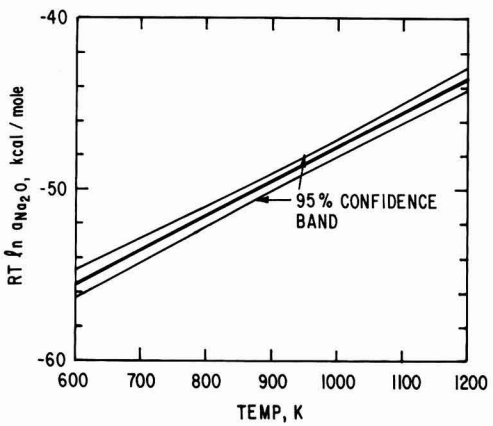


Fig. 3. Estimate of $RT \ln a_{Na_2O}$ vs. temperature showing the 95% confidence band.

Although β-alumina and β''-alumina exhibit limited stoichiometric ranges, two values each for x_β (9 and 10) and for $x_{\beta''}$ (5 and 6) were assigned for the estimates. Starting with Eq. [2] for the β-alumina phase, the values of x_β, c_β (−80.5 and −65.15 kcal/mole), and the high and low values for $RT \ln a_{Na_2O}$ (−54.761 and −56.357 kcal/mole) were combined to yield the $RT \ln a_{Al_2O_3}$ estimates for β''-, β-alumina coexistence; the estimated value is −1.870 ± 0.990 kcal/mole. $c_{\beta''}$ values were then computed for $x_{\beta''} = 5$ and 6. The estimate of $RT \ln a_{Na_2O}$ and $RT \ln a_{Al_2O_3}$ for $NaAlO_2$, β''-alumina coexistence were then made by simultaneous solutions of Eq. [2] for $NaAlO_2$ and β''-alumina. The estimate of $RT \ln a_{Na_2O}$ is −38.198 ± 1.540 kcal/mole, the corresponding estimate of $RT \ln a_{Al_2O_3}$ being −5.083 ± 1.540 kcal/mole. Table VII summarizes the estimates of the Na_2O and Al_2O_3 activities at 600 K for pairs of coexistent phases between $NaAlO_2$ and α-Al_2O in the pseudobinary system.

Conclusions

The Na_2O activity at 600 K for β''-, β-alumina ceramic electrolytes is $\sim 5.75 \times 10^{-21}$, the estimated Al_2O_3 activity being ~0.208. The estimated Na_2O and Al_2O_3 activities at 600 K for $NaAlO_2$, β''-alumina equilibrium coexistence are $\sim 1.21 \times 10^{-14}$ and 0.014, respectively.

Manuscript submitted June 20, 1985; revised manuscript received Oct. 28, 1985.

General Electric Company assisted in meeting the publication costs of this article.

REFERENCES

1. F. G. Will, *This Journal*, **123**, 834 (1976).
2. T. Kaneda, J. B. Bates, J. C. Wang, and H. Engstrom, *Mater. Res. Bull.*, **14**, 1053 (1979).
3. I. Yasui and R. H. Doremus, *J. Am. Ceram. Soc.*, **60**, 296 (1977).
4. I. Yasui and R. H. Doremus, *This Journal*, **125**, 1007 (1978).
5. R. D. Armstrong, T. Dickinson, and J. Turner, *Electrochim. Acta*, **19**, 187 (1974).
6. G. J. Tennenhouse, R. L. Ku, R. H. Richman, and T. J. Whalen, *Bull. Am. Ceram. Soc.*, **53**, 523 (1975).
7. R. H. Richman and G. J. Tennenhouse, *J. Am. Ceram. Soc.*, **58**, 63 (1975).
8. D. K. Shetty, A. V. Virkar, and R. S. Gordon, in "Fracture Mechanics of Ceramics," No. 4, R. L. Bradt and D. P. H. Hasselman, Editors, p. 652, Plenum Press, New York (1978).
9. A. V. Virkar and G. R. Miller, in "Fast Ion Transport in Solids," P. Vashista, J. N. Mundy, and G. K. Shenoy, Editors, p. 87, Elsevier North Holland, Inc., New York (1979).

10. A. V. Virkar, L. Viswanathan, and D. R. Biswas, *J. Mater. Sci.*, **15**, 302 (1980).
11. A. V. Virkar, *ibid.*, **16**, 1142 (1981).
12. R. W. Davidge, G. Tappin, J. R. McLaren, and G. J. May, *J. Am. Ceram. Soc.*, **58**, 771 (1979).
13. M. P. J. Brennan, *Electrochim. Acta*, **15**, 621 (1980).
14. L. C. DeJonghe, L. Feldman, and P. Millett, *Mater. Res. Bull.*, **14**, 589 (1979).
15. N. K. Gupta and G. J. Tennenhouse, *This Journal*, **126** 1451 (1979).
16. L. C. DeJonghe, L. Feldman, and A. Buechele, *J. Mater. Sci.*, **16**, 780 (1981).
17. R. C. DeVries and W. L. Roth, *J. Am. Ceram. Soc.*, **52**, 364 (1969).
18. M. G. Barker, P. G. Gadd, and M. J. Begley, *J. Chem. Soc., Chem. Comm.*, 379 (1981).
19. I. Barin and O. Knacke, "Thermochemical Properties of Inorganic Substances," Springer-Verlag, New York-Heidelberg (1973), and I. Barin, O. Knacke, and O. Kubaschewski, "Thermochemical Properties of Inorganic Substances, Supplement," Springer-Verlag, New York-Heidlberg (1977).
20. N. S. Choudhury, *This Journal*, **120**, 1663 (1973).
21. F. A. Elrefaie and W. W. Smeltzer, *ibid.*, **128**, 1443 (1981).
22. G. Rog, S. Kozinski, and A. Kozlowska-Rog, *Electrochim. Acta*, **28**, 43 (1983). The Na_2O-activity for α-alumina, β-alumina coexistence determined by these authors are essentially in agreement with Ref. (21).
23. A. Dubreuil, M. Malenfant, and A. D. Pelton, *This Journal*, **128**, 2006 (1981).
24. M. W. Breiter, N. S. Choudhury, and E. L. Hall, To be published.
25. W. B. Nelson, C. B. Morgan, and P. Caporal, "1979 STATPAC Simplified—A short introduction to how to run STATPAC, a general statistical package for data analysis," Report no. 78CRD276, General Electric Corporate Research and Development, Schenectady, NY (Dec. 1978).

Thermochemical Stability of β- and β″-Alumina Electrolytes in Na/S Cells

II. Assessment

N. S. Choudhury*[1]

General Electric Corporate Research and Development, Schenectady, New York 12301

ABSTRACT

The degradation of β- and β″-alumina electrolytes in Na/S cells is assessed from a thermochemical viewpoint. Two probable schemes for the S-side degradation are considered: (*i*) Na_2O-leaching and (*ii*) free Al_2O_3 liberation. The probable degradation mechanism at the Na electrode, considered in this assessment, involves reactions leading to the liberation of metallic Al. The assessment indicates that α- and β-alumina with low Na_2O activity are thermodynamically stable, while the other soda-rich phases in the Na_2O-Al_2O_3 system are unstable to the Na_2O leaching reactions. On the other hand, thermodynamic stability to the reaction with Na is favored by high Na_2O activity and qualifies soda-rich β″-alumina and other soda-rich compounds as stable phases. Thus, the existence of any phase in the Na_2O-Al_2O_3 system which would be stable at both the Na and the S electrode, is negated by the assessment.

The estimates of the Na_2O and Al_2O_3 activities given in Table VII, Part I (1) are utilized to examine the thermodynamic feasibility of probable chemical reactions involving the components of the electrodes of the Na/S cells and the β- and β″-alumina electrolytes. The pertinent free energy data used in this assessment are taken from the compilations of Barin, Knacke, and Kubaschewski (2). The cell operating temperature is assumed to be 600 K and the potential for S, Na_2S_5 coexistence is taken as 2.08V with respect to Na, *i.e.*, the cell open-circuit emf in the "two-phase" region.

Probable Reactions at the S Electrode

In addition to the presence of sulfur, carbon is also present at this electrode as current collector. Because Al_2O_3 is relatively stable, it is assumed that no compounds of Al with S or C are formed. Thus, the probable reactions of interest may involve the formation of the condensed phases, *e.g.*, Na_2CO_3, Na_2SO_4, Na_2SO_3, or gaseous products SO_2, CO, and finally O_2. Two possible reaction schemes may be considered. One involves progressive quasi-steady-state "leaching" of Na_2O from the electrolyte to form the various reaction products, together with the formation of a soda-poor electrolyte, without significant change in $a_{Al_2O_3}$. This mechanism may be particularly applicable to the compositions in β″- + β-alumina two-phase field or for infinitesimal change in the electrolyte composition at any particular instant of time. The other mechanism involves liberation of free Al_2O_3 as a result of the reactions. These two reaction schemes are considered in further detail in the following paragraphs.

Na_2O "leaching" mechanism.—In this situation, the various possible reactions can be written as follows

$$3[Na_2O] + C = Na_2CO_3 + 4Na^+ + 4e \quad [1]$$

$$3[Na_2O] + S = Na_2SO_3 + 4Na^+ + 4e \quad [2]$$

$$4[Na_2O] + S = Na_2SO_4 + 6Na^+ + 6e \quad [3]$$

$$[Na_2O] + C = CO + 2Na^+ + 2e \quad [4]$$

$$2[Na_2O] + S = SO_2 + 4Na^+ + 4e \quad [5]$$

$$2[Na_2O] = O_2 + 4Na^+ + 4e \quad [6]$$

where $[Na_2O]$ represents Na_2O in the electrolyte at the prevailing activity. Treating a_{Na_2O} as a variable, the reactions may be graphically represented in a plot of RT ln a_{Na_2O} *vs.* E (where E is the potential at the electrode with respect to Na) as in Fig. 1. It is apparent from the figure, that for the stability against the Na_2O leaching reactions (at the cell open-circuit potential), a RT ln a_{Na_2O} value of less than ~ -60 kcal/mole ($a_{Na_2O} \leq 1.4 \times 10^{-22}$) is desirable. A lower value may be needed if the cell charging practice demands the S-electrode potential to deviate significantly from the cell open-circuit potential.

With reference to Table VII, Part I (1), soda-poor β-alumina (*i.e.*, in coexistence with α-Al_2O_3) should be stable, while soda-rich β″-alumina unstable to many of the above reactions. The estimated RT ln a_{Na_2O} for β-, β″-alumina coexistence (the material of practical interest) is shown in Fig. 1; which indicates that the β-, β″-alumina

*Electrochemical Society Active Member.
[1]Present address: General Electric/Knolls Atomic Power Laboratory, Schenectady, New York 12301.

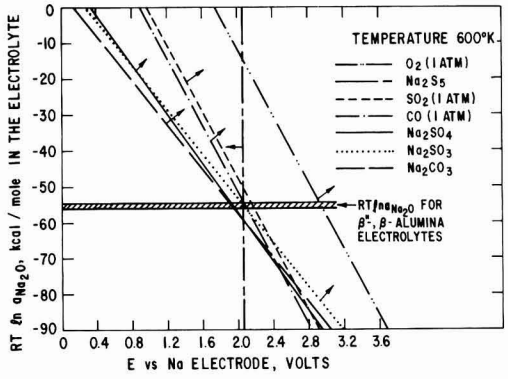


Fig. 1. *RT* ln a_{Na_2O} vs. potential plots for various Na_2O leaching reactions at the S electrode. Illustrating the thermodynamic instability of β"-, β-alumina electrolytes at potentials >-2.08V.

ceramic may be somewhat susceptible to some of the leaching reactions at the cell open-circuit potential.

Liberation of free Al_2O_3.—The mechanisms involving the liberation of free Al_2O_3 should probably consider the formation of metastable Al_2O_3 phases rather than α-Al_2O_3. For example, if β-Al_2O_3 is decomposed, the resulting structure of Al_2O_3 will most probably be "spinel like" instead of the α-Al_2O_3 phase. However, because neither free energy nor structural data are available for the metastable Al_2O_3 decomposition products, the reactions considered here will, by necessity, assume the formation of α-Al_2O_3. The following reactions are possible

$$3Na_2O \cdot xAl_2O_3 + C = 3xAl_2O_3 + Na_2CO_3 + 4Na^+ + 4e \quad [7]$$

$$3Na_2O \cdot xAl_2O_3 + S = 3xAl_2O_3 + Na_2SO_3 + 4Na^+ + 4e \quad [8]$$

$$4Na_2O \cdot xAl_2O_3 + S = 4xAl_2O_3 + Na_2SO_4 + 6Na^+ + 6e \quad [9]$$

$$Na_2O \cdot xAl_2O_3 + C = xAl_2O_3 + CO + 2Na^+ + 2e \quad [10]$$

$$2Na_2O \cdot xAl_2O_3 + S = 2xAl_2O_3 + SO_2 + 4Na^+ + 4e \quad [11]$$

$$2Na_2O \cdot xAl_2O_3 = 2xAl_2O_3 + O_2 + 4Na^+ + 4e \quad [12]$$

The equilibrium potentials (*vs.* Na reference) for these reactions involving β-alumina ($x = 9$) and β"-alumina ($x = 5$) are given in Table I. It is apparent from the table that only the soda-rich β"-alumina is susceptible to the free Al_2O_3 liberating reaction [9] at the cell open circuit, while the β-, β"-alumina coexistent phases, as well as the soda-poor β-alumina should be stable.

It should be pointed out that post-test examinations, conducted in this laboratory, normally indicate no visible S-side degradation.

Probable Reaction with Na

The possibility of Na reacting with a soda-poor phase in the Na_2O-Al_2O_3 system to liberate free aluminum and form a Na_2O-rich phase has been considered (3). To reiterate, the reaction may be written as follows

$$6Na + [Al_2O_3] = 3[Na_2O] + 2Al \quad [13]$$

where $[Al_2O_3]$ and $[Na_2O]$ represent Al_2O_3 and Na_2O in the material at the prevailing activities. The free energy change for reaction [13] may be written as

$$\Delta G = 3RT \ln a_{Na_2O} - RT \ln a_{Al_2O_3} + 3\Delta G^\circ_{Na_2O} - \Delta G^\circ_{Al_2O_3}$$

For the material to be stable with Na, ΔG must be positive, *i.e.*

$$(3RT \ln a_{Na_2O} - RT \ln a_{Al_2O_3}) \geq -113.9 \text{ kcal at } 600 \text{ K} \quad [14]$$

This is graphically illustrated in Fig. 2 which also shows the regions of existence of the pertinent phases according to the present estimates. It is apparent from the figure that α-Al_2O_3, β-alumina, as well as β"-alumina in equilibrium with β-alumina are not thermodynamically stable against the reaction. Because the line of stability crosses over the spread in the estimates of the Na_2O and Al_2O_3 activities for high-soda β"-alumina, and also because of the uncertainty in the free energy data, it is not clear whether high-soda β"-alumina is stable against the reaction. However, a major portion of the spread of the Na_2O- and Al_2O_3-activity estimates is above the stability line. Thus, high-soda β"-alumina is perhaps stable. Although β"-alumina may not be subjected to phase transformation in contact with Na, an increase in Na_2O activity (and corresponding decrease in Al_2O_3 activity), in accordance with reaction [13], may occur for the β"-alumina phase (in equilibrium with β-alumina), resulting in lattice strains. It is also apparent from Fig. 2 that $NaAlO_2$ and other Na_2O-rich phases should be thermodynamically stable with Na.

In addition to the formation of free Al considered in reaction [13], one may consider the formation of various suboxides of Al, or other defect complexes (for example: Al^{+3} ion, electron pair) involving the incorporation of excess Na in the β- or β"-alumina lattice. One, of course, needs further thermodynamic information to make such calculations. However, it is quite likely that the formation of suboxides or defect complexes may represent intermediate steps to the liberation of free Al. Thus, the widely observed blackening of the electrolytes in contact with

Table I. Equilibrium potentials, volts (vs. Na), for various reactions involving liberation of free Al_2O_3

Reaction	For β-alumina in equilibrium with α-Al_2O_3	For β-alumina in equilibrium with β"-alumina	For β"-alumina in equilibrium with β-alumina	For β"-alumina in equilibrium with $NaAlO_2$
7	2.75, 2.24	2.48	2.24	2.19
8	2.89, 2.39	2.62	2.38	2.34
9	2.55, 2.11	2.32	2.10	2.06
10	2.64, 2.31	2.46	2.30	2.27
11	2.71, 2.38	2.54	2.37	2.35
12	3.49, 3.16	3.32	3.15	3.12

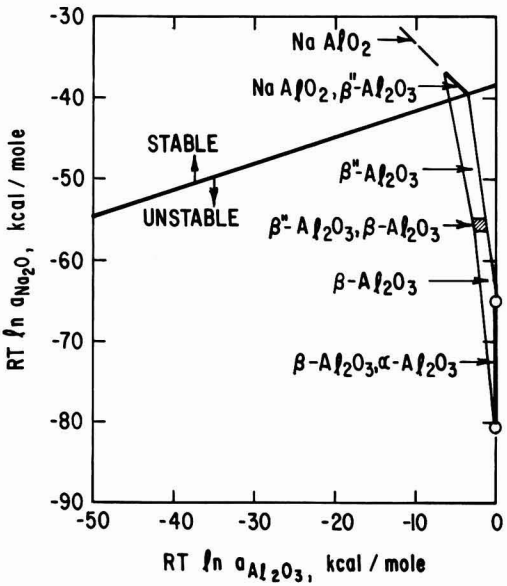


Fig. 2. *RT* ln a_{Na_2O} vs. *RT* ln $a_{Al_2O_3}$ plot defining the stability of the phases in the Na_2O-Al_2O_3 system against Na attack.

Na may be manifestations of these intermediate steps. Interestingly, DeJonghe *et al.* (4, 5) have attributed the coloration of the electrolytes in contact with Na to be due to the introduction of oxygen vacancies, compensated by electrons. In their experiments, the sodium metal was saturated with oxygen; this would mean that the Na_2O activity in the metal was unity. Because the Na_2O activity in the electrolyte is less than unity, the creation of oxygen vacancies by diffusion of oxygen from the electrolyte to the metal is a thermodynamic impossibility. From the Na_2O activity in β-, β″-alumina electrolytes, and the solubility of oxygen in Na of ~145 ppm (6) at 600 K, a concentration of $\sim 10^{-20}$ ppm of oxygen may be calculated; below this concentration, oxygen may diffuse from the electrolyte to the metal. As this low value of oxygen concentration in sodium metal is not practically achievable, oxygen diffusion out of the electrolyte cannot be responsible for the observed coloration.

Concluding Remarks

Certain potential thermodynamic instability problems for the β″- or β-alumina electrolytes in the environment of the Na/S cells were identified. The considerations given in this assessment are mainly thermodynamic, *i.e.*, even though certain reactions may be favorable, the kinetics may be slow enough to be insignificant over the projected life of the Na/S cells. The major conclusions drawn from this assessment are:

1. The α-Al_2O_3, and β-alumina (with a_{Na_2O} less than $\sim 10^{-22}$) phases are thermodynamically stable in the environment of the S electrode. Other phases in the Na_2O-Al_2O_3 system are unstable.
2. The α-Al_2O_3, β-alumina, and β″-alumina (with low soda activity) phases are thermodynamically unstable in contact with Na. β″-alumina (with high Na_2O activity) and other soda-rich phases should be stable with Na.
3. There does not exist any phase in the Na_2O-Al_2O_3 system which is thermodynamically stable at the Na as well as the S electrode.

Acknowledgments

The author wishes to thank his colleagues at General Electric and Chloride Silent Power Limited for many helpful discussions.

Manuscript submitted June 20, 1985; revised manuscript received Oct. 28, 1985.

General Electric Company assisted in meeting the publication costs of this article.

REFERENCES

1. N. S. Choudhury, *This Journal*, **133,** 417 (1986).
2. I. Barin and O. Knacke, "Thermochemical Properties of Inorganic Substances," Springer-Verlag, New York-Heidelberg (1973), and I. Barin, O. Knacke, and O. Kubaschewski, "Thermochemical Properties of Inorganic Substances, Supplement," Springer-Verlag, New York-Heidelberg (1977).
3. N. S. Choudhury, *This Journal*, **120,** 1663 (1973).
4. L. C. De Jonghe and A. Buechele, *J. Mater. Sci.*, **17,** 885 (1982).
5. L. C. De Jonghe, *This Journal*, **129,** 752 (1982).
6. O. J. Foust, Editor, "Sodium-NaK Engineering Handbook," Vol. 1, p. 240, Gordon and Breach Science Publishers (1972).

Thermochemistry and Structure of Low Pressure Chemically Vapor Deposited and Bulk SiO_2-P_2O_5 and SiO_2-GeO_2 Glasses

Maria Huffman*

Department of Chemistry, Arizona State University, Tempe, Arizona 85287

Alexandra Navrotsky

Department of Geological and Geophysical Sciences, Princeton University, Princeton, New Jersey 08544

Fabio S. Pintchovski*

Motorola Incorporated, Advanced Product Research and Development Laboratories, Austin, Texas 78721

ABSTRACT

Heterogeneously (film) and homogeneously low pressure chemically vapor deposited ("snow") SiO_2-P_2O_5 and SiO_2-GeO_2 glass samples have been prepared at various temperatures. Bulk glass samples have also been made by melting the oxides. High temperature transposed drop and solution calorimetry have provided thermochemical data on the two binary glass systems. SiO_2-P_2O_5 LPCVD film and "snow" samples are metastable relative to bulk or annealed samples by up to ~152 kJ mol^{-1}. The "snow" samples are the most metastable. With increasing temperature of deposition, the total excess enthalpy stored in the film samples decreases. The 703 K deposited film samples are the most stable energetically. There is also indication of a negative heat of mixing in SiO_2-P_2O_5 binary glasses. Bulk SiO_2-GeO_2 glasses mix nonideally with a negative heat of mixing of -12.8 ± 1.5 kJ mol^{-1} at the 50 mole percent composition. Infrared spectroscopy showed Si-OH and Si-H species present in the as-deposited LPCVD samples. These species disappear on annealing. Scanning electron microscopy showed that films have a smooth surface in general but bubbles are present, especially in the annealed samples. "Snows" present a variety of surface morphologies and very high surface areas.

Binary SiO_2 based oxide glasses deposited by low pressure chemical vapor deposition (LPCVD) as thin films on various substrates have been of considerable interest (1). SiO_2-P_2O_5 films are widely used by the semiconductor industry as interlayer dielectrics and as protective layers over aluminum metallization (2, 3, 4). SiO_2-GeO_2 glasses are used primarily in fiber optics (5, 6). This system, in addition to having possible semiconductor uses, is of significant geochemical interest since germanates are used as analogues of high pressure silicates (7, 8).

*Electrochemical Society Active Member.

Chemical, dielectric, thermal and optical properties, reaction kinetics, deposition rates, and structure of SiO_2-P_2O_5 LPCVD glasses have been studied extensively (9-16, 29). However, SiO_2-GeO_2 LPCVD glasses have been studied in less detail.

There has been a lack of thermochemical information on these binary amorphous systems. In this study, high temperature calorimetry has been utilized to obtain thermodynamic data on a variety of LPCVD SiO_2-P_2O_5 film and "snow" samples (powdery LPCVD deposits) with varying phosphorus concentrations and on two SiO_2-GeO_2

LPCVD samples. One bulk SiO_2-P_2O_5 and a series of SiO_2-GeO_2 glass samples have also been prepared and studied. Infrared spectroscopy was combined with existing Raman results to obtain structural information and scanning electron microscopy was used to observe the surface morphology.

The purpose of this paper is to understand the variations of properties of LPCVD amorphous materials over a wide range of preparation and annealing conditions and not to optimize properties over a small range of processing conditions used by the semiconductor industry.

Experimental

Sample preparation and characterization.—The furnace and gas flow system used for the depositions has been described elsewhere (17).

Two kinds of SiO_2-P_2O_5 LPCVD amorphous samples have been made: thin film and "snow". Samples have been deposited at three different temperatures: 523 K, 643 K, and 703 K. The gases used for the SiO_2-P_2O_5 deposition were SiH_4, 10% PH_3/Ar, and O_2. The film samples (3-5 μm thick) were deposited on ~0.4-0.5 mm thick stainless steel wafers, 100 mm in diameter, so that they could be separated from the substrate by a simple bending motion for further study. The "snows" deposit on the colder ends of the LPCVD furnace walls during each run and were collected from a specific area each time.

To obtain various P_2O_5 contents in the glasses, the PH_3 flow was adjusted. In general, the $O_2/SiH_4 + PH_3$ ratio was kept at ~1:1, with the O_2 flowing at ~94 cm^3/min. The pressure in the LPCVD furnace was ~400 mtorr. SiO_2-P_2O_5, films have been obtained ranging in composition from 3.6 to 7.5 mole percent (m/o) P_2O_5 and "snows" ranging from 3.5 to 10.8 m/o P_2O_5. No samples with higher P_2O_5 content were prepared because they are hygroscopic. All samples (films and "snows") were analyzed for phosphorus by the wet chemical method of complexing with molybdate (18). The accuracy of the analyses varied from ~0.2 m/o for samples with less than 7 m/o P_2O_5 to ~0.3 m/o for samples containing 8-11 m/o P_2O_5. The LPCVD SiO_2-P_2O_5 samples contained small amounts of metallic impurities from the stainless steel substrates (10-1000 ppm). The samples did not lose any phosphorus, even after storage for a few months in desiccators containing P_2O_5 and Drierite.

For further calorimetric, spectroscopic, and annealing studies, small amounts of sample (~50 mg) were heated at 1173 K in air (at atmospheric pressure) for 35h in alumina crucibles. No crystallization and no phosphorus loss were observed.

One bulk SiO_2-P_2O_5 sample was also prepared. The use of P_2O_5 was avoided since it is extremely hygroscopic. Instead, $(NH_4)_2HPO_4$ (Fisher Scientific Company certified A.C.S.) and silica gel were used. The silica gel was prepared by the general method of Hamilton and Henderson (19). In brief, tetraethyl orthosilicate (TEOS) $(C_2H_5O)_4Si$ (J. T. Baker Chemical Company, Phillipsburg, NJ 08865) calibrated for actual Si content, was mixed with ethanol and a small amount of ammonium hydroxide. The masses of the reagents were calculated so as to produce a set quantity of final product (8-10g). The gelled mixture was first left to dry at room temperature to drive off the excess fluid. Then, it was placed in a drying oven overnight at 383 K. After grinding, the gel was dried once more overnight at 1173 K. The final product was pure white. To prepare the SiO_2-P_2O_5 glass sample, $(NH_4)_2HPO_4$ and dry silica gel were ground for 20 min and then melted at 1573 K for 3h. After melting, some tridymite was present as indicated by x-ray diffraction. The sample was reground and remelted at 1673 K for 24h. A very homogeneous glass containing 6.2 (± 0.2) m/o P_2O_5 was obtained. This sample was analyzed for phosphorus using the electron microprobe.

One set of SiO_2-GeO_2 LPCVD samples was obtained. The deposition temperature was 703 K and the gases used were SiH_4, GeH_4, and O_2. The $O_2/SiH_4 + GeH_4$ ratio was 1:1, with pressure being ~400 mtorr. The film sample (~3 μm thick) was again collected on stainless steel wafers. As a result, there was a small amount of metallic impurities in the sample (10-1000 ppm). The GeO_2 film content was 3.6 m/o. The reason for not obtaining films with higher GeO_2 content is that the LPCVD deposition rates for such glasses are very slow, and runs of several days duration would be necessary.

Therefore, in order to obtain more information on the SiO_2-GeO_2 binary, bulk glass samples were prepared. Silica gel and high purity crystalline GeO_2 (predominantly hexagonal modification) (Sylvania Corporation) were used. The two compounds were ground and then melted at 1673 K for 48h in order to obtain crystal-free glasses. Thus, one 49.7 and one 56.5 m/o GeO_2 SiO_2-GeO_2 sample were prepared. In order to obtain a higher GeO_2-content glass and to avoid prolonged melting (since Ge is quite volatile at high temperatures), a 49.7 m/o GeO_2 sample and the required amount of crystalline GeO_2 was added to make an ~83 m/o GeO_2 sample. The materials were ground together and then melted for 3h at 1473 K. X-ray diffraction showed no crystals present. All SiO_2-GeO_2 samples were analyzed for Ge content by atomic absorption spectroscopy. The accuracy of these analyses is noted in Tables V and VI. The homogeneity of the samples was checked by the electron microprobe. The 49.7 m/o GeO_2 sample was homogeneous (the Ge count-rate on various grains was ~±2%). The other two samples were somewhat inhomogeneous (the Ge count-rate on various grains was ~7%). The 83 m/o GeO_2 sample contained many bubbles and voids. No phase separation was evident in the glass.

High temperature calorimetry.—The calorimeter used is of the Tian-Calvet type operating at 973 K and has been described elsewhere (20). In this study, three types of experiments have been performed: "transposed temperature drop" calorimetry, solution calorimetry, and "transposed temperature drop-solution" calorimetry. In transposed temperature drop calorimetry, small amounts of the sample (20-40 mg) are placed into a Pt capsule which is then dropped from room temperature into the calorimeter at 973 K. Two processes can be associated with this step. First, the sample heats from room temperature to calorimeter temperature, absorbing an amount of heat equal to its heat content, H_{973}-H_{298}. A second process can occur in a metastable sample (such as "snow" and film LPCVD samples) which may also transform very rapidly from its original metastable structural and thermodynamic state to a stable or less metastable configuration at 973 K. The Pt capsule with the sample can be retrieved and then the drop experiment can be repeated. From the second drop, the heat content of the transformed sample can be obtained. The difference between first and second drops is the enthalpy (at room temperature) associated with the transformation.

In solution calorimetry, a sample (15-30 mg) is thermally equilibrated in the hot calorimeter and subsequently dissolved in molten $2PbO \cdot B_2O_3$. From this type of experiment, one can obtain the heat of solution of a sample and compare the heat of solution of different metastable forms which do not interconvert at 973 K. Thus, transposed-temperature-drop calorimetry is useful when the rates of transformation are rapid (complete transformation in half an hour or less) and solution calorimetry is useful when the rates of transformation are slow (no change in several hours in the calorimeter).

When transformation occurs on an intermediate time scale (partial transformation in a few hours), neither of the above two methods is suitable for getting the total stored enthalpy. The bulk GeO_2-SiO_2 glass samples, which devitrify partially in several hours, are such a case. For them, a combination of the above methods, called "drop-solution" calorimetry, was used. Two variants of this method were utilized. For powdered samples, a small amount of sample (20-30 mg) was encapsulated in Pt. A piece of Pt was placed on top of the sample and in the same capsule in order to make the whole capsule sufficiently heavy to fall properly. The top of the capsule

Table I. Drop calorimetry results on SiO_2-P_2O_5 glasses

Drop	Deposition T(K) "Snow"	Film	m/o P_2O_5 Snow	m/o P_2O_5 Film	Snow SiO_2-P_2O_5 H_{973}-H_{298} (kJ mol^{-1})	Film SiO_2-P_2O_5 H_{973}-H_{298} (kJ mol^{-1})
1	344-673	703	10.8	7.5	−20.57 ± 4.89[a] (2)[b]	38.33 ± 1.66 (2)
2	344-673	703	10.8	7.5	43.20 ± 0.51 (2)	44.62 ± 0.62 (2)
1	344-673	703	3.5	4.4	−74.48 ± 1.24 (2)	36.28 ± 0.47 (2)
2	344-673	703	3.5	4.4	39.48 ± 1.56 (2)	43.58 ± 2.22 (2)
1	344-673	703	8.8	6.6	−23.62 ± 0.50 (2)	36.44 ± 0.59 (2)
2	344-673	703	8.8	6.6	41.90 ± 4.75 (2)	42.36 ± 1.57 (2)
1	419-533	643	3.7	3.7	−13.81 ± 0.71 (2)	25.32 ± 1.36 (2)
2	419-533	643	3.7	3.7	30.19 ± 5.12 (2)	42.01 ± 0.35 (2)
3	419-533		3.7		33.48 ± 4.62 (2)	
1	419-533	643	7.3	5.9	−65.34 ± 3.70 (2)	25.21 ± 1.10 (2)
2	419-533	643	7.3	5.9	40.88 ± 3.20 (2)	41.70 ± 2.81 (2)
1	419-533	643	5.3	3.6	−112.06 ± 12.02 (5)	22.68 ± 0.88 (2)
2	419-533	643	5.3	3.6	40.26 ± 5.95 (5)	42.87 ± 0.21 (2)
1	327-455	523	10.8	7.2	−48.23 ± 9.30 (4)	9.15 ± 0.50 (2)
2	327-455	523	10.8	7.2	43.89 ± 4.38 (2)	44.31 ± 0.06 (2)

[a] ± 1σ (standard deviation of the data), significant figures carried to avoid round-off errors in subsequent calculations.
[b] Number of successful experiments.

was left open. The capsule was dropped from room temperature into molten $2PbO \cdot B_2O_3$ and kept in a Pt crucible in the calorimeter at 973 K. The dissolution of the sample is very fast. Also, for glass samples that were in the form of large pieces, encapsulation in Pt was not necessary. Glass pieces of approximately 40 mg were simply dropped into the flux from room temperature. These samples dissolved easily and rapidly in the lead borate flux and no stirring apparatus was required. After each run, the flux was checked visually to ensure that all the sample had dissolved completely.

The enthalpy of the "drop-solution" process consists of two contributions: (*i*) the heat content H_{973}-H_{298} of the initial glass (and the platinum, when used) and (*ii*) the enthalpy of solution of the glass in lead borate at 973 K. The heat content of the GeO_2-SiO_2 glass has been measured by drop experiments, so the heat of solution can be calculated.

Infrared spectroscopy.—A Nicolet MX-1 FT-IR Spectrometer was used. Approximately 1 mg of sample was ground with ~115 mg of KBr and pelletized. Before taking the spectra, the disks were placed in a drying oven at 373 K for about 24h.

Scanning electron microscopy (SEM).—An ISI-SS40 Scanning Electron Microscope was used. All samples were gold coated.

Results and Discussion

High temperature calorimetry.—Table I contains the results of drop calorimetry on the SiO_2-P_2O_5 samples. For both types of samples, "snow" and film, the first drop is less endothermic than the second one. Similar behavior has been found for SiO_2 LPCVD samples (17). The rapid release of energy during the first drop is most dramatic for the "snow" samples. Its magnitude ranges from ~47 to ~152 kJ/mol, while for the film samples, the excess heat released from the first drop ranges from ~6 to ~35 kJ/mol. All film samples become less metastable with increasing temperature of deposition. Finally, the heat effects measured in the second (or third) drop on all film samples (which contain < 8 m/o P_2O_5) are very similar to values of H_{973}-H_{298} for bulk SiO_2 glass (41.9 kJ mol^{-1}) (21, 22).

The results of solution calorimetry for all the SiO_2-P_2O_5 samples are listed in Table II. The heats of solution of P_2O_5 containing samples are all more exothermic than the heat of solution of bulk SiO_2 glass (−11.30 kJ mol^{-1}). This is a consequence of the P_2O_5 content, since the heat of solution of P_2O_5 is very exothermic [−470.93 kJ mol^{-1} for crystalline P_2O_5 as calculated from the reaction $3CaO + P_2O_5 \rightarrow Ca_3(PO_4)_2$ at 985 K (22, 23) and −492.69 kJ mol^{-1} for P_2O_5 liquid, as calculated from the heat of fusion (21.76 kJ mol^{-1} (24)] and the above reaction. The heat of solution data for both "snow" and film SiO_2-P_2O_5 samples are plotted *vs.* composition in Fig. 1. In general, the enthalpies of solution are less negative than the straight line joining P_2O_5 liquid to SiO_2 glass (Fig. 1). This means that the heat of mixing in the SiO_2-P_2O_5 binary at 973 K is negative. The "snows," even though they release more energy in the drop experiments than the films, seem to have less negative heats of solution than the films. However, these differences are marginal when the uncertainties in the measured values are taken into consideration.

The solution calorimetric data at 973 K refer to P_2O_5 liquid and to glasses on the SiO_2-rich side. Were one to try to calculate the heats of mixing with respect to glassy end members (SiO_2 and P_2O_5 glasses), data on the glass transition temperature and the heat capacity of P_2O_5 glass and liquid would be needed. For P_2O_5, T_g is 473 K (25). Some heat capacity data for crystalline P_2O_5 are reported (22) but C_p data for glass and liquid are not known. Nevertheless, the effect of this correction would be to make the heat of solution of hypothetical P_2O_5 glass under calori-

Table II. Solution calorimetry results on SiO_2-P_2O_5 glasses

Sample	m/o P_2O_5	Deposition T(K)	Anneal T(K)	Anneal t(h)	ΔH_{sol} (kJ mol^{-1})	
Snow	10.8	344-673	973	20	−37.13 ± 0.33[a]	(2)[b]
Snow	8.8	344-673	973	20	−26.26 ± 1.75	(2)
Snow	3.5	344-673	973	20	−21.42	(1)
Snow	7.3	419-533	973	20	−38.56 ± 3.10	(2)
Snow	5.3	419-533	973	20	−21.36 ± 1.63	(2)
Snow	3.7	419-533	973	20	−17.32 ± 0.35	(2)
Snow	10.8	327-455	973	20	−41.80 ± 1.19	(2)
Film	7.5	703	973	20	−37.72 ± 0.68	(2)
Film	7.5	703	1173	20	−36.20 ± 1.12	(2)
Film	6.6	703	973	20	−37.03 ± 1.71	(2)
Film	6.6	703	1173	20	−35.31 ± 3.46	(3)
Film	4.4	703	973	35	−27.16 ± 2.37	(2)
Film	4.4	703	1173	20	−23.31 ± 0.42	(2)
Film	3.6	643	973	35	−36.55 ± 3.58	(2)
Film	3.6	643	1173	20	−36.51 ± 0.69	(2)
Film	3.7	643	973	35	−32.99 ± 3.82	(2)
Film	3.7	643	1173	35	−31.43 ± 2.43	(2)
Film	5.9	643	973	35	−45.17 ± 1.86	(2)
Film	5.9	643	1173	35	−36.57 ± 0.77	(2)
Film	7.2	503	973	20	−51.51 ± 0.94	(2)
Film	7.2	523	1173	35	−49.75 ± 0.77	(2)

[a] ± 1σ (standard deviation of the data), significant figures carried to avoid round-off errors in subsequent calculations.
[b] Number of successful experiments.

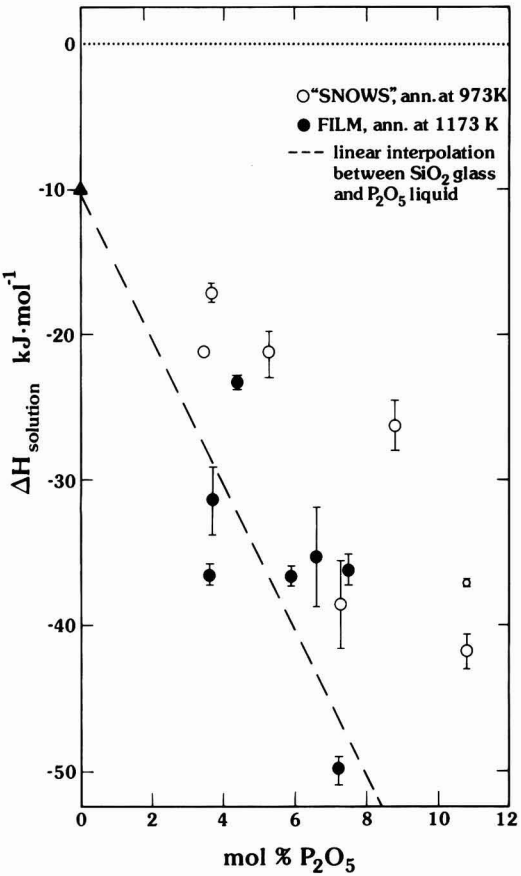


Fig. 1. Heat of solution of annealed film and "snow" SiO_2-P_2O_5 LPCVD samples (kJ · mol^{-1}) vs. composition. Total length of error bars is 2σ.

metric conditions less negative than that of the liquid. Thus, the points for the binary SiO_2-P_2O_5 glasses may lie closer to a straight line joining SiO_2 glass and P_2O_5 glass than to the line drawn which joins SiO_2 glass and P_2O_5 liquid. It is concluded that the substitution of P_2O_5 into SiO_2 in the glassy state is either ideal or slightly exothermic in terms of enthalpy.

Table III. Comparison between film LPCVD and bulk SiO_2-P_2O_5 glasses

Sample	m/o P_2O_5	H_{973}-H_{298} 2nd drop (kJ mol^{-1})	ΔH_{sol} (kJ mol^{-1})
Bulk	6.2	43.22 ± 2.66[b] (2)[c]	−30.06 ± 0.38 (2)
703 K film	6.6	42.36 ± 1.57 (2)	−37.03 ± 1.71 (2)
703 K film ann.[a]	6.6		−35.31 ± 3.46 (3)
643 K film	5.9	41.70 ± 2.81 (2)	−45.17 ± 1.86 (2)
643 K film ann.[a]	5.9		−36.57 ± 0.77 (2)

[a] Sample annealed at 1173 K for 35h, in air.
[b] ± 1σ (standard deviation of the data), significant figures carried to avoid round-off errors in subsequent calculations.
[c] Number of successful experiments.

Table III compares H_{973}-H_{298} and the enthalpy of solution of a bulk sample, deposited films, and annealed films of similar P_2O_5 content (5.9-6.6%). The heat contents are similar. The heats of solution of annealed films are more similar to those of bulk material than they are to those of initially deposited films. This similarity was also observed in comparing annealed SiO_2 LPCVD films to bulk silica glass (17). Thus, both SiO_2 and SiO_2-P_2O_5 films tend to approach the energetic state of bulk glass on annealing. This observation is relevant to the semiconductor industry since phosphosilicate LPCVD layers are annealed routinely during device processing.

The total stored excess enthalpy (relative to the annealed SiO_2-P_2O_5 LPCVD samples) is the sum of the excess enthalpy in the drop and in the solution experiments (Table IV). This is plotted in Fig. 2 against composition. The various "snow" samples show somewhat irregular behavior. The 344-673 K "snows," after a significant increase in the total stored enthalpy at 3.5 m/o P_2O_5, display a smoother decrease to a slightly higher value than that for pure SiO_2 "snow" for the 8.8 and 10.8 m/o P_2O_5 samples. The two batches of 419-533 K pure SiO_2 "snows" (from two nominally identical runs) have slightly different total stored enthalpies. Then, with increasing P_2O_5 content, there is an initial decrease in the total stored enthalpy for the 3.7 m/o P_2O_5 sample followed by a

Table IV. Total stored enthalpy of the SiO_2-P_2O_5 LPCVD samples

Sample	m/o P_2O_5	Deposition T(K)	Enthalpy difference Drop (kJ mol^{-1})	Solution (kJ mol^{-1})	Total stored enthalpy (kJ mol^{-1})
Film	0.0	703	19.4[b] ± 0.3[a]	2.8[b] ± 0.4[c]	22.1 ± 0.5[e]
Film	4.4	703	7.3[f] ± 2.3	3.9[d] ± 2.4	11.2 ± 3.3
Film	6.6	703	5.9[f] ± 1.6	1.7[d] ± 3.9	7.6 ± 4.2
Film	7.5	703	6.3[f] ± 1.8	1.5[d] ± 1.3	7.8 ± 2.2
Film	0.0	643	22.8[b]	10.4[b] ± 0.4	33.3 ± 0.4
Film	3.6	643	20.2[f] ± 0.9	0.0[d] ± 3.7	20.2 ± 3.8
Film	3.7	643	16.7[f] ± 1.4	0.8[d] ± 4.5	17.5 ± 4.7
Film	5.9	643	16.5[f] ± 3.0	8.5[d] ± 2.0	24.9 ± 3.6
Film	0.0	523	42.9[b] ± 1.1	0.9[b] ± 2.0	43.8 ± 2.2
Film	7.2	523	35.7[f] ± 0.5	1.8[d] ± 1.2	36.9 ± 1.3
Snow	0.0	344-673 (703)	14.7[b] ± 0.2	32.3[b] ± 0.6	47.0 ± 0.7
Snow	3.5	344-673 (703)	113.8[f] ± 2.0	~0[g]	113.8 ± 2.0
Snow	8.8	344-673 (703)	65.5[f] ± 4.8	~0[g]	65.5 ± 4.8
Snow	10.8	344-673 (703)	63.8[f] ± 4.9	~0[g]	63.8 ± 4.9
Snow	0.0	419-533 (643)	103.4[b] ± 3.8	−1.6[b] ± 1.7	101.8 ± 4.1
Snow	0.0	419-533 (643)	78.7[b] ± 2.3	0.3[b] ± 0.2	79.0 ± 2.3
Snow	3.7	419-533 (643)	47.3[f] ± 4.7	~0[g]	47.3 ± 4.7
Snow	5.3	419-533 (643)	152.3[f] ± 13.4	~0[g]	152.3 ± 13.4
Snow	7.3	419-533 (643)	106.2[f] ± 4.9	~0[g]	106.2 ± 4.9
Snow	0.0	327-455 (523)	61.7[b] ± 1.5	−1.8[b] ± 0.7	59.9 ± 1.6
Snow	10.8	327-455 (523)	92.1[f] ± 10.3	~0[g]	92.1 ± 10.3

[a] Errors propagated from drop experiments.
[b] Difference calculated from bulk SiO_2 glass, see Ref. (17).
[c] Errors propagated from solution experiments.
[d] Difference calculated from 1173 K annealed film sample.
[e] Errors calculated by propagation of errors of a and c.
[f] Difference calculated from 1st and 2nd (or 3rd) drop experiments, Table I.
[g] Not known, assumed zero.

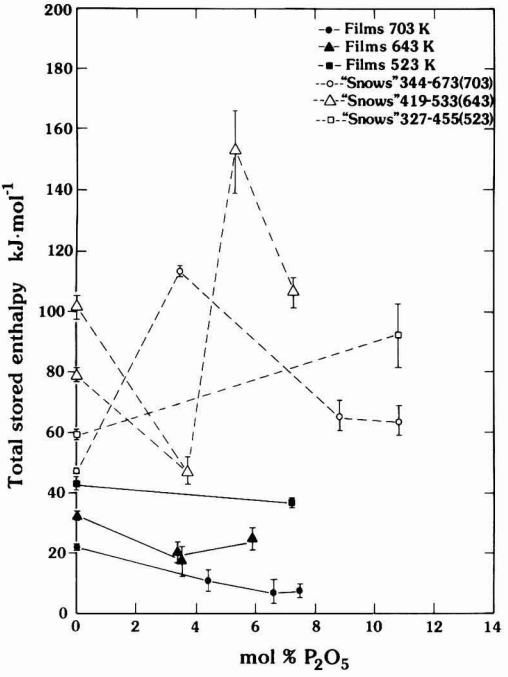


Fig. 2. Total stored enthalpy (kJ mol^{-1}) of the "snow" SiO_2-P_2O_5 samples (dashed lines) and films (solid lines) vs. composition. Total length of error bars is 2σ.

significant increase for the 5.3 m/o P_2O_5 "snow" and a decrease to a value slightly higher than that for pure SiO_2 "snow" for the 7.3 m/o P_2O_5 sample. Finally, for the 327-455 K "snows," the 10.8 m/o P_2O_5 sample displays a higher total stored enthalpy than the undoped SiO_2 "snow." Such irregular behavior is not surprising, since these samples are porous, possess very large surface areas, and are probably slightly chemically inhomogeneous.

The film samples, on the other hand, show much more systematic behavior (Fig. 2). In general, with increasing temperature of deposition, the total stored excess enthalpy is lowered, again suggesting a tendency to approach the bulk glass state. For the 523 K film containing 7.2 m/o P_2O_5, there is a slight decrease in the total stored enthalpy when compared to the pure SiO_2 film sample. After an initial decrease in the total stored enthalpy of the 3.6 and 3.7 m/o P_2O_5 films deposited at 643 K, there is a small increase to a value still smaller than for SiO_2 film for the 5.9% P_2O_5 sample. For the 703 K samples, there is a smooth decrease in total stored enthalpy until the 7.5 m/o P_2O_5 film has a stored enthalpy less than that of the undoped SiO_2 sample. This overall decrease in total stored enthalpy with increasing P_2O_5 content is most pronounced in the highest temperature film samples. The structural reasons for this variation in stored enthalpy are not known in detail. The IR spectra suggest the disappearance of P-OH, Si-OH, and Si-H species on annealing (see below). This may be accompanied by changes in the geometry of the phosphosilicate network or in the distribution of PO_4 tetrahedra in the structure, but no direct evidence exists for this. What is known is that increasing P_2O_5 doping decreases the viscosity and reflow temperature of SiO_2-P_2O_5 films (26, 27). There is evidence that preannealing at temperatures near 973 K, well below reflow temperatures of about 1273 K, improves the subsequent flow characteristics at higher temperatures (28). Such an anneal also decreases the hygroscopicity of the films (29). We take these observations and our enthalpies of annealing as evidence for significant structural and

Table V. Drop calorimetry results on SiO_2-GeO_2 glasses

Drop	Sample	m/o GeO_2	H_{973}-H_{298} (kJ mol^{-1})
1 & 2	Bulk	0	41.83[a] ± 0.12[b] (2)
1	"Snow" CVD 344-673 K	2.7 ± ~ 0.2	−46.48 ± 5.19 (2)
2	"Snow" CVD 344-673 K		39.66 ± 1.76 (2)
1	Film CVD 703 K	3.6 ± ~ 0.2	23.05 ± 1.00 (2)
2	Film CVD 703 K		40.46 ± 0.33 (2)
1	Bulk	49.7 ± ~ 2.8	40.29 ± 0.38 (2)
2	Bulk		42.05 ± 0.96 (2)
1	Bulk	56.5 ± ~ 2.8	41.09 ± 0.67 (2)
2	Bulk		42.38 ± 1.46 (2)
1	Bulk	82.9 ± ~ 2.8	41.67 ± 1.53 (3)
2	Bulk		43.01 (1)
1	Bulk	100	44.56 ± 0.03 (2)

[a] From Ref. (20) and (21).
[b] ± 1σ (standard deviation of the data), significant figures carried to avoid round-off errors in subsequent calculations.

thermodynamic relaxation of the films in the range 600-1000 K. Such relaxation would be expected to occur more readily with increasing temperature and with increasing phosphorus content, and for the higher deposition temperatures and higher phosphorus contents, could occur during deposition. This would explain the observed excess enthalpies. At the lowest deposition temperature, 523 K, all films would have a large excess enthalpy which anneals only at much higher temperatures. At higher deposition temperatures, 643 K and especially 703 K, considerable relaxation could occur during deposition of films with higher P_2O_5 content, causing the total stored enthalpy to decrease with increasing P_2O_5 concentration. Such relaxation may have a direct relation to the reflow properties after anneal during device processing. Although all films tend to approach the energetic state of bulk glass after annealing, the fact that the high-P_2O_5 high-temperature films begin to do so during deposition may make them desirable, relatively stable materials for certain semiconductor device applications.

The LPCVD SiO_2-GeO_2 samples have been examined together with the bulk samples that have been prepared. The bulk samples cover the whole compositional range from SiO_2 to GeO_2, thus making it possible to obtain information on the mixing of the two end members, SiO_2 glass and GeO_2 glass. Calorimetric results are listed in Tables V amd VI. Results for the heat content of germania glass are in good agreement with the literature (22), as is the molar enthalpy of solution of GeO_2 glass (30).

The heats of solution from Table VI have been fitted by least squares techniques. A quadratic equation is the simplest expression that fits the seven points along the SiO_2-GeO_2 join. Thus, (in kJ mol^{-1})

$$\Delta H_{sol} = -35.5(\pm 1.4) + 76.6(\pm 6.8)x - 51.0(\pm 5.9)x^2 \quad [1]$$

where x is the mol fraction of SiO_2. The coefficient of determination R^2 for the fit is 0.94.

Table VI. Drop-solution calorimetry results on SiO_2-GeO_2 glasses

Sample	m/o GeO_2	ΔH_{sol} (kJ mol^{-1})
Bulk	0	−11.30 ± 0.21[a] (2)[b]
"Snow" CVD 344-673 K	2.7 ± ~ 0.2	−12.13 ± 0.54 (2)
Film CVD 703 K	3.6 ± ~ 0.2	−7.53 ± 0.92 (3)
Bulk	49.7 ± ~ 2.8	−11.62 ± 0.95 (3)
Bulk	56.5 ± ~ 2.8	−8.20 ± 2.09 (3)
Bulk	82.9 ± ~ 2.8	−27.32 ± 1.51 (3)
Bulk	100	−33.81 ± 1.63 (3)

[a] ± 1σ (standard deviation of the data), significant figures carried to avoid round-off errors in subsequent calculations.
[b] Number of successful experiments.

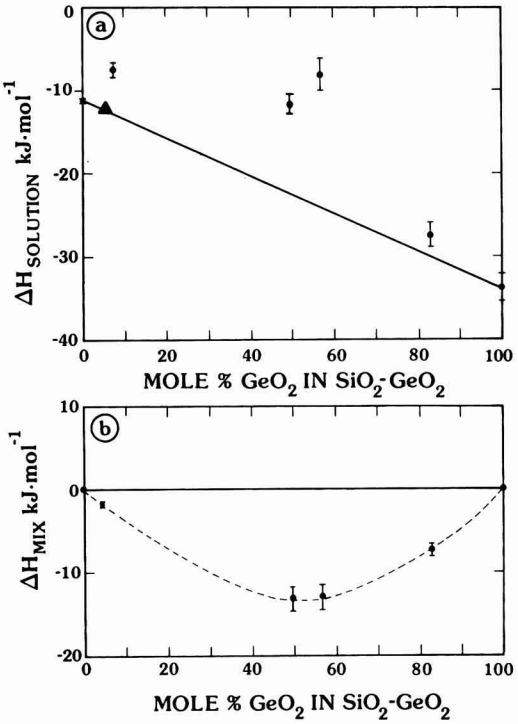


Fig. 3. a. Heat of solution (kJ mol^{-1}) of various SiO_2-GeO_2 samples along the whole compositional range including the end members. The triangle refers to the one LPCVD "snow" sample and is not included in the calculations. Total length of error bars is 2σ. b. Heat of mixing (kJ mol^{-1}) of the samples in part a. Total length of error bars is 2σ.

The resulting heat of mixing is given by Eq. [2] (in kJ mol^{-1}) (see Fig. 3)

$$\Delta H_{mix} = -51.0(\pm 5.9)x(1-x) \quad [2]$$

The negative heat of mixing (-12.8 ± 1.5 kJ mol^{-1} at the 50 m/o composition) implies an energetic stabilization of intermediate compositions, resulting, presumably, from atomic or molecular level structural readjustments. These results suggest that the glassy SiO_2-GeO_2 system behaves in a manner more complex than what is expected for a simple ideal substitution of Ge for Si in a tetrahedral framework. This is in contrast to the ideal mixing seen in glasses along the $NaAlSi_3O_8$-$NaAlGe_3O_8$ pseudobinary (31).

Earlier work by Riebling (32) suggests that the volumes of mixing in the SiO_2-GeO_2 binary are slightly positive. At the 50 m/o composition the molar volume of the binary is ~0.6% higher than a linear combination of end-member volumes. Measurements in this study are similar, with a 0.7% larger volume at the 50 m/o composition. These positive excess volumes contrast with the negative excess enthalpies, suggesting that the structural rearrangements causing these features may be quite subtle. Schlichting and Neumann (33) reported significant deviations from average behavior in the thermal expansivities of intermediate composition glasses, again pointing to complex behavior.

According to Smith and Isaacs (34) the longer Ge-O distance (when compared to Si-O) plays a more significant role in determining density (and thus molar volume) than does the smaller Ge-O-Ge bond angle (133° compared to 144° for Si-O-Si). Also, in GeO_2 glass not all tetrahedra are always linked to four others (35). Thus the GeO_2 glass structure is more open and more weakly bonded than that of silica glass. The enthalpy, volume, and expansivity data may reflect this structural complexity.

Infrared spectroscopy.—Figures 4 and 5 show the powder IR spectra of the SiO_2-P_2O_5 LPCVD film and "snow" samples deposited at 703 K and 643 K, respectively, and Fig. 6 shows the spectrum of the bulk SiO_2-P_2O_5 sample. Variations in peak intensities in the various P_2O_5 content glasses are due to small variations in the sample size used for making the disks. Thus, the figures cannot be used to compare absolute intensities.

A few main features can be seen in the spectra. First, the major features of the silicate framework are practically unchanged, *i.e.*, the 1100 and 800 cm^{-1} bands characteristic of the bulk SiO_2 glass spectrum are present. This is not surprising, since all the SiO_2-P_2O_5 samples have low P_2O_5 contents. However, some subtle differences are present.

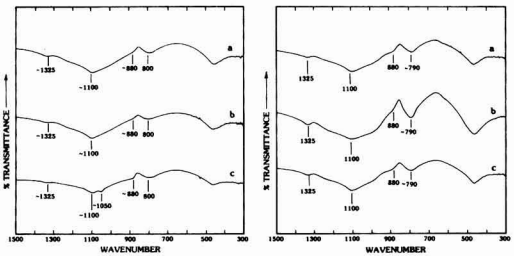


Fig. 4. Powder infrared spectra of as-deposited (left) and annealed (1173 K) (right) LPCVD SiO_2-P_2O_5 films; a: 7.5 m/o P_2O_5 b: 6.6 m/o P_2O_5, and c: 4.4 P_2O_5. Samples deposited at 703 K. Region from 1500-300 cm^{-1}.

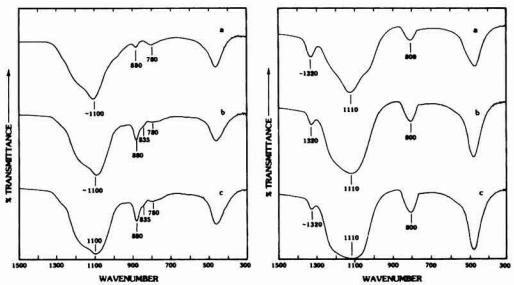


Fig. 5. Powder infrared spectra of as-deposited (left) and annealed (1173 K) (right) LPCVD "snow" SiO_2-P_2O_5 samples deposited at 643 K. a: 7.3 m/o P_2O_5 b: 5.3 m/o P_2O_5, and c: 3.7 m/o P_2O_5. Region from 1500-300 cm^{-1}.

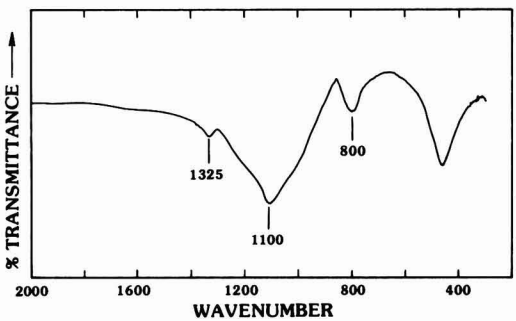
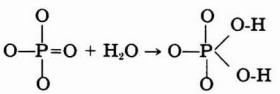


Fig. 6. Powder infrared spectrum of bulk SiO_2-P_2O_5 glass containing 6.2 m/o P_2O_5. Region from 2000-300 cm^{-1}.

In the film samples, an unexpected 880 cm^{-1} band is present and it is much more pronounced in the "snow" samples. In general, it disappears upon annealing. Its absence from the bulk SiO_2-P_2O_5 sample suggests that it may be associated with the LPCVD process. Raman studies on pure P_2O_5 glass and on the SiO_2-P_2O_5 binary have been performed (5, 36, 37). From the Raman spectra of P_2O_5 glass, it was concluded that this glass is a three-connected network in which each phosphorus atom is surrounded almost tetrahedrally by three bridging oxygen atoms and one double-bonded oxygen (36). For the phosphosilicate glasses, characteristic bands occur at 700, 1140, and 1330 cm^{-1}, which are attributable to O-P=O, P-O-Si, and P=O vibrations, respectively (35). The only major band in the samples in this study is that assigned to P=O.

The most important other feature seen in the IR spectra of the SiO_2-P_2O_5 samples is the band at 1325 cm^{-1}. This is attributed to the P=O bonds (15). This band is also present in the spectrum of bulk SiO_2-P_2O_5 glass (6.2 m/o P_2O_5, Fig. 6) and in all the annealed film and "snow" LPCVD samples. However, the same band is either absent or only slightly visible in the as-deposited samples. This may suggest that when there is H_2O present in a sample, the P=O bonds are broken



[3]

When the sample is annealed, P=O bonds form since H_2O is driven off from the sample (15). In the high frequency region bands associated with Si-OH and Si-H species were found [3680 and 2260 cm^{-1}, respectively (38, 39)] which disappear on annealing. There are cases where the 1325 cm^{-1} band is slightly visible in the as-deposited samples (film SiO_2-P_2O_5 samples) (Fig. 4). For these samples, the high frequency spectra show traces of Si-OH and Si-H species or an absence of these species. On annealing at 1173 K, the 1325 cm^{-1} band becomes more prominent, suggesting that there is a small degree of P=O bond breaking in the as-deposited samples. The above results agree well with reported IR data on LPCVD SiO_2-P_2O_5 glasses (14, 15, 16).

In the spectra of the as-deposited "snow" LPCVD SiO_2-P_2O_5 samples deposited during the 643 K LPCVD runs, there are some small and unexplained differences in the region between 750 and 880 cm^{-1}. Especially unusual is a shoulder appearing at ~835 cm^{-1}. No such feature is present in the film SiO_2-P_2O_5 samples.

The spectra of the film and "snow" SiO_2-GeO_2 samples have been compared to those of bulk SiO_2 glass. The differences between the spectrum of the annealed SiO_2-GeO_2 film sample and those of bulk SiO_2 glass are minimal and are consistent with the very low GeO_2 content (3.6 m/o). The same is true for the "snow" SiO_2-GeO_2 spectra. The major difference is the 880 cm^{-1} band present in the as-deposited "snow" sample which disappears on annealing. This feature is generally seen in all LPCVD "snow" samples, including pure SiO_2, the SiO_2-GeO_2 sample, and the SiO_2-P_2O_5 "snows." In all these systems, this peak disappears on annealing. The origin of this band is unclear, although interpretations in terms of oxygen-deficient species have been proposed (40).

For pure GeO_2 glass, the Raman spectrum exhibits a band at ~416 cm^{-1}. This is attributed to the symmetric Ge-O-Ge mode and two weak bands at 858 and 973 cm^{-1} assigned to TO and LO splitting of the antisymmetric Ge-O-Ge vibrational mode (41). Figure 7 shows the IR spectrum of GeO_2 glass, of hexagonal crystalline GeO_2, and of a devitrified GeO_2 sample after an 8h anneal at 973 K in the calorimeter. The evolution from glass to crystal is evident. For hex-GeO_2, bands at ~875 and ~960 cm^{-1} are observed which most probably correspond to the 853 and

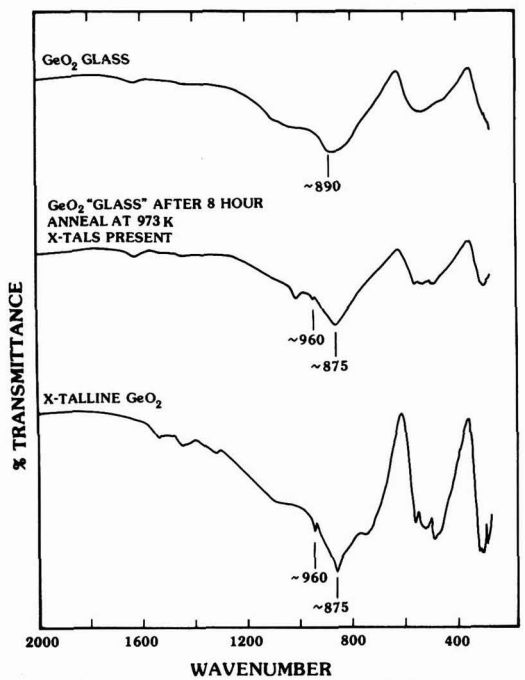


Fig. 7. Powder infrared spectra of GeO_2 bulk glass, GeO_2 glass undergoing devitrification, and of the hexagonal form of crystalline GeO_2. Region from 2000-300 cm^{-1}.

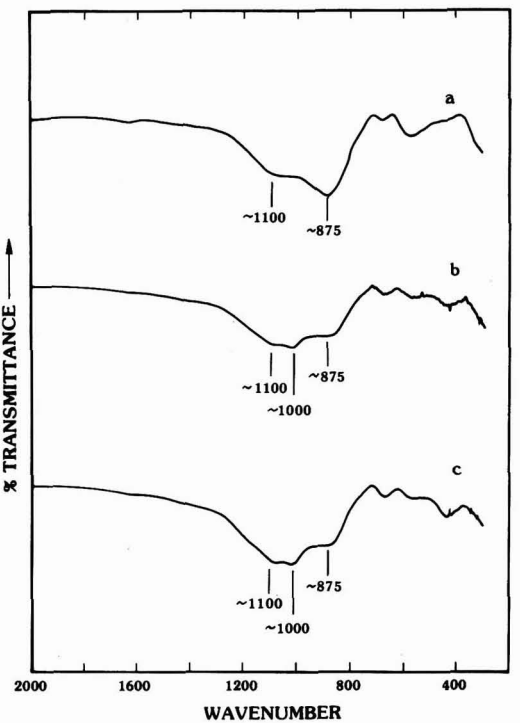


Fig. 8. Powder infrared spectra of SiO_2-GeO_2 bulk glasses. a: 82.9 m/o GeO_2, b: 56.5 m/o GeO_2, and c: 49.7 m/o GeO_2. Region from 2000-300 cm^{-1}.

973 cm^{-1} Raman bands. Similar observations have been made on the IR spectrum of hex-GeO_2 by Lippincott *et al.* (42). In vitreous GeO_2, the Ge-O-Ge antisymmetric stretching is also observed at ~890 cm^{-1}. This indicates the similarity between glass and hexagonal GeO_2, in that both consist of tetrahedrally coordinated GeO_2 units.

An analysis of the structures of glasses along the SiO_2-GeO_2 join by Raman spectroscopy has been given by Sharma *et al.* (43). On adding SiO_2 to GeO_2 glass, the band at ~1100 cm^{-1} starts to appear and also a band in the vicinity of 930-980 cm^{-1}, attributed to the antisymmetric Ge-O-Si vibration, appears (43). Figure 8 presents the IR spectra of the bulk SiO_2-GeO_2 glasses. As the GeO_2 content decreases (Fig. 8a, b, c), the SiO_2 features can be seen more clearly; *i.e.*, the 1100 cm^{-1} band attributed to Si-O-Si antisymmetric stretching. With increasing SiO_2 content, a band appears at ~1000 cm^{-1} which could be assigned to the antisymmetric Ge-O-Si vibrational mode. Finally, the 875 cm^{-1} band (assigned to Ge-O-Ge stretching) is seen in all the SiO_2-GeO_2 samples and it diminishes in intensity as the samples become more SiO_2 rich.

Scanning electron microscopy (SEM).—SEM micrographs of various "snow" and film SiO_2-P_2O_5 samples are shown in Fig. 9. The film samples have a smooth surface in general, but (see Fig. 9a and b) bubbles, which become more prominent in the annealed samples, can be present.

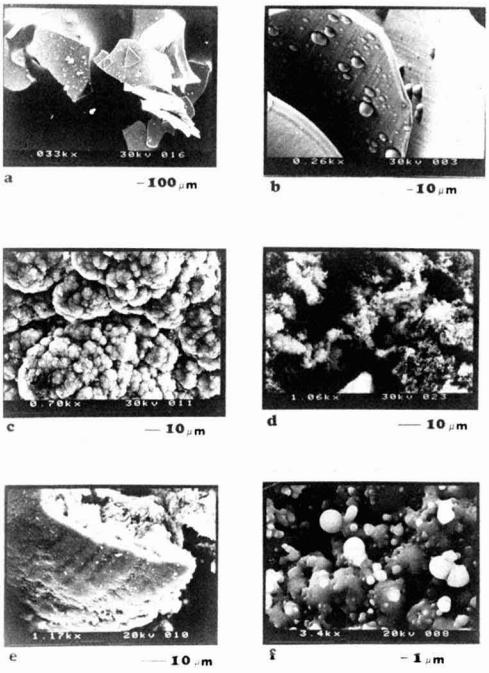


Fig. 9. a. SEM micrograph of as-deposited film LPCVD SiO_2-P_2O_5 deposited at 523 K containing 7.2 m/o P_2O_5. Mag. 33x. General overview-bubbles. b. Close-up of same sample but annealed. Mag. 260x. Bubbles can be clearly seen. Larger single bubbles are about 20-25 μm in diam and smaller ones are much less than 10 μm in diam. c. SEM micrograph of as-deposited LPCVD "snow" SiO_2-P_2O_5 deposited at 643 K. Sample contains 3.7 m/o P_2O_5. Cauliflower-like surface. Mag. 700x. d. SEM micrograph of as-deposited LPCVD "snow" SiO_2-P_2O_5 deposited at 523 K. Sample contains 10.8 m/o P_2O_5. Very porous surface. Mag. 1060x. e. SEM micrograph of annealed LPCVD "snow" SiO_2-P_2O_5 deposited at 703 K. Sample contains 8.8 m/o P_2O_5. Partly porous surface. Mag. 1170x. f. SEM micrograph of annealed LPCVD "snow" SiO_2-P_2O_5 deposited at 703 K. Sample contains 8.8 m/o P_2O_5. Even though same sample as in part c, surface is unique. Spherules present. Most prominent ones have a diam of about 3 μm. Mag. 3400x.

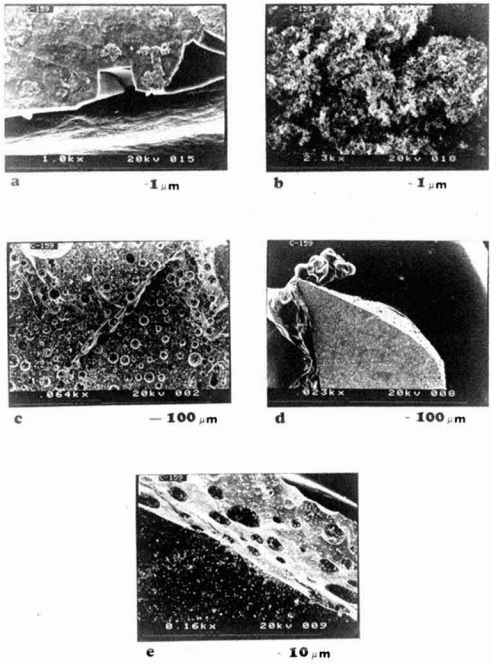


Fig. 10. a. SEM micrograph of as-deposited LPCVD film SiO_2-GeO_2 deposited at 703 K and containing 3.6 m/o GeO_2. Mag. 1000x. b. SEM micrograph of as-deposited "snow" LPCVD SiO_2-GeO_2 deposited at 703 K and containing 2.7 m/o GeO_2. Surface very porous. Mag. 2300x. c. SEM micrograph of bulk SiO_2-GeO_2 glass containing 82.9 m/o GeO_2. Numerous air bubbles and voids present. Bubbles vary in diam size. Most prominent ones are about 80-100 μm in diam. Mag. 64x. d. Same sample as in part a. Micrograph of glass surface and edge. Bubbles and voids can be seen. Mag. 23x. e. Same sample as in parts a, b. Close-up of the edge from part b. Voids and a few bubbles can be clearly seen. Voids range from ~20μm to ~100μm in diam. Bubbles are about 40 μm in diam.

We suggest that these bubbles are caused by hydrogen gas which is trapped in the films during the very long deposition runs, since at the deposition conditions in this study, H_2 is a by-product of the oxidation of SiH_4. The "snow" samples present a variety of surface morphologies (see Fig. 9c-f). This variability may indicate heterogeneity which may give rise to some of the scatter in the calorimetric data for these samples.

The film LPCVD SiO_2-GeO_2 sample exhibits a slightly rougher surface than the SiO_2-P_2O_5 film samples (Fig. 10a). This roughness is due to the stainless steel substrate. No bubbles are seen. However, the "snow" SiO_2-GeO_2 sample is very typical and similar to other "snows" (17) (Fig. 10b). Figure 10c through e shows the bulk SiO_2-GeO_2 glass containing 83 m/o GeO_2 which contains numerous air bubbles and voids.

Conclusions

High temperature calorimetry has provided thermodynamic data on two LPCVD glass systems, SiO_2-P_2O_5 and SiO_2-GeO_2, and on bulk SiO_2-GeO_2 glass samples.

The as-deposited LPCVD SiO_2-P_2O_5 samples are metastable with respect to annealed films by ~6 to ~152 kJ mol^{-1}. The "snow" samples are more metastable than the films. There is also an indication that the heat of mixing in the SiO_2-P_2O_5 binary is negative. From the point of view of semiconductor processing, the above study suggests the following conclusions: (*i*) The 703 K deposited SiO_2-P_2O_5 films, being energetically least metastable, may offer an advantageous starting point for further processing. (*ii*) At higher deposition temperatures

(703 K especially), the P_2O_5 richer films may relax somewhat during the actual LPCVD process, causing a decrease in the total stored enthalpy of these samples when compared to the undoped SiO_2 films deposited at the same temperature.

Data on the SiO_2-GeO_2 binary indicate that the two end members mix nonideally with a negative heat of mixing of -12.8 ± 1.5 kJ mol^{-1} at the 50 m/o composition.

Our results from IR spectroscopy agree well with those reported on both SiO_2-P_2O_5 and SiO_2-GeO_2 samples. Si-OH and Si-H species are present in the as-deposited LPCVD samples and disappear on annealing.

It is interesting to note that observations on the thermodynamic properties and the nature of vapor deposited amorphous and vitreous states of water have been made (44, 45), which are similar to our results. In particular, the fact that the structure and thermodynamic properties of vapor deposited materials (as-deposited amorphous water or LPCVD samples) differ from those of materials in the glassy state (vitreous water or other bulk glasses) and also depend on deposition conditions and heat-treatments (annealing).

Acknowledgments

We would like to thank Dr. Paul McMillan for his comments on the spectroscopy. Special thanks are given to Ms. Susan Selkirk for the drafting and to Mr. Patrick Trusty for the SEM work. This research was supported by NSF grant DMR 8211127. This work is part of M. Huffman's Ph.D. thesis.

Manuscript submitted July 15, 1985; revised manuscript received Oct. 21, 1985.

REFERENCES

1. K. Soto, Y. Nishi, and T. Abe, in "Thin Film Dielectrics," F. Vratny, Editor, p. 378, The Electrochemical Society Softbound Proceedings Series, New York, NY (1969).
2. M. M. Schlacter, E. S. Schlegel, R. S. Keen, Jr., R. A. Lathlaen, and G. L. Schnable, *IEEE Trans. Electron Devices*, **ed-17,** 1077 (1970).
3. L. H. Kaplan and M. E. Lowe, *This Journal*, **118,** 1649 (1971).
4. A. W. Fisher, J. A. Amick, H. Hyman, and J. H. Scott, Jr., *RCA Rev.*, **29,** 533 (1968).
5. W. A. Sproson, K. B. Lyons, and J. W. Fleming, *J. Non-Cryst. Solids*, **45,** 69 (1981).
6. D. L. Nash, J. R. Simpson, and D. L. Wood, *Ceram. Bull.*, **63,** 726 (1984).
7. A. Navrotsky, *J. Solid State Chem.*, **6,** 21 (1973).
8. A. E. Ringwood, "Composition and Petrology of the Earth's Mantle," McGraw Hill, New York (1975).
9. B. J. Baliga and S. K. Ghandi, *J. Appl. Phys.*, **44,** 990 (1973).
10. W. Kern, G. L. Schnable, and A. W. Fisher, *RCA Rev.*, **37,** 3 (1976).
11. P. J. Tobin and J. B. Price, 408 RNP presented at The Electrochemical Society Meeting, Boston, MA, May 6-11, 1979.
12. D. M. Brown, M. Garfinkel, M. Ghezzo, E. A. Taft, A. Tenney, and J. Wong, *J. Cryst. Growth*, **17,** 276 (1972).
13. M. Shibata and K. Sugawara, *This Journal*, **122,** 155 (1975).
14. J. Wong, AIP Conference Proceedings, Vol. 31, pp. 237-243 (1976).
15. R. M. Levin, *This Journal*, **129,** 1765 (1982).
16. A. S. Tenney and M. Ghezzo, *ibid.*, **120,** 1276 (1973).
17. M. Huffman, A. Navrotsky, and F. Pintchovski, *ibid.*, In press.
18. "Standard Methods for the Examination of Water and Wastewater," 12th ed., pp. 230-234 American Public Health Assoc., American Water Works Assoc., Water Pollution Control Feder.
19. D. L. Hamilton and C. M. B. Henderson, *Mineral. Mag.* **36,** 832 (1968).
20. A. Navrotsky, *Phys. Chem. Min.*, **2,** 89 (1977).
21. P. Richet, Y. Bottinga, L. Denielou, J. P. Petitet, and C. Tequi, *Geochim. Cosmochim. Acta*, **46,** 2639 (1982).
22. R. A. Robie, B. S. Hemingway, and J. R. Fisher, "Thermodynamic Properties of Minerals and Related Substances at 298.15 K and 1 Bar (10^5 Pascals) Pressure and at Higher Temperatures," Geological Survey Bulletin 1452 (1978).
23. H. R. Westrich and A. Navrotsky, *Am. J. Sci.*, **281,** 1091 (1981).
24. H. Rawson, "Inorganic Glass-Forming Systems," chap. 9, Academic Press, Inc., London and New York (1967).
25. A. Eisenberg, H. Farb, and L. G. Cool, *J. Polym. Sci.*, Part A-2, **4,** 855 (1966).
26. W. Kern, *RCA Rev.*, **34,** 655 (1973); *Solid State Technol.*, **17,** No. 3, 35 and No. 4, 78, 89 (1974).
27. G. E. Moore, U.S. Pat. 3,825,442 (1974).
28. W. Kern, R.C.A. Labs, Princeton, NJ, Personal communication, 1985.
29. R. A. Levy, S. M. Vincent, and T. E. McGahan, *This Journal*, **132,** 1472 (1985).
30. A. Navrotsky, *J. Inorg. Nucl. Chem.*, **33,** 1119 (1971).
31. C. Capobianco and A. Navrotsky, *Am. Mineral.*, **67,** 718 (1982).
32. E. F. Riebling, *J. Am. Ceram. Soc.*, Disc. and Notes, **51,** 406 (1968).
33. J. Schlichting and A. Neumann, 8 EPTC Proceedings, p. 167, Pion Publication, Great Britain (1982).
34. G. S. Smith and P. B. Isaacs, *Acta Crystallogr.*, **17,** 842 (1964).
35. A. J. Leadbetter and A. C. Wright, *J. Non-Cryst. Sol.*, **7,** 23 (1972).
36. F. L. Galeener and J. C. Mikkelsen, Jr., *Solid State Commun.*, **30,** 505 (1979).
37. A. Saissy, J. Botineaue, A. Azema, and F. Gives, *J. Phys. Paris Lett.*, 40, L-355 (1979).
38. G. E. Walrafen and S. R. Samanta, *J. Chem. Phys.*, **69,** 493 (1978).
39. G. H. A. M. van der Steen and H. van den Boom, *J. Non-Cryst. Solids*, **23,** 279 (1977).
40. W. A. Pliskin and P. P. Castrucci, *This Journal*, **115,** 85 (1968).
41. F. L. Galeener and G. Lucovsky, *Phys. Rev. Lett.*, **37,** 1474 (1976).
42. E. R. Lippincott, A. Van Valkenburg, C. E. Weir, and E. N. Bunting, *J. Res. Nat. Bur. Stand.*, **61,** 61 (1958).
43. S. K. Sharma and D. W. Matson, *J. Non-Cryst. Solids*, **69,** 81 (1984); S. K. Sharma, D. W. Matson, and J. A. Philpotts, *ibid.*, In press.
44. G. P. Johari, *Philos. Mag.*, **35,** (4), 1077 (1977).
45. E. Mayer and R. Pletzer, *J. Chem. Phys.*, **80,** (6), 2939 (1984).

Releasing Material for the Growth of Shaped Silicon Crystals

Y. Maeda, T. Yokoyama, I. Hide, T. Matsuyama, and K. Sawaya

Hoxan Corporation, Hoxan Research Laboratories, Kikusui, Sapporo, Japan

ABSTRACT

A mold coating material for a melt-shaped crystal growth technique has been developed. After studying the contact angle and reaction between the molten silicon and other various high melting point materials, it was found that for shaped crystal growth with a lower impurity contamination level, a combination coating of Si_3N_4 and SiO_2 is suitable for a mold coating material. A double layer coating was applied to the graphite mold base. The bottom layer in the mold, which had a 100-150 μm thickness, consisted of Si_3N_4 that had been formed by nitriding a spray-coated Si powder. The 200 μm thick top layer consisted of a Si_3N_4-SiO_2 material. It had been produced by oxidizing a sprayed-on coating consisting of Si_3N_4 powder mixed in a silanol liquid. Using the mold prepared with these coatings, a melt-shaped crystal growth technique was carried out by the spinning-casting process. Polycrystalline silicon sheets, with a 10 × 10 cm rectangular dimension and 0.5 mm thickness the size of a mold cavity, were obtained without adhesion to the mold. The sheet had an oxygen content of 1.7 ppm and a carbon content of 0.33 ppm. The mold was usable repeatedly up to 10 times.

For many applications of semiconductor silicon, conventional crystal growth techniques such as the Czochralski pulling method are typically used for producing cylindrical crystal ingots. The final shape required is usually formed by grinding the ingot into a regular cylinder and slicing it into wafers. In large-scale production, approximately one-half of this expensive crystalline material is lost as a result of carrying out these various shaping processes.

Up until now, various silicon melt-growth processes have been developed. As an unconventional crystallization technique from the melt, a typical ingot technique of directional solidification is the "casting" technique (1). In this case, the ingot mold is a crucible into which silicon melt is poured directly with solidification occurring in a fixed temperature environment. The crucible is made of graphite or quartz. The quartz crucible cannot be used repeatedly because of solidification-conglutination of silicon. In the case of the graphite, one undesirable consequence is contamination due to the reaction between the crucible and molten silicon. Saito *et al.* (2) reported that by using silicon nitride powder to coat the inner surface of graphite crucibles, a solidified polycrystalline ingot could be taken out without destroying the crucible. Silicon nitride powder acts as an interface releasing agent between silicon and the crucible. However, a difficult problem is the contamination which results from the silicon nitride powder (having a low purity of 99.9%) mixing with molten silicon as the powder is poured into the crucible.

Another technique for shaping silicon material directly is ribbon growth (3, 4), in which a continuous silicon sheet is pulled upward from the melt. In the capillary action shaping technique and the edge supported pulling technique, a wettable die or filament is immersed in the melt. Ciszek (5) has carried out many experiments to study die material and filament material characteristics in relation to the silicon melt. In these materials, besides graphite and quartz, mullite was noteworthy for filament material. However, it is difficult to obtain high purity (more than 99.9%) mullite economically. Until now, only graphite has been used with this sheet growth technique. Yet to be solved are such problems as carbon contamination and shaping controllability.

The authors (6) have proposed a mold shaping technique for forming a silicon sheet directly from the melt: the so-called spinning method utilizes the centrifugal force generated by spinning the melt. What distinguishes this process is simplicity, ease of control, and an extremely high formation rate, 4s per sheet has been obtained. The key to controlling sheet formation and impurity contamination is the contact interface between mold material and silicon melt. Thus, it is required that impurity contamination from mold materials be prevented while the solidified sheet is being formed from the liquid phase; furthermore, the solidified sheet should pull off the mold without adhesion.

The subject of the present study is to find mold or coating materials to satisfy these requirements; and to carry out sheet formation using them. In this paper, the reaction of various high melting point materials with silicon is studied. Using studies of wetting behavior of the melt with these high melting point materials and the contact angle observed between them, a possible coating material was found. A process for applying coatings to the mold will be discussed. Using this mold, silicon sheets have been prepared and their material characteristics are studied.

Experimental

The reaction of silicon with various high melting point materials.—Molten silicon reacts with every material. At temperatures over 1412°C, (the melting point of silicon) however, materials can be classified roughly as wetting or nonwetting in relation to silicon. Typical nonwetting materials are quartz and boron nitride (BN). As a result of using quartz as the crucible for Cz pulling, the silicon is free of contamination except for oxygen. As a mold material, however, quartz cracks when it comes in contact with silicon, owing to the difference of volume expansion when the silicon solidified and adhered to the quartz. Bickler *et al.* (7) tried to form silicon sheets using the sheet casting technique with a BN mold. The silicon sheet can be easily removed from a mold, because of the nonadhesive effect at solidification. Despite this advantage, the IR technique has not been put to practical use, because of undesirably heavy boron doping into silicon.

Wettable materials have various contact angles with molten silicon. Ciszek described graphite, SiC, B_4C, and CVD-Si_3N_4 as possible die materials for ribbon pulling because they have low contact angles which are necessary to induce capillary action.

In this study, various experiments have been carried out to observe the reaction between silicon and various high melting point materials. The high melting point compounds were hot-pressed into cylindrical forms, 10 mm diameter and 5 mm length. The compounds had no binder and hot-pressed densities were more than 90% of the theoretical limit. The raw materials for each compound were composed of 200-350 mesh powder. The materials used in this experiment had purity levels of 99.5-99.99%. Each sample was prepared by putting a polysilicon lump on a high melting point substrate which was then put on a quartz plate. This sample was heated in a carbon resistance furnace with an atmosphere of continuously flowing inert gas. Polysilicon started to melt at a furnace temperature of over 1430°C. After melting was confirmed visually, the temperature was held for 5 min before the heat was turned off and the sample allowed to cool. The sample, which now consisted of solidified silicon combined with the material substrate, was partly ground. The contact interface with the previously molten silicon was observed by micrograph.

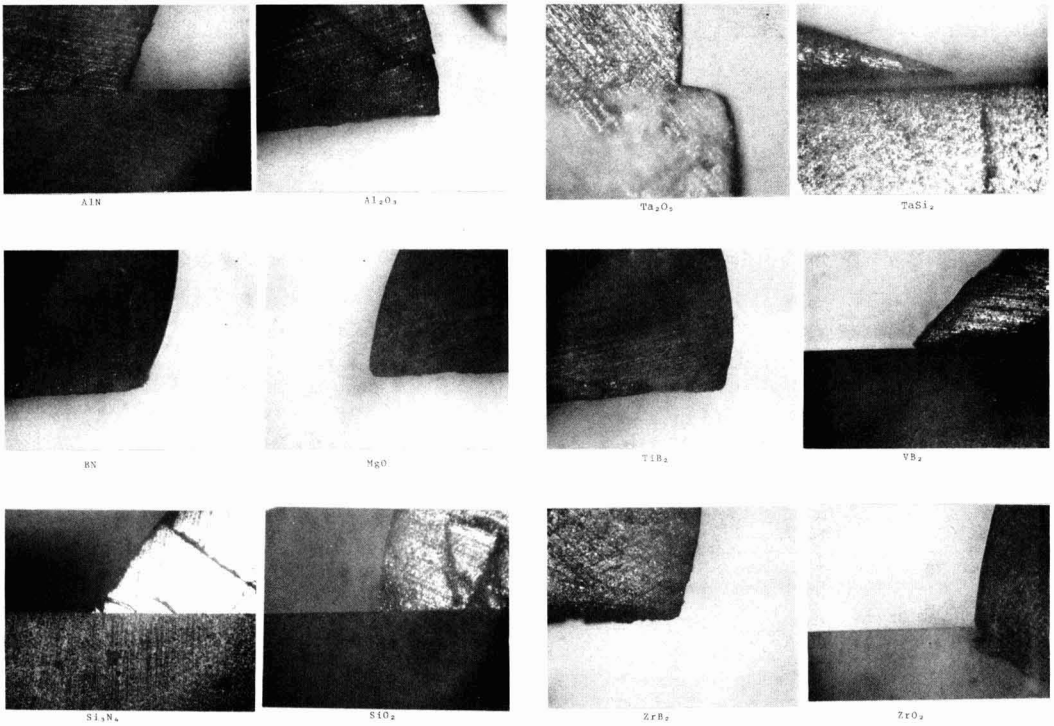


Fig. 1. Close-ups (50×) of one edge of frozen Si on various substrates

Figure 1 shows photomicrographs of various contact areas. The contact angle was observed by measuring the angle between the silicon surface slope and the material substrate.

The contact angle and the reaction between silicon and various high melting point materials are summarized in Table I. In this table, the reaction conditions are categorized as follows: (*i*) silicon and substrate separated from each other without adhesion; (*ii*) wetting was not observed but adhesion occurred; (*iii*) wetted; (*iv*) wetted and permeated; and (*v*) thorough reaction with loss of original shape.

A releasing or mold coating material for melt-solidified silicon, which is a goal in the present study, belongs to either category (*i*) or (*ii*) materials.

In addition, a problem with these materials is the doping effect of the silicon. BN is excellent for releasing, but is unsuitable because of contamination from heavy boron doping in excess of $10^{19}/cm^3$. Similarly, boron compounds such as B_4C and VB_2 produce excessive boron doping, despite their potential as releasing materials.

From the contact angle, reaction condition and doping effect in groups A and B of Table I, only SiO_2 and Si_3N_4 have a great potential, relative to other high melting point materials, as a releasing or a mold coating material for silicon. The simple use of these materials as a coating layer or a mold material is difficult because of the adhesion of melt-solidified silicon. Therefore, a morphological study of the various factors retained by these materials was conducted in the following experiment to formulate a releasing or mold coating material.

Mold coating and shaped crystal growth.—The purpose of the present study is to form a solidified silicon sheet from the melt in a mold without adhesion and contamination. The coating material, acting as a releasing agent, should effectively produce a large contact angle with the silicon melt as well as be nonreactive and physically durable.

In this study, an attempt was made to apply Si_3N_4 and SiO_2 coatings to a mold base. Mold coatings which have a double layer structure, as shown in Fig. 2, were prepared. For the first layer, silicon powder, with an average particle size of 5 μm and a purity level of 99.999%, was deposited with a thickness of 100-150 μm on the surface of a graphite substrate. Two procedures were used for silicon deposition. A spray of silicon powder solution, with either pure water or a natural cellulose inert vehicle, was used. The sprayed substrate was then dried in an oven and baked at 1450°C for 2h in a furnace with nitrogen gas flowing. At this time, a "knife-hard" 100-150 μm thick Si_3N_4 layer was formed on the graphite substrate surface. A nitride ratio of more than 99% of the layer was confirmed by a weight measurement check.

Next, for the second layer, a compound coating layer of Si_3N_4 and SiO_2 was formed on the first Si_3N_4 layer surface. Si_3N_4 powder, the base material in this coating layer, was produced in a quartz crucible by the previously mentioned procedure using silicon powder (5 μm particle size and 99.999% purity). This powder was first mixed into a silanol solution $R_3Si(OH)$ and then sprayed on the surface to a thickness of 200 μm. This was baked in an oxidizing atmosphere at 400°C for 20 min. In this process, a SiO_2 layer was formed which functioned as a coating around

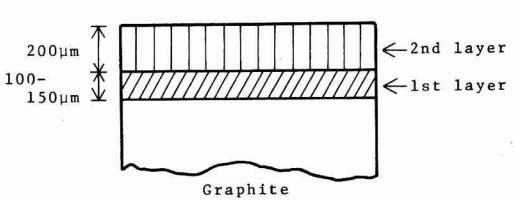


Fig. 2. Double layer structure coated on a graphite substrate. 1st layer: Si powder nitrided to Si_3N_4. 2nd layer: Si_3N_4 powder + SiO_2.

Table I. Reactions between silicon and high melting point material

Material	Melting point °C	Reaction	Contact angle	Material	Melting point °C	Reaction	Contact angle
AlN	2200 ~ 2400	B	117°	SiO_2	1550	B	96.5°
Al_2O_3	2044	B	93°	Ta	2850	C	—
B_4C	1770 ~ 2450	B	101°	TaC	4000	D	—
BN	3000	A	122.5°	TaN	2100 ~ 2500	D	—
BeO	2550	B	—	Ta_2O_5	1880	B	85°
C	3500	E	—	$TaSi_2$	2200	B	20°
CrB_2	2200 ~	C	—	TiB_2	2790	B	109°
Cr_3C_2	1830 ~ 1900	D	—	TiC	3067	D	—
$CrSi_2$	1490	D	—	TiN	2950	C	—
HfC	3950	D	—	TiO_2	1830	D	—
HfN	3310	C	—	$TiSi_2$	1540	C	—
HfO_2	2758 ± 25	C	—	VB_2	2100 ~ 2450	B	45°
$HfSi_2$	1700 ~ 1750	C	—	VC	2700	D	—
LaB_6	2210	B	94°	VN	2050 ~ 2360	E	—
MgO	2825	B	82°	VO_2	1967	D	—
Mo_2B_5	2140 ± 15	D	—	VSi_2	1660 ~ 1700	C	—
Mo_2C	2480 ~ 2522	E	—	W	3382	C	—
$MoSi_2$	1870 ~ 2030	C	—	WB	2800 ~ 2920	C	—
Nb	2740	C	—	WC	2785	D	—
NbC	3870	D	—	WO_3	1473	E	—
NbN	2050 ~ 2300	D	—	WSi_2	2170	C	—
Nb_2O_5	1520	D	—	ZrB_2	3040	B	101°
$NbSi_2$	1950 ~ 2630	C	—	ZrC	3420	D	—
Pt	1774	D	—	ZrN	2980	C	—
SiC	2830	E	—	ZrO_2	2700	C	80°
Si_3N_4	1600 ~ 1900	B	51°	$ZrSi_2$	1520 ~ 1700	C	—

A, silicon and substrate separated from each other without adhesion.
B, wetting was not observed but adhesion occurred.
C, wetted.
D, wetted and permeated.
E, thorough reaction with loss of original shape.

Si_3N_4 particles as well as a link between the layers. SiO_2 layer thickness was not measured, but its existence was confirmed by the x-ray diffraction pattern. The second layer was not as hard as the first layer, but firmly maintained surface integrity.

Using molds treated with the double coating layer, shaped crystals for silicon sheets were grown from the melt directly by utilizing the spinning method (8). In this experiment, semiconductor grade polysilicon was used. Polysilicon was melted in a quartz crucible at 1450°C. The molds, at 1400°C, were spun via a rotating shaft at 400 rpm. Molten silicon was poured into the center of the spinning molds and spread into the mold cavities by centrifugal force. Solidified silicon sheets, having the mold cavity shape, were then formed after a proper cooling time.

Figure 3 shows the mold and an as-formed solidified silicon sheet. The sheets, taken from the mold without adhesion, have a metallic glossy and smooth surface and are 10 × 10 cm square and 0.5 mm thick (the same size as the mold cavity). The prepared mold cavity surface maintained its previous coating condition in the silicon contact area. This clearly demonstrates that repeated use of molds is possible. In fact, in the present experiment, the molds were reused 3-10 times without any particular retreatments. In the cases where fewer possible reuse times were found, problems existed in the coating process for the mold, which resulted in nonuniformity in the coating thickness. It was found that an improvement in the coating process made a long reuse life possible.

Characteristics of shaped silicon sheet.—The characteristics of silicon sheet obtained in the above experiment were measured and the results are shown in Table II. The size and thickness of the sheet is the same as the mold cavity size. Minimum thickness of 0.1 mm was experimentally possible. Although the thickness is not closely controllable after being treated with the coating layers, when using a cavity width that is as narrow as possible, thicknesses of 0.08-0.12 mm were obtained. The surface has an average roughness of 15 μm and a metallic gloss. Crystal structure was polycrystalline and columnar. Average grain size, obtained by measuring grain number per unit area, was approximately 5.3 mm. Using as primary material a nondoped semiconductor grade polysilicon, the silicon sheet exhibited a maximum resistivity of 32 Ω-cm when measured by the microwave noncontact method. It was p-type electrically conductive material as determined by the thermoelectric electromotive force method. Using activation analysis, the impurity contamination of the sheet was found to be as follows: oxygen content—$1.5 \times 10^{17}/cm^3$ (1.7 ppm) and carbon content—$3.9 \times 10^{16}/cm^3$ (0.33 ppm).

Discussion

Although silicon is strongly reactive with other materials, the shaped crystal growth technique is required for large scale uses. In this study, the reaction between silicon and high melting point materials has been investigated. For shaping silicon in molds, large contact angle materials such as A1N, and B_4C, and BN are effective as mold materials. But when considering contamination, it was found that only SiO_2 and Si_3N_4 were suitable materials for investigation. Oxygen was localized as an interstitial in solid silicon (9), and the solubility of nitrogen was less than 2 orders of magnitude smaller than that of either carbon or oxygen (10); thus, these doping effects were relatively controllable.

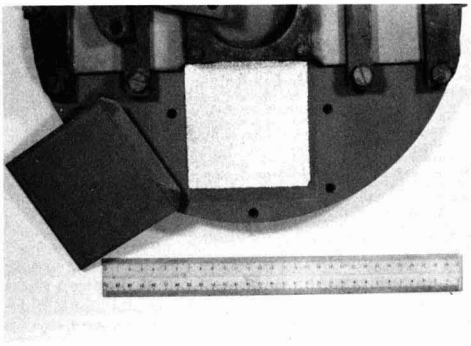


Fig. 3. Mold and as-formed silicon sheet. A rectangular mold shows a surface which was in contact with melt-solidified silicon.

Table II. Characteristics of the sheet obtained in this study

Size	10 cm × 10 cm rectangular
Thickness	0.5 mm
Surface morphology	Metallic glossy and smooth surface
Surface roughness	Average 15 μm
Crystal structure	Polycrystalline columnar structure
Grain size	Average 5.3 mm
Resistivity	32 Ω-cm
Electrical conductive type	p type
Oxygen content	1.7 ppm
Carbon content	0.33 ppm

Using a combination of SiO_2 and Si_3N_4, mold material for silicon melt-solidified crystal growth was made. A double layer was coated on the surface of a graphite base material. The first layer, Si_3N_4, formed by using silicon powder as starting material, performed the following functions: it prevented diffusion from the base material and also acted as a mechanically firm base for the second coating layer. The second layer consisted of an application of Si_3N_4 powder (previously produced by silicon powder nitriding) covered with a thin SiO_2 film; also, the SiO_2 formed a binder between Si_3N_4 particles. The solidification process of the silicon melt in the mold is not known, but it appears that both the contact angle of the melt with the mold surface and the Si_3N_4 particle size in the second layer produce a releasing effect. Silicon has a volume expansion of 9% on solidification. This volume expansion in the mold is alleviated in all directions: an increase of surface direction is accommodated by the tapered edges of the mold cavity, and an increase in thickness (perpendicular direction to the surface) by the elasticity of the second coating layer.

The present study has been carried out to obtain silicon sheets for solar cells. Grain size, sheet size, and impurity properties obtained are sufficient for this application. Solar cell efficiencies more than 11% AM 1.5 have been achieved. Furthermore, the high growth rate for shaped sheets, which was obtained by the use of this mold coating, could contribute to cost reductions within the solar cell industry. The advantages of obtaining a 0.1 mm thick silicon sheet, shaped to a specific mold size with a high growth rate, could bring about large scale applications of shaped silicon crystals, such as a polycrystalline layer on a monocrystal wafer. Further studies on the solidification process of the silicon melt as it occurs in the coated mold are required in order to expand the application possibilities.

Manuscript submitted June 17, 1985; revised manuscript received Oct. 21, 1985.

Hoxan Corporation assisted in meeting the publication costs of this article.

REFERENCES

1. B. Authier, *Adv. Solid State Phys.*, **18,** 1 (1978).
2. T. Saito, A. Shimura, and S. Ichikawa, in "Proceedings of the 15th Photovoltaic Specialists Conference," p. 576, Institute of Electrical and Electronics Engineers (1981).
3. K. V. Ravi, *J. Cryst. Growth*, **39,** 1 (1977).
4. T. F. Ciszek, J. L. Hurd, and M. Schietzelt, *This Journal*, **129,** 2838 (1982).
5. T. F. Ciszek, "Crystals 5-Silicon," p. 190, Springer-Verlag, New York-Heidelberg (1981).
6. Y. Maeda, T. Yokoyama, and I. Hide, *IEEE Trans. Electron Devices*, **ed-31,** 708 (1984).
7. D. B. Bickler, L. E. Sanchez, and W. J. Sampson, in "Proceedings of the 14th Photovoltaic Specialists Conference," p. 36, Institute of Electrical and Electronics Engineers (1980).
8. Y. Maede, T. Yokoyama, and I. Hide, *J. Cryst. Growth*, **65,** 331 (1983).
9. F. A. Johnson, *Proc. Phys. Soc.*, **73,** 265 (1959).
10. T. Nozaki, Y. Yatsurugi, N. Akiyama, Y. Endo, and Y. Makide, *J. Radio Anal. Chem.*, **19,** 109 (1974).

Technical Notes

Evaluations of Plasma Silicon-Oxide Film (P-SiO) by Infrared Absorption

A. Takamatsu, M. Shibata, M. Ishida, H. Sakai, and T. Yoshimi

Hitachi Limited, Musashi Works, Hitachi Microcomputer Engineering Limited, 1450 Josuihon-cho, Kodaira-shi, Tokyo, 187 Japan

As LSI systems shrink and become more densely integrated, LSI insulating films are becoming more important and are required to be of better quality and reliability.

Recently, a plasma-activated silicon-oxide film (P-SiO) (1-3) has been developed and used either as a final passivation or as a multilayer interconnect in VLSI devices.

However, the properties of insulating films deposited by plasma-CVD (chemical vapor deposition) are strongly affected by the various plasma conditions in the reactor. The properties of the plasma change with such parameters as the reactor geometry, RF power, RF frequency, and deposition pressure, making it difficult to optimize the deposition conditions to give best film quality. The deposition of P-SiO films is usually optimized by measuring the chemical etch rate, refractive index, film stress, and film density. However, these properties do not always furnish data suitable for evaluating the moisture resistance of passivation films, a property which directly affects the reliability of LSI devices incorporating such films. Thus, a better method of evaluating the quality of P-SiO films, especially their moisture resistance, is required.

The work described in this paper, a new evaluating method of P-SiO films by infrared absorption measurements (4, 5) in connection with pressure-cooker testing (PCT) was developed. The method was then used to determine the best deposition conditions for producing highly moisture-resistant films.

Experiments

P-SiO films were deposited in a plasma-activated reaction system with a lateral quartz tube. To obtain film of

uniform thickness, silicon wafers were set on the center of a susceptor boat constructed of graphite plates. The reaction gases used were SiH_4 and N_2O. In all experiments, the N_2O:SiH_4 ratio, RF frequency, and deposition temperature were kept constant at 28, 450 kHz, and 400°C, respectively. The silicon wafers on which P-SiO films were deposited had a resistivity of more than 1 Ω-cm and a diameter of 100 mm.

After the P-SiO deposition, the backs of the samples were etched with silicon etchant ($HF/HNO_3/CH_3COOH$) to clean them and to eliminate infrared scattering during the measurements.

Initial infrared spectra of 0.5-μm thick P-SiO films were then taken using a Hitachi EPI-G2 spectrophotometer. The samples were then pressure-cooker tested to check the moisture resistance of films, by treating them with steam at 2 atm and 121°C. The samples were then removed from the cooker and the infrared spectra were measured again. The PCT and infrared absorption measurements were repeated until the PCT time reached 500h.

Results

The dependence of the infrared spectra of P-SiO on the RF power density is shown in Fig. 1.

The infrared spectra of SiO_2 films are known to show a 1000-1100 cm^{-1} band, a 810 cm^{-1} band, and a 450 cm^{-1} band originating from the Si-O bond, plus 3650 cm^{-1}, 3330 cm^{-1}, and 880 cm^{-1} bands originating from Si-OH, H_2O, and Si-H (Si_2O_3) (2, 4) respectively.

The infrared spectra of the P-SiO deposited under a low power density of 60W showed 3650 and 3330 cm^{-1} bands whose absorbance decreased, thus increasing RF power density. As the RF power density increased, the wave number of the Si-O stretching band increased from 1060 to 1080 cm^{-1}, approaching that of thermally grown silicon

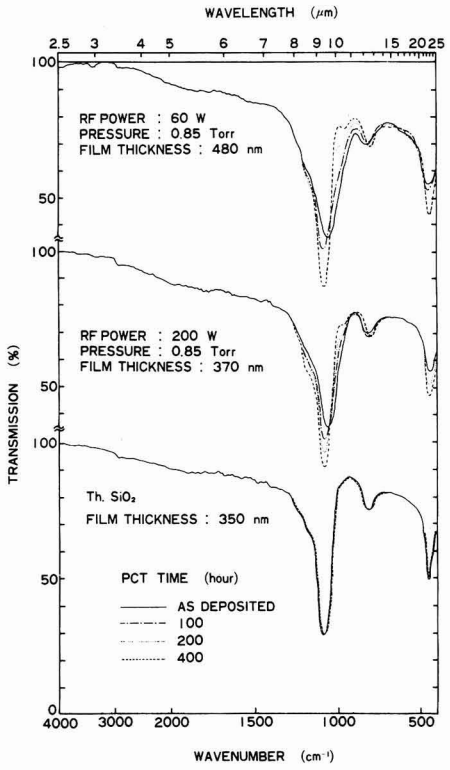


Fig. 1. Dependence of infrared spectra of P-SiO on RF power density

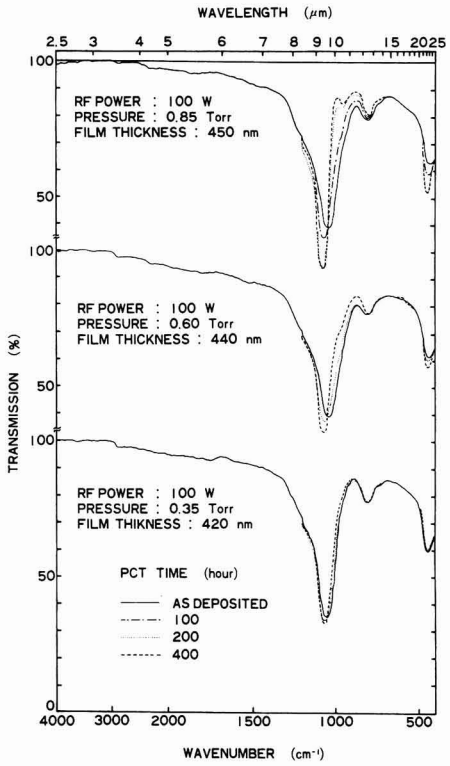


Fig. 2. Dependence of infrared spectra of P-SiO on deposition pressure.

oxide, which has a 1090 cm^{-1} absorption band. In addition, the absorbance of the Si-O bands increased and the

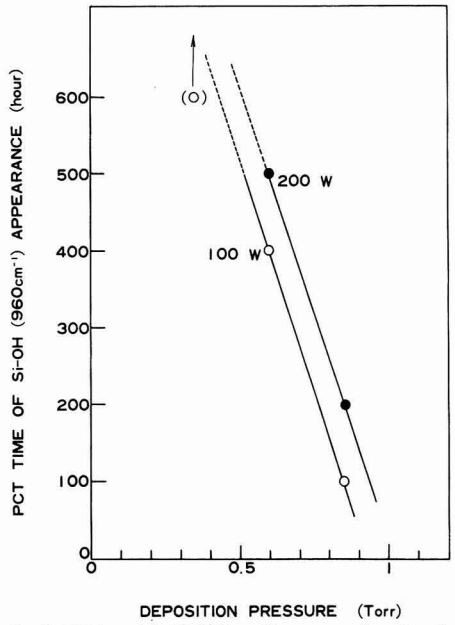


Fig. 3. PCT time of Si-OH (960 cm^{-1}) appearance ($t_{Si\text{-}OH}$) vs. deposition pressure with RF power density as parameter.

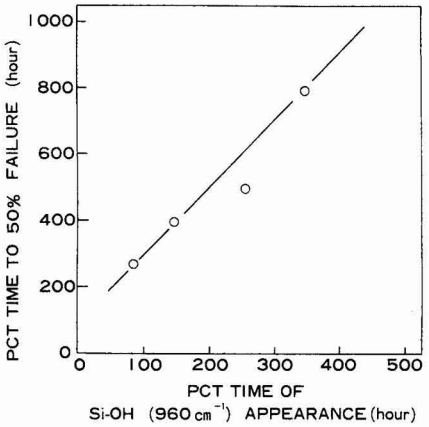


Fig. 4. PCT time to 50% failure vs. PCT time of Si-OH (960 cm^{-1}) appearance ($t_{Si\text{-}OH}$).

half-bandwidths of the Si-O bands (1080, 810, and 450 cm^{-1}) decreased.

The dependence of the infrared spectra of the P-SiO on the deposition pressure is shown in Fig. 2. There was no significant difference among P-SiO films at pressures of 0.35-0.85 torr.

Typical changes in the infrared spectra of the P-SiO after pressure-cooker testing are shown in Fig. 1 and 2. At a PCT time of 100h, the infrared spectra of the P-SiO at low power density (60W) and high deposition pressure (0.85 torr) are different from those of as-deposited films, suggesting that the P-SiO deposited at low RF power density and high deposition pressure absorbs H_2O easily during PCT. However, the P-SiO deposited at high power density (200W) showed a slight change in the Si-O bands, while the P-SiO deposited at low deposition pressure (0.35 torr) showed no change in the Si-O bands.

P-SiO absorbs moisture by the following mechanism: first, the wave number of the Si-O stretching band increases, accompanied by an increase in the absorbance and a decrease in the half-bandwidth. At the same time, the 810 and 450 cm^{-1} bands gradually increase in absorbance and decrease in half-bandwidth. Second, a 960 cm^{-1} band, assumed to come from Si-OH (2, 4), appears and increases with the PCT time. Third, the changes in the Si-O bands saturate when their configuration comes to resemble that of thermally grown silicon oxide. The absorbance of the 960 cm^{-1} bands also saturates at this stage. During all of these stages, hardly any increases in the 3650 and 3330 cm^{-1} bands are observed. Thermally grown silicon oxide treated in the same way, as a reference, showed no change in its infrared spectra after 500h PCT.

The P-SiO deposited at high power density and low deposition pressure showed the most stable film properties with the least change in the Si-O bands after PCT, while at low RF power density or high deposition pressure, the P-SiO was unstable. These post-PCT phenomena are assumed to be due to porosity and lack of oxygen in the P-SiO. Under the PCT conditions, water molecules entering the P-SiO cause the formation Si-OH bonds and an increase in the number of Si-O bonds (6). Thus, the absorbance of the Si-O bands increases and a Si-OH band appears. P-SiO with stable infrared spectra before and after PCT is expected to be more reliable, since it consists of dense, stoichiometric SiO_2.

Table I. Properties of P-SiO.

Measurement \ Film	P-SiO	CVD SiO_2	Th. SiO_2
RF power desity (W)	200	—	—
Pressure (Torr)	0.6	760	—
Temperature (℃)	400	400	1000
Gas ratio	N_2O/SiH_4 28	O_2/SiH_4 14	Wet O_2
BHF-etch rate (nm/min)	200	450	120
P-etch rate (Å/sec)	6	20	2
Refractive index	1.47	1.44	1.46
Stress (dynes/cm^2)	-2.8×10^9	$+2.8\times10^9$	-3×10^9
Density (g/cm^3)	2.30	2.17	2.23

The PCT time at which the Si-OH (960 cm^{-1}) band appeared ($t_{Si\text{-}OH}$) was used as a further measure of the film quality. This was defined as the time when the absorbance of the 960 cm^{-1} band reached 0.02/μm, and is shown as a function of deposition pressure for two different RF power densities in Fig. 3. As the deposition pressure decreases, $t_{Si\text{-}OH}$ increases linearly. At a constant deposition pressure, $t_{Si\text{-}OH}$ is larger for the P-SiO deposited at the higher RF power density.

The above results show that the PCT time of Si-OH appearance corresponds to the amount of Si-O band change in the P-SiO after PCT.

The reliability of the P-SiO was investigated by fabricating LSI's with 1.5 μm thick P-SiO as the final passivation film. The PCT time to 50% failure in 64K bit DRAM test patterns *vs.* the PCT time of Si-OH appearance is shown in Fig. 4. It is clear that the PCT time of Si-OH appearance corresponds to the reliability of the silicon devices and that deterioration of the P-SiO causes the devices to fail.

Other properties of the P-SiO films, such as their refractive index, density, and chemical etch rate, are given in Table I. The values match those of thermally grown silicon oxide and are superior to those of CVD SiO_2.

In conclusion, infrared absorption measurements combined with PCT can effectively optimize the deposition conditions for the P-SiO. A high RF power density and low deposition pressure give the P-SiO with the best moisture resistance.

Manuscript submitted May 14, 1984; revised manuscript received *ca.* Oct. 1, 1985.

Hitachi, Limited assisted in meeting the publication costs of this article.

REFERENCES

1. J. R. Hollahan, *This Journal*, **126**, 930 (1981).
2. A. C. Adams, F. B. Alexander, C. D. Capio, and T. E. Smith, *ibid.*, **128**, 1545 (1981).
3. A. Takamatsu, M. Shibata, H. Sakai, and T. Yoshimi, *ibid.*, **131**, 1865 (1984).
4. W. A. Pliskin, *J. Vac. Sci. Technol.*, **14**, 1064 (1977).
5. N. Nagashima, H. Suzuki, K. Tanaka, and S. Nishida, *This Journal*, **121**, 434 (1974).
6. W. Noll, in "Chemistry and Technology of Silicones," p. 589, Academic Press, New York and London (1978).

Thermal Oxidation of Undoped LPCVD Polycrystalline-Silicon Films

C. Y. Lu and N. S. Tsai

AT&T Bell Laboratories, Reading, Pennsylvania 19603-0856

The thermal oxidation of polycrystalline-silicon (polysilicon) films is technologically important because of the widespread use of these films in integrated-circuit fabrication. Polysilicon films are often oxidized directly after a phosphorus predeposition or arsenic implantation without a subsequent drive-in diffusion. Thus, the dopant concentration is not uniform throughout the thickness of the polysilicon layer, making the analysis of the oxidation behavior fairly complicated (1, 2). Most work has been concentrated on the issue of doping-enhanced oxidation of polysilicon films (1-6), and only a few papers reported the oxidation data on undoped polysilicon films (3, 4, 7). However, these early data were either obtained from atmospheric pressure chemical vapor deposited (APCVD) polysilicon films (7), or for a limited temperature range (700°-850°C) in only wet oxygen (3), or for a specific oxidation time (4). In addition to its own merit as a fundamental interesting problem, the oxidation rate of undoped low pressure chemical vapor deposited (LPCVD) polysilicons films is important for integrated-circuit processing designs in some specific applications. In this work, we report the oxidation data for LPCVD polysilicon films prepared at 630° and 575°C; both wet and dry oxidations were done from 20 min to 4h, and from 1h to 6h, respectively.

Experimental

Polysilicon films of 6500Å thickness were deposited onto thermally oxidized silicon wafers by LPCVD at 630° and 575°C. The polysilicon layer thicknesses were measured by Nanospec interferometer and stylus surface profilometer, and were confirmed by transmission electron microscope (TEM) observations. It was known that as-deposited films at 575°C were amorphous silicon (α-Si) or microcrystalline silicon with very small crystallites (8). The samples were then divided into three groups: (*i*) 630°C LPCVD polysilicon films; (*ii*) 575°C LPCVD amorphous silicon films which received a preoxidation N_2 annealing at 1100°C for 30 min to convert them into polysilicon films (8); (*iii*) 575°C LPCVD α-Si films without preannealing, but in which recrystallization should occur while the films were oxidized. Although the low temperature (575°C) deposited polysilicon (later referred to as α-poly) may have control problems due to recrystallization during post-deposition heat-treatments (9), it may be a potential candidate for critical IC applications because of its high quality in terms of structural perfection and surface roughness (8).

The oxidation process in this work included the usual ramping procedures, that is, it started at 850°C with a ramping rate of 10°C/min up and 3°C/min down. All the oxidation thicknesses were measured by a stylus surface profilometer on more than five spots over 4-in. wafers. A Nanospec interferometer could not give reasonable measurement results for oxidized films because of the multilayer structures and the unknown refractive indexes of polysilicon oxide and α-poly oxide.

Results and Discussion

Figure 1 shows the oxidation thickness of polysilicon (630°C), α-poly (575°C) without preannealing treatment, and α-poly (575°C) with 1100°C N_2 preannealing at 900° and 1050°C in wet oxygen. Results for single-crystal Si with orientation <100> and <111> were also plotted in Fig. 1 for comparison. Figure 2 shows the corresponding data for dry oxidation.

An approximate relation $d_{ox} \simeq Kt^n$ has been shown by Sunami (3) to model the oxidation of polysilicon films, where K and n are empirical constants used for curve

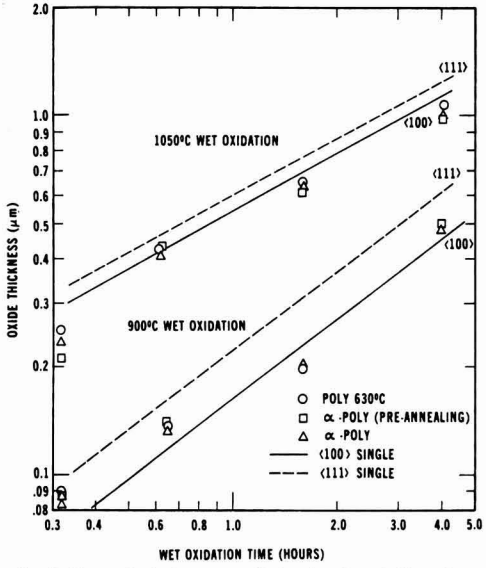


Fig. 1. Wet oxide thickness vs. oxidation time for polysilicon deposited at 630°C, α-poly (575°C) with and without pre-annealing, and single-crystal silicon.

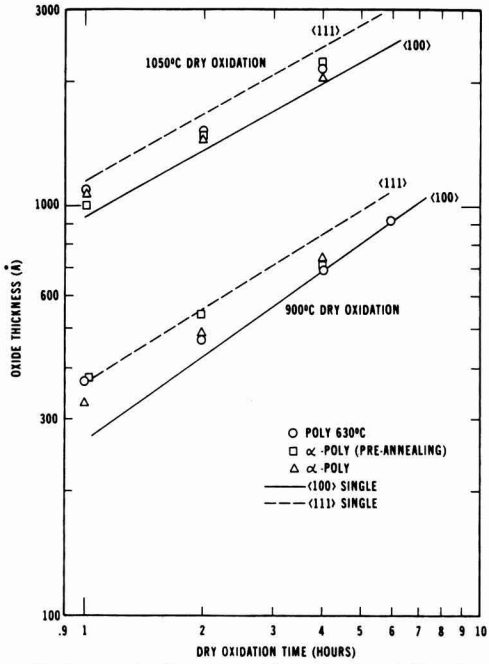


Fig. 2. Dry oxide thickness vs. oxidation time for polysilicon deposited at 630°C, α-poly (575°C) with and without pre-annealing, and single-crystal silicon.

fitting. For undoped single-crystal silicon, n is always between 1.0 (linear oxidation region) and 0.5 (parabolic oxidation). It is evident in Fig. 1 and 2 that the slope of d_{ox} *vs.* t curves for both 630° and 575° polysilicons is slightly less than that for single-crystal silicon. Similar lower values of n have been observed in the data of Barnes *et al.* (5), and Saraswat *et al.* (1), for heavily P- and As-doped polysilicon films. There were no significant differences within measurement error among the three different kinds of polysilicon films. Because the oxidation rates of undoped polysilicon films were smaller than that of (111) silicon and greater than that of (100) silicon (except 1050°C, wet oxidation), the orientation effect of polysilicon crystallites must play a more dominate role than the effect of grain-boundary enhanced oxidation. This is quite different from the thermal oxidation of heavily doped polysilicon films in which dopant segregation at the grain boundaries plays a major role in the oxidation process (1). In n-type doped polysilicon, the dopant concentration in the grain boundaries can be in excess of 10^{22} cm^{-3}. It was speculated by Saraswat and Singh (1) that a large fraction of this dopant segregates into the oxide, resulting in an increase in the parabolic rate constant and, therefore, in an increased oxidation rate. In order to understand the relationship between the grain-boundary enhanced oxidation with dopant segregation, a systematic study should be done on the oxidation rate of boron-doped polysilicon films, which has no dopant segregation at the grain boundaries. To the authors' knowledge, no such experiment has been reported.

Summary

In summary, the thermal oxidation kinetics of undoped LPCVD polysilicon films, deposited at 630° or 575°C (α-poly) and oxidized in dry and wet oxygen have been studied. It was found that oxide thickness grown on undoped polysilicon films were in general smaller than that for (111) but larger than that for (100) single-crystal silicon. Similar oxidation behavior was reported for dry oxidation of APCVD polysilicon films (7), and wet oxidation at low temperatures (700°-850°C) (3). The slope of the polysilicon oxidation curve (d_{ox} *vs.* time) is only slightly less than that of single-crystal silicon. No significant differences between the oxidation behavior of as-deposited polysilicon (630°C) and recrystallized polysilicon (575°C, α-poly) were observed.

Acknowledgments

The authors would like to thank G. Jones, D. Bingaman of AT&T Technology System for helping to prepare LPCVD polysilicon films, and the staff in the Models Laboratory for sample oxidation and measurements. We, also, would like to thank C. A. Goodwin for discussions with us and T. T. Sheng for TEM analysis.

Manuscript submitted July 22, 1985; revised manuscript received Nov. 5, 1985.

AT&T Bell Laboratories assisted in meeting the publication costs of this article.

REFERENCES

1. K. C. Saraswat and H. Singh, *This Journal*, **129**, 2321 (1982).
2. E. Kinsbron, S. P. Murarka, T. T. Sheng, and W. T. Lynch, *ibid.*, **130**, 1555 (1983).
3. H. Sunami, *ibid.*, **125**, 892 (1978).
4. T. I. Kamins, *ibid.*, **126**, 838 (1979).
5. J. J. Barnes, J. M. DeBlasi, and B. E. Deal, *ibid.*, **126**, 1779 (1979).
6. L. Baldi, C. Ferla, and M. Toshi, Abstract 168, p. 441, The Electrochemical Society Extended Abstracts, Vol. 80-1, St. Louis, MO, May 11-16, 1980.
7. T. I. Kamins and E. L. MacKenna, *Metall. Trans.*, **2**, 2292 (1971).
8. G. Harbeke, L. Krausbauer, E. F. Steigmeier, A. E. Weidner, H. F. Kappert, and G. Neugebaur, *This Journal*, **131**, 675 (1984).
9. T. I. Kamins, *ibid.*, **127**, 686 (1980).

Rapid Isothermal Annealing of Sputtered Phosphorus-Doped Silicon Films

T. Serikawa and A. Okamoto

Nippon Telegraph and Telephone Corporation, Musashino Electrical Communication Laboratory, 3-9-11, Midoricho, Musashino-shi, Tokyo, 180 Japan

Phosphorus-doped polycrystalline silicon (polysilicon) films have played a major role in the astronomical success of the metal-oxide-semiconductor field effect transistor (MOSFET). Phosphorus is introduced in films *in situ* during deposition and by external doping after deposition, for example, via ion implantation. The films are usually annealed in a furnace at a high temperature near 1000°C for 10 min. This annealing reduces film resistivity to values that make polysilicon films useful as conductors. Recent advanced MOSFET's, however, very much require a low temperature process of short duration, because it is necessary to precisely control dopant profiles of arsenic, boron, and phosphorus introduced in the silicon substrate. For this requirement, several researchers have developed large area incoherent energy sources which perform rapid isothermal annealing (RIA) (1-7). In RIA, the entire wafer is heated to 900°C or higher for times on the order of 10s.

Silicon films have usually been deposited by chemical vapor deposition (CVD). The films are also prepared by sputtering at a substrate temperature lower than that for CVD. Moreover, the silicon films may easily be phosphorus-doped *in situ* during deposition by generating phosphorus vapor in a sputtering chamber (8). The films are annealed for application to electrodes and conductors in MOSFET's in a similar manner to those of CVD silicon films. This note therefore presents data obtained by rapid isothermal annealing of sputtered phosphorus-doped silicon films.

Experimental

Silicon films, 500 nm thick, were deposited on 1 μm thick oxidized, 4 in. diam silicon wafers. This was accomplished by the RF planar magnetron sputtering of 99.9995% pure silicon target in argon-phosphorus vapor mixtures (8). Phosphorus vapor was generated by heating solid red phosphorus in a crucible mounted in the sputtering chamber. The films contained phosphorus with a concentration of about 6×10^{20} cm^{-3}. The details of deposition conditions are listed in Table I.

The sputtered phosphorus-doped silicon films were rapidly isothermal annealed by high intensity quartz

Table I. Conditions of sputter-deposition

Sputtering power	: 3.0 kW
Sputtering gas pressure	: 2.0 Pa
Crucible temperature	: 360°C
Deposition rate	: 120 nm/min
Substrate temperature	: <100°C
Background pressure	: $<1.0 \times 10^{-5}$ Pa

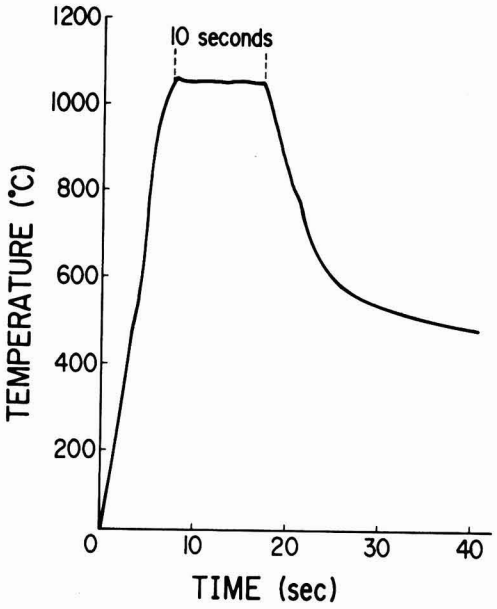


Fig. 1. Temperature-time profile for a 10s at 1050°C

tungsten lamps, that were enclosed by water-cooled reflective walls (4). A typical temperature-time profile is shown in Fig. 1 for nominal 1050°C, 10s annealing. The temperature was measured by a Chromel-Alumel thermocouple. The wafers in these experiments were annealed at set-point temperatures which ranged from 680° to 1100°C for 10s. For comparison, some wafers were annealed at 1100°C for 20 min in a conventional furnace.

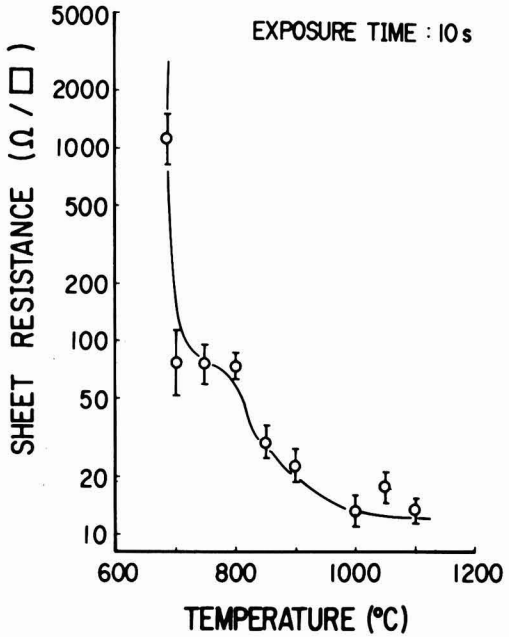


Fig. 2. Sheet resistance vs. annealing temperature for 10s exposure in nitrogen atmosphere.

The wafers were analyzed subsequent to annealing using a sheet resistance measurement and the x-ray diffraction technique. Sheet resistance was measured by the four-point technique. Film composition profiles were measured by Auger electron spectroscopy (AES) (9). Auger data were collected using the electron gun of 3.0 keV energy and 2.8×10^{-7}A beam current. The Auger phosphorus peak at 120 eV, silicon peak at 91 eV, and oxygen peak at 511 eV were monitored for depth profiles. The ion beam used for sputter etching was argon ion at 2.25 keV.

Results and Discussion

Figure 2 plots the sheet resistance relative to annealing temperature for 10s intervals. At temperatures below 600°C, the sheet resistance decrease is small. Therefore, in the figure, data ranging from 680° to 1100°C in annealing temperature will be described. Annealing at temperatures higher than 700°C drastically decreases sheet resistance. Moreover, annealing at 1000°C brings it down to 15 Ω/□, whose value is applicable to electrodes and conductors in MOSFET's (11). However, annealing temperature beyond 1000°C has a small influence on sheet resistance.

Phosphorus concentration profiles of as-deposited and rapid isothermal annealed films are shown in Fig. 3a and 3b. These profiles are compared with those of conventional furnace annealed films at 1100°C for 20 min (Fig. 3c). The phosphorus concentration was calculated using AES spectrum peak height. The as-deposited film of Fig. 3a indicates a uniform phosphorus concentration profile, which remains in spite of both annealings of Fig. 3b and 3c. This is due to the fact that the loss of phosphorus from doped silicon film by out-diffusion is small. This fact differs from those cases in which highly phosphorus-doped single-crystal silicon substrate and CVD polysilicon films are either rapid isothermal annealed or furnace annealed (3, 5, 6, 10). The silicon film annealed in the furnace was oxidized to a thickness of 45.5 nm as indicated in Fig. 3c. Moreover, phosphorus was not detected in the oxidized layer by AES. On the other hand, the rapid isothermal annealed silicon film (Fig. 3b) indicates the presence of a very thin oxidized layer.

X-ray diffractometry was done on the 1100°C, RIA, and furnace annealed silicon films. The resultant spectra are shown in Fig. 4. Examination of these spectra shows that both annealed films exhibit (111), (220), (311), and (200) reflections of polysilicon films. The furnace annealed film shows an x-ray spectrum quite similar to that of RIA. Grain sizes were calculated from the (111) reflection peak in the x-ray spectra for RIA and furnace annealing. The RIA and furnace annealed films have a small grain size of about 60 nm, in spite of high annealing temperature of 1100°C.

The as-deposited, phosphorus-doped silicon films are amorphous. The films were crystallized at 700°C of RIA annealing temperature, resulting in drastically decreasing sheet resistance (12). Argon atoms are contained in the silicon films during sputter-deposition. The grain size of the silicon films containing argon atoms is small even after high temperature annealing (13). Consequently, any increase in annealing temperature beyond 1000°C does not substantially decrease the sheet resistance, as shown in Fig. 2.

Conclusion

In situ phosphorus-doped silicon films, 500 nm thick, were deposited by the RF planar magnetron sputtering in phosphorus vapor at a low substrate temperature. RIA at a temperature range of 680°-1100°C for 10s was carried out on the phosphorus-doped silicon films. Annealing at temperatures higher than 700°C drastically brought sheet resistance down to 15 Ω/□. The film grain size was small and about 600 nm after 1100°C temperature annealing. Moreover, it was found that a uniform phosphorus concentration profile was maintained following RIA.

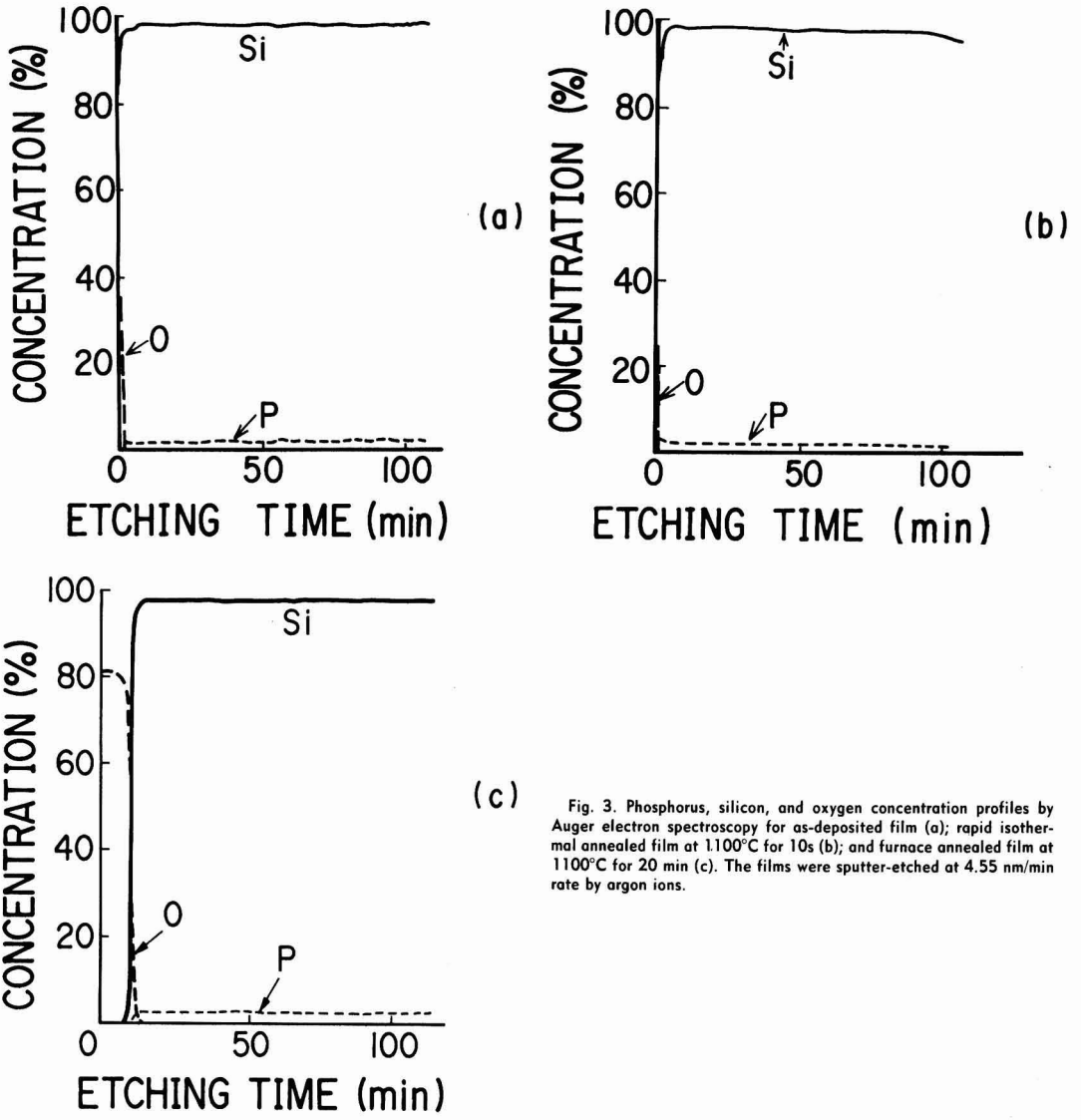


Fig. 3. Phosphorus, silicon, and oxygen concentration profiles by Auger electron spectroscopy for as-deposited film (a); rapid isothermal annealed film at 1100°C for 10s (b); and furnace annealed film at 1100°C for 20 min (c). The films were sputter-etched at 4.55 nm/min rate by argon ions.

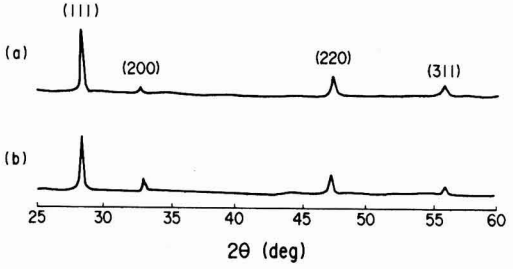


Fig. 4. X-ray spectra of rapid isothermal annealed film at 1100°C for 10s (a); and furnace annealed at 1100°C for 20 min (b).

Acknowledgments

The authors wish to express their sincerest thanks to Akiteru Ishimoto for his valuable suggestions and encouragement.

Manuscript submitted Jan. 14, 1985; revised manuscript received Aug. 27, 1985.

Nippon Telegraph and Telephone Corporation assisted in meeting the publication costs of this article.

REFERENCES

1. A. Gat, *IEEE Electron. Device Lett.*, **EDL-2,** 85 (1981).
2. R. A. Powell, R. Chow, C. Thidandam, R. T. Fucks, I. A. Bleck, and J. D. T. Pan, *ibid.*, **EDL-4,** 380 (1983).
3. K. Takebayashi, T. Yokoyama, M. Yoshida, and M. Inoue, *This Journal,* **130,** 2271 (1983).
4. T. Yachi, *IEEE Electron. Device Lett.*, **EDL-5,** 217 (1984).
5. S. R. Wilson, W. M. Paulson, and R. B. Gregory, *J. Appl. Phys.*, **55,** 4162 (1984).
6. T. O. Sedgwick, F. M. d'Heurle, and S. A. Cohen, *This Journal,* **131,** 2446 (1984).
7. S. J. Krause, S. R. Wilson, W. M. Paulson, and R. B. Gregory, *Appl. Phys. Lett.*, **45,** 778 (1984).
8. T. Serikawa and A. Okamoto, *J. Vac. Sci. Technol. A,*

1788 (1985).
9. O. K. T. Wu and A. N. Saxena, *This Journal*, **132**, 932 (1985).
10. S. P. Murarka, *J. Appl. Phys.*, **56**, 2225 (1984).
11. T. I. Kamins, *This Journal*, **126**, 833 (1979).
12. J. Kato and S. Iwamatsu, *ibid.*, **131**, 1145 (1984).
13. A. Bhattacharyya and K. N. Ritz, *ibid.*, **131**, 2143 (1984).

Temperature Response of GaAs in a Rapid Thermal Annealing System

T. R. Block, C. W. Farley,* and B. G. Streetman*

Microelectronics Research Center, Department of Electrical and Computer Engineering, The University of Texas, Austin, Texas 78712

Rapid thermal annealing (RTA) systems are used to heat semiconductors for short periods of time, usually seconds. This technique has a variety of applications in the processing of Si and III-V compound semiconductors (1). In an RTA system which uses radiant energy to heat the semiconductors, one might expect to find variations in the temperature response of materials due to their different absorption properties. An investigation of GaAs and Si shows that this is indeed the case, and that the temperature variation is quite pronounced.

Experimental

The RTA system used in these experiments is similar to that described by Davies and Kennedy (2), and consists of a heating chamber containing two elliptically shaped cavities which focus light produced by two 2 kW tungsten filament quartz lamps onto a sample suspended at the center of the chamber. A microprocessor controls power to the lamps with a thermocouple for temperature feedback. Samples are suspended on very thin (~250 μm thick) silica slides inside a silica tube which allows annealing in a selected gas ambient.

Semi-insulating (100) GaAs doped with Cr, p-type (100) GaAs doped with 7×10^{17} cm^{-3} Zn, and n-type (100) Si doped with 4×10^{15} P were cut into samples ~8 mm × 8 mm. Holes were etched into the GaAs using a 20% bromine-methanol etch and a mask of CVD deposited SiO_2, and into the Si using a solution of pyrocatechol, ethylene diamine, and water (3). 200 nm of CVD SiO_2 containing 7% P was then deposited on each sample. K-type thermocouples (0.002 in. diam wire) were glued into the holes with a mixture of Aremco no. 516 cement (ZrO) and either ground GaAs or Si using a procedure similar to that suggested by Cohen *et al.* (4). Such small thermocouples were used to insure that the temperature response of the samples would be little affected by the thermocouples.

Throughout the experiments, the GaAs samples were either thermally isolated from each other or placed on a larger piece of silicon to thermally connect them, as shown in Fig. 1. Temperature feedback to the controller was provided by the Si sample. These two configurations were then submitted to a heat cycle consisting of a preheat at 300°C for 30s to stabilize initial conditions, then an instantaneous change of setpoint to 750°C, a hold at this temperature for 30s (counted after the sample is within 30°C of 750°C), and then a change of the setpoint back to zero. The heat cycling was done in a stagnant N_2 atmosphere.

Results and Discussion

Temperature response curves for the thermally isolated samples are shown in Fig. 2. Curve (a) is the programmed setpoint and curve (b) is the thermocouple output of the Si sample. The Zn doped and semi-insulating GaAs samples are shown as curve (c) and (d), respectively.

Clearly, GaAs couples to the radiant flux differently than Si, exhibiting a drastically different temperature response. Comparison of doped *vs.* semi-insulating GaAs in Fig. 2 shows the tremendous effect of free carrier concentration on the temperature response, an effect also found in silicon by Seidel *et al.* (5). However this is not enough to explain the data completely. At 750°C the free carrier concentration of Si is greater than that of the doped GaAs, yet GaAs is at a higher temperature. This effect must be due to basic differences in the bulk material properties, for example direct *vs.* indirect bandgap, size of

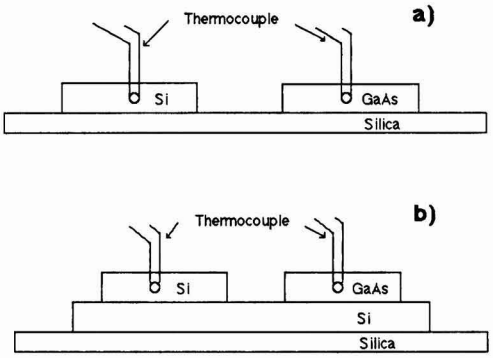


Fig. 1. Schematic diagram of sample configuration for (a) thermally isolated and (b) thermally connected cases.

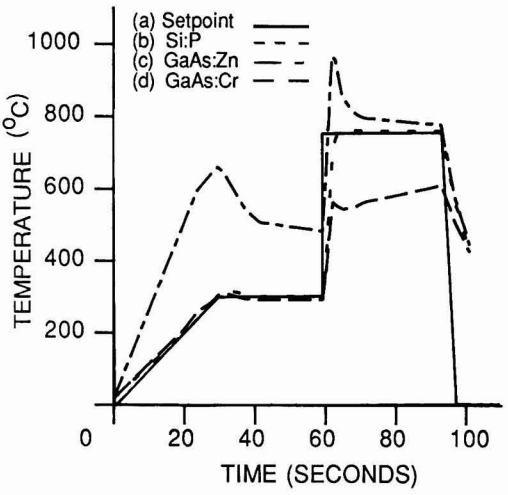


Fig. 2. Temperature response curve for thermally isolated samples: (a) temperature setpoint, (b) P doped Si, (c) Zn doped GaAs, and (d) Cr doped GaAs.

*Electrochemical Society Active Member.

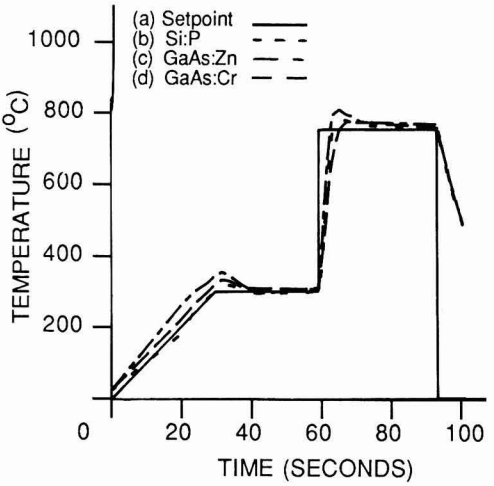


Fig. 3. Temperature response curve for thermally connected samples: (a) temperature setpoint, (b) P doped Si, (c) Zn doped GaAs, and (d) Cr doped GaAs.

bandgap, optical absorption parameters, and thermal conductivity. Theoretical work by Borisenko *et al.* (6) predicts different heating rates for materials with different emissivities. Another factor may be a shift in the frequency distribution of the tungsten lamps' output at different power levels (due to blackbody radiation at different temperatures). As the lamp power is cut back to hold the sample at temperature, the light shifts to longer wavelengths, which may affect the relative amounts of band-to-band *vs.* free carrier excitation.

Results for the thermally connected samples are shown in Fig. 3. Curves (a) and (b) are again the programmed setpoint and the Si sample response, (c) and (d) the Zn doped and semi-insulating GaAs samples.

When the materials are put in thermal contact, their temperature behavior becomes similar. The significant temperature overshoot of setpoint is due to thermal lags in the control loop from the configuration in Fig. 1b. In actual anneals, the large piece of Si pictured in Fig. 1b would contain the thermocouple. In such a setup, we have observed negligible temperature overshoot and the temperature difference between GaAs and Si is usually less than 15°C at 750°C. It should be noted that this annealing arrangement requires good thermal contact of the sample to the large Si susceptor. We also found the temperature response to be sensitive to gas flow in the system. A high flow rate resulted in a GaAs temperature 50°C higher than the temperature of the Si susceptor at 750°C. The source of this phenomenon is not clear; the anneals were therefore performed in a stagnant atmosphere.

These results point to an important fact: GaAs behaves quite differently from Si in a rapid thermal annealing system. Consequently, the temperature of the GaAs must be used to control the system. This can be done either directly, by using a pyrometer looking at the GaAs or indirectly, by having the GaAs in isothermal contact to a susceptor to which a thermocouple is attached. The latter method is the less complicated of the two and avoids problems pyrometers themselves face in a radiant RTA system (7).

Acknowledgments

The authors acknowledge support from the Joint Services Electronics Program under contract No. AFOSR F49620-82-C-0033 and the National Science Foundation under grant no. ECS-8420002. We also wish to thank D. Neikirk and S. Lester for useful discussion during the course of the experiments.

Manuscript submitted Oct. 4, 1985.

The University of Texas assisted in meeting the publication costs of this article.

REFERENCES

1. J. F. Gibbons, D. M. Dobkin, M. E. Greiner, J. L. Hoyt, and W. G. Opyd, *Mater. Res. Soc. Symp. Proc.*, **23,** 37 (1984).
2. D. E. Davies and E. F. Kennedy, *Electronics Lett.*, **18,** no. 7, 282 (1982).
3. K. E. Bean, *IEEE Trans. Electron. Devices*, **ed-25,** 1185 (1978).
4. S. A. Cohen, T. O. Sedgewick, and J. L. Speidell, *Mater. Res. Soc. Symp. Proc.*, **23,** 321 (1984).
5. T. E. Seidel, D. E. Lischner, C. S. Pai, and S. S. Lau, *J. Appl. Phys.*, **57,** (4), 1317 (1985).
6. V. E. Borisenko, V. V. Gribkovskii, V. A. Labunov, and S. G. Yudin, *Phys. Status Solidi A*, **86,** 573 (1984).
7. C. Russo, *Nucl. Instrum. Methods*, **B6,** 298 (1985).

JOURNAL OF THE ELECTROCHEMICAL SOCIETY

ACCELERATED

BRIEF COMMUNICATIONS

FEBRUARY
1986

Potential Corrosion of Metals by Atmospheric Organic Acids

T. E. Graedel, C. McCrory-Joy,* and J. P. Franey

AT&T Bell Laboratories, Murray Hill, New Jersey 07974

Most metals corrode when exposed to the earths' atmosphere. Moisture and molecular oxygen are involved in this degradation, as are a number of atmospheric trace species. Attention has generally been focused on the strong mineral acids and their precursors, with NO, NO_2, H_2S, SO_2, and HCl being most frequently singled out as likely principal corrodents.

With the increased analytical efforts recently being directed at trace species within precipitation, it has become apparent that organic acids may have a role to play in atmospheric materials corrosion as well. Formic and acetic acids were first inferred to be present in rain by Galloway and Likens.[1] Subsequent studies have confirmed this detection and added other species.[2-7] It is clear that the presence of organic acids in precipitation is the rule rather than the exception.

The concentrations of organic acids in precipitation are typically a few micromolar, with concentrations as low as about 0.6 μM having been measured in remote areas[5] and concentrations as high as about 80 μM having been measured in urban areas.[2] Several organic acids are commonly present, with formic and acetic acids being generally the most abundant. Strong inorganic acids in precipitation appear to have a smaller proportional fraction of natural sources than do the organic acids. As a result, organic acids contribute some 18-35% of the free acidity in precipitation samples from industrially-developed regions of the world[8] and as much as two-thirds of the free acidity in remote area[5] precipitation.

The atmospheric chemistry of organic acids is of more than academic interest to the corrosion scientist because organic acids degrade many metals and alloys. Two widely known examples are the "bronze disease" caused by acetic acid emission from wood shavings used as packing materials[9] and the deterioration of lead roofing due to volatile acids from oak beams.[10] A more general survey of the scientific literature reveals that organic acids are also known to be capable of degrading aluminum,[11] brass,[12] cadmium,[13] cobalt,[10] copper,[13] indium,[10] iron,[14] magnesium,[10] manganese,[10] nickel,[12] solder,[15] steel,[16] tin,[17] titanium,[18] and zinc.[13]

Given these perspectives from atmospheric chemistry and metallurgy, it appeared useful to investigate whether evidence could be found for organic acids or their ions in the corrosion films formed on metal exposed to precipitation. For this purpose we studied copper used in statuary and exposed to the atmosphere for approximately one hundred years[19] and copper used as a roofing material and exposed to the atmosphere for approximately forty years. The copper in each case was polycrystalline, and of the "electrolytic tough pitch" type (i.e., with the inclusion of oxides to add structural strength).

For the determination of ionic species and their concentrations, a Dionex 2120i ion chromatograph was used with an AS3 separator column, an AG3 guard column, and an AFS1 suppressor. A flow rate of 2.0 ml/min was selected for the .0022 M Na_2CO_3/ .0028 M $NaHCO_3$ eluent.

To obtain the first sample, sections of filter paper soaked with water were applied to an undisturbed region of the statuary copper and allowed to dry. Subsequent extraction of the filter paper and characterization of the extract by ion chromotography indicated the presence of sulfate and chloride. Wiping the surface with sections of cloth or filter paper wetted with acetone appeared to be a more effective procedure because a considerable amount of residue was collected. Ion chromatograms of the corresponding extracts indicated the presence of acetate, formate, chloride, nitrate, and sulfate in the residue. Appropriate blanks were prepared by treating sections of cloth or filter paper in the same way except for contact with the surface.

A common characteristic of copper exposed to the atmosphere is that a portion of the blue-green corrosion film generally runs down vertical surfaces and discolors masonry beneath it. This circumstance had occurred on the statuary copper, so we obtained a small portion of discolored mortar from the statue pedestal. Residue was collected by lightly scraping an area of the pedestal surface with a stainless steel spatula. A weighed sample of the material was extracted with a volume of warm water for one hour. Acetate, formate, chloride, nitrate, and sulfate ions were again detected.

A patina scraping from a portion of the roofing copper comprised our third sample. A weighed portion of this material was extracted with water using the same procedure used for the pedestal sample. The corresponding ion chromatogram was qualitatively the same as that obtained for the surface and pedestal samples. Extraction of cut sections of the roof carried out by placing the whole sections in water without scraping was relatively ineffective. No acetate or formate was detected and relatively weak signals for chloride and sulfate were observed.

The semi-quantitative results for the organic acids and inorganic ions in the samples are presented in Table 1. (The relative results in the table are more reliable than are the absolute values, since our experience indicates the absolute reproducibility of wiped and scraped samples is not particularly high and since the ionic solubilities differ from ion to ion and perhaps for the different sample matrices as well.) The table demonstrates that the amounts of formate and acetate ions present in the copper corrosion layers differ substantially from sample to sample. For sample 1, the wipe sample, sulfate ion concentrations are the highest, those of chloride ion next.

*Electrochemical Society Active Member.

Nitrate and the organic acid anions are clearly present at lower abundances. The high sulfate levels are doubtless due to brochantite [$Cu(SO_4) \cdot 3Cu(OH)_2$], the main constituent of the green patina which forms on copper.[20] The chloride ion source is sea salt and gaseous HCl. Gaseous nitric acid is the probable source of the nitrate ion. The organic acid anions constitute about 0.1% of the total ion concentration. Samples 2 and 3 were treated so as to sample a range of depths of the patina. The resulting ionic concentrations are much higher. In each case, the concentrations of acetate ion are significantly higher than are those of the formate ion. In these latter samples the total organic acid anion concentrations approach 1% of the total ion concentration and are of the same order of magnitude as that of the nitrate ion.

The presence of formate and acetate ions in the corrosion films from field exposures is consistent with similar results obtained in the laboratory[13] and from indoor surfaces[21] by other workers. Except for a passing mention by Vernon and Whitby in 1929[22] of combined carboxylic acids in patina films, neither formate, acetate, or their corresponding acids has previously been reported in analyses of outdoor atmospheric corrosion products. The source of the indoor organic acids is not known, but they may enter buildings along with outdoor air used in ventilation and air conditioning.

Thus, we know that organic acids are present in precipitation, that they are potentially harmful to a number of metals and alloys, and that they are incorporated into the corrosion films that form on copper exposed to the atmosphere in at least two different geographical locations. What can be said about the severity of their impact? One way to assess the impact is to note that significant degradation of several metals including copper was noted by Clarke and Longhurst[12] using vapor phase acetic acid concentrations sufficient to give solution concentrations of $\sim 150\ \mu M$. This is only slightly greater than organic acid concentrations in precipitation over continents. Therefore, atmospheric concentrations of organic acids may be sufficiently high to corrode a number of different metals to a significant degree.

In summary, organic acids are ubiquitous in atmospheric droplets at concentrations that are probably high enough to corrode metals and alloys. Our examinations of copper samples exposed to the atmosphere for extended periods show the presence of incorporated formate and acetate ions. We conclude that it is likely that organic acids play a role in the degradation of materials exposed to the atmosphere.

REFERENCES

[1] J. N. Galloway and G. E. Likens, *Water Air Soil Poll.*, **6**, 241 (1976).
[2] M. J. Barcelona, H. M. Liljestrand, and J. J. Morgan, *Anal. Chem.*, **52**, 321 (1980).
[3] W. A. Hoffman, Jr., S. E. Lindberg, and R. R. Turner, *Environ. Sci. Technol.*, **14**, 999 (1980).
[4] J. N. Galloway, G. E. Likens, W. C. Keene, and J. M. Miller, *J. Geophys. Res.*, **87**, 8771 (1982).
[5] W. C. Keene, J. N. Galloway, and J. D. Holden, Jr., *J. Geophys. Res.*, **88**, 5122 (1983).
[6] G. E. Likens, E. S. Edgerton, and J. N. Galloway, *Tellus*, **35B**, 16 (1983).
[7] R. B. Norton, J. M. Roberts, and B. J. Huebert, *Geophys. Res. Lett.*, **10**, 517 (1983).
[8] W. C. Keene and J. N. Galloway, *Atmos. Environ.*, **18**, 2491 (1984).
[9] U. R. Evans, *Chem. Ind.*, 706 (1951).
[10] P. D. Donovan and J. Stringer, *British Corr. J.*, **6**, 132 (1971).
[11] S. P. Kuznetsova, G. A. Budnevskaya, and N. P. Zhuk, *Prot. Metals*, **14**, 275 (1978).
[12] S. G. Clarke and E. E. Longhurst, *J. Appl. Chem., Lond.*, **11**, 435 (1961).
[13] D. Knotková-Čermáková and J. Vlčková, *British Corr. J.*, **6**, 17 (1971).
[14] E. Laengle, *Schweiz. Arch. Angew. Wiss. Tech.*, **34**, 109, 147 (1968).
[15] M. A. Fawsy, G. H. Sedahmed, and A. A. Mohamed, *Surf. Technol.*, **14**, 257 (1981).
[16] G. Reinhard and C. Irmscher, *Werk. Korros.*, **32**, 377 (1981).
[17] F. A. Lowenheim, R. A. Woofter, and R. R. Hartwell, in *Corrosion Resistance of Metals and Alloys*, 2nd ed., F. L. LaQue and H. R. Copson, Eds., 259 (1963).
[18] E. Heitz, *Adv. Corros. Sci. Technol*, **4**, 149 (1974).

[19] We thank John Robbins of the U.S. National Park Service for his assistance in obtaining the statuary copper samples.

[20] E. Mattsson and R. Holm, in Publication STP-435, Amer. Soc. for Testing and Materials, Philadelphia, 187 (1968).
[21] J. D. Sinclair, AT&T Bell Laboratories, private communication, 1985.
[22] W. H. J. Vernon and L. Whitby, *J. Inst. Metals*, **42**, 181 (1929).

TABLE 1. Surface Extract Concentrations of Ions on Copper Exposed to the Atmosphere for Extended Periods

	Ion Concentration, M/(cm² surface)				
Sample	Formate	Acetate	Cl^-	NO_3^-	SO_4^{2-}
1 (wipe sample, 100y exposure)	$>1\times10^{-11}$	$>3\times10^{-11}$	5.0×10^{-9}	4.7×10^{-10}	1.8×10^{-8}
2 (runoff scraping, 100y exposure)	6×10^{-11}	5×10^{-10}	3.9×10^{-8}	2.4×10^{-9}	6.6×10^{-8}
3 (patina scraping, 40y exposure)	9×10^{-11}	3×10^{-9}	4.4×10^{-8}	3.5×10^{-9}	4.8×10^{-7}

Manuscript received Oct. 29, 1985.

AT&T Bell Laboratories assisted in meeting the publication costs of this article.

A Self-Contained Miniature Hydrogen Reference Electrode

Fritz G. Will*

General Electric Company, Corporate Research and Development, Schenectady, New York 12301

Traditionally, hydrogen reference electrodes require a supply of tank hydrogen, accompanied by the inconvenience of regulators, pipes and valves. Furthermore, the H_2 must be purified to avoid contamination of the electrolyte with CO and organic impurities. In many sensitive electrode studies, such as in chemisorption and electrocatalysis, post-purification of the tank H_2 with Pd diffusers is essential, thus resulting in increased complexity.

To overcome the shortcomings of the conventional H_2 reference electrode, a "dynamic H_2 electrode" was *proposed*[1]. It relies on the passage of a small current between two electrodes. At least one of these is a platinized Pt electrode on which H_2 is continually being evolved while O_2 is formed on a second inert electrode. The two electrodes must be positioned such that the O_2 does not affect the H_2 electrode potential, and the gases must be properly vented. As the dynamic H_2 electrode is cathodically polarized, correction must be made for the magnitude of the polarization corresponding to the applied current. This is best accomplished by calibrating against a conventional H_2 electrode. Typical corrections are between 15 and 40mV.[1]. A constant current source must be employed if accuracy within a few mV is to be achieved. As both the dynamic H_2 electrode and its counter electrode must be kept electrically floating, a battery with a large series resistor is used to simulate a constant current source. As the battery voltage decreases with time, the potential of the dynamic H_2 electrode is subject to slow drift, typically amounting to less than 5 mV in 2 days.[1]

The novel self-contained H_2 reference electrode described here avoids both the inconveniences of the conventional H_2 reference electrode and the shortcomings of the dynamic H_2 electrode. It does not require an external supply of H_2 nor a source of electrical power. It is a true reversible H_2 reference electrode that maintains its potential as well as a conventional H_2 reference electrode. Furthermore, the electrode lends itself to miniaturization and is portable if desired.

The self-contained H_2 electrode is based on the use of a partially immersed platinized Pt electrode,[2] its emerging part in contact with a hermetically sealed H_2 bubble. The design utilizes the fact that the emerging part of such a partially immersed electrode is covered with a meniscus and thin film of electrolyte.[2] Such a thin electrolyte film allows dissolved H_2 to diffuse faster to the electrode surface than the boundary layer of electrolyte created by H_2 bubbles dispersed in bulk electrolyte.[2]

Figures 1 and 2 show schematic drawings of electrolytic cells employing two different types of self-contained H_2 electrodes.[3,4]. The H_2 reference electrode in Fig. 1 consists of a platinized Pt wire of 1mm diameter, sealed into a long glass capillary whose opening is located close to the test electrode. The lower narrow end of the glass tubing functions as a Luggin capillary while the upper larger diameter part is sealed hermetically to a ground glass joint. This feature makes the H_2 electrode readily removable and transportable. The H_2 electrode in Fig. 2 consists of a platinized Pt wire sealed into the upper end of a short glass capillary, whereas the lower narrow end is *permanently cemented* into a polymer cell housing.

The self-contained H_2 reference electrodes are prepared for operation by filling the glass capillary with electrolyte under vacuum, followed by electrolytic generation of H_2 on the Pt wire.[3] Any inert auxiliary electrode can be used as the O_2-evolving anode which is then removed after use. The H_2 formed on the Pt wire displaces electrolyte at the top end of the glass capillary. Electrolysis is continued until 1/4 to 3/4 of the Pt wire is surrounded by H_2 gas. A current of

*Electrochemical Society Active Member.

Key Words: Gas, Cell, Potential

0.04A produces an H_2 bubble of 2 cm length in a glass tube of 0.4 cm inner diameter in approximately 1 minute.

The useful life of the self-contained H_2 electrode depends on the rate of H_2 loss, unless gradual poisoning of the Pt black catalyst occurs earlier. If the Pt wire is sealed properly, the rate of H_2 loss is determined by diffusion into the bulk electrolyte. For a lower capillary portion of 2 cm length and 0.1 cm diameter, H_2 out-diffusion occurs in approximately 5 years. The rate of catalyst poisoning depends on the purity of the electrolyte, more specifically, the concentration of organic impurities, CO and metal ions reducible at the H_2 potential. The fact that the Pt wire is in contact with electrolytically generated H_2 greatly reduces the rate of poisoning.

As a measure of the long-term stability of the self-contained H_2 reference electrode, its potential was monitored against a conventional H_2 reference electrode as a function of time. Ultra-pure H_2 was employed for the latter. The potential varied by less than $\pm$ 0.5 mV over the time period of several days. Self-contained H_2 electrodes were observed to have potentials within less than 0.5 mV against one another.

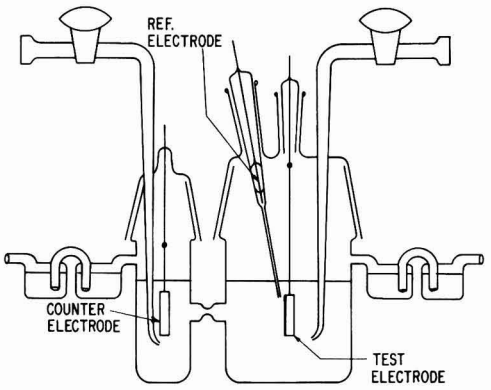


Fig. 1. Schematic drawing of electrolytic cell showing removable self-contained H_2 reference electrode.

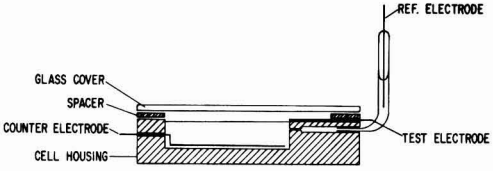


Fig. 2. Schematic drawing of electrolytic cell showing miniature self-contained H_2 reference electrode cemented to cell housing. Length of reference electrode capillary 2 cm.

REFERENCES

1. J. Giner, J. Electrochem. Soc., 111, 376 (1964).
2. F.G. Will, ibid., 110, 145 (1963); 110, 152 (1963).
3. F.G. Will and H.J. Hess, Final Report NASA CR 72777, March 15, 1971.
4. F.G. Will and H.J. Hess, J. Electrochem. Soc. 120, 1 (1973).

Manuscript submitted Oct. 31, 1985; revised manuscript received Dec. 10,1985.
General Electric Corporate Research and Development assisted in meeting the publication costs of this article.

THE ELECTROCHEMICAL SOCIETY, INC.

The Electrochemical Society is an international society concerned with a broad range of phenomena related to electrochemical science and technology and solid state science and technology.

OBJECTIVES

1. The advancement of the theory and practice of electrochemistry, electrometallurgy, electrothermics, electronics, and allied subjects.
2. The encouragement of research and the dissemination of knowledge in the fields of electrochemical science and technology and solid state science and technology.
3. The assurance of the availability of adequate training in the fields of electrochemistry and solid state science for chemists, engineers, metallurgists, physicists, solid state scientists, and others in related subjects.

BENEFITS OF MEMBERSHIP

1. The assurance of being kept aware of pertinent scientific and technical developments through the JOURNAL OF THE ELECTROCHEMICAL SOCIETY and other Society publications.
2. The opportunity to contribute to the advancement of science and technology through support of Society activities.
3. The stimulation of personal association and technical exchange with fellow scientists and engineers.

DIVISIONS

The activities of the Society are carried on by its nine Divisions and two Groups as follows:

Battery
Corrosion
Dielectrics and Insulation
Electrodeposition
Electronics
  New Electronic Technologies
  Semiconductors
Energy Technology Group
High Temperature Materials
Industrial Electrolytic
Luminescence and Display Materials Group
Organic and Biological Electrochemistry
Physical Electrochemistry

SECTIONS

Local Sections of the Society have been organized in the following cities and regions:

Boston
Canadian
Chicago
Cleveland
Columbus
Detroit
European
Indianapolis
Japan
Metropolitan New York
Midland (Michigan)
National Capital Area
North Texas
Oregon
Pacific Northwest
Philadelphia
Pittsburgh
Rocky Mountain
San Francisco
Southern California-Nevada
Southern Wisconsin
Twin Cities

JOURNAL OF THE ELECTROCHEMICAL SOCIETY

REVIEWS AND NEWS

FEBRUARY
1986

SECTION NEWS

Chicago Section

The Chicago Section held its second meeting of the 1985-1986 season at the Holiday Inn, Willowbrook, on November 11, 1985. The speaker was Dr. John Appleby of the Electric Power Research Institute. Dr. Appleby lectured on "Electric Power Generation in the 21st Century."

The Chicago Section Officers' Night was held at the Amoco Research Center, Naperville, Illinois, on December 3, 1985. Dr. Bruce E. Deal, Vice-President of the Society and a Scientific Consultant at the Schlumberger/Fairchild Research Center in Palo Alto, California, spoke on "Current Advances in Semiconductor Device and Processing Technology."

Cleveland Section

On Thursday, November 7, Dr. Fritz Will, Vice-President of The Electrochemical Society, addressed the Cleveland Section. Dinner and the meeting were held at the Cleveland Engineering Society. Nineteen people attended. The Past-Chairman's Pin (1983-1984) was awarded to Prof. Uziel Landau, CWRU, prior to the talk.

The technical talk concerned Dr. Will's own work: "Electrochemistry of p-Doped Polyacetylene." General concerns of ECS members were addressed at the meeting.

Columbus Section

Recent events of the Columbus Section include a lunchtime meeting held at the Chemical Abstracts Service on November 26, 1985. Following lunch, a tour of Chemical Abstracts' impressive facilities was held.

Dr. Fred Kohl of the NASA-Lewis Research Center in Cleveland, Ohio, addressed the December 10, 1985, joint meeting of the ECS, the American Chemical Society, and the American Institute of Chemical Engineers with a seminar entitled "Materials Science in Space –or– The Sky is NOT the Limit!" Dr. Kohl described existing and planned materials science experiments as well as the methods in which "ground" experiments lead to space experiments. The talk, which was held at Battelle Columbus Laboratories, was attended by over 100 members as well as by representatives of a local television station, which provided coverage of the meeting on the local news later that evening.

Detroit Local Section

Dr. Fritz G. Will, Vice-President of The Electrochemical Society, addressed the Detroit Local Section at the Schmid Haus, Warren, on November 21st, 1985. The meeting was attended by 34 members of the Society and was sponsored by Bioanalytical Systems, West Lafayette, IN.

Dr. Will spoke about the current membership and financial status of the Society, followed by a talk on "Electrochemistry of p-Doped Polyacetylene Batteries." The talk covered studies of the electrochemical kinetics of p-doped polyacetylene, charge-discharge behavior of polyacetylene batteries, and photoacoustic spectroscopic studies of the structure of p-doped polyacetylene.

National Capitol Section

The December meeting of the National Capitol Section was held on December 5, 1985, at Georgetown University, Washington, DC. The guest speaker, Dr. Fritz G. Will of General Electric Corporate Research and Development, Schenectady, NY, presented a talk entitled "Electrochemistry of p-Doped Polyacetylene." In this talk, Dr. Will discussed the use of polyacetylene polymer films as electrode materials in lithium-polyacetylene batteries. It was shown that the overall rate of reaction at polyacetylene electrodes is controlled by the rate of diffusion of the dopant within the polymer. The behavior of these electrodes was described using a semi-infinite diffusion model that incorporated the experimentally measured diffusive properties of the dopant. Prior to the technical portion of his presentation, Dr. Will, who is currently Vice-President of the Society, presented a brief summary of the financial and membership status of the Society.

Attending the meeting were approximately 35 persons, both members and nonmembers. The attendants represented the National Bureau of Standards, U.S. Bureau of Mines, Naval Research Laboratory, Georgetown University, American University, University of Maryland (Baltimore County), Johns Hopkins University, W. R. Grace & Co., and other governmental, academic, and industrial organizations in the Washington, DC, area.

North Texas Section

The November meeting of the North Texas Section was held on November 7, 1985, at the Holiday Inn in Richardson, Texas. Fred Streiter of Honeywell's Optoelectronic Division was the guest speaker for the evening. In his talk, entitled "Is GaAs Real?", he discussed the current status of GaAs technology and its role in the future of the semiconductor industry. Forty-two members and guests attended the dinner meeting and discussion.

The North Texas Section set up a booth at Semicon Southwest, held in Dallas in October. Members distributed membership application forms and literature concerning the Society's business and activities. Interest was high, and all available literature was distributed.

The most recent meeting of the North Texas Section was held on December 12, 1985. Dr. Ronald Enstrom of RCA, Vice-President of The Electrochemical Society, discussed "Electronic Materials and The Electrochemical Society." The relationship of various electronic materials and studies to improvements in their electronic device characteristics was illustrated and discussed. Twenty-four members and visitors attended the meeting.

In an effort to encourage new membership in the Society and participation in the local section, the dinner at the latest meeting was free for new member applicants and half price for first-time visitors. Several applications were received. The North Texas Section plans to continue this policy at future dinner meetings.

Oregon Section

The November meeting of the Oregon Section of The Electrochemical Society was held at the Oregon Graduate Center on the evening of November 20, 1985. Mr. Joel Pollack of Tektronix presented a lecture on "Liquid Crystal Shutter Technology and Applications." Twenty-two people enjoyed the lecture and demonstrations of the applications of liquid crystal color displays, including a color stereo video tape. The lecture was followed with an informal social hour with refreshments of wine and cheese. The next section meeting is scheduled for January 15, 1986.

Southern Wisconsin Section

The November 6, 1985, meeting of the Southern Wisconsin Section was held at the Quality Inn South in Madison, Wisconsin. Our guest speaker was Dr. Marc A. Anderson, Professor of Water Chemistry at the University of Wisconsin, Madison. His presentation was titled "In situ Cylindrical Internal Reflectance— FTIR Studies of Oxide/Aqueous Solution Interface." Dr. Anderson emphasized the importance of multiple quantitative and qualitative testing of aqueous solutions. Twenty-six people attended the session.

In December, the Southern Wisconsin Section of The Electrochemical Society met at Marquette University in Milwaukee. The guest speaker was Dr. Bruce Deal, a scientific consultant at the Schlumberger/Fairchild Research Center in Palo Alto, California. Dr. Deal's program was titled "Current Advances in Semiconductor Device and Processing Technology." Dr. Deal's talk gave an historical overview of semiconductor technology and some of the important trends and advances that we can expect in the future. This presentation was given before an audience of twenty-two.

NEW MEMBERS

It is a pleasure to announce the following new members of The Electrochemical Society as recommended by the Admissions Committee and approved by the Board of Directors in November, 1985.

Active Members

Foster, M.B., Bedford, IN
Hopkins, R. M., St. John, Newfoundland, Canada
Hsu, C., Laguna Hills, CA
Inoue, T., Pasadena, CA
Johansson, T., Ljungaverk, Sweden
Johnson, B. E., Niagara Falls, NY
Jucha, B., Celeste, TX
Langlais, F., Talence, France
Leung, D. L., Manhattan Beach, CA
Lory, E., Princeton, NJ
Lund, H., Aarhus, Denmark
Mammone, R. J., South Plainfield, NJ
Mattson, B., Sunnyvale, CA
Navarro, R. R., Chula Vista, CA
Oh, J. M., Albany, OR
Pearce, R. H., Trumbull, CT
Philipossian, A., Wilmington, MA
Roehr, E., Milwaukee, WI
Samantaray, P. K., San Jose, CA
Sayka, T., Security, CO
Semkow, K. W., St. Louis, MO
Tyler, W. W., New Haven, CT
Wehlin, P., Stockholm, Sweden

Student Members

Bartz, J. A., Madison, WI
Dimpault-Darcy, E., College Station, TX
Hsiao, Y.-J., Chicago, IL
Jordan, K. G., Berkeley, CA
Kembaiyan, K. T., Hoboken, NJ
Landsberger, L. M., Stanford, CA
Lee, J. Y., Berkeley, CA
Rudnicki, J. D., Oakland, CA
Simonsen, L. R., Ann Arbor, MI
Toth, J., Pasadena, CA

Reinstatement

Storck, A., Nancy, France

Member Representative

Dunlop, J. D., Clarksburg, MD

POSITIONS WANTED

Please address replies to the box number shown, c/o The Electrochemical Society, Inc., 10 South Main Street, Pennington, NJ 08534-2896.

Electronics Materials Engineer—B.S.Ch.E. with broad experience in semiconductor wafer fabrication, clean gases, chemicals, D. I. H_2O and plastic encapsulation. Recent work in passive transponders for article surveillance labels, web-fed rotary manufacture/lamination of papers, foils, films, and adhesives. Publications and patents. Seeks industrial position with growth. Reply Box C-261.

Ph.D. Electrochemist/Metallurgist—Industrial/academic background. Specializes in passivation, oxidation, electrodeposition, and alloy development. Extensive R&D experience in electronic packaging. Versatile, innovative. Patents and publications. Seeking university or industrial R&D position. Reply Box C-262.

Electrochemical/Chemical Engineer—Ph.D. seeks challenging entry level position in R&D. Research experience in electrochemical membrane transport, cyclic voltammetry, surface electrochemistry. Strong academic background in electrochemistry and chemical engineering. Will also consider academic position. Reply Box C-263.

ELECTROCHEMICAL ENGINEER

Life Systems, Inc. a growing high technology Aerospace R&D Company has an immediate need for an individual possessing proven talents and experience in electrochemistry to join our team of creative research professionals. A steady increase in our work load has created the need for more of the highly skilled people responsible for our success to date. Long term projects include Aerospace life support and advanced power storage systems development for the NASA Space Station Program and the development of commercially viable products from our Company's engineering technology.

Your responsibilities will require you to direct the activities required to develop water electrolysis systems technology for multiple applications which will include regenerative fuel cells, O_2 generation and bulk H_2 generation. Cell sizes vary from 0.1 ft^2 to 1.0 ft^2 with modules to >30 cells. Your primary focus will be on new applications of recent technology, logical development cycles, and high quality results. In addition you will be expected to assume responsibility for the management and marketing of assigned technology programs. This position requires an MS Degree (Ph.D. preferred) and 5 + years of related experience coupled with strong verbal and written communications skills.

Our interdisciplinary approach to R&D provides the ideal career environment for technical professionals who share our interest in practical applications of advanced science. Our team is strong in sophisticated system and subsystem integration and unique control/monitoring instrumentation. We offer a superior compensation package with fringe benefits that are customized to meet your needs, challenging assignments and respect for good work. If you are interested in challenges we can provide, send resume with salary history to:

Manager, Recruitment

Life Systems, Inc.

24755 Highpoint Road
Beachwood, OH 44122

An Equal Opportunity Employer M/F/H/V

REVIEWS & NEWS INDEX

Section News 45C

New Members 46C

Meetings Calendar 47C

Call for Papers - San Diego, California, Meeting 57C-64C

ADVERTISERS' INDEX

Life Systems 46C

McMaster University 47C

Bioanalytical Systems 52C

The Electrosynthesis Company 53C

Princeton Applied Research 54C

DIRECTOR

INSTITUTE FOR MATERIALS RESEARCH
McMASTER UNIVERSITY

McMaster University is seeking applications and/or nominations to fill the position of Director of the Institute for Materials Research. The Institute is a unique interdisciplinary organization with the primary objective of furthering high quality fundamental and applied research in materials. The Director is expected to provide leadership in planning for the directions of materials research at McMaster. The Director is also expected to establish and maintain both the academic environment and physical facilities that are essential for the pursuit of forefront scientific and engineering research in materials.

It is expected that the appointee to this position will be a distinguished scientist or engineer who has achieved international recognition through scholarly contributions to materials research. The appointee will be given a tenured academic appointment at the rank of Professor in an appropriate Department in either the Faculty of Engineering or Science. To further the objectives of the Institute, the University provides the Director with a discretionary budget that supplements the externally generated infrastructure funding.

McMaster would prefer the appointee to start on July 1, 1986 but a later starting date can be negotiated. Salary is also open to negotiation. Applications and nominations should include a current curriculum vitae and the names of three referees who are familiar with the individual's previous contributions. These should be sent to: Dr. A.C. Heidebrecht, Dean of Engineering, or Dr. R.F. Childs, Dean of Science, McMaster University, Hamilton, Ontario, L8S 4L7, CANADA.

In accordance with Canadian immigration regulations, priority will be given to Canadian citizens and permanent residents in Canada.

Nominations for the Electronics Division Award

Nominations for the 1987 Electronics Division Award of The Electrochemical Society are now being solicited. The Electronics Division Award is presented annually in order to give recognition to active members of the Society who have made outstanding scientific contributions and enhanced the scientific stature of the Society by presentation of this work in papers in the Journal and at Society meetings.

To be considered, a nominee must be a member of the Society and have been an author or co-author in the publication of more than one paper in the *Journal* and/or presentation of more than one full paper or more than two recent newspapers at a Society meeting within the previous five years.

Nominations must be accompanied by supporting data, such as a list of publications, patents, activities, and a brief summary outlining the accomplishment on which the award will be based. Nominations should be submitted **before** May 1, 1986, to the Chairman of the Committee, W. A. Pliskin, Department 025, Building 300-48A, IBM Corporation, Hopewell Junction, NY 12533.

MEETINGS CALENDAR

8th Symposium on Applied Surface Analysis
June 4-6, 1986
University of Dayton
Dayton, Ohio

For further information, contact J. S. Murday, Naval Research Laboratory, Washington, DC 20375, or J. T. Grant, Research Institute, University of Dayton, Dayton, OH 45469.

American Chemical Society
Division of Colloid and Surface Chemistry
Symposium on Photochemical and Electrochemical Surface Science: Corrosion
April 14-17, 1986
191st National Meeting, New York, NY

For further information, contact A. Wieckowski, University of Illinois, Box 56-5, 1209 W. California, Urbana, IL 61801, or call 217-333-7943.

American Institute of Chemical Engineers
Kinetics of Industrial Electrochemical Reactions
November 2-7, 1986
Annual Meeting, Miami, Florida

For further information, contact: B. Savinell, Department of Chemical Engineering, University of Akron, Akron, OH 44325. Telephone 216-375-7943; R. Selman, Department of Chemical Engineering, Illinois Institute of Technology, 10 W. 33rd St., Chicago, IL 60616. Telephone 312-567-3037; or H. Saltsburg, Department of Chemical Engineering, University of Rochester, Rochester, NY 14627. Telephone 716-275-4582.

American Institute of Chemical Engineers
Mathematical Modelling of Batteries and Fuel Cells
November 2-7, 1986
Annual Meeting, Miami, Florida

For further information, contact: R. E. White, Department of Chemical Engineering, Texas A&M University, College Station, TX 77843-3122. Telephone 409-845-3307; or R. Pollard, Department of Chemical Engineering, University of Houston, Houston, TX 77004. Telephone 713-749-4407.

13th International Symposium on Gallium Arsenide
and Related Compounds
September 28-October 1, 1986
Caesars Palace, Las Vegas, Nevada

For further information, contact C. M. Wolfe, Washington University, Box 1127, St. Louis, MO 63130. Telephone 314-889-6149.

Nominations Solicited for the Eighth Electrochemical Society Award in Solid State Science and Technology

Nominations are solicited by the Honors and Awards Committee for the Solid State Science and Technology Award. Since establishment of the biennial award in 1972, the recipients have been the following:

1973 William G. Pfann

1975 Harry C. Gatos

1977 Robert N. Hall

1979 Morton B. Panish

1981 Gerald L. Pearson

1983 Nick Holonyak, Jr.

1985 Jerry M. Woodall

The next award will be presented at the Spring 1987 Meeting of the Society.

The recipient of the Award must have made distinguished contributions to the field of solid state science. The recipient need not be a member of the Society, and there are no restrictions regarding age, sex, race, citizenship, or place of origin.

The Award consists of a silver medal together with a bronze replica and the sum of $1500. The recipient will deliver an address to the Society on a subject related to the contributions for which the Award is presented.

This is one of the Society's most prestigious awards, and we urge all members of the Society to give serious consideration to possible candidates. If you wish to suggest or nominate a candidate, please fill out the Award Search Form that appears on page ___ of This Journal and mail to:

The Electrochemical Society, Inc.
10 South Main Street
Pennington, NJ 08534-2896

Nomination forms may also be obtained from Society Headquarters. If the Committee needs more information, the nominator will be contacted. If possible, please submit the nominations by March 1, 1986 to facilitate consideration by the Committee. Nominations close at the opening of the Spring 1986 Meeting.

Call for Applications for the Student Research Grants of the Battery Division of The Electrochemical Society, Inc.

Applications are being solicited for the 1986 Student Research Grants of the Battery Division of The Electrochemical Society, Inc.

The purpose of the Battery Division in offering these awards is to aid promising young scientists and engineers in their initial research in the field of electrochemical energy storage. It is also the intent of the Division to recognize excellent student performance and to provide significant encouragement to talented young people who are considering research careers in the field of electrochemical power sources.

The amount of each grant is $1000.00, payable to the recipient, which is to be used in carrying out the recipient's current or proposed research program. The grant is for one year only and is not renewable.

To be eligible to receive a grant a person must be enrolled in a college or university or have been accepted for enrollment. The application for the award must include:

1. Transcripts of all post-secondary school academic work.
2. An outline of the research project to be engaged in during the next year (limit to two typewritten double-spaced pages).
3. A statement which describes the relationship of the project to the field of electrochemical power sources (limit to one typewritten double-spaced page).
4. A letter of recommendation from the applicant's research supervisor.

In addition, the applicant may submit a record of achievements in industrial work if he or she believes it is pertinent. All application materials are to be sent to: Prof. Drannan Hamby, Department of Chemistry, Linfield College, McMinnville, Oregon 97128. Deadline for receipt of completed applications is **March 1, 1986.**

Recipients will be selected on the basis of past academic performance, past record of research productivity if applicable, merit of proposed research and recommendation of the research supervisor. The total number of awards given in any year is limited by the availability of Battery Division funds as determined by the Battery Division Executive Committee. In the event that there are no qualified applicants, no awards will be made.

THE ELECTROCHEMICAL SOCIETY, INC.
AWARD SEARCH FORM

Name of Award: _____

Submit to: The Electrochemical Society, Inc.
10 South Main Street
Pennington, NJ 08534-2896

Date: _____

Name of Nominee: _____
(Last) (First) (Middle Initial)

Nominee's occupation/position/affiliation: _____

_____

Current address: _____

_____

Proposed citation (30 words or less): For _____

_____

_____

_____

Submitted by: _____ Occupation/position: _____

Current address: _____

_____

Phone: _____

Are you willing to prepare the nomination forms yourself? ☐ Yes ☐ No

If YES, it is not necessary to complete the balance of this form. Mail this form to the above address. The Headquarters office will send you a copy of the nomination form and the current award rules concerning this award which also gives instructions for the preparation of the nomination.

If NO, please complete the rest of this form before mailing.

Potential endorsers:
(Persons familiar with nominee, who can probably attest to his/her contributions and to the importance thereof.)

A. Name	B. Name	C. Name
Position/Title	Position/Title	Position/Title
Address	Address	Address
City Zip	City Zip	City Zip

List major achievements and honors to support nomination:

_____

_____

_____

_____

_____

_____

Suggested nominator(s): _____

_____

Submission of this form does not replace the necessity of a complete Nomination Form.

CALL FOR RECENT NEWS PAPERS AND EXTENDED RECENT NEWS PAPERS

Boston, Massachusetts Meeting May 4-9, 1986

DUPLICATE copies of a 75-word abstract of a Recent News Paper, for a 10-minute presentation, must be *RECEIVED* by the Symposium Chairman not later than March 5, 1986.
DUPLICATE copies of a 75-word abstract, and ALSO a 200-300 word abstract of an Extended Recent News Paper, for a 20-minute presentation, must be *RECEIVED* by the Symposium Chairman not later than March 12, 1986.

ELECTRONICS DIVISION AND DIELECTRICS AND INSULATION DIVISION

Recent News Papers and Extended Recent News Papers are invited for the sessions sponsored by the Electronics Division and Dielectrics and Insulation Division for the 1986 Spring Meeting in Boston, Massachusetts. The time allotted for the 75-word Recent News Paper will be 10 minutes, including 2 minutes for discussion. The time allotted for the Extended Recent News Paper will be 20 minutes, including the question/answer period.

The Extended Recent News Paper requires, in addition to the 75-word abstract, a 200-300 word abstract in duplicate, and should be received significantly earlier than the normal dead-line date because these papers will be reviewed for technical content, appropriateness of the paper, time limitations, duplication of materials, etc. Topics for Recent News Papers and Extended Recent News Papers include:

1. Silicon Materials Science and Technology
2. Electrochemistry In Electronic Packaging
3. Electrochemical Sensors for Biomedical Applications
4. Aluminum Surface Treatment Technology
5. Pattering Science and Technology
6. Silicon On Insulators
7. Organic Semiconductors
8. Electrodeposition of Semiconductors
9. Surface Modification of High Temperature Materials
10. Film Structures and Their Properties
11. Silicon-Based Structural Ceramics

Copies of all abstracts, as outlined above, should be sent to the Recent News Papers Symposium Chairman: W. A. Pliskin, IBM Corporation, Department 025, Internal Zip 48A, Route 52, Hopewell Junction, NY 12533. Please note that the deadlines are for RECEIVING the papers and not for mailing them.

Call for Nominations for the 1987 H. H. Uhlig Award of the Corrosion Division

Nominations are solicited for the H. H. Uhlig Award of the Corrosion Division, to be presented at the 1987 Fall Meeting of the Society in Honolulu, Hawaii.

The Corrosion Division has established this Award, formerly known as the Outstanding Achievement Award, to recognize excellence in corrosion research and outstanding technical contributions to the field of corrosion science.

The recipient will receive a scroll, a $500 award, and, if required, financial assistance toward travel expenses to attend the Society Meeting at which the Award is made. The recipient is required to attend the Society Meeting at which the Award is given and to present an Award lecture to the Corrosion Division.

For the nominee to be considered for the Award, the nomination must be accompanied by supporting documents, such as a biography, list of publications, professional activities, and a brief summary of the outstanding contributions on which the Award is to be based. Five (5) copies of each nomination with supporting documents should be submitted to the Award Committee Chairman, Dr. T. R. Beck, Electrochemical Technology Corporation, 1601 Dexter Avenue North, Seattle, WA, 98109. Deadline for receipt of nominations by the Award Committee Chairman is **June 1, 1986.**

THE ELECTROCHEMICAL SOCIETY
SHORT COURSE
RESIST SCIENCE AND TECHNOLOGY

Sunday, May 4, 1986, Sheraton Boston Hotel
Limited attendance—Advance registration required

The Electrochemical Society will sponsor a short course in conjunction with the 169th Meeting of the Society in Boston at the Sheraton Boston Hotel on Sunday, May 4, 1986. The course will consist of four lectures, two from 9:00 AM to noon, and two from 1:30 to 4:30 PM. Copies of the slides, along with an outline and bibliography will be distributed to each registrant at the time of the course. The registration fee is $150 for members and $200 for nonmembers. The fee covers the course, luncheon, and text material; it is not applicable to any other activities of the Society's 169th Meeting. The attached registration form and a check for the correct registration fee must be received not later than April 4, 1986, at The Electrochemical Society, Inc., 10 South Main St., Pennington, N.J. 08534-2896.

RESIST SCIENCE AND TECHNOLOGY

Michael P. C. Watts

AZ Photoresist Products, American Hoechst Corporation, Sunnyvale, California

Elsa Reichmanis

AT&T Bell Labs, Murray Hill, New Jersey

This course will cover the theory and applications of resist science and technology in semiconductor lithography. It is intended to provide a working guide to current commercial practices and an introduction to the current research activities for the "next generation." The course should be of interest as an introduction to the technology for process engineers and researchers and as a "refresher" for experienced lithographers.

The first half of the course will involve discussions of the optical lithography hardware, resist chemistry, and resist process operations used in production-integrated circuit manufacture. The discussion of lithography hardware and ancillary processes, plasma etching, etc. will be restricted to "what the resist scientist must know to survive." Emphasis will be placed on resist chemistry and process technology. Both the control of specific process operations that is required to achieve linewidth control and related metrology problems will also be described.

Multilayer resist systems provide a method for extending the range of conventional optical lithography. The various two- and three-layer processes will be described along with examples of what they can achieve and the penalty of use.

The second half of the course will parallel the first half in a discussion of resists for the "next generation," *e.g.*, electron beam, x-ray, and deep UV lithography. Emphasis will be placed on the various resist chemistries, reflecting the current status of these technologies. Some of the process implications of these new technologies will be discussed.

SHORT COURSE REGISTRATION FORM

RESIST SCIENCE AND TECHNOLOGY

Payment Enclosed:

☐ ECS Member—$150.00 ☐ Nonmember—$200.00

Name _____

Address _____

City, State, Zip _____

Business Affiliation _____

Please return this form by April 4, 1986, with your payment to:
The Electrochemical Society, Inc., 10 South Main St., Pennington, N.J. 08534-2896.

You don't have to be made of money to afford Electrochemistry

Chemical instrumentation is expensive! Acquisition of MS, NMR, FTIR, and ESCA can involve a capital expense measured in multiples of $100,000. The information gained justifies the investment. Electrochemical techniques provide unique thermodynamic, kinetic, and mechanistic information which is simply not available from spectroscopic instrumentation. The cost-benefit analysis is in your favor if you work with transition metal complexes, biochemical redox reactions, thin-films, and chemically modified surfaces. For an order of magnitude less, you could learn more. Our BAS-100 Electrochemical Analyzer does most of the work, giving you time to think.



BAS

2701 Kent Ave
West Lafayette
Indiana 47906

Telex: 276141
(317) 463-4527

SIX PROVEN PRODUCTS FROM ESC TO IMPROVE YOUR ELECTROCHEMISTRY...

Low Cost, High Current Digital Coulometer



Model 640: Single current range 1 mA to 1 Amp; external shunts to 10,000 Amps*

Low Cost, High Sensitivity Digital Coulometer



Model 630: Five current ranges, 10 µAmps to 100 mAmps: high accuracy

Microprocessor Based Computing Coulometer



Model 680: Integrates currents from 10^{-9} to 10^{5} Amps with external shunts* Optional data interface

IR Measurement System



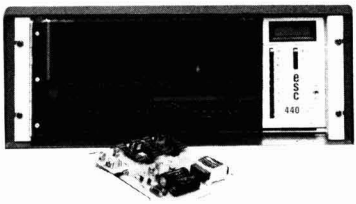
Model 800: Determine potential losses due to Ohmic resistance; specimen currents up to 10 Amps. Other systems up to 100 Amps.

Potentiostatic Controller



Models 410 and 415: Convert your lab power supply into a Potentiostat. Two models; 1 Amp or 5 Amps.

Multichannel Potentiostat



Model 440: Ten independent potentiostats in modular form for corrosion research.

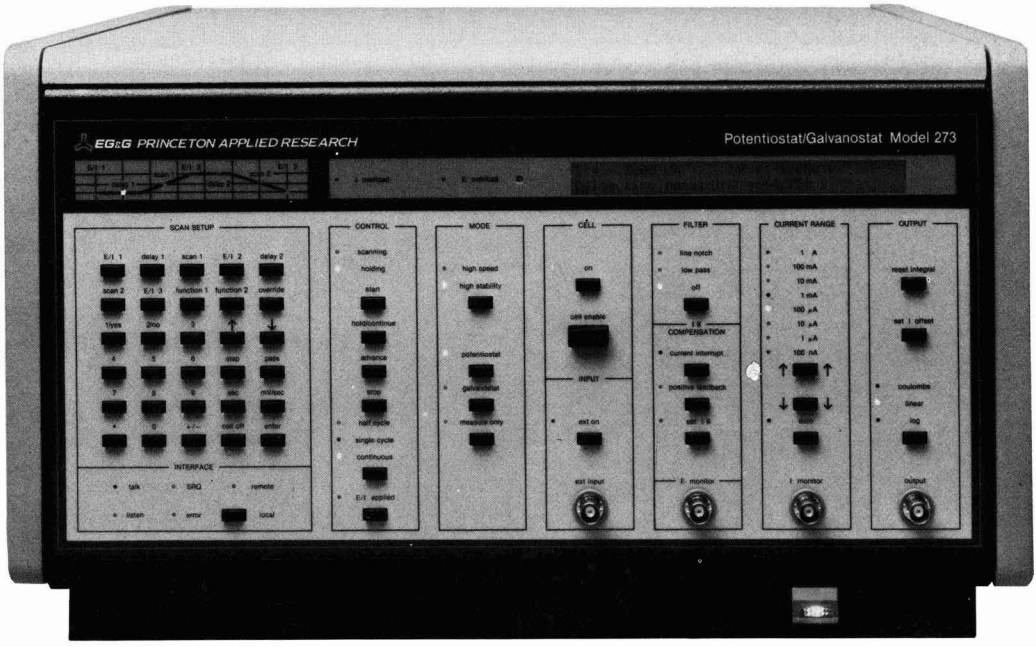
*Optional

THE ELECTROSYNTHESIS CO., INC.
P.O. BOX 16, E. Amherst, N.Y. 14051
Telephone: (716) 684-0513
Telex: 854091

European Representative:

ELECTROCELL AB, P.O. Box 34,
S-184 00 Akersberga, Sweden
Telephone: 46(0) 764/60040
Telex: 15313 ECAB S

The NEW BENCHMARK for Electrochemical Research Instrumentation



Our new MODEL 273 POTENTIOSTAT/GALVANOSTAT is the most versatile electrochemical research instrument you can buy. As a manually-controlled potentiostat, it provides features such as waveform generation and current, log current, and coulomb outputs. As a computer-controlled potentiostat, it offers both RS232 and GPIB Interfaces together with an expanded version of our easy to use Electrochemical Command Set.

The Model 273 is functionally equivalent to a rack of research instruments, yet its price is significantly lower and its performance is remarkably better. A completely new design allows both extraordinarily low noise operation and a hefty compliance of ±100 V. Current measurements can autorange over eight decades from 1 A to 100 nA full scale! A front panel control lets you optimize the Model 273 for either high-speed or high stability operation. The Model 273/97 IR compensation option uses the current-interrupt technique and includes a 5 μs A/D converter.

We even offer a less expensive version of the Model 273 without front-panel controls. It's called the Model 272. For corrosion studies, up to eight Model 272's or 273's can be used with our new Model 351 Corrosion Measurement Console.

Sound intriguing? Write or call for more details.

"See us at Corrosion '86, Booths 725 and 727"

EG&G PRINCETON APPLIED RESEARCH

P.O. BOX 2565 • PRINCETON, NJ 08540. U.S.A. • 609/452-2111 • TELEX: 843409

APPLICATION FOR ADMISSION

TO

The Electrochemical Society, Inc.

Return completed application to:

Secretary
The Electrochemical Society, Inc.
10 South Main Street, Pennington, New Jersey 08534-2896
609-737-1902

For office use only

Date Rec'd. _____ $ _____

Notice of Ackn. _____

Checked: _____

Approved: _____

To the Board of Directors of The Electrochemical Society, Inc:

Please print complete name and address as it should appear on mailings.

Name: _____

Address: _____

_____

_____

_____

_____

Business Telephone: (include area code) _____

I hereby make application for admission to The Electrochemical Society, Inc., as an _____ member, and enclose the amount of $_____ covering the first year's dues. (Please see reverse side for proper class of membership and dues applying thereto, noting the options with regard to the date of election and active life membership and the credit available for nonmember meeting registration.)

1. Date of Birth: _____ (month) _____ (day) _____ (year)

2. Please check LOCAL SECTION with which you wish to affiliate:

—— Boston (05)	—— Detroit (25)	—— Midland (Mich.) (40)	—— Philadelphia (70)	—— So. Calif.-Nevada (90)
—— Canadian (60)	—— European (27)	—— Natl. Capital Area (45)	—— Pittsburgh (75)	—— Southern Wisconsin (92)
—— Chicago (10)	—— Indianapolis (30)	—— North Texas (55)	—— Rocky Mountain (80)	—— Twin Cities (96)
—— Cleveland (15)	—— Japan (33)	—— Oregon (62)	—— San Francisco (85)	—— None (99)
—— Columbus (20)	—— Metropolitan N.Y. (35)	—— Pacific Northwest (65)	—— South Texas (88)	

3. Please indicate your DIVISIONAL and GROUP interests, noting your primary interest(s) with the number 1 and secondary interest(s) with the number 2.

—— Battery (AO)	—— Electronics (EO)	—— Industrial Electrolytic (IO)
—— Corrosion (BO)	☐ New Electronic Technologies (E1)	—— Luminescence and Display Materials (KO)
—— Dielectrics and Insulation (CO)	☐ Semiconductors (E3)	—— Organic and Biological Electrochemistry (FO)
—— Electrodeposition (DO)	—— Energy Technology (GO)	—— Physical Electrochemistry (JO)
	—— High Temperature Materials (HO)	

4. Education:

Institution	Dates Attended	Major Subject	Degree Earned

5. Work Experience:

Name of Employer (current, followed by previous)	Dates	Position

6. The Society's Constitution provides that two Active Members of the Society (who can substantiate the above record) must recommend you for admission to membership. It will facilitate the handling of your application if you are able to have your references sign this application form; if this is not convenient, please list their names and addresses. On a student application, only a single faculty member recommendation with signature (including title and and institution) is required.

Name (please print)	Signature	Address
Name (please print)	Signature	Address

The undersigned certifies that the above statements are correct and agrees, if elected to the Society, to be governed by its Constitution and Bylaws and to promote the objects of the Society as stated in its Constitution.

Date _____ 19 —

_____
(Signature)

Rev. 7/85

EXTRACTS FROM THE CONSTITUTION AND BYLAWS

CONSTITUTION—Article II

Membership

Section 1. The individual membership shall consist of Active, Honorary and Emeritus Members. The Board of Directors may from time to time authorize other classifications of membership as defined in the Bylaws of the Society.

(Active Member—Annual Dues $50.00)

Active Member

Section 2. An Active Member shall be interested in electrochemistry or allied subjects and possess a Bachelor's degree, or its equivalent, in engineering or natural science. In lieu of a Bachelor's degree, or its equivalent, any combination of years of undergraduate study and years of relevant work experience in electrochemistry or allied subjects adding to at least seven years shall be required. Election to Active Membership shall require the recommendation of two Active Members in good standing.

BYLAWS—Article II

Non-Voting Membership
(Student Member—Annual Dues $10.00)

Student Member

Section 1. Student Member. A Student Member shall be a full-time undergraduate or graduate student registered for a degree in natural science or engineering. The applicant for Student Membership shall be recommended by a member of the faculty of the school. Upon graduation with a Bachelor's degree or equivalent in natural science or engineering, the Student Member may apply for Active Membership. The application shall be approved by two Active Members of the Society in good standing. If the Student Member enters graduate school as a full-time student, the person may choose to apply for Active Membership or remain a Student Member.

BYLAWS—Article XXI

Dues and Fees

Dues

Section 1. The annual dues for Active Members shall be fifty dollars. The annual dues for Student Members shall be ten dollars. Each member shall receive the JOURNAL OF THE ELECTROCHEMICAL SOCIETY.

Date of Election

Section 2. When individuals are elected to membership, they must elect to initiate their membership as of January 1 or July 1 of the year of election; or, if elected during the last quarter, January 1 of the year following election. In the case of a July 1 election for starting membership, dues will be prorated.

Active Life Membership

Section 3. Any Active Member who shall pay in one lump sum the amount equivalent to two-thirds of the remaining dues to age sixty-five at the time of payment, but not less than an amount of 5 years of full dues, shall be exempt from payment of any further dues and shall be considered an Active Member during the remainder of his or her life.

Nonmember Meeting Registration Credit

BOARD OF DIRECTORS ACTION OF OCTOBER 9, 1960

If application for new membership is received within four months of the payment of nonmember registration at a Society Meeting by the applicant, the difference between the nonmember and member registration fees shall be credited toward the first year's dues.

CONSTITUTION—Article III

Admission and Dismissal of Members

Section 1. Application for individual membership shall be in writing on a form adopted by the Board of Directors.

Section 2. The Admissions Committee shall be a rotating committee consisting of three members. One member shall be appointed each year by the President with the approval of the Board of Directors for a term of three years to replace the outgoing member. This Committee shall receive from the Secretary all properly executed and properly recommended applications for admission which he has received from persons desirous of becoming members of the Society. It shall be the duty of this Committee, after examining the credentials of applicants, to make appropriate recommendation to the Board as to approval or rejection of the applications. Unanimous approval of an applicant by this Committee shall be required before the candidate's name may be submitted to the Board of Directors for election. The election to membership shall be by a mail vote of the Board of Directors. The candidate shall be considered elected two weeks after the date the proposed membership list is mailed to the Board if no negative votes have been received by the Secretary. If a candidate receives one negative vote, his application shall then be considered and voted upon at the next meeting of the Board of Directors. Two negative votes cast at this meeting shall exclude a candidate. The Board of Directors may refuse to elect a candidate who, in its opinion, is not qualified for membership. The names of those elected shall be announced to the Society. Duly elected candidates shall have all the rights and privileges of membership as soon as their entrance fee, if any, and dues for the current year have been paid.

Section 3. A member desiring to resign shall send a written resignation to the Office of the Society.

Section 4. Upon the written request of ten or more Active Members that, for cause stated therein, a member be dismissed, the Board of Directors shall consider the matter and, if there appears to be sufficient reason, shall advise the accused of the charges against him. He shall then have the right to present a written defense, and to appear in person before a meeting of the Board of Directors, of which meeting he shall receive notice at least twenty days in advance. Not less than two months after such meeting the Board of Directors shall finally consider the case and, if in the opinion of the majority of the Board of Directors a satisfactory defense has not been made and the accused member has not in the meantime tendered his resignation he shall be dismissed from the Society.

Section 7. The entrance fee, if any, annual dues and any other payments to be made by the members of the Society shall be paid in accordance with regulations set forth in the Bylaws.

Section 8. Any member delinquent in dues after April 1 shall not receive the Society's publications and will not be allowed to vote in any Society election until such dues are paid. All members in arrears for one year after April 1 shall lose their membership status and can be reinstated only by action of the Board of Directors.

All members receive a subscription to the Journal of The Electrochemical Society.

Call for Papers
170th Meeting
San Diego, California, October 19-24, 1986

Selected symposium topics and planned General Sessions are described in the following pages.

Procedure for Submitting Papers

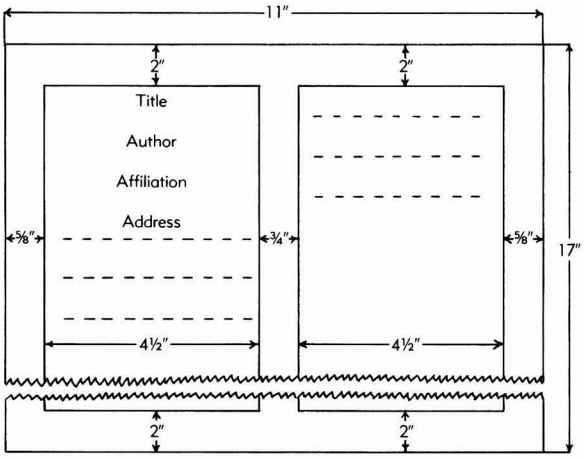
1. Submit one original 75-Word Abstract on the attached form or a facsimile together with one original Extended Abstract to The Electrochemical Society, Inc., 10 South Main St., Pennington, NJ 08534-2896. The deadline for receipt of **both** the 75-Word and Extended Abstract at The Electrochemical Society Headquarters Office is **May 1, 1986.**

2. Send a copy of **both** the 75-Word and Extended Abstract to the appropriate organizing symposium or General Session chairman listed. **No paper will be considered unless both the 75-Word and Extended Abstract are received at Society Headquarters by May 1, 1986. Both abstracts and the oral presentation are required in English.**

Instructions for Preparation of Extended Abstract

1. New Deadline—Extended Abstract must be submitted with the 75-Word Abstract by **May 1, 1986.**

2. All scheduled papers will be published in the EXTENDED ABSTRACTS volume for this meeting. The volume is published photo-offset directly from typewritten copy submitted by the author. The volume will be 7 × 10 in.; therefore, it is essential that the typing be clear and all lettering should be the size of ordinary type or at least 1/16 in. high so that it will be legible after reduction. The EXTENDED ABSTRACTS volume is in a double-column format. Camera-ready typing mats may be obtained from The Electrochemical Society, Inc., 10 South Main St., Pennington, NJ 08534-2896, or you may use any white bond paper 11 × 17 in. The diagram below gives the dimensions of the Extended Abstract form.



A. Use black typewriter ribbon only; type single-spaced.

B. Opaque lacquer may be used for corrections.

C. Type title, author(s), affiliation(s), and address(es) at top of first column (see diagram).

D. Tables and figures must be securely mounted within the margins with rubber cement.

E. Place references and figures after text.

3. The text of the abstract, including references, must not exceed one page (two columns) in length. An additional two columns are permitted for figures, if necessary. Papers exceeding this limit will be returned or rejected.

Mailing Instructions

Mail the original Extended Abstract together with the original 75-Word Abstract to The Electrochemical Society, Inc., 10 South Main St., Pennington, NJ 08534-2896 and a copy to the organizing chairman **for receipt before May 1, 1986.**

Notification of Paper Acceptance

Programming for this meeting will occur in early June. Organizing chairmen will notify those authors whose papers have not been accepted. In early August, a complete packet of program materials, including an Advance Program, will be sent to the presenting authors. Coauthors will receive a meeting packet without an Advance Program.

Manuscript Publication in the JOURNAL OF THE ELECTROCHEMICAL SOCIETY

Upon presentation, all meeting papers become the property of The Electrochemical Society, Inc. However, presentation incurs no obligation to publish. If publication in the JOURNAL OF THE ELECTROCHEMICAL SOCIETY is desired, papers should be submitted as promptly as possible in full manuscript form in order to be considered. "Instructions to Authors" for JOURNAL publication are available from the Society Headquarters office and are published monthly in the JOURNAL. If publication elsewhere is desired after presentation, written permission from Society Headquarters is required.

San Diego, California, Meeting Symposia Plans—Fall 1986
October 19-24, 1986

Extended Abstract must be submitted with the 75-Word Abstract by May 1, 1986

BATTERY

Lithium Battery

Papers on all aspects of lithium batteries are invited for presentation in this symposium. Both the primary and the rechargeable types will be included. Some examples of specific topics are: 1. recent technological developments on the well-known primary lithium systems such as Li/MnO_2, Li/CF_x, Li/SO_2, Li/$SOCl_2$; 2. basic studies to gain new insight into the chemistry and the electrochemistry of the above systems; 3. exploratory studies on couples other than those mentioned above; 4. new developments in lithium rechargeable systems including the systems based on new types of conducting polymers; and 5. new developments in improving the safety of lithium batteries.

Lithium battery papers dealing with electrochemical and thermal modeling will also be included in this symposium.

Publication of a proceedings volume is being considered. Papers published in a proceedings volume may also be submitted to the **Journal**, but must be received no later than 6 months after the date of the symposium at which the paper was presented.

Suggestions and inquiries are solicited and should be sent to the Symposium Chairman: A. N. Dey, DURACELL, Inc., Duracell Research Center, 37 "A" St., Needham, MA 02194.

Stored Hydrogen Batteries

Contributions on any aspect of research, development, and operation of batteries in which hydrogen performs an electrochemical energy storage function are welcome at this symposium.

Sessions on nickel-hydrogen, silver-hydrogen, and regenerative fuel cells are anticipated, as is a session on novel battery systems where electrochemically regenerable hydrogen is used on discharge.

Papers ranging from theoretical to applied aspects of electrode or cell design, fabrication,and behavior are most welcome, as are papers on life and performance of cells and batteries. The symposium will provide a forum for discussion of existing and particularly new applications.

Publication of a proceedings volume is being considered. 75-word and extended abstracts must be submitted by May 1, 1986. Papers published in a proceedings volume may also be submitted to the **Journal**, but must be received no later than 6 months after the date of the symposium at which the paper was presented.

Suggestions and inquiries should be sent to the Symposium Chairman: C. K. Dyer, Bell Communications Research, RM. 1D-335, Murray Hill, NJ 07974.

Sodium-Sulfur Battery

This symposium will provide a forum for discussion of theoretical, basic, and applied research, and of development, application, and commercialization of sodium-sulfur batteries. Papers on all aspects of the sodium-sulfur battery—design, manufacture, modeling, operating characteristics, reliability, and cost—are solicited. In addition, papers on fundamental and applied research on the sodium and sulfur electrodes, on electrolyte manufacture, on performance and characterization, on corrosion, and on other aspects of supporting research such as failure mechanisms are encouraged. Panel discussions are planned.

Publication of a proceedings volume is being considered. Papers published in a proceedings volume may also be submitted to the **Journal**, but must be received no later than 6 months after the date of the symposium at which the paper was presented.

Suggestions and inquiries should be sent to the Symposium Co-Chairmen: A. Landgrebe, Dept. of Energy, Washington, DC 20585; or R. D. Weaver, Electric Power Research Institute, 3412 Hillview Ave., P. O. Box 10412, Palo Alto, CA 94303.

General Session

Papers concerning any aspects of batteries and fuel cells not included in the topic areas of the symposia are welcome.

Suggestions and inquiries should be sent to the Session Chairman: J. S. Wilkes, Seller Research Laboratory, U.S. Air Force Academy, Colorado Springs, CO 80840-6528.

BATTERY/PHYSICAL ELECTROCHEMISTRY

Electrochemical and Thermal Modeling of Battery, Fuel Cell, and Photoenergy Conversion Systems

This symposium will be devoted to recent progress in the engineering modeling of electrochemical energy conversion systems, *i.e.*, batteries, fuel cells, and photovoltaic or photoelectrochemical devices. Papers are invited covering all modeling aspects of engineering analysis and design of these systems. Topics include, but are not limited to: 1. electrode stationary and transient performance models for both battery and gas-diffusion electrodes, including flow-through electrodes; 2. electrode characterization by modeling *in situ* response to stationary operation and modulation of operational variables; 3. wetting and gas-liquid distribution in gas-diffusion electrodes; 4. modeling of structural change in electrodes and of diagnostics for performance decay; 5. performance decay analysis by mathematical modeling; 6. models treating heat-transfer and the interaction of temperature and current distributions in large-scale devices by various numerical techniques; 7. models for the effect of grid or current collector geometry on performance; 8. microcalorimetric analysis of battery performance, self-discharge, and endurance; 9. geometric effects in design and performance of photovoltaic devices; 10. scaling up of batteries, fuel cells, and photovoltaic devices; and 11. general models for the interaction of system design and performance economics.

Papers are invited covering all types of batteries, fuel cells, and photovoltaic and other energy conversion devices. Of special interest are systems currently in use or being developed for commercialization. This includes, but is not limited to: lithium-thionylchloride and other lithium cells, lead-acid, nickel-cadmium, nickel-zinc, zinc-halogen, zinc-redox, sodium-sulfur and lithium alloy-metal sulfide batteries; phosphoric acid, alkaline, molten carbonate and solid oxide fuel cells; and all types of photovoltaic devices with associated electrical storage systems.

A few keynote papers will be invited for review and highlighting of general features of battery, fuel cell, and photovoltaic modeling, and the state of the art in numerical techniques of modeling.

Publication of a proceedings volume which will be available at the time of the meeting is being planned. Manuscripts will be due by May 1, 1986. Papers published in a proceedings volume may also be submitted to the **Journal**, but must be received no later than 6 months after the date of the symposium.

Suggestions and inquiries should be sent to the Symposium Co-Chairmen: J. R. Selman, Dept. of Chemical Engineering, Illinois Institute of Technology, 10 West 33rd St., Chicago, IL 60616; or H. C. Maru, Energy Research Corp., 3 Great Pasture Rd., Danbury, CT 06810.

BATTERY/PHYSICAL ELECTROCHEMISTRY/INDUSTRIAL ELECTROLYTIC

Fuel Cell Electrochemistry and Electrolysis

This symposium will focus on recent advances in electrocatalysis and electrolyte development for fuel cell and electrolysis applications. Advances in the catalysis of low temperature reforming reactions to produce hydrogen are also of great interest. A number of topics will be addressed by invited papers, including the following: electrocatalysis by metals, metal alloys, and organometallic catalysts; low temperature reforming of methanol; direct electrochemical oxidation of methane and methanol; and new electrolytes for fuel cell and electrolysis applications. Papers should deal with the areas of oxygen evolution and reduction, hydrogen evolution and oxidation, direct anodic oxidation of organic molecules, effects of single crystal orientations, the role of catalyst particle size, chemisorption, the catalytic role of UPD species, and techniques for monitoring the structure of the catalyst and the electrode interface. Contributed papers are solicited on all of the above topics.

Suggestions and inquiries should be sent to the Symposium Co-Chairmen: W. E. O'Grady, Brookhaven National Laboratory, Dept. of Applied Science, Upton, NY 11973; or P. N. Ross, University of California, Lawrence Berkeley Laboratory, Materials and Molecular Research Div., Berkeley, CA 94720.

CORROSION

Surfaces, Inhibition, and Passivation Norman Hackerman 75th Birthday Symposium

Papers are invited for this symposium honoring Norman Hackerman in all areas of corrosion science and electrochemistry in which Dr. Hackerman has made outstanding contributions and has provided special insights. Pertinent topics for this symposium include, but are not limited to: the physical chemistry, surface chemistry, or electrochemistry of corrosion processes; adsorption onto metal or oxide surfaces; the electrical double layer; passivation and passive films; and corrosion inhibition.

Publication of a proceedings volume, which will be available at the symposium, is being planned. Camera-ready manuscripts are due on May 1, 1986 (to E. McCafferty, address below); the usual 75-word and extended abstracts are also due on May 1, 1986 to The Electrochemical Society Headquarters. Papers published in a proceeding volume may also be submitted to the **Journal**, but must be received no later than 6 months after the date of the symposium at which the paper was presented.

Detailed instructions on manuscript preparation are available from, and the completed manuscript should be sent to, E. McCafferty.

Suggestions and inquiries should be sent to the Symposium Co-Chairmen: R. Brodd, Amoco Research Center, P. O. Box 400, Naperville, IL 60566; or E. McCafferty, Naval Research Laboratory, Code 6314, Washington, DC 20375-5000.

Corrosion Protection by Organic Coatings

This symposium will provide a forum for presentation and discussion of papers describing fundamental and engineering aspects of the protection of metals by polymer coatings. Papers dealing with the general mechanism of the protection of metals by polymer coatings, mass transport in polymer coatings, surface pretreatment and modification, adhesion, electrochemical and electrophoretic formation of polymer coatings, nondestructive evaluation of polymer-coated metals, innovative accelerated testing, and life prediction of polymer-coated metals are particularly encouraged. Papers that describe the combined use of corrosion inhibitors and pigments, or cathodic protection with polymer coatings are also solicited.

Publication of a proceedings volume is planned. Authors are required to submit a manuscript by the date of the meeting. Detailed instructions on manuscript preparation are available from M. Kendig. Papers published in a proceedings volume may also be submitted to the **Journal**, but must be received no later than 6 months after the date of the symposium at which the paper was presented.

Suggestions and inquiries should be sent to the Symposium Co-Chairmen: M. W. Kendig, Rockwell International Science Center, 1049 Camino dos Rios, Thousand Oaks, CA 91360; or H. Leidheiser, Jr., Center for Surface and Coatings Research, Sinclair Laboratory 7, Lehigh University, Bethlehem, PA 18015.

General Session

Papers on all aspects of low and high temperature corrosion and associated phenomena will be considered. Experimental techniques for the study of corrosion processes and corrosion products are also of interest.

Suggestions and inquiries should be sent to the Session Chairman: E. McCafferty, Naval Research Laboratory, Code 6314, Washington, DC 20375-5000.

CORROSION/HIGH TEMPERATURE MATERIALS

Corrosion of Aerospace Materials

This symposium will address theoretical and experimental aspects of the corrosion of new alloys and structural composites with metal, organic, and ceramic matrices. Papers are solicited on materials appropriate for room temperature and elevated temperature aerospace applications. Corrosion effects observed in aqueous, high temperature oxidation, and sulfidation environments, as well as those specific to low earth orbiting satellites are welcome. Areas of interest include, but are not limited to: 1. fundamental corrosion and stress-corrosion studies; 2. mechanisms of degradation; 3. effects of corrosion on mechanical properties; and 4. new techniques developed and adapted for material evaluation in aerospace environments.

Suggestions and inquiries should be sent to the Symposium Co-Chairmen: S. G. Fishman, Office of Naval Research, Materials Div., 800 North Quincy St., Arlington, VA 22217; or J. R. Pickens, Martin Marietta Laboratories, 1450 South Rolling Rd., Baltimore, MD 21227.

DIELECTRICS AND INSULATION/ELECTRONICS

Isolation and Trench Technology

This symposium will address all aspects of semiconductor isolation as well as related technologies involving trench integration into device structures. In particular, both theoretical and experimental papers are solicited in the following areas: 1. isolation processes and improvements thereon; 2. trench structures in integrated device applications; 3. modeling of grown or deposited oxide isolation, trench isolation, and trench structures for capacitance; 4. improved materials and process capability for isolation (e.g., high pressure oxidation, plasma oxidation, CVD improvements, etc.); 5. methods and results of the characterization of isolation and trench structures; and 6. reliability and yield issues with isolation and trench structures.

Publication of a proceedings volume is being considered. Papers for this volume must be provided, in a camera-ready form, at the time of the presentation. Papers published in a proceedings volume may also be submitted to the **Journal**, but must be received no later than 6 months after the date of the symposium at which the paper was presented.

Suggestions and inquiries should be sent to the Symposium Co-Chairmen: J. L. Mauer, 11-261, IBM Research, Yorktown Heights, NY 10598; or B. Kemlage, B330-81E, IBM East Fishkill, Hopewell Junction, NY 12533.

Sixth Symposium on Plasma Processing

Speakers have been invited to present papers on the following topics: etching, deposition, electrical and spectroscopic diagnostics, modeling, damage and surface modification, fundamentals of plasma/surface interactions, and new directions in dry processing.

Contributed papers on these and related topics are solicited. Contributors should specify their preference for a poster presentation or for an oral presentation of their papers. All efforts will be made to accommodate requests.

Please note that a separate symposium on Silicon Nitride and Silicon Oxide is planned for this meeting.

All abstracts (both 75-word and extended) must be sent both to the The Electrochemical Society and to G. C. Schwartz, IBM East Fishkill, Zip 48A, Rt. 52, Hopewell Junction, NY 12533.

A proceedings volume of the symposium will be published and distributed shortly after the meeting. Acceptance of a paper for presentation at the meeting obligates the authors to submit a typed camera-ready copy of the paper, including a list of key words for the subject index, by November 24, 1986. Instructions for preparation and submission of the camera-ready copy of the paper will be mailed to the authors with the notification of acceptance of a paper. Papers published in a proceedings volume may also be submitted to the **Journal**, but must be received no later than 6 months after the date of the symposium at which the paper was presented.

Suggestions and inquiries should be sent to the Symposium Co-Chairmen: R. A. Gottscho, AT&T Bell Laboratories, Rm. 7A-321, Murray Hill, NJ 07974; G. S. Mathad, IBM East Fishkill, Zip 40E, Hopewell Junction, NY 12533; or G. C. Schwartz, IBM East Fishkill, Zip 48A, Hopewell Junction, NY 12533.

Sixth Symposium on Plasma Processing Recent News Papers Session

Recent News Papers and Extended Recent News Papers are invited for the Sixth Symposium on Plasma Processing.

A special call for Recent News Papers will appear in the June, July, and August 1986 issues of the JOURNAL.

Copies of all abstracts should be sent to the Session Chairman: G. C. Schwartz, IBM East Fishkill, Zip 48A, Hopewell Junction, NY 12533.

Multilevel Metallization Interconnection and Contact Technologies

Papers are solicited on all aspects of multilevel metallization, interconnections, and contacts for both semiconductor and packaging technologies. Areas of interest are processes for high performance wiring, the effects of multilevel wiring on design and wireability, yield and reliability issues, and modeling and analysis. Some suggested topics are: 1. contact and conductor metals; 2. deposition conditions; 3. patterning techniques; 4. insulator technologies; 5. planarization processes; 6. electrical characterization; 7. geometry considerations.

Publication of a proceedings volume is being considered. Papers published in a proceedings volume may also be submitted to the **Journal**, but must be received no later than 6 months after the date of the symposium at which the paper was presented.

Suggestions and inquiries should be sent to the Symposium Co-Chairmen: L. B. Rothman, IBM Corp., Bldg. 330, Zip T-82, Hopewell Junction, NY 12533; T. Herndon, MIT Lincoln Laboratories, Rm. B-161, Lexington, MA 02173; or D. V. McCaughan, Marconi Electronic Devices, Lincoln Industrial Park, Doddington, Rd., Lincoln, England LN6 3LF.

DIELECTRICS AND INSULATION/ELECTRONICS/HIGH TEMPERATURE MATERIALS

Silicon Nitride and Silicon Dioxide Thin Insulating Films

The purpose of this symposium is to provide a forum for the presentation and discussion of topics concerning the fundamental characteristics of silicon nitride and silicon dioxide films. The objective is to link material studies and technological application to allow for clearer design and design processing considerations for the fabrication of devices and integrated circuits (LSI/VLSI) which incorporate silicon nitride and silicon dioxide films. The symposium will include both invited and contributed papers covering a wide range of topics related to silicon nitride and silicon dioxide including film preparation, characterization, modeling, processing, device physics, present applications, and future requirements of the insulators in VLSI and VHSIC.

Both experimental and theoretical contributed papers are solicited from the following general areas: 1. film preparation (CVD, LPCVD, plasma, ion implantation, sputtering, thermal nitridation, thermal oxidation, etc.); 2. film and film/substrate interface analysis by RBS, AES, XPS, SIMS, and other new and novel analysis techniques; 3. charge trapping, characteristics and origin of traps, and role of interface states; 4. defects and impurities and their effects on electronic processes for solid-state devices and circuits; 5. optical and electrical properties, electronic structure, tunneling phenomena, charge transport, and dielectric breakdown; 6. silicon nitride/silicon dioxide dual dielectrics and interfaces; 7. silicon dioxide and/or silicon nitride films for nonvolatile semiconductor memories (write/erase characteristics, retention, endurance, temperature effects, aging, modeling, reliability, and radiation hardness); 8. films for multilayer-metal IC's and for potential use in VLSI; 9. insulating films on compound semiconductors (passivation studies, interfaces, electrical and optical properties of devices); 10. plasma science and plasma processing technology for silicon nitride and silicon dioxide films; and 11. quality verification, environmental effects, new applications, and new devices.

As part of this symposium, a special one-day mini-symposium titled "Mechanisms and Kinetics for Growth of Thin Thermal SiO_2," is planned. All papers will be invited and will include various proposed kinetic models and mechanisms for the thermal oxidation of silicon in dry oxygen over the thickness range 0-300Å, which is not adequately described by the Deal-Grove general oxidation relationship. For further information, contact B. E. Deal, Fairchild Research Center, 4001 Miranda Ave., Palo Alto, CA 94304; or C. R. Helms, Electronics Laboratories, Stanford University, Stanford, CA 94305.

Publication of proceedings volume is being considered. Papers for this volume must be provided, in a camera-ready copy form, at the time of presentation. Papers published in a proceedings volume may also be submitted to the **Journal**, but must be received no later than 6 months after the date of the symposium at which the paper was presented.

Suggestions and inquiries should be sent to the Symposium Co-Chairmen: V. J. Kapoor, Dept. of Electrical and Computer Engineering, ML No. 30, University of Cincinnati, Cincinnati, OH 45221; R. A. Turi, NCR Corp., 8181 Byers Rd., Miamisburg, OH 45342; T. A. Dellin, Sandia National Laboratories, P.O. Box 5800, Albuquerque, NM 87185; or K. T. Hankins, Harris Corp., P.O. Box 883, Melbourne, FL 32901.

ELECTRODEPOSITION

Electrodeposition Technology, Theory and Practice

This symposium will review the state of the art of the field of electrodeposition in various industries, and will cover plating of individual metals and metal alloys. It will include theory and practice of plating solutions, mechanism of deposition, deposition techniques, cell design, modeling of film growth and plating cells, and automation technology for plating. This symposium will consist primarily of tutorials and a selected number of contributed papers.

Publication of a proceedings volume is being considered. Camera-ready manuscripts for the proceedings volume are due at the time of paper presentation. Papers published in a proceedings volume may also be submitted to the **Journal**, but must be received no later than 6 months after the date of the symposium at which the paper was presented.

Suggestions and inquiries should be sent to the Symposium Co-Chairmen: L. T. Romankiw, IBM T. J. Watson Research Center, P.O. Box 218, Yorktown Heights, NY 10598; or D. R. Turner, 59 Susan Dr., Chatham, NJ 07928.

General Session

Papers are solicited in the area of theoretical and experimental investigations and applications involving electrodeposition, electrophoretic deposition, anodic dissolution, anodization and etching, electrochemical engineering (including plating equipment), and plant design and operation.

Suggestions and inquiries should be sent to the Session Chairman: T. C. Franklin, Dept. of Chemistry, Baylor University, Waco, TX 76798.

ELECTRODEPOSITION/PHYSICAL ELECTROCHEMISTRY

Electrosolidification

Electrocrystallization as well as the fundamentals of other redox-mediated transitions involving condensed phases are subjects for which papers are solicited. Suitable topics for the symposium include the formation of metallic, compound-inorganic and organic materials, their structures, properties, and transformations, and the experimental techniques for investigating them. The involved kinetics including stochastic processes and the development of fractal structures are also welcome topics. Papers involving the modeling of the above processes are also solicited.

Publication of a proceedings volume is being considered. Papers published in a proceedings volume may also be submitted to the **Journal**, but must be received no later than 6 months after the date of the symposium at which the paper was presented.

Suggestions and inquiries should be sent to the Symposium Co-Chairmen: R. Weil, Dept. of Materials and Metallurgical Engineering, Stevens Institute of Technology, Hoboken, NJ 07030; or J. D. Porter, AT&T Bell Laboratories, Rm. 6E-307, Murray Hill, NJ 07974.

ELECTRONICS

Entrepreneurship in the Semiconductor Industry

This symposium is the third in a series on the business aspects of the electronics industry and will focus on the role of the entrepreneur in the development of the electronics business. It will be comprised entirely of invited papers.

Silicon Valley and Route 128 have become home to a multitude of new dynamic, high technology, electronically oriented, start-up companies. Some have grown to industry giants; others have gone belly up and passed into obscurity. The speakers at this symposium will described factors that contribute to both outcomes.

Suggestions and inquiries should be sent to the Symposium Chairman: F. J. Strieter, 7814 Fallmeadow Ln., Dallas, TX 75248.

ELECTRONICS/DIELECTRICS AND INSULATION

Second Symposium on Automated IC Manufacturing (AIM II)

This symposium will focus on all aspects of automation related to front-end IC fabrication and manufacture. In this context, the phrase "automation" is meant to imply computer control of equipment, mechanized/automated material handling, computer network architecture for equipment communication/control, IC factory planning and logistics, in-process monitoring, and data collection and analysis. "Front-end IC fabrication and manufacture," means those operations involved in the development, prototyping, and volume manufacturing of IC circuits in the "cleanroom."

Original technical work or substantial review papers are solicited. A plenary session with invited presentations by industry and university leaders in the field of IC fabrication automation is also being planned for this symposium.

Papers are solicited for the following sessions and topics: 1. CAM systems architecture and network, information systems for wafer/lot tracking, and process and operations management and control; 2. IC factory modeling, simulation, and capacity planning systems, on-line lot/batch dispatching and scheduling systems; 3. chemical and wafer/cassette handling in the lab, with emphasis on cleanliness, reliability, flexibility, and maintainability of such systems; the impact of such systems on clean room design; 4. contamination detection sensors and systems for particles, organics, etc., contamination detection and monitoring procedures, personnel and garment requirements and control, electrostatic, ionic and radiation-induced "contamination"; 5. interface to equipment for process control and data collection and local, real-time data reduction and feedforward control; and 6. engineering data collection, analysis, and correlation, and engineering feedback and process feed-forward.

Publication of a proceedings volume is being considered. Papers published in a proceedings volume may also be submitted to the **Journal**, but must be received no later than 6 months after the date of the symposium at which the paper was presented.

Suggestions and inquiries should be sent to the Symposium Co-Chairmen: M. Parikh, Asyst Technologies, 46309 Warm Springs Blvd., Fremont, CA 94539; V. Akins, CTX International, 3821 East Broadway Rd., Suite 8, Phoenix, AZ 85040; or R. Miller, IBM T. J. Watson Research Center, Yorktown Heights, NY 10598.

Ion Implantation of Compound Semiconductors

This symposium will address those areas of ion implantation in compounds which are of paramount importance to the electronic device fabrication. Papers are solicited dealing with fundamental issues of defects, impurity migration and activation, encapsulation and annealing, transient processing, range distributions, recoil effects, and related problems. Papers dealing with more specific device applications of ion implantation in compounds are also welcome. Methods for monitoring and analyzing the effects of ion implantation and annealing will be included, with special emphasis on promising new techniques for characterizing implanted layers in a device-fabrication environment. Papers are solicited dealing with the applications of ion implantation in multilayer heterostructures. This subject will include basic studies of layer mixing, effects of implantation damage and annealing on interfaces, special effects in stained-layer superlattices and related issues. Device applications of implantation in multilayers will be included, with the emphasis on special effects arising from the ion implantation. New types of implantation procedures, such as combinations of implantation with MBE growth, are welcomed.

Publication of a proceedings volume is being considered. Manuscripts, in camera-ready form, will be required at the time of the meeting. Details of manuscript preparation will be provided with the acceptance of abstracts. Papers published in a proceedings volume may also be submitted to the **Journal**, but must be received no later than 6 months after the date of the symposium at which the paper was presented.

Suggestions and inquiries should be sent to the Symposium Co-Chairmen: B. Schwartz, AT&T Bell Laboratories, Rm. 2C-314, Murray Hill, NJ 07974; or B. G. Streetman, Dept. of Electrical and Computer Engineering, University of Texas, Austin, TX 78712.

Process Physics and Modeling in Semiconductor Technology

This symposium is intended to provide a forum for presenting modeling research in various semiconductor integrated circuit process technologies. The symposium focuses on both the mechanistic (physical modeling) and numerical (simulation) aspects of process modeling. Papers are solicited on the recent developments in IC process and technology modeling. Specifically, the following topics are included: ion implantation, channeling theory, diffusion, defect-diffusion interactions, kinetics of oxide growth, chemical vapor deposition, doping and autodoping in epitaxial growth, rapid thermal annealing of defects, etching and deposition, gettering, metal-silicide reaction kinetics, lithography, and pattern transfer. Emphasis is placed on the physical understanding of the processes, as well as numerical treatments such as finite elements, Monte Carlo techniques, etc.

Publication of a proceedings volume is being considered. Authors of accepted papers will be asked to submit camera-ready copies of the manuscript, which will be reviewed. Papers published in a proceedings volume may also be submitted to the **Journal**, but must be received no later than 6 months after the date of the symposium at which the paper was presented.

Suggestions and inquiries should be sent to the Symposium Co-Chairmen: G. R. Srinivasan, IBM East Fishkill Laboratory, Zip 37A, Hopewell Junction, NY 12533; J. Plummer, McCullough 114, Integrated Circuits Laboratory, Stanford University, Stanford, CA 94305; or D. Antoniadis, Massachusetts Institute of Technology, Rm. 39-227, Cambridge, MA 02139.

Joint General Session

Papers are solicited on all aspects of electronic materials and processng technologies except those covered by the special symposia. Topics of interest include: electronic materials preparation, characterization, interactions, and device applications; basic chemistry and physics of materials and device processing; process and device modeling; sensor technology; and computer-aided manufacturing of electron devices and integrated circuits. Of particular interest are new or novel materials and processes.

Suggestions and inquiries should be sent to the Session Co-Chairmen: W. M. Bullis, Siltec Silicon, 423 National Ave., Mountain View, CA 94043; G. C. Schwartz, IBM Corp., Dept. 206, Bldg. 300-48A, Hopewell Junction, NY 12533; or H. R. Huff, Monsanto Electronic Materials Co., P.O. Box 10123, Palo Alto, CA 94303.

Joint Recent News Papers Session

Recent News Papers and Extended Recent News Papers consisting of topics covered by the symposia and sessions being sponsored or co-sponsored by the Electronics and Dielectrics and Insulation Divisions are invited for presentation.

A special call for Recent News Papers will appear in the June, July, and August 1986 issues of the **Journal**.

Suggestions and inquiries should be sent to the Session Chairman: G. C. Schwartz, IBM Corp., Dept. 206, Bldg. 300-48A, Hopewell Junction, NY 12533.

ELECTRONICS/DIELECTRICS AND INSULATION

State-of-the-Art Program on Compound Semiconductors (SOTAPOCS V)

This is the fifth of a new series of special symposia intended to provide a forum for the presentation and discussion of the latest developments in areas involving compound semiconductor processing. Original papers and reviews dealing with all aspects of compound semiconductors are solicited for this program. In recognition of the interdependence between materials properties, fabrication processes and device characteristics, papers which correlate these topics for high speed, microwave, millimeter wave, photonic, optoelectronics, and sensing devices (discrete and integrated circuits) are welcome.

Of particular interest are papers in the following general areas: materials growth technologies; gate and interconnect technologies, fine feature patterning: lithography, etching, plasma process; ion implantation/capping/annealing; dielectrics/passivation; surface/interface effects; metal-semiconductor interactions—Schottky barriers, ohmic contacts; radiation effects; via formation/packaging techniques; field limiting effects; manufacturing trends/status.

The symposia are also aimed at providing a forum for synergistic interactions between those working in compound semiconductors and those involved in silicon technologies.

To ensure the timely nature of the SOTAPOCS V effort, a special deadline has been set. Abstracts will be accepted until July 1, 1986. The standard 75-word Electrochemical Society abstract (refer to form in this Call for Papers) is sufficient for paper presentation at SOTAPOCS V. There is no need to submit an Extended Abstract.

Abstracts, suggestions, and inquiries should be sent to the Symposium Co-Chairmen: A. D. M. Chen, General Electric Co., Electronics Laboratory, Syracuse, NY 13221; C. E. Weitzel, Motorola, Inc., Semiconductor R&D Laboratory, Phoenix, AZ 85008; or R. E. Enstrom, RCA Laboratories, Princeton, NJ 08540.

ELECTRONICS/LUMINESCENCE AND DISPLAY MATERIALS

Microstructured Sensors

This symposium covers the emerging field of microstructured sensors. This covers fabrication, device design, reliability, and stability for two- and three-dimensional structures pertaining to all sensor technologies. Work in all aspects including theoretical, experimental, and state-of-the-art applications are within the scope of this symposium. Papers on micromechanical structures, electronic and optical devices in single component or array format for biological, industrial, and military applications are solicited.

Publication of a proceedings volume is being considered jointly with the "Robotics for Use in Manufacturing Devices" and "Sensors for Robot Applications" symposia. Papers published in a proceedings volume may also be submitted to the **Journal**, but must be received no later than 6 months after the date of the symposium at which the paper was presented.

Suggestions and inquiries should be sent to the Symposium Co-Chairmen: H. H. Busta, Gould Research Center, 40 Gould Center, Rolling Meadows, IL 60008; or S. C. Pyke, SOHIO Research Center, 4440 Warrensville Center Rd., Cleveland, OH 44128.

ENERGY TECHNOLOGY

Electrolyte Management in Electrochemical Energy Systems

Proper management of electrolyte is very important for attaining maximum possible energy output and longevity. The purpose of this symposium is to provide a common forum to bring out various approaches being utilized in different systems. Topics of interest include, but are not limited to: 1. optimization of amount of electrolyte, composition and additives to minimize ohmic, activation, and diffusion polarizations; 2. flow and transport characteristics and concentration profiles of electrolyte under steady-state and transient operating conditions; 3. estimation of electrolyte redistribution, loss, or degradation at operating conditions and approaches to minimize the same; 4. approaches for impregnation, storage, and replenishment of electrolyte; 5. approaches for minimizing shunt currents or secondary currents, resulting from electrolyte films in inactive areas and liquid manifolds; and 6. capillary balance of electrolyte in various porous components, and electrolyte/electrode interface considerations.

Electrochemical systems with electrolyte pool, fixed electrolyte, flow systems and solid electrolyte are expected to be covered in this symposium.

Suggestions and inquiries should be sent to the Symposium Co-Chairmen: H. C. Maru or M. Klein, Energy Research Corp., 3 Great Pasture Rd., Danbury, CT 06810.

General Session

Papers are solicited on the fundamental and applied aspects of energy conversion, storage, and transmission not covered by current symposia. Of particular interest are new developments in photoelectrochemistry and novel methods for energy storage, conversion, and transmission. Papers on the application of electrochemistry for environmental cleanup are also welcome.

Suggestions and inquiries should be sent to the Session Co-Chairmen: D. S. Ginley, Sandia National Laboratories, Div. 1154, Albuquerque, NM 87185; or V. Jalan, Giner, Inc., 14 Spring St., Waltham, MA 02154.

ENERGY TECHNOLOGY/BATTERY

Protonic and Hydroxyl Electrolytes for Use in Electrochemical Devices

This symposium will be devoted to papers that focus on new types of protonic and hydroxyl electrolytes and novel electrochemical applications of same. Relevant topics include new H^+ and OH^- electrolytes for fuel cells, batteries, electrodeposition, sensors, electrophoresis, etc. Both solid and liquid electrolytes are to be covered. Subject matter will cover a range of topics, including preparation characterization, physical aspects, and applications.

Publication of a proceedings volume is being considered. Papers published in a proceedings volume may also be submitted to the **Journal**, but must be received no later than 6 months after the symposium at which the paper was presented.

Suggestions and inquiries should be sent to the Symposium Co-Chairmen: E. Findl, 15730 Hartsook St., Encino, CA 91436; or C. R. Martin, Dept. of Chemistry, Texas A&M University, College Station, TX 77843.

ENERGY TECHNOLOGY/PHYSICAL ELECTROCHEMISTRY

Semiconductor-Electrolyte Interfaces

This symposium will address the chemistry, electrochemistry, and physics of semiconductor-electrolyte interfaces. Invited are papers treating the relationship between the interfacial chemistry and carrier recombination; charge transport or corrosion behavior; localization effects on charge transport; photoetching of semiconductors; photoelectrochemical solar cells; nonsolar applications, such as in chemical sensors, electronic and other possible industrial applications; photoelectrochemistry on semiconducting powders; electroluminescence at semiconductor-electrolyte contacts; electrocatalysis and surface modifications of semiconductor electrodes.

Suggestions and inquiries should be sent to the Symposium Co-Chairmen: M. Tomkiewicz, Dept. of Physics, Brooklyn College of CUNY, Brooklyn, NY 11210; or A. B. Ellis, Dept. of Chemistry, University of Wisconsin, Madison, WI 53706.

HIGH TEMPERATURE MATERIALS/CORROSION/ DIELECTRICS AND INSULATION/ ELECTRODEPOSITION

Protective Coatings at Elevated Temperatures

This symposium will address the fundamental and applied aspects of coatings for high temperature applications. Presentations on ceramic as well as metallic coatings are solicited. Review papers outlining recent progress in the several fields of high temperature coatings are planned for the different sessions. Areas of interest include, but are not limited to: 1. fabrication techniques, including plasma spraying, chemical and physical vapor deposition, pack cementation, and electrodeposition; 2. degradation mechanisms including substrate/coating interactions, oxidation, erosion, and hot corrosion; 3. effects of coatings on the mechanical properties of the substrate/coating system; and 4. the role of coatings in fiber-reinforced composites.

Suggestions and inquiries should be sent to the Symposium Co-Chairmen: R. L. Jones, Naval Research Laboratory, Code 6170, 4555 Overlook Ave. SE, Washington, DC 20375-5000; or K. L. Luthra, General Electric Co., Corporate Research and Development, 3B6, K1, Schenectady, NY 12301.

INDUSTRIAL ELECTROLYTIC/HIGH TEMPERATURE MATERIALS

Industrial Electrolysis of Fused Salts

This symposium will bring together scientists who are concerned with research, development, and operation of a variety of industrial fused salt processes and will commemorate the 100th anniversary of the invention by Hall and Heroult that led to our present industrial aluminum electrolysis. There will be particular emphasis on the synergy among discoveries, modeling, and prediction arising from laboratory research and the reaffirmation or impact of this work in industrial cells.

A commemorative session will include presentations on the history, the state of the art, and the future of the Hall-Heroult process, as well as reports on current research and development efforts.

For a general session, papers are solicited on topics concerned with other industrial fused salt processes, including the extraction of other metals.

A special session will focus on materials aspects, the development of materials often being the key for progressing development in fused salt processes. Contributions on the electrochemical and refractory aspects of materials essential to light metal extraction and other processes are invited, particularly discussions on methods to determine the stability of materials and the electrochemistry of advanced electrode materials.

Publication of a proceedings volume is being considered. Papers published in a proceedings volume may also be submitted to the **Journal**, but must be received no later than 6 months after the date of the symposium at which the paper was presented.

Suggestions and inquiries should be sent to the Symposium Co-Chairmen: R. Keller, R.D. 3, Roundtop Rd., Export, PA 15632; N. E. Richards, Reynolds Metals Co., P.O. Box 1200, Sheffield, AL 35660; or K. H. Stern, Naval Research Laboratory, Code 6170, Washington, DC 20375.

LUMINESCENCE AND DISPLAY MATERIALS

Physics and Chemistry of Lamp Phosphors

Papers are invited for this symposium on any aspect of lamp phosphor physics and chemistry. Examples of desired topics include new phosphors; studies of absorption, energy transfer, and emission properties as influenced by chemical composition or preparation procedure; properties of luminescent single crystals of lamp phosphors; mechanisms of and experimental searches for multiple-photon emission processes; studies of the influence of synthesis procedures on phosphor properties; studies of efficiency and of nonradiative processes influencing efficiency; studies of maintenance mechanisms.

Suggestions and inquiries should be sent to the Symposium Co-Chairmen: W. A. McAllister, N. A. Philips Lighting Center, Dept. 8006, 1 Westinghouse Plaza, Bloomfield, NJ 07003; T. E. Peters, GTE Laboratories, 40 Sylvan Rd., Waltham, MA 02254; or W. H. White, Pennsylvania State University, College Park, PA 16802.

Lamp Manufacture and Performance

Papers are invited for this symposium on any lamp type that incorporates luminescent materials, such as linear, compact, or folded lamps and suitable high intensity discharge lamps. Pertinent topics include lamp design and processing characteristics such as phosphor selection criteria (color, CRI, particle size, etc.), multiple coatings, and barrier coatings. Papers are also invited on shape, electrical design and processing steps, to the extent that they interact with lamp performance and/or selection of luminescent materials.

Suggestions and inquiries should be sent to the Symposium Co-Chairmen: M. V. Hoffman, General Electric Co., Nela Park, Cleveland, OH 44112; or E. A. Dale, GTE Lighting Center, 100 Endicott St., Danvers, MA 01923.

Light Modulation in Optical Information Processing

The purpose of this symposium is to establish a forum for the discussion and review of recent developments in optical processing, including the generation modulation, deflection, and scattering of light. This symposium will cover both materials and device research and technology. With respect to materials, papers are solicited on, *e.g.*, the theory of and physical origins of optical nonlinearities and other materials characteristics useful for optical processing devices, limitations to device performance due to fundamental materials properties, technological difficulties encountered in the growth of optically active materials and in processing these materials into devices, new materials with enhanced or different optical properties—including new organic polymers—and novel structures such as multilayer quantum well structures, and materials suitable for them. With respect to devices, papers are solicited on spatial light modulators, bistable optical devices, volume holographic optical elements, integrated optics waveguides, laser deflection systems, storage technology, and any novel optical modulation device concepts. Pertinent review talks are planned.

Suggestions and inquiries should be sent to the Symposium Co-Chairmen: J. M. Flaherty, W. J. Shafer Associates, Corporate Pl., 128, Bldg. 2, Suite 300, Wakefield, MA 01880; or T. Soules, General Electric Co., Nela Park, Cleveland, OH 44121.

X-Ray Imaging

We invite papers for this symposium on all topics of interest in x-ray imaging. Representative topics include: new x-ray phosphors, their preparation and characterization; surface treatment of x-ray phosphors, x-ray intensifying screen structures and their fabrication; new binder systems; film-screen systems including dyes, pigments, and special substrates; absorption efficiency, persistence or lag; phosphor screen evaluation including MTF, sharpness, and noise; phosphor conversion efficiency and the loss mechanisms; scintillation spectroscopy; time-resolved spectroscopy with x-ray sources; photodiode systems; image processing; filmless radiography; digital radiography, thermoluminescence after x-ray irradiation; optically stimulated luminescence and storage phosphors and panels; phosphor stabilization through screen design, additives, and resins, the use of x-ray phosphors in nondestructive testing; and dual energy techniques.

Suggestion and inquiries should be sent to the Symposium Co-Chairmen: L. Brixner, E. I. du Pont de Nemours and Company, Experimental Sta. 356-339, Wilmington, DE 19898; S. Larach, RCA Laboratories, Princeton, NJ 08540; or M. Tecotzky, DigiRad Corp., 1047 Elwell Ct., Palo Alto, CA 94303.

Picosecond and Faster Phenomena in Luminescence

This symposium will address topics concerning ultrafast luminescent phenomena. Original work and substantial review papers in this area are solicited. Representative topics are studies of ultrafast phenomena in luminescence, absorption, or Raman spectroscopies; the generation and characterization of fast light pulses; and studies of picosecond processes in solids, semiconductors, dielectrics, magnetic materials, or ions in crystals.

Suggestions and inquiries should be sent to the Symposium Co-Chairmen: R. R. Alfano, Institute for Ultrafast Spectroscopy and Lasers, City College, City University of New York, New York, NY 10031; or H. G. Brittain, Dept. of Chemistry, Seton Hall University, South Orange, NJ 07079.

General Session

The general session covers all topics of luminescence and display materials cited in our scope of interests, except those covered by specific symposia at this meeting. Representative topics include: the physics and chemistry of phosphors; inorganic, organic, and organometallic phosphors; lasers; thermoluminescence; chemiluminescence; luminescence of biological materials; and molecular spectroscopy.

Suggestions and inquiries should be sent to the Session Co-Chairmen: P. Toch, Raytheon Co., New Products Center, Foundry Ave., Waltham, MA 02254; or S. S. Trond, RCA Corp., New Holland Ave., Lancaster, PA 17604.

Recent News Papers Session

Recent News Papers and Extended Recent News Papers consisting of topics covered by the symposia and sessions being sponsored or co-sponsored by the Luminescence and Display Materials Group are invited for presentation.

A special call for Recent News Papers will appear in the June, July, and August 1986 issues of the **Journal**.

Suggestions and inquiries should be sent to the Session Chairman: T. E. Peters, GTE Laboratories, 40 Sylvan Rd., Waltham, MA 02254.

LUMINESCENCE AND DISPLAY MATERIALS/DIELECTRICS AND INSULATION

Materials and Fabrication Techniques for Display Devices

This symposium, like its predecessors in the Fall meetings in 1976 and 1983, focuses both on the material breakthroughs which allow new display devices and the improvements in fabrication or manufacturing techniques which allow new display technologies. There will be review papers on current technologies and invited papers by recognized experts in the various subtopics. Contributed papers are solicited in topics such as: 1. liquid crystal display technology (liquid crystal materials, bistable effects, LCD device fabrication techniques such as alignment, packaging, backlighting, color filtering, etc.); 2. active matrix addressed displays (active matrix materials, thin film transistors, semiconductor and gate insulator materials and fabrication methods, their characterization and failure mechanisms, TFT performance characteristics, other active elements, etc.); 3. electroluminescent displays (materials, multicolor displays and fabrication techniques such as passivation, light absorbing black layer, etc.); 4. CRT technology (color phosphor materials, shadow mask metallurgy and fabrication, cathodes, contrast enhancement materials, and antireflection thin films); 5. vacuum fluorescent displays (fabrication techniques, low voltage color phosphors, and deposition methods); 6. electrochemical displays (electrophoretic, electrochemichromic, and electrochemiluminescent display devices; their fabrication and packaging techniques); 7. phosphors (phosphors for various display applications, their synthesis and characterization, their degradation mechanisms); 8. any new material, property, or fabrication technique which may have applicability in future devices or technologies. Papers are solicited that deal with either the fundamental aspects or the applications of robots in semiconductor materials processing and device fabrication, and electronic parts assembly.

Publication of a proceedings volume is being considered. Papers published in a proceedings volume may also be submitted to the **Journal,** but must be received no later than 6 months after the symposium at which the paper was presented.

Suggestions on paper submissions and invited papers and other inquiries should be sent to the Symposium Co-Chairmen: I. F. Chang, Institute of Systems Science, National University of Singapore, Heng Mui Keng Terrace, Kent Ridge, Singapore 0511; or C. C. Wang, RCA Laboratories, Princeton, NJ 08540.

LUMINESCENCE AND DISPLAY MATERIALS/ELECTRONICS

Sensors for Robot Applications

This symposium covers the promise and the problems in the emerging field of robotic sensors, particularly the recent advances in vision, touch, motion, and adaptive sensors needed for robots. Work on all aspects, including theoretical, experimental, and state-of-the-art applications of sensors to robots are desired. Special emphasis will be placed on devices and systems. Papers are solicited that treat the applications to robotics of: sensors for electromagnetic radiation; biological sensors; electro-optic sensors; magneto-optic sensors; velocity, acceleration, and motion sensors; pressure and force sensors; robotic vision arrays; electrochemical sensors; sensor signal processing and novel and adaptive sensors.

Publication of a proceedings volume is being considered jointly with the "Robotics for Use in Manufacturing Devices" and "Microstructured Sensors" symposia. Papers published in a proceedings volume may also be submitted to the **Journal,** but must be recevied no later than 6 months after the symposium at which the paper was presented.

Suggestions and inquiries should be sent to the Symposium Co-Chairmen: J. Masi, Dept. of Electrical Engineering, Western New England College, Springfield, MA 01119; and G. Beni, Dept. of Electrical and Computer Engineering, University of California, Santa Barbara, CA 93106.

LUMINESCENCE AND DISPLAY MATERIALS/ELECTRONICS/NEW TECHNOLOGY SUBCOMMITTEE

Robotics for Use in Manufacture of Electronic Devices

Future plans in wafer fabrication processing and device assembly include automation systems that will reduce total system operating costs while providing repeatability and increased output. This session is on the application of robots in this high technology environment. As electronic devices decrease in size and increase in complexity, they become more difficult to handle. The use of computer-controlled mechanics with sensory feedback and some level of program adaptability (*i.e.,* of robots) becomes more important. The robot system has to be integrated into an in-line process, often in a cleanroom environment. Fundamental problems exist in monitoring materials processing, precision handling, inspection and testing, and assembly and packaging. The robot system must therefore be clean, precise, and intelligent. Possible applications include the automation of process control in a fabrication sequence, material handling both within and between work stations, and assembly and packaging of the completed devices. System integration is also an extremely important issue. Papers are solicited that deal with either the fundamental aspects or the applications of robots in semiconductor materials processing and device fabrication, and electronic parts assembly.

Publication of a proceedings volume is being considered jointly with the "Sensors for Robot Applications" and "Microstructured Sensors" symposia. Papers published in a proceedings volume may also be submitted to the **Journal,** but must be recieved no later than 6 months after the symposium at which the paper was presented.

Suggestions and inquiries should be sent to the Symposium Co-Chairmen: S. Hackwood, Dept. of Electrical and Computer Engineering, University of California, Santa Barbara, CA 93106; or D. L. Nelson, Office of Naval Research, Chemistry Div. (413), 800 North Quincy St., Arlington, VA 22217-5000.

PHYSICAL ELECTROCHEMISTRY

General Session

Papers concerning any aspect of physical electrochemisty not included in the topic areas of symposia at this meeting are welcome.

Suggestions and inquiries should be sent to the Session Chairman: B. Miller, AT&T Bell Laboratories, Rm. 1D-350, Murray Hill, NJ 07974.

PHYSICAL ELECTROCHEMISTRY/HIGH TEMPERATURE MATERIALS/BATTERY

Solid Electrolytes

This symposium covers the fundamental properties of new solid electrolyte materials as well as the application of solid electrolytes in practical electrochemical devices. Papers are solicited on the following or related topics: enhanced ionic transport in glasses and polymers at ambient temperatures and the resulting influence upon the performance of solid electrolyte cells, batteries, sensors and display devices; degradation and stability of solid electrolytes, including both bulk phenomena and interfacial effects; relation of structure to conductivity in new solid electrolyte materials; and optical properties of solid electrolytes. Both theoretical and experimental studies are welcome.

Suggestions and inquiries should be sent to the Symposium Co-Chairmen: B. B. Owens, Dept. of Chemical Engineering and Materials Science, 151 Amundson Hall, University of Minnesota, Minneapolis, MN 55455; or B. Dunn, Dept. of Materials Science and Engineering, 6531 Boelter Hall, University of California, Los Angeles, CA 90024.

Extended Abstract must be submitted with the 75-Word Abstract by May 1, 1986

75-Word Abstract Form

Extended Abstract must be submitted with the 75-Word Abstract by May 1, 1986

San Diego, California—October 19-24, 1986

Submit to: The Electrochemical Society, Inc.
10 South Main Street, Pennington, NJ 08534-2896
With a copy to the Organizing Chairman

Abstract No. .....
(to be assigned by the Society)

Schedule for .....
(Title of Symposium)

Sponsored by .....
(Division/Group)

Title of paper .....

.....

Authors (Underline name of author presenting paper.) .....

.....

Business affiliation and address .....

.....

.....
(State or Country) (ZIP Code) (Telephone No.)

(Type abstract in this area—double-spaced.)

Do you require any audiovisual equipment?

- ☐ **35 mm (2 x 2 in.) slide projector**
- ☐ **Vu-Graph**
- ☐ **Specify other (subject to availability and cost)**

Has the information in this abstract been presented verbally, submitted for publication, or published?
☐ **Yes** ☐ **No**
If the answer is yes, please provide the reference (except in the case of invited review presentations). _____

Is a full length paper on this work to be submitted for Society Journal publication? ☐ **Yes** ☐ **No**

Papers presented before a Society technical meeting become the property of the Society and may not be published elsewhere without written permission of the Society. Papers presented at Society technical meetings must be authored by a member or sponsored by an active member.

.....
Insert name of Society member author or sponsor

This form should accompany your Extended Abstract.

THE ELECTROCHEMICAL SOCIETY PATRON MEMBERS

AT&T Bell Laboratories
Murray Hill, NJ

Dow Chemical Co.
Inorganic Chemicals Dept.
Midland, MI

ELTECH Systems Corp.
Chardon, OH

Exxon Research and Engineering Co.
Corporate Research
Advanced Energy Systems Laboratory,
Materials and Catalysis Sciences Laboratory
Linden, NJ
Technology Department
Chemical Engineering Technology Div.
Materials Technology Div.
Florham Park, NJ

Fujitsu Limited
Tokyo, Japan

General Electric Co.
Chemical Laboratory, Knolls Atomic Power Laboratory,
Schenectady, NY
Chemical Products, Engineering
& Technical Support, Cleveland, OH
Materials & Process Laboratory, Large Steam
Turbine-Generator Dept., Schenectady, NY
Research and Development Center,
Inorganic Materials Laboratory
Schenectady, NY

General Electric Co. (continued)
Signal Processing & Communication Laboratory,
Schenectady, NY
Semiconductor Products Dept.,
Syracuse, NY

International Business Machines Corp.
New York, NY

Olin Corp.
Chemicals Div.
Charleston Technology Center
Charleston, TN

Philips Research Laboratories
Eindhoven, The Netherlands

Tadiran, Israel Electronics Industries, Ltd.
Tel Aviv, Israel

Union Carbide Corp.
Battery Products Div.
Corporate Research Dept.
Danbury, CT

Westinghouse Electric Corp.
Electronic Tube Div., Elmira, NY
Nuclear Center, Monroeville, PA
Semiconductor Div., Youngwood, PA
Research Laboratories, Pittsburgh, PA

THE ELECTROCHEMICAL SOCIETY SUSTAINING MEMBERS

The Aerospace Corp.
Los Angeles, CA

Airco Industrial Gases
Murray Hill, NJ

Air Products and Chemicals, Inc.
Allentown, PA

Allied Corporation
C&D Power Systems
Plymouth Meeting, PA

Aluminum Co. of America
New Kensington, PA

AMAX Inc.
Greenwich, CT

AMP Inc.
Harrisburg, PA

Analog Devices, Inc.
Norwood, MA

Applied Materials, Inc.
Santa Clara, CA

ASARCO, Inc.
South Plainfield, NJ

AT&T Technologies
Princeton, NJ

AT&T Teletype Corp.
Skokie, IL

Ballard Research, Inc.
North Vancouver, B.C., Canada

Battelle Memorial Institute
Columbus, OH

Bioanalytical Systems Inc.
West Lafayette, IN

Boeing Co.
Seattle, WA

BP Research Centre
Middlesex, England

Brown, Boveri & Co., Ltd.
Research Center
Baden, Switzerland

C-I-L Inc.
Industrial Chemicals Div.
Montreal, Que., Canada

Comdial Semiconductor, Inc.
Sunnyvale, CA

Cominco Ltd.
Trail, B.C., Canada

COMSAT Laboratories
Clarksburg, MD

Corning Glass Works
Corning, NY

Crawford & Russell Inc.
Stamford, CT

CSIRO Division of Mineral Chemistry
Port Melbourne, Victoria, Australia

Diamond Shamrock Chemicals Co.
Painesville, OH

Duracell Inc.
A Division of Duracell International
Tarrytown, NY (2 memberships)

Duro-Test Corp.
North Bergen, NJ

Eagle-Picher Industries, Inc.
Electronics Div.
Joplin, MO

Eastman Kodak Co.
Rochester, NY

ECO Energy Conversion
Newton, MA

EG&G Princeton Applied Research Corp.
Princeton, NJ

Elcap Electronics Ltd.
Tai Po, Hong Kong

Electric Power Research Institute
Palo Alto, CA

Electrochemical Technology Corp.
Seattle, WA

Energy Conversion Devices, Inc.
Troy, MI

Energy Development Associates
A Gulf and Western Co.
Greensboro, NC

Engelhard Corp.
Engelhard Industries Div.
Iselin, NJ

Ever Ready Co. (Holdings) Ltd.
Whetstone, London, England

Exide Corp.
Yardley, PA

Exmet Corp.
Bridgeport, CT

SUSTAINING MEMBERS (CONTINUED)

Fairchild Camera & Instrument Corp.
Research & Development Laboratory
Palo Alto, CA

Focus Semiconductor Systems, Inc.
Sunnyvale, CA

Ford Motor Co.
Dearborn, MI

The Gates Corporation
Denver, CO

General Motors Corp.
Delco-Remy Div., Anderson, IN
Research Laboratories Div.
Warren, MI

Gould Inc.
Gould Research Center
Rolling Meadows, IL

GTE Laboratories
Waltham, MA

GTE Sylvania Inc.
Chemical & Metallurgical Div.
Towanda, PA

Heliotronic GmbH
Burghausen, Germany

Hewlett Packard Co.
Loveland, CO

Hewlett Packard Laboratories
Palo Alto, CA

Hill Cross Co., Inc.
West New York, NJ

Hitachi, Ltd.
Central Research Laboratory
Tokyo, Japan

Hoechst-Uhde Corp.
Englewood Cliffs, NJ

Honeywell, Inc.
Power Sources Center
Horsham, PA

Hughes Research Laboratories
Div. of Hughes Aircraft Co.
Malibu, CA

IMI Marston Limited
Wolverhampton, England

International Lead Zinc Research Organization, Inc.
New York, NY

Johnson Controls, Inc.
Milwaukee, WI

Kaiser Aluminum & Chemical Corp.
Pleasanton, CA

KBI
a division of Cabot Corp.
Boyertown, PA

Kerr-McGee Chemical Corp.
Chemical Corporation, Oklahoma City, OK
Technical Center, Oklahoma City, OK

Leclanche S. A.
Yverdon, Switzerland

Lockheed Missiles & Space Co., Inc.
Research Laboratory
Palo Alto, CA

LSI Logic Corp.
Santa Clara, CA

Marathon Battery Co.
Waco, TX

Max-Planck-Institut f. Festkorperforschung
Stuttgart, Germany

Medtronic Energy Technology
Minneapolis, MN

Mepco/Electra, Inc.
Columbia, SC

Microwave Associates, Inc.
Burlington, MA

Molycorp, Inc.
New York, NY

Monsanto Co.
St. Louis, MO

Motorola Inc.
Phoenix, AZ

M&T Chemicals Inc.
Detroit, MI

NEC Corporation Central Research Laboratories
Kawasaki, Japan

Nippon Telegraph and Telephone Corporation
Tokyo, Japan

Noranda Research Centre
Pointe Claire, Que., Canada

North American Philips Lighting Corp.
Bloomfield, NJ

Northern Telecom
Ottawa, Ont., Canada

Occidental Chemical Corporation
Research & Development
(2 memberships)
Grand Island, NY

Olin Corp.
Metals Research Laboratories
New Haven, CT

OMI International Corp.
Udylite/Sel-Rex
Warren, MI

Perkin-Elmer Corp.
Norwalk, CT

Philips Laboratories, Inc.
Briarcliff Manor, NY

Prototech Co.
Newton Highlands, MA

Public Service Electric and Gas Co.
PSE&G Research Corp.
Newark, NJ

Rayovac Corp.
Madison, WI

RCA Corp.
Color Picture Tube Div.
Lancaster, PA

Reynolds Metals Co.
Reduction Research Div.
Sheffield, AL

Rockwell International
El Segundo, CA

SAB NIFE AB
Oskarshamn, Sweden

SAFT America, Inc.
Power Sources Division,
Valdosta, GA
Advanced Battery Systems Division,
Cockeysville, MD

Sandia National Laboratories
Albuquerque, NM

Sanyo Electric Co., Ltd.
Osaka, Japan

Schlumberger-Doll Research
Ridgefield, CT

J. C. Schumacher Co.
Oceanside, CA

Shipley Company, Inc.
Newton, MA

Siemens Aktiengesellschaft
Munich, Germany

Siltec Corp.
Menlo Park, CA

Sonnenschein GmbH
Budingen, Germany

Sprague Electric Co.
North Adams, MA

Standard Telecommunication Laboratories Ltd.
Essex, England

St. Joe Minerals Corp.
Monaca, PA

Tektronix, Inc.
Beaverton, OR

Texas Instruments Inc.
Attleboro, MA
Dallas, TX

Toshiba Corp.
Toshiba Research and Development Center
Kawasaki, Japan

Toyota Central Research and Development Labs, Inc.
Nagoya, Japan

Tracor Applied Science, Inc.
Alexandria, VA

Varian Associates
Palo Alto, CA

VARTA Batterie AG
Kelkheim, Germany

Wacker Chemitronic
Burghausen, Germany

Wilson Greatbatch Ltd.
Clarence, NY

Xerox Corp.
Webster Research Center
Rochester, NY

Yardney Corp.
Pawcatuck, CT

Yuasa Battery Co., Ltd.
Osaka, Japan

11 881,2529